



Sudip Bhattacharyya
Alessandro Papitto
Dipankar Bhattacharya *Editors*

Millisecond Pulsars

Astrophysics and Space Science Library

Volume 465

Series Editor

Steven N. Shore, Dipartimento di Fisica “Enrico Fermi”, Università di Pisa,
Pisa, Italy

The Astrophysics and Space Science Library is a series of high-level monographs and edited volumes covering a broad range of subjects in Astrophysics, Astronomy, Cosmology, and Space Science. The authors are distinguished specialists with international reputations in their fields of expertise. Each title is carefully supervised and aims to provide an in-depth understanding by offering detailed background and the results of state-of-the-art research. The subjects are placed in the broader context of related disciplines such as Engineering, Computer Science, Environmental Science, and Nuclear and Particle Physics. The ASSL series offers a reliable resource for scientific professional researchers and advanced graduate students.

Series Editor:

STEVEN N. SHORE, Dipartimento di Fisica “Enrico Fermi”, Università di Pisa, Pisa, Italy

Advisory Board:

F. BERTOLA, University of Padua, Italy

C. J. CESARSKY, Commission for Atomic Energy, Saclay, France

P. EHRENFREUND, Leiden University, The Netherlands

O. ENGVOLD, University of Oslo, Norway

E. P. J. VAN DEN HEUVEL, University of Amsterdam, The Netherlands

V. M. KASPI, McGill University, Montreal, Canada

J. M. E. KUIJPERS, University of Nijmegen, The Netherlands

H. VAN DER LAAN, University of Utrecht, The Netherlands

P. G. MURDIN, Institute of Astronomy, Cambridge, UK

B. V. SOMOV, Astronomical Institute, Moscow State University, Russia

R. A. SUNYAEV, Max Planck Institute for Astrophysics, Garching, Germany

More information about this series at <https://link.springer.com/bookseries/5664>

Sudip Bhattacharyya • Alessandro Papitto •
Dipankar Bhattacharya
Editors

Millisecond Pulsars



Springer

Editors

Sudip Bhattacharyya
Department of Astronomy and Astrophysics
Tata Institute of Fundamental Research
Mumbai
Maharashtra, India

Alessandro Papitto
INAF Osservatorio Astronomico di Roma
Monte Porzio Catone
Roma, Italy

Dipankar Bhattacharya
Inter-University Centre for Astronomy and
Astrophysics
Pune, India

ISSN 0067-0057

ISSN 2214-7985 (electronic)

Astrophysics and Space Science Library

ISBN 978-3-030-85197-2

ISBN 978-3-030-85198-9 (eBook)

<https://doi.org/10.1007/978-3-030-85198-9>

© Springer Nature Switzerland AG 2022

This work is subject to copyright. All rights are reserved by the Publisher, whether the whole or part of the material is concerned, specifically the rights of translation, reprinting, reuse of illustrations, recitation, broadcasting, reproduction on microfilms or in any other physical way, and transmission or information storage and retrieval, electronic adaptation, computer software, or by similar or dissimilar methodology now known or hereafter developed.

The use of general descriptive names, registered names, trademarks, service marks, etc. in this publication does not imply, even in the absence of a specific statement, that such names are exempt from the relevant protective laws and regulations and therefore free for general use.

The publisher, the authors, and the editors are safe to assume that the advice and information in this book are believed to be true and accurate at the date of publication. Neither the publisher nor the authors or the editors give a warranty, expressed or implied, with respect to the material contained herein or for any errors or omissions that may have been made. The publisher remains neutral with regard to jurisdictional claims in published maps and institutional affiliations.

Cover illustration: Artistic impression of a millisecond pulsar in a binary system including the magnetic field structure and the surrounding accretion disk. Reproduced from <https://svs.gsfc.nasa.gov/10144>.
Credits: Dana Berry (Skyworks Digital; Lead Animator), Michael McClare (HTSI; writer); NASA.

This Springer imprint is published by the registered company Springer Nature Switzerland AG.
The registered company address is: Gewerbestrasse 11, 6330 Cham, Switzerland

Preface

Observing pulsars provides a unique view of the physics of matter at densities exceeding those of atomic nuclei and magnetic fields not reproducible on Earth. The unparalleled stability and frequency of the pulsations make them very accurate clocks. The discovery of a radio pulsar in the late sixties itself proved the very existence of neutron stars. The quickest spinning pulsars allow attaining the highest accuracy. It is no surprise that pulsars spinning with a period of a few milliseconds had a substantial impact on many fields in astronomy and physics. Modelling the pulse arrival times of the 59 ms Hulse & Taylor binary pulsar unveiled how the orbit was shrinking at the exact rate due to gravitational waves, more than 30 years before the actual detection by the *LIGO/VIRGO* interferometers. Later, a double pulsar system provided the most stringent tests of the predictions of General Relativity to date. The outstanding stability of the spin of millisecond pulsars allowed the masses of two dozen neutron stars to be precisely measured and even discovered the first planets ever detected outside the Solar System. Regularly monitoring arrays of radio millisecond pulsars may unveil the stochastic background of gravitational waves due to the interaction of supermassive black holes at the centre of galaxies. Millisecond X-ray pulsars can even be used as a navigation tool for interplanetary probes, as the recently launched NICER/Sextant mission aims at demonstrating.

What is the behaviour of the strong nuclear interaction? What are the constituents at ultrahigh densities in neutron star cores? How do old neutron stars in binaries evolve? How does their magnetosphere interact with the surrounding plasma to accelerate particles and emit radiation observed at all wavelengths? These are just a few of the questions that millisecond pulsars are helping us answer and will settle shortly with the next generation of instruments. Although almost 40 years have passed since the discovery of the first radio millisecond pulsar, their number keeps growing. The progress in high timing resolution detectors and the opening of new observing windows are the key drivers. The late 1990s greeted the discovery of a millisecond pulsar shining at X-ray energies. The GeV gamma-ray band followed in the late 2010s, more recently joined by the visible and the ultraviolet wavebands.

Millisecond pulsars are a very diverse class of sources, as their emission owes to different mechanisms at the various stages of their complex evolutionary history. The *recycling* scenario established an evolutionary link between neutron stars in X-ray binaries being spun-up by mass accretion and radio millisecond pulsars whose emission is due to particles accelerated in their rotating magnetosphere. Incidentally, the discovery of millisecond pulsars in 1982 bridged the community of radio (and later gamma-ray) astronomers who looked for faint coherent signals from pulsars in binaries with X-ray astronomers who dealt with the much brighter accretion-powered binaries. The need for a genuine multi-wavelength approach in the study of these systems has only become more evident with the discovery of millisecond pulsars switching back and forth accretion and rotation-powered regimes over a few days, or perhaps even less.

Currently, we know more than 500 rotation-powered radio millisecond pulsars and two dozen accretion-powered X-ray progenitors. Although the bias in detecting very quickly spinning radio pulsars has considerably diminished, the shortest spin period ever observed (1.4 ms) lies well above the Keplerian break-up limit predicted by most of the equations of state proposed for neutron star matter. Some mechanisms must limit the acceleration imparted by mass accretion. The steady emission of gravitational waves seems a crucial ingredient. Theoretical works are ever more timely, as the sensitivity of gravitational wave detectors starts to graze the expected flux of millisecond pulsars.

The speed and compactness of millisecond pulsars make them truly relativistic objects. They spin so quickly that particles at their equator travel at more than ten per cent the speed of light. Also, the long accretion phase which spun them up made them more massive than younger neutron stars. Special and general relativistic effects significantly modify the trajectory and energy of photons emitted from spots on their surface, such as those observed at X-ray energies from spin-powered millisecond pulsars or during outbursts and thermonuclear bursts in accreting millisecond pulsars. The corresponding oscillation pattern encodes information on the mass and the size of the neutron star. Modelling the X-ray pulse profiles of millisecond pulsars stands out as one of the most accurate and effective ways to constrain the equation of state models of neutron stars from observations. Recently, modelling of data collected by the *NICER* mission provided the first long-awaited simultaneous measurements of the mass and radius of a spin-powered millisecond pulsar, unveiling an unexpectedly complex magnetic field configuration. Soon the X-ray polarimetry window is going to reopen, thanks to the forthcoming launch of the Imaging X-ray Polarimetry Explorer (*IXPE*) and X-ray Polarimeter Satellite (*XPoSat*), and the planned enhanced X-ray Timing and Polarimetry (*eXTP*) mission. These missions may help hold the long-standing promise of the high energy astrophysics of supplying theoretical nuclear physics the pressure-density relation required to understand how the strong interaction behaves at sub-nuclear distances.

Our knowledge and understanding of the properties of millisecond pulsars have rapidly progressed during the last decades. A book that could sum up the recent progress in observations and theory seemed timely. The idea of actually writing it originated from a session on millisecond pulsars that we convened as part of the

42nd Scientific Assembly of the Committee on Space Research (COSPAR) that took place in Pasadena, USA, in July 2018.

This book covers in nine chapters the many multi-faceted aspects of millisecond pulsars. Radio millisecond pulsars are the vast majority. The rotation of the magnetic field of these pulsars powers such emission and causes the neutron star to spin down steadily. In Chap. 1, the authors (B. Bhattacharyya & J. Roy) provide an introduction to rotation-powered pulsars and a general description of the properties of the ~ 500 radio millisecond pulsars discovered so far.

The last decade also saw the somehow unexpected discovery that rotation-powered millisecond pulsars are also bright gamma-ray sources, summing up to roughly half of the whole population of gamma-ray pulsars. Nowadays, targeting unidentified Fermi sources has become an efficient way to discover both the magnetospheric pulsed emission of millisecond pulsars and the continuous emission from intra-binary shocks that characterize pulsars in compact binaries. D. F. Torres and J. Li summarize the current results on the gamma-ray emission from millisecond pulsars in Chap. 2.

The high energy emission of millisecond pulsars somehow resembles slower gamma-ray pulsars and suggests a similar emission mechanism taking place in the outer magnetosphere of the pulsar. However, the exact location and physics of these objects are still not fully known. A. K. Harding discusses in Chap. 3 the current understanding of the emission physics of millisecond pulsars, as well as the outstanding problems.

Soon after the discovery of a radio pulsar in a binary in 1975, Bisnovatyi-Kogan and Komberg argued that accretion of the mass lost by the companion star could have spun up the neutron star. When radio astronomers eventually saw a 1.6 ms millisecond pulsar in 1982, scientists swiftly argued that a previous X-ray bright evolutionary phase had to have occurred. The weakly magnetized neutron star had to be spun up by the accretion of the mass transferred by a sub-solar companion star through a disk. In 1998, the detection of millisecond X-ray pulsations from an X-ray transient observed by the *Rossi X-ray Timing Explorer* eventually crowned with success the significant efforts to find the accreting progenitors of millisecond pulsars. Accreting millisecond X-ray pulsars are the evolutionary link between neutron star low mass X-ray binaries and spin-powered millisecond pulsars, or, at least, a sub-sample of them (the so-called black widows and redbacks). In Chap. 4, T. Di Salvo and A. Sanna review the observed spectral and timing properties, putting particular attention to peculiar systems and the latest discoveries. They address the long-term spin and orbital evolution of some specific sources, as well as some of the unsolved problems.

A few accreting neutron stars in low mass X-ray binaries show coherent brightness oscillations during some of the thermonuclear X-ray bursts originating from their surface. This phenomenon has a high potential to understand the extreme physics of the stellar surface, including modes of oscillations and thermonuclear flame spreading as the accreted matter burns, and to measure neutron star parameters. In Chap. 5, S. Bhattacharyya presents the current observational and theoretical

understanding of burst oscillations, as well as the main problems of the field yet to be solved.

A few *transitional* millisecond pulsars that switch back and forth radio and X-ray pulsar regimes in response to variations of the mass accretion rate are one of the most recent add-ons to the zoo of millisecond pulsars. These pulsars eventually demonstrated how close the evolutionary link between accretion and rotation-powered millisecond pulsar is. Transitional millisecond pulsars showcase over a few days (or perhaps less) all the possible outcomes of the interaction between the pulsar wind of particles and radiation and matter in an accretion disc. A. Papitto and D. de Martino review in Chap. 6 the main observational results obtained in the last decade, highlighting the numerous enigmas yet to be solved and the vast discovery potential yet to be explored.

The observed orbital and stellar properties of each binary system hosting a millisecond pulsar represent a present-day snapshot of how the binary reached that configuration and provide clues and constraints to the secular evolution. In Chap. 7, F. D'Antona and M. Tailo review how much the current understanding of the binary evolution can account for these fossil records and their group properties. They focus on the fundamental role of the close-by neutron star in altering the structure of the donor star, compared to an ordinary stellar companion.

Whereas the old millisecond pulsars we observe are relatively weakly magnetized neutron stars, about ten per cent of neutron stars are assumed to be born as magnetars. Millisecond rotation at birth is key to the generation of their tremendous magnetic fields. Formation mechanisms comprise the collapse of a quickly spinning stellar core or a white dwarf and the merging of two (light) neutron stars. A powerful rotation-driven emission of electromagnetic and/or gravitational waves should follow soon after a millisecond magnetar is born. This emission can contribute significantly to the radiative output of long and short Gamma-Ray Bursts, Hyper Luminous Supernovae and Fast Radio Bursts. S. Dall'Osso and L. Stella discuss in Chap. 8 the conditions to form a millisecond magnetar and how it can be observed, with an emphasis on the possibility of detecting the associated GW signal.

Neutron stars are unparalleled natural laboratories to investigate the fundamental constituents of matter and their interactions under extreme conditions not replicable in terrestrial laboratories. I. Bombaci discusses in Chap. 9 some of the present models for the equation of state (EoS) of dense matter, their application to neutron star physics, and the possibility of transitions to a quark deconfined phase in the star, with the resulting realization of two coexisting families of compact stars in nature.

This book includes substantial background introductory material and recent theoretical and multi-wavelength observational results. It aims at providing professional astronomers, graduate students and other beginners a timely summary of the enormous progress in the field of millisecond pulsars during the last decades. We warmly thank all the authors of the chapters for their dedication to keeping

the information included in this book as comprehensive and up-to-date as possible, especially considering the additional challenges posed by the pandemic.

Mumbai, India

Sudip Bhattacharyya

Roma, Italy

Alessandro Papitto

Pune, India

Dipankar Bhattacharya

October 2021

Contents

1 Radio Millisecond Pulsars	1
Bhaswati Bhattacharyya and Jayanta Roy	
1.1 Introduction to Parameters of Radio MSPs	1
1.2 Properties of Radio MSPs	4
1.2.1 Spectra and Luminosity	4
1.2.2 Pulse Profile and Polarisation Properties	6
1.3 Searches for Radio MSPs	7
1.3.1 Search Techniques	11
1.3.2 Targeted Searches	13
1.3.3 Wide Field Surveys	18
1.4 Timing of MSPs	19
1.4.1 MSPs as Sensitive Gravitational Wave Detectors	20
1.4.2 MSPs as Gravity Probes	21
1.4.3 Eclipsing MSPs: Probing Intra-Binary Material	24
References	27
2 The High-Energy Emission of Millisecond Pulsars	33
Diego F. Torres and Jian Li	
2.1 Millisecond Pulsars in the <i>Fermi</i> -LAT Era	33
2.2 Do Accreting Millisecond Pulsars Shine in Gamma-Rays?	38
2.3 Gamma-Ray Emission from Transitional Millisecond Pulsars	41
2.4 More on Redbacks, and Black Widows in the Context of Gamma-Ray Binaries	46
References	49
3 The Emission Physics of Millisecond Pulsars	57
Alice K. Harding	
3.1 Introduction	57
3.2 Global Magnetosphere Models	58
3.2.1 Vacuum Retarded Dipole	59
3.2.2 Force-Free and Dissipative Models	59
3.2.3 Kinetic Models	60

3.3	Multiwavelength Emission Models	61
3.3.1	Polar Cap Models	63
3.3.2	Outer Gap Models	63
3.3.3	Slot Gap and Annular Gap Models	64
3.3.4	Current Sheet Models	65
3.3.5	Light Curve Modeling	66
3.4	Pairs and Death Lines	72
3.5	Thermal X-ray Emission and Field Structure	74
3.6	Millisecond Pulsars in Binary Systems	76
3.7	Outstanding Problems	78
	References	80
4	Accretion Powered X-ray Millisecond Pulsars	87
	Tiziana Di Salvo and Andrea Sanna	
4.1	How to Spin Up a Neutron Star: The Recycling Scenario	87
4.1.1	Evolution of Rotation-Powered Neutron Stars in the $P - \dot{P}$ Diagram	88
4.1.2	Low-Mass X-ray Binaries and Accretion onto a Neutron Star	90
4.2	The Discovery of Accreting X-ray Millisecond Pulsars: The Missing Link in the Recycling Scenario	93
4.3	Timing and Spectral Properties of AMXPs	96
4.3.1	Spectral Properties	96
4.3.2	Short-Term Variations of the Spin During Outbursts	100
4.3.3	Long-Term Variations of the Spin	103
4.3.4	Long-Term Timing of the Orbital Period	107
4.3.5	Non-conservative Mass Transfer?	111
4.4	Summary and Open Questions	113
	References	117
5	Nuclear-Powered X-ray Millisecond Pulsars	125
	Sudip Bhattacharyya	
5.1	Introduction	125
5.1.1	Thermonuclear X-ray Bursts	126
5.1.2	Burst Oscillations: Discovery and Growth of the Field	129
5.2	Observational Aspects	133
5.2.1	Frequency and Coherence	133
5.2.2	Amplitude	135
5.2.3	Harmonic Content	136
5.2.4	Energy Dependence	137
5.2.5	Connection with Accretion-Powered Pulsations	138
5.2.6	Superburst Oscillations	140
5.3	Burst Rise Oscillations and Thermonuclear Flame-Spreading	141
5.3.1	Theory of Flame-Spreading	142
5.3.2	Evidence of Flame-Spreading	142

5.4	What Causes Burst Decay Oscillations	145
5.4.1	Surface Modes	146
5.4.2	Cooling Wake	146
5.5	Conclusion	147
	References	148
6	Transitional Millisecond Pulsars	157
	Alessandro Papitto and Domitilla de Martino	
6.1	Introduction	157
6.2	The Population of Millisecond Pulsar Binaries	158
6.3	Changes of State in Millisecond Pulsars	160
6.4	Transitional Millisecond Pulsars	163
6.4.1	PSR J1023+0038—FIRST J102347.6-003841	163
6.4.2	IGR J18245-2452—PSR J1824-2452I	163
6.4.3	XSS J12270-4859—PSR J1227-4853	164
6.5	The Three States of Transitional Millisecond Pulsars	164
6.5.1	The Rotation-Powered State	164
6.5.2	Accretion Outbursts	169
6.5.3	The Sub-luminous Disc State	172
6.5.4	Candidate Transitional Millisecond Pulsars	178
6.6	Models and Open Questions	181
6.6.1	The Rotation-Powered State	181
6.6.2	The Accretion-Disc State	183
6.7	Conclusions	189
	References	189
7	Origin and Binary Evolution of Millisecond Pulsars	201
	Francesca D'Antona and Marco Tailo	
7.1	Introduction	201
7.2	The Origin of Millisecond Pulsars	202
7.2.1	The Formation of Single Neutron Stars	202
7.2.2	Formation of Neutron Stars in Binaries	203
7.2.3	The MSP Formation	204
7.2.4	Binary and Single MSPs and the Globular Clusters Environment	205
7.3	Concepts of Binary Evolution	207
7.3.1	The Roche Lobe and the Radius Evolution of Single Stars	207
7.3.2	The Radius Change due to Mass Loss	208
7.3.3	The Losses of Angular Momentum: Primary Mechanisms	211
7.3.4	The Approach of a Donor to the Roche Lobe Contact	213
7.4	Cataclysmic Binaries as a Comparison Key Study	215
7.4.1	Extension of the CB Evolution Scheme to X-ray Binaries ...	217
7.4.2	Comparisons and the Birthrate Problem	218

7.5	The P_{orb} Versus M_d Plane as a Tracer of the NS to MSP Evolution	219
7.5.1	Double NS Remnants	220
7.5.2	Intermediate Mass Cases A, B or C	222
7.5.3	The Evolution to MSPs with Companion Low Mass White Dwarfs	222
7.6	Short Period, Low-mass Companion Systems: The Mixed Bag	224
7.6.1	The Radius Reaction when a Source of Irradiation Is Present	225
7.6.2	The Consequence of X-ray Irradiation: Mass Transfer Cycles	227
7.6.3	The MSP Illumination	230
7.6.4	The ‘Evaporation’ Model: A Role for the Black Widows Stage?	231
7.6.5	The Evolution Close to P_{bif}	234
7.7	Summary and (a few of the) Questions Left Open	236
7.7.1	Why the Evolution Close to P_{bif} Has Such a Dominant Role?	236
7.7.2	Conclusions	237
	References	238
8	Millisecond Magnetars	245
	Simone Dall’Osso and Luigi Stella	
8.1	Introduction	245
8.2	Millisecond Magnetars as Gamma-Ray Burst Central Engines	250
8.3	Millisecond Magnetars and Supernovae	257
8.4	Gravitational Waves from Millisecond Spinning Magnetars	259
8.5	Fast Radio Bursts and Millisecond Magnetars	264
8.6	Conclusions	269
	References	269
9	The Equation of State of Neutron Star Matter	281
	Ignazio Bombaci	
9.1	Introduction	281
9.2	Neutron Star Physics in a Nutshell: Basic Concepts	282
9.2.1	The Role of Weak Interaction and Pauli Principle	284
9.3	Nuclear Matter and Nucleon Stars	288
9.3.1	Isospin-Asymmetric Nuclear Matter	289
9.3.2	β -stable Nuclear Matter: Role of the Nuclear Interactions	293
9.3.3	Nucleon Stars Properties	296
9.4	Hyperons in Neutron Stars: The Hyperon Puzzle	298
9.4.1	β -stable Hyperonic Matter	299
9.4.2	Hyperon Stars	301
9.4.3	Hyperonic Three-Body Interactions as Possible Solutions of the Hyperon Puzzle	303

Contents	xv
9.5 Quark Matter in Neutron Stars	305
9.5.1 β -stable Strange Quark Matter	307
9.5.2 Strange Stars	309
9.6 Two Coexisting Families of Compact Stars.....	310
References	314
Index	319

Contributors

Bhaswati Bhattacharyya National Centre for Radio Astrophysics, Tata Institute of Fundamental Research, Pune, India

Sudip Bhattacharyya Department of Astronomy and Astrophysics, Tata Institute of Fundamental Research, Mumbai, India

Ignazio Bombaci Dipartimento di Fisica “Enrico Fermi”, Università di Pisa & INFN Sezione di Pisa, Largo Bruno Pontecorvo, Pisa

Simone Dall’Osso Gran Sasso Science Institute, L’Aquila, Italy

Franca D’Antona INAF Osservatorio Astronomico di Roma, Roma, Monte Porzio Catone, Italy

Domitilla de Martino INAF – Osservatorio Astronomico di Capodimonte, Napoli, Italy

Tiziana Di Salvo Università degli Studi di Palermo, Dipartimento di Fisica e Chimica - Emilio Segrè, Palermo, Italy

Alice Harding Astrophysics Science Division, NASA/Goddard Space Flight Center Greenbelt, Greenbelt, MD, USA

Jian Li Deutsches Elektronen-Synchrotron DESY, Zeuthen, Germany

Alessandro Papitto INAF Osservatorio Astronomico di Roma, Roma, Italy

Jayanta Roy National Centre for Radio Astrophysics, Tata Institute of Fundamental Research, Pune, India

Andrea Sanna Università degli Studi di Cagliari, Dipartimento di Fisica, Monserato, Italy

Luigi Stella INAF Osservatorio Astronomico di Roma, Roma, Monte Porzio Catone, Italy

Marco Tailo Dipartimento di Fisica e Astronomia ‘Galileo Galilei’, Univ. di Padova, Padova, Italy

Diego Torres Institute of Space Sciences (ICE, CSIC), Barcelona, Spain
Institut d’Estudis Espacials de Catalunya (IEEC), Barcelona, Spain
Institució Catalana de Recerca i Estudis Avançats (ICREA), Barcelona, Spain

Chapter 1

Radio Millisecond Pulsars



Bhaswati Bhattacharyya and Jayanta Roy

Abstract The extreme timing stability of radio millisecond pulsars (MSPs) combined with their exotic environment and evolutionary history makes them excellent laboratories to probe matter in extreme condition. Population studies indicate that we have discovered less than five per cent of the MSPs of our Galaxy, implying that a huge majority of radio MSPs are waiting to be discovered with improved search techniques and more sensitive surveys. In this chapter, we provide an overview of the present status of ongoing and upcoming surveys for MSPs. Observed spectra, profile and polarisation properties of known radio MSPs are also summarised. Finally, we describe how the timing studies of radio MSPs enable a huge science return including attempts to detect gravitational waves using an array of MSPs, gravity tests using individual interesting MSP systems, as well as probing the intra-binary material using eclipses observed in MSPs in compact binary systems.

1.1 Introduction to Parameters of Radio MSPs

Millisecond pulsars (MSPs) are rapidly rotating neutron stars (rotational period of few tens of milliseconds) with very small spin-down rates. Whereas the spin period of the radio pulsars span around four orders of magnitude (1.4 ms to 23 s), MSPs are defined here by a periodicity < 30 ms. With extremely stable periods and very low period derivative values, MSPs are the most precise celestial clocks and occupy the bottom-left corner in the $P - \dot{P}$ diagram (see Fig. 1.1, where blue squares mark MSPs; see also Fig. 4.1). Since rotation-powered pulsars spin down at a rate which depends on the magnetic field strength and the spin period of the pulsar, it is inferred that the magnetic field of an MSP is a few orders of magnitude weaker than an *ordinary*, slower pulsar. MSPs are assumed to have acquired their high rotational rate by accretion of matter, and thereby transfer of angular momentum, from a

B. Bhattacharyya (✉) · J. Roy

National Centre for Radio Astrophysics, Tata Institute of Fundamental Research, Pune, India
e-mail: bhaswati@ncra.tifr.res.in; jroy@ncra.tifr.res.in

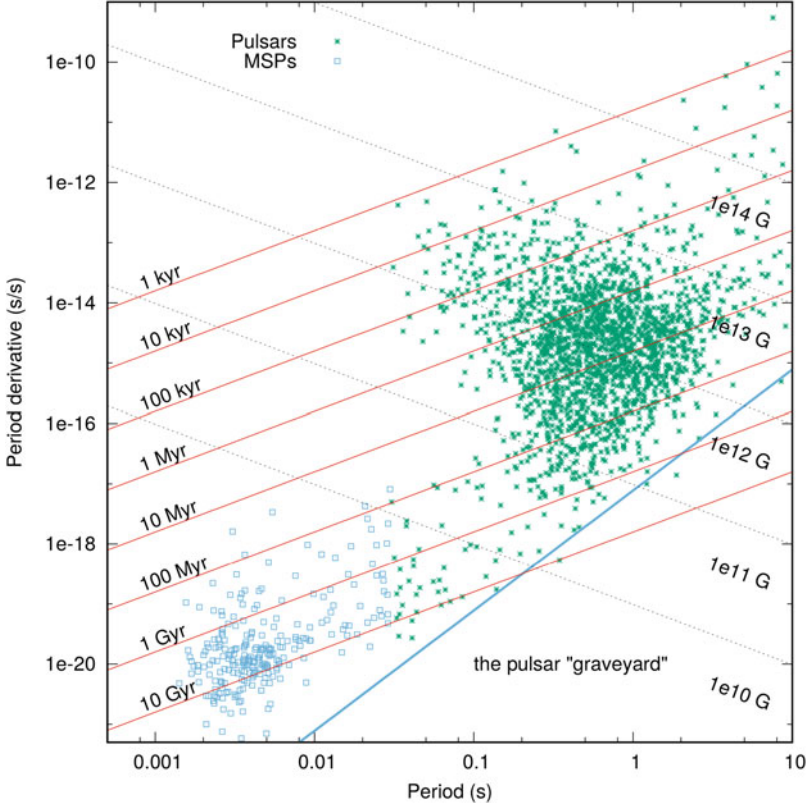


Fig. 1.1 Period versus period derivative of the *ordinary* ($P > 30$ ms) pulsar and the millisecond pulsars. Data taken from the ATNF pulsar catalogue ([67], <http://www.atnf.csiro.au/research/pulsar/psrcat>)

low mass ($< M_{\odot}$) companion star in a binary system [1, 12]. Mass accretion is also possibly responsible for the decay of the magnetic field of the neutron star. Such a recycling scenario (discussed in Sect. 4.1) is now supported by observational evidences of accreting millisecond pulsars (see Chap. 4) and of a few transitional systems switching states between radio MSP and low-mass X-ray binaries (see Chap. 6).

MSPs are still a small population compared to the classical *ordinary* pulsars (spin period > 30 ms). A total of 512 MSPs are reported in the lists maintained by E. Ferrara and D. Lorimer¹ and by P. Freire,² as of November 2020, whereas 2450 slower *ordinary* pulsars are listed in the Australia Telescope National Facility

¹ Available at <http://astro.phys.wvu.edu/GalacticMSPs/>.

² Available at <http://www.naic.edu/~pfreire/GCpsr.html>.

Table 1.1 Parameters of the known radio MSPs

Parameters	Range of values (units)
Spin period (P)	1.4–30 ms
Spin period derivative (\dot{P})	10^{-18} – 10^{-22}
Magnetic field strength (B)	10^7 – 10^9 G
Age	10^7 – 10^{11} years
Dispersion measure (DM)	2.6–540 pc cm $^{-3}$
DM distance (d)	0.11–49 kpc
Flux density (S_{1400})	0.01–150 mJy
Companion mass (M_{cmin})	0.009–1.39 M_\odot
Orbital period (P_b)	0.065–669 days
Eccentricity (e)	0–0.95
Semi-major axis (A_1)	0.0018–100 lt-sec

(ATNF) database [67].³ The parameters of the MSPs listed in the ATNF pulsar catalog are summarised in Table 1.1. The recycling scenario of MSPs suggests that most of them should be part of a binary system, and this actually occurs in >80% of the known systems.

MSPs in binary systems have an orbital period ranging from 75 min to 669 days, and a mass of the companion star between 0.009 and 1.39 M_\odot (see also Fig. 6.1). More than 60% of the binaries hosting an MSP have an orbital period $P_b > 1$ day. These large-period binary MSPs essentially fall into three groups, depending on the mass of the companion star. The majority (~85%) have a low-mass (<0.4 M_\odot) Helium white dwarf companion, but higher-mass (seemingly Carbon–Oxygen) white dwarfs, as well as neutron star companions are also found. The mass of the companion increases as a function of orbital period, following theoretical expectations [76]. Most of the MSPs are in nearly circular orbit with only ~8% of known binaries having known eccentricity value >0.1. Tauris and Savonije [96] and Hui et al. [43] analysed the observed orbital properties of a binary MSPs with a white dwarf companion and reported a positive correlation between the orbital period and the eccentricity. However, different trends were obtained for MSPs with a Helium white dwarf companion, and MSPs with a Carbon–Oxygen white dwarf. They also reported two gaps in the distribution of orbital period (between 35–50 days and between 2.5–4.5 days). On the other hand, MSPs in binaries with a short ($P_b < 1$ day) orbital period also include eclipsing pulsars (see Sect. 1.4.3) either with a non degenerate main-sequence companion with a mass in the range 0.1–0.8 M_\odot (dubbed *redbacks*) or with a <0.06 M_\odot brown dwarf (termed *black widows*). The reader is referred to the Chap. 7 for a detailed discussion of the origin and evolutionary channels of MSPs.

D. Lorimer [61] estimated the presence of around 40,000 MSPs in the Galaxy, indicating that a large number of MSPs are waiting to be discovered. Presently, only ~15% of the ~3000 known pulsars are MSPs, either in the Galactic disk or in

³ Available at <https://www.atnf.csiro.au/research/pulsar/psrcat/>.

globular clusters. Thus, it is possible that the known parameter range of the MSPs does not represent the true distribution.

This chapter presents a overview of radio millisecond pulsars. Sect. 1.2 details spectra and polarisation properties of the MSPs. Searches for radio MSPs are detailed in Sect. 1.3. Some aspects of the timing studies of radio MSPs are presented in Sect. 1.4.

1.2 Properties of Radio MSPs

1.2.1 Spectra and Luminosity

Kramer et al. [49] compared the spectral dependence of the flux density S_ν on the frequency ν observed from *ordinary* ($P > 30$ ms) pulsars and MSPs in the 0.7–3.1 GHz band. They concluded that the average spectra of MSPs are steeper than *ordinary* pulsars. They derived a mean spectral index of the power-law relationship $S_\nu \propto \nu^\alpha$ of $\alpha = (-1.8 \pm 0.1)$ for a set of 32 MSPs located in the Galactic disk and a mean index of $\alpha = (-1.60 \pm 0.04)$ for *ordinary* pulsars in the same frequency range. The median values for both samples were -1.8 and -1.7 , respectively. However, they also pointed out that the steeper spectral index for MSPs could be due to the selection bias of having fainter (and farther) *ordinary* pulsars in the sample, with a relatively flatter spectral index. Indeed, restricting the data set to sources that are closer than 1.5 kpc, they found that mean spectral index of MSPs and *ordinary* pulsars are similar ($\alpha = -1.6 \pm 0.2$ for MSPs and $\alpha = -1.7 \pm 0.1$ for *ordinary* pulsars), with a median value of -1.65 and -1.66 , respectively. Note that a more recent study by Bates et al. [11] based on larger sample of *ordinary* pulsars reported that the distribution of the spectral index has a mean of -1.4 and a standard deviation of 1.0. Although the number of MSPs has increased drastically in last two decades since the study by Kramer et al. [49], the flux at more than one observing frequency was reported only for a small fraction of the newly discovered MSPs. In a more recent study, Dai et al. [27] investigated 24 MSPs observed with the Parkes 64-m telescope in three bands, centred at 730, 1400 and 3100 MHz. Figure 1.2 plots the flux density spectra of these MSPs. They reported that the spectra of a few pulsars significantly deviated from a single power-law across the observing bands. Although a spectral steepening at high frequencies was observed for a few MSPs, for some other a spectral flattening was instead observed. Dai et al. [27] also studied the pulse phase-resolved spectral index of MSPs and found that different profile components have different spectral indices which overlap with one another. We conclude that considering the observed diversity of the spectral properties of MSPs, and in the absence of systematic flux measurements for a large sample of MSPs, it is not possible to draw a firm conclusion from the comparison of the steepness of the spectra of MSPs and *ordinary* pulsars.

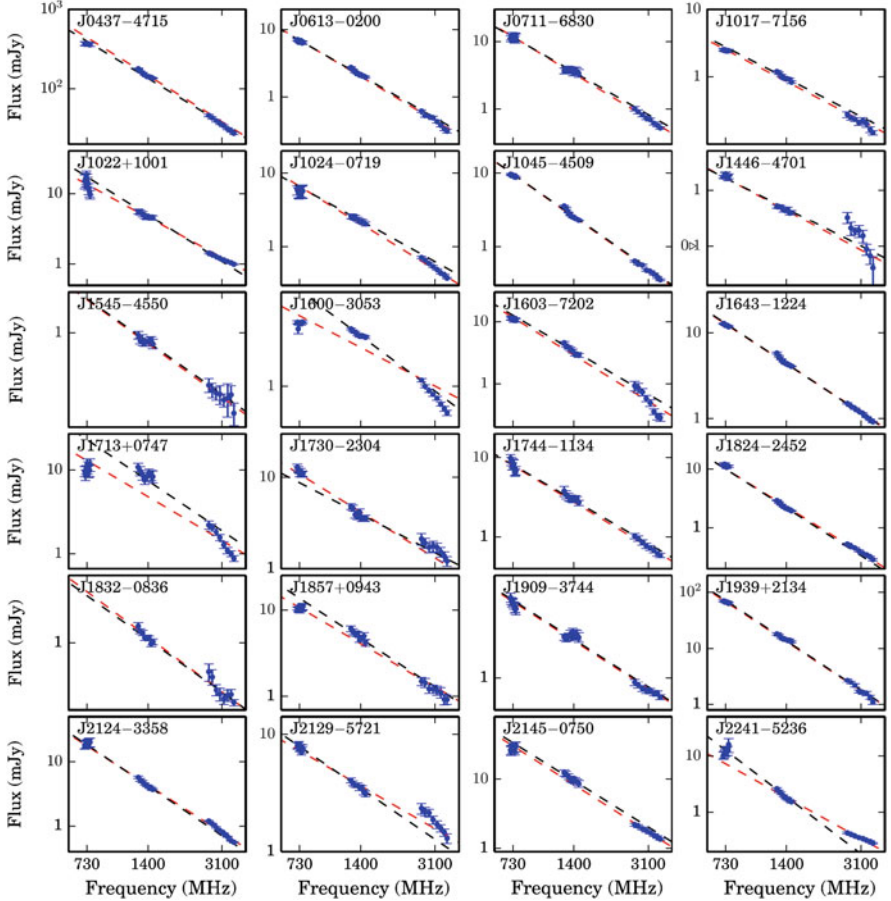


Fig. 1.2 Flux density spectra for 24 MSPs. The red and black lines are for spectral index spectra fitted with power law α_1 and α_2 , respectively. Credit: Dai et al., MNRAS, 449, 3223 (2015) [27]

Ordinary pulsars exhibit low-frequency turn overs in the spectra, while this is still debated for MSPs. Kuzmin et al. [54] analysed the spectra of 30 MSPs down to 100 MHz, and most of them did not exhibit any low frequency turn over. On the other hand, Kunyoshi et al. [53] found that one forth of the MSPs for which the spectrum was observed down to 100 MHz (i.e., 10 out of 39 MSPs) showed evidence of a turn over.

MSPs tend to be less luminous and less efficient radio emitters compared to ordinary pulsars. To obtain this result, Kramer et al. [49] used a luminosity estimator $S \times d^2$ equal to the product of the average flux density observed at 1.4 GHz times the square of the distance, and found that the luminosity of MSPs are an order of magnitude fainter than ordinary pulsars. They also restricted the comparison of the luminosity distribution to sources within a distance of 1.5 kpc, and concluded

that the luminosity difference becomes less prominent. In addition, they noted that some high luminosity MSPs (which should be easy to detect) are missing and that isolated MSPs are generally fainter than the ones in binaries, which could be attributed to different evolutionary history.

1.2.2 Pulse Profile and Polarisation Properties

Xilouris et al. [100] reported that the pulse profiles of MSPs are slightly more complex than *ordinary* pulsars. They considered the number of Gaussian components required to represent the pulse profile as a measure of their complexity. They found that MSP profiles could be fitted with four Gaussian components on average, whereas three components were enough for *ordinary* pulsar.

Ordinary pulsars follow a systematic behaviour, where the observed pulse profile becomes narrower at higher frequencies, which is known as the ‘radius to frequency mapping’ [63, 81]. Xilouris et al. [100] reported a much less marked dependence on frequency for MSP profiles, instead. They identified three categories of MSPs: (i) almost no dependence, (ii) a very slow ‘radius to frequency mapping’, and (iii) contrary to ‘radius to frequency mapping’. They suggested that the observed profile complexity, including the low-level emission and the unusual features identified in some of the MSPs, could result from emission from outer gaps [87]. The sample of MSPs studied by Dai et al. [27] also confirmed that most MSPs have very wide profiles with multiple components. The majority of the MSPs in their sample showed a duty cycle higher than 50%, with the profile components which did not show an appreciable dependence on the observing frequency.

Whereas the investigation by Dai et al. [27] covered the frequency range 730–3100 MHz in three bands, a more recent study by Kondratiev et al. [47] presented a census of MSPs using the LOw-Frequency ARray (*LOFAR*) in the frequency range 110–188 MHz. They found that the separation between the different components of the profiles seen at low-frequency by *LOFAR* was compatible with that seen at higher frequencies. Also the width of the profiles was similar at different frequencies. Thus low-frequency observations also supported that there was very little pulse profile dependence on frequency. This is different from the classical pulsars and indicates a more compact emission region in the MSP magnetosphere and possibly higher multipolar components. In addition, the observed pulse shapes indicated that the emission beam of MSPs are narrower than the classical pulsars. Ravi et al. [85] suggested that the features of MSPs radio profiles represent caustics in the emission beam. They proposed that the radio emission of MSPs could originate in wide beams higher up in the pulsar magnetosphere (up to or even beyond the null charge surface). The physics of the emission of MSPs is thoroughly discussed in Chap. 3.

Xilouris et al. [100] also studied for the first time the polarization profiles of MSPs and found that the polarization degree is higher than in *ordinary* pulsars. In addition, the swings of the polarization position angle of MSPs are flatter. The

polarization position angle curves of the MSPs exhibit smaller excursions and cannot be described by rotating vector model (RVM, [80]). This warrants different models to explain the MSP polarization properties. To address this, some models suggested emission from locations which extend over a substantial fraction of the light cylinder [8]. In addition, it is possible that special geometries of MSPs in binaries [21], or the existence of higher multipole moments in the magnetosphere of MSPs [66], can explain the observed polarization properties for individual MSPs.

Dai et al. [27] reported that the secondary pre- and post-cursors peaks in the profile generally have a higher fractional linear polarization than the main pulse. They also observed that the circular polarization showed complicated variations with both frequency and pulse phase, and different pulse components often had different signs of circular polarization. They studied the distributions of the fractional linear and circular polarization across the frequency bands, finding that although the fractional linear polarization was similar across three bands, both the fractional and net circular polarization decreased at lower frequencies. They further reported that the polarization angle sweep for all the MSPs of their sample were extremely complicated and could not be fitted using the RVM. As an example, Fig. 1.3 shows the polarization profile of MSP J0437–47. They also noted that the polarisation angle profile could significantly evolve across the observing frequency band.

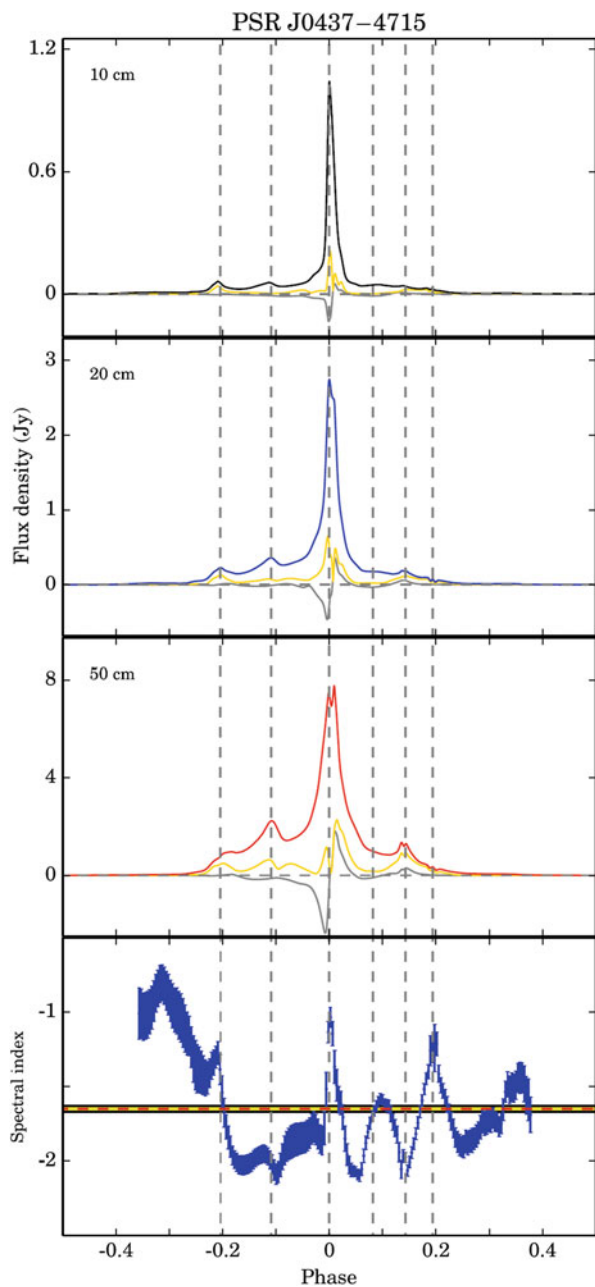
1.3 Searches for Radio MSPs

The improvement in the technique of analysis made the rate of discovery of pulsars in ongoing surveys at major telescopes to increase dramatically over the last decade (see Fig. 1.4). However, the population of currently known MSPs (~ 500) is less than one per cent of the predicted number of potentially observable radio pulsars in the Galaxy (1.2×10^5 ; [35]). The *PsrPopPy*⁴ code is widely used to infer predictions on the underlying unseen population of MSPs [11]. Once the survey specifications are given as input, the *PsrPopPy* simulation can predict the number of MSPs that can be potentially discovered. For example, *PsrPopPy* simulations predicted that ~ 3000 MSPs will be discovered by the Square Kilometre Array (SKA, [45]; see Fig. 1.5). Thus, population studies indicate that many MSPs are waiting to be discovered. A large fraction of the MSPs are faint sources requiring sensitive searches and improved analysis techniques to be discovered.

The sensitivity of the pulsar survey is calculated using the radiometer equation. A pulsar will be detectable (with a 5σ detection significance) in a survey made of an incoherent array of smaller telescopes, if it exceeds some minimum flux density

⁴ <https://github.com/samb8s/PsrPopPy>.

Fig. 1.3 The polarization profile of PSR J0437–4715 and phase-resolved results. The spectral index observed at different pulse phases is reported in the bottom panel. The leading and trailing parts have steeper spectral indices, whereas the outer edges of the profile have flatter spectra. Credit: Dai et al., MNRAS, 449, 3223 (2015) [27]



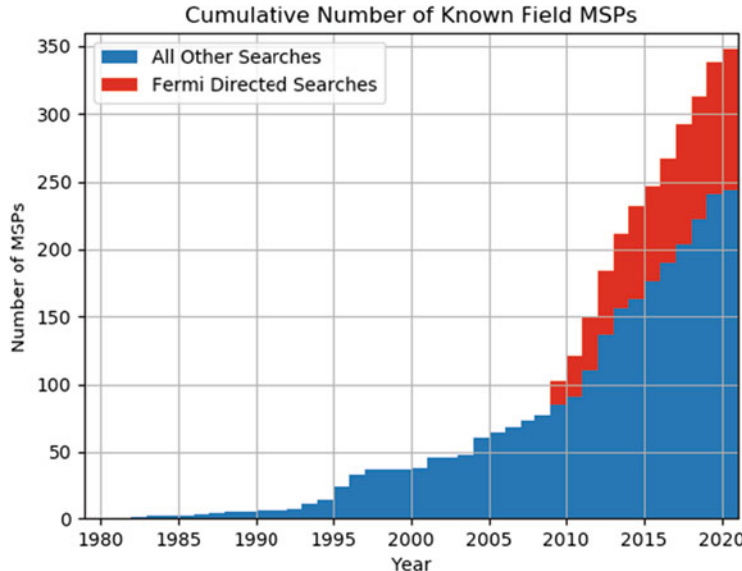


Fig. 1.4 Cumulative number of known MSPs in the Galactic field. Fermi-directed searches have contributed to one-third of this number. Figure courtesy of Paul Ray

(S_{pulsar}) that can be calculated using the radiometer equation:

$$S_{\text{pulsar}} \sim 5 \frac{T_{\text{rec}} + T_{\text{sky}}}{G \sqrt{B N_p N_a t}} \sqrt{\frac{w}{P - w}} \quad (1.1)$$

where T_{rec} and T_{sky} are the temperatures of the receiver and sky, respectively, G the gain of individual antennas, B the bandwidth, N_p the number of orthogonal polarizations needed to construct the total intensity, N_a the number of antennas, t the integration time, w the effective pulse width (including all instrumental smearing), and P the pulse period. The limiting sensitivity of different surveys can be calculated using the survey parameters in this equation. The discovery of new MSPs is hampered by their radio faintness and requires deeper searches with larger telescopes. Ongoing searches with the Green Bank Telescope (*GBT*), the Parkes telescope, Effelsberg, Arecibo, the Giant Metrewave Radio Telescope (*GMRT*), and the Five hundred meter Aperture Spherical Telescope (*FAST*) have discovered a good number of MSPs, bringing the total number of MSP in the Galactic field to ~ 353 ⁵ and total number of MSPs in Globular cluster to 147. Some of the major radio telescopes that are actively discovering MSPs are large single dish telescopes (e.g. Arecibo, *GBT*, Parkes), and their limiting sensitivity has almost been

⁵ <http://astro.phys.wvu.edu/GalacticMSPs/GalacticMSPs.txt>.

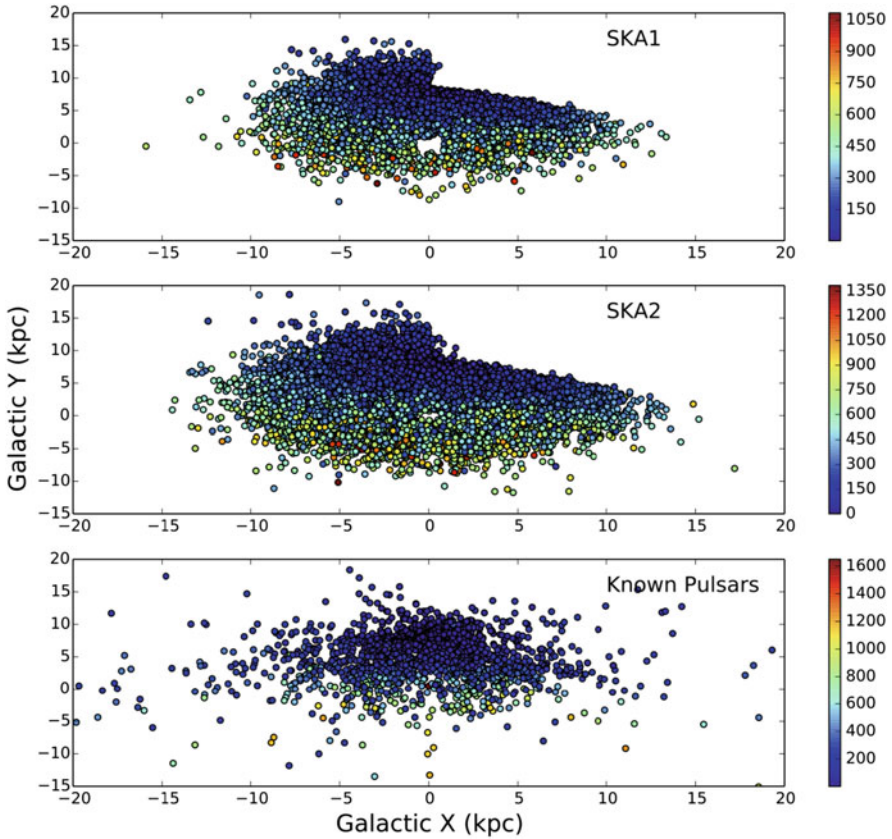


Fig. 1.5 *PsrPopPy* simulation of the number of pulsars expected to be found with the *SKA* along with their distribution throughout the Galaxy, projected onto the Galactic plane, compared to the distribution of currently known pulsars. The color coding indicates the approximate range of dispersion measures of the simulated pulsars. Credit: Keane et al., in “Advancing Astrophysics with the Square Kilometre Array”, Proceedings of Science, PoS(AASKA14), id. 040 (2015), [45]

reached. Thus, large arrays of many smaller telescopes are the future to increase the sensitivity, and this will ultimately lead to the world’s largest telescope, the Square Kilometer Array (*SKA*).

In spite of the fact that the rate of discovery of pulsars in ongoing surveys at major telescopes has increased dramatically over the last decade, the presently known population is a very small fraction of the predicted number of MSPs. Since MSPs are intrinsically faint and most of the MSPs are part of binary systems, a binary acceleration search (and sometimes jerk search, i.e., searching up to period double derivatives) is also required, in addition to a search for dispersion measure and periodicity. The details of search techniques are described in Sect. 1.3.1. Targeted searches and wide-area blind surveys are two popular ways to look for the large

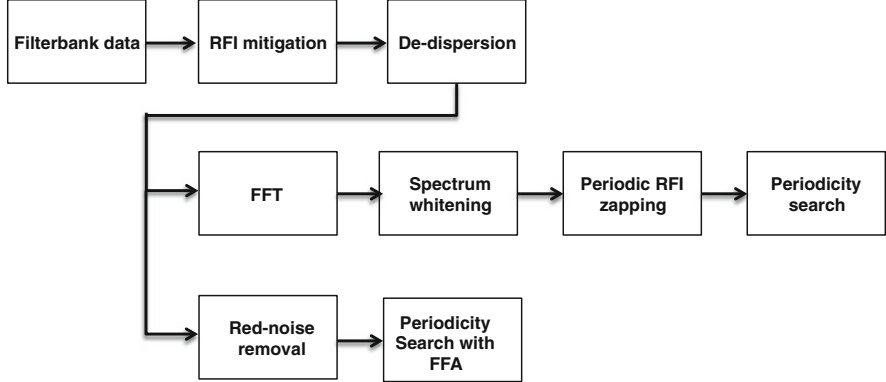


Fig. 1.6 Functional blocks for pulsar search processing. The de-dispersed time samples are processed concurrently using frequency-domain search (with Fast Fourier Transforms) and time-domain periodicity search (with Fast Folding Algorithm, FFA)

number of the MSPs which are yet unseen. In Sects. 1.3.2 and 1.3.3 we describe these two MSP search techniques.

1.3.1 Search Techniques

Pulsar search processing is a computing-intensive task. Figure 1.6 shows a typical functional block diagram for a search analysis. The time-frequency filterbank data from the telescope are first processed to excise broad-band and narrow-band radio frequency interference (RFI). RFI mitigated filterbank data are then fed into a de-dispersion transform module, which corrects for the frequency dependent dispersive delays at various trial dispersion measure (DM) values. The pipeline performs a periodicity search for each of the de-dispersed time-series. The periodicity search in frequency-domain involves Fast Fourier Transforms (FFT), spectrum whitening to remove the instrumental red-noise, and masking periodic RFIs (e.g. impulsive signals from AC power-line). In parallel, the de-dispersed time-series can also be searched for periodic signals in the time-domain. The increase in computing power enhanced the sensitivity of on-going surveys with large single dishes or interferometric arrays, making them progress through a hitherto unexplored parameter space. Since the majority of MSPs are in binaries, a periodicity search requires the correction of the line-of-sight acceleration caused by the orbital motion of the pulsar. Thus, in addition to the constant acceleration search, for systems like double neutron star binaries with higher companion mass, the assumption of constant spin frequency-derivative over the span of the observation is no longer valid. The periodicity search employs a jerk search, i.e. searching over the period and the first two period-derivatives that corrects the binary acceleration effect on much shorter

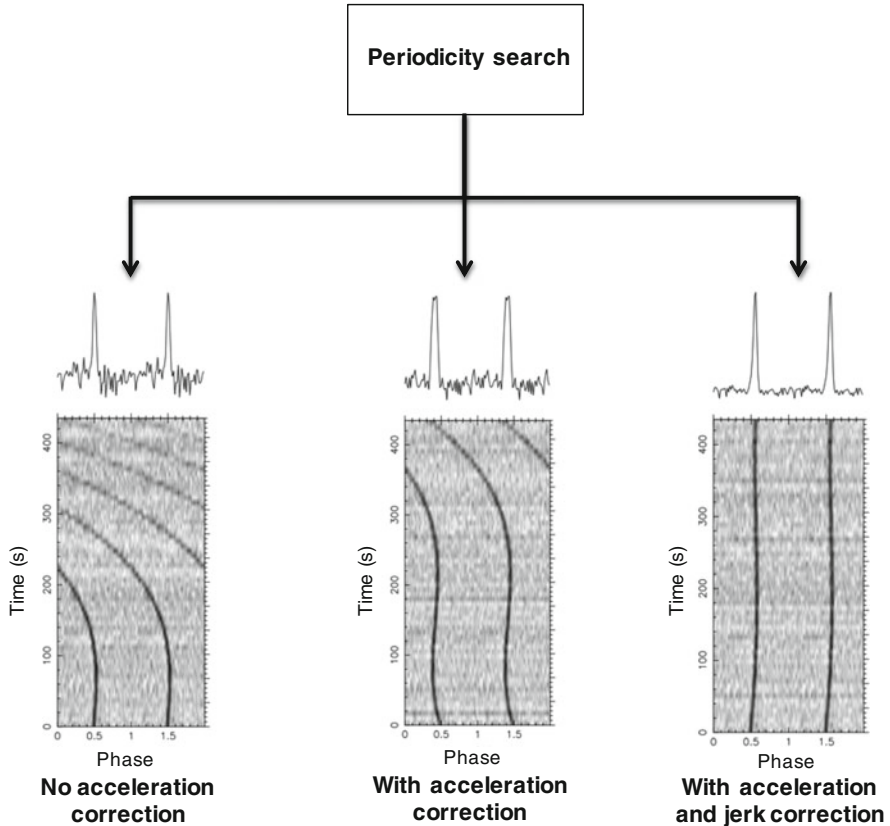


Fig. 1.7 The effect of line-of-sight acceleration for a simulated system containing a pulsar in 1.2 h circular orbit with companion mass of $1.4 M_{\odot}$. The tracks indicate the pulse intensities as function of time and the averaged pulse profiles are shown on the top

time scales even for a fraction of the orbit. Figure 1.7 shows the improvement obtained in a periodicity search that involves no acceleration, a constant acceleration and acceleration+jerk, respectively. The comparison is done for a simulated system containing a 22 ms pulsar and a neutron star companion ($1.4 M_{\odot}$) in a 1.2 h circular orbit. Correcting for the binary acceleration significantly enhances the signal-to-noise (S/N) of the signal, making a detection much easier. However such an acceleration (and jerk) search increases the pulsar search processing cost by more than an order of magnitude. For example, Anderson et al. [2] reported an increase by a factor of ~ 80 of the processing time while searching for highly accelerated pulsars in Terzan 5 globular cluster. A new 2.93 ms pulsar, J1748–2446 am, was discovered with the jerk search which had not been detected before with an acceleration-only search [2]. Discovering such systems is important as they provide unique laboratories to test the theories of gravity (see Sect. 1.4.2). The population of non-recycled slow pulsars (period > 100 ms) contains several interesting objects, such as

pulsars showing pulse intermittence, drifting and nulling, all of which are important probes of the emission physics. We also know two ultra-slow pulsars with a period longer than 10 s; these pulsars graze the theoretical death-line and are interesting to probe the conditions at which the radio emission is expected to cease. The instrumental red-noise and radio frequency interference (RFI) reduce the search sensitivity at the low frequency end of the power spectrum of the detected time series, where the signal from these objects is strongest. In addition, due to the shorter duty cycle of long period pulsar, the number of harmonics used in the frequency-domain periodicity search limits the signal recovery from the power spectrum. For this reason, the ongoing surveys (e.g. [19] for HTRU survey, [72] for PALFA survey, [70] for SUPERB survey) also perform a time-domain search with a Fast Folding Algorithm (FFA; [92]), simultaneously to the frequency-domain periodicity search.

1.3.2 Targeted Searches

Targeted searches are more sensitive to pulsars compared to wide-area surveys that cover the sky blindly. They allow deeper searches through longer observations (making the surveys more sensitive) as well as multiple visits per source. This is precious because in some cases a pulsar can be missed in a single observation due to scintillation, eclipses, or acceleration in a binary system. Such deep observations can characterise specific environments in unique ways. Targeted surveys also probe different types of MSPs, so probing the evolutionary links between different classes.

1.3.2.1 Follow-Up of High Energy Sources

The radio and the high-energy ends of electromagnetic spectrum are highly complementary in pulsar searches, since the highest sensitivity and resolution is attained in the radio domain but the largest observable energy output (though smaller in terms of photon counting statistics) is attained at higher energies (see Chap. 2).

Targeted searches of high-energy sources proved particularly efficient compared to blind surveys for pulsars, especially for the *Fermi* directed searches. Since August 4, 2008, the Giga-electron-volt γ -ray sky has been surveyed by the *Fermi* Large Area Telescope (*LAT*, [6]), the primary instrument on-board the *Fermi* Gamma-ray Space Telescope. An increasing number of unassociated γ -ray point sources appear at each *Fermi* LAT catalog release. Targeted searches for radio pulsations at the position of such unassociated LAT point sources is coordinated by the *Fermi* Pulsar Search Consortium (PSC). Till now, 95 new MSPs are been discovered in this effort,⁶ which amounts to about one third of the total known Galactic MSP population. Figure 1.4 plots the cumulative number of known Galactic MSPs

⁶ <https://confluence.slac.stanford.edu/display/GLAMCOG/Public+List+of+LAT-Detected+Gamma-Ray+Pulsars>.

discovered over the years. It is evident that Fermi directed surveys considerably enhanced the number of MSPs. Figure 1.8 shows the Galactic distribution of the MSPs discovered in Fermi directed surveys, and Table 1.2 summarises the existing and ongoing efforts in Fermi-directed search for millisecond pulsation.

Since MSPs have been spun-up by accretion of matter lost by a companion star, many of them are naturally expected to be part of binary systems. LMXB/MSP transitional systems are considered as direct observational evidences of this hypothesis, as it is described in detail in Chap. 6 of this book. On the other hand, the formation of isolated MSPs has not been understood yet. Their existence could be linked to a class of MSPs in very compact binary orbits ($P_b < 1$ day), known as spider MSPs, whose companion masses are either brown dwarfs (black widows, where $0.01 M_{\odot} < M_c < 0.05 M_{\odot}$) or main sequence stars (redbacks, where $0.1 M_{\odot} < M_c < 0.4 M_{\odot}$) [86]. The eclipses of the radio signal observed from these systems are caused by plasma ejected by the radio pulsar wind, and which surrounds the system. This process could evaporate completely the companion star of black widows, so producing isolated MSPs. The majority of spider MSP systems were discovered in the radio surveys of unassociated Fermi-ray sources.

1.3.2.2 Searches in Globular Clusters

Pulsars in globular clusters (GCs) are among the most interesting to study the pulsar population. From slow to millisecond pulsars, isolated to binary, GC pulsars have provided a variety of exciting science results. Over the last few decades, 157 pulsars have been discovered in 30 GCs, the vast majority of which are MSPs. Figure 1.9 plots the histogram of isolated and binary MSPs in individual globular clusters. Many of the GC MSPs are in exotic binary systems compared to the population found in Galactic field. They include the fastest spinning pulsar, highly eccentric binaries, and MSPs in peculiar evolutionary phases such as redbacks, black widows and a transitional MSP (e.g. [28, 30, 39, 42, 71, 82]). The high stellar densities in GCs lead to a high probability of close stellar interactions through which binaries form and subsequently evolve. GCs also hold the possibility of hosting ultra-fast spinning pulsars like sub-millisecond pulsars created through multiple episodes of recycling, which would provide stringent constraints on the neutron star equation-of-state [55]. Additionally, one can learn about the cluster dynamics, gas content (e.g., [29, 38]) and magnetic field, as well as about the MSP formation and evolution (thanks to the high number of sources; e.g., [84]). The dense, highly interacting environment in clusters core could in principle host the rarest system, like a holy-grail MSP—black hole binary or even an MSP—MSP binary.

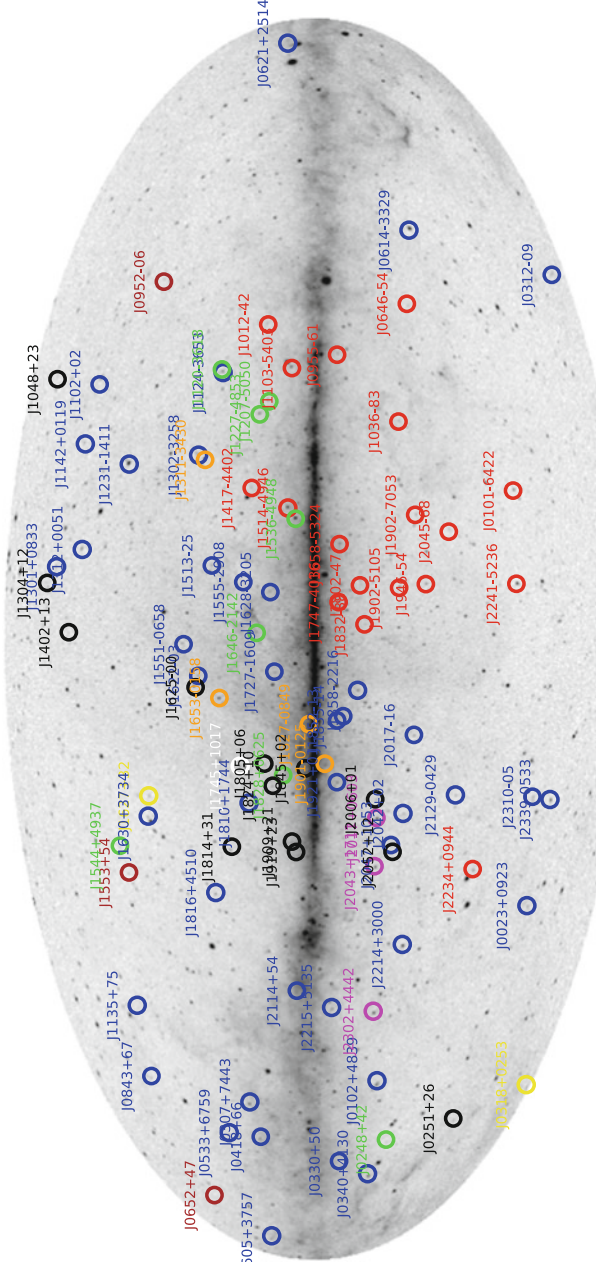


Fig. 1.8 Galactic distribution of the MSPs discovered in Fermi directed surveys. Discoveries by different telescopes are marked in different colours. GBT in blue, Parkes in red, GMRT in green, Nancay in magenta, white is Effelsberg, orange is LAT, black is Arecibo, brown is LOFAR and yellow is FAST. Figure courtesy of Paul Ray

Table 1.2 Summary table for ongoing targeted and wide field searches for MSPs

Telescope	Survey name	S_{min}^a (mJy)	Frequency (MHz)	# MSP discovered	Status
GBT	Fermi-directed	0.06–0.08	350, 820, 2000 ^b	45	Ongoing [83]
Arecibo	Fermi-directed	–	300–500, 1214–1537	14	Ongoing
Parkes	Fermi-directed	0.2	1262–1518	18	Dormant[20]
GMRT	Fermi-directed	0.3–0.9	306–338, 607–639	8	Restarting[13]
LOFAR	Fermi-directed	1.1	115–154	3	Ongoing[10, 75]
Nancay	Fermi-directed	–	1344–1472	3	Dormant[24]
Effelsberg	Fermi-directed	0.02–0.06	1180–1420	1	Dormant[9]
FAST	Fermi-directed	–	–	2	Ongoing
MeerKAT ^c	Fermi-directed	0.02–0.06	900–1680	–	Starting
CHIME ^d	CHIME/Pulsar	0.2	400–800	–	Starting[23]
Arecibo	327 MHz Drift	0.5	300–350	10	Ongoing ^e [68]
Arecibo	PALFA	–	1214–1537	8	Ongoing[73]
GBT	GBNCC survey	0.74	300–400	24	Ongoing ^f [69]
LOFAR	LOTAAS	1.2	119–151	2	Ongoing ^g [89]
Parkes	SUPERB	0.2–0.7	1182–1582	2	Ongoing ^h [46]
GMRT	GHRSS	0.2–0.5	300–500	2	Ongoing ⁱ [14, 15]
MeerKAT ^c	TRAPUM–UHF	–	544–1088	–	Starting

^a S_{min} is the limiting flux density at the frequency at which the survey was conducted. A value is reported if available in related publication/webpage

^b 100, 200 and 800 MHz bandwidth centered at 350, 820 and 1500 MHz

^c Part of TRAPUM project. From private communication with Ben Stappers

^d For CHIME/Pulsar the sensitivity limit is for single transit and multi-day stacking search is planned for the targeted survey

^e <https://www.naic.edu/~deneva/drift-search/>

^f <http://astro.phys.wvu.edu/GBNCC/>

^g <http://www.astron.nl/lotaas/>

^h <https://sites.google.com/site/publicsuperb>

ⁱ <http://www.ncra.tifr.res.in/ncra/research/research-at-ncra-tifr/research-areas/pulsarSurveys/GHRSS>

1.3.2.3 Galactic Centre MSPs

Scattering is the main hindrance in searches for MSPs in the Galactic centre region, since it causes a temporal broadening of pulses and a reduction of the pulse signal-to-noise ratio (S/N). The discovery of a MSP near the Galactic Centre region would be of immense importance, as it would be a very useful tool to measure the magnetised ISM in such extreme environment, and especially to probe the space-time surrounding the nearest super-massive black hole, Sgr A* [59]. It is conjectured that General Relativity and other perturbations experienced by Galactic Centre pulsars would be so large that even a low precision pulsar timing could suffice. Liu et al. [59] illustrated that even with moderate timing precision, a binary MSP in a close orbit around Sgr A* ($P_b < 1$ yr) would allow the observation of relativistic

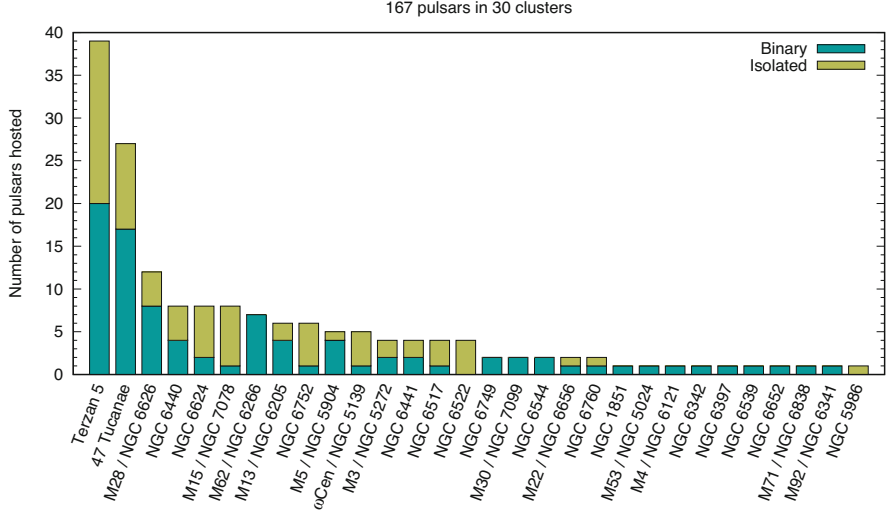


Fig. 1.9 Histogram of pulsars in globular clusters. Credit: A. Ridolfi, www3.mpifr-bonn.mpg.de/staff/pfreire/GCpsr.html. Reproduced with permission

effects, like time dilation, Shapiro delay and relativistic peri-center precession. It is expected that soon after the discovery of such an MSP, relativistic effects could be measured allowing an accurate measure of the mass of Sgr A* and unprecedented gravity tests. Pulsar timing has the potential of increasing the testing and diagnostic precision of gravity tests by at least three orders of magnitude In comparison with the best predicted precision of infrared astrometry and Doppler measurements.

To date, there are six active radio pulsars (all relatively slow *ordinary* pulsars) within $15'$ (~ 36 pc) of Sgr A*. Figure 1.10 shows the distribution of these pulsars close to the Galactic Centre. This is a very small fraction of the ~ 1000 pulsars (inclunding MSPs) expected to lie within the central pc around Sgr A* [22, 99]. Most of the targeted searches of the Galactic Centre are performed at relatively high frequencies to minimise the loss of pulse power due to scattering, as the temporal broadening has a strong frequency dependence $\propto \nu^{-4}$. However, pulsars become less luminous at such high frequencies because of their steep spectrum, which is described by a power-law spectrum with an index ~ -1.7 . The fact that a fraction of pulsars have relatively flatter spectral index, combined with the detection of a few pulsars, motivated high frequency searches in the Galactic Centre. The discovery of more pulsars towards the Galactic Centre would help determine the optimum frequency for targeted searches in the Galactic Centre. For example, measurements of pulse broadening in PSR J1745–2900 found that the degree of scattering toward the Galactic Centre is less than previously predicted [91]. This study also suggested that the scattering region could be distant from the Galactic Centre.

Periodicity searches that take into account the correction for the for orbital motion (commonly known as acceleration and jerk searches; see Sect. 1.3.1) are

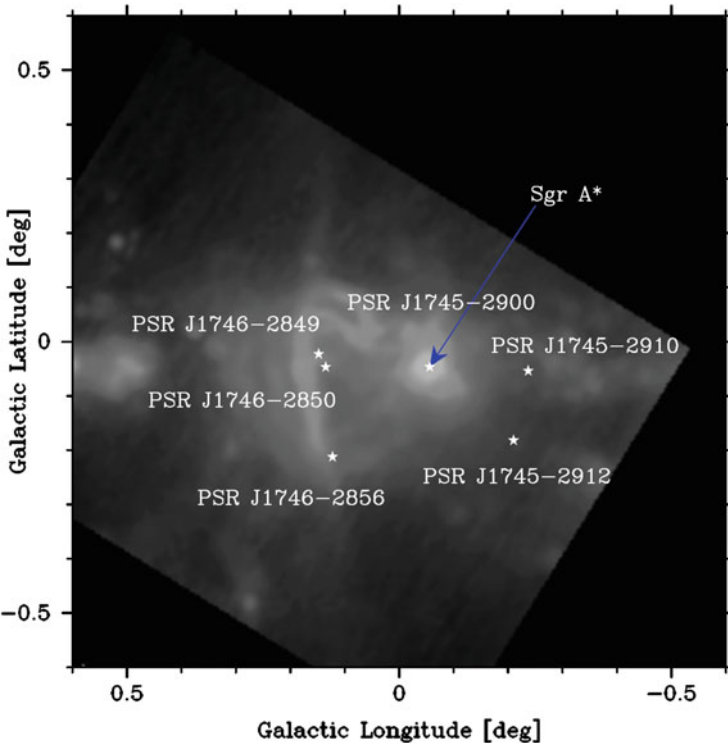


Fig. 1.10 The positions of known radio pulsars in the central 0.5° toward the GC overlaid on a 10.55 GHz continuum map made with the Effelsberg telescope. Future discovery of any MSP near to the Sgr A* will be very useful for gravity tests. Credit: Eatough et al., in “Advancing Astrophysics with the Square Kilometre Array”, Proceedings of Science, PoS(AASKA14), id. 045 (2015), [34]

employed to search for millisecond pulsars in Galactic Centre region. Searches for transient sources are also relevant for the Galactic Centre region, because some pulsars may have strong single pulses or giant pulses, and are more easily detected by single-pulse detection algorithms.

1.3.3 Wide Field Surveys

The location of the majority of the pulsars cannot be predicted accurately. Thus, blind searches over large areas of the sky are the best way to search for new pulsars. There are a few factors that have to be considered in the design a blind survey, (i) the intrinsic steep spectra of MSPs (spectral index $\alpha \sim -1.7$), (ii) the dispersion delays which scale as v^{-2} and can be corrected, (iii) scattering, whose effect scales as v^{-4} and cannot be corrected, (iv) the sky temperature, and (v) the field-of-view

of the telescope. Low-frequency surveys are favoured as pulsars are intrinsically stronger, the field-of-view is larger, and scattering is relatively mild, especially for relatively higher galactic latitudes. Indeed, the most efficient all-sky pulsar searches are conducted within the radio frequency range between ~ 100 MHz and ~ 1 GHz, for Galactic latitudes $|b| > 5^\circ$. Of the 396 MSPs listed in ATNF pulsar catalog, 35% are at $|b| < 5^\circ$, indicating the need for sensitive off-galactic plane surveys. The major, ongoing low-frequency pulsar surveys are listed in Table 1.2. They are being conducted from 100 MHz to up till 1400 MHz with a sensitivity reaching up to 0.2 mJy. Considering the population model, these surveys will result in a significant number of interesting individual MSPs in the near future.

Pulsar searches with the future world's largest telescope, the Square Kilometre Array (*SKA*) featuring a wide field-of-view, high sensitivity, multi-beaming and sub-arraying capabilities, coupled with advanced pulsar search backends, aims at going ten times deeper than any ongoing wide-field survey resulting in discovering a large fraction of the Galactic pulsar population [45]. This will also increase the number of MSPs suitable for high precision timing for the detection of gravitational waves (see Sect. 1.4.1), double pulsars to test the theories of gravity (Sect. 1.4.2), and interesting individual system like triples (Sect. 1.4.2). The holy grail, a Pulsar-Black hole binary will be the long-sought-after system that the SKA is expected to find. The SKA1-Mid, which will be located in South Africa and operate from 350 MHz, is expected to find 700 MSPs (Fig. 1c of [94]). The SKA1-Low, which will be located in Australia and operate from 50 to 350 MHz, is expected to find a few hundreds nearby MSPs. The SKA1-Low will have 500 tied-array beams over an observing bandwidth of 100 MHz, sampled at 100 μ s, while the SKA1-Mid will produce 1500 tied-array beams over an observing bandwidth of 300 MHz sampled at 64 μ s [57]. The SKA pulsar search backend can correct for 350 ms^{-2} line-of-sight acceleration for a pulsar with 2 ms spin-period. For a typical SKA observations duration of 540 s, with this acceleration limit SKA can detect pulsar with a $15 M_\odot$ black hole in a 5 h orbit (seen in Fig. 1.11 taken from [94]). NS-NS or NS-WD binaries as compact as an hour could also be detected with the SKA.

1.4 Timing of MSPs

Pulsar timing probes interesting individual pulsar properties, like glitches [90], profile state changes [64], nulling [7], intermittency [50] and binary evolution. The timing of pulsars located in the Galactic plane also aids the investigation of properties of the interstellar medium through the measure of scattering effects, as well as via dispersion (DM) and rotation measure (RM) studies. Pulsar timing measures the deviation of the observed pulse arrival times from the values predicted with a timing model assumed beforehand. The measured deviations could be caused by un-modelled effects, like the low-frequency gravitational wave background or the curvature of the space-time in a compact massive binary. The high rotational stability [62], compactness (second only to black holes), and their presence in binary

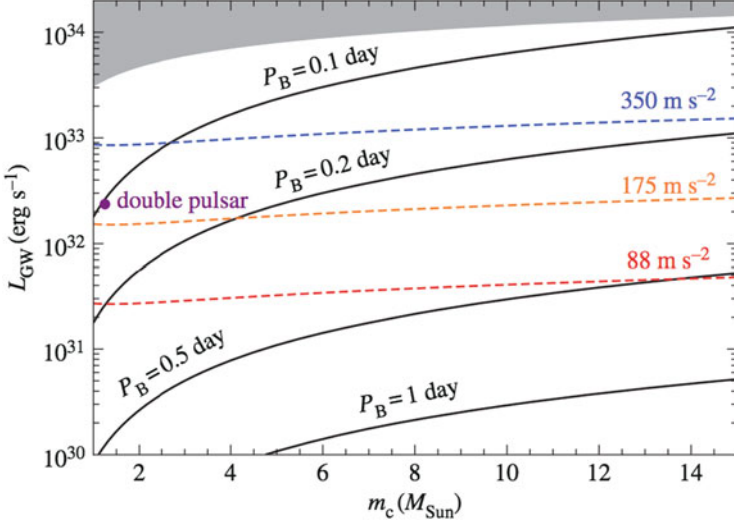


Fig. 1.11 The binary pulsar search space that the SKA will be sensitive to. A typical SKA observation will last about 540 s with an acceleration search range up to 350 ms^{-2} . The higher GW luminosity for compact orbits (shorter P_B) with higher companion mass (m_c) gives a higher binary acceleration. Credit: Stappers et al., Philos. Trans. R. Soc. A, 376, 2120 (2018), reproduced with permission of the Royal Astronomical Society, [94]

systems, make MSPs ideal laboratories to test the physics of gravity [19, 51, 95], to use them as detectors for long-wavelength gravitational waves [33, 37] and to constrain the equation of state of matter at supra-nuclear densities ([3, 31]; see the discussion in Chap. 9).

1.4.1 MSPs as Sensitive Gravitational Wave Detectors

A Pulsar Timing Array (PTA) exploits the accurate pulse arrival time measurements of a large set of high-timing precision MSPs distributed across the sky, in order to detect the space-time vibrations caused by the stochastic Gravitational Waves (GWs) background [33, 37, 56]. As the timing span and precision increase, the timing residuals become dominated by red noise components, either from the GW background or from intrinsic pulsar timing noise. A significant fraction of the pulsar timing noise is produced by turbulence in the free electron density of the interstellar plasma. At present, one of the most crucial challenges for the PTAs is to disentangle the influence of the interstellar medium from other sources of noise. Changes in the dispersion measure and/or the influence of scattering can adversely affect the arrival times. In order to separate the red noise components from the GW background, the non-white components of timing residuals due to the

interstellar medium and/or the profile evolution with frequency need to be mitigated. Then, the detection of the stochastic GW background can be probed from the angular correlation between the residuals of the arrival times of pairs of pulsars distributed across the sky, which is called Hellings and Downs curve [41]. Through these detections, a PTA aims at revealing the cosmic population of inspiralling supermassive black holes binaries (SMBHBs) in merging galaxies. These systems are expected to emit GWs in the nanohertz frequency range, which is invisible to space-based and ground-based GWs detectors like *LISA* and *LIGO* [18]. At present, there are three main PTA efforts: the EPTA (European Pulsar Timing Array⁷), NANOGrav (North American Nanohertz Observatory for Gravitational Waves⁸) and the PPTA (Parkes Pulsar Timing Array⁹). A PTA is sensitive to GWs with frequencies ranging from $1/($ timing-span) to $1/($ cadence). Assuming a timing-span of 10 years and a weekly cadence, at the low frequencies (10^{-9} – 10^{-6} Hz) GWs are detectable through long-term timing observations of the most stable pulsars. All the three PTAs already provide stringent limits on the amplitude of the GW background around 10^{-15} , ruling out some of the theoretical models for the stochastic GW background [94]. The timing measurements from the eight telescopes used for the PTAs around the world are combined to form the International Pulsar Timing Array (IPTA) data set. This improves the cadence and the frequency range of the observations. In the recent second data release of the IPTA [74], the combined high-precision timing data for 65 MSPs regularly observed by the three PTAs were considered. The significantly higher quality of these data promises to improve the limits on the isotropic stochastic low-frequency GW background obtained, so far. The GW landscape shown in Fig. 1.12 highlights the GW radiation expected from a variety of sources at frequencies ranging from nHz to kHz. The advent of SKA will increase the current limit of 10^{-15} on the isotropic stochastic GW background by more than an order of magnitude. Besides improving the timing precision using sensitive instrument like the SKA, an increase in the number of MSPs that can be timed with good precision is also expected to contribute significantly to the PTA's sensitivity. According to Manchester et al. [65], for a GW amplitude of 10^{-16} , a 5 year-long timing campaign with an ideal PTA that uses 100 pulsars can achieve a higher significance than a 20 year-long campaign with 20 pulsars (see Fig. 1.13).

1.4.2 *MSPs as Gravity Probes*

MSPs in compact binaries with a white dwarf or a neutron star companion offer extreme environments to carry out stringent test of gravity. As the signal from the pulsar propagates through curved space-time across the binary, we can perform

⁷ www.epta.eu.org.

⁸ www.nanograv.org.

⁹ www.atnf.csiro.au/research/pulsar/ppta.

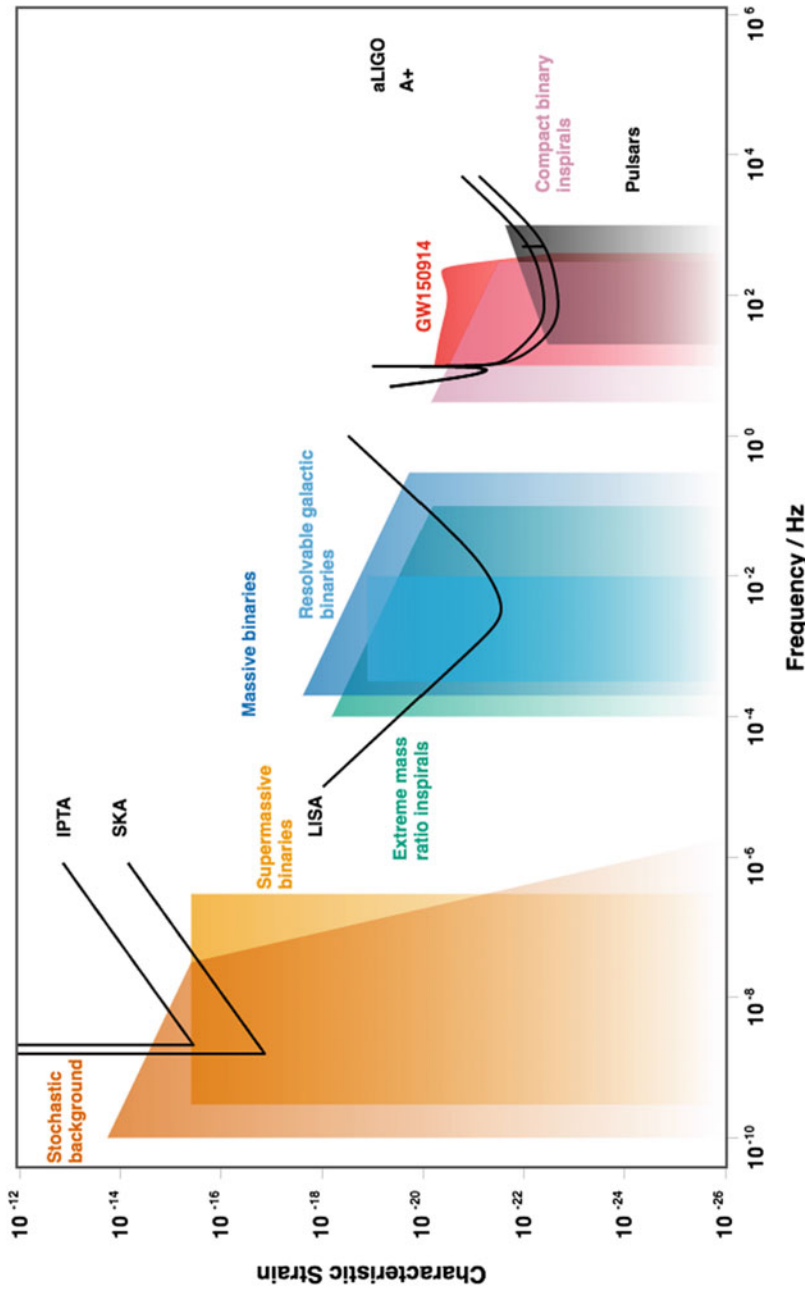


Fig. 1.12 Variation of the amplitudes of the gravitational wave radiation from variety of sources over the spectrum. Ground-based interferometers (e.g. LIGO and future instruments), space-based interferometers (e.g. LISA), and pulsar timing (e.g. IPTA and SKA) probe the spectrum from nHz to kHz range from the cosmological population of SMBHBs to compact object inspirals. Produced with <http://gwplotter.com/>

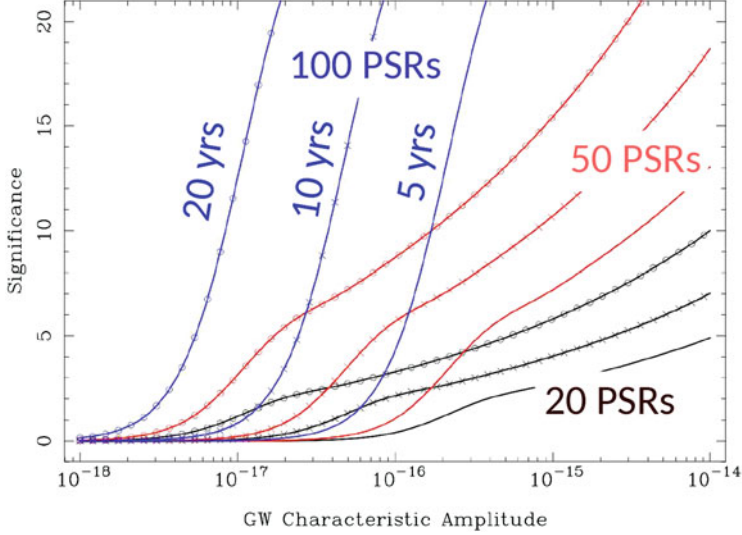


Fig. 1.13 Detection significance of the isotropic stochastic GW background using an ideal PTA, as a function of the signal strength, the number of MSPs in the PTA, and data time span. In this simulation, a variable number of MSPs is considered (20, 50 and 100), whereas the data span 5, 10 and 20 years, respectively. The RMS noise in the timing residuals is taken as 100 ns and a weekly cadence is assumed. For a GW amplitude of 10^{-16} , 5 years timing campaign with 100 pulsars can achieve higher significance than 20 years timing campaign with 20 pulsars. Credit: Manchester et al., Classical Quant. Grav., 30, 22 (2013), reproduced with permission of the IOP, [65]

precision tests of gravity to search for tiny deviations from GR [48]. In addition to the five Keplerian binary parameters like the orbital period P_b , the eccentricity of the orbit e , the projected semi-major axis of the pulsar orbit $a_p \sin i$, the longitude of periastron ω , and the epoch of periastron passage of the pulsar T_0 , there are few “Post-Keplerian” (PK) parameters which measure the relativistic effects in pulsar timing [62]. The PK parameters are the relativistic advance of the periastron described as a time derivative of the angle of periastron $\dot{\omega}$, the orbital decay due to gravitational wave emission described as time derivative of the orbital period \dot{P}_b , a combination of gravitation redshift and time dilation described by Einstein delay parameter γ , a Shapiro delay due to the curvature of space-time around the companion described by a ‘shape’ s and a range ‘ r ’ parameter, and the relativistic deformation of the orbit described by δ_θ and δ_r [62]. Different theories of gravity can be tested by comparing their predictions of the PK parameters for a binary system with those measured from timing studies. The Hulse-Taylor pulsar, B1913+16 [44] first provided an evidence for GW emission from the measure of a few PK parameters [97]. Later, all the PK parameters could be measured for the exceptional

double pulsar system, PSR J0737–3039A/B, so probing the deviations from GR by less than 0.05% [51]. A recent study of two double neutron star systems (DNS) allowed the investigation of a hitherto unexplored relativistic parameter space while probing the formation and evolution of the DNS population. One of the DNS is in the most accelerated binary system PSR J1757–1854 [19], and the other is the most massive DNS system with the highest asymmetric mass ratio PSR J1913+1102 [36]. Also, PSR J0337+1715, a mildly relativistic hierarchical triple system with two white dwarfs, provided a unique laboratory to perform some of the most stringent tests of the strong equivalence principle (SEP), the universality of free fall [5]. Finally, a yet to be found pulsar-black hole binary would be a holy-grail to trace the space–time around the most extreme gravitating system using the nature’s best clocks. Finding such systems and performing high precision timing studies to reveal black hole properties with unprecedented sensitivities [60] is one of the main goal of the SKA.

1.4.3 Eclipsing MSPs: Probing Intra-Binary Material

Black widow and redback spiders are eclipsing binary MSPs that can provide a variety of information on:

- the accretion history and the evolutionary link between accreting X-ray pulsars and radio MSP (see also Chaps. 6 and 7);
- the high energy emission from the intra-binary shock produced by the interaction between the pulsar and the stellar wind (see also Chap. 2);
- the eclipse mechanism and the properties of the eclipsing medium, such as magnetic field strength, temperature, clumping of material (described in this section and in Chap. 6).

Black widow and redback pulsars are fast spinning MSPs in compact binaries with a low-mass companion. These systems were named in this way as the pulsar wind is energetic enough to ablate the companion star, or at least to eject the matter that the latter transfers to the neutron star. The matter flung out by the pulsar wind is responsible for the observation of irregular eclipses of the radio signal. MSPs are naturally expected to be part of binary systems due to their formation in recycled scenario [12]. Whereas the majority of the observed MSP systems are in binaries, a small fraction of these (<20%) is isolated. It was argued that complete evaporation of the companion of a black widow MSP is one of the ways to form isolated MSPs [1]. Thus, these systems were proposed to be the evolutionary link connecting accreting X-ray pulsars and isolated millisecond pulsars. However, it is not clear yet whether the companion in black widow systems system will be actually

eventually evaporated. The mass loss rates determined by the recent studies for some of the systems indicates that it would be impossible to ablate the companion star completely within a Hubble time [78].

Both black widow and redback spider MSPs have compact orbits with orbital periods in the 0.1–1 day range; black widows have very-low mass (0.01–0.06 M_⊙) brown dwarf companions, whereas the redback systems have moderate mass (0.2–0.8 M_⊙) main-sequence companion stars. As discussed in Sect. 1.3.2, the number of black widow and redback spider pulsars increased significantly thanks to targeted pulsar searches from γ -ray selected sources. Before the launch of Fermi, only two such eclipsing black widow systems were known in the Galactic field, PSR B1957+20 [40] and PSR J2051–0827 [93]. Presently there are >40 known black widow MSPs and 20 redback MSPs (with parameters listed in the catalogue maintained by A. Patruno¹⁰). Compared to other MSPs, the spider MSP systems are found to have on average higher values of spin-down energy-loss rate ($\dot{E} \sim 10^{34} \text{ erg s}^{-1}$) making these systems good γ -ray pulsar candidates emission [86].

The majority of the black widow and redback systems are eclipsed for a large fraction of the orbital period (>10%, i.e., larger than the fraction of the orbit subtended by the companion’s Roche lobe). These eclipses are caused by the material of the very low mass companion blown by the pulsar wind. The energy flux of the isotropic pulsar wind of spider MSPs, at the distance of the companion, is at least four order of magnitudes larger than other MSPs (\dot{E}/a^2 , where a is the distance to the companion, for the black widow and redback systems is $\sim 10^{34} \text{ erg/s/R}_\odot^2$, whereas \dot{E}/a^2 for other MSPs are $10^{29} - 10^{30} \text{ erg/s/R}_\odot^2$). Table 1.3 lists the observed properties of black widow and redback MSPs. A higher value of \dot{E}/a^2 indicates that an active interaction between the pulsar and its companion is likely. During the eclipse, the radio flux density regularly drops below the detection threshold throughout the companion superior conjunction, with an excess of DM near the eclipse boundaries. Figure 1.14 shows the flux density observed for the black widow MSP system PSR J2051–0827 [78]. It is shown that at 345 MHz the MSP is never detected between orbital phases, 0.23–0.27, with a corresponding increase of the DM value near the eclipse boundary.

Thompson et al. [98] described possible mechanisms for the observed eclipses. Most of the observational studies of the black widow and redback spider systems pointed to cyclo-synchrotron absorption as the most likely eclipse mechanism (e.g. PSR B1957+20 [35], PSR J2051–0827 [78, 79, 93], PSR J1810+1744 [77], J1227–4853 [52, 88]). While the earlier studies used only timing observations (e.g.[35, 93]), some of more recent studies (e.g.[52, 78, 88]) used simultaneous timing and imaging observations to probe the eclipse mechanism. In addition, polarisation study at the eclipse boundary has been performed [26, 58, 78], resulting in measurement of the magnetic field in the eclipse region. In addition to the main eclipse, random short

¹⁰ <https://apatruno.wordpress.com/about/millisecond-pulsar-catalogue/>.

Table 1.3 Parameters for eclipsing binary millisecond pulsar systems (adopted from Kudale et al. [52])

Pulsar name	Excess DM (pc cm ⁻³)	\dot{E}/a^2 ^a (10^{35}) ($erg/s/R_\odot^2$)	Eclipse duration ^b	n	Reference
J1023+0038 (RB)	0.15(700)	0.33	40(685)	-0.41	[4]
J1048+2339 (RB)	0.008(327)	0.03	57(327)	-	[32]
J1227–4853(RB)	0.079(607)	0.29	64(607)	-0.44	[52]
J1227–4853 ^c (RB)	0.035(607)	-	6(607)	-	[52]
J1544+4937 (BW)	0.027(607)	0.11	13(322)	-	[13]
J1723–2837 (RB)	-	0.04	26(1520)	-	[25]
B1744–24A (RB)	0.6(1499.2)	-	~50 ^d (820)	-	[16]
J1810+1744 (BW)	0.015(325)	0.18	13(149)	-0.41	[77]
J1816+4510 (RB)	0.01(149)	0.08	24(121)	-0.49 ^e	[79]
B1957+20 (BW)	0.01(149)	0.22	18(121)	-0.18	[16]
J2051–0827 (BW)	0.13(705–4023)	0.06	28(149)	-0.41	[78, 79]
J2215+5135 (RB)	-	0.28	66(149)	-0.21 ^e	[17, 78]

Parameters presented in different columns of this table are,

Column 1: indicate redback (RB) or black widow (BW)

Column 2: the excess dispersion around eclipse boundary.

Column 3: \dot{E}/a^2 , \dot{E} is spin-down energy of the pulsar and a is distance to the companion

Column 4: eclipse duration with corresponding frequency in parenthesis

Column 5: index of power-law dependence (n) of full eclipse duration with frequency

^a Using <https://apatrano.wordpress.com/about/millisecond-pulsar-catalogue/>

^b Eclipse duration (in % of orbit) includes non-detection and associated ingress, egress transition

^c Parameters for excess dispersion observed around inferior conjunction

^d For majority of the observed eclipses. Eclipse duration are observed to be variable and sometimes completely enshrouding the pulsar [16]

^e Estimated power law index using all available frequency measurements from the recent literature.

duration eclipses have also been reported from a few spider MSPs (e.g., in the case of PSR J1544+4937, [13]). A recent study by Kudale et al. [52] has reported a flux decrease near the pulsar inferior conjunction of PSR J1227–4853. This can be interpreted as caused by mass loss through the L2 Lagrangian point for a system that has a rapid orbital evolution.

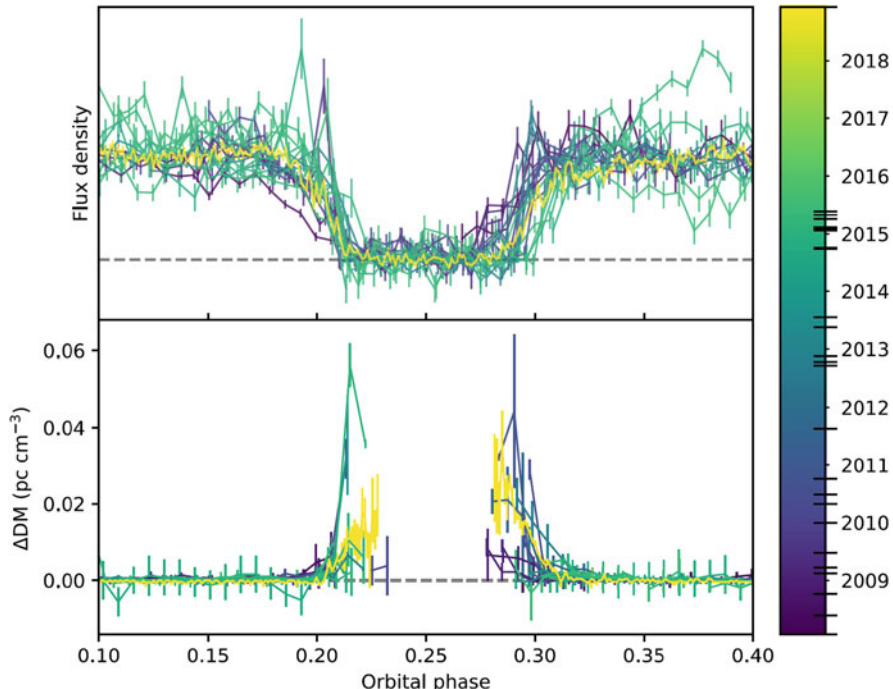


Fig. 1.14 Measured flux densities of PSR J2051–0827 for 345 MHz observations covering the eclipse region, with each normalised so the the out-of eclipse mean flux density is unity. The horizontal dashed line represents detection limit of the telescope. Bottom: Deviation from mean out-of-eclipse dispersion measures for the same set of observations. 1σ uncertainties from the simultaneous DM and scattering fits are shown with the error bars. Credit: Polzin et al., MNRAS; 490, 889 (2019), [78]

References

1. Alpar, M.A., Cheng, A.F., Ruderman, M.A., Shaham, J.: A new class of radio pulsars. *Nature* **300**(5894), 728–730 (1982). <https://doi.org/10.1038/300728a0>
2. Andersen, B.C., Ransom, S.M.: A Fourier Domain “Jerk” Search for Binary Pulsars. *Astrophys. J. Lett.* **863**(1), L13 (2018). <https://doi.org/10.3847/2041-8213/aad59f>
3. Antoniadis, J., Freire, P.C.C., Wex, N., et al.: A massive pulsar in a compact relativistic binary. *Science* **340**(6131) (2013). <https://doi.org/10.1126/science.1233232>
4. Archibald, A.M., Stairs, I.H., Ransom, S.M., et al.: A radio pulsar/X-ray binary link. *Science* **324**(5933), 1411 (2009). <https://doi.org/10.1126/science.1172740>
5. Archibald, A.M., Gusinskaia, N.V., Hessels, J.W.T., et al.: Universality of free fall from the orbital motion of a pulsar in a stellar triple system. *Nature* **559**(7712), 73–76 (2018). <https://doi.org/10.1038/s41586-018-0265-1>
6. Atwood, W.B., Abdo, A.A., Ackermann, M., et al.: The large area telescope on the fermi gamma-ray space telescope mission. *Astrophys. J.* **697**(2), 1071–1102 (2009). <https://doi.org/10.1088/0004-637X/697/2/1071>
7. Backer, D.C.: Pulsar nulling phenomena. *Nature* **228**(5266), 42–43 (1970). <https://doi.org/10.1038/228042a0>

8. Barnard, J.J., Arons, J.: Wave propagation in pulsar magnetospheres: refraction of rays in the open flux zone. *Astrophys. J.* **302**, 138 (1986). <https://doi.org/10.1086/163979>
9. Barr, E.D., Guillemot, L., Champion, D.J., et al.: Pulsar searches of Fermi unassociated sources with the Effelsberg telescope. *Mon. Not. R. Astron. Soc.* **429**(2), 1633–1642 (2013). <https://doi.org/10.1093/mnras/sts449>
10. Bassa, C.G., Pleunis, Z., Hessels, J.W.T., et al.: LOFAR discovery of the fastest-spinning millisecond pulsar in the galactic field. *Astrophys. J. Lett.* **846**(2), L20 (2017). <https://doi.org/10.3847/2041-8213/aa8400>
11. Bates, S.D., Lorimer, D.R., Rane, A., Swiggum, J.: PSRPOPPY: an open-source package for pulsar population simulations. *Mon. Not. R. Astron. Soc.* **439**(3), 2893–2902 (2014). <https://doi.org/10.1093/mnras/stu157>
12. Bhattacharya, D., van den Heuvel, E.P.J.: Formation and evolution of binary and millisecond radio pulsars. *Phys. Rep.* **203**(1–2), 1–124 (1991). [https://doi.org/10.1016/0370-1573\(91\)90064-S](https://doi.org/10.1016/0370-1573(91)90064-S)
13. Bhattacharyya, B., Roy, J., Ray, P.S., et al.: GMRT discovery of PSR J1544+4937: an eclipsing black-widow pulsar identified with a fermi-LAT source. *Astrophys. J. Lett.* **773**(1), L12 (2013). <https://doi.org/10.1088/2041-8205/773/1/L12>
14. Bhattacharyya, B., Cooper, S., Malenta, M., et al.: The GMRT high resolution southern sky survey for pulsars and transients. I. Survey description and initial discoveries. *Astrophys. J.* **817**(2), 130 (2016). <https://doi.org/10.3847/0004-637X/817/2/130>
15. Bhattacharyya, B., Roy, J., Stappers, B.W., et al.: The GMRT high-resolution southern sky survey for pulsars and transients. II. New discoveries, timing, and polarization properties. *Astrophys. J.* **881**(1), 59 (2019). <https://doi.org/10.3847/1538-4357/ab2bf3>
16. Bilous, A.V., Ransom, S.M., Demorest, P.: Unusually bright single pulses from the binary pulsar B1744-24A: a case of strong lensing? *Astrophys. J.* **877**(2), 125 (2019). <https://doi.org/10.3847/1538-4357/ab16dd>
17. Broderick, J.W., Fender, R.P., Breton, R.P., et al.: Low-radio-frequency eclipses of the redback pulsar J2215+5135 observed in the image plane with LOFAR. *Mon. Not. R. Astron. Soc.* **459**(3), 2681–2689 (2016). <https://doi.org/10.1093/mnras/stw794>
18. Burke-Spolaor, S., Taylor, S.R., Charisi, M., et al.: The astrophysics of nanohertz gravitational waves. *Astron. Astrophys. Rev.* **27**(1), 5 (2019). <https://doi.org/10.1007/s00159-019-0115-7>
19. Cameron, A.D., Barr, E.D., Champion, D.J., et al.: An investigation of pulsar searching techniques with the fast folding algorithm. *Mon. Not. R. Astron. Soc.* **468**(2), 1994–2010 (2017). <https://doi.org/10.1093/mnras/stx589>.
20. Camilo, F., Kerr, M., Ray, P.S., Saz Parkinson, P.M., Wood, K.S., et al.: Parkes radio searches of fermi gamma-ray sources and millisecond pulsar discoveries. *Astrophys. J.* **810**(2), 85 (2015). <https://doi.org/10.1088/0004-637X/810/2/85>
21. Chen, K., Ruderman, M.: Origin and radio pulse properties of millisecond pulsars. *Astrophys. J.* **408**, 179 (1993). <https://doi.org/10.1086/172578>
22. Chennamangalam, J., Lorimer, D.R.: The galactic centre pulsar population. *Mon. Not. R. Astron. Soc.* **440**, L86–L90 (2014). <https://doi.org/10.1093/mnrasl/slu025>
23. CHIME/Pulsar Collaboration, Amiri, M., Bandura, K.M., Boyle, P.J., et al.: The CHIME pulsar project: system overview. e-prints. arXiv:2008.05681 (2020)
24. Cognard, I., Guillemot, L., Johnson, T.J., et al.: Discovery of two millisecond pulsars in fermi sources with the Nançay radio telescope. *Astrophys. J.* **732**(1), 47 (2011). <https://doi.org/10.1088/0004-637X/732/1/47>
25. Crawford, F., Lyne, A.G., Stairs, I.H., et al.: PSR J1723-2837: an eclipsing binary radio millisecond pulsar. *Astrophys. J.* **776**(1), 20 (2013). <https://doi.org/10.1088/0004-637X/776/1/20>
26. Crowter, K., Stairs, I.H., McPhee, C.A., et al.: The GBT 350-MHz drift scan pulsar survey – III. Detection of a magnetic field in the eclipsing material of PSR J2256-1024. *Mon. Not. R. Astron. Soc.* **495**(3), 3052–3064 (2020). <https://doi.org/10.1093/mnras/staa933>

27. Dai, S., Hobbs, G., Manchester, R.N., et al.: A study of multifrequency polarization pulse profiles of millisecond pulsars. *Mon. Not. R. Astron. Soc.* **449**(3), 3223–3262 (2015). <https://doi.org/10.1093/mnras/stv508>
28. D’Amico, N., Possenti, A., Manchester, R.N., et al.: An eclipsing millisecond pulsar with a possible main-sequence companion in NGC 6397. *Astrophys. J. Lett.* **561**(1), L89–L92 (2001). <https://doi.org/10.1086/324562>
29. D’Amico, N., Possenti, A., Fici, L., et al.: Timing of millisecond pulsars in NGC 6752: evidence for a high mass-to-light ratio in the cluster core. *Astrophys. J. Lett.* **570**(2), L89–L92 (2002). <https://doi.org/10.1086/341030>
30. DeCesar, M.E., Ransom, S.M., Kaplan, D.L., et al.: A highly eccentric 3.9 millisecond binary pulsar in the globular cluster NGC 6652. *Astrophys. J. Lett.* **807**(2), L23 (2015). <https://doi.org/10.1088/2041-8205/807/2/L23>
31. Demorest, P.B., Pennucci, T., Ransom, S.M., et al.: A two-solar-mass neutron star measured using Shapiro delay. *Nature* **467**(7319), 1081–1083 (2010). <https://doi.org/10.1038/nature09466>
32. Deneva, J.S., Ray, P.S., Camilo, F., et al.: Multiwavelength observations of the redback millisecond pulsar J1048+2339. *Astrophys. J.* **823**(2), 105 (2016). <https://doi.org/10.3847/0004-637X/823/2/105>
33. Detweiler, S.: Pulsar timing measurements and the search for gravitational waves. *Astrophys. J.* **234**, 1100–1104 (1979). <https://doi.org/10.1086/157593>
34. Eatough, R., Lazio, T.J.W., Casanellas, J., et al.: Observing radio pulsars in the galactic centre with the square kilometre array. In: *Proceedings of Science, Advancing Astrophysics with the Square Kilometre Array (AASKA14)*, PoS(AASKA14), id. 45 (2015)
35. Faucher-Giguère, C.A., Kaspi, V.M.: Birth and evolution of isolated radio pulsars. *Astrophys. J.* **643**(1), 332–355 (2006). <https://doi.org/10.1086/501516>
36. Ferdman, R.D., Freire, P.C.C., Perera, B.B.P., et al.: Asymmetric mass ratios for bright double neutron-star mergers. *Nature* **583**(7815), 211–214 (2020). <https://doi.org/10.1038/s41586-020-2439-x>
37. Foster, R.S., Backer, D.C.: Constructing a pulsar timing array. *Astrophys. J.* **361**, 300 (1990). <https://doi.org/10.1086/169195>
38. Freire, P.C., Kramer, M., Lyne, A.G., et al.: Detection of ionized gas in the globular cluster 47 tucanae. *Astrophys. J. Lett.* **557**(2), L105–L108 (2001). <https://doi.org/10.1086/323248>
39. Freire, P.C.C., Ransom, S.M., Bégin, S., et al.: Eight new millisecond pulsars in NGC 6440 and NGC 6441. *Astrophys. J.* **675**(1), 670–682 (2008). <https://doi.org/10.1086/526338>
40. Fruchter, A.S., Stinebring, D.R., Taylor, J.H.: A millisecond pulsar in an eclipsing binary. *Nature* **333**(6170), 237–239 (1988). <https://doi.org/10.1038/333237a0>
41. Hellings, R.W., Downs, G.S.: Upper limits on the isotropic gravitational radiation background from pulsar timing analysis. *Astrophys. J. Lett.* **265**, L39–L42 (1983). <https://doi.org/10.1086/183954>
42. Hessels, J.W.T., Ransom, S.M., Stairs, I.H., et al.: A radio pulsar spinning at 716 Hz. *Science* **311**(5769), 1901–1904 (2006). <https://doi.org/10.1126/science.1123430>
43. Hui, C.Y., Wu, K., Han, Q., et al.: On the orbital properties of millisecond pulsar binaries. *Astrophys. J.* **864**(1), 30 (2018). <https://doi.org/10.3847/1538-4357/aad5ec>
44. Hulse, R.A., Taylor, J.H.: Discovery of a pulsar in a binary system. *Astrophys. J. Lett.* **195**, L51–L53 (1975). <https://doi.org/10.1086/181708>
45. Keane, E., Bhattacharyya, B., Kramer, M., et al.: A cosmic census of radio pulsars with the SKA. In: *Proceedings of Science, Advancing Astrophysics with the Square Kilometre Array (AASKA14)*, PoS(AASKA14), id. 40 (2015)
46. Keane, E.F., Barr, E.D., Jameson, A., et al.: The survey for pulsars and extragalactic radio bursts – I. Survey description and overview. *Mon. Not. R. Astron. Soc.* **473**(1), 116–135 (2018). <https://doi.org/10.1093/mnras/stx2126>
47. Konratiev, V.I., Verbiest, J.P.W., Hessels, J.W.T., et al.: A LOFAR census of millisecond pulsars. *Astron. Astrophys.* **585**, A128 (2016). <https://doi.org/10.1051/0004-6361/201527178>

48. Kramer, M.: Gravity tests with pulsars. In: Weltevrede, P., Perera, B.B.P., Preston, L.L., Sanidas S. (eds.) *Pulsar astrophysics the next fifty years*, vol. 337, pp. 128–133 (2018). <https://doi.org/10.1017/S1743921317009243>
49. Kramer, M., Xilouris, K.M., Lorimer, D.R., et al.: The characteristics of millisecond pulsar emission. I. Spectra, pulse shapes, and the beaming fraction. *Astrophys. J.* **501**(1), 270–285 (1998). <https://doi.org/10.1086/305790>
50. Kramer, M., Lyne, A.G., O'Brien, J.T., et al.: A periodically active pulsar giving insight into magnetospheric physics. *Science* **312**(5773), 549–551 (2006). <https://doi.org/10.1126/science.1124060>
51. Kramer, M., Stairs, I.H., Manchester, R.N., et al.: Tests of general relativity from timing the double pulsar. *Science* **314**(5796), 97–102 (2006). <https://doi.org/10.1126/science.1132305>
52. Kudale, S., Roy, J., Bhattacharyya, B., et al.: Study of eclipses for redback pulsar J1227-4853. *Astrophys. J.* **900**(2), 194 (2020). <https://doi.org/10.3847/1538-4357/aba902>
53. Kuniyoshi, M., Verbiest, J.P.W., Lee, K.J., et al.: Low-frequency spectral turn-overs in millisecond pulsars studied from imaging observations. *Mon. Not. R. Astron. Soc.* **453**(1), 828–836 (2015). <https://doi.org/10.1093/mnras/stv1604>
54. Kuzmin, A.D., Losovsky, B.Y.: No low-frequency turn-over in the spectra of millisecond pulsars. *A&A* **368**(1), 230–238 (2001). <https://doi.org/10.1051/0004-6361:20000507>
55. Lattimer, J.M., Prakash, M.: Neutron star structure and the equation of state. *Astrophys. J.* **550**(1), 426–442 (2001). <https://doi.org/10.1086/319702>
56. Lee, K.J., Bassa, C.G., Janssen, G.H., et al.: The optimal schedule for pulsar timing array observations. *Mon. Not. R. Astron. Soc.* **423**(3), 2642–2655 (2012). <https://doi.org/10.1111/j.1365-2966.2012.21070.x>
57. Levin, L., Armour, W., Baffa, C., et al., SKA TDT Team: Pulsar searches with the SKA. In: Weltevrede, P., Perera, B.B.P., Preston, L.L., Sanidas, S. (eds.) *Pulsar Astrophysics the Next Fifty Years*, vol. 337, pp. 171–174 (2018). <https://doi.org/10.1017/S1743921317009528>
58. Li, D., Lin, F.X., Main, R., et al.: Constraining magnetic fields through plasma lensing: application to the Black Widow pulsar. *Mon. Not. R. Astron. Soc.* **484**(4), 5723–5733 (2019). <https://doi.org/10.1093/mnras/stz374>
59. Liu, K., Wex, N., Kramer, M., et al.: Prospects for probing the spacetime of Sgr A* with pulsars. *Astrophys. J.* **747**(1), 1 (2012). <https://doi.org/10.1088/0004-637X/747/1/1>
60. Liu, K., Eatough, R.P., Wex, N., Kramer, M.: Pulsar-black hole binaries: prospects for new gravity tests with future radio telescopes. *Mon. Not. R. Astron. Soc.* **445**(3), 3115–3132 (2014). <https://doi.org/10.1093/mnras/stu1913>
61. Lorimer, D.R.: Binary and millisecond pulsars. *Living Rev. Relativ.* **11**(1), 8 (2008). <https://doi.org/10.12942/lrr-2008-8>
62. Lorimer, D.R., Kramer, M.: *Handbook of Pulsar Astronomy*, vol. 4. Cambridge Univ. Press, Cambridge (2004)
63. Lyne, A.G., Manchester, R.N.: The shape of pulsar radio beams. *Mon. Not. R. Astron. Soc.* **234**, 477–508 (1988). <https://doi.org/10.1093/mnras/234.3.477>
64. Lyne, A., Hobbs, G., Kramer, M., et al.: Switched magnetospheric regulation of pulsar spin-down. *Science* **329**(5990), 408 (2010). <https://doi.org/10.1126/science.1186683>
65. Manchester, R.N., IPTA: the international pulsar timing array. *Classical Quantum Gravity* **30**(22), 224010 (2013). <https://doi.org/10.1088/0264-9381/30/22/224010>
66. Manchester, R.N., Johnston, S.: Polarization properties of two pulsars. *Astrophys. J. Lett.* **441**, L65 (1995). <https://doi.org/10.1086/187791>
67. Manchester, R.N., Hobbs, G.B., Teoh, A., Hobbs, M.: The Australia telescope national facility pulsar catalogue. *Astron. J.* **129**(4), 1993–2006 (2005). <https://doi.org/10.1086/428488>
68. Martinez, J.G., Gentile, P., Freire, P.C.C., et al.: The discovery of six recycled pulsars from the arecibo 327 MHz drift-scan pulsar survey. *Astrophys. J.* **881**, 166 (2019). <https://doi.org/10.3847/1538-4357/ab2877>
69. McEwen, A.E., Spiewak, R., Swiggum, J.K., et al.: The green bank north celestial cap pulsar survey. V. Pulsar census and survey sensitivity. *Astrophys. J.* **892**(2), 76 (2020). <https://doi.org/10.3847/1538-4357/ab75e2>

70. Morello, V., Keane, E.F., Enoto, T., et al.: The survey for pulsars and extragalactic radio bursts – IV. Discovery and polarimetry of a 12.1-s radio pulsar. *Mon. Not. R. Astron. Soc.* **493**(1), 1165–1177 (2020). <https://doi.org/10.1093/mnras/staa321>
71. Papitto, A., Ferrigno, C., Bozzo, E., et al.: Swings between rotation and accretion power in a binary millisecond pulsar. *Nature* **501**(7468), 517–520 (2013). <https://doi.org/10.1038/nature12470>
72. Parent, E., Kaspi, V.M., Ransom, S.M., et al.: The implementation of a fast-folding pipeline for long-period pulsar searching in the PALFA survey. *Astrophys. J.* **861**(1), 44 (2018). <https://doi.org/10.3847/1538-4357/aac5f0>
73. Parent, E., Kaspi, V.M., Ransom, S.M., et al.: Eight millisecond pulsars discovered in the arecibo PALFA survey. *Astrophys. J.* **886**(2), 148 (2019). <https://doi.org/10.3847/1538-4357/ab4f85>
74. Perera, B.B.P., DeCesar, M.E., Demorest, P.B., et al.: The international pulsar timing array: second data release. *Mon. Not. R. Astron. Soc.* **490**(4), 4666–4687 (2019). <https://doi.org/10.1093/mnras/stz2857>
75. Pleunis, Z., Bassa, C.G., Hessels, J.W.T., et al.: A millisecond pulsar discovery in a survey of unidentified fermi γ -ray sources with LOFAR. *Astrophys. J. Lett.* **846**(2), L19 (2017). <https://doi.org/10.3847/2041-8213/aa83ff>
76. Podsiadlowski, P., Rappaport, S., Pfahl, E.D.: Evolutionary sequences for low- and intermediate-mass X-ray binaries. *Astrophys. J.* **565**(2), 1107–1133 (2002). <https://doi.org/10.1086/324686>
77. Polzin, E.J., Breton, R.P., Clarke, A.O., et al.: The low-frequency radio eclipses of the black widow pulsar J1810+1744. *Mon. Not. R. Astron. Soc.* **476**(2), 1968–1981 (2018). <https://doi.org/10.1093/mnras/sty349>
78. Polzin, E.J., Breton, R.P., Stappers, B.W., et al.: Long-term variability of a black widow's eclipses – A decade of PSR J2051-0827. *Mon. Not. R. Astron. Soc.* **490**(1), 889–908 (2019). <https://doi.org/10.1093/mnras/stz2579>
79. Polzin, E.J., Breton, R.P., Bhattacharyya, B., et al.: Study of spider pulsar binary eclipses and discovery of an eclipse mechanism transition. *Mon. Not. R. Astron. Soc.* **494**(2), 2948–2968 (2020). <https://doi.org/10.1093/mnras/staa596>
80. Radhakrishnan, V., Cooke, D.J.: Magnetic poles and the polarization structure of pulsar radiation. *Astrophys. Lett.* **3**, 225 (1969)
81. Rankin, J.M.: Toward an empirical theory of pulsar emission. VI. The geometry of the conal emission region. *Astrophys. J.* **405**, 285 (1993). <https://doi.org/10.1086/172361>
82. Ransom, S.M., Hessels, J.W.T., Stairs, I.H., et al.: Twenty-one millisecond pulsars in terzan 5 using the green bank telescope. *Science* **307**(5711), 892–896 (2005). <https://doi.org/10.1126/science.1108632>
83. Ransom, S.M., Ray, P.S., Camilo, F., et al.: Three millisecond pulsars in fermi LAT unassociated bright sources. *Astrophys. J. Lett.* **727**(1), L16 (2011). <https://doi.org/10.1088/2041-8205/727/1/L16>
84. Rasio, F.A., Pfahl, E.D., Rappaport, S.: Formation of short-period binary pulsars in globular clusters. *Astrophys. J. Lett.* **532**(1), L47–L50 (2000). <https://doi.org/10.1086/312555>
85. Ravi, V., Manchester, R.N., Hobbs, G.: Wide radio beams from γ -ray pulsars. *Astrophys. J. Lett.* **716**(1), L85–L89 (2010). <https://doi.org/10.1088/2041-8205/716/1/L85>
86. Roberts, M.S.E.: Surrounded by spiders! New black widows and redbucks in the Galactic field. In: van Leeuwen, J. (ed.) *Neutron Stars and Pulsars: Challenges and Opportunities After 80 Years*, vol. 291, pp. 127–132 (2013). <https://doi.org/10.1017/S174392131202337X>
87. Romani, R.W., Yadigaroglu, I.A.: Gamma-ray pulsars: emission zones and viewing geometries. *Astrophys. J.* **438**, 314 (1995). <https://doi.org/10.1086/175076>
88. Roy, J., Ray, P.S., Bhattacharyya, B., et al.: Discovery of Psr J1227-4853: a transition from a low-mass X-ray binary to a redback millisecond pulsar. *Astrophys. J. Lett.* **800**(1), L12 (2015). <https://doi.org/10.1088/2041-8205/800/1/L12>
89. Sanidas, S., Cooper, S., Bassa, C.G., et al.: The LOFAR tied-array all-sky survey (LOTAAS): survey overview and initial pulsar discoveries. *Astron. Astrophys.* **626**, A104 (2019). <https://doi.org/10.1051/0004-6361/201935609>

90. Shemar, S.L., Lyne, A.G.: Observations of pulsar glitches. *Mon. Not. R. Astron. Soc.* **282**(2), 677–690 (1996). <https://doi.org/10.1093/mnras/282.2.677>
91. Spitler, L.G., Lee, K.J., Eatough, R.P., et al.: Pulse broadening measurements from the galactic center pulsar J1745-2900. *Astrophys. J. Lett.* **780**(1), L3 (2014). <https://doi.org/10.1088/2041-8205/780/1/L3>
92. Staelin, D.H.: Fast folding algorithm for detection of periodic pulse trains. *IEEE Proc.* **57**, 724–725 (1969). <https://doi.org/10.1109/PROC.1969.7051>
93. Stappers, B.W., Bailes, M., Lyne, A.G., et al.: Probing the eclipse region of a binary millisecond pulsar. *Astrophys. J. Lett.* **465**, L119 (1996). <https://doi.org/10.1086/310148>
94. Stappers, B.W., Keane, E.F., Kramer, M., et al.: The prospects of pulsar timing with new-generation radio telescopes and the Square Kilometre Array. *Philos. Trans. R. Soc. Lond. A* **376**(2120), 20170293 (2018). <https://doi.org/10.1098/rsta.2017.0293>
95. Stovall, K., Freire, P.C.C., Chatterjee, S., et al.: PALFA discovery of a highly relativistic double neutron star binary. *Astrophys. J. Lett.* **854**(2), L22 (2018). <https://doi.org/10.3847/2041-8213/aaad06>
96. Tauris, T.M., Savonije, G.J.: Formation of millisecond pulsars. I. Evolution of low-mass X-ray binaries with $P_{\text{orb}} > 2$ days. *Astron. Astrophys.* **350**, 928–944 (1999)
97. Taylor, J.H., Weisberg, J.M.: A new test of general relativity – gravitational radiation and the binary pulsar PSR 1913+16. *Astrophys. J.* **253**, 908–920 (1982). <https://doi.org/10.1086/159690>
98. Thompson, C., Blandford, R.D., Evans, C.R., Phinney, E.S.: Physical processes in eclipsing pulsars: eclipse mechanisms and diagnostics. *Astrophys. J.* **422**, 304 (1994). <https://doi.org/10.1086/1086173728>
99. Wharton, R.S., Chatterjee, S., Cordes, J.M., et al.: Multiwavelength constraints on pulsar populations in the galactic center. *Astrophys. J.* **753**(2), 108 (2012). <https://doi.org/10.1088/0004-637X/753/2/108>
100. Xilouris, K.M., Kramer, M., Jessner, A., et al.: The characteristics of millisecond pulsar emission. II. Polarimetry. *Astrophys. J.* **501**(1), 286–306 (1998). <https://doi.org/10.1086/305791>

Chapter 2

The High-Energy Emission of Millisecond Pulsars



Diego F. Torres and Jian Li

Abstract This chapter provides a phenomenological appraisal of the high-energy emission of millisecond pulsars. We comment on some of their properties as a population, as well as consider the special cases of transitional pulsars, other redbacks, and black widow systems.

2.1 Millisecond Pulsars in the *Fermi*-LAT Era

The *Fermi* gamma-ray telescope was launched on June 11, 2008. The main instrument onboard *Fermi* is the Large Area Telescope (LAT). The LAT is an imaging high-energy gamma-ray telescope working in the energy range from 20 MeV to above 300 GeV. The LAT has a large field of view (20% sky coverage at any time), as well as a significant effective area (on the scale of 10^4 cm^2). LAT is mostly operating in a survey mode, scanning the whole sky every three hours. Because of its large effective area and field of view, maximized with a survey strategy, *Fermi*-LAT has been the main working horse in gamma-ray pulsar research since its launch. During the three decades after the discovery of what was meant to be the first gamma-ray pulsar (i.e., the Crab pulsar, PSR B0531+21; [34]), only seven pulsars were known to emit in gamma-rays. Within only six months since its launch, Fermi-LAT has increased this number to 46 [4], and later to 117 in three years [6]. Until December

D. F. Torres (✉)

ICREA & Institute of Space Sciences (ICE, CSIC), & Institut d'Estudis Espacials de Catalunya, Barcelona, Spain

e-mail: dtorres@ice.csic.es; dtorres@ieec.uab.es

J. Li

Deutsches Elektronen Synchrotron DESY, Zeuthen, Germany

e-mail: jian.li@desy.de

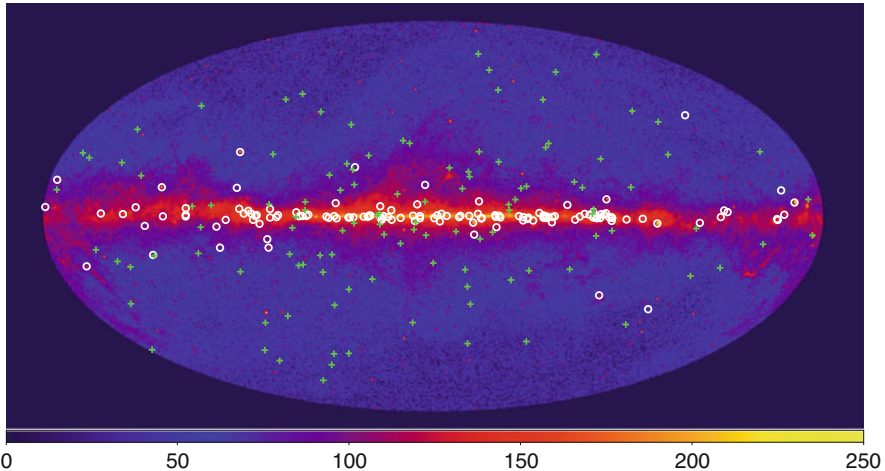


Fig. 2.1 Eight years of *Fermi*-LAT observations: all-sky map above 1 GeV. Gamma-ray millisecond pulsars are shown with green crosses while other gamma-ray pulsars are shown with white circles. The map in the background is adapted from Fig. 1 of Smith et al., arXiv:1706.03592 (2017), [106]

27, 2019, the number of *Fermi*-LAT detected gamma-ray pulsars reached 250.¹ This population is composed of 115 millisecond pulsars (MSPs, $P < 30$ ms) and 135 young, non-recycled pulsars ($P > 30$ ms). Their positions are shown in Fig. 2.1, on the background of the eight-years *Fermi*-LAT all sky map above 1 GeV (see e.g., [106]). Gamma-ray MSPs (in short, referred to as gMSPs in what follows) are scattered at larger Galactic latitude in comparison to gamma-ray young pulsars, which are mainly distributed in the Galactic plane. This is consistent with most of MSP being of recycled nature (neutron-star formation in an evolving binary system and spin-up due to accretion from the binary companion; see Sect. 4.1 for details on the recycling scenario), leading to a larger age of their population.

This chapter provides a phenomenological appraisal of the high-energy emission of millisecond pulsars. We comment on some of their properties as a population, as well as consider the especial cases of transitional pulsars (see also Chap. 6 for the phenomenology of these sources), other redbacks, and black widow systems (see also Sects. 1.4.3 and 6.5.1). An interesting and complementary overview can be found in the work of Smith et al. [106]. Chapter 3 in this same volume will deal with theoretical aspects of the high-energy emission from millisecond pulsars beyond what we mention here (see also Venter et al. [117]).

Besides the obviously faster spin period (\dot{P}) and much smaller value of period derivative (\ddot{P}), many different characteristics have been revealed when comparing

¹ See the updated list at <https://confluence.slac.stanford.edu/display/GLAMCOG/Public+List+of+LAT-Detected+Gamma-Ray+Pulsars>.

Table 2.1 Gamma-ray millisecond pulsar varieties as of December 27, 2019

Category	#	Fraction
Known gamma-ray MSP	115	
... with radio pulsation	112	97.4%
... without radio pulsation	3	2.6%
... Isolated	24	20.9%
... In binaries	91	79.1%
Redbacks	10	
Black widows	21	

the population of gMSPs with that of the gamma-ray young pulsars observed by *Fermi*-LAT, as reported in the gamma-ray pulsar catalogs [4, 6]. Among these differences, we can emphasize that gMSPs have lower gamma-ray luminosities compared to gamma-ray young pulsars, which explains why gMSPs are often detected at nearer distances. Gamma-ray pulsars are multi-wavelength objects and many of them are bright also in X-rays. The observed gamma-ray to X-ray flux ratio is lower for gMSPs, and it is less scattered than that observed for the gamma-ray young pulsars. The spectra of gamma-ray pulsars are usually modelled by a power-law with exponentially cutoff. The power-law index Γ shows a mild correlation with the spin down power \dot{E} for gMSPs and gamma-ray young, radio-quiet pulsars, with a Pearson correlation factor of 0.58 and 0.68, respectively. The cutoff energy E_{cut} correlates with the magnetic field strength at light cylinder, with a Pearson correlation factor of 0.52 for gMSPs and 0.64 for gamma-ray young, radio-quiet pulsars. Again, some dispersion is found also here. The Vela [67] and Crab [22] pulsar, both of which are gamma-ray young pulsars, have also been detected by Imaging Atmospheric Cherenkov Telescopes at very high energies (VHE) above 100 GeV. No gMSP has been detected in the VHE range so far.

We note that most of the 115 currently known *Fermi*-LAT gMSPs are also detected having radio pulsations (see Table 2.1). We show the distribution of P and \dot{E} of gMSPs with and without radio pulsations in Fig. 2.2. No difference can be drawn. Roughly 80% of *Fermi*-LAT detected gMSPs are in binary systems (see Table 2.1). The distribution of P and \dot{E} comparing isolated gMSPs and gMSPs in binaries is also shown in Fig. 2.2. The spin-down power distribution is consistent between these two populations. However, the spin period of isolated gMSPs shows a hint for a bimodal distribution, which is different from that found of gMSPs in binary systems. However, we caveat that the current population of isolated gMSPs is comparably small (24, see Table 2.1). It is expected that a future catalog of *Fermi*-LAT gamma-ray pulsars may shed light on this point, having higher statistics.

Among MSPs in binaries, there are two interesting sub-groups known as redbacks (RBs) and black widows (BWs), on which we provide further details below. They are tight binaries ($P_{orb} < 1$ day) with a low mass companion star (BWs, $M_{companion} \ll 0.1 M_{Sun}$, e.g., [64]; RBs, $M_{companion} \sim 0.2 - 0.4 M_{Sun}$, see e.g., [52]). In these cases, the strong pulsar wind is continuously ablating their companion star, leading to mass loss as indicated by the irregular eclipses of the

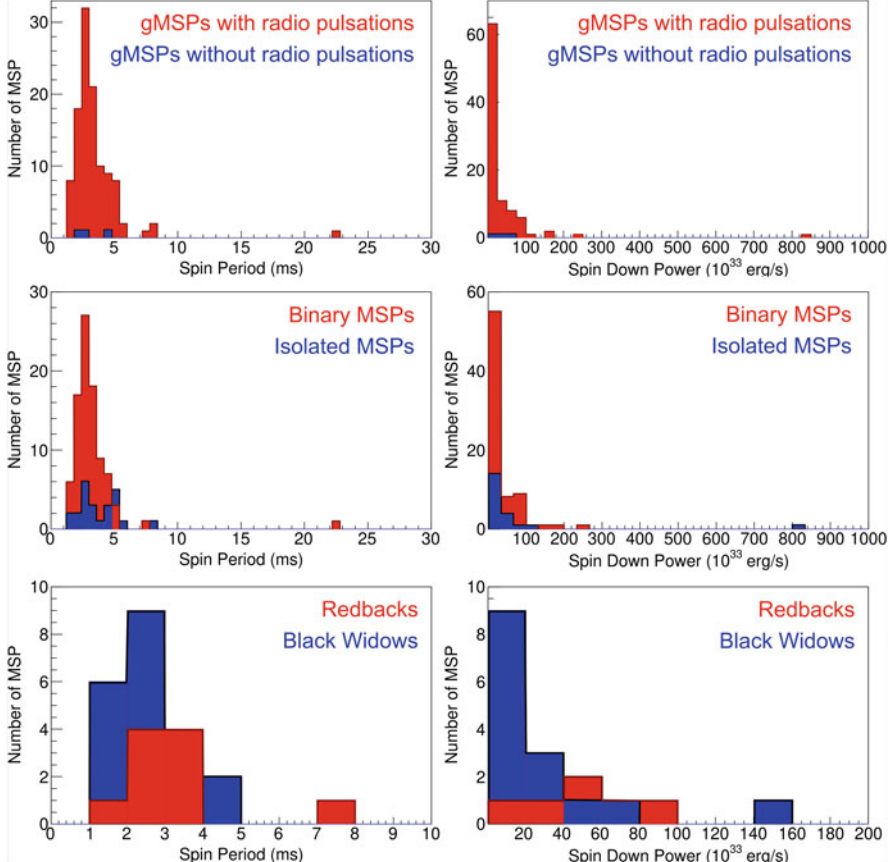


Fig. 2.2 Top: Distribution of pulsar spin periods and spin down powers of the gMSPs with and without radio pulsation. Middle: *ibid.* but for isolated gMSPs and gMSPs in binaries. Bottom: *ibid.* but for redbacks and black widows

radio pulsed emission, which are in turn caused by the absorption and scattering of the ejected matter. Many of these systems have been discovered by radio surveys in our Galaxy (see the ATNF Pulsar Catalog;² [83]). *Fermi*-LAT detected 10 RB and 21 BW (see the Millisecond Pulsar Catalogue maintained by A. Patruno³). The spin period distributions of these RBs and BWs are consistent, while the RBs may have a wider spin down power distribution than BWs (Fig. 2.2). However, again, a large uncertainty still exists because of the small population considered, and these apparent differences have to be taken with extreme caution for the moment.

² <http://www.atnf.csiro.au/people/pulsar/psrcat/>.

³ <https://apatruno.wordpress.com/about/millisecond-pulsar-catalogue/>.

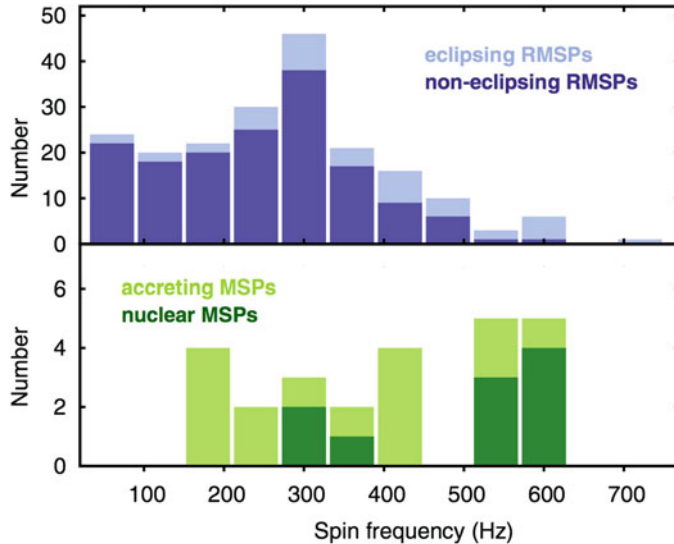


Fig. 2.3 Spin frequency distribution of binary non-eclipsing and eclipsing rotation-powered millisecond pulsars, and nuclear-powered and accreting millisecond pulsars. Credit: Papitto et al., A&A, 566, A64 (2014), reproduced with permission © ESO

In a greater context, the comparison of the spin frequency distributions of different samples of MSPs can be used to test theories describing the spin evolution of NSs as they evolve from the accretion to the rotation-powered stages of the recycling scenario. For instance, to study whether accreting MSPs are faster than binary millisecond radio pulsars (RMSPs), as noted by several authors (e.g., see [62, 69, 110] and references therein). Considering the total population, and not just the gMSPs, the spin frequency distributions of binary millisecond pulsars have been recently studied by Papitto et al. [90] (see Fig. 2.3). They found that even though accreting MSPs are on-average faster than RMSPs by ~ 100 Hz, comparing the two distributions could not exclude the possibility that they come from the same parent distribution. Simulations revealed that to detect a 3σ difference to the rotational-powered MSP distribution there need to be at least 50 accreting MSPs. Assuming a normal distribution, this implies that if the spin frequency distributions of accreting MSPs and RMSPs are different, the difference would be visible when the number of known accreting MSPs has increased by more than a factor of three. Only nuclear MSPs, i.e., nuclear-powered millisecond pulsars, with coherent-oscillations observed exclusively during thermonuclear type I X-ray bursts, are significantly faster than the rotational-powered MSPs. Patruno et al. [94] later concluded to a higher statistical significance that the observed population of RMSPs (excluding RBs and BWs) is slower than accreting MSPs in LMXBs (including also nuclear MSPs). In addition, two populations of MSPs in LMXBs were identified (clustering around 300 and 575 Hz), with the spin distribution of the population of RMSPs

being compatible with the slower one. Taking all of this into account, an obvious question arises.

2.2 Do Accreting Millisecond Pulsars Shine in Gamma-Rays?

Accretion-powered millisecond pulsars (AMSPs, see Chap. 4 for a broad review) normally orbit a low-mass companion star ($\sim 1 M_{\odot}$ or less) and show coherent X-ray pulsations. The latter are caused by the impact of an accretion stream onto the neutron star surface. Thus, the coherent pulsations observed in the X-ray light curves (especially during outburst) occurs as a result of a kinetic, thermal process in nature, where at least part of the matter in the accretion flow is channeled to the surface of the star. The prototypical source for this class is SAX J1808.4–3658, the first AMSP discovered [118]. Can such an accreting environment be also prone to the production of higher-energy gamma-rays? How? Can a radio and gamma-ray pulsar arise in periods of quiescence when accretion is not that dramatic? These questions have unclear answers for the moment.

Despite radio pulsations have not been detected from AMSPs up to the moment of writing⁴ (see, e.g., [36, 72]; the case of transitional pulsars is discussed in the next section), some indications of an active pulsar state occurring in generic AMSPs during X-ray quiescence have been put forward. The amount of optical light reprocessed by the companion star during X-ray quiescence in SAX J1808.4–3658 [70] is compatible with irradiation by a radio pulsar [35]. Also, the decrease of the spin period of the neutron stars between consecutive outbursts is similar to the rate observed from MSPs [93]. However, these are only indirect hints that such a scenario is not ruled out, not proof of its existence.

In gamma-rays, specially interesting due to their unscathed escape from significant absorption, the sky region of several AMSPs was investigated by Xing et al. [120], leading to no detections. The orbital uncertainties, as well as the limited time span of their search (4 years) could perhaps have played a role in their lack of detection of any candidate. Indeed, the impact of the orbital uncertainties on the timing of pulsars in binary systems is large. Caliandro et al. [37] recently presented an analytical study aimed to understand this impact on pulsation searches for uncertainties in each of the orbital parameters and validated it with numerical simulations. Their Table 3 summarizes the results.

Xing et al. [122] later reported a barely significant modulation of SAX J1808.4–3658 at the spin-period, although perhaps the most relevant indication of gamma-ray emission from accreting millisecond pulsars is to be found in the work by de Oña

⁴ Recently, optical and UV pulsations have been detected during a bright X-ray outburst of the AMSP SAX J1808.4–3658, and interpreted as likely driven by synchro-curvature radiation in the pulsar magnetosphere, or just outside [18].

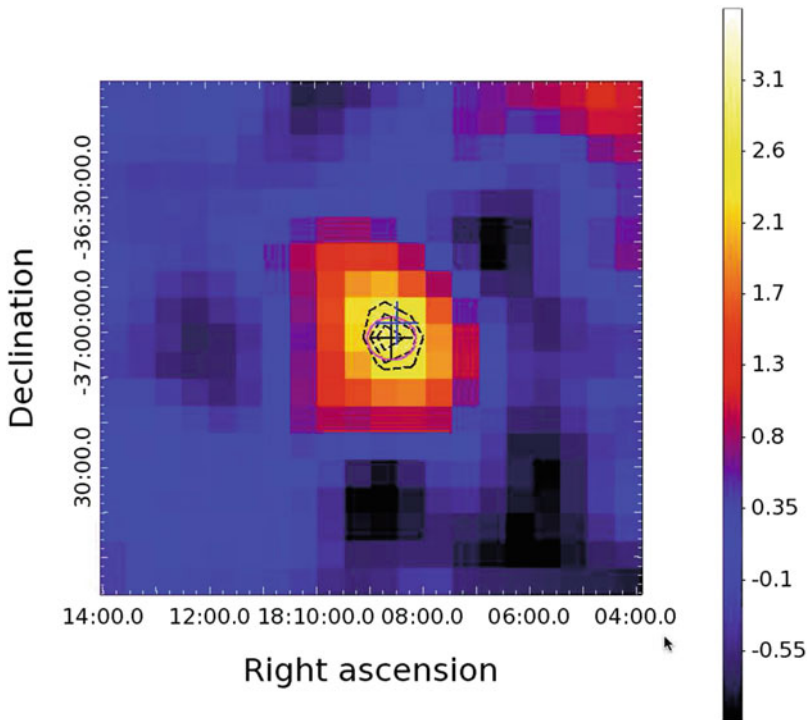


Fig. 2.4 Image created using 6 years of data from the Large Area Telescope on board the Fermi Gamma-ray Space Telescope. *Fermi*-LAT residual $2^\circ \times 2^\circ$ (using a pixel size of $0.1^\circ \times 0.1^\circ$) count map above 1 GeV of the SAX J1808.4–3658 region smoothed with a Gaussian of width $\sigma = 0.3^\circ$ (units of the scale on the right are counts). The best-fit position of the gamma-ray source is marked with a black cross whereas the position of SAX J1808.4–3658 is marked in blue. Credit: de Oña Wilhelmi et al., MNRAS, 456, 2647 (2016)

Wilhelmi et al. [56]. They revealed a point gamma-ray source at a significance of $\sim 6\sigma$ with a position compatible with that of SAX J1808.4–3658 within 95% confidence level (see Fig. 2.4). Its flux and spectral parameters resulted compatible with that of 3FGL J1808.4–3703, a source in the 3FGL catalogue that is also compatible with the position of SAX J1808.4–3658. De Oña Wilhelmi et al. [56] could not claim an association by timing, though, given that the search for gamma-ray pulsations is limited by the uncertainties in the ephemeris and position of the source as well as by its dim character. However, they did rule out the existence of other possible obvious candidates to producing the gamma-rays observed beside the AMSP. If proven true, SAX J1808.4–3658 in X-ray quiescence will be similar to, for instance, PSR J1311–3430 [95, 96], also a fast MSP (~ 2.5 ms) in a compact binary system (~ 2 h). The spectral parameters are also compatible within the current statistics to the ones found in other MSPs, with a hard spectrum and a turn over at a few GeV.

If the detection of SAX J1808.4–3658 is confirmed, the implication is that the AMSP would be active in gamma-rays along the whole quiescent state. The fully opposite alternative from associating gamma-ray emission to ASMPs could come from the possibility that the former is transient, and perhaps linked with outburst events.

A recent search for gamma-ray emission from AMSPs from this perspective have been presented by Xing et al. [123]. They reported hints for detection of GRO J1008–57, a Be X-ray binary with transient X-ray pulsar, detectable during X-ray outbursts of the source, having a period of 93.5 s [45]. Interestingly, the magnetic field of the pulsar is known to be the highest among the Be XRBs, likely as high as 8×10^{12} G [104]. GRO J1008–57 shows type-I X-ray outbursts at each periastron passage (e.g., [114]), produced by the interaction between the neutron star and the circumstellar disk around the Be companion (e.g., [97]), and also, occasionally, type-II outbursts. Xing et al. [123] proposed that the source also occasionally flares in gamma-rays, following giant X-ray outbursts. Li et al. [77] have also earlier proposed a similar case for the transient gamma-ray behavior detected as GRO J1036–55 and AGL J1037–5708 to be associated with the HMXB 4U 1036–56. In fact, their table 1 shows a list of unidentified transient gamma-ray sources in the Galactic plane with possible binary nature. However, although not yet ruled out, evidence for an association is circumstantial in all these cases, since at the end of the day, it is mostly based on positional coincidence: the occurrence of the gamma-ray emitting events did not precisely coincide with any X-ray outbursts involved. In the case of GRO J1008–57, not even a uniform displacement (all after, or all before) of the putative gamma-ray emission and the outburst is found (see, e.g., Figure 5 of [123]).

From a theoretical perspective, it is unclear how an accreting scenario could lead to gamma-ray pulsations. Based on the work by Cheng et al. [40], Romero et al. [100] suggested that hadronic process, in which hadrons accelerated from the magnetosphere of the neutron star could impact the surrounding accretion disk, could lead to observable gamma-ray emission. They applied this model to A 0535+26 back in EGRET times. However, no further *Fermi*-LAT detection of the source has been found, and additionally, in this model one would also expect a significant neutrino yield [21] which has not been detected either (see, e.g., [1, 7]). Bednarek [27, 28] proposed that gamma-rays can be produced at a turbulent and magnetized transition region formed due to the balance between the magnetic pressure and the pressure injected by the accreting matter. Depending on the accretion level, matter can either accrete or be expelled away, similarly to a propeller. However, it is unclear in these models how the pulsations could be maintained, and in particular, how could a magnetosphere sustain penetration of accreting matter without being disrupted. We discuss more on this in the next section, related to transitional pulsars.

The recent radio detection of an evolving jet from a strongly-magnetised accreting X-ray pulsar have been also put forward [101, 115]. Whereas the nature of origin of the radio emission (whether in a jet, or otherwise) may be yet unclear, the fact that there is likely non-thermal emission in these environments is not. The

same region of non-thermal particle acceleration can also be prone to gamma-ray production.

At this time, however, we can safely conclude that it is yet unclear whether gamma-ray emission from purely AMSPs has or has not been detected yet. The dim character of the expected emission and slow increase in signal-to-noise ratio with time in a gamma-ray background-dominated domain play against a ready confirmation. Further observations of the most promising candidates are needed in order to reach to a definite claim. In particular, AMSP transient emission would be certainly detectable (provided it reaches to sufficiently high energy, of course) by the Cherenkov Telescope Array [41]. The capabilities of the latter in comparison with *Fermi*-LAT are much better for shorter events, e.g., it can be up to tens of thousands of times for sensitive for events lasting an hour or less. This capability may open a yet-unchartered transient gamma-ray sky.

2.3 Gamma-Ray Emission from Transitional Millisecond Pulsars

PSR J1023+0038 [23, 107] was the first source for which two different states (accretion and rotational) were suggested. Later on, swings between a rotation-powered MSP state and an accretion-powered low mass X-ray binaries (LMXB) state were caught on a few-weeks timescale in the transient system IGR J18245–2452 [89]. Such timescales could then be compatible with those of the accretion flow. XSS J12270–4859 [26, 53–55], has also been observed to transition. These systems are called transitional pulsars. The varied and complex phenomenology of these transitions is also broadly reviewed by Chap. 6 in this book, which should be read concurrently with this section to get a full panorama. We shall only provide here some comments describing the multi-wavelength phenomenology, focusing on what relates to describing the gamma-ray properties of these sources.

We have clearly defined states at the two extremes of the transition: On the one hand, at high mass inflow rates, the radio pulsar is likely shut-off, the system is bright in X-rays ($L_X > 10^{36} \text{ erg s}^{-1}$). This is an accretion state, similar to other AMSPs in LMXB. On the other hand, at sufficiently low mass inflow rates, the magnetosphere likely dominates the scenario and is in full fledge up to the light cylinder, the radio pulsar is active, the disk disappears and the system is instead dimmer in X-rays ($L_X \sim 10^{32} \text{ erg s}^{-1}$).

The most interesting behavior happens in between these two extremes, where all three sources mentioned have been observed to be in a sub-luminous accretion state, with X-ray luminosities in between (of the order of ($L_X \sim 10^{33} \text{ erg s}^{-1}$)). In this sub-luminous state (also called, active state) these systems vary their X-ray fluxes from a low to a high mode (spending most of the time in the latter) with occasional flaring. Whereas the states (both the radio pulsar and sub-luminous state) can be stable along years, the mode-changing within the sub-luminous state,

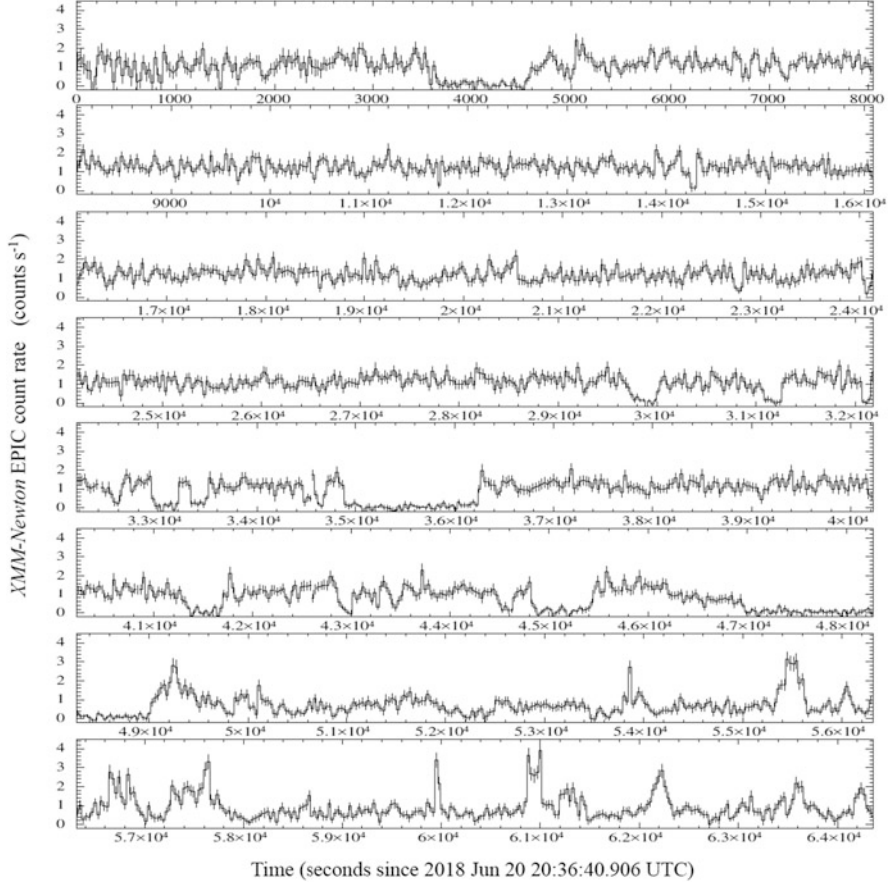


Fig. 2.5 An example of a sub-luminous state for a transitional pulsar. 0.3–10 keV background-subtracted and exposure-corrected light curve of CXOU J110926.4–650224, as obtained with XMM–Newton EPIC with a time bin of 30 s. Credit: Coti Zelati et al., A&A, 622, A211 (2019), reproduced with permission ©ESO

which has been seen in all transitional sources, can be very fast, and has been often found on a time scale of a few seconds. What causes such rapid changes is not yet well understood. Figure 2.5 provides a graphical example of the evolution of the X-ray luminosity in one of the transitional pulsars candidates, CXOU J110926.4–650224. General features regarding the variability are generic in all members of the class. In fact, such features of the sub-luminous state are the defining characters of transitional pulsars as we understand them now, although the community is still calling them candidates until the rotational state is observed (what may well never happen in our lifetime, given the decades-long duration of the sub-luminous states in the prototypical sources). At least five candidates to transitional pulsar systems have been identified. Coti Zelati et al. [51] list their properties (see their Table 6,

as well as provide detailed references for them all). They all share in the general features of the sub-luminous states, with their high and low modes, but have not been observed to undergo a state transition so far.

It is interesting to note that the gamma-ray emission also transitions from quiescence to the active state simultaneously with the X-rays and optical flux. For instance, in the cases of J1023+0038 [107], and J1227–4853 [73] (by the way, both being RB systems), their gamma-ray flux was observed to vary by a factor of 2 to 5. Recently, Torres et al. [113] considered 7 years of *Fermi*-LAT data to search transitions between states in all redbacks and black widows. Figure 2.6 shows the long-term light curves and the spectra of the transitional millisecond pulsars J1023+0038 and J1227–4853. Regarding the spectra, high-energy cutoffs at a few GeV are established for the high gamma-ray state of PSR J1023+0038 and for both states of PSR J1227–4853. In the light curves, the state transitions are indicated with dotted vertical lines. The red lines in Fig. 2.6 show the flux upper limits. The dotted horizontal green line indicates $TS = 12$ (which for *Fermi*-LAT is roughly equivalent to about 3.5σ confidence level). In the analysis by Torres et al. [113], the smallest time bin so that a state transition similar to those found in the known transitional pulsars would be detected with high confidence was defined for each system analysed. For instance, in the case of J1023+0038 and J1227–4853 this time bin is 8 and 53 days, respectively, and the light curve under these bins are shown in the second row of Fig. 2.6. With this method, it can be seen that whereas in the low state, the flux evolution is compatible with being constant, the high gamma-ray state conflicts with a constant flux. For instance, for J1227–4853, it is ruled out with a significance of 4.7σ , likely indicating the action of shorter-timescale phenomena also in gamma-rays. Indeed, under the current understanding of transitional pulsars, it is expected that at least in the low mode of the sub-luminous state the rotationally-powered MSP is active again (and with it, the gamma-ray emission) [39, 81]. If this is true, by adjoining all low-mode periods of the sub-luminous state one should be able to acquire a gamma-ray signal. This signal should in principle be the pure contribution of the MSP. This test is however hampered by the fact that one would need a constant monitoring to determine all the low-mode periods in the light curve, given that with the historic simultaneous X-ray/gamma-ray data, adjoining all such already-determined periods does not allow for enough statistics to be acquired. No significant upper limit can be put.

Using the same binning method referred above, Torres et al. [113] found no hint for a state transition for most of the studied pulsars, two black-widow systems, PSR J2234+0944 and PSR J1446–4701 have an apparent variability that is reminiscent of the transitions in PSR J1023+0038 and PSR J1227–4853.

Evidence for gamma-ray pulsations in J1023+0038 during the quiescent state has been presented by Archibald et al. [24]. They presented evidence at the 3.7σ confidence level (using gamma-ray data from 2008 to 2012, before the transition). Currently in the active state, pulsations remain hidden. Additionally, X-ray pulsations at the neutron star spin period have been earlier observed to exist both in the quiescent state and in the high mode of the active state [25]. These high-mode pulsations were initially understood in terms of intermittent, and partial,

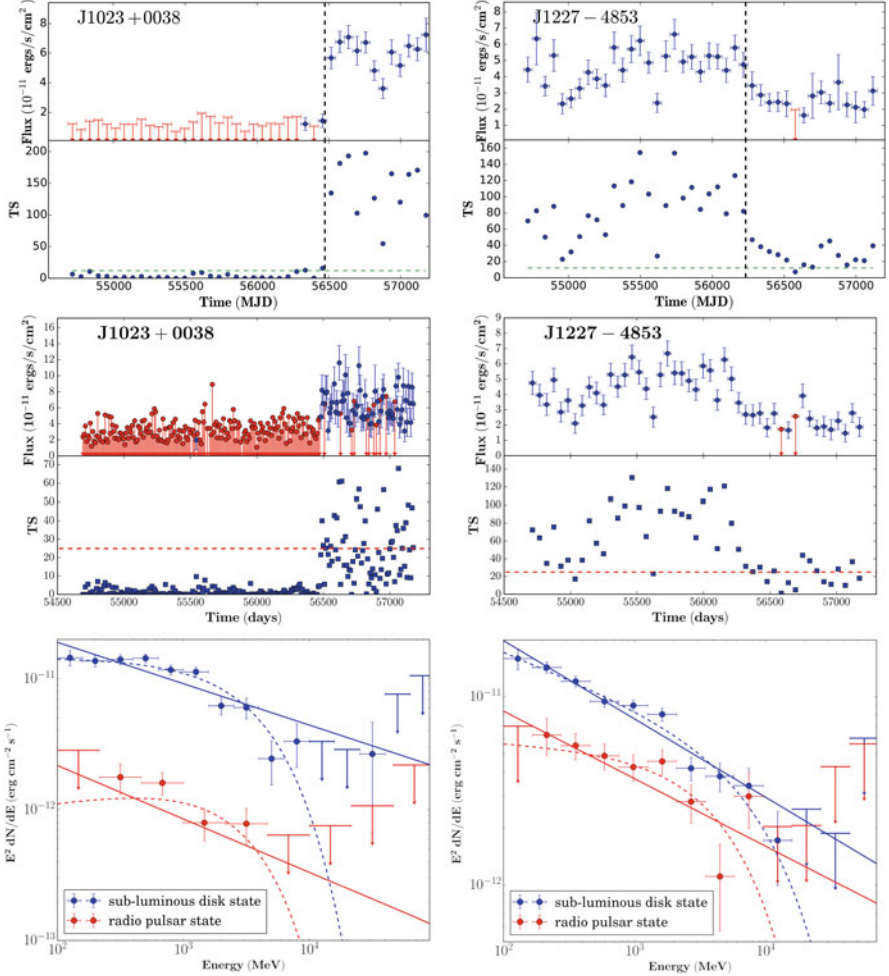


Fig. 2.6 The first row shows the long-term light curves of the transitional millisecond pulsars J1023+0038 and J1227-4853. The already known [26, 107] state transitions are indicated with dotted vertical lines. The red lines show the flux upper limits. The dotted horizontal green line indicates $TS = 12$. The second row shows the same data but analyzed using a smaller time bin defined by simulations. The third row shows the *Fermi*-LAT spectra of J1023+0038 (left) and J1227-4853 (right), in radio pulsar state (red) and sub-luminous disk state (blue). Credit: Torres et al., ApJ, 836, 68 (2017) © AAS. Reproduced with permission

mass accretion onto the NS surface. The 1.69 ms spin period of PSR J1227-4853 (in system XSS J12270-4859) was also recently discovered in gamma-rays, once the source transitioned to a rotation-powered MSP, as inferred from decreases in optical, X-ray, and gamma-ray flux from the source [73].

Transitional pulsars are then the only low-mass X-ray binaries from which emission at energies of few GeVs has been undoubtedly observed. The immediate interpretation that has been put forward is that the gamma-ray emission is due to a disk/pulsar wind shock, similar to gamma-ray binaries (see below, and, e.g., [50, 79, 107, 109]). In these scenarios, a rotation-powered pulsar must be active even in the presence of an accretion disk, when the radio coherent pulsation is washed out by the enshrouding of the system by intra-binary material. In more detail, Stappers et al. [107] and Coti Zelati et al. [50] proposed that the pulsar wind/mass in-flow shock is the region where the gamma-ray emission is generated. Instead, Takata et al. [109] and Li et al. [79] interpreted the gamma-ray emission through inverse Compton scattering of UV disk photons directly by the wind. Here, the X-rays are due to synchrotron emission taking place in the shock between the pulsar wind and the plasma in-flow. Such a shock would be expected to be stronger in the sub-luminous disk state when a larger fraction of the pulsar wind would be intercepted.

However, the observation of coherent X-ray pulsations –with an rms amplitude of ≈ 6 per cent during the accretion disk state– is difficult to reconcile with these interpretations. If these are rotation-powered, then when a disk is present the pulsed flux increases more than one order of magnitude with respect to the case of an unperturbed magnetosphere. What makes this happen? In fact, one would expect that the larger the plasma density, the more shorted out the electric fields which power the electron/positron acceleration should be. Also the total energy reservoir would be in doubt. The sum of the average luminosity observed from J1023+0038 in just the 0.3–79 keV and 0.1–100 GeV energy bands amounts to $\simeq 1.7 \times 10^{34} \text{ erg s}^{-1}$, a value that implies a spin-down power conversion efficiency of $>40\%$. Depending on how the source emits in the 1–10 MeV energy range, where we lack observational tools, the total luminosity would significantly exceed the spin down power. Strong flickering (as observed in X-rays) makes the case for the spin-down power being the lone source of energy even more unlikely.

Models in which most of the matter in the disc would have to be propelled away were also constructed [39, 63, 87, 91], and have shown to be successful in describing the gamma-ray emission. In here, the emission is due to self-synchrotron Compton emission originated at the turbulent boundary between a propelling magnetosphere and the disk in-flow. At lower energies, the X-ray emission is contributed by synchrotron emission from the same region, and by the luminosity emitted by the accretion flow. The inability of observationally separating these contributions limits the model testing. However, the recent detection of optical pulses (during high and flare modes) at a flux level compatible with a power law extrapolation from X-rays [17, 92] is intriguing. The pulsed luminosity observed in the visible band is too large to be produced by reprocessing of accretion-powered X-ray emission or cyclotron emission by electrons in the accretion columns above the pulsar polar caps. Instead, it was interpreted as an indication that a rotation-powered pulsar was active. It is not yet settled whether optical pulses are produced in a magnetospheric environment (as in other millisecond pulsars) or are perhaps the result of a mini pulsar wind nebula. In the latter scenario, proposed by Papitto et al. [92] and Veledina et al. [116], the

striped pulsar wind meets the accretion disk within a few light cylinder away from the pulsar, and this intrabinary shock provides the synchrotron radiation.

2.4 More on Redbacks, and Black Widows in the Context of Gamma-Ray Binaries

Gamma-ray binaries are binary systems producing most of their electromagnetic output in gamma rays above 1 MeV (see the review by Dubus [58]). Their multi-wavelength emission are orbitally modulated from radio to TeV. Additionally, in at least one case, a super-orbital modulated signal has been found [8, 13, 42, 43, 76, 78]. There are only a handful of known gamma-ray binaries: six in the Galaxy: PSR B1259–63 [5, 10, 38], LS I+61 303 [2, 14, 66], LS 5039 [3, 9, 11, 46, 66], 1FGL J1018.6–5856 [61, 68, 75], HESS J0632+057 [12, 16, 32, 80], 4FGL J1405.1–6119 [49]), and one in the Large Magellanic Cloud, CXOU J053600.0–673507 [48]. The currently known gamma-ray binaries are all high mass X-ray binary systems, hosting a massive O or Be star and a compact object. Except for PSR B1259–63, hosting a 48 ms pulsar, the nature of the compact objects in such binaries is unknown. Colliding wind (pulsar/stellar wind) interaction (e.g., [57, 84]), pulsar wind zone processes (e.g., [29, 31, 105]), a transitioning pulsar scenario (e.g., [88, 112, 126]), and microquasar jets (see e.g., Bosch-Ramon & Khangulyan [33] for a review) have been proposed as the origin of the gamma-ray emission for one or several gamma-ray binaries. None of these gamma-ray binaries have a known pulsar with a period classifying it as MSP. There might be chance, however, that some of the binaries with a yet unknown companion has a millisecond pulsar in the system, although it would have to be a newborn neutron star, given the short-lived nature of the companion. Other X-ray binary systems also show gamma-ray emission. Transient gamma-ray emission from V404 Cyg has been observed by *Fermi*-LAT in coincidence with the brightest radio and hard X-ray flare during its 2015 June outburst [82]. Cyg X-1 [15, 85, 102] and Cyg X-3 [47, 60, 111] have also been detected in gamma rays. However, their spectral energy distributions (SEDs) peak at X-ray energies, and their gamma-ray emission is not recurrent in every orbit. Thus, we do not consider V404 Cyg, Cyg X-1 and Cyg X-3 as gamma-ray binaries (and of course, none seem to contain a millisecond pulsar as compact object).

In RBs and BWs, the collision between stellar wind and pulsar wind also produces and intra-binary shock, which is thought to accelerate particles to relativistic energies similarly as in gamma-ray binaries. Synchrotron emissions from these intra-binary shocks are observed in X-rays having orbital modulation, both for RBs and BWs (e.g., see [65, 98, 99]), while gamma-rays are expected to arise through inverse Compton scattering (e.g., see [30, 111]). X-ray emission of about half of the BWs are dominated by the thermal emission from MSP surface and did not reveal much shock emission. Some BWs show a clear non-thermal X-ray component but except in some cases, e.g. PSR B1957+20 [71], their orbital light curves are

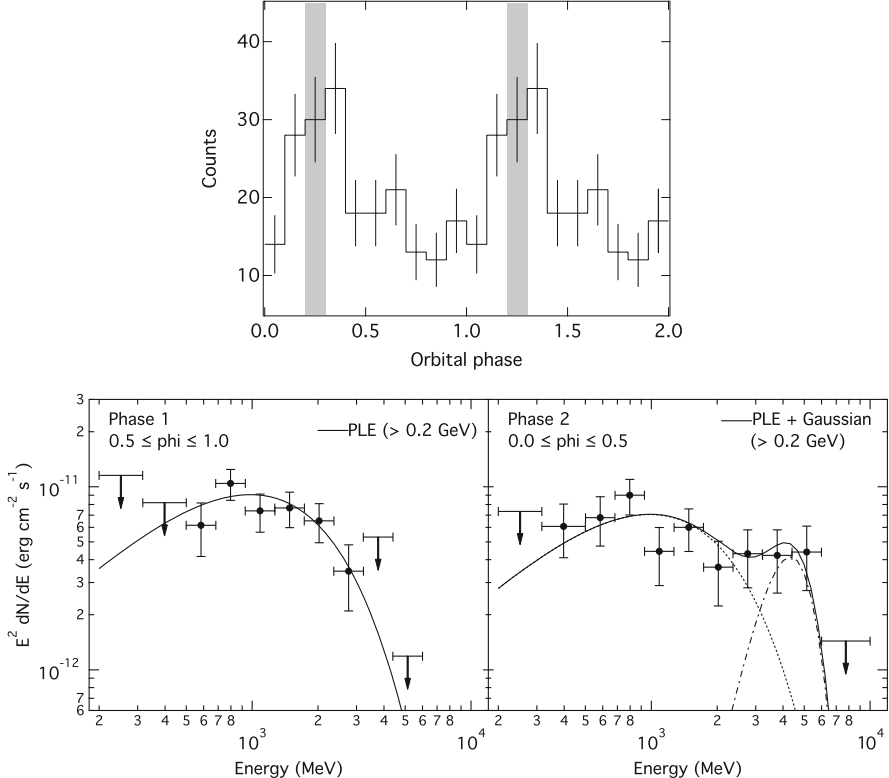


Fig. 2.7 Top: gamma-ray light curve of PSR B1957+20 above 2.7 GeV folded at the orbital period. Bottom: gamma-ray spectrum for the low (orbital phase 1, 0.5–1.0) and high (orbital phase 2, 0.0–0.5) states. Credit: Wu et al., ApJ, 761, 181 (2012) © AAS. Reproduced with permission

not clearly defined due low statistics. RBs, on the contrary, nearly always show a clear non-thermal X-ray spectra components and orbital modulated light curve, also thought to be driven by the intra-binary shock (see e.g., [99]). In RBs and BWs, the intra-binary shock induced gamma-ray emission manifests as orbital modulation in light curves and spectra. For instance, the gamma-ray orbital light curve of BW PSR B1957+20 above 2.7 GeV from [119] is shown in Fig. 2.7. The modulation is apparent to eye. The corresponding gamma-ray spectra for the low (orbital phase 1, 0.5–1.0) and high (orbital phase 2, 0.0–0.5) states are shown in Fig. 2.7. An orbital phase related spectral modulation is detected [119].

The search for intra-binary shock-induced gamma-ray emission in RBs and BWs is difficult since gMSP themselves are much brighter gamma-ray sources. To minimize the contamination of gMSPs, a search during their off-peak phases is preferred. Valid timing ephemerides is then a prerequisite for the search, but the timing noise of gMSPs, orbital solution uncertainties and orbital period fluctuation of RBs & BWs make the task difficult. Out of 10 RBs and 21 BWs detected by *Fermi*-LAT,

Table 2.2 RBs and BWs with intra-binary shock-induced gamma-ray emission

Name	RB/BW	Orbital modulation in light curve	References
PSR B1957+20	BW	$\sim 2.3\sigma$	[119]
PSR J1311–3430	BW	$\sim 3.5\sigma$	[19, 121]
PSR J0610–2100	BW	$\sim 2\sigma$	[59]
PSR J2241–5236	BW	$\sim 4.4\sigma$	[20]
PSR J1023–0038	RB	$\sim 3.2\sigma$	[125]
PSR J1227–4853	RB	$\sim 3.0\sigma$	[121]
2FGL J0523.3–2530	RB candidate	$\sim 4.0\sigma$	[124]
3FGL J2039.6–5618	RB candidate	$\sim 4.0\sigma$	[86]

there are only 2 RBs and 4 BWs showing hints (above 3σ) of intra-binary shock-induced gamma-ray emission (see Table 2.2 for details and references). Besides that, 2 RBs candidates also show hints of orbital modulated gamma-ray emission. In RBs and BWs, the currently observed X-ray and gamma-ray emissions from intra-binary shock resemble those in gamma-ray binaries, peaking above 1 MeV. In this perspective, RBs and BWs in Table 2.2 are potential gamma-ray binaries. However, the current gamma-ray orbital modulation of RBs and BWs are all below 5σ . Future observations are needed to increase the significance and confirm their classification as gamma-ray binaries.

In fact, we note that a number of still unidentified *Fermi*-LAT sources may host a BW or a RB pulsar, which could have been not yet detected as such because it was not observed in the radio band, or because its radio signal was scattered and absorbed by matter enshrouding the system, or because no X-ray variable counterpart has been discovered yet.

Closing Comments: MSPs at Home

As closing comments we would like to draw attention to the radio-quiet MSPs. As we have seen, essentially all rotationally powered MSPs have been discovered through their radio pulsations. This is of course limiting our knowledge of the population to those MSPs that are nearby, bright and with radio emission beamed toward us. Whereas it is true that MSPs are expected to have wider radio beams, visible from a larger range of viewing angles, thus making radio-bright pulsars the most common (see, e.g., the population studies by Story et al. [108]), there is also an obvious observational bias. The problem is that precise position-dependent barycentering corrections need to be applied to photon arrival times to account for the Doppler shift due to *Fermi*'s motion through the solar system. Without the radio detection, the localization of a gamma-ray source suspected to be a pulsar (e.g., see [103]) cannot be better than a few arcmin, much larger than the arc second precision

required to detect gamma-ray pulsations from MSPs. Hundreds of thousands of sky locations covering the source localization region must therefore be searched. This tremendous computational effort has been outsourced on the distributed volunteer computing system Einstein@Home [74]. This allowed to search for pulsations from more than 150 pulsar-like unidentified sources (those having curved spectra and low flux variability). This survey discovered several MSPs, now even a radio quiet MSPs, see [44], promoting the hope of obtaining a more unbiased sample.

Acknowledgments We acknowledge support from grants PGC2018-095512-B-I00, SGR2017-1383, and AYA2017-92402-EXP. Jian Li further acknowledges the support from the Alexander von Humboldt Foundation. We also acknowledge the fruitful discussions with the international team on “Understanding and unifying the gamma rays emitting scenarios in high mass and low mass X-ray binaries” of the ISSI (International Space Science Institute), Beijing.

References

1. Aartsen, M.G., Abraham, K., Ackermann, M., et al., IceCube Collaboration: All-sky search for time-integrated neutrino emission from astrophysical sources with 7 yr of IceCube data. *Astrophys. J.* **835**(2), 151 (2017). <https://doi.org/10.3847/1538-4357/835/2/151>
2. Abdo, A.A., Ackermann, M., Ajello, M., et al.: Fermi LAT observations of LS I +61°303: first detection of an orbital modulation in GeV gamma rays. *Astrophys. J. Lett.* **701**(2), L123–L128 (2009). <https://doi.org/10.1088/0004-637X/701/2/L123>
3. Abdo, A.A., Ackermann, M., Ajello, M., et al.: Fermi/LAT observations of LS 5039. *Astrophys. J. Lett.* **706**(1), L56–L61 (2009). <https://doi.org/10.1088/0004-637X/706/1/L56>
4. Abdo, A.A., Ackermann, M., Ajello, M., et al.: The first fermi large area telescope catalog of gamma-ray pulsars. *Astrophys. J. Suppl. Ser.* **187**(2), 460–494 (2010). <https://doi.org/10.1088/0067-0049/187/2/460>
5. Abdo, A.A., Ackermann, M., Ajello, M., et al.: Discovery of high-energy gamma-ray emission from the binary system PSR B1259-63/LS 2883 around periastron with Fermi. *Astrophys. J. Lett.* **736**(1), L11 (2011). <https://doi.org/10.1088/2041-8205/736/1/L11>
6. Abdo, A.A., Ajello, M., Allafort, A., et al.: The second fermi large area telescope catalog of gamma-ray pulsars. *Astrophys. J. Suppl. Ser.* **208**(2), 17 (2013). <https://doi.org/10.1088/0067-0049/208/2/17>
7. Acciari, V.A., Aliu, E., Araya, M., et al.: Gamma-ray observations of the be/pulsar binary 1A 0535+262 during a giant X-ray outburst. *Astrophys. J.* **733**(2), 96 (2011). <https://doi.org/10.1088/0004-637X/733/2/96>
8. Ackermann, M., Ajello, M., Ballet, J., et al.: Associating long-term γ -ray variability with the superorbital period of LS I +61°303. *Astrophys. J. Lett.* **773**(2), L35 (2013). <https://doi.org/10.1088/2041-8205/773/2/L35>
9. Aharonian, F., Akhperjanian, A.G., Aye, K.M., et al.: Discovery of very high energy gamma rays associated with an X-ray binary. *Science* **309**(5735), 746–749 (2005). <https://doi.org/10.1126/science.1113764>
10. Aharonian, F., Akhperjanian, A.G., Aye, K.M., et al.: Discovery of the binary pulsar PSR B1259-63 in very-high-energy gamma rays around periastron with HESS. *Astron. Astrophys.* **442**(1), 1–10 (2005). <https://doi.org/10.1051/0004-6361:20052983>
11. Aharonian, F., Akhperjanian, A.G., Bazer-Bachi, A.R., et al.: 3.9 day orbital modulation in the TeV γ -ray flux and spectrum from the X-ray binary LS 5039. *Astron. Astrophys.* **460**(3), 743–749 (2006). <https://doi.org/10.1051/0004-6361:20065940>

12. Aharonian, F.A., Akhperjanian, A.G., Bazer-Bachi, A.R., et al.: Discovery of a point-like very-high-energy γ -ray source in Monoceros. *Astron. Astrophys.* **469**(1), L1–L4 (2007). <https://doi.org/10.1051/0004-6361:20077299>
13. Ahnen, M.L., Ansoldi, S., Antonelli, L.A., et al.: Super-orbital variability of LS I +61°303 at TeV energies. *Astron. Astrophys.* **591**, A76 (2016). <https://doi.org/10.1051/0004-6361/201527964>
14. Albert, J., Aliu, E., Anderhub, H., et al.: Variable very-high-energy gamma-ray emission from the microquasar LS I +61 303. *Science* **312**(5781), 1771–1773 (2006). <https://doi.org/10.1126/science.1128177>
15. Albert, J., Aliu, E., Anderhub, H., et al.: Very high energy gamma-ray radiation from the stellar mass black hole binary cygnus X-1. *Astrophys. J. Lett.* **665**(1), L51–L54 (2007). <https://doi.org/10.1086/521145>
16. Aliu, E., Archambault, S., Aune, T., et al., H. E. S. S. Collaboration: Long-term TeV and X-ray observations of the gamma-ray binary HESS J0632+057. *Astrophys. J.* **780**(2), 168 (2014). <https://doi.org/10.1088/0004-637X/780/2/168>
17. Ambrosino, F., Papitto, A., Stella, L., et al.: Optical pulsations from a transitional millisecond pulsar. *Nat. Astron.* **1**, 854–858 (2017). <https://doi.org/10.1038/s41550-017-0266-2>
18. Ambrosino, F., Miraval Zanon, A., Papitto, A., et al.: Optical and ultraviolet pulsed emission from an accreting millisecond pulsar. *Nat. Astron.* **5**, 552 (2021). <https://doi.org/10.1038/s41550-021-01308-0>
19. An, H., Romani, R.W., Johnson, T., et al.: High-energy Variability of PSR J1311-3430. *Astrophys. J.* **850**(1), 100 (2017). <https://doi.org/10.3847/1538-4357/aa947f>
20. An, H., Romani, R.W., Kerr, M.: Signatures of intra-binary shock emission in the black widow pulsar binary PSR J2241-5236. *Astrophys. J. Lett.* **868**(1), L8 (2018). <https://doi.org/10.3847/2041-8213/aaedaf>
21. Anchordoqui, L.A., Torres, D.F., McCauley, et al.: Neutrinos from accreting neutron stars. *Astrophys. J.* **589**(1), 481–486 (2003). <https://doi.org/10.1086/374551>
22. Ansoldi, S., Antonelli, L.A., Antoranz, P., et al.: Teraelectronvolt pulsed emission from the Crab Pulsar detected by MAGIC. *Astron. Astrophys.* **585**, A133 (2016). <https://doi.org/10.1051/0004-6361/201526853>
23. Archibald, A.M., Stairs, I.H., Ransom, S.M., et al.: A radio pulsar/X-ray binary link. *Science* **324**(5933), 1411 (2009). <https://doi.org/10.1126/science.1172740>
24. Archibald, A.M., Kaspi, V.M., Hessels, J.W.T., et al.: Long-term radio timing observations of the transition millisecond pulsar PSR J1023+0038. e-prints. arXiv:1311.5161 (2013)
25. Archibald, A.M., Bogdanov, S., Patruno, A., et al.: Accretion-powered pulsations in an apparently quiescent neutron star binary. *Astrophys. J.* **807**(1), 62 (2015). <https://doi.org/10.1088/0004-637X/807/1/62>
26. Bassa, C.G., Patruno, A., Hessels, J.W.T., et al.: A state change in the low-mass X-ray binary XSS J12270-4859. *Mon. Not. R. Astron. Soc.* **441**(2), 1825–1830 (2014). <https://doi.org/10.1093/mnras/stu708>
27. Bednarek, W.: Gamma-rays from the vicinity of accreting neutron stars inside compact high-mass X-ray binaries. *Astron. Astrophys.* **495**(3), 919–929 (2009). <https://doi.org/10.1051/0004-6361:200811063>
28. Bednarek, W.: TeV gamma-rays from accreting magnetars in massive binaries. *Mon. Not. R. Astron. Soc.* **397**(3), 1420–1425 (2009). <https://doi.org/10.1111/j.1365-2966.2009.14893.x>
29. Bednarek, W.: A model for the two component γ -ray spectra observed from the γ -ray binaries. *Mon. Not. R. Astron. Soc.* **418**(1), L49–L53 (2011). <https://doi.org/10.1111/j.1745-3933.2011.01141.x>
30. Bednarek, W.: Modulated gamma-ray emission from compact millisecond pulsar binary systems. *Astron. Astrophys.* **561**, A116 (2014). <https://doi.org/10.1051/0004-6361/201322595>
31. Bednarek, W., Sitarek, J.: Gamma-rays from nebulae around binary systems containing energetic rotation-powered pulsars. *Mon. Not. R. Astron. Soc.* **430**(4), 2951–2959 (2013). <https://doi.org/10.1093/mnras/stt098>

32. Bongiorno, S.D., Falcone, A.D., Stroh, M., et al.: A new TeV binary: the discovery of an orbital period in HESS J0632+057. *Astrophys. J. Lett.* **737**(1), L11 (2011). <https://doi.org/10.1088/2041-8205/737/1/L11>
33. Bosch-Ramon, V., Khangulyan, D.: Understanding the very-high emission from microquasars. *Int. J. Mod. Phys. D* **18**(3), 347–387 (2009). <https://doi.org/10.1142/S0218271809014601>
34. Browning, R., Ramsden, D., Wright, P.J.: Detection of pulsed gamma radiation from the Crab Nebula. *Nat. Phys. Sci.* **232**(31), 99–101 (1971). <https://doi.org/10.1038/physci232099a0>
35. Burderi, L., Riggio, A., di Salvo, T., et al.: Timing of the 2008 outburst of SAX J1808.4-3658 with XMM-Newton: a stable orbital-period derivative over ten years. *Astron. Astrophys.* **496**(2), L17–L20 (2009). <https://doi.org/10.1051/0004-6361/200811542>
36. Burgay, M., Burderi, L., Possenti, A., et al.: A search for pulsars in quiescent soft X-ray transients. I. *Astrophys. J.* **589**(2), 902–910 (2003). <https://doi.org/10.1086/374690>
37. Caliandro, G.A., Torres, D.F., Rea, N.: Impact of the orbital uncertainties on the timing of pulsars in binary systems. *Mon. Not. R. Astron. Soc.* **427**(3), 2251–2274 (2012). <https://doi.org/10.1111/j.1365-2966.2012.22091.x>
38. Caliandro, G.A., Cheung, C.C., Li, J., et al.: Gamma-ray flare activity from PSR B1259-63 during 2014 periastron passage and comparison to its 2010 passage. *Astrophys. J.* **811**(1), 68 (2015). <https://doi.org/10.1088/0004-637X/811/1/68>
39. Campana, S., Coti Zelati, F., Papitto, A., et al.: A physical scenario for the high and low X-ray luminosity states in the transitional pulsar PSR J1023+0038. *Astron. Astrophys.* **594**, A31 (2016). <https://doi.org/10.1051/0004-6361/201629035>
40. Cheng, K.S., Ruderman, M.: Stationary accelerators around keplerian disks of aligned magnetized collapsed objects: pair production and gamma-ray emission. *Astrophys. J.* **373**, 187 (1991). <https://doi.org/10.1086/170036>
41. Cherenkov Telescope Array Consortium, Acharya, B.S., Agudo, I., Al Samarai, I., et al.: Science with the Cherenkov Telescope Array (2019). <https://doi.org/10.1142/10986>
42. Chernyakova, M., Neronov, A., Molkov, S., et al.: Superorbital modulation of X-ray emission from gamma-ray binary LSI +61 303. *Astrophys. J. Lett.* **747**(2), L29 (2012). <https://doi.org/10.1088/2041-8205/747/2/L29>
43. Chernyakova, M., Babyk, I., Malyshev, D., et al.: Study of orbital and superorbital variability of LSI +61° 303 with X-ray data. *Mon. Not. R. Astron. Soc.* **470**(2), 1718–1728 (2017). <https://doi.org/10.1093/mnras/stx1335>
44. Clark, C.J., Pletsch, H.J., Wu, J., et al.: Einstein@Home discovers a radio-quiet gamma-ray millisecond pulsar. *Sci. Adv.* **4**(2), eaao7228 (2018). <https://doi.org/10.1126/sciadv.aao7228>
45. Coe, M.J., Bird, A.J., Hill, A.B., et al.: Now you see it, now you don't – the circumstellar disc in the GRO J1008-57 system. *Mon. Not. R. Astron. Soc.* **378**(4), 1427–1433 (2007). <https://doi.org/10.1111/j.1365-2966.2007.11878.x>
46. Collmar, W., Zhang, S.: LS 5039 – the counterpart of the unidentified MeV source GRO J1823-12. *Astron. Astrophys.* **565**, A38 (2014). <https://doi.org/10.1051/0004-6361/201323193>
47. Corbel, S., Dubus, G., Tomsick, J.A., et al.: A giant radio flare from Cygnus X-3 with associated γ -ray emission. *Mon. Not. R. Astron. Soc.* **421**(4), 2947–2955 (2012). <https://doi.org/10.1111/j.1365-2966.2012.20517.x>
48. Corbet, R.H.D., Chomiuk, L., Coe, M.J., et al.: A luminous gamma-ray binary in the large magellanic cloud. *Astrophys. J.* **829**(2), 105 (2016). <https://doi.org/10.3847/0004-637X/829/2/105>
49. Corbet, R.H.D., Chomiuk, L., Coe, M.J., et al.: Discovery of the galactic high-mass gamma-ray binary 4FGL J1405.1-6119. *Astrophys. J.* **884**(1), 93 (2019). <https://doi.org/10.3847/1538-4357/ab3e32>
50. Coti Zelati, F., Baglio, M.C., Campana, S., et al.: Engulfing a radio pulsar: the case of PSR J1023+0038. *Mon. Not. R. Astron. Soc.* **444**(2), 1783–1792 (2014). <https://doi.org/10.1093/mnras/stu1552>

51. Coti Zelati, F., Papitto, A., de Martino, D., et al.: Prolonged sub-luminous state of the new transitional pulsar candidate CXOU J110926.4-650224. *Astron. Astrophys.* **622**, A211 (2019). <https://doi.org/10.1051/0004-6361/201834835>
52. D'Amico, N., Lyne, A.G., Manchester, R.N., et al.: Discovery of short-period binary millisecond pulsars in four globular clusters. *Astrophys. J. Lett.* **548**(2), L171–L174 (2001). <https://doi.org/10.1086/319096>
53. de Martino, D., Falanga, M., Bonnet-Bidaud, J.M., et al.: The intriguing nature of the high-energy gamma ray source XSS J12270-4859. *Astron. Astrophys.* **515**, A25 (2010). <https://doi.org/10.1051/0004-6361/200913802>
54. de Martino, D., Belloni, T., Falanga, M., et al.: X-ray follow-ups of XSS J12270-4859: a low-mass X-ray binary with gamma-ray Fermi-LAT association. *Astron. Astrophys.* **550**, A89 (2013). <https://doi.org/10.1051/0004-6361/201220393>
55. de Martino, D., Papitto, A., Belloni, T., et al.: Multiwavelength observations of the transitional millisecond pulsar binary XSS J12270-4859. *Mon. Not. R. Astron. Soc.* **454**(2), 2190–2198 (2015). <https://doi.org/10.1093/mnras/stv2109>
56. de Oña Wilhelmi, E., Papitto, A., Li, J., Rea, N., et al.: SAX J1808.4-3658, an accreting millisecond pulsar shining in gamma rays? *Mon. Not. R. Astron. Soc.* **456**(3), 2647–2653 (2016). <https://doi.org/10.1093/mnras/stv2695>
57. Dubus, G.: Gamma-ray binaries: pulsars in disguise? *Astron. Astrophys.* **456**(3), 801–817 (2006). <https://doi.org/10.1051/0004-6361:20054779>
58. Dubus, G.: Gamma-ray emission from binaries in context. *C. R. Phys.* **16**(6–7), 661–673 (2015). <https://doi.org/10.1016/j.crhy.2015.08.014>
59. Espinoza, C.M., Guillemot, L., Çelik, Ö., et al.: Six millisecond pulsars detected by the Fermi Large Area Telescope and the radio/gamma-ray connection of millisecond pulsars. *Mon. Not. R. Astron. Soc.* **430**(1), 571–587 (2013). <https://doi.org/10.1093/mnras/sts657>
60. Fermi LAT Collaboration, Abdo, A.A., Ackermann, M., Ajello, M., et al.: Modulated high-energy gamma-ray emission from the microquasar cygnus X-3. *Science* **326**(5959), 1512 (2009). <https://doi.org/10.1126/science.1182174>
61. Fermi LAT Collaboration, Ackermann, M., Ajello, M., Ballet, J., et al.: Periodic emission from the gamma-ray binary 1FGL J1018.6-5856. *Science* **335**(6065), 189 (2012). <https://doi.org/10.1126/science.1213974>
62. Ferrario, L., Wickramasinghe, D.: The birth properties of Galactic millisecond radio pulsars. *Mon. Not. R. Astron. Soc.* **375**(3), 1009–1016 (2007). <https://doi.org/10.1111/j.1365-2966.2006.11365.x>
63. Ferrigno, C., Bozzo, E., Papitto, A., et al.: Hiccup accretion in the swinging pulsar IGR J18245-2452. *Astron. Astrophys.* **567**, A77 (2014). <https://doi.org/10.1051/0004-6361/201322904>
64. Fruchter, A.S., Stinebring, D.R., Taylor, J.H.: A millisecond pulsar in an eclipsing binary. *Nature* **333**(6170), 237–239 (1988). <https://doi.org/10.1038/333237a0>
65. Gentile, P.A., Roberts, M.S.E., McLaughlin, M.A., et al.: X-ray observations of black widow pulsars. *Astrophys. J.* **783**(2), 69 (2014). <https://doi.org/10.1088/0004-637X/783/2/69>
66. Hadasch, D., Torres, D.F., Tanaka, T., et al.: Long-term monitoring of the high-energy γ -ray emission from LS I +61°303 and LS 5039. *Astrophys. J.* **749**(1), 54 (2012). <https://doi.org/10.1088/0004-637X/749/1/54>
67. H. E. S. S. Collaboration, Abdalla, H., Aharonian, F., Ait Benkhali, et al.: First ground-based measurement of sub-20 GeV to 100 GeV γ -rays from the Vela pulsar with H.E.S.S. II. *Astron. Astrophys.* **620**, A66 (2018). <https://doi.org/10.1051/0004-6361/201732153>
68. H. E. S. S. Collaboration, Abramowski, A., Aharonian, F., Ait Benkhali, et al.: Discovery of variable VHE γ -ray emission from the binary system 1FGL J1018.6-5856. *Astron. Astrophys.* **577**, A131 (2015). <https://doi.org/10.1051/0004-6361/201525699>
69. Hessels, J. W. T.: The observed spin distributions of millisecond radio and X-ray pulsars. A Decade of Accreting Millisecond X-ray Pulsars **1068**, 130 (2008). <https://doi.org/10.1063/1.3031183>

70. Homer, L., Charles, P.A., Chakrabarty, D., van Zyl, L.: The optical counterpart to SAX J1808.4-3658: observations in quiescence. *Mon. Not. R. Astron. Soc.* **325**(4), 1471–1476 (2001). <https://doi.org/10.1046/j.1365-8711.2001.04567.x>
71. Huang, R.H.H., Kong, A.K.H., Takata, J., et al.: X-ray studies of the black widow pulsar PSR B1957+20. *Astrophys. J.* **760**(1), 92 (2012). <https://doi.org/10.1088/0004-637X/760/1/92>
72. Iacolina, M.N., Burgay, M., Burderi, L., et al.: Search for pulsations at high radio frequencies from accreting millisecond X-ray pulsars in quiescence. *Astron. Astrophys.* **519**, A13 (2010). <https://doi.org/10.1051/0004-6361/201014025>
73. Johnson, T.J., Ray, P.S., Roy, J., et al.: Discovery of gamma-ray pulsations from the transitional redback PSR J1227-4853. *Astrophys. J.* **806**(1), 91 (2015). <https://doi.org/10.1088/0004-637X/806/1/91>
74. Knispel, B., Allen, B., Cordes, J.M., et al.: Pulsar discovery by global volunteer computing. *Science* **329**(5997), 1305 (2010). <https://doi.org/10.1126/science.1195253>
75. Li, J., Torres, D.F., Chen, Y., et al.: INTEGRAL observations of the γ -ray binary 1FGL J1018.6-5856. *Astrophys. J. Lett.* **738**(2), L31 (2011). <https://doi.org/10.1088/2041-8205/738/2/L31>
76. Li, J., Torres, D.F., Zhang, S., et al.: Unveiling the super-orbital modulation of LS I +61°303 in X-rays. *Astrophys. J. Lett.* **744**(1), L13 (2012). <https://doi.org/10.1088/2041-8205/744/1/L13>
77. Li, J., Torres, D.F., Zhang, S., et al.: INTEGRAL and swift observations of the be X-ray binary 4U 1036-56 (RX J1037.5-5647) and its possible relation with γ -ray transients. *Astrophys. J.* **761**(1), 49 (2012). <https://doi.org/10.1088/0004-637X/761/1/49>
78. Li, J., Torres, D.F., Zhang, S.: Spectral analysis in orbital/superorbital phase space and hints of superorbital variability in the hard X-rays of LS I +61°303. *Astrophys. J. Lett.* **785**(1), L19 (2014). <https://doi.org/10.1088/2041-8205/785/1/L19>
79. Li, K.L., Kong, A.K.H., Takata, J., et al.: NuSTAR observations and broadband spectral energy distribution modeling of the millisecond pulsar binary PSR J1023+0038. *Astrophys. J.* **797**(2), 111 (2014). <https://doi.org/10.1088/0004-637X/797/2/111>
80. Li, J., Torres, D.F., Cheng, K.S., et al.: GeV detection of HESS J0632+057. *Astrophys. J.* **846**(2), 169 (2017). <https://doi.org/10.3847/1538-4357/aa7f7>
81. Linares, M., Bahramian, A., Heinke, C., et al.: The neutron star transient and millisecond pulsar in M28: from sub-luminous accretion to rotation-powered quiescence. *Mon. Not. R. Astron. Soc.* **438**(1), 251–261 (2014). <https://doi.org/10.1093/mnras/stt2167>
82. Loh, A., Corbel, S., Dubus, G., et al.: High-energy gamma-ray observations of the accreting black hole V404 Cygni during its 2015 June outburst. *Mon. Not. R. Astron. Soc.* **462**(1), L111–L115 (2016). <https://doi.org/10.1093/mnrasl/slw142>
83. Manchester, R.N., Hobbs, G.B., Teoh, A., Hobbs, M.: The Australia telescope national facility pulsar catalogue. *Astron. J.* **129**(4), 1993–2006 (2005). <https://doi.org/10.1086/428488>
84. Maraschi, L., Treves, A.: A model for LS I +61 303. *Mon. Not. R. Astron. Soc.* **194**, 1P–5 (1981). <https://doi.org/10.1093/mnras/194.1.1P>
85. McConnell, M.L., Ryan, J.M., Collmar, W., et al.: A high-sensitivity measurement of the MeV gamma-ray spectrum of cygnus X-1. *Astrophys. J.* **543**(2), 928–937 (2000). <https://doi.org/10.1086/317128>
86. Ng, C.W., Takata, J., Strader, J., et al.: Evidence on the orbital modulated gamma-ray emissions from the redback candidate 3FGL J2039.6-5618. *Astrophys. J.* **867**(2), 90 (2018). <https://doi.org/10.3847/1538-4357/aae308>
87. Papitto, A., Torres, D.F.: A propeller model for the sub-luminous state of the transitional millisecond pulsar PSR J1023+0038. *Astrophys. J.* **807**(1), 33 (2015). <https://doi.org/10.1088/0004-637X/807/1/33>
88. Papitto, A., Torres, D.F., Rea, N.: Possible changes of state and relevant timescales for a neutron star in LS I +61°303. *Astrophys. J.* **756**(2), 188 (2012). <https://doi.org/10.1088/0004-637X/756/2/188>

89. Papitto, A., Ferrigno, C., Bozzo, E., et al.: Swings between rotation and accretion power in a binary millisecond pulsar. *Nature* **501**(7468), 517–520 (2013). <https://doi.org/10.1038/nature12470>
90. Papitto, A., Torres, D.F., Rea, N., Tauris, T.M.: Spin frequency distributions of binary millisecond pulsars. *Astron. Astrophys.* **566**, A64 (2014). <https://doi.org/10.1051/0004-6361/201321724>
91. Papitto, A., Torres, D.F., Li, J.: A propeller scenario for the gamma-ray emission of low-mass X-ray binaries: the case of XSS J12270-4859. *Mon. Not. R. Astron. Soc.* **438**, 2105 (2014). <https://doi.org/10.1093/mnras/stt2336>
92. Papitto, A., Ambrosino, F., Stella, L., et al.: Pulsating in unison at optical and X-ray energies: simultaneous high time resolution observations of the transitional millisecond pulsar PSR J1023+0038. *Astrophys. J.* **882**(2), 104 (2019). <https://doi.org/10.3847/1538-4357/ab2fdf>
93. Patruno, A., Bult, P., Gopakumar, A., et al.: Accelerated orbital expansion and secular spin-down of the accreting millisecond pulsar SAX J1808.4-3658. *Astrophys. J. Lett.* **746**(2), L27 (2012). <https://doi.org/10.1088/2041-8205/746/2/L27>
94. Patruno, A., Haskell, B., Andersson, N.: The spin distribution of fast-spinning neutron stars in low-mass X-ray binaries: evidence for two subpopulations. *Astrophys. J.* **850**, 106 (2017). <https://doi.org/10.3847/1538-4357/aa927a>
95. Pletsch, H.J., Guillemot, L., Fehrmann, H., et al.: Binary millisecond pulsar discovery via gamma-ray pulsations. *Science* **338**(6112), 1314 (2012). <https://doi.org/10.1126/science.1229054>
96. Ray, P.S., Ransom, S.M., Cheung, C.C., et al.: Radio detection of the fermi-LAT blind search millisecond pulsar J1311-3430. *Astrophys. J. Lett.* **763**(1), L13 (2013). <https://doi.org/10.1088/2041-8205/763/1/L13>
97. Reig, P.: Be/X-ray binaries. *Astrophys. Space Sci.* **332**(1), 1–29 (2011). <https://doi.org/10.1007/s10509-010-0575-8>
98. Roberts, M.S.E., McLaughlin, M.A., Gentile, P.A., et al.: X-ray studies of redbacks. e-prints. arXiv:1502.07208 (2015)
99. Roberts, M.S.E., Al Noori, H., Torres, R.A., et al.: X-ray and optical properties of black widows and redbacks. In: Weltevrede, P., Perera, B.B.P., Preston, L.L., Sanidas, S. (eds.) *Pulsar Astrophysics the Next Fifty Years*, vol. 337, pp. 43–46 (2018). <https://doi.org/10.1017/S1743921318000480>
100. Romero, G.E., Kaufman Bernadó, M.M., Combi, J.A., Torres, D.F.: Variable gamma-ray emission from the Be/X-ray transient A0535+26? *Astron. Astrophys.* **376**, 599–605 (2001). <https://doi.org/10.1051/0004-6361:20011044>
101. Russell, T.D., Degenaar, N., Wijnands, R., et al.: The radio-bright accreting millisecond X-ray pulsar IGR J17591-2342. *Astrophys. J. Lett.* **869**(1), L16 (2018). <https://doi.org/10.3847/2041-8213/aaf4f9>
102. Sabatini, S., Tavani, M., Striani, E., et al.: Episodic transient gamma-ray emission from the microquasar cygnus X-1. *Astrophys. J. Lett.* **712**(1), L10–L15 (2010). <https://doi.org/10.1088/2041-8205/712/1/L10>
103. Saz Parkinson, P.M., Xu, H., Yu, P.L.H., Salvetti, D., Marelli, M., Falcone, A.D.: Classification and ranking of fermi LAT gamma-ray sources from the 3FGL catalog using machine learning techniques. *Astrophys. J.* **820**(1), 8 (2016). <https://doi.org/10.3847/0004-637X/820/1/8>
104. Shrader, C.R., Sutaria, F.K., Singh, K.P., Macomb, D.J.: High-energy spectral and temporal characteristics of GRO J1008-57. *Astrophys. J.* **512**(2), 920–928 (1999). <https://doi.org/10.1086/306785>
105. Sierpowska-Bartosik, A., Torres, D.F.: Pulsar wind zone processes in LS 5039. *Astropart. Phys.* **30**(5), 239–263 (2008). <https://doi.org/10.1016/j.astropartphys.2008.09.009>
106. Smith, D.A., Guillemot, L., Kerr, M., et al.: Gamma-ray pulsars with Fermi. e-prints. arXiv:1706.03592 (2017)

107. Stappers, B.W., Archibald, A.M., Hessels, et al.: A state change in the missing link binary pulsar system PSR J1023+0038. *Astrophys. J.* **790**(1), 39 (2014). <https://doi.org/10.1088/0004-637X/790/1/39>
108. Story, S.A., Gonthier, P.L., Harding, A.K.: Population synthesis of radio and γ -ray millisecond pulsars from the galactic disk. *Astrophys. J.* **671**(1), 713–726 (2007). <https://doi.org/10.1086/521016>
109. Takata, J., Li, K.L., Leung, G.C.K., et al.: Multi-wavelength emissions from the millisecond pulsar binary PSR J1023+0038 during an accretion active state. *Astrophys. J.* **785**(2), 131 (2014). <https://doi.org/10.1088/0004-637X/785/2/131>
110. Tauris, T.M.: Spin-down of radio millisecond pulsars at genesis. *Science* **335**(6068), 561 (2012). <https://doi.org/10.1126/science.1216355>
111. Tavani, M., Bulgarelli, A., Piano, G., et al.: Extreme particle acceleration in the microquasar CygnusX-3. *Nature* **462**(7273), 620–623 (2009). <https://doi.org/10.1038/nature08578>
112. Torres, D.F., Rea, N., Esposito, P., et al.: A magnetar-like event from LS I +61°303 and its nature as a gamma-ray binary. *Astrophys. J.* **744**(2), 106 (2012). <https://doi.org/10.1088/0004-637X/744/2/106>
113. Torres, D.F., Ji, L., Li, J., Papitto, A.r., Rea, N., de Oña Wilhelmi, E., Zhang, S.: A search for transitions between states in redbacks and black widows using seven years of fermi-LAT observations. *Astrophys. J.* **836**(1), 68 (2017). <https://doi.org/10.3847/1538-4357/836/1/68>
114. Tsygankov, S.S., Wijnands, R., Lutovinov, A.e.A., et al.: The X-ray properties of Be/X-ray pulsars in quiescence. *Mon. Not. R. Astron. Soc.* **470**(1), 126–141 (2017). <https://doi.org/10.1093/mnras/stx1255>
115. van den Eijnden, J., Degenaar, N., Russell, T.D., et al.: An evolving jet from a strongly magnetized accreting X-ray pulsar. *Nature* **562**(7726), 233–235 (2018). <https://doi.org/10.1038/s41586-018-0524-1>
116. Veledina, A., Nättilä, J., Beloborodov, A.M.: Pulsar wind-heated accretion disk and the origin of modes in transitional millisecond pulsar PSR J1023+0038. *Astrophys. J.* **884**(2), 144 (2019). <https://doi.org/10.3847/1538-4357/ab44c6>
117. Venter, C., Harding, A.K., Grenier, I.: High-energy emission properties of pulsars. e-prints. arXiv:1802.00204 (2018)
118. Wijnands, R., van der Klis, M.: A millisecond pulsar in an X-ray binary system. *Nature* **394**(6691), 344–346 (1998). <https://doi.org/10.1038/28557>
119. Wu, E.M.H., Takata, J., Cheng, K.S., et al.: Orbital-phase-dependent γ -ray emissions from the black widow pulsar. *Astrophys. J.* **761**(2), 181 (2012). <https://doi.org/10.1088/0004-637X/761/2/181>
120. Xing, Y., Wang, Z.: Search for gamma-ray emission from four accreting millisecond pulsars with fermi/LAT. *Astrophys. J.* **769**(2), 119 (2013). <https://doi.org/10.1088/0004-637X/769/2/119>
121. Xing, Y., Wang, Z.: Discovery of gamma-ray orbital modulation in the black widow PSR J1311-3430. *Astrophys. J. Lett.* **804**(2), L33 (2015). <https://doi.org/10.1088/2041-8205/804/2/L33>
122. Xing, Y., Wang, Z., Jithesh, V.: Possible fermi detection of the accreting millisecond pulsar binary SAX J1808.4-3658. e-prints. arXiv:1502.00733 (2015)
123. Xing, Y., Wang, Z.: The likely Fermi detection of the Be X-ray binary GRO J1008-57: hint for gamma-ray production in neutron-star X-ray binaries. e-prints. arXiv:1902.00828 (2019)
124. Xing, Y., Wang, Z., Ng, C.Y.: Fermi variability study of the candidate pulsar binary 2FGL J0523.3-2530. *Astrophys. J.* **795**(1), 88 (2014). <https://doi.org/10.1088/0004-637X/795/1/88>
125. Xing, Y., Wang, Z.X., Takata, J.: Possible modulated γ -ray emission from the transitional millisecond pulsar binary PSR J1023+0038. *Res. Astron. Astrophys.* **18**(10), 127 (2018). <https://doi.org/10.1088/1674-4527/18/10/127>
126. Zamanov, R., Marti, J., Marziani, P.: Be/X-ray binary LSI+61303 in terms of ejector-propeller model. In: The Second National Conference on Astrophysics of Compact Objects, p. 50 (2001)

Chapter 3

The Emission Physics of Millisecond Pulsars



Alice K. Harding

Abstract Understanding the physics of rotation-powered millisecond pulsars (MSPs) presents a number of challenges compared to that of the non-recycled pulsar population. Even though their fast rotation rates can produce high spin-down power and accelerating electric fields, their relatively low surface magnetic fields make the production of electron-positron pairs required for radio emission difficult. The Fermi Gamma-Ray Space Telescope has discovered pulsed γ -rays from a large fraction of the MSP population which have gamma-ray light curves surprisingly similar to those of young pulsars. However, their very compact magnetospheres enable magnetic fields at the light cylinder that are comparable to those of the most energetic pulsars. This fact and recent global magnetosphere models showing that particle acceleration takes place near and beyond the light cylinder, now makes the γ -rays from MSPs plausible. The large increase in binary systems harboring MSPs has revitalized the study of shock acceleration and high-energy emission in such systems, with many showing orbitally-modulated X-rays. This chapter will review the history and our current studies of the mechanisms for multiwavelength emission from MSPs.

3.1 Introduction

Rotation-powered pulsars display emission over a broad range of wavelengths from radio to TeV γ -rays. Millisecond pulsars (MSPs) have broadband spectra that are similar to those of non-recycled (normal) pulsars, with coherent radio emission components, incoherent UV to X-ray thermal and/or non-thermal components and non-thermal γ -ray components that extend to GeV energies. Differences in emission between normal pulsars and MSPs are present but more subtle. MSPs tend to have on average steeper radio spectra and radio pulse profiles that are wider and

A. K. Harding (✉)

Theoretical Division, Los Alamos National Laboratory, Los Alamos, NM, USA

more complex (see Chap. 1 for more details), hotter thermal X-ray spectra and harder γ -ray spectra (see Chap. 2), and to date no MSPs have detected emission at energies greater than 20 GeV. By contrast, several young pulsars have detected pulsed emission above 50 GeV, including the Crab pulsar with pulsations up to 2 TeV [3], the Vela pulsar with pulsations up to 7 TeV [34], the Geminga pulsar with pulsations above 75 GeV [72] and PSR B1706–44 with pulsations up to 70 GeV [101]. Despite these differences, the physics and mechanisms of MSP emission is much the same as for normal pulsars. Due to their very rapid rotation rates (up to several hundred Hz) and despite their much lower surface magnetic fields ($\sim 10^8$ G), MSPs have higher spin-down power on average than normal pulsars. There are, however, challenges to emission modeling that are specific to MSPs. The low surface magnetic fields greatly hinder magnetic one-photon pair production in a dipole field that is needed for the operation of the pair cascades that are thought to be responsible for both the creation of plasma for the magnetosphere and for radio emission. This problem, as well as recent observational results, strongly suggest that non-dipolar magnetic fields are present near the surface of MSPs. Therefore, complex surface field structure may be a hallmark and a driver of MSP emission physics. It may also be a direct consequence of their history of spin-up by accretion in Low Mass X-ray Binaries (LMXB) (see Chap. 4).

Consequently, this chapter will begin with a review of the structure and physics of the global pulsar magnetosphere, as we presently understand it, pointing out the yet unsolved problems. We will then review models for the broadband non-thermal emission, with specific predictions for MSPs. The physics of pair cascades and their operation in MSPs, as well as the implications for radio death lines and magnetic field structure, are discussed in Sect. 3.4. In Sect. 3.5, the heating of the neutron star surface by energetic particles from the pair cascades, which produce the observed thermal X-ray components, will be reviewed. This section will also discuss the recent modeling of the thermal X-ray light curves observed by Neutron Star Interior Composition Explorer (NICER) and its implications for the magnetic field structure of MSPs. The large number of γ -ray MSPs discovered by the *Fermi Large Area Gamma-Ray Telescope* has led to a factor of seven increase in the number of exotic binary systems known as Black Widows and Redbacks, whose MSPs are heating and ablating their companions with their pulsar winds, producing intra-binary shocks that are accelerating particles (see Chap. 2). Section 3.6 will review the high-energy emission from these systems. Finally, Sect. 3.7 will discuss the outstanding problems in modeling MSP emission.

3.2 Global Magnetosphere Models

Since the emission physics of pulsars is closely tied to the geometry of the magnetic and electric fields, it is important to first discuss the global solutions for the electrodynamics of a rotating dipole field and how these have evolved with increasingly better computational power.

3.2.1 Vacuum Retarded Dipole

At the time pulsars were first discovered in 1967, the only global magnetosphere solution that existed was the vacuum retarded dipole (VRD) [33] that describes the electric and magnetic fields of a star rotating at rate Ω with a magnetic dipole field in vacuum. The analytic VRD solution showed that a very strong quadrupole electric field is induced near the star with a large component parallel to the magnetic field. This electric field falls off as $1/r^4$, much faster than the magnetic dipole field, $1/r^3$. At large distance from the star, $r \sim R_{LC} = c/\Omega$, where the corotation velocity reaches c the displacement current distorts the magnetic field, causing it to sweep back opposite to the direction of rotation. Well beyond the light cylinder, the solution becomes an electromagnetic wave as imposed by the far-field boundary condition.

Although the VRD magnetic field structure was a more realistic alternative than the static vacuum dipole and was used over several decades for pulsar emission modeling (see Sect. 3.3), it is completely lacking some essential elements needed for a physical description of a pulsar magnetosphere, namely charges and currents. Very early in the pulsar modeling game, [40] noted that a magnetized neutron star cannot be surrounded by a vacuum since the strong parallel electric fields, E_{\parallel} , about the surface would pull charges from the star to fill the magnetosphere. This concept of a magnetosphere filled with plasma however, was not easy to fully model. Early N-body simulations [70], allowing either sign of charge to be pulled from the neutron star and accelerated by the vacuum E_{\parallel} for an aligned rotator failed to fill the magnetosphere with charge. Rather, it showed that two separated regions of static and opposite charge form above the polar caps (dome) and along the equator (torus) with no currents, producing a dead pulsar (electrosphere) solution. However, with the advent of global kinetic plasma simulations (see Sect. 3.2.3) it has been shown that diocotron instabilities [82] as well as the production of electron-position pairs above the neutron star surface prevents a stable electrosphere solution.

3.2.2 Force-Free and Dissipative Models

The Force-Free (FF) magnetosphere is the solution to Maxwell's Equations for a rotating star with a dipole field, ignoring plasma pressure and requiring that the electric field parallel to the magnetic field is zero everywhere ($\mathbf{E} \cdot \mathbf{B} = 0$). In this special case (force-free and ideal MHD), the charge density in the magnetosphere is equal to the Goldreich-Julian charge [40], $\rho_{GJ} = -\Omega \cdot \mathbf{B}/2\pi c$, where Ω and B are the pulsar rotation rate and magnetic field, which is the density required to locally screen the E_{\parallel} . The equation describing the fields and currents of an aligned FF magnetosphere, the ‘Pulsar Equation’ introduced by Michel [76], was first solved numerically by Contopoulos et al. [28]. The current density distribution across the polar cap in this solution shows that the current flows out along field lines near

the magnetic poles and returns to the star along a current sheet (where magnetic field lines of opposite polarity merge) and separatrix (along the last open field line that separates the open and closed magnetosphere, those field lines that close within R_{LC}) (see also [106]). Numerical solutions for oblique FF magnetospheres were derived by solving the time-dependent Maxwell's Equations [61, 102], showing that the return current region becomes more distributed and axisymmetric with increasing inclination angle. FF magnetospheres have polar caps that are larger than those of vacuum magnetospheres and shifted backward toward the trailing edge [8, 53].

The FF models however still do not describe real pulsars since there is no E_{\parallel} acceleration and no radiation. If the FF condition $\mathbf{E} \cdot \mathbf{B} = 0$ is relaxed, dissipative magnetosphere solutions can be found for different values of a macroscopic conductivity σ [20, 62, 71]. These solutions span the range between vacuum and FF magnetospheres and showed self-consistent regions of E_{\parallel} that exist along the separatrix and current sheet. However, the dissipative models are not completely self-consistent since the microphysics that creates the σ distribution is not specified.

3.2.3 Kinetic Models

To fully compute the self-consistent feedback between particle motions and fields, kinetic plasma simulations are needed. Particle-in-Cell (PIC) models provide a method to track the feedback between particles and fields by solving the time-dependent Maxwell's Equations and the particle equations of motion simultaneously (actually in alternating time steps). The first PIC simulations of a pulsar magnetosphere were performed by Philippov and Spitkovsky [83], using a 3D Cartesian grid and injecting pair plasma ($e^+ - e^-$ pairs) throughout the computational domain and by Chen and Beloborodov [24] using a 2D spherical grid. Cerutti et al. [21] using a spherical 2D PIC code showed that injecting enough pair plasma only above the neutron star surface could produce a near-FF solution for an aligned rotator. Simulations requiring arbitrary thresholds on particle energies for pair injection found that pair production must occur in the current sheet as well as at the polar caps to create a FF solution [24, 85]. Using a 3D Cartesian PIC code, [65] found that if a larger rate of pairs is injected, everywhere or just from the neutron star surface [17], FF magnetospheres can be formed at all inclination angles without the need for pair production in the current sheet. For increasing injection rates, the E_{\parallel} is screened over a larger part of the magnetosphere and confined more to the current sheet, where the highest energy particles are found (see Fig. 3.1).

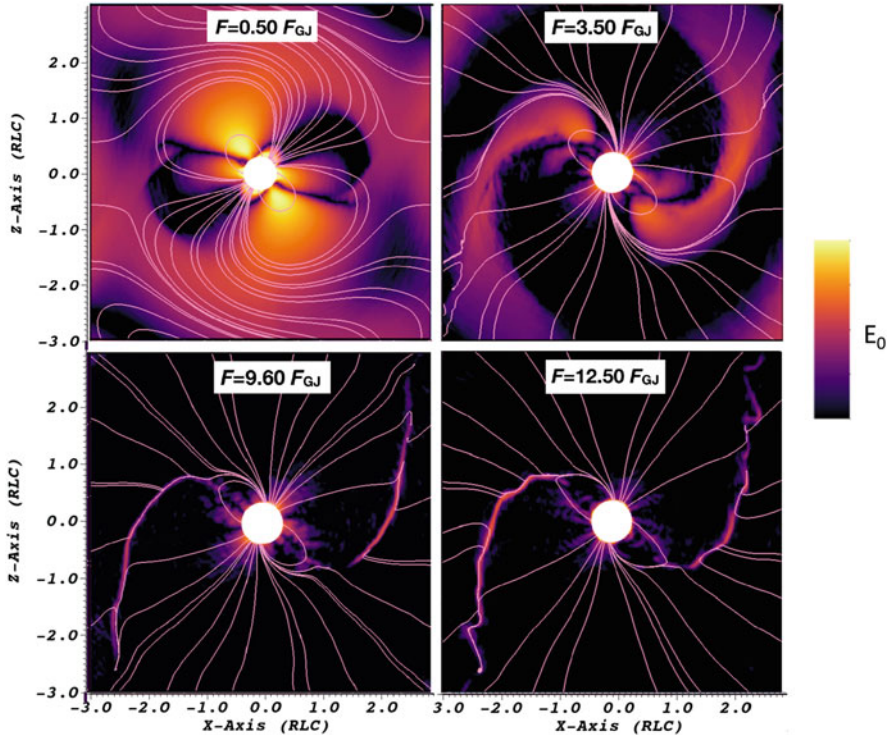


Fig. 3.1 3D kinetic simulations of a global pulsar magnetosphere with $\alpha = 45^\circ$ showing the magnetic field (pink lines) and accelerating electric field E_0 distribution (color scale) in the poloidal plane of the dipole and spin axis, for different pair injection rates in units of the Goldreich-Julian rate. Credit: Brambilla et al. ApJ, 858, 81 (2018) © AAS. Reproduced with permission

3.3 Multiwavelength Emission Models

It is clear that pulsar non-thermal emission occurs at a variety of different sites throughout the magnetosphere across wavelength bands (see Fig. 3.2). From the morphology of pulse profiles and their polarization, the radio emission seems to be originating on open field lines above the polar caps. Many normal pulsars show the “S”-shaped swing of polarization position angle predicted by the Rotating Vector Model [90]. MSP radio emission (see Chap. 1) is generally more complicated than that of normal pulsars, with wider, more complex profiles and polarization patterns that are harder to interpret. By contrast, the high-energy emission from MSPs (see Chap. 2) is more similar to that of normal pulsars. Thanks to the many detections of pulsed γ -ray emission from both normal and MSPs by *Fermi* [1], it is now clear that most of the high-energy emission from pulsars comes from the outer magnetosphere. As discussed in Sect. 3.2, global magnetosphere models have shown that most of the particle acceleration and high-energy emission occurs near the

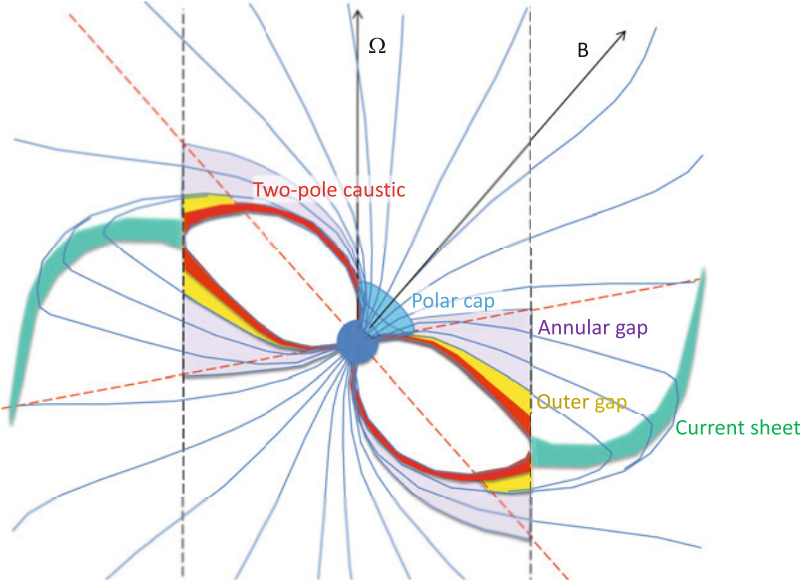


Fig. 3.2 Location of polar cap/radio (blue) and high-energy emission in the outer gap (yellow), two-pole caustic (red), annular gap (purple) and current sheet (green) models in the meridional plane containing the spin and magnetic axes of a near force-free magnetosphere. The dashed black lines denote the light cylinder and the dotted red lines show projections of the null-charge surface

current sheet outside the light cylinder. In the global models, the structure of the fields, currents and current sheets scale with the light cylinder independent of the pulsar period or surface magnetic field strength. Therefore, similarity of the high-energy emission in normal pulsars and MSPs is to be expected. However, even at high energies, there are notable differences both observationally and theoretically. In the X-ray domain, two groups of MSPs with different emission characteristics have often been discussed, with one group being more energetic with spectra dominated by non-thermal emission and narrow pulse profiles, and the other group being less energetic with spectra dominated by thermal emission and broad, sinusoidal-like pulse profiles [9]. At GeV energies, there are three classes of MSPs with distinct γ -ray profile characteristics: Class I show narrow double-peaked profiles where the first peak trails the radio peak by one or two tenths of a period, behavior very similar to that of normal γ -ray pulsars; Class II have phase-aligned γ -ray and radio profiles [42], like the Crab pulsar and PSR B0540-69; Class III have broader, non-standard γ -ray profiles with the first peak leading the radio peak, a behavior unique to MSPs. Class I MSP γ -ray profiles tend to have larger phase lags with the radio peaks than do normal pulsars.

3.3.1 *Polar Cap Models*

Emission models for MSPs have paralleled those of normal pulsars, with the early models placing the high-energy emission at the polar caps followed by models placing the emission near (but inside) the light cylinder and present-day models having emission near the current sheet. Because of their short periods and larger polar caps, MSPs have voltage drops above the polar caps that are similar to some young pulsars. Consequently, polar cap models for normal pulsars [31] were adopted for MSP high-energy emission [18, 112] and predicted detectable fluxes of curvature radiation (CR) and inverse-Compton scattering (ICS) emission from primary accelerated particles scattering thermal X-rays from the neutron star polar cap. However, because MSPs have very low surface magnetic fields, particles must be accelerated to higher energies to emit more energetic photons in order to pair produce. Also, since the field line radius of curvature is smaller due to the larger polar caps, the CR energy loss rate is higher and the particles may become radiation-reaction limited before producing pair-creating photons [73]. In the extreme case, which may include most MSPs as well as older normal pulsars, the voltage drop will not be high enough to produce enough electron-positron pairs to screen the fields near the polar caps, allowing acceleration of particles and radiation to extend to high altitude along the open field lines [78]. In such “pair-starved polar cap” (PSPC) models, the high-energy emission could be visible over a much larger fraction of the sky compared to polar cap emission that is limited to a very small emission cone. Harding et al. [51] applied the PSPC regime to model high-energy emission from MSPs, proposing that the primary CR spectrum would extend above 10 GeV if the observer line of sight crossed near the magnetic poles. They also predicted that *Fermi* would detect the cumulative emission from the many MSPs that inhabit globular clusters.

3.3.2 *Outer Gap Models*

Vacuum gaps in the outer magnetosphere can develop in a charge-separated magnetosphere between the null charge line where the Goldreich-Julian charge, ρ_{GJ} , changes sign and the light cylinder, if particles of one sign flow out along open field lines but there are no charges below to replace them [27]. Outer gaps also require that there be no polar cap pair cascades that send a super-Goldreich-Julian particle flux into the gap. The gap accelerates primary charges to produce CR, but near the light cylinder pairs are created by the photon-photon process, using thermal X-rays from the neutron star surface, since the field is too low for magnetic pair production. The 3D geometry of the outer gap was modeled by Romani and Yadigaroglu [98], using the [33] retarded vacuum dipole magnetic field and emission up to but inside the light cylinder, producing γ -ray light curves with one or two peaks from the same rotational hemisphere.

High-energy emission from outer gaps of MSPs has been explored by Zhang and Cheng [121] and Zhang et al. [126] (see also [105]). In outer gap models for normal

pulsars, the polar cap heating from accelerated particles flowing down from the gap give a surface temperature much higher than observed. The solution to this problem is to reflect the hot thermal emission back to a larger fraction of the neutron star surface with resonant Compton scattering by particles near the star created in pair cascades [120]. However, for MSPs with very low surface fields, the pair cascades from downward flowing gap-accelerated particles do not occur for dipole fields so that multipole fields near the neutron star surface are required to create enough pairs. The predicted spectra consist of two thermal X-ray components (one hotter from a heated polar cap and one cooler from the emission reflected to most of the neutron star), a non-thermal downward-going X-ray SR component from near-surface pairs and an upward-going high energy γ -ray synchro-curvature component from the outer gap. This model thus predicts that the phase shift between the non-thermal X-ray pulse and γ -ray pulse will be large, which is not consistent with MSPs such as PSR B1821–24 and PSR J0218+4232 whose non-thermal X-ray and γ -ray peaks are in phase. Using a similar outer gap model, [57] were able to fit a number of phase-averaged γ -ray spectra of MSPs measured by *Fermi*. Lyutikov [74] proposed a model where the high-energy (GeV) emission is cyclotron self-Compton radiation by a spectrum of particles accelerated and counter-streaming in the outer gaps. This model can produce the observed Crab spectrum from UV to VHE γ -rays.

3.3.3 Slot Gap and Annular Gap Models

In polar cap models, the Poisson Equation solution for E_{\parallel} varies over the polar cap, decreasing to zero at the last open field line that borders the force-free fully conducting closed field region. The slot gap (SG) is a narrow set of field lines near this boundary in which particles accelerate more slowly and never radiate photons with high-enough energy to produce pairs before the magnetic field drops too low. In the SG, the E_{\parallel} is never screened by pairs and particle acceleration and radiation continue up to high altitude [5]. High-energy emission can thus be produced over a large range of radii from the neutron star surface to near the light cylinder [79]. Along trailing field lines, the observed phase differences of radiation due to the curved field is canceled by aberration and light travel time delays, forming caustics so that all the radiation arrives to the observer in phase. In such a two-pole caustic model (TPC, [37]) caustic patterns from both magnetic poles form one or two peaks with variable spacing in the light curves. The slot gap produces light curves like those of the TPC model, with varied separation of peaks that have phase lags with the radio peaks [52], similar to those of *Fermi* pulsars (see Sect. 3.3.5).

The annular gap model is geometrically similar to the slot gap with two distinct regions of the polar cap: the annular field lines are those that cross the null charge surface within the light cylinder and are located at the outer edge of the polar cap while the core field lines are those interior to the annular gap [88, 89]. Unlike the outer gap, the annular gap model assumes that the magnetosphere is not charge-separated but consists of a quasi-neutral pair plasma. In the core region, the E_{\parallel} is screened at a low altitude by pairs since the local charge density ρ has the same sign as ρ_{GJ} , but in the annular gap the pairs do not screen the E_{\parallel} since ρ has the opposite

sign as ρ_{GJ} and acceleration can continue to high altitude. The caustics of the γ -ray light curves from annular gaps are similar to those of the slot gap and can also fit many of the *Fermi* pulsar light curves [35] and in particular several MSPs [36].

3.3.4 Current Sheet Models

Pulsed high-energy emission from the current sheet was first proposed by Kirk et al. [68] based on the striped pulsar wind discussed by Coroniti [29]. The emission was assumed to come from a region at 10 to 100 R_{LC} where the field energy of the wind is at least partly converted to particle energy. The particles then radiate Doppler-boosted SR and an observer will see a pulse of emission each time the current sheet crosses the light-of-sight. With the emissivity assumed to be uniform throughout the current sheet, the radio lags are larger than those seen in *Fermi* pulsar light curves. Later versions of the striped-wind model [80, 81] using the geometric wind solution of [12] placed the emission closer to the R_{LC} , within 50 R_{LC} , and modeled the predicted polarization signatures that could match the observed optical polarization of the Crab pulsar.

Dissipative global MHD models show that the regions of acceleration do lie mostly outside the light cylinder near the current sheet. Using global models with infinite conductivity σ (FF) inside the light cylinder and finite σ outside the light cylinder and assuming that the accelerated particles radiate CR at GeV energies, [64] found that the predicted particle acceleration and radiation patterns matched the characteristics of the *Fermi* pulsars. Phase-resolved spectra in dissipative magnetospheres [16] are able to account for the variation of the spectral index and cutoff energy as a function of pulse phase seen for bright *Fermi* pulsars [32]. It was also seen that σ should increase with spin-down power \dot{E} . Since σ in these models is physically tied to the density of pairs in different parts of the magnetosphere, it is expected that pulsars with higher \dot{E} create a larger number of pairs.

Harding and Kalapotharakos [45] used the magnetic field structure of FF magnetospheres to model broad-band radiation from young pulsars and MSPs, calculating trajectories of particles along field lines from the neutron star surface to $2R_{\text{LC}}$. CR, SR and synchrotron-self Compton (SSC) emission was produced by both primary particles accelerating in an assumed E_{\parallel} and electron-positron pairs produced in polar cap pair cascades. The computed spectra show pair SR components at optical to hard X-ray energies, CR components from primaries at energies up to several GeV and SSC components from pairs at very-high energy (VHE) extending to a TeV for the Crab pulsar and energetic MSPs. While the SSC component for the Crab peaks in the spectral energy distribution (SED) around 1–10 GeV and contributes to the *Fermi* spectrum, the SSC components from MSPs such as PSR B1821–24 and B1937+21 have SED peaks at higher energies near 100 GeV. The MSP SSC components are however suppressed by Klein-Nishina effects and are not predicted to be detectable by current VHE telescopes, but could eventually be detectable by CTA. The pairs produced by MSPs have much higher energies than those of young pulsars since in their low magnetic fields the pair-producing photons must have

higher energies. Harding et al. [54] extended the model of [45] to both lower (IR and optical) and higher (up to 100 TeV) photon energies to reveal an additional spectral component above 10 TeV from primary particles inverse-Compton scattering pair SR. Such a VHE component could account for the recent pulsed emission detected by HESS above 7 TeV from the Vela pulsar [34]. Similar 10 TeV emission is also expected from Crab-like pulsars and energetic MSPs [55].

While global PIC models also show that most particle acceleration is located in the current sheet, the surface magnetic fields and particle energies they can treat numerically are limited to $B \lesssim 10^6$ G and $\gamma \lesssim 10^3$ to resolve the plasma frequency, cyclotron frequency and skin depth. Since this magnetic field and energy are well below those of pulsars, it is necessary to scale-up the simulation results to model high-energy emission. There have generally been two approaches to this problem, neither completely satisfactory. The approach of [22] and [84] is to model the synchro-curvature radiation from the PIC-energy particles, which will be in the SR regime given the very low particle energies, and scale-up the photon spectra to GeV energies. However, it is not clear that the PIC-modeled particle dynamics will be the same as it would be if the particles were to be accelerated to the much higher realistic pulsar energies. Also, the particles with higher energy and small pitch angles will be in a different regime of synchro-curvature emission and may be closer to the CR regime. The alternate approach of [65] is to scale up the surface magnetic field and consequent E_{\parallel} and particle energies to those of a real pulsar on trajectories that are calculated in parallel with those of the PIC particles. In this case, they find that particles reach $\gamma \sim 10^7 - 10^8$ in the radiation-reaction limited regime where the acceleration is balanced by CR losses. The CR spectra reach γ -ray energies with cutoffs around a few GeV, similar to those of *Fermi* pulsar spectra. The drawback to this approach is the need to artificially suppress the particle pitch angles at low altitudes since their gyro-motion is very small and cannot be resolved by PIC models.

3.3.5 Light Curve Modeling

A variety of the above emission models have been used to fit multi-wavelength light curves of MSPs. Venter et al. [114] used geometric versions of outer gap (OG) and slot gap models, as well as the PSPC model to perform by-eye fits to both γ -ray and radio light curves to eight MSPs with detected γ -ray pulsations. They used the two-pole caustic (TPC) model [37] as the geometric version of the slot gap. The radio light curves were fit with cone beams centered on the magnetic poles at relatively low altitude [103]. It was found that most of the MSP light curves in their sample were best fit with TPC or OG models, while only two were better fit with PSPC models. The TPC/OG fits were MSPs whose γ -ray peaks lagged the radio peaks (Class I), while the MSPs fit by PSPC models had radio peaks that lagged the γ -ray peaks (Class III), thus identifying two of the three distinct classes of MSP high-energy light curves. Several years later, *Fermi* discovered pulsations from MSPs

whose γ -ray peaks were aligned in phase with their radio peaks [42] (Class II). Some of these MSPs were already known to have non-thermal X-ray peaks that were also aligned with their radio peaks. Venter et al. [115] (see also [59]) fit the γ -ray and radio light curves of several MSPs of this class with altitude-limited OG and TPC models (see Fig. 3.3), where the emission in the gaps was limited between minimum and maximum radii. The radio emission of these pulsars was found to be at much higher altitude compared to the cone beam emission near the polar caps and formed caustics similar to those of the γ -ray emission. The Class II MSPs thus have light curve characteristics close to that of the Crab pulsar and the Crab-like PSR B0540–69 in the Large Magellanic Cloud, whose radio, optical, X-ray and γ -ray peaks are all aligned in phase. It is likely that for the short periods and small magnetospheres of both Crab-like pulsars and MSPs, the radio emission occurs at large altitudes relative to the light cylinder where the emission forms caustics that are in phase with the high-energy emission.

Johnson et al. [59] performed more formal fits of the same OG, TPC, PSPC and altitude-limited OG and TPC models to 40 MSP light curves of the *Fermi* second γ -ray pulsar catalog [1]. Using a maximum Likelihood technique, they found that Class I and Class II MSP light curves are best fit with either OG or TPC models in about equal numbers while Class III MSPs were exclusively fit with PSPC models. The MSP light curves that prefer OG models tend to have little or no off-peak emission (See Fig. 3.3, top) while those that prefer TPC models tend to have significant levels of off-peak emission and/or two equal widely spaced peaks. In this sample, the Class II MSPs with aligned radio and γ -ray peaks tend to have the shortest periods and the highest surface fields and spin-down power. The Class III MSPs tend to have the lowest spin-down power. The light curve fits also showed that MSPs have a wider distribution of inclination α and viewing angles ζ than normal pulsars whose α and ζ values are higher [86]. Chang et al. [23] fit the light curves of Class II MSPs using altitude-limited TPC and energy-dependent OG models in VRD magnetic fields but added a perturbation factor to modify the fields due to effects of currents.

Several of the Class II MSPs, notably PSR B1821–24 [58] and J1939+2048 (See Fig. 3.3, bottom), not only have radio peaks that are aligned with X-ray and γ -ray peaks but also radio peaks that are not aligned with high-energy peaks but are possibly at phases of magnetic poles. This suggests that MSPs can have both normal radio components above the polar caps as well as high-altitude caustic components. These two types of radio emission can be identified by their predicted distinctive polarization, with polar cap radio components showing RVM-like S-shaped position angle swings and high polarization degree while the caustic components show fast sweeps of position angle and depolarization at the peaks [38]. This behavior is in fact seen in the radio polarization of PSR B1821–24 [10], where the high-energy aligned radio peaks show caustic polarization and the polar cap radio peak shows RVM polarization. These MSPs are similar to the Crab pulsar which has both caustic radio peaks aligned with high-energy peaks and a polar cap radio precursor.

Although OG and SG/TPC models each have some of the elements that can match observed γ -ray pulsar characteristics, neither model is able to satisfactorily fit all the MSP light curves [113]. This result was also found for fits of OG and

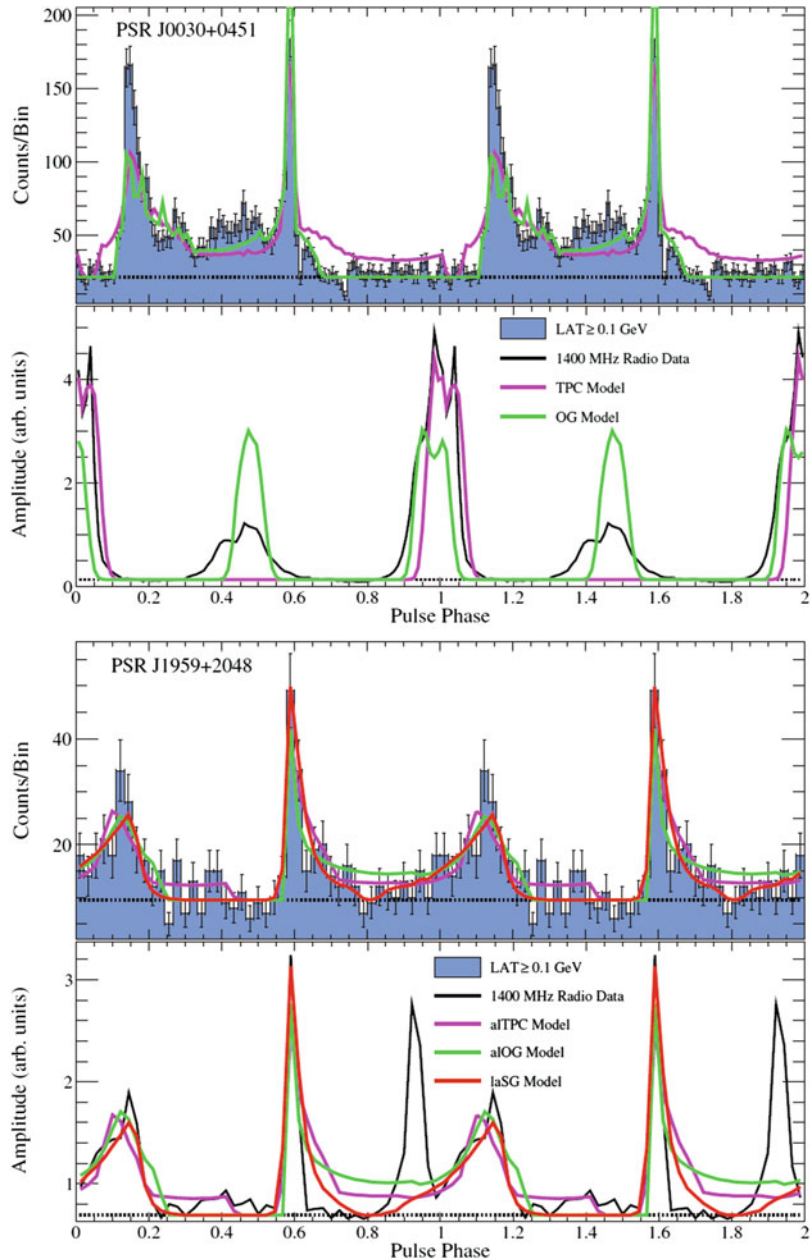


Fig. 3.3 Examples of joint γ -ray (top) and radio (bottom) light curve fits of two *Fermi* MSPs. J0030+0451 (top panels) is a Class I MSP while J1939+2048 (bottom panels) is a Class II MSP having both polar cap and caustic radio peaks. Credit: Johnson et al. ApJS, 213, 6 (2014) © AAS. Reproduced with permission

TPC models to the light curves of young *Fermi* pulsars [86]. Ultimately, the reason for the failure of OG and SG/TPC model light curve fitting is that neither is the correct physical model for pulsar high-energy emission. As discussed above, global dissipative MHD and PIC simulations showed that the main emission is not inside the light cylinder but from the current sheet. The original OG and TPC models were not able to include the current sheet emission since they used the VRD whose magnetic field structure requires particle trajectories along field lines outside the light cylinder to be super-luminal. On the other hand, in force-free and dissipative magnetospheres particle trajectories along magnetic field lines remain sub-luminal at all radii. Furthermore, the model light curves of emission using MHD and PIC global magnetospheres combine some of the best elements of both OG and SG/TPC models, such as very low off-peak emission, bridge emission between the peaks and emission from both hemispheres (Fig. 3.4).

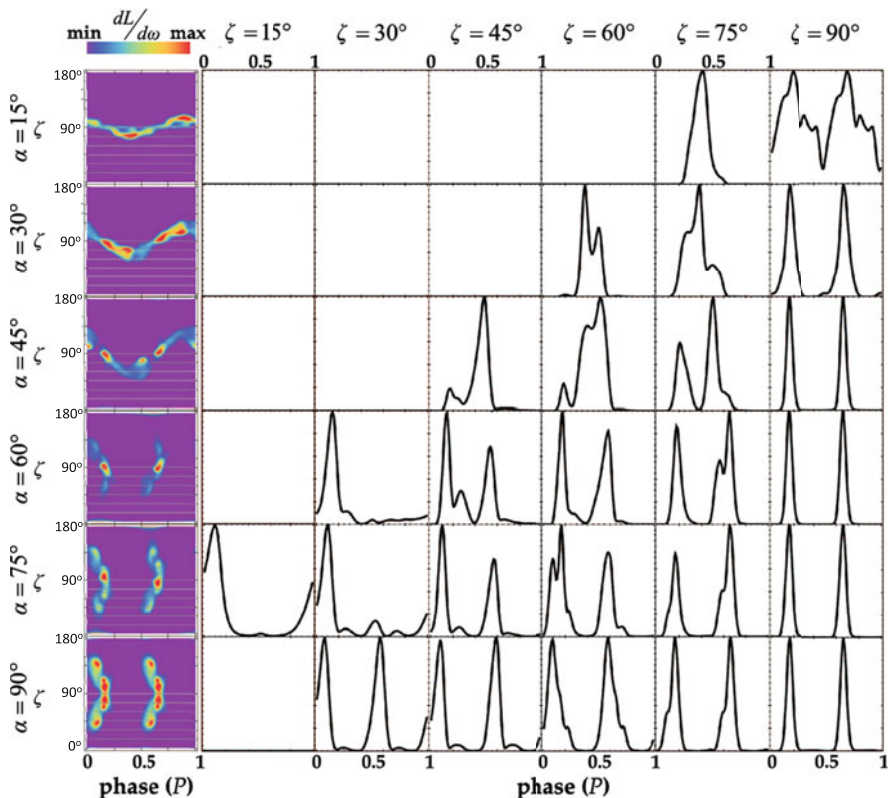


Fig. 3.4 Skymaps of high-energy luminosity per solid angle $dL/d\omega$ at different inclination angles α and light curves at observer angles ζ , for a dissipative MHD magnetosphere model, FIDO, having infinite conductivity (force-free) inside the light cylinder and a finite conductivity outside. Credit: Kalapotharakos et al., ApJ, 793, 97 (2014) © AAS. Reproduced with permission

Bai and Spitkovsky [8] modeled the geometry of high-energy emission and light curves using FF magnetosphere models assuming emission along the last open field line, or separatrix, that extended from the neutron star surface to beyond the light cylinder into the current sheet. The caustics that appear in the emission sky maps in this “separatrix model”, as in other current sheet emission models, are stagnation caustics formed as the particles near and outside the light cylinder must drift backward along field lines to counteract the field sweepback. The particles are thus able to maintain sub-luminal velocities with their trajectories parallel to field lines as they move out nearly radially. The emission from these particles at different radii in the current sheet will all arrive in phase to form the caustics. Depending on magnetic inclination and viewing angle, light curves can have one or two peaks of varying separation. In the double-peaked light curves, the peaks come from opposite hemispheres similar to those of TPC models and unlike the one-hemisphere OG models.

Sky maps (distribution of emission as a function of observer angle and phase with respect to the rotation axis) and light curves from dissipative magnetospheres were explored by Kalapotharakos et al. [64] who used the self-consistent E_{\parallel} distribution of the models to accelerate particles and emit CR emission. It was found that models with infinite σ inside R_{LC} and large but finite σ outside R_{LC} or FIDO (Force-free Inside Dissipative Outside) models were able to match the light curve characteristics of young *Fermi* pulsars, particularly the γ -ray peak separation vs. radio lag. Importantly, matching the radio lags requires the distribution of emission in the 3D current sheet to be non-uniform and non-axisymmetric. Models with uniform emission throughout the current sheet produce larger radio lags not compatible with the data. Cao and Yang [19] also modeled light curves from dissipative magnetosphere models calculated using a pseudo-spectral method [20], different from the MHD methods used by Kalapotharakos et al. [62] and Li et al. [71]. They explored both geometric models with uniform emissivity along fields and uniform σ , and emission from particles accelerated by the self-consistent E_{\parallel} from a FIDO emissivity distribution. A succession of sky maps and light curves for dissipative magnetospheres with uniform increasing σ show that light curve peaks progressively move to later phase with σ increasing from zero (vacuum) to near-FF, confirming the previous results of [63]. Since uniform emissivity and σ models do not match *Fermi* radio lags, they confirm that FIDO models with non-uniform emission in the current sheet is a better match to the data.

The FIDO dissipative models do a good job matching the radio lags of young pulsar light curves assuming that the radio phase is equal to the magnetic pole phase, which would be true if the radio emission occurs relatively near the neutron star surface. While this assumption may be justified for young pulsars, the *Fermi* MSPs have larger radio lags on average that do not fit FIDO models as well. This is likely because in the smaller magnetospheres of MSPs the radio emission height is a large fraction of R_{LC} , with the phase shift from aberration and retardation adding to the γ -ray model phase lag from the magnetic pole. If the γ -ray model light curves were known to be accurate, the observed MSP radio lags would give us information on their radio emission heights. This may be possible as the γ -ray

models improve. Additionally, NICER is accurately measuring phases of thermal X-ray peaks of MSPs, which locate the phase of the magnetic poles, relative to the radio peak phases [92]. Using NICER observations in conjunction with *Fermi* and radio data will further constrain both γ -ray and radio models (see Sect. 3.5).

The sky maps and high-energy light curves in PIC models are similar to those of the striped wind and current sheet models, showing one or two peaks with varying phase separation, but are sensitive to the assumptions made in artificially scaling up the PIC particle energies to those of real pulsars, as discussed in Sect. 3.3.4. The γ -ray light curves computed from scaling up SR of PIC particles to γ -ray energies [22, 84], shown in Fig. 3.5, have model phase lags from the magnetic pole that are larger than the radio lags of young pulsars, but might better agree with those of MSPs. That would imply however, that MSP radio emission occurs at

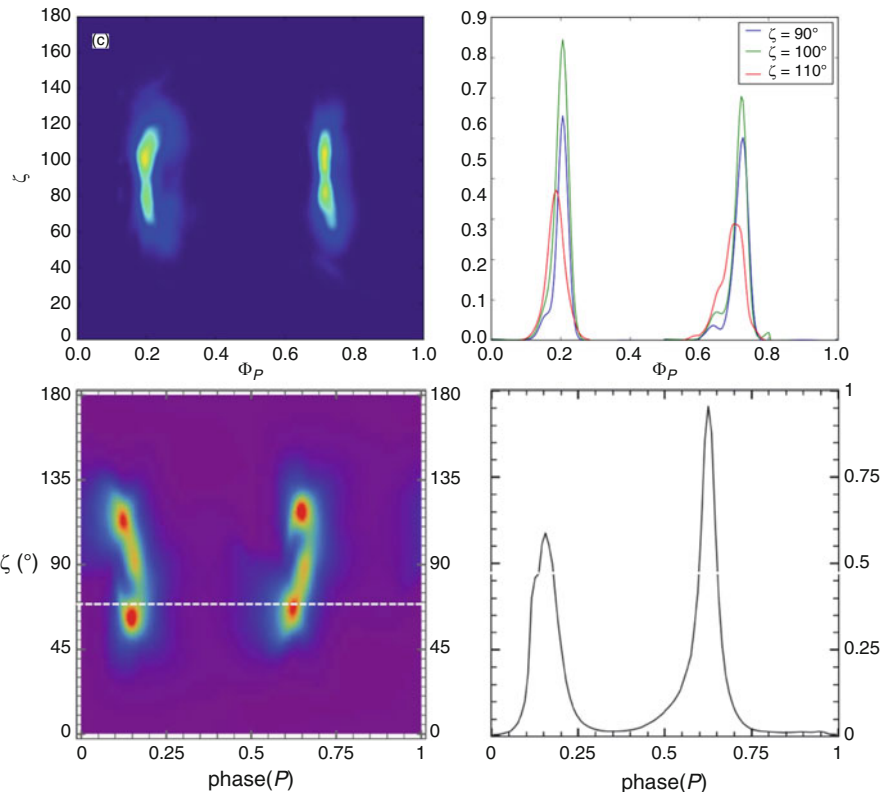


Fig. 3.5 High-energy sky maps (left) and light curves (right) from PIC current sheet models. Top row is for $\alpha = 60^\circ$ and light curves are for three values of ζ from [84]. Bottom row is for $\alpha = 75^\circ$, and light curves are for $\zeta = 70^\circ$ from [65]. Phase 0 and 0.5 in these plots are the phases of the magnetic poles. Credit: Kalapotharakos et al., ApJ, 857, 44 (2018) © AAS. Reproduced with permission

the neutron star surface. The light curves computed from CR of PIC particle with scaled-up energies [65], also shown in Fig. 3.5, have smaller model phase lags from the magnetic pole that agree better with radio phase lags of young pulsars and even allow for some additional lag from aberration and retardation of radio emission located above the neutron start surface. Interestingly, the sky maps and light curves of the PIC models of [65] agree with those of the MHD FIDO models that do not need to be scaled up since they can be computed for realistic pulsar fields. This implies that CR emission models are consistent for both dissipative MHD and PIC approaches, with the caveat that the dissipative models must assume an arbitrary σ distribution.

3.4 Pairs and Death Lines

The production of electron-positron pairs is believed to be an essential element of pulsar physics, providing the plasma to fill the magnetosphere and supply the wind particles, the charges and the currents, as well as the pairs needed for coherent radio emission. There are several sites in the magnetosphere where pair production and cascades can occur: at the polar caps, in the outer gaps, in the current sheet and at the Y-point, where the separatrices from opposite poles merge. Since the latter three sites can only supply pairs on a limited range of field lines near the separatrix, polar cap pair cascades are required at minimum to supply pairs throughout the rest of the magnetosphere and particularly to facilitate the radio emission above the polar caps. Electromagnetic pair cascades at the polar caps [30, 104] are enabled through the QED process of one-photon pair production [39], where a single photon can convert to an electron-positron pair in a magnetic field that is strong enough to supply the additional momentum required. The pair production threshold, $\epsilon > 2mc^2 / \sin \theta$, where ϵ is the photon energy in mc^2 , requires the photon momentum to have an angle θ to the local magnetic field. Since relativistic particles accelerated along the field lines radiate photons within a narrow angle of their direction, the photons must travel some distance across curved field to acquire the angle to create a pair. The particle acceleration length plus the physics of pair production thus sets the length scale of the polar gaps since once pairs are created they screen the surface E_{\parallel} and limit the particle acceleration. The polar cap pair cascades can be initiated by either CR or by inverse Compton photons from accelerated particles scattering thermal X-ray from the neutron star surface [47, 49, 122, 123]. The pairs will be produced with non-zero pitch angles and will radiate SR that can produce more generations of pairs until the photons eventually can escape the magnetosphere. The total number of cascade pairs per primary particle is the pair multiplicity which can reach up to $\sim 10^4$ in dipole fields.

Outer gap pair cascades must rely on photon-photon pair creation since the magnetic fields in the outer magnetosphere are too low for one-photon pair creation. The CR by primary particles accelerated by the gap interact with thermal X-rays from the neutron star surface, or non-thermal X-rays from the gap cascade in the

case of Crab-like pulsars, to produce secondary pairs that then radiate SR. The pairs screen the gap E_{\parallel} to limit the width and voltage of the gap. In the original outer gap model [27], the current through the gap is sustained entirely by the gap pair cascades so that the outer gap dies if the gap cascades cannot take place. However, [56] noted that the self-sustained gap current alone cannot account for the observed luminosity of γ -ray pulsars and proposed that there must be external currents in the outer gaps.

As pulsars age and spin down, the gap voltage drops below that required to radiate pair-producing photons. One can define boundaries in period P and period derivative \dot{P} space that define a “death line” for pair production in the gaps. The location of the death line will depend on the particular gap model, with the outer gap death lines in \dot{P} vs. P space [125] located above those of polar cap death lines. Since pairs are thought to be a requirement for radio emission, the polar cap pair death line has been adopted as the death line for pulsar radio emission. Given the angle dependence of the one-photon pair threshold, the curvature of the near surface magnetic field is important in determining the polar cap death line. In a pure dipole field, the death line for producing pairs by CR occurs at a pulsar age $\sim 10^7$ yr for normal pulsars which is much less than the maximum age $\sim 10^8$ yr of observed radio pulsars ([49, 99]). In the MSP population, the CR pair death line is even more restrictive with only a handful of MSPs lying above the line. Although [124] found that the death line for producing pairs by IC photons lies below the entire normal and MSP populations, IC pair cascades produce very low pair multiplicity [49] that may not be sufficient for radio emission. It has therefore been suggested that multipole fields are present near the neutron star to enable CR pair cascades in older pulsars and MSPs ([6]). Multipolar fields have a smaller field line radius of curvature and can produce larger E_{\parallel} than dipole fields, both of which allow more robust pair cascades ([50]). As will be discussed in Sect. 3.5, there is now strong evidence that at least some MSPs do have multipole fields near their surface.

More recent global models of the pulsar magnetosphere have substantially changed the earlier models assuming steady-state polar cap and outer gap cascades. The FF solutions showed that the global magnetosphere requires a current distribution along open magnetic field lines that is different from the Goldreich-Julian current density $J_{GJ} = \rho_{GJC}$ assumed by previous polar cap and outer gap models (Timokhin 2006). In the global FF magnetosphere, regions of current density $J > J_{GJ}$ (super-GJ), $0 < J < J_{GJ}$ (sub-GJ) and $J < 0$ (anti-GJ) exist across the polar caps, with a distribution that depends on magnetic inclination. In this picture, the main current ($J > 0$) flows out over most of the polar cap while the return current ($J < 0$) occurs in regions that connect to the (spin) equatorial current sheet. In order for polar cap accelerators and the pair cascades they produce to provide the currents required by the global model, they must be time-dependent rather than steady-state. Time-dependent models of vacuum gap pair cascades were developed by Timokhin [107] and for Space-Charge Limited Flow (SCLF) gaps by Timokhin and Arons [108], showing that in both cases the accelerators produce bursts of pairs that fully screen the electric field, halting acceleration until the pair cloud exits the gap, followed by renewed acceleration and another burst of pair production. In non-

steady polar gaps the E_{\parallel} is higher than in steady gaps, so that the maximum pair multiplicity for CR cascades can reach a higher value $\sim 10^5$ [109].

Some PIC models of pulsar magnetospheres have attempted to include pair production where PIC particles reach a specified threshold energy [24, 85]. Although such an approach cannot resolve the actual microphysics of pair production, it shows the possible locations in the global magnetosphere where pair production could take place. These locations are places where particles are accelerated to high energies such as above the polar caps, at the Y-point, and in the current sheet. The simulations suggest that the polar caps can supply pairs and/or currents along field lines with super-GJ current $J > J_{\text{GJ}}$, but in the return current regions with anti-GJ current $J < 0$, pairs from the Y-point and current sheet may be needed.

3.5 Thermal X-ray Emission and Field Structure

The surface thermal emission from MSPs, which are well past the age when neutron star cooling would be important, is most likely caused by heating by back-flowing energetic particles from pair cascades at the polar caps or in the outer magnetosphere, and from global return currents. Early models of pulsar polar cap acceleration concluded that some flux of particles returning to the neutron star surface was inevitable, since the electrons and positrons of the pairs that are produced by the upward accelerating particles will move in opposite directions in the electric field. Since the downward-moving particles, produced near the top of the gap, will gain nearly the full gap voltage before they reach the surface, this energy will be deposited in the NS surface layers and heat the polar cap. Vacuum gaps (e.g. Ruderman & Sutherland 1975) that spontaneously break down through pair cascades produce equal numbers of energetic upward and downward particles, and thus a higher level of polar cap heating than the SCLF gaps (e.g. [7]) that return only a small fraction of positrons to screen the electric field. The steady SCLF gaps were shown to produce polar cap heating temperatures and luminosities that are in agreement with observed thermal X-ray components [4, 48, 49], whereas the vacuum gaps can produce polar caps much hotter than observed. Outer gaps [27] break down in a way similar to that of polar vacuum gaps, returning a flux of energetic particles to the NS that is equal to the flux of upward energetic particles. [43] noted that a flux of returning particles from outer gaps that was equal to the flux of outward-going particles needed to produce the γ -ray emission of the Geminga pulsar would heat the polar caps to a temperature much higher than observed, suggesting that some mechanism for reprocessing the thermal emission from heating is needed (see also [120]). Even in the non-steady SCLF case, there are nearly equal fluxes of upward and downward moving particles, and thus high levels of polar cap heating, during the pair formation and screening part of the cycle [108]. The average polar cap heating luminosity then depends on the duty cycle of the time-dependent pair cascades, which depends on the time required for the pair cloud from each cycle to clear the accelerator. Although the pair cascade duty cycle and thus the

actual polar cap heating luminosity is difficult to assess with present calculations, it is possible to estimate by assuming that the pair cloud exits the gap on a timescale $\sim R/c$, where R is the neutron star radius. This approximate heating gives surface temperatures that agree with those observed for both normal and MSPs [110].

The pattern of polar cap heating will depend on the current distribution across the polar cap which, as discussed above, is a function of magnetic inclination. It also depends on what type of accelerator (vacuum or SCLF) is operating. With free supply of both signs of charge, thought to be the case for all except magnetar-strength magnetic fields [75], SCLF gaps will operate. For time-dependent SCLF gaps [108], pair cascades (and polar cap heating) occur only in regions with super-GJ or anti-GJ current. No pair cascades (and no polar cap heating) occur in regions of sub-GJ current since a flow of low-energy primary electrons alone can supply the current. For aligned rotators, most of the polar cap has sub-GJ current and is not heated, surrounded by a ring of anti-GJ return current adjacent to the last open field lines. As the inclination increases, the region of anti-GJ current increases toward the direction of the spin equator (and current sheet) while the region of sub-GJ current shrinks. At inclinations above around 45° , a region of super-GJ current appears and grows on the equatorial side of the anti-GJ current, while the sub-GJ region continues to shrink. At inclination of 90° , a region of super-GJ current covers nearly the entire polar cap. Thus, for most inclination angles, the heated area is either nearly symmetric around the outside of the polar cap or covers a large part of the polar cap that is nearly symmetric about the poloidal plane containing the magnetic and spin axes.

The heated areas inferred from observed thermal components of MSPs are typically much smaller than the polar cap area [9]. A study of the 2D heated area of centered and offset polar caps for the case of a steady-state SCLF gap [48] shows that the hot spot radius is predicted to be much smaller than the canonical polar cap radius $R_{PC} = R(\Omega R/c)^{1/2}$. The hot spot radius is $R_{hot} \sim 0.03 - 0.1 R_{PC}$, which for MSPs is $R_{hot} \sim 50 - 100$ m. Most of the heating occurs near the center of the polar cap because the gap voltage is largest near the magnetic axis, where the radius of curvature is largest and screening by cascades from CR photons is least effective. Observed thermal components of MSPs typically have hot spot radii of around 100 m [13, 15], in agreement with the theoretical heated area. Thermal X-ray light curve fitting of several MSPs indicates that the hot spots are offset from the magnetic axis [14], implying offset dipoles or multipoles (Fig. 3.6).

Recent fitting of the thermal X-ray light curves of MSP J0030–0451 observed by NICER to obtain constraints on the neutron star mass and radius require two or three heated spots all in the same hemisphere (see Fig. 3.6), with the observer direction in the opposite hemisphere [77, 93]. The spots are thus not antipodal as would be expected for a star-centered dipole field. Furthermore, one spot is much smaller than the polar cap size and the other main spot is a very extended crescent or ellipse. These results strongly suggest that this MSP has a non-dipolar and very offset magnetic field [11]. Gralla et al. [41] showed that a combined dipole plus quadrupole field can produce hot spots similar to what is inferred from the NICER data, but the spots are antipodal since the fields were star centered. Chen et al.

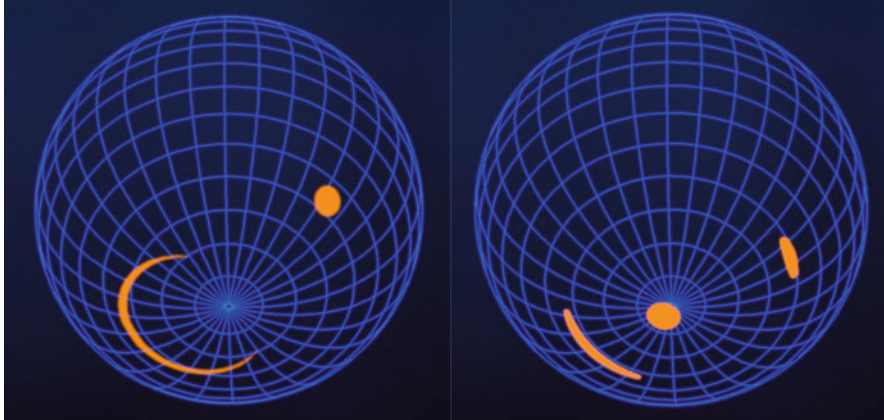


Fig. 3.6 Heated spots viewed 144° from the rotation axis, as inferred from fitting of the NICER X-ray waveforms of PSR J0030+0451 by two independent groups: [93] (left panel), [77] (right panel). Illustration credit: NASA Goddard Space Flight Center

[26] explored a vacuum NS-centered dipole plus a quadrupole offset along the spin axis by $0.4R$ whose polar caps resemble the hot spot shapes found by Riley et al. [93]. They then used a global FF model, matching model γ -ray light curves to Fermi data to determine the magnetic inclination angle which is not constrained by the NICER waveform modeling alone. Kalapotharakos et al. [66] took a different approach, first determining configurations of dipole and quadrupole components, both with arbitrary offset and orientation, whose hot spots produce thermal X-ray light curves that accurately fit those of NICER. They found several degenerate field configurations with different offsets, orientations (including dipole inclination angle) and quadrupole-to-dipole ratio that all match the NICER data. Using these solutions, they then computed the γ -ray light curves in a FF magnetosphere to compare with those of Fermi, finding a configuration with magnetic inclination angle $\sim 90^\circ$, dipole offset $\sim 0.4R$ and quadrupole offset $\sim 0.3R$ that is compatible with both NICER and Fermi data. In this field configuration, the surface quadrupole B_Q at the polar caps has a strength that is about 10 times that of the dipole field, which for J0030–0451 is $B_D = 2.2 \times 10^8$ G.

3.6 Millisecond Pulsars in Binary Systems

The majority ($\sim 80\%$) of rotation-powered MSPs are in binary systems, which is not unexpected given that their progenitors are Low Mass X-Ray Binaries (LMXBs). A class of binary MSPs are in very close systems in which the pulsar wind is heating the companion star and interacting with its induced wind or magnetosphere to form an intra-binary shock. This class is divided into two main groups called

Black Widows, whose companions are extremely light (a few Jupiter masses) and severely ablated, and Redbacks with heavier (several tenths of Solar masses) but also heated companions. The number of Black Widow and Redback MSPs has recently increased from four to nearly 30 with pointed radio searches of *Fermi* unidentified γ -ray sources that discover new MSPs [91]. The radio pulsar ephemerides and orbital solution then allow a detection of the γ -ray pulsations. In a few cases, optical observations of *Fermi* sources have revealed the binary orbital periods by detecting the intensity variations of heated and unheated sides of the companions in these tidally-locked systems [95, 97]. This then allowed successful blind searches for the γ -ray pulsations [69, 87].

Many of the Black Widows and Redbacks show non-thermal X-ray emission modulated at the orbital period and two show orbitally-modulated γ rays, strongly suggesting that the intra-binary shocks are accelerating particles to ultra-relativistic energies. Most also show eclipses of the MSP pulsed radio emission that indicate absorption or scattering by the companion wind or atmosphere. The intra-binary bow shock forms along the pressure balance surface between the pulsar wind and companion star wind or magnetosphere [44, 119] and wraps around one of the two stars depending on which pressure is dominant (see Fig. 3.7). Both single- and double-peaked X-ray light curves are seen, with the majority of sources showing the X-ray peak(s) at inferior conjunction when the pulsar is in front of the companion, whereas the radio eclipses occur at superior conjunction. If the X-ray peaks are produced by the radiation of accelerated particles flowing along the shock, then peaks at inferior conjunction require that the shock wraps around the pulsar. Mildly Doppler-boosted SR from shock-accelerated particles can explain the shapes of the observed X-ray light curves [96, 117, 118].

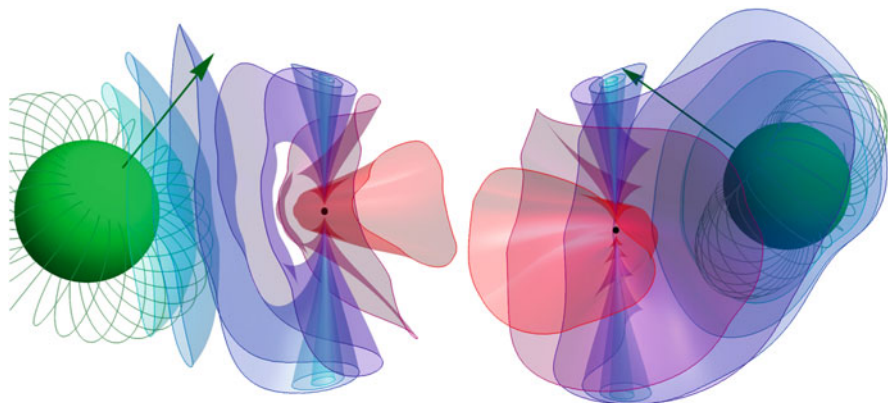


Fig. 3.7 Views of isobaric surfaces for an anisotropic wind of a pulsar with magnetic inclination $\alpha = 15^\circ$ and misaligned dipole magnetosphere of the companion. Isobar colors scale from green to red with increasing surface field strength of the companion star. Credit: Wadiasingh et al., ApJ, 869, 120 (2018) © AAS. Reproduced with permission

MSP binaries are particularly good sources in which to study properties of pulsar wind shocks since they occur much closer to the pulsars than those in pulsar wind nebulae. The shock-accelerated particle energies could reach as high as several TeV [44] if diffusive acceleration limited by SR losses is occurring. Reconnection alone will produce lower maximum particle energies that are limited to $\gamma_{\max} \sim \gamma_w \sigma_w$, where γ_w is the wind bulk flow Lorentz factor and σ_w is the ratio of the electromagnetic to particle energy density in the wind [67]. If diffusive shock acceleration (DSA) dominates, the particle spectrum will have an index $-\delta$ where $\delta = (r + 2)/(r - 1)$ and r is the shock compression ratio, if the injected (upstream) spectrum is steeper than $-\delta$. If the upstream spectrum is flatter than $-\delta$, then the accelerated spectrum retains its slope, with the particles just moving up in energy [60]. Since the injected particle spectrum, the pair spectrum from the MSP, has an index $p \sim 1.5$ (Harding & Muslimov 2011) which is flatter than $\delta = 2$ of a shock with maximum $r = 4$, this will also be the accelerated particle spectral slope. The expected SR photon spectral index would then be $-(p + 1)/2$ or ~ 1.25 . If magnetic reconnection dominates the particle acceleration, the particle spectral index could be as hard as $p \sim 1$ producing a SR spectrum with photon index ~ 1 . Since observed power-law spectra of intra-binary shock emission in MSP binaries is ~ 1 [94], either of these processes would be compatible. However, the maximum particle energy could discriminate between DSA and reconnection. Detection of VHE emission above 1 TeV from IC scattering of shock-accelerated particles on thermal radiation from the companion would argue in favor of DSA or at least some combination of reconnection and DSA [100]. The IC component is predicted to be detectable by Air-Cherenkov telescopes for several MSP binaries [111], as shown in Fig. 3.8. Both the maximum particle energy and pair multiplicity have implications for a contribution of MSP binaries [116] to the energetic cosmic-ray positron excess observed by AMS2 [2].

3.7 Outstanding Problems

In the area of emission physics, MSPs provide many interesting puzzles that suggest a number of topics for future investigation. One of the most fundamental questions is: How do MSPs produce electron-positron pairs? If their magnetic fields are purely dipolar, all but a few known MSPs should not be producing any pairs, much less the high multiplicities required for radio emission and for the γ -ray pulses from near-FF magnetospheres. As was discussed in Sect. 3.5, one proposed solution is that MSPs have more complex multipole fields near their surface. Higher multipoles can have a local field strength that is much higher than what is inferred from the spin-down rate and will have smaller radii of curvature, both of which enhance magnetic pair creation. Multipole fields can also produce offset and/or larger polar caps that will increase the surface E_{\parallel} . There is independent evidence that MSPs have non-dipolar fields from the thermal X-ray profile fits which suggest non-antipodal surface hot spots in several sources. However, if MSPs really have the magnetic field

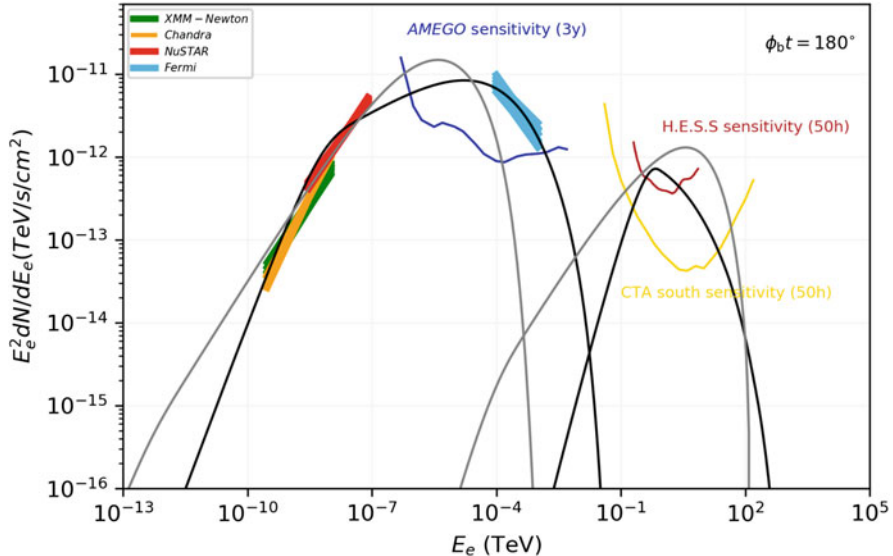


Fig. 3.8 Model SR and IC emission components from particles accelerated at the intra-binary shock in the Redback system containing MSP J1723–2837. Spectra are shown for two models that match the X-ray data but predict different GeV and TeV spectra. Credit: Van der Merwe et al., ApJ, 904, 91 (2020) © AAS. Reproduced with permission

configuration with the extreme offset inferred by the NICER waveform modeling, what effect does it have on the γ -ray light curves that are well reproduced by dipole magnetospheres? There is evidence that the offset field configurations inferred by the NICER data have some effect on the γ -ray light curves but that the γ -ray data may also help in narrowing down degenerate field configurations. What is the geometry and visibility of the radio beams in this case? Finally, is the inferred field configuration stable? Another proposed solution is suggested by PIC models of “weak pulsars”, those that cannot produce enough pairs to fill their magnetospheres [24]. Chen et al. [25] find that pulsars can have global states with intermittent pair production and current flow by which they can reach a near-FF magnetosphere. Global magnetosphere simulations with non-dipolar fields will be needed to answer some of these questions.

Another unresolved question, that applies to normal pulsars as well as MSPs is: What is the GeV emission mechanism? As discussed in Sects. 3.3 and 3.3.5, CR, SR and IC have all been proposed. A resolution of this issue could come from improvements in detected VHE emission components. The maximum photon energy of the pulsed emission will provide a direct lower limit on the maximum energy of the accelerated particles. The maximum photon energies of 2 TeV for Crab and around 7 TeV for Vela already requires particle energies of at least these energies. This tends to disfavor SR and IC for the GeV emission, since the CR losses of particles with this high an energy can easily dominate. Polarization observations

could also distinguish between these different mechanisms since CR is predicted to have a higher degree of polarization than either SR or IC [46].

There are many outstanding problems in the physics of emission from intra-binary shock accelerated particles. The mechanism by which particles are accelerated in pulsar wind termination shocks has been an outstanding issue for decades primarily for pulsar wind nebulae. It has now become a central question for the growing number of Black Widow and Redback binary systems that show emission from intra-binary shocks. As discussed in Sect. 3.6, detection of a VHE emission component from IC can constrain the particle maximum energy. Detecting both the VHE component and the cutoff of the SR spectrum, $E_{\text{SR}} \propto B_s \gamma^2$, would give a measure of the magnetic field at the shock, B_s . One might then constrain the σ_w of the wind and distinguish between reconnection and DSA, if one of these mechanisms does not provide a consistent picture.

I would like to thank Christo Venter for a careful reading of the manuscript and for many helpful suggestions, Zorawar Wadiasingh for comments and suggestions, and Matthew Baring for illuminating discussions.

References

1. Abdo, A.A., et al.: The second fermi large area telescope catalog of gamma-ray pulsars. *Astrophys. J. Suppl. Ser.* **208**, 17 (2013)
2. Accardo, L., et al.: High statistics measurement of the positron fraction in primary cosmic rays of 0.5–500 GeV with the alpha magnetic spectrometer on the international space station. *Phys. Rev. Letters* **113**, 121101 (2014)
3. Ansoldi, S., et al.: Teraelectronvolt pulsed emission from the Crab Pulsar detected by MAGIC. *Astron. Astrophys.* **585**, A133 (2016)
4. Arons, J.: Pair creation above pulsar polar caps – steady flow in the surface acceleration zone and polar CAP X-ray emission. *Astrophys. J.* **248**, 1099 (1981)
5. Arons, J.: Pair creation above pulsar polar caps – geometrical structure and energetics of slot gaps. *Astrophys. J.* **266**, 215 (1983)
6. Arons, J.: Pulsars as gamma-ray sources. *Astron. Astrophys. Suppl. Ser.* **120**, 49 (1996)
7. Arons, J., Scharlemann, E.T.: Pair formation above pulsar polar caps: structure of the low altitude acceleration zone. *Astrophys. J.* **231**, 8654 (1979)
8. Bai, X.N., Spitkovsky, A.: Modeling of gamma-ray pulsar light curves using the force-free magnetic field. *Astrophys. J.* **715**, 1282 (2010)
9. Becker, W.: X-ray mmission from pulsars and neutron stars. In: Neutron Stars and Pulsars, Astrophysics and Space Science Library, vol. 357, p. 91. Springer, Berlin (2009). ISBN 978-3-540-76964-4
10. Bilous, A.V., Pennucci, T.T., Demorest, P., Ransom, S.M.: A broadband radio study of the average profile and giant pulses from PSR B1821-24A. *Astrophys. J.* **803**, 83 (2015)
11. Bilous, A.V. et al.: A nicer view of PSR J0030+0451: evidence for a global-scale multipolar magnetic field. *Astrophys. J. Lett.* **887**, L23 (2019)
12. Bogovalov, S.: On the physics of cold MHD winds from oblique rotators. *Astron. Astrophys.* **349**, 1017 (1999)
13. Bogdanov, S.: The nearest millisecond pulsar revisited with XMM-Newton: improved mass-radius constraints for PSR J0437-4715. *Astrophys. J.* **762**, 96 (2013)
14. Bogdanov, S., Rybicki, G.B., Grindlay, J.E.: Constraints on neutron star properties from X-ray observations of millisecond pulsars. *Astrophys. J.* **670**, 668 (2007)

15. Bogdanov, S., Grindlay, J.E., Rybicki, G.B.: Thermal X-rays from millisecond pulsars: constraining the fundamental properties of neutron stars. *Astrophys. J.* **689**, 407 (2008)
16. Brambilla, G., Kalapotharakos, C., Harding, A.K., Kazanas, D.: Testing dissipative magnetosphere model light curves and spectra with fermi pulsars. *Astrophys. J.* **804**, 84 (2015)
17. Brambilla, G., Kalapotharakos, C., Timokhin, A., Harding, A.K., Kazanas, D.: Electron-positron pair flow and current composition in the pulsar magnetosphere. *Astrophys. J.* **858**, 81 (2018)
18. Bulik, T., Rudak, B., Dyks, J.: Spectral features in gamma-rays expected from millisecond pulsars. *Mon. Not. R. Astron. Soc.* **317**, 97 (2000)
19. Cao, G., Yang, X.: Modeling gamma-ray light curves with more realistic pulsar magnetospheres. *Astrophys. J.* **874**, 166 (2019)
20. Cao, G., Zhang, L., Sun, S.: An oblique pulsar magnetosphere with a plasma conductivity. *Mon. Not. R. Astron. Soc.* **461**, 1068 (2016)
21. Cerutti, B., Philippov, A., Parfrey, K., Spitkovsky, A.: Particle acceleration in axisymmetric pulsar current sheets. *Mon. Not. R. Astron. Soc.* **448**, 606 (2015)
22. Cerutti, B., Philippov, A.A., Spitkovsky, A.: Modelling high-energy pulsar light curves from first principles. *Mon. Not. R. Astron. Soc.* **457**, 2401 (2016)
23. Chang, S., Zhang, L., Li, X., Jiang, Z.: Modelling gamma-ray light curves of phase-aligned millisecond pulsars. *Mon. Not. R. Astron. Soc.* **475**, 2185 (2018)
24. Chen, A., Beloborodov, A.: Electrodynamics of axisymmetric pulsar magnetosphere with electron-positron discharge: a numerical experiment. *Astrophys. J.* **795**, 22 (2014)
25. Chen, A.Y., Cruz, F., Spitkovsky, A.: Filling the magnetospheres of weak pulsars. *Astrophys. J.* **889**, 69 (2020)
26. Chen, A.Y., Yuan, Y., Vasilopoulos, G.: A numerical model for the multiwavelength lightcurves of PSR J0030+0451. *Astrophys. J.* **893**, 38 (2020)
27. Cheng, K.S., Ho, C., Ruderman, M.: Energetic radiation from rapidly spinning pulsars. I – outer magnetosphere gaps. II – Vela and Crab. *Astrophys. J.* **300**, 500 (1986)
28. Contopoulos, I., Kazanas, D., Fendt, C.: The axisymmetric pulsar magnetosphere. *Astrophys. J.* **511**, 351 (1999)
29. Coroniti, F.V.: Magnetically striped relativistic magnetohydrodynamic winds: the crab Nebula revisited. *Astrophys. J.* **349**, 538 (1990)
30. Daugherty, J.K., Harding, A.K.: Electromagnetic cascades in pulsars. *Astrophys. J.* **252**, 337 (1982)
31. Daugherty, J.K., Harding, A.K.: Gamma-ray pulsars: emission from extended polar CAP cascades. *Astrophys. J.* **458**, 278 (1996)
32. DeCesar, M.: Using Fermi Large Area Telescope Observations to Constrain the Emission and Field Geometries of Young Gamma-ray Pulsars and to Guide Millisecond Pulsar Searches. Ph.D. Thesis, University of Maryland (2013)
33. Deutsch, A.J.: The electromagnetic field of an idealized star in rigid rotation in vacuo. *Ann. Astro.* **18**, 1 (1955)
34. Djannati-Atai, A., et al.: Probing Vela pulsar down to 20 GeV with H.E.S.S. II observations. *AIP Conf. Proc.* **1792**(1), 040028 (2017)
35. Du, Y.J., Qiao, G.J., Han, J.L., Lee, K.J., Xu, R.X.: The annular gap model for γ -ray emission from young and millisecond pulsars. *Mon. Not. R. Astron. Soc.* **404**, 2671 (2010)
36. Du, Y.J., Qiao, G.J., Chen, D.: Radio and gamma-ray pulsed emission from millisecond pulsars. *Astrophys. J.* **763**, 29 (2013)
37. Dyks, J., Rudak, B.: Two-pole caustic model for high-energy light curves of pulsars. *Astrophys. J.* **598**, 1201 (2003)
38. Dyks, J., Harding, A.K., Rudak, B.: Relativistic effects and polarization in three high-energy pulsar models. *Astrophys. J.* **606**, 1125 (2004)
39. Erber, T.: High-energy electromagnetic conversion processes in intense magnetic fields. *Rev. Mod. Phys.* **38**, 626 (1966)
40. Goldreich, P., Julian, W.H.: Pulsar electrodynamics. *Astrophys. J.* **157**, 869 (1969)

41. Gralla, S.E., Lupsasca, A., Philippov, A.: Inclined pulsar magnetospheres in general relativity: polar caps for the Dipole, Quadrupole, and Beyond. *Astrophys. J.* **851**, 137 (2017)
42. Guillemot, L., et al.: Pulsed gamma rays from the original millisecond and black widow pulsars: a case for caustic radio emission? *Astrophys. J. Astrophys. J.* **744**, 33 (2012)
43. Halpern, J.P., Ruderman, M.: Soft X-ray properties of the geminga pulsar. *Astrophys. J.* **415**, 286 (1993)
44. Harding, A.K., Gaisser, T.K.: Acceleration by pulsar winds in binary systems. *Astrophys. J.* **358**, 561 (1990)
45. Harding, A.K., Kalapotharakos, C.: Synchrotron self-compton emission from the crab and other pulsars. *Astrophys. J.* **811**, 63 (2015)
46. Harding, A.K., Kalapotharakos, C.: Multiwavelength polarization of rotation-powered pulsars. *Astrophys. J.* **840**, 73 (2017)
47. Harding, A.K., Muslimov, A.G.: Particle acceleration zones above pulsar polar caps: electron and positron pair formation fronts. *Astrophys. J.* **508**, 328 (1998)
48. Harding, A.K., Muslimov, A.G.: Pulsar polar cap heating and surface thermal X-ray emission. I. Curvature radiation pair fronts. *Astrophys. J.* **556**, 987 (2001)
49. Harding, A.K., Muslimov, A.G.: Pulsar polar cap heating and surface thermal X-ray emission. II. Inverse compton radiation pair fronts. *Astrophys. J.* **568**, 862 (2002)
50. Harding, A.K., Muslimov, A.: Pulsar pair cascades in magnetic fields with offset polar caps. *Astrophys. J.* **743**, 181 (2011)
51. Harding, A.K., Usov, V.V., Muslimov, A.G.: High-energy emission from millisecond pulsars. *Astrophys. J.* **622**, 531 (2005)
52. Harding, A.K., Stern, J.V., Dyks, J., Frackowiak, M.: High-altitude emission from pulsar slot gaps: the crab pulsar. *Astrophys. J.* **680**, 1376 (2008)
53. Harding, A.K., DeCesar, M.E., Miller, M.C., Kalapotharakos, C., Contopoulos, I.: gamma-ray pulsar light curves in vacuum and force-free geometry. In: 2011 Fermi Symposium Proceedings – eConf C110509 (2011)
54. Harding, A.K., Kalapotharakos, C., Barnard, M., Venter, C.: Multi-TeV emission from the vela pulsar. *Astrophys. J.* **869**, 18 (2018)
55. Harding, A.K., Venter, C., Kalapotharakos, C.: Very-high-energy emission from pulsars. *ApJ.* **923**, 194 (2021)
56. Hirotani, K., Shibata, S.S.: Electrodynamic structure of an outer gap accelerator: location of the gap and the gamma-ray emission from the crab pulsar. *Astrophys. J.* **558**, 216 (2001)
57. Jiang, Z.J., Chen, S.B., Li, X., Zhang, L.: Phase-averaged gamma-ray spectra from rotation-powered millisecond pulsars. *Mon. Not. R. Astron. Soc.* **437**, 2957 (2014)
58. Johnson, T.J., et al.: Broadband pulsations from PSR B1821-24: implications for emission models and the pulsar population of M28. *Astrophys. J.* **778**, 106 (2013)
59. Johnson, T.J., et al.: Constraints on the emission geometries and spin evolution of gamma-ray millisecond pulsars. *Astrophys. J. Suppl. Ser.* **213**, 6 (2014)
60. Jones, F.C., Ellison, D.C.: The plasma physics of shock acceleration. *Space Sci. Rev.* **58**, 259 (1991)
61. Kalapotharakos, C., Contopoulos, I.A.: Three-dimensional numerical simulations of the pulsar magnetosphere: preliminary results. *Astron. Astrophys.* **496**, 495 (2009)
62. Kalapotharakos, C., Kazanas, D., Contopoulos, I., Harding, A.K.: Gamma-ray light curves from pulsar magnetospheres with finite conductivity. *Astrophys. J.* **749**, 2 (2012)
63. Kalapotharakos, C., Harding, A.K., Kazanas, D., Contopoulos, I.: Gamma-ray light curves from pulsar magnetospheres with finite conductivity. *Astrophys. J.* **754**, L1 (2012)
64. Kalapotharakos, C., Harding, A.K., Kazanas, D.: Gamma-ray emission in dissipative pulsar magnetospheres: from theory to fermi observations. *Astrophys. J.* **793**, 97 (2014)
65. Kalapotharakos, C., Brambilla, G., Timokhin, A., Harding, A.K., Kazanas, D.: Three-dimensional kinetic pulsar magnetosphere models: connecting to gamma-ray observations. *Astrophys. J.* **857**, 44 (2018)
66. Kalapotharakos, C., Wadiasingh, Z., Harding, A.K., Kazanas, D.: The multipolar magnetic field of millisecond PSR J0030+0451. *ApJ.* **907**, 63 (2021)

67. Kandel, D., Romani, R.W., An, H.: The synchrotron emission pattern of intrabinary shocks. *Astrophys. J.* **879**, 73 (2019)
68. Kirk, J.G., Skjaeraasen, O., Gallant, Y.A.: Pulsed radiation from neutron star winds. *Astron. Astrophys.* **388**, L29 (2002)
69. Kong, A.K.H., et al.: Discovery of an unidentified fermi object as a black widow-like millisecond pulsar. *Astron. Astrophys.* **747**, L3 (2012)
70. Krause-Polstorff, J., Michel, F.C.: Electrosphere of an aligned magnetized neutron star. *Astron. Astrophys.* **144**, 72 (1985)
71. Li, J., Spitkovsky, A., Tchekhovskoy, A.: Resistive solutions for pulsar magnetospheres. *Astrophys. J.* **746**, 60 (2012)
72. Lopez, M., Ceribellab, G., Schweizerb, T., Garciaab, J.R., Dazzic, F., For the MAGIC Collaboration: Detection of the Geminga pulsar with the MAGIC telescopes. In: Proceedings of Science (ICRC 2019), vol. 728 (2019)
73. Luo, Q., Shibata, S., Melrose, D.B.: High-energy emission from millisecond pulsars: polar cap models. *Mon. Not. R. Astron. Soc.* **318**, 943 (2000)
74. Lyutikov, M.: Inverse compton model of pulsar high-energy emission. *Mon. Not. R. Astron. Soc.* **431**, 2580 (2013)
75. Medin, Z., Lai, D.: Condensed surfaces of magnetic neutron stars, thermal surface emission, and particle acceleration above pulsar polar caps. *Mon. Not. R. Astron. Soc.* **382**, 1833 (2007)
76. Michel, F.C.: Rotating magnetospheres: an exact 3-D solution. *Astrophys. J.* **180**, L133 (1973)
77. Miller, M.C., et al.: PSR J0030+0451 mass and radius from nicer data and the implications for the properties of neutron star matter. *Astrophys. J. Lett.* **887**, L24 (2019)
78. Muslimov, A.G., Harding, A.K.: Particle acceleration in pair-starved pulsars. *Astrophys. J.* **617**, 471 (2004)
79. Muslimov, A.G., Harding, A.K.: High-altitude particle acceleration and radiation in pulsar slot gaps. *Astrophys. J.* **606**, 1143 (2004)
80. Petri, J.: A unified polar cap/striped wind model for pulsed radio and gamma-ray emission in pulsars. *Mon. Not. R. Astron. Soc.* **412**, 1870 (2011)
81. Petri, J.: High-energy emission from the pulsar striped wind: a synchrotron model for gamma-ray pulsars. *Mon. Not. R. Astron. Soc.* **424**, 2023 (2012)
82. Petri, J., Heyvaerts, J., Bonazzola, S.: Diocotron instability in pulsar electrospheres. *Astron. Astrophys.* **387**, 520 (2002)
83. Philippov, A., Spitkovsky, A.: Ab initio pulsar magnetosphere: three-dimensional particle-in-cell simulations of axisymmetric pulsars. *Astrophys. J.* **785**, L33 (2014)
84. Philippov, A., Spitkovsky, A.: Ab-initio pulsar magnetosphere: particle acceleration in oblique rotators and high-energy emission modeling. *Astrophys. J.* **855**, 94 (2018)
85. Philippov, A., Spitkovsky, A., Cerutti, B.: Ab initio pulsar magnetosphere: three-dimensional particle-in-cell simulations of oblique pulsars. *Astrophys. J.* **801**, L19 (2015)
86. Pierbattista, M., et al.: Light-curve modelling constraints on the obliquities and aspect angles of the young Fermi pulsars. *Astron. Astrophys.* **575**, 3 (2015)
87. Pletsch, H.J., et al.: Binary millisecond pulsar discovery via gamma-ray pulsations. *Science* **338**, 1314 (2013)
88. Qiao, G.J., Lee, K.J., Wang, H.G., Xu, R.X., Han, J.L.: The inner annular gap for pulsar radiation: gamma-ray and radio emission. *Astrophys. J.* **606**, L49 (2004)
89. Qiao, G.-J., Lee, K.-J., Zhang, B., Wang, H., Xu, R.: An annular gap acceleration model for gamma-ray emission of pulsars. *Chin. J. Astron. Astrophys.* **7**, 496 (2007)
90. Radhakrishnan, V., Cooke, D.J.: Magnetic poles and the polarization structure of pulsar radiation. *Astrophys. J. Lett.* **3**, 225 (1969)
91. Ray, P., et al.: Radio searches of fermi LAT sources and blind search pulsars: the Fermi pulsar search consortium. In: 2011 Fermi Symposium Proceedings – eConf C110509 (2011)
92. Ray, P., et al.: Discovery of soft X-ray pulsations from PSR J1231–1411 using NICER. *Astrophys. J.* **878**, L22 (2019)
93. Riley, T., et al.: A nicer view of PSR J0030+0451: millisecond pulsar parameter estimation. *Astrophys. J. Lett.* **887**, L21 (2019)

94. Roberts, M.S.E., et al.: X-ray studies of redbacks. In: 2014 Fermi Symposium Proceedings – eConf C14102.1 (2015)
95. Romani, R.W.: 2FGL J1311.7-3429 joins the black widow club. *Astrophys. J.* **754**, L25 (2012)
96. Romani, R.W., Sanchez, N.: Intra-binary shock heating of black widow companions. *Astrophys. J.* **828**, 7 (2017)
97. Romani, R.W., Shaw, M.S.: The orbit and companion of probable γ -ray pulsar J2339-0533. *Astrophys. J.* **743**, L26 (2011)
98. Romani, R.W., Yadigaroglu, I.-A.: Gamma-ray pulsars: emission zones and viewing geometries. *Astrophys. J.* **438**, 314 (1995)
99. Ruderman, M. A., Sutherland, P. G.: Theory of pulsars: polar gaps, sparks, and coherent microwave radiation. *Astrophys. J.* **196**, 51 (1975)
100. Sironi, L., Spitkovsky, A.: Acceleration of particles at the termination shock of a relativistic striped wind. *Astrophys. J.* **741**, 39 (2011)
101. Spir-Jacob, M., Djannati-Atai, A., Mohrmann, L., Giavitto, L., Khelifi, B., Rudak, B., Venter, C., Zanin, R., for the H.E.S.S. Collaboration: Detection of sub-100 GeV gamma-ray pulsations from PSR B1706-44 with H.E.S.S. In: Proceedings of Science (ICRC 2019), vol. 799 (2019)
102. Spitkovsky, A.: Time-dependent force-free pulsar magnetospheres: axisymmetric and oblique rotators. *Astrophys. J.* **648**, L51 (2006)
103. Story, S.A., Gonthier, P.L., Harding, A.K.: Population synthesis of radio and gamma-ray millisecond pulsars from the galactic disk. *Astrophys. J.* **671**, 713 (2007)
104. Sturrock, P.A.: A model of pulsars. *Astrophys. J.* **164**, 529 (1971)
105. Takata, J., Cheng, K.S., Taam, R.E.: X-ray and gamma-ray emissions from rotation powered millisecond pulsars. *Astrophys. J.* **745**, 100 (2012)
106. Timokhin, A.N.: On the force-free magnetosphere of an aligned rotator. *Mon. Not. R. Astron. Soc.* **368**, 1055 (2006)
107. Timokhin, A.: Time-dependent pair cascades in magnetospheres of neutron stars - I. Dynamics of the polar cap cascade with no particle supply from the neutron star surface. *Mon. Not. R. Astron. Soc.* **408**, 2092 (2010)
108. Timokhin, A., Arons, J.: Current flow and pair creation at low altitude in rotation-powered pulsars' force-free magnetospheres: space charge limited flow. *Astrophys. J.* **429**, 20 (2013)
109. Timokhin, A., Harding, A.K.: On the polar cap cascade pair multiplicity of young pulsar. *Astrophys. J.* **810**, 144 (2015)
110. Timokhin, A., Harding A.K.: On the maximum pair multiplicity of pulsar cascades. *Astrophys. J.* **871**, 12 (2019)
111. Van Der Merwe, C. J. T., Venter, C., Wadiasingh, Z., Harding, A.K., Baring, M. G.: X-Ray through Very High Energy Intrabinary Shock Emission from Black Widows and Redbacks. *ApJ.* **904**, 91 (2020)
112. Venter, C., de Jager, O.C.: Spectral constraints for millisecond pulsars due to general relativistic frame dragging. *Ap. Space Sci.* **297**, 399 (2005)
113. Venter, C., Harding, A.K.: High-energy pulsar models: developments and new questions. *Astron. Nachr./AN* **335**(3), 268 (2014)
114. Venter, C., Harding, A.K., Guillemot, L.: Probing millisecond pulsar emission geometry using light curves from the Fermi/large area telescope. *Astrophys. J.* **707**, 800 (2009)
115. Venter, C., Johnson, T.J., Harding, A.K.: Modeling phase-aligned gamma-ray and radio millisecond pulsar light curves. *Astrophys. J.* **744**, 34 (2012)
116. Venter, C., Kopp, A., Harding, A.K., Gonthier, P.L., Busching, I.: Cosmic-ray positrons from millisecond pulsars. *Astrophys. J.* **807**, 130 (2015)
117. Wadiasingh, Z., Harding, A.K., Venter, C., Bottcher, M.: High-energy emission from black widows and redbacks. HEASA2015 (2015) [arXiv:1512.07320v1]
118. Wadiasingh, Z., Harding, A.K., Venter, C., Bottcher, M., Baring, M.G.: Constraining relativistic bow shock properties in rotation-powered millisecond pulsar binaries. *Astrophys. J.* **839**, 80 (2017)

119. Wadiasingh, Z., Venter, C., Harding, A.K., Bottcher, M., Kilian, P.: Pressure balance and intrabinary shock stability in rotation-powered-state redback and transitional millisecond pulsar binary systems. *Astrophys. J.* **869**, 120 (2018)
120. Wang, F.Y.-H., Ruderman, M., Halpern, J.P., Zhu, T.: Models for X-ray emission from isolated pulsars. *Astrophys. J.* **498**, 373 (1998)
121. Zhang, L., Cheng, K.S.: X-ray and gamma-ray emission from millisecond pulsars. *Astron. Astrophys.* **398**, 639 (2003)
122. Zhang, B., Harding, A.K.: Full polar cap cascade scenario: gamma-ray and X-ray luminosities from spin-powered pulsars. *Astrophys. J.* **532**, 1150 (2000)
123. Zhang, B., Qiao, G.J., Han, J.L.: Inverse compton scattering: gap parameters, energy loss of the particles, and possible implications for pulsar radio emission. *Astrophys. J.* **491**, 891 (1997)
124. Zhang, B., Harding, A.K., Muslimov, A.G.: Radio pulsar death line revisited: is PSR J2144-3933 anomalous? *Astrophys. J.* **531**, 135 (2000)
125. Zhang, L., Cheng, K.S., Jiang, Z.J., Leung, P.: Gamma-ray luminosity and death lines of pulsars with outer gaps. *Astrophys. J.* **604**, 317 (2004)
126. Zhang, L., Fang, J., Chen, S.B.: High-energy properties of pulsed emission from millisecond pulsars. *Astrophys. J.* **666**, 1165 (2007)

Chapter 4

Accretion Powered X-ray Millisecond Pulsars



Tiziana Di Salvo and Andrea Sanna

Abstract The discovery in 1998 of the first accreting millisecond X-ray pulsar started an exciting season of continuing discoveries. In the last 20 years, thanks to the extraordinary performance of astronomical detectors in the radio, optical, X-ray, and Gamma-ray bands, astrophysicists had the opportunity to thoroughly investigate the so-called recycling scenario: the evolutionary path leading to the formation of a Millisecond-spinning Pulsar. In this chapter we review the general properties of Accreting Millisecond X-ray Pulsars, which provide the first evidence that neutron stars are spun up to millisecond periods by accretion of matter and angular momentum from a (low-mass) companion star. We describe the general characteristics of this class of systems with particular attention to their spin and orbital parameters, their short-term and long-term evolution, as well as the information that can be drawn from their X-ray spectra.

4.1 How to Spin Up a Neutron Star: The Recycling Scenario

Millisecond Pulsars (hereafter MSPs) are fast-spinning Neutron Stars (NS), here defined to have a period shorter than 30 ms, and hence a spin frequency higher than 30 Hz. Now we know that the vast majority of these fast-spinning NS are in binary systems with a low-mass ($<1 M_{\odot}$) companion star and possess a relatively weak magnetic field (less than 10^8 – 10^9 Gauss). Moreover, a large amount of these systems are found in Globular Clusters (old clusters of stars). It was soon realised that these NS must belong to old systems in order to have the time for the magnetic

T. Di Salvo (✉)

Università degli Studi di Palermo, Dipartimento di Fisica e Chimica – Emilio Segrè, Palermo, Italy

e-mail: tiziana.disalvo@unipa.it

A. Sanna

Università degli Studi di Cagliari, Dipartimento di Fisica, Monserrato, Italy

e-mail: andrea.sanna@dsf.unica.it

field to decay from the large strength in young NS (usually above 10^{12} Gauss) to their present, much lower strength. It was therefore proposed that old NS are spun up to millisecond periods by the accretion of matter and angular momentum during a Low-Mass X-ray Binary (hereafter LMXB) phase; this is the so-called *recycling scenario* (see, e.g., [10]). Once a *recycled* NS reaches a high spin frequency, even if its magnetic field has decayed, the rotation-powered emission mechanism (which depends on the fourth power of the spin frequency, see below) can be re-activated; hence, at the end of the accretion phase, when the companion star has lost its atmosphere and/or has detached from its Roche lobe, the NS should be visible as a rotation-powered MSP.

4.1.1 Evolution of Rotation-Powered Neutron Stars in the $P - \dot{P}$ Diagram

According to the recycling scenario, a newly born NS should have on average a relatively slow spin period (above few tens of milliseconds) and a relatively strong magnetic field; an example is given by the Crab pulsar, a 33 ms isolated pulsar with a magnetic field of $\sim 4 \times 10^{12}$ Gauss discovered in 1968 at the center of a young, ~ 1000 -years old, supernova remnant called the Crab Nebula. The magnetic field, rotating at the spin period of the NS, behaves as a rotating magnetic dipole which emits radiation according to Larmor's formula (e.g. [70]):

$$P_{\text{rad}} = \frac{2}{3} \frac{(\ddot{\mu}_\perp)^2}{c^3} = \frac{2}{3} \frac{\mu_\perp^2 \Omega^4}{c^3} = \frac{2}{3c^3} (BR^3 \sin \alpha)^2 \left(\frac{2\pi}{P} \right)^4, \quad (4.1)$$

where $\mu_\perp = BR^3 \sin \alpha$ is the component of the magnetic dipole moment perpendicular to the rotation axis, B and R are the surface magnetic field and the NS radius, respectively, α is the angle between the rotation axis and the magnetic dipole axis, Ω is the spin angular frequency of the NS and P its spin period. In this case the (pulsed) emission is usually visible in the radio (and often in the gamma-ray) band; it is mainly due to synchrotron emission of charge currents, formed by electrons and positrons extracted from the NS surface by the intense Lorentz force due to the magnetic field and the fast rotation, moving along curved open magnetic field lines ([70]; see also Chap. 3). Because of this emission, the NS loses rotational energy and slows down, according to the relation (see, e.g., [129]):

$$\dot{E} = \frac{d}{dt} \left(\frac{1}{2} I \Omega^2 \right) = I \Omega \dot{\Omega} \simeq -\frac{\mu^2 \Omega^4}{c^3} (1 + \sin^2 \alpha), \quad (4.2)$$

where $I \propto MR^2$ is the moment of inertia of the NS, M its mass, and $\mu = B_0 R^3 / 2$ is the magnetic moment, where B_0 is the magnetic field strength at the poles. Solving this equation for B_0 and inserting typical values of $I \simeq 10^{45}$ g cm², $R \simeq 10^6$ cm

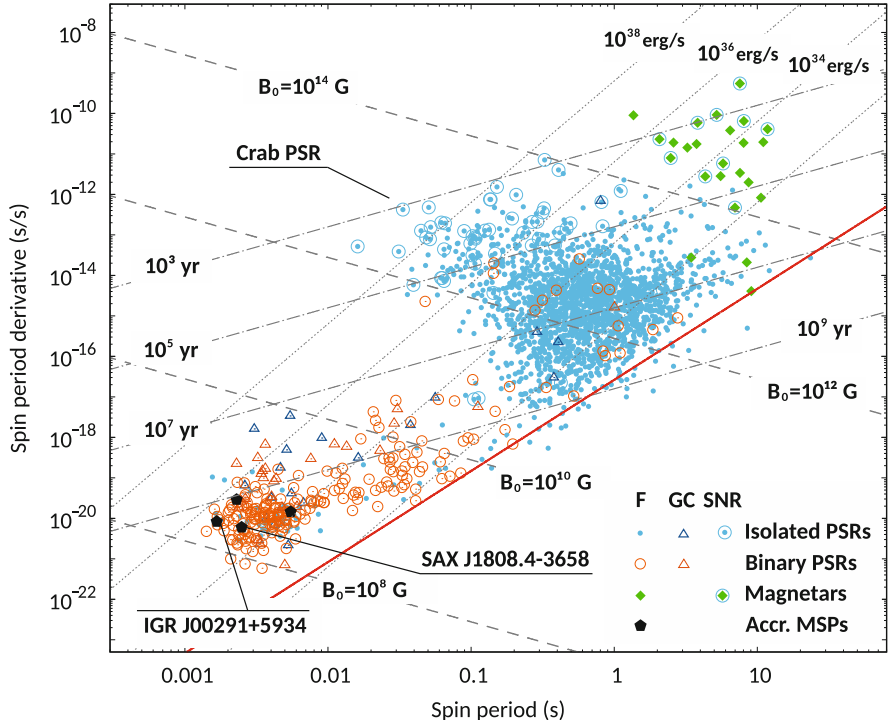


Fig. 4.1 P - \dot{P} diagram of rotation-powered pulsars (blue and orange symbols refer to isolated and binary pulsars, respectively), accreting MSPs (black pentagons) and magnetars (green diamonds). Different symbols mark pulsars found in the Galactic field, in globular clusters and supernova remnants, respectively (see the legend at the lower-right corner of the panel). Lines of constant magnetic field (evaluated using Eq. 4.3), spin-down age ($\tau = P/2\dot{P}$) and spin-down power (Eq. 4.2 evaluated for $\alpha = 0$) are plotted with dashed, dotted and dot-dashed lines, respectively. The red solid line marks a pulsar death line, evaluated using a polar cap vacuum gap model in a multipolar field with curvature radiation as the source of electron/positron pairs [140]. Figure courtesy of A. Papitto

and $\alpha = 90^\circ$, gives:

$$B_0 \sim 6 \times 10^{19} (P \dot{P})^{1/2} \text{ Gauss}, \quad (4.3)$$

which allows to relate the magnetic field strength to the spin period and its derivative, and hence to give an estimate of the magnetic field once the spin period and its derivative are measured. Figure 4.1 shows the measured values of the spin period and period derivative from the ~ 3000 rotation-powered pulsar listed in the ATNF pulsar catalogue ([76], available at <https://www.atnf.csiro.au/research/pulsar/psrcat/>) at the moment of writing this chapter, and from the four AMXPs for which a secular spin evolution was measured (see Table 4.2). Dashed lines in such a P - \dot{P} diagram indicate constant magnetic field values evaluated using Eq. 4.3.

In the hypothesis that the magnetic field does not change significantly with time, a pulsar moves from left to right in the $P - \dot{P}$ diagram along a constant. From Eq. (4.2) we can estimate the pulsar characteristic age $\tau = P/(2\dot{P})$, defined as the timescale necessary to bring the pulsar from its initial period P_0 to the current period P at the observed spin-down rate by assuming $P_0 \ll P$. For instance, the characteristic age of the Crab pulsar comes out to be ~ 2.5 kyr. Dot-dashed lines in Fig. 4.1 mark a few values of constant pulsar characteristic age.

In the meantime, the NS magnetic field rapidly decays due to mechanisms not fully understood yet, probably ohmic dissipation (see, e.g., [132] for a review), perhaps with a contribution due to accretion of matter in the subsequent LMXB phase (see, e.g., [38]). This causes the pulsar to detach from a constant magnetic field line (see dashed lines in Fig. 4.1), and to move towards the bottom of the $P - \dot{P}$ diagram. Below the so-called death line (see the red solid line in Fig. 4.1), the NS enters the graveyard region where the rotation-powered pulsar switches off because not enough spin-down power is available to feed the emission mechanism (see Sect. 3.4). At this point, if the NS is in a binary system with a low-mass star (lighter than $1 M_\odot$), the latter may be able to fill its Roche-lobe due to nuclear evolution and/or losses of the orbital angular momentum caused by Magnetic Braking (MB) of the companion star and/or Gravitational Radiation (GR). This scenario envisages mass-transfer phases in which the system will start emitting in X-rays and will be observed as a LMXB. At the end of the LMXB phase, the NS, spun-up to millisecond periods by the accretion of matter and its angular momentum, can exit the graveyard and appear in the bottom-left portion of the $P - \dot{P}$ diagram (where most of the pulsars are actually hosted in binary systems, marked by orange symbols in Fig. 4.1), being observed as a rotation-powered MSP.

4.1.2 Low-Mass X-ray Binaries and Accretion onto a Neutron Star

LMXBs are (Gyr-old) binary systems in which a low-mass star transfers matter onto a compact object via Roche lobe overflow. Matter passing through the inner Lagrangian point has a large specific angular momentum (because of the rotation of the system around its center of mass) that inhibits radial accretion. Matter starts to spiral-in around the compact object creating a structure usually defined as *accretion disk*, in which internal torques transfer angular momentum outwards, allowing the accreting plasma to slowly approach the compact object. The mechanical energy of matter is partially dissipated in the disk which emits a blackbody-like spectrum with a temperature increasing towards the center. If the compact object is a NS, the rest of the mechanical energy of the matter is released when the accreting matter reaches the surface of the NS, giving a total luminosity of $\sim GM_{NS}\dot{M}/R_{NS}$, where \dot{M} is the mass accretion rate onto the NS. This implies an efficiency in the conversion of rest mass energy to luminosity of $\eta = GM_{NS}/(c^2 R_{NS}) \sim 0.21$ for a $1.4 M_\odot$

NS with 10 km radius. The mass accretion rate onto the NS is limited by radiation pressure which can be high enough to balance the gravitational force towards the NS. This happens at the so-called Eddington limit; in the hypothesis of stationary and spherical accretion, the maximum luminosity of the system is given by: $L_{Edd} \simeq 1.3 \times 10^{38} (M/M_\odot) \text{ erg s}^{-1}$. For a NS with $M_{NS} = 1.4 M_\odot$, the Eddington limit is given by $L_{Edd} \simeq 2.5 \times 10^{38} \text{ erg s}^{-1}$ (appropriate for helium-rich material and a moderate, $z = 1.2$, gravitational redshift correction factor; [133]), corresponding to a mass accretion rate of $\dot{M}_{Edd} \sim 1.3 \times 10^{18} \text{ g s}^{-1} \sim 2 \times 10^{-8} M_\odot \text{ yr}^{-1}$. At the Eddington luminosity, the blackbody emission from the NS surface will reach a temperature of about 20 million K, corresponding to $\sim 2 \text{ keV}$ in photon energy. This implies that the emission from the innermost region of the system will be mainly in the X-ray band. At such high luminosity, the strong radiation pressure can drive strong outflows of matter and the inner part of the disk may inflate and form a geometrically thick and optically thick disk, also known as *thick disk*. In general, besides the blackbody-like components produced by the accretion disk and the NS surface, the X-ray spectrum of a LMXB is often complicated by the presence of a hot electron corona in the central part of the system, which up-scatters soft photons coming from the disk and/or the NS surface, producing hard Comptonization spectra.

In the case of a magnetised NS, the accretion flow towards the NS can be halted by the magnetosphere depending on the magnetic field strength (see also the discussion focused on the changes of state of MSPs, presented in Sect. 6.3). For a dipolar magnetic field, the magnetic energy ($B^2/8\pi$) increases at small radii and can overcome the Kinetic energy ($\rho v^2/2$) of the (free-falling) in-falling matter at the magnetospheric radius (which delimits the NS magnetosphere); inside this radius (charged) particles are forced to flow along the magnetic field lines and will be accreted at the NS polar caps. For spherical accretion, this radius is called Alfvén radius and it is given by:

$$R_A = \left(\frac{\mu^4}{2GM_{NS}\dot{M}^2} \right)^{1/7} \sim 3.7 \times 10^6 \mu_{26}^{4/7} \dot{M}_{-10}^{-2/7} (M/M_\odot)^{-1/7} \text{ cm} \quad (4.4)$$

where μ_{26} is the magnetic moment (BR^3) in units of 10^{26} Gauss cm³ and \dot{M}_{-10} is the mass accretion rate in units of $10^{-10} M_\odot \text{ yr}^{-1}$. It is easy to deduce that, in order to have a magnetospheric radius larger than the NS radius for a mass accretion rate of about 10% of the Eddington limit, the magnetic field should be higher than 10^8 Gauss. In this case, under the hypothesis of magnetic axis not aligned with the NS spin axis, accretion onto the polar caps can produce a lighthouse signal visible as X-ray (accretion-powered) pulsations, which give us a direct measure of the NS spin period. For disk-fed accretion flows, the ram pressure of matter is concentrated in the disk plane, allowing it to penetrate further the NS magnetosphere and reducing the magnetospheric radius, r_m , with respect to the Alfvén radius, by a factor $\sim 0.3 - 0.5$ (see, e.g., [16, 56]).

The interaction of the accretion flow with the NS magnetosphere allows an exchange of angular momentum between the accreting matter and the NS which results in a spin-up or spin-down of the NS (see, e.g., [55] for a first study of the torques exerted by the accreting matter onto the NS). Assuming that the inner accretion disk is truncated at the magnetospheric radius and defining the corotation radius r_{CO} as the radius at which the Keplerian angular velocity of the disk, $\omega_K(r)$, matches the NS angular velocity Ω_0 , that is $r_{CO} = (GM_{NS}/\Omega_0^2)^{1/3} \sim 2.8 \times 10^6 (M/M_\odot)^{1/3} P_{ms}^{2/3}$ cm (where P_{ms} is the NS spin period in milliseconds), we can envisage the following three possibilities:

(i) $r_m < r_{CO}$, i.e. the inner disk rotates faster than the magnetosphere and exerts a positive torque spinning-up the NS. In this case the spin-up torque is given at zero order by: $I\Omega\dot{\Omega} = \dot{M}(GM_{NS}r_m)^{1/2}$, i.e. by the mass accretion rate onto the NS times the specific angular momentum at the magnetospheric radius (the latter also has a weak dependence on the mass accretion rate, as $\dot{M}^{-2/7}$). According to Ghosh and Lamb [55], the rate of change of the NS period is:

$$\frac{\dot{P}}{P} = -3 \times 10^{-8} f \frac{P}{1ms} \left(\frac{L_X}{10^{37} ergs^{-1}} \right)^{6/7} yr^{-1}, \quad (4.5)$$

where the dimensionless parameter f is expected to be of the order of unity. This demonstrates that in the LMXB phase the NS can be efficiently spun-up by accretion torques within its lifetime. Moreover, it can be shown that, for a slow-rotating low-magnetic field NS, it is enough to accrete no more than $\sim 0.1\text{--}0.2 M_\odot$ to spin-up the NS to millisecond periods (see, e.g., [17]), unless the mass transfer is highly non conservative. Hence, for a NS it is in principle possible to reach mass-shedding spin periods before the gravitational collapse into a black hole.

(ii) $r_m > r_{CO}$, i.e. the Keplerian velocity at the inner accretion disk is lower than the angular velocity of the NS and this causes a spin-down torque onto the NS. Indeed, in this case, the centrifugal barrier should prevent matter to penetrate the magnetosphere, giving the so-called *propeller effect*. However, magneto-hydrodynamic simulations by Romanova et al. [116] suggest that this is true only when the magnetospheric radius is very large when compared to r_{CO} ($r_m \gg r_{CO}$, strong propeller regime), otherwise matter can still (at least in part) penetrate the magnetosphere and accrete onto the NS (weak propeller regime), allowing the possibility to observe spin-down during (low-rate) accretion phases. The latter may also be favoured by some threading of the magnetic field lines by the accretion disk beyond the corotation radius (see, e.g., [73, 111, 134], and references therein) when magnetic field lines are not completely shielded by current sheets at the magnetospheric radius. In this case, threading of the magnetic field can result in both a spin-up (due to threading inside r_{CO}) and a spin-down (due to threading outside r_{CO}), and the balance of the two, plus the material torque, gives the net torque exerted onto the NS. The possibility to have a spin-down of the NS during accretion phases for fast rotators has been studied by Rappaport et al. [111] and Kluzniak et al. [73]; these authors argue that the accretion disk structure around a

fast pulsar will adjust itself so that the inner edge of the disk, also known as the truncation radius, will remain fixed near r_{CO} while accretion will continue. In this case, the net torque onto the NS is given by the accretion torque of matter captured at the corotation radius decreased by a spin-down torque due to the magnetic field drag on the accretion disk, which, at a first order of approximation, can be expressed as $\mu^2/(9r_{CO}^3)$, resulting in the net torque:

$$\tau_{NS} = 2\pi I \dot{v}_{NS} = \dot{M}(GM_{NS}r_{CO})^{1/2} - \frac{\mu^2}{9r_{CO}^3}. \quad (4.6)$$

(iii) $r_m \sim r_{CO}$, in this case matter loaded by the magnetic field will have the same angular velocity of the NS and no net torque is expected onto the NS, meaning that the NS will be at the spin equilibrium. In this case, the equilibrium period is given by:

$$P_{eq} = 0.5\mu_{26}^{6/7} L_{37}^{-3/7} R_6^{-3/7} (M/M_\odot)^{-2/7} \text{ ms}, \quad (4.7)$$

where R_6 is the NS radius in units of 10^6 cm. This means that a NS can reach in principle a spin equilibrium period shorter than a millisecond. However, the maximum spin frequency that a NS can attain also depends on its Equation of State (EoS, see, e.g., [85] for a review), which sets the mass-shedding spin limit depending on the mass-radius relation. The fastest-spinning NS known to date is PSR J1748–2446ad, a rotation-powered pulsar spinning at 716 Hz [64]. This spin frequency is, however, not high enough to put strong constraints onto the NS EoS and it is not clear yet whether other mechanisms (e.g. GR emission, a relatively large magnetic field, observational bias, and so on) can be responsible of the lack of ultra-fast spinning NS (see, e.g., [9, 18, 32, 94, 107]).

4.2 The Discovery of Accreting X-ray Millisecond Pulsars: The Missing Link in the Recycling Scenario

From what is discussed above, it appears clear that NS can be spun-up to millisecond periods or below, depending on the constraints imposed by the EoS of ultra-dense matter, during the accretion phase in a LMXB. However, till 1998, no LMXB was found to show any coherent pulsation at such low periods. The fact that the vast majority of LMXBs do not show coherent pulsations is still a fascinating enigma. Several possible explanations have been invoked to interpret this fact, but none of them is fully satisfactory (see also [105] and references therein, for further discussion of this issue). Thanks to the large effective area ($\sim 6500 \text{ cm}^2$) and good timing capabilities ($\sim 1 \mu\text{s}$) of the NASA satellite Rossi X-ray Timing Explorer (*RXTE*), in 1998 it discovered the first LMXB, SAX J1808.4–3658, to show coherent pulsations (at about 401 Hz; [137]). This was the first direct confirmation

of the recycling scenario, since it demonstrated that LMXBs could indeed host a fast-spinning NS. Doppler effects visible in the spin period of the pulsar revealed the ~ 2 h orbital period of the system [33]. The final confirmation of the recycling scenario arrived only in 2013, when Papitto et al. [92] discovered a transient system, IGR J18245–2452, showing accretion-powered pulsations during the X-ray outburst and rotation-powered radio pulsations during X-ray quiescence (see Sect. 6.4.2). This source, which is one of the members of the so-called *transitional* MSP class thoroughly discussed in Chap. 6, is the direct evidence of the fact that, when accretion stops, the rotation-powered pulsar mechanism should resume on a short timescale.

SAX J1808.4–3658, first discovered in 1996 by the Wide Field Camera (WFC) on board the X-ray satellite BeppoSAX, is a transient system, which spends most of the time in quiescence (with X-ray luminosity around a few 10^{31} erg s $^{-1}$, [28]) and shows month-long X-ray outbursts every ~ 3 yr, during which it reaches an X-ray luminosity in the range 10^{36} – 10^{37} erg s $^{-1}$. Now we know about two dozens of these systems, belonging to the class of Accreting Millisecond X-ray Pulsars (hereafter AMXPs), most of them discovered by *RXTE* and the ESA satellite *XMM-Newton*, and more recently by *NuSTAR* and *NICER*. All of them are transient systems, although with very different behaviour (see Table 2 in [78] for an overview). X-ray outbursts usually last from a few days to less than three months. Most of the AMXPs have shown just one outburst since their discovery, while a few sources show recurrent outbursts. The shortest outburst recurrence time is about a month, registered for the globular cluster source NGC 6440 X-2, with an outburst duration of less than 4–5 days, whereas the longest outburst has been observed from HETE J1900.1–2455, and has lasted for about 10 years (up to late 2015 when the source returned to quiescence; [41]).

Another peculiar behaviour is the intermittency of the pulsations, which is important because the understanding of this phenomenon could give insights on the lack of X-ray pulsations in the large majority of NS LMXBs. This phenomenon was observed for the first time in the AMXP HETE J1900.1–2455, which went into X-ray outburst in 2005 and showed X-ray pulsations at 377 Hz. However, after the first 20 days of the outburst, pulsations became intermittent for about 2.5 yr [54], and then disappeared with very stringent upper limits on the pulsed fraction ($<0.07\%$; [99]). The most peculiar behaviour was observed from Aql X-1, a transient LMXB showing regular outbursts more or less every 0.5–1 year (see, e.g., [29]); it showed coherent pulsations in only one 150-s data segment out of a total exposure time of ~ 1.5 Ms from more than 10 years of *RXTE* monitoring [31]. Another AMXP showing intermittency of pulsations is SAX J1748.9–2021, where pulsations were detected sporadically in several data segments and in three out of four outbursts observed by the source (see, e.g., [101]). Note that these AMXPs may have a long-term average mass accretion rate higher than the other AMXPs. To explain this *intermittent* behaviour, it has been proposed that the accreting matter could screen

Table 4.1 Accreting X-ray pulsars in low mass X-ray binaries

Source	$\nu_s(P)$ [Hz][ms]	P_{orb} [hr]	f_x [M_\odot]	$M_{c,\min}$ (M_\odot)	Companion type	Ref.
Accreting millisecond X-ray pulsars						
Aql X-1	550 (1.8)	18.95	1.4×10^{-2}	0.56	MS	[31, 81]
IGR J17591–2342	527 (1.9)	8.80	1.5×10^{-2}	0.37	MS	[123]
Swift J1749.4–2807	518 (1.9)	8.82	5.5×10^{-2}	0.59	MS	[3, 40]
SAX J1748.9–2021	442 (2.3)	8.77	4.8×10^{-4}	0.1	MS	[1, 26]
IGR J17498–2921	401 (2.5)	3.84	2.0×10^{-3}	0.17	MS	[89]
XTE J1814–338	314 (3.2)	4.27	2.0×10^{-3}	0.17	MS	[79, 136]
IGR J1824–2453	254 (3.9)	11.03	2.3×10^{-3}	0.17	MS	[92]
IGR J17511–3057	245 (4.1)	3.47	1.1×10^{-3}	0.13	MS	[88]
IGR J00291+5934	599 (1.7)	2.46	2.8×10^{-5}	0.039	BD	[53]
IGR J17379–3747	468 (2.1)	1.88	8×10^{-5}	0.056	BD	[122]
SAX J1808.4–3658	401 (2.5)	2.01	3.8×10^{-5}	0.043	BD	[135, 137]
HETE J1900.1–2455	377 (2.7)	1.39	2.0×10^{-6}	0.016	BD	[48, 72]
XTE J1751–305	435 (2.3)	0.71	1.3×10^{-6}	0.014	He WD	[39, 80]
MAXI J0911–655	340 (2.9)	0.74	6.2×10^{-6}	0.024	He WD?	[118]
NGC6440 X–2	206 (4.8)	0.95	1.6×10^{-7}	0.0067	He WD	[2]
Swift J1756.9–2508	182 (5.5)	0.91	1.6×10^{-7}	0.007	He WD	[74]
IGR J17062–6143	164 (6.1)	0.63	9.1×10^{-8}	0.006	He WD?	[130]
IGR J16597–3704	105 (9.5)	0.77	1.2×10^{-7}	0.006	He WD	[121]
XTE J0929–314	185 (5.4)	0.73	2.9×10^{-7}	0.0083	C/O WD	[52, 59]
XTE J1807–294	190 (5.3)	0.67	1.5×10^{-7}	0.0066	C/O WD	[30, 39]

ν_s is the spin frequency, P_b the orbital period, f_x is the X-ray mass function, $M_{c,\min}$ is the minimum companion mass, calculated for an inclination $\sin i = 1$ of the binary system and for an assumed NS mass of $1.4 M_\odot$. The companion types are: WD = White Dwarf, BD = Brown Dwarf, MS = Main Sequence, He Core = Helium Star

Adapted and updated from Patruno and Watts [99]

the NS magnetic field, weakening it by orders of magnitude on a few hundred days timescale, hampering the possibility to effectively channel the accretion flow towards the NS polar caps (see, e.g., [99]). However, it is not clear yet whether this hypothesis can explain all the phenomenology observed in AMXPs, and more observations and theoretical efforts are needed to reach a satisfactory explanation of this puzzling behaviour.

In Table 4.1, we list the main properties of the AMXPs known to date. The following sections will be dedicated to the description of the main results obtained to date on the spectral and timing properties of this class of sources.

4.3 Timing and Spectral Properties of AMXPs

4.3.1 Spectral Properties

In the vast majority of the AMXPs, the X-ray luminosity during outburst remains below 10% the Eddington luminosity, and the spectra do not show transitions between hard and soft spectral states, as it usually happens for non-pulsating LMXBs (harbouring a NS or a black hole, see, e.g., [47]). For this reason, AMXPs are often referred to as hard X-ray transients. Hence, their spectra are quite similar to the spectra usually observed for NS LMXBs in the hard state, with little spectral evolution during the X-ray outburst. In particular, the X-ray continuum is composed of one or two blackbody-like components and an unsaturated Comptonization component, usually with cutoff energies (corresponding to the electron temperature of the Comptonizing cloud, often called *corona*) of tens of keV [57, 58, 109]. In this case, the presence of a *reflection* of the hard Comptonized photons off the cold accretion disk is expected. This reflection component usually contains discrete features, such as the fluorescence iron line at 6.4–6.7 keV (depending on the iron ionization state), which are smeared by Doppler and relativistic effects due to the large velocity of matter in the inner accretion disk (see Fig. 4.2 where these spectral components are indicated). The precise modelling of these features may give information about some important physical parameters as the ionization state

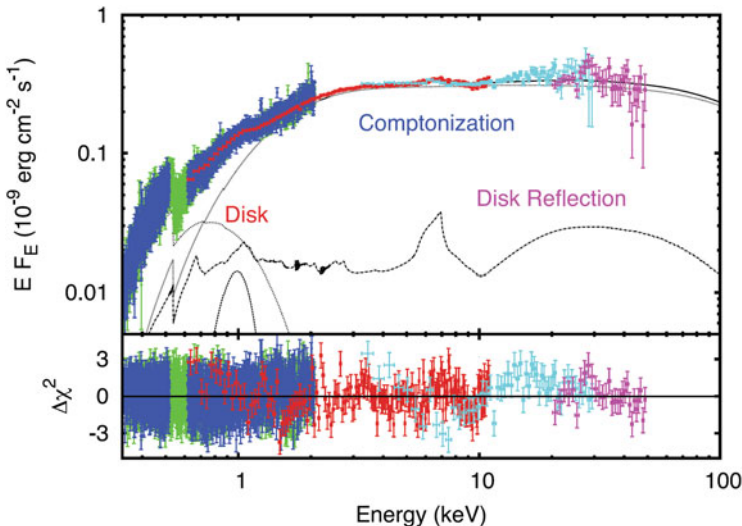


Fig. 4.2 Broad-band spectrum of the AMXP HETE J1900.1–2455 in outburst as observed by *XMM-Newton* (blue, green and red points) and *RXTE* (cyan and magenta points). The single spectral components used to fit the X-ray spectrum are indicated in the figure. The Gaussian feature at 0.98 keV may be identified with Fe L α or He-like Ne K α transition. Credits: Papitto et al. MNRAS, 429, 3411 (2013)

of matter in the inner accretion disk, the inclination of the system with respect to the line of sight, the radius at which the inner accretion disk is truncated, the outer radius of the emitting region in the disk, and the index of the emissivity law in the disk, which is $\propto r^{\text{index}}$.

The inner disk radius is an important parameter since it may be useful to obtain an estimate of the magnetospheric radius, which can be compared to the corotation radius of the source in order to test the accretion torque paradigm described above. Together with discrete features (emission lines and absorption edges), the hard photons impinging the disk are scattered by Thomson/(direct) Compton effect, generating a continuum spectrum (with a shape similar to the primary Comptonization spectrum) which is usually evident as an excess of emission between 10 and 30 keV named Compton hump. The spectral shape of this continuum is also sensitive to the inclination angle of the system and the ionization state of matter in the disk. The latter is measured through the parameter $\xi = L_X/(n_e r^2)$, where L_X is the bolometric X-ray luminosity of the ionizing continuum, n_e is the electron density in the disk atmosphere and r is the distance of the disk from the center of the system. For high values of the ionization parameter ξ , photoelectric absorption of soft X-rays in the disk is suppressed and this results in a strong reflection continuum, which increases at soft X-ray energies instead of decreasing.

Most, but not all, of the AMXPs have been observed with moderate/high resolution instruments in order to perform a broad-band spectral analysis and look for reflection features. In the following, we describe the main spectral results obtained for the available sample of AMXPs, with particular attention to reflection features and the constraints that can be inferred on the inner accretion flow. Indeed, a relatively small inner disk radius is implied for most of the AMXPs for which a spectral analysis has been performed and a broad iron line has been detected in moderately high resolution spectra. The AMXP IGR J17511–3057, observed by *XMM-Newton* for 70 ks and *RXTE* [88], showed both a broad iron line and the Compton hump at ~ 30 keV. In this case, the inner disc radius was at ≥ 40 km from the NS center, assuming a $1.4 M_\odot$ NS, with an inclination angle between 38° and 68° (see also [95]). The AMXP and transitional pulsar IGR J18245–2452 observed by *XMM-Newton* [92], showed a broad iron line at 6.7 keV (identified as K α emission from Fe XXV) with a width of ~ 1.6 keV, corresponding to $R_{in} \simeq 17.5 R_g$ (where $R_g = GM_{NS}/c^2$ is the gravitational radius) or ~ 36.7 km for a $1.4 M_\odot$ NS. For comparison, the inner disk radius derived from the blackbody component was quite similar, 28 ± 5 km. The (intermittent) AMXP HETE J1900–2455, observed by *XMM-Newton* for ~ 65 ks [93], showed a broad iron line at 6.6 keV (Fe XXIII–XXV) and an intense and broad line at ~ 0.98 keV, visible both in the pn and in the RGS spectra, compatible with being produced in the same disk region (see Fig. 4.3, right panel). In this case, the inner disc radius was estimated to be $25 \pm 15 R_g$, with an inclination angle ranging between 27° and 34° . A moderately broad, neutral Fe emission line was observed during the 2015 outburst of IGR J00291+5934 observed by *XMM-Newton* and *NuSTAR* [119]. Fitted with a Gaussian profile, the line centroid was at an energy of 6.37 ± 0.04 keV with a $\sigma = 80 \pm 70$ eV, while using a *diskline* profile, the line parameters were poorly constrained. The newly discovered

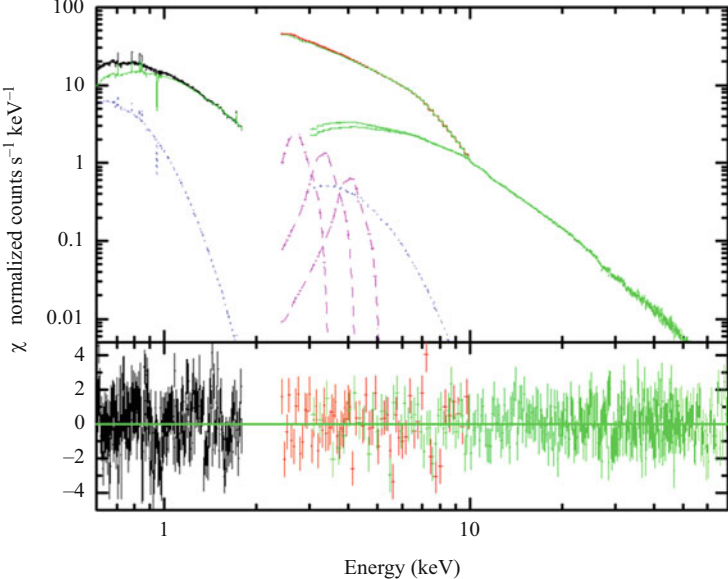


Fig. 4.3 Broad-band spectrum of the AMXP SAX J1808.4–3658 during its 2015 outburst as observed by *XMM-Newton* (black and red points) and *NuSTAR* (green points). The model includes a blackbody component, the *relxill/CP* component, which includes the Comptonization continuum and the smeared reflection component, and three low-energy features modelled with *disklines*. Credit: Di Salvo et al. MNRAS, 483, 767 (2019)

AMXP, MAXI J0911–655, observed by *XMM-Newton* and *NuSTAR* [119], showed the presence of a weak, marginally significant and relatively narrow emission line in the range 6.5–6.6 keV, modelled with a Gaussian profile with σ ranging between 0.02 and 0.2 keV, identified with a K α transition from moderate-to-highly ionized iron.

The (intermittent) AMXP SAX J1748.9–2021, observed by *XMM-Newton* for ~ 115 ks and *INTEGRAL* [108], was caught at a relatively high luminosity of $\sim 5 \times 10^{37}$ erg/s corresponding to $\sim 25\%$ of the Eddington limit for a $1.4 M_{\odot}$ NS, and, exceptionally for an AMXP, showed a spectrum compatible with a soft state. The broad-band spectrum was in fact dominated by a cold thermal Comptonization component (electron temperature of ~ 2 keV) with an additional hard X-ray emission described by a power-law (photon index $\Gamma \sim 2.3$), typically detected in LMXBs in the soft state (see, e.g., [44]). In addition, a number of broad (Gaussian $\sigma = 0.1$ –0.4 keV) emission features, likely associated to reflection processes, were observed in the *XMM-Newton* spectrum. A broad iron line was observed at an energy of ~ 6.7 –6.8 keV, consistent with a Fe XXV K α transition produced in the disc at a distance of ~ 20 –43 R_g (~ 42 –90 km), with an inclination angle of ~ 38 –45°. The other broad emission lines may be associated to K-shell emission of S XVI (2.62 keV), Ar XVIII (3.32 keV) and Ca XX or Ca XIX (4.11 keV).

or 3.90 keV, respectively), and are compatible with coming from the same emission region as the iron line.

High-quality X-ray spectra of SAX J1808.4–3658 were obtained during the 2008 outburst with *XMM-Newton* [87] and *Suzaku* [25] and during the 2015 outburst with *XMM-Newton* (which observed the source at the peak of the outburst) and *NuSTAR*, which observed the source four days later [46]. The 2015 spectrum of SAX J1808.4–3658 taken with *NuSTAR* was quite similar to the 2008 spectra; the continuum emission was modelled with one or two blackbody-like components and a hard Comptonization component with an electron temperature >40 keV. On the other hand, the 2015 *XMM-Newton* spectrum was surprisingly much softer, with an electron temperature below 10 keV and a much colder blackbody component (corresponding to a large radius, >100 km, for the emitting surface, [46]). In all the cases, a reflection component was also required to model both the broad iron line and the Compton hump observed on top of the continuum (the composite broadband spectrum of SAX J1808.4–3658 observed during the 2015 outburst is shown in Fig. 4.3). All the smearing parameters were quite similar in the 2008 and 2015 spectra, with the exception of the ionization parameter, much higher during the 2015 *XMM-Newton* observation ($\log \xi \sim 3.5$), which also showed broad emission lines from highly ionized elements (S XVI, Ar XVIII and Ca XIX-XX) at low energies. In particular, the inner disk radius was $\sim 10 R_g$, corresponding to about 20 km; in comparison, the corotation radius of the system is $31m_{1.4}^{1/3}$ km, where $m_{1.4}$ is the NS mass in units of $1.4 M_\odot$, indicating that the disk was truncated inside the corotation radius during the outburst, as expected from the observed timing properties of the source. However, the inclination angle required by spectral fits turned out to be high (usually values $>60^\circ$ were required; the tighter constraint comes from the 2015 *XMM-Newton* spectrum, where $i = 58^\circ - 64^\circ$; [46]). This result is in agreement with evidences from the 2015 *XMM-Newton* spectrum of discrete absorption features, namely an absorption edge at ~ 7.4 keV from neutral or mildly ionized iron and at least two absorption lines, possibly from K transitions of highly ionized (He-like) Ne IX (at 0.947 keV) and Mg XI (at 1.372 keV). These lines were relatively broad (implying a velocity dispersion of $\sigma_v \sim 0.01c$) and blue-shifted at a velocity a few percent the speed of light [46]. If confirmed, these lines may suggest the presence of a weakly relativistic outflowing wind towards the observer. A high inclination angle is also compatible with other estimates (see, e.g., [12, 42, 69, 135]). However, high values for the inclination angle of the system look at odd when considered together with optical estimates of the radial velocity of the companion star [37, 48], since they imply quite low values of the NS mass, $M_{NS} \sim 0.5 - 0.8 M_\odot$. These results may indicate some problem with the interpretation of the reflection component and/or the need of more precise measurements of the radial velocity of the companion star.

It is noteworthy that reflection features are not always observed in AMXPs. Indeed, no evidence of iron emission lines or reflection humps has been reported for IGR J16597–3704 observed by *Swift* and *NuSTAR* [121], IGR J17379–3747 observed by *XMM-Newton* [122], XTE J1807–294 observed by *RXTE*, *XMM-*

Newton and *INTEGRAL* [49], and XTE J1751–305 observed by *XMM-Newton* [83]. Similar results have been reported for the 2018 outburst of the AMXP SWIFT J1756.9–2508 monitored by several satellites such as *NICER*, *Swift*, *XMM-Newton*, *NuSTAR* and *INTEGRAL* [124]. Evidences of iron emission lines in the 6–7 keV band have been, however, reported from the analysis of *RXTE* observations of the source during its 2007 and 2009 outbursts [103].

4.3.2 Short-Term Variations of the Spin During Outbursts

Accretion torque theories can be tested by studying the spin variations of AMXPs during accretion phases. These studies can provide valuable information on the mass accretion rate and magnetic field of the NS in these systems, as well as their spin evolution. Coherent timing has been performed on several sources of the sample, with sometimes controversial results (see [27] for a recent review). Some sources seem to show spin-up during outbursts (e.g. IGR J00291+5934, XTE J1751–305, XTE J1807–294, IGR J17511–3057), while other sources seem to show spin-down even during accretion phases (e.g. XTE J0929–314, XTE J1814–338, IGR J17498–2921 and IGR J17591–2342). Although some AMXPs show pulse phase delays distributed along a second order polynomial, indicating an almost constant spin frequency derivative, other sources show strong timing noise (e.g. SAX J1808–3658, HETE 1900–2455), sometimes correlated with sharp variations of the X-ray flux [102], which can hamper any clear measurement of the spin derivative.

The first AMXP for which a spin derivative has been measured is the fastest spinning (~ 599 Hz, in a 2.46 hr orbit) among these sources, IGR J00291+5934. It is now generally accepted that this source shows spin up at a rate of $\sim (5\text{--}8) \times 10^{-13}$ Hz s $^{-1}$ ([50, 63, 90, 98]; see the top panel of Fig. 4.4). Burderi et al. [22] have attempted to fit the phase delays vs. time with physical models taking into account the observed decrease of the X-ray flux as a function of time during the X-ray outburst, with the aim of getting a reliable estimate of the mass accretion rate onto the compact object. Because the X-ray flux, which is assumed to be a good tracer of the mass accretion rate, is observed to decrease along the outburst, this variation has to be considered in Eq. (4.6) in order to obtain the correct value of the mass accretion rate, and hence of the spin frequency derivative, at the beginning of the outburst as well as its variation during the outburst. This approach has been successfully applied to the timing of the 2014 outburst of the so-called *bursting pulsar*, GRO J1744–28, an X-ray pulsar with a spin frequency of 2.14 Hz in a 11.83 days orbit around a $0.2 M_{\odot}$ companion star. Sanna et al. [120] were able in this way to obtain a good fit of the pulse phase delays versus time, deriving a frequency spin-up of $\sim 9 \times 10^{-12}$ Hz/s and inferring a distance to the source between 3.4 and 4.1 kpc, assuming a disk viscous parameter α in the range of 0.1–1. In the case of IGR J00291+5934, this technique gave a spin frequency derivative at the beginning of the outburst of $\dot{\nu} \sim 1.2(2) \times 10^{-12}$ Hz s $^{-1}$, corresponding to a mass accretion rate of $\sim 7 \times 10^{-9} M_{\odot}/\text{yr}$ and a peak bolometric luminosity of $\sim 7 \times 10^{37}$ erg/s

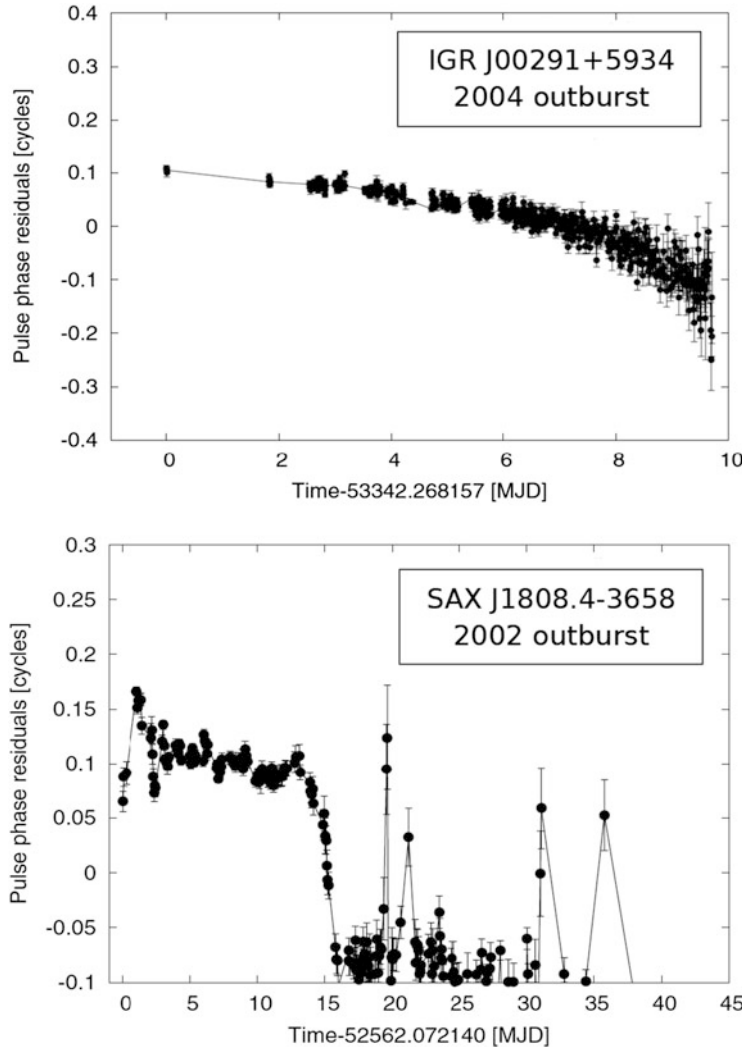


Fig. 4.4 Phase residuals of the fundamental frequency for the AMXP SAX J1808.4–3658 (bottom Panel) and IGR J00291+5934 (top Panel). Figure adapted from Patruno et al. ApJL, 698(1), L60–L63 (2009)

for the 2004 outburst. This is at least one order of magnitude higher than the X-ray luminosity inferred from the observed X-ray flux, assuming a distance of 4.2 kpc. Once we will have a direct, independent, estimate of the distance to the source, we will have the possibility to test the \dot{M} vs. X-ray luminosity relation, torque theories and/or the physical parameters of the NS in this system.

A recent example of an AMXP showing spin-down while accreting is given by IGR J17591–2342. This source has been extensively monitored by *NICER* during

its outburst starting from 2018 August 15 up to 2018 October 17 for a total exposure time of ~ 101 ks distributed into 37 dedicated observations. X-ray pulsations have been detected uninterruptedly for almost 60 days allowing to accurately investigate the NS spin frequency evolution. Phase-coherent timing analysis of the frequency fundamental and second harmonic components revealed a statistically significant negative frequency derivative $\dot{\nu} \sim -7 \times 10^{-14}$ Hz/s [126] (see, however, [75] for different results from the timing analysis). Further analysis of the X-ray pulse phase evolution of IGR J17591–2342, adopting a physical model that accounts for the accretion material torque as well as the magnetic threading of the accretion disc in regions where the Keplerian velocity is slower than the magnetosphere velocity, allowed to constrain the NS magnetic field to be $B_{eq} = 2.8(3) \times 10^8$ G [126].

A similar spin frequency evolution has been reported for the AMXPs IGR J17498–2921 ($\dot{\nu} = -6.3(1.9) \times 10^{-14}$ Hz/s; [89]), XTE J1814–338 ($\dot{\nu} = -6.7(7) \times 10^{-14}$ Hz/s; [86]), and XTE J0929–314 ($\dot{\nu} = -9.2(4) \times 10^{-14}$ Hz/s; [52]). These observations indicate that spin-down during accretion phases is possible and requires a magnetic threading of the accretion disk.

The best studied, as well as most discussed source, is certainly the first discovered AMXP, SAX J1808–3658. Differently from all the other AMXPs, this source shows X-ray outbursts almost regularly every 2–4 years. So far, eight outbursts have been observed from this source with instruments with a high-time resolution, each lasting about one month. The pulse phase evolution during the outburst showed a strong timing noise, with phases going up and down without any clear correlation with flux variations, or remaining constant for a long time before jumping to another constant phase value (see, e.g., [60–62]). In the attempt to gain information on the spin variations in this source, Burderi et al. [21] have analysed separately the fundamental and second harmonic of the pulse profile during the 2002 outburst of the source, finding that while the phases of the fundamental were dominated by timing noise (see Fig. 4.4, bottom panel), the second harmonic showed a more regular behaviour. This suggests that the phase jump in the fundamental (clearly visible in the bottom panel of Fig. 4.4) was not related to an intrinsic spin variation (which would have affected the whole pulse profile), but was instead caused by a change of the shape of the pulse profile, leaving the possibility that the second harmonic is a better tracer of the NS spin evolution. A similar behavior of the second harmonic has also been observed in other AMXPs (e.g. [91, 112, 114]). Under this hypothesis, the fitting of the second harmonic phase delays revealed a spin-up of SAX J1808–3658 at the beginning of the 2002 outburst of $\dot{\nu} = 4.4(8) \times 10^{-13}$ Hz s $^{-1}$, corresponding to a mass accretion rate of $\dot{M} \sim 1.8 \times 10^{-9} M_\odot$ yr $^{-1}$, and a constant spin-down, of $\dot{\nu}_{sp} = -7.6(1.5) \times 10^{-14}$ Hz s $^{-1}$, dominating the phase delays at the end of the outburst. The mass accretion rate inferred from timing was only a factor of 2 larger than the inferred X-ray bolometric luminosity at the beginning of the outburst, that is $\sim 10^{37}$ ergs s $^{-1}$. The spin-down can be interpreted in terms of the threading of the accretion disk by the NS magnetic field outside the corotation radius, which, in agreement with expectations, appears to be more relevant at the end of the outburst, when the mass accretion rate significantly

decreases. The derived magnetic field, $B = (3.5 \pm 0.5) \times 10^8$ G, is perfectly in agreement with other, independent, constraints (see [21], and references therein).

The latest outburst shown by SAX J1808.4–3658 in 2019 was monitored with *NICER* for one month and a total exposure of 355.4 ks. Timing analysis of these data showed that the pulse profile was dominated by the fundamental (the second harmonic was significantly detected only in a handful of intervals) and the relative phase delays showed a clear parabolic trend typical of a spin-down at the rate of $\dot{v} = -3.02(13) \times 10^{-13}$ Hz s⁻¹ [15]. Since these phase shifts appear to be correlated with the source flux, the authors interpreted this trend in terms of hot-spot drifts on the stellar surface, driven by changes in the mass accretion rate.

Other recent results regard phase-coherent timing analysis of the outburst of the AMXPs SWIFT J1759–2508 and IGR J17379–3737, which allowed to set upper limits on the spin frequency derivative of $\dot{v} < |1.4| \times 10^{-12}$ Hz/s [14, 125] and $-0.5 \times 10^{-14} < \dot{v} < 0.9 \times 10^{-14}$ Hz/s [15], respectively.

4.3.3 Long-Term Variations of the Spin

AMXPs for which more than one outburst has been observed with high time resolution instruments, allow us to estimate the long term spin evolution by comparing the averaged spin frequency measured in each outburst. To date only eight AMXPs have been observed in different outbursts: SAX J1808.4–3658, IGR J00291+5934, XTE J1751–305, Swift J1756.9–2508, IGR J17379–3747, IGR J17511–3057, NGC 6440 X–2, and SAX J1748.9–2021 (although, with relatively low S/N and short outburst duration for some of these sources, see Table 4.2).

The best constrained long-term spin evolution was obtained for SAX J1808.4–3658 (see the top panel of Fig. 4.5), for which the secular spin evolution has been measured over a 13 year time span (between 1998 and 2011), showing a constant long-term spin-down at a rate of $\sim -1 \times 10^{-15}$ Hz s⁻¹ (see [105], and references therein). Because of the stability of the spin-down rate over the years, the most likely explanation appears to be loss of angular momentum via magnetic-dipole radiation, which is expected for a rapidly rotating NS with a magnetic field. The measured spin-down is consistent with a polar magnetic field of $(1.5–2.5) \times 10^8$ G, in agreement with other estimates. The spin frequency measured during the 2015 outburst had a large uncertainty because of strong timing noise of the fundamental. Interestingly, the spin frequency measured using the phases of the second harmonic fell very close (less than 2σ) from the value predicted by the secular evolution [117]. In the 2019 outburst, the second harmonic was significantly detected only in a few *NICER* snapshots and the exact value of the spin frequency inferred from the fundamental depends on the adopted timing solution. Bult et al. [15] have fitted the phase delays using a linear model (which leaves large residuals), a quadratic model (indicating a spin-down during the outburst), and a flux-adjusted model (under the hypothesis that phase variations with time originate from a hot-spot drifting on the

Table 4.2 Accreting millisecond X-ray pulsars: secular spin and orbital evolution

Source	N	P_{orb} (s)	T_{ASC} (MJD)	\dot{P}_{orb} (10^{-11} s/s)	$\dot{\nu}$ (10^{-15} Hz/s)	Ref.
NGC 6440 X-2	4	3457.8929(7)	55318.04809(2)	± 8	± 500	[13]
SAX J1748.9–2021	4	31554.868(3)	52191.52737(3)	3.9(1.1)	–	[127]
IGR J00291+5934	4	8844.07673(3)	53345.16192640(5)	-0.007(22)	-3.0(8)	[90, 98, 100, 119]
IGR J17379–3747	3	6765.84521(3)	53056.03926(12)	-0.25(23)	–	[122]
SAX J1808.4–3658	8	7249.1541(2)	50914.79449(4)	0.17(6)	-1.01(7)	[15, 128]
Swift J1756.9–2508	3	3282.3519(5)	54265.28087(10)	0.15(28)	-0.48(6)	[14, 124]
IGR J17511–3057	2	12487.50(7)	57107.85882(8)	4.4(7)	–	[115]
IGR J1751–305	2	2545.342(2)	52368.0129023(4)	± 1.4	-5.5(1.2)	[113]

N is the number of outbursts observed, P_{orb} is the orbital period, T_{ASC} is the time of passage from the Ascending Node and the reference of the orbital solution, \dot{P}_{orb} is the orbital period derivative, and $\dot{\nu}$ is the long-term spin frequency derivative

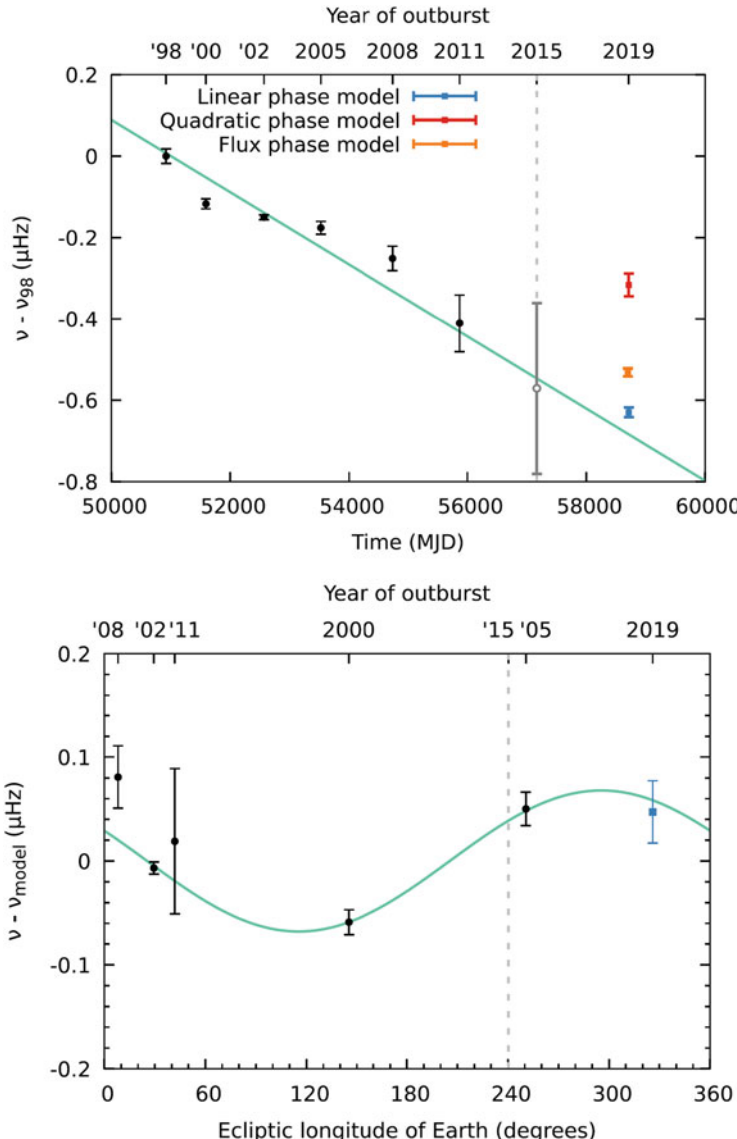


Fig. 4.5 *Top Panel:* Secular spin frequency evolution of the AMXP SAX J1808.4–3658 calculated relatively to the 1998 epoch. Black points represent measurements obtained with *RXTE* while colored squared represent the *NICER* measurements obtained for the 2019 outburst of the source for three different models (see [15] for more details). The solid line indicates the spin evolution best-fit model. *Bottom Panel:* Spin frequency measurements of the AMXP SAX J1808.4–3658 relative to the best-fit spin-down model as a function of the Earth’s ecliptic longitude. Credit: Bult et al., ApJ, 898, 38 (2020), reproduced with permission of the AAS

stellar surface, driven by changes in the mass accretion rate). The linear and flux-adjusted models gave a spin frequency relatively close to the secular spin-down trend, while the quadratic model gave a frequency lying significantly above the trend (see Fig. 4.5, top panel). Considering the linear model (which provides the frequency value closest to the expected trend), the long-term evolution of the spin showed a modulation around a constant spin-down behaviour at the Earth’s orbital period (see bottom panel of Fig. 4.5), which has been used to astrometrically refine the source coordinates.

A long-term spin-down has also been measured for IGR J00291+5934 between the 2004 and 2008 outbursts, at a rate of $-4.1(1.1) \times 10^{-15} \text{ Hz s}^{-1}$ [63, 90, 98]. This value is larger than that observed in SAX J1808.4–3658, as expected given that IGR J00291+5934 spins at a higher frequency. The less accurate spin measurement obtained from the *XMM-Newton* observation of its 2015 outburst could only set an upper limit on the spin-down since the previous outburst as $|\dot{\nu}| < 6 \times 10^{-15} \text{ Hz s}^{-1}$ (see [119] and references therein). If interpreted in terms of magneto-dipole emission, the measured spin-down translates into an estimate of the NS magnetic field of $(1.5 - 2) \times 10^8 \text{ G}$. Another possibility is given by the spin-down torque associated with the emission of GR, strongly dependent on the NS spin, which has also been proposed as a limiting factor for the maximum spin frequency observed for a NS (to date 716 Hz, [64]). Assuming that the long-term spin-down observed in IGR J00291+5934, the fastest spinning AMXP known to date, is due to this mechanism, the measurement of the average spin-down in this source translates to an upper limit on the average mass quadrupole moment of $Q \lesssim 2 \times 10^{36} \text{ g cm}^2$ [63]. Under this hypothesis, it is possible to predict that the long-term spin-down in IGR J00291+5934 should be a factor 7.6 higher than in SAX J1808.4–3658. The large uncertainties on these measurements prevent at the moment to assess this prediction, but it can be checked with future, high-quality, monitoring of the spin frequency in these systems.

The long-term spin evolution has been constrained for a few other sources of the sample of AMXPs. After the discovery of X-ray pulsations during the 2018 outburst of IGR J17379–3747, pulsations from this source have been discovered also in the *RXTE* archival data of its 2004 and 2008 outbursts after applying the binary ephemeris. Combining the barycentric spin frequency values from the three outbursts, an upper limit on the secular spin derivative has been estimated, $-8.3 \times 10^{-13} \text{ Hz/s} < \dot{\nu} < 1.1 \times 10^{-12} \text{ Hz/s}$. This corresponds to an upper limit on the magnetic field strength of $B < 2.8 \times 10^9 \text{ G}$, under the assumption of a NS radius of 10 km and an angle $\alpha \simeq 10^\circ$ between the magnetic hotspot and the rotational pole [122]. Swift J1756.9–2508 has been detected three times (2007, 2009 and 2018) in outburst since its discovery, which allowed the detection of a long-term spin-down derivative of $-4.8(6) \times 10^{-16} \text{ Hz/s}$ [125], corresponding to a NS superficial magnetic field $1.5 \times 10^8 < B_{eq} < 2.2 \times 10^8 \text{ G}$ (consistent with the value reported by Mukherjee et al. [84]).

4.3.4 Long-Term Timing of the Orbital Period

The study of the orbital evolution in Low Mass X-ray Binary systems is very important to constrain the evolutionary path leading to the formation of rotation-powered MSPs, and hence to obtain information on the progenitors of fast-rotating NS and on the recycling scenario (see Chap. 7 in this book). In this section, we discuss the long-term changes of the orbital period observed from AMXPs, which however reflect changes on timescales relatively short with respect to the secular evolution of the binary systems. Nonetheless, measuring the long-term orbital evolution can in principle be useful to probe alternative theories of Gravity. In fact, since the difference in the orbital period evolution of binaries interpreted with General Relativity (GR) and other theories of Gravity (e.g. Brans-Dicke gravity) is related to the mass difference of the two members of the binary system [139], these sources provide prime candidates for constraining deviations from GR [110]. In this framework, AMXPs are the most promising candidates for an experimental test on these alternative theories, because the companion star is, in most cases, a very light white dwarf or even a brown dwarf [12], and the primary stars are millisecond pulsars with orbital periods accurately determined.

However, these studies require a large baseline (tens of years) of data to be able to constraint the orbital period derivative. Hence, one of the main difficulty is given by the limited number of AMXPs observed recurrently into X-ray outburst. To date, only eight AMXPs have more than one outburst observed with high-time resolution instruments since their discovery, and therefore only a few constraints on the orbital period derivative have been derived to date (see Table 4.2). Moreover, long-term orbital solutions show sometimes residuals that are complex and difficult to interpret. Understanding these complex orbital residuals is therefore of fundamental importance, since it would allow to constrain the orbital period evolution in these systems, at least on a dynamical timescale, providing hints on their evolutionary paths or at least important information on the long-term dynamical behaviour of these systems (e.g., to measure the mass transfer rate and deduce the presence of outflows).

The best constraint on the orbital evolution of an AMXP obtained so far, comes again from SAX J1808.4–3658, which has shown eight X-ray outbursts to date, allowing to follow its orbital period over 21 years. As reported in Fig. 4.6, for each outburst the time of passage of the NS through the ascending node (T^* , which is the most sensitive parameter to variations of the orbital period) can be derived and plotted versus time. The orbital residuals (with respect to a constant orbital period) were dominated by a clear parabolic trend up to the 2015 outburst, with residuals with respect to this trend of the order of a few seconds [117]. Interpreting this parabolic trend with a constant orbital period derivative gave a best-fit value of $\dot{P}_{orb} = 3.6(4) \times 10^{-12} \text{ s s}^{-1}$, which implied a fast orbital expansion. The origin of the observed \dot{P}_{orb} is still not fully understood, yet, and different possible mechanisms have been proposed over the years [23, 45, 60, 104, 106]. However, there is consensus on the fact that conservative mass transfer is not compatible with

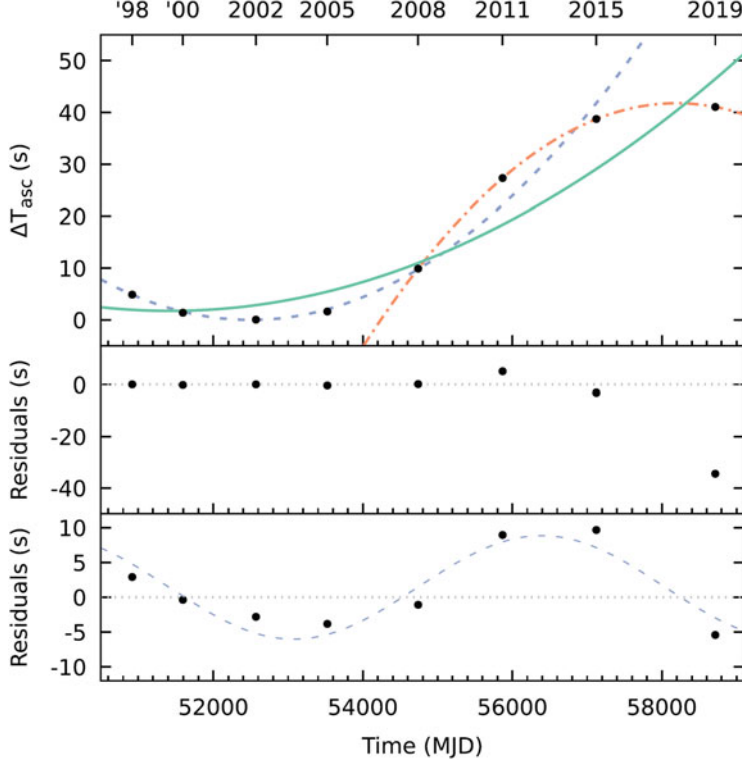


Fig. 4.6 Orbital evolution of the AMXP SAX J1808.4–3658. The dashed, dashed-dot and solid curves represent the parabolic trends fit between 1998–2008, 2008–2019, and 1998–2019 subsets of the data, respectively. Residuals relative to the 1998–2008 and 1998–2019 parabolic models are shown in the middle and bottom panels, respectively. The dashed line shown in the bottom panel represents a sinusoid with a 18.2 yr period and 7 s amplitude that has been inserted to tentatively describe the residuals (see [15] for more details). The solid line indicates the spin evolution best-fit model. Credit: Bult et al., ApJ, 898, 38 (2020)

the observed value of \dot{P}_{orb} for SAX J1808.4–3658. This can be easily demonstrated by estimating the mass-loss rate from the secondary star as a function of the observed orbital period derivative (see, e.g., [23]), which implies a mass transfer of the order of $2 \times 10^{-9} M_{\odot} \text{ yr}^{-1}$. This mass transfer rate is much larger than the mass accretion rate onto the NS, considering that the source accretes matter for about a month every 2–4 yr with a bolometric luminosity at the peak of the outburst barely reaching $10^{37} \text{ erg s}^{-1}$ (corresponding to a maximum mass accretion rate of $\sim 10^{-9} M_{\odot} \text{ yr}^{-1}$). The average mass accretion rate over the 17 years from 1998 to 2015 is indeed three orders of magnitude below, $\sim 2 \times 10^{-11} M_{\odot} \text{ yr}^{-1}$.

A non-conservative mass transfer can explain the large orbital period derivative assuming that the mass transfer rate is $\dot{M} \sim 10^{-9} M_{\odot} \text{ yr}^{-1}$, and that most of the transferred matter is expelled from the system, instead of being accreted onto

the NS, with the specific angular momentum at the inner Lagrangian point (see [23, 45]). In this case, the non-conservative mass transfer may be a consequence of the so-called *radio-ejection* model, extensively discussed by Burderi et al. [18, 19] and Ferraro et al. [51], which reports the discovery of the first tidally-distorted companion star to a millisecond (radio) pulsar and proposes that a fraction of the matter transferred by the companion star could be swept out by the (radiative and high-energy particles) pressure of the pulsar wind. Alternatively, the large orbital period derivative observed in SAX J1808.4–3658 has been interpreted as the effect of short-term angular momentum exchange between the donor star and the orbit [61, 104], resulting from variations in the spin of the companion star (holding the star out of synchronous rotation) caused by intense magnetic activity driven by the pulsar irradiation, the so-called Applegate & Shaham mechanism (hereafter A&S; [7]). In this case, the orbital period should oscillate, alternating epochs of orbital period increase and decrease, because of the gravitational quadrupole-coupling to the orbit. However, according to this mechanism, the system should evolve to longer orbital periods, because of mass and angular momentum loss, on a timescale of 10^8 yr (for a 2-hr orbital period and a companion mass of $0.1 - 0.2 M_\odot$), thus implying a strong orbital period derivative, similar to that inferred from the quadratic trend observed in SAX J1808.4–3658. In this framework, the orbital residuals in SAX J1808.4–3658 up to 2015 may be interpreted as small oscillations of few-seconds amplitude caused by the A&S mechanism superposed on a global orbital period derivative induced by the strong mass-loss from the system [117]. Alternatively, variations of the orbital period with respect to the global parabolic trend may be caused by random fluctuations of the mass transfer (and loss) rate.

The latest outburst of SAX J1808.4–3658 in 2019, however, shows an abrupt flattening of the parabolic trend ([15]; see the top panel of Fig. 4.6). Indeed, the measurements between 2008 and 2019 taken alone seem to imply an orbital contraction of the orbit in the last 10 years, with an orbital period derivative of $\dot{P}_{orb} \simeq -5.2 \times 10^{-12} \text{ s s}^{-1}$. Alternatively, fitting all the measurements with a global parabolic trend, gives an orbital period derivative of $\dot{P}_{orb} = 1.6 \pm 0.7 \times 10^{-12} \text{ s s}^{-1}$. As shown in the bottom panel of Fig. 4.6, the residuals around this mean trend show a sinusoidal-like, 7-s amplitude, oscillation with a period of approximately 18.2 years. Additional monitoring of future outbursts is needed to confirm the presence of oscillations around a steadily expanding orbit, or, instead, a ~ 20 s amplitude modulation around a constant (or much less variable) orbital period.

A very different evolution was found for IGR J0029+5934 (see Fig. 4.7) which has orbital parameters very similar to those of SAX J1808.4–3658, and it is considered its orbital twin. IGR J0029+5934 has shown only four outbursts since its discovery, but tight upper limits could be derived on its orbital period derivative, $|\dot{P}_{orb}| < 5 \times 10^{-13} \text{ s s}^{-1}$ (90% confidence level; [100, 119]). This implies a much slower orbital evolution, on a timescale longer than ~ 0.5 Gyr, as compared to the fast (at least up to 2015) orbital evolution of SAX J1808.4–3658, ~ 70 Myr. Although the orbital evolution observed in IGR J0029+5934 was obtained using only four points with large error bars, and more measurements are needed to confirm this result, it seems to be compatible with the expected timescale of mass transfer

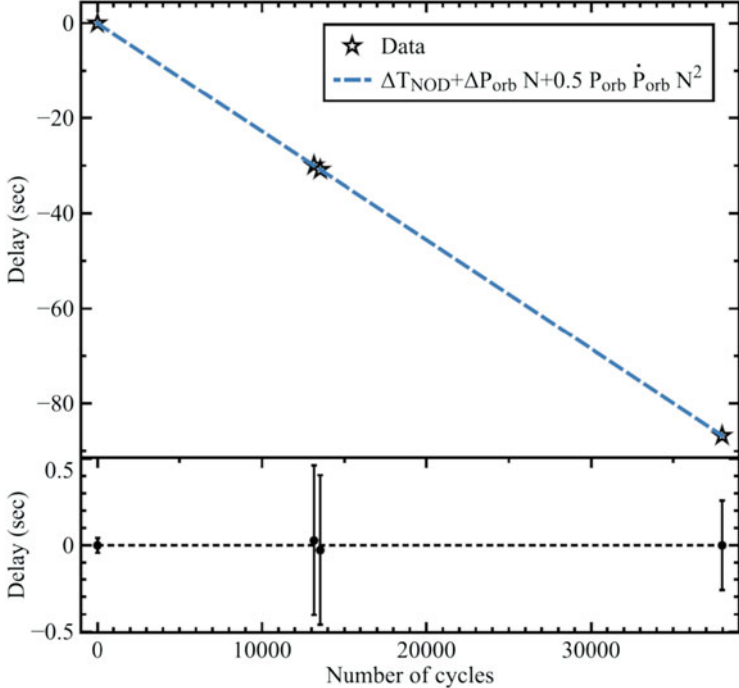


Fig. 4.7 Orbital evolution of the AMXP IGR J00291+5934. The cyan dashed line represents the best-fitting parabola used to model the data. Residuals in seconds of the time delays with respect to the best-fitting timing solution are shown in the bottom panel. Credit: Sanna et al., MNRAS, 466, 2910 (2017)

driven by angular momentum loss via GR, with no need of A&S mechanism or non-conservative mass transfer.

What causes such an enormous difference between the orbital evolution of two sources with very similar orbital parameters? Tailo et al. [131] have studied the effects of irradiation of the companion star in order to reproduce the evolution of SAX J1808.4–3658 (see Sect. 7.6.2 for a discussion of the model employed). They have simulated the binary evolution of its possible progenitor system, starting at an orbital period of ~ 6.6 h and taking into account angular momentum losses via magnetic braking (MB) and gravitational radiation (GR). They also considered the effects of illumination of the donor by both the X-ray emission during accretion phases and the spin-down luminosity of the pulsar. They showed that pulsar irradiation is a necessary ingredient to reach the correct orbital period when the donor mass is reduced to the actual value of 0.04 – $0.06 M_\odot$. Also it is shown that irradiation alters the internal structure of the donor, causing the companion star to be not completely convective at the values of mass observed for the system and keeping the MB active along the whole evolution (see also [35]). The secular mass transfer proceeds through cycles: the donor reacts to the irradiation by expanding

and starting a phase of large mass-transfer; consequently, mass loss dominates the period evolution. When the thermal relaxation of the envelope takes over, the star radius shrinks and the system detaches (see also [8] and references therein). In this framework, SAX J1808.4–3658 and IGR J0029+5934 may be at different phases of this cycle, with the first in a phase of high mass transfer rate (and a fast orbital evolution) and the latter in an almost detached phase (with a low mass transfer rate and slow orbital evolution). In both cases, a non-conservative mass transfer is implied with matter expelled from the system by the radiation pressure of the pulsar, that should be stronger in the case of IGR J0029+5934 because of its faster rotation. More details on the orbital evolution of these systems from a theoretical point of view can be found in Chap. 7 of this book.

In order to test this or other models for the orbital evolution in these systems it is important to continue monitoring the behavior of these and other sources. Other AMXPs have shown more than one outburst for which an orbital solution has been obtained. The long-term evolution of the time of passage at the ascending node of SAX J1748.9–2021 has been clearly observed after combining the orbital solutions of the five observed outbursts to date (in 2001, 2005, 2010, 2015 and 2018). Although marginally significant ($\sim 3.5\sigma$ confidence level), an orbital period derivative of $\dot{P}_{\text{orb}} = 3.9(1.1) \times 10^{-11} \text{ s/s}$ has been determined [127], suggesting again a fast orbital expansion of the system. In the case of IGR J17379–3747, the combination of the ephemerides obtained for the observed outbursts allowed to set an upper limit on the orbital period derivative of $-4.4 \times 10^{-12} < \dot{P}_{\text{orb}} < 9.4 \times 10^{-12}$ [122]. Swift J1756.9–2508 has been detected in outburst three times (2007, 2009 and 2018) since its discovery; the orbital timing of the source set an upper limit on the orbital period derivative of $-4.1 \times 10^{-12} < \dot{P}_{\text{orb}} < 7.1 \times 10^{-12}$ [125]. Riggio et al. (in prep.) analysed a *NuSTAR* observation of the 2015 outburst of IGR J17511–3057, obtaining a new local orbital solution. Combining that with the orbital solution of the 2011 outburst [114], they inferred an orbital period derivative of $\dot{P}_b = 4.4(7) \times 10^{-11} \text{ s s}^{-1}$, suggesting a fast orbital expansion of the binary system similar to that reported for SAX J1748.9–2021. These results are summarised in Table 4.2.

4.3.5 Non-conservative Mass Transfer?

Despite the reduced statistics, the majority of the results suggests that these sources are undergoing a fast orbital expansion, notwithstanding the low averaged mass accretion rate observed from these sources.

Besides AMXPs, one of the most evident example of non-conservative mass transfer has been given by the slowly rotating (spin period of ~ 0.59 s, [71]) X-ray pulsar and eclipsing LMXB 4U 1822–37, which shows a persistent X-ray luminosity of $\sim 10^{36}$ erg/s and an orbital period of ~ 5.57 h, measured from the periodic eclipse of the X-ray source and confirmed through the timing of the X-ray pulsations. The compilation of the eclipse times over the last 40 years showed a fast orbital

expansion at a rate of $\dot{P}_{orb} \sim 1.5 \times 10^{-10} M_{\odot}/yr$ (see, e.g., [36, 82]). The delays of the eclipse arrival times with respect to a constant orbital period showed a clear parabolic trend, which implies a constant orbital period derivative more than three orders of magnitude larger than what is expected from conservative mass transfer driven by MB and GR (e.g. [24, 68]). Mechanisms based on the gravitational quadrupole coupling of the companion star with the orbit (see, e.g., [6, 7]) have been investigated, but resulted not suitable since the ($\sim 0.3 M_{\odot}$) companion star lacks enough internal power to produce such a large orbital period variation (e.g. [82]).

A possible explanation is given by a highly non conservative mass transfer, in which the companion star transfers mass at a high rate. Most of the transferred mass would be then expelled from the system by the strong radiation pressure of the central source emitting at the Eddington limit. In fact, it has been proposed that 4U 1822–37 is accreting at the Eddington limit (while just 1% of the total X-ray luminosity is visible due to the high inclination angle, $80\text{--}85^\circ$, [68]), while the companion star is transferring at a higher rate (of the order of seven times Eddington, [24]), and most of the transferred mass is expelled from the system by the radiation pressure producing strong outflows and winds.

Indeed, there are other indirect evidences of a non-conservative mass transfer in AMXPs. Marino et al. [78] have analysed a sample of AMXPs, starting from XTE J0929–314 [77], finding that the averaged (over the time since their discovery) X-ray luminosity of most sources of the sample is significantly lower than what would be predicted by conservative mass transfer driven by GR and/or MB. Comparing their averaged X-ray luminosity with that predicted for a conservative mass transfer, a lower limit on the source distance may be estimated. Based on a sample of 18 sources, strong evidence of a non-conservative mass transfer was found for five sources, for which the estimated distance lower limits turned out to be significantly larger than their known distances, while hints of mass outflows were found in further six sources of the sample. The discrepancy can be fixed under the hypothesis of a non-conservative mass transfer in which a fraction of the mass transferred onto the compact object is swept away from the system, likely due to the radiation pressure of the rotating magnetic dipole and/or pulsar wind (see an artistic impression of the *accretion* and *ejection* phases in Fig. 4.8). Interestingly, the possibility of strong outflows from these systems has been recently confirmed by general-relativistic MHD simulations [97] showing how the interaction of a turbulent accretion flow with the electromagnetic wind of the pulsar can lead to the transition of a rotational-powered pulsar to the accreting state, causing in turn the formation of relativistic jets whose power can greatly exceed the power of the pulsar wind. If the accretion rate is below a critical value, the pulsar may instead expel the accretion stream.

A similar argument has also been proposed for the black-hole X-ray Binary and microquasar V404 Cyg [141]; considering X-ray observations of its two outbursts, the authors found that the average mass accretion rate was substantially lower than the predicted mass-loss rate from the low-mass giant donor; to fix this discrepancy,

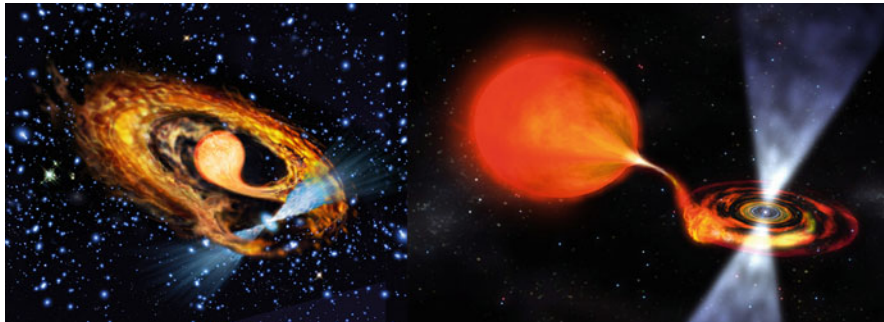


Fig. 4.8 Artistic impression of a system during the accretion phase (*right panel*) and during a radio ejection phase *left panel*. Credits: NASA & ESO. Reproduced with permission

they propose that a large fraction of the mass flowing from the donor leaves the binary in the form of outflows from the accretion disc around the accretor. We can conclude that, regardless of the nature of the accretor and the radiation emitted, it seems that radiation pressure has an important role in limiting the accretion of matter onto the compact object and in initiating a non-conservative mass transfer in LMXB systems, which may be a common feature in these systems, possibly related (as a cause or consequence) to the transient behavior itself.

4.4 Summary and Open Questions

Despite the amount of information we have gained in the last two decades of observations and theoretical studies of AMXPs, several issues still remain to be addressed, as for instance the torque imparted by the accreting matter onto the NS, in most cases hidden behind the strong timing noise shown by pulse profiles of AMXPs. Is the spin-up or spin-down of the NS overwhelmed by the large timing noise? Moreover, what is the origin of this large timing noise? Movements of the hot spot on the NS surface caused by flux variations have been proposed to explain the large timing noise, although it is not clear why in some sources (e.g. SAX J1808.4–3658) it appears to be much stronger than in others (e.g. IGR J00291+5934). Even more puzzling are the orbital residuals observed in SAX J1808.4–3658 and the different behaviour observed in IGR J00291+5934, as well as the role of non-conservative mass transfer in AMXPs and LMXBs in general. Beside that, there are other important issues that should be addressed and are briefly described in the following.

The discovery of AMXPs and the subsequent discovery of transitional millisecond pulsars (see Chap. 6 for further details) has confirmed the recycling scenario. As a consequence of that, we have improved our understanding of the formation of millisecond pulsars, which are accelerated by the accretion of matter and angular

momentum during the LMXB phase, and of the evolutionary path linking the LMXB progenitors to the end products of the evolution, i.e. black-widow pulsars and redbacks (see Chap. 1, 2, and 7), possibly through the transitional phase (see Chap. 6). Nevertheless, several open questions remain to be addressed, the first one regarding pulsations themselves. In fact, apart from the presence of coherent pulsations, AMXPs resemble the behaviour of transient LMXBs of the atoll class. Both the spectral properties and the aperiodic and quasi-periodic variability (so-called QPOs) of AMXPs and not-pulsating LMXBs are very similar ([138]; see also [105] for a review). Similar to LMXBs, AMXPs show type-I X-ray bursts and all the associated phenomenology, as for example the presence of (quasi-coherent) oscillations at the spin frequency of the NS during type-I X-ray bursts (thoroughly discussed in Chap. 5). From the observation of burst oscillations we know that many NS in LMXBs indeed rotate at millisecond periods. However, despite all these similarities, the large majority of LMXBs harbouring a NS does not show coherent pulsations, not even when the mass accretion rate decreases (for instance in transient systems) enough to allow the magnetosphere to expand outside the NS surface. The observation of an intermittent behaviour of coherent pulsations in some AMXPs (see, e.g., the case of Aql X-1 or HETE J1900.1–2455) has suggested that magnetic field burial caused by accretion of fresh matter may play a role (see, e.g., [38] and references therein). However, it is not clear whether this can explain the lack of pulsations in most of LMXBs or other factors contribute in hampering the detection of pulsations in these sources. For instance, there may be a smearing of the pulsations by an optically thick corona, a smearing of pulsations due to gravitational light bending, alignment of the NS magnetic and rotational axes, onset of MHD instabilities at the disk/magnetospheric boundary. None of these models, however, furnish a satisfactorily explanation valid for all the cases (see a discussion in [27, 105]).

Even more puzzling is the lack of radio pulsations in both AMXPs and LMXBs during X-ray quiescence (see also Sect. 6.5.2). In principle, when the accretion of matter stops during (long) quiescent periods, the mechanism producing radio (or gamma-ray) pulsations should resume and the millisecond pulsar should shine in radio (or gamma-ray) as a rotation-powered pulsar. However, this has been observed to date in just one source, the AMXP and transitional pulsar IGR J18245–2452 (J18245 hereafter) in the Globular Cluster M28 ([92]; see 6.4.2), demonstrating that the transition between the rotation-powered and the accretion-powered regime can occur on short timescales (in about 10 days or even less). It is worth noting that the other few sources belonging to the transitional millisecond pulsar class (see Chap. 6), also show radio pulsations during X-ray quiescence and X-ray pulsations during the so-called disk state with (possibly) a low-level of accretion. However, none of these sources ever showed an X-ray outburst to date similar to the one showed by J18245 or the other AMXPs. The compelling possibility that these systems could swiftly switch from accretion-powered to rotation-powered magnetodipole emitters during quiescence gives the opportunity to study a phase that could shed new light on the not yet cleared up radio pulsar emission mechanism. Therefore, if the swing between the rotation-powered and the accretion-powered

pulsar can happen on fast timescales, why is this observed just in few cases? Why radio millisecond pulsations at the known spin period have never been detected in other LMXBs or AMXPs during X-ray quiescence?

In the framework of the so-called radio-ejection model [18], the radio pulsar mechanism switches on when a significant reduction of the mass-transfer rate occurs. The accretion of matter onto the NS is then inhibited by the radiation pressure from the radio pulsar, which may be capable of ejecting out of the system most of the matter overflowing from the companion-star Roche lobe. One of the strongest predictions of this model is the presence, during the radio-ejection phase, of a strong wind of matter emanating from the system (see an artistic impression of a system in the *radio-ejection* phase in the left panel of Fig. 4.8). The non-detection of radio pulsations in this situation may be due to free-free absorption of the radio signal interacting with the ejected matter. A possibility to test this scenario is, therefore, to perform deep (tens of hours) radio observations of these sources at high radio frequency (above 5–6 GHz), since the cross-section of free-free absorption decreases with frequency as ν^{-2} (see, e.g., [66, 67]). However, the question remains: why do transitional millisecond pulsars, and J18245 in particular, behave in a different way, showing radio pulsations when the X-ray emission is off? Perhaps, a favourable geometry, e.g. a relatively low inclination angle of the system, may reduce the amount of matter along our line of sight, since most of the matter is expected to lie in the equatorial plane, and therefore reduce the amount of free-free absorption in these systems. Alternatively, pulsating radio emission should be searched in systems with long orbital periods, in which the matter transferred by the companion star is spread over a wide orbit.

Despite the fact that radio pulsations remain elusive in AMXPs, sporadic detection of transient emission in the radio band has been reported in a few cases. On the other extreme of the electromagnetic spectrum, in the gamma-ray band, searches of AMXPs counterpart is also quite difficult. Because of the paucity of photons at such high energies, in order to obtain a statistically significant detection, it is necessary to integrate over several years. The analysis of ~ 6 yr of data from the Large Area Telescope on board the Fermi gamma-ray Space Telescope (Fermi-LAT) revealed a possible gamma-ray counterpart of SAX J1808.4–3658, at a significance of $\sim 6\sigma$, with a position compatible with that of the source within the 95% confidence level ([43], see Sect. 2.2 in this book). However, the search for coherent pulsations did not produce a significant detection taking into account the number of trials. Uncertainties in the source position, orbital motion of the pulsar as well as the intrinsic evolution of the pulsar spin, which still are not known with enough precision to maintain the phase over years, are likely the causes of the non detection. A precise knowledge of the spin and orbital parameters of AMXPs is of fundamental importance to allow deep searches of their counterparts in the gamma-ray band, which has the advantage of not suffering the free-free absorption as in the radio band, but the disadvantage of the reduced number of photons, which requires folding over years in order to reach the statistics needed for detecting a (weak) pulsed signal.

On other other hand, searches of the optical counterpart of these systems has given interesting, unexpected results. In several AMXPs, the optical counterpart during X-ray quiescence appears surprisingly luminous, inconsistent with both intrinsic emission from the companion star and X-ray reprocessing (e.g. [39, 40, 65]). In fact, the optical counterpart shows an approximately sinusoidal modulation with photometric minimum at the superior conjunction of the pulsar. The lack of ellipsoidal, double-humped variations, rules out an origin from intrinsic emission from the companion star, while it is best explained as caused by the irradiated surface of the companion star. Given the lack of significant X-ray emission during quiescence, this has been interpreted as a strong (indirect) evidence that a rotating magneto-dipole powers the quiescent emission of AMXPs [20, 28]. In fact, the magnetic dipole rotator, if active during quiescence, has a bolometric luminosity given by the Larmor formula and may power the reprocessed optical emission.

Even more puzzling is the recent discovery of optical pulsations at the NS spin period in one of the transitional pulsars, PSR J1023+0038 [4, 96], the first time ever from a millisecond pulsar. Optical pulsations, with a maximum pulsed optical luminosity of $L_{pulse} \simeq 0.01L_{opt} \simeq 10^{31} \text{ erg s}^{-1}$, were observed when the source was in a bright active state corresponding to an X-ray luminosity of $7 \times 10^{33} \text{ erg s}^{-1}$ (see Sect. 6.5.3 in this book). More recently, optical and UV coherent pulsations were observed in the AMXP SAX J1808.4–3658 [5] with a similar optical luminosity and pulsed fraction as observed in PSR J1023+0038. Optical pulsations in SAX J1808.4–3658 were observed during the rising phase of the 2019 outburst (at an X-ray luminosity of several $10^{34} \text{ erg s}^{-1}$), and during the decay of the outburst at a similar X-ray luminosity level. Several options have been order to explain the large optical pulsed luminosity, while a clear explanation still remains elusive. Certainly, future optical observations with a fast photometer during X-ray quiescence or at the peak of an X-ray outburst, possibly performed simultaneously to high-time resolution X-ray observations, will give further information able to discriminate among different possibilities.

One of the most important, yet open questions about AMXPs is their spin period distribution and, most of all, the minimum spin period for a NS. Since (recycled) millisecond pulsars have been accelerated during the LMXB phase, we expect that the minimum period of a NS is reached during this accretion phase, before the starting of the (non-accreting) spin-down phase caused by the emission of the magnetic dipole rotator. Hence, we expect that the fastest spinning NS should reside in an AMXP. Since the maximum frequency of a NS depends on its compactness, that is on its mass to radius ratio, the detection of the maximum spin frequency of NS may give strong and important constraints on the EoS of ultra-dense matter. However the distribution of spin frequencies of the ensemble of AMXPs has an abrupt cutoff at about 730 Hz (see, e.g., [94, 107]), well below the maximum spin frequency allowed by the majority of realistic EoS. We are left therefore with the following questions: is the maximum frequency of NS telling us something related to the EoS of ultra-dense matter? Alternatively, which is the factor limiting the spin of NS well below the maximum possible possible frequency? Several possibilities have been proposed as a limiting factor for the NS rotation, such as emission of

Gravitational Radiation [11, 34], possibly made even more required by the effect of non-steady accretion [9], the presence of a (not yet completely decayed) magnetic field [105], bias caused by a fast orbital motion [18], and so on. However, none of these possibilities seems to be able to explain all the phenomenology of AMXPs and LMXBs, and further investigation is needed to assess this fascinating question. To this aim, future X-ray missions, with large effective area and fast timing capabilities, such as *Athena*, possibly coupled with polarimetric capabilities, as is the case of the enhanced X-ray Timing and Polarimetry mission, *eXTP*, may be fundamental to put forward the research in this field and to open a new era of exciting discoveries on millisecond pulsars.

References

1. Altamirano, D., Casella, P., Patruno, A., et al.: Intermittent millisecond X-ray pulsations from the neutron star X-ray transient SAX J1748.9-2021 in the globular cluster NGC 6440. *Astrophys. J. Lett.* **674**(1), L45 (2008). <https://doi.org/10.1086/528983>
2. Altamirano, D., Patruno, A., Heinke, C.O., et al.: Discovery of a 205.89 Hz accreting millisecond X-ray pulsar in the globular cluster NGC 6440. *Astrophys. J. Lett.* **712**(1), L58–L62 (2010). <https://doi.org/10.1088/2041-8205/712/1/L58>
3. Altamirano, D., Cavecchi, Y., Patruno, A., et al.: Discovery of an accreting millisecond pulsar in the eclipsing binary system SWIFT J1749.4-2807. *Astrophys. J. Lett.* **727**(1), L18 (2011). <https://doi.org/10.1088/2041-8205/727/1/L18>
4. Ambrosino, F., Papitto, A., Stella, L., et al.: Optical pulsations from a transitional millisecond pulsar. *Nat. Astron.* **1**, 854–858 (2017). <https://doi.org/10.1038/s41550-017-0266-2>
5. Ambrosino, F., Miraval Zanon, A., Papitto, A., et al.: Optical and ultraviolet pulsed emission from an accreting millisecond pulsar. *Nat. Astron.* **5**, 552 (2021). <https://doi.org/10.1038/s41550-021-01308-0>
6. Applegate, J.H.: A mechanism for orbital period modulation in close binaries. *Astrophys. J.* **385**, 621 (1992). <https://doi.org/10.1086/170967>
7. Applegate, J.H., Shaham, J.: Orbital period variability in the eclipsing pulsar binary PSR B1957+20: evidence for a tidally powered star. *Astrophys. J.* **436**, 312 (1994). <https://doi.org/10.1086/174906>
8. Benvenuto, O.G., De Vito, M.A., Horvath, J.E.: Evolution of redback radio pulsars in globular clusters. *Astron. Astrophys.* **598**, A35 (2017). <https://doi.org/10.1051/0004-6361/201628692>
9. Bhattacharya, S., Chakrabarty, D.: The effect of transient accretion on the spin-up of millisecond pulsars. *Astrophys. J.* **835**(1), 4 (2017). <https://doi.org/10.3847/1538-4357/835/1/4>
10. Bhattacharya, D., van den Heuvel, E.P.J.: Formation and evolution of binary and millisecond radio pulsars. *Phys. Rep.* **203**(1–2), 1–124 (1991). [https://doi.org/10.1016/0370-1573\(91\)90064-S](https://doi.org/10.1016/0370-1573(91)90064-S)
11. Bildsten, L.: Gravitational radiation and rotation of accreting neutron stars *Astrophys. J. Lett.* **501**(1), L89 (1998). <https://doi.org/10.1086/311440>
12. Bildsten, L., Chakrabarty, D.: A brown dwarf companion for the accreting millisecond pulsar SAX J1808.4-3658. *Astrophys. J.* **557**(1), 292–296 (2001). <https://doi.org/10.1086/321633>
13. Bult, P., Patruno, A., van der Klis, M.: Coherent timing of the accreting millisecond pulsar NGC 6440 X-2. *Astrophys. J.* **814**(2), 138 (2015). <https://doi.org/10.1088/0004-637X/814/2/138>

14. Bult, P., Altamirano, D., Arzoumanian, Z., et al.: On the 2018 outburst of the accreting millisecond X-ray pulsar swift J1756.9-2508 as seen with NICER. *Astrophys. J.* **864**(1), 14 (2018). <https://doi.org/10.3847/1538-4357/aad5e5>
15. Bult, P., Chakrabarty, D., Arzoumanian, Z., et al.: Timing the pulsations of the accreting millisecond pulsar SAX J1808.4-3658 during its 2019 outburst. *Astrophys. J.* **898**(1), 38 (2020). <https://doi.org/10.3847/1538-4357/ab9827>
16. Burderi, L., King, A.R.: A firm upper limit to the radius of the neutron star in SAX J1808.4-3658. *Astrophys. J. Lett.* **505**(2), L135–L137 (1998). <https://doi.org/10.1086/311611>
17. Burderi, L., Possenti, A., Colpi, M., et al.: Neutron stars with submillisecond periods: a population of high-mass objects? *Astrophys. J.* **519**(1), 285–290 (1999). <https://doi.org/10.1086/307353>
18. Burderi, L., Possenti, A., D'Antona, F., et al.: Where may ultrafast rotating neutron stars be hidden? *Astrophys. J. Lett.* **560**(1), L71–L74 (2001). <https://doi.org/10.1086/324220>
19. Burderi, L., D'Antona, F., Burgay, M.: PSR J1740-5340: accretion inhibited by radio ejection in a binary millisecond pulsar in the globular cluster NGC 6397. *Astrophys. J.* **574**(1), 325 (2002). <https://doi.org/10.1086/340891>
20. Burderi, L., Di Salvo, T., D'Antona, F., et al.: The optical counterpart to SAX J1808.4-3658 in quiescence: evidence of an active radio pulsar? *Astron. Astrophys.* **404**, L43–L46 (2003). <https://doi.org/10.1051/0004-6361:20030669>
21. Burderi, L., Di Salvo, T., Menna, M.T., et al.: Order in the chaos: spin-up and spin-down during the 2002 outburst of SAX J1808.4-3658. *Astrophys. J. Lett.* **653**(2), L133–L136 (2006). <https://doi.org/10.1086/510666>
22. Burderi, L., Di Salvo, T., Lavagetto, G., et al.: Timing an accreting millisecond pulsar: measuring the accretion torque in IGR J00291+5934. *Astrophys. J.* **657**(2), 961–966 (2007). <https://doi.org/10.1086/510659>
23. Burderi, L., Riggio, A., di Salvo, T., et al.: Timing of the 2008 outburst of SAX J1808.4-3658 with XMM-Newton: a stable orbital-period derivative over ten years. *Astron. Astrophys.* **496**(2), L17–L20 (2009). <https://doi.org/10.1051/0004-6361/200811542>
24. Burderi, L., Di Salvo, T., Riggio, A., et al.: New ephemeris of the ADC source 2A 1822-371: a stable orbital-period derivative over 30 years. *Astron. Astrophys.* **515**, A44 (2010). <https://doi.org/10.1051/0004-6361/200912881>
25. Cackett, E.M., Altamirano, D., Patruno, A., et al.: Broad relativistic iron emission line observed in SAX J1808.4-3658. *Astrophys. J. Lett.* **694**(1), L21–L25 (2009). <https://doi.org/10.1088/0004-637X/694/1/L21>
26. Cadelano, M., Pallanca, C., Ferraro, F.R., et al.: The optical counterpart to the accreting millisecond X-ray pulsar SAX J1748.9-2021 in the globular cluster NGC 6440. *Astrophys. J.* **844**(1), 53 (2017). <https://doi.org/10.3847/1538-4357/aa7b7f>
27. Campana, S., Di Salvo, T.: Accreting pulsars: mixing-up accretion phases in transitional systems. *Astrophys. Space Sci. Libr.* **457**, 149 (2018). <https://doi.org/10.1007/978-3-319-97616-7-4>
28. Campana, S., D'Avanzo, P., Casares, J., et al.: Indirect evidence of an active radio pulsar in the quiescent state of the transient millisecond pulsar SAX J1808.4-3658. *Astrophys. J. Lett.* **614**(1), L49–L52 (2004). <https://doi.org/10.1086/425495>
29. Campana, S., Coti Zelati, F., D'Avanzo, P.: Mining the Aql X-1 long-term X-ray light curve. *Mon. Not. R. Astron. Soc.* **432**(2), 1695–1700 (2013). <https://doi.org/10.1093/mnras/stt604>
30. Campana, S., Ravasio, M., Israel, G.L., et al.: XMM-newton observation of the 5.25 millisecond transient pulsar XTE J1807-294 in outburst. *Astrophys. J. Lett.* **594**(1), L39–L42 (2003). <https://doi.org/10.1086/378258>
31. Casella, P., Altamirano, D., Patruno, A., et al.: Discovery of coherent millisecond x-ray pulsations in aquila X-1. *Astrophys. J. Lett.* **674**(1), L41 (2008). <https://doi.org/10.1086/528982>
32. Chakrabarty, D.: The spin distribution of millisecond X-ray pulsars. In: Wijnands, R. et al. (eds.) *A Decade of Accreting Millisecond X-ray Pulsars*. American Institute of Physics Conference Proceedings, vol. 1068, pp. 67–74 (2008). <https://doi.org/10.1063/1.3031208>

33. Chakrabarty, D., Morgan, E.H.: The two-hour orbit of a binary millisecond X-ray pulsar. *Nature* **394**(6691), 346–348 (1998). <https://doi.org/10.1038/28561>
34. Chakrabarty, D., Morgan, E. H., Muno, M. P., et al.: Nuclear-powered millisecond pulsars and the maximum spin frequency of neutron stars. *Nature* **424**, 42 (2003). <https://doi.org/10.1038/nature01732>
35. Chen, W.C.: An evolutionary channel towards the accreting millisecond pulsar SAX J1808.4-3658. *Mon. Not. R. Astron. Soc.* **464**(4), 4673–4679 (2017). <https://doi.org/10.1093/mnras/stw2747>
36. Chou, Y., Hsieh, H.E., Hu, C.P., et al.: Orbital and spin parameter variations of partial eclipsing low mass X-ray binary X 1822-371. *Astrophys. J.* **831**(1), 29 (2016). <https://doi.org/10.3847/0004-637X/831/1/29>
37. Cornelisse, R., D'Avanzo, P., Muñoz-Darias, T., et al.: Phase-resolved spectroscopy of the accreting millisecond X-ray pulsar SAX J1808.4-3658 during the 2008 outburst. *Astron. Astrophys.* **495**(1), L1–L4 (2009). <https://doi.org/10.1051/0004-6361:200811396>
38. Cumming, A., Zweibel, E., Bildsten, L.: Magnetic screening in accreting neutron stars. *Astrophys. J.* **557**(2), 958–966 (2001). <https://doi.org/10.1086/321658>
39. D'Avanzo, P., Campana, S., Casares, J., et al.: The optical counterparts of accreting millisecond X-ray pulsars during quiescence. *Astron. Astrophys.* **508**(1), 297–308 (2009). <https://doi.org/10.1051/0004-6361/200810249>
40. D'Avanzo, P., Campana, S., Muñoz-Darias, T., et al.: A search for the near-infrared counterpart of the eclipsing millisecond X-ray pulsar Swift J1749.4-2807. *Astron. Astrophys.* **534**, A92 (2011). <https://doi.org/10.1051/0004-6361/201117841>
41. Degenaar, N., Ootes, L.S., Reynolds, M.T., et al.: A cold neutron star in the transient low-mass X-ray binary HETE J1900.1-2455 after 10 yr of active accretion. *Mon. Not. R. Astron. Soc.* **465**(1), L10–L14 (2017). <https://doi.org/10.1093/mnrasl/slw197>
42. Deloye, C.J., Heinke, C.O., Taam, R.E., et al.: Optical observations of SAX J1808.4-3658 during quiescence. *Mon. Not. R. Astron. Soc.* **391**(4), 1619–1628 (2008). <https://doi.org/10.1111/j.1365-2966.2008.14021.x>
43. de Ofá Wilhelmi, E., Papitto, A., Li, J., et al.: SAX J1808.4-3658, an accreting millisecond pulsar shining in gamma rays? *Mon. Not. R. Astron. Soc.* **456**(3), 2647–2653 (2016). <https://doi.org/10.1093/mnras/stv2695>
44. Di Salvo, T., Iaria, R., Burderi, L., et al.: The broadband spectrum of MXB 1728-34 observed by BeppoSAX. *Astrophys. J.* **542**(2), 1034–1040 (2000). <https://doi.org/10.1086/317029>
45. di Salvo, T., Burderi, L., Riggio, A., et al.: Orbital evolution of an accreting millisecond pulsar: witnessing the banquet of a hidden black widow? *Mon. Not. R. Astron. Soc.* **389**(4), 1851–1857 (2008). <https://doi.org/10.1111/j.1365-2966.2008.13709.x>
46. Di Salvo, T., Sanna, A., Burderi, L., et al.: NuSTAR and XMM-Newton broad-band spectrum of SAX J1808.4-3658 during its latest outburst in 2015. *Mon. Not. R. Astron. Soc.* **483**(1), 767–779 (2019). <https://doi.org/10.1093/mnras/sty2974>
47. Done, C., Gierliński, M., Kubota, A.: Modelling the behaviour of accretion flows in X-ray binaries. Everything you always wanted to know about accretion but were afraid to ask. *Astron. Astrophys. Rev.* **15**(1), 1–66 (2007). <https://doi.org/10.1007/s00159-007-0006-1>
48. Elebert, P., Callanan, P.J., Filippenko, A.V., et al.: Optical photometry and spectroscopy of the accretion-powered millisecond pulsar HETE J1900.1-2455. *Mon. Not. R. Astron. Soc.* **383**(4), 1581–1587 (2008). <https://doi.org/10.1111/j.1365-2966.2007.12667.x>
49. Falanga, M., Bonnet-Bidaud, J.M., Poutanen, J., et al.: INTEGRAL spectroscopy of the accreting millisecond pulsar XTE J1807-294 in outburst. *Astron. Astrophys.* **436**(2), 647–652 (2005). <https://doi.org/10.1051/0004-6361:20042575>
50. Falanga, M., Kuiper, L., Poutanen, J., et al.: INTEGRAL and RXTE observations of accreting millisecond pulsar IGR J00291+5934 in outburst. *Astron. Astrophys.* **444**(1), 15–24 (2005). <https://doi.org/10.1051/0004-6361:20053472>

51. Ferraro, F.R., Possenti, A., D'Amico, N., et al.: The bright optical companion to the eclipsing millisecond pulsar in NGC 6397. *Astrophys. J. Lett.* **561**(1), L93 (2001). <https://doi.org/10.1086/324563>
52. Galloway, D.K., Chakrabarty, D., Morgan, E.H., et al.: Discovery of a high-latitude accreting millisecond pulsar in an ultracompact binary. *Astrophys. J. Lett.* **576**(2), L137–L140 (2002). <https://doi.org/10.1086/343841>
53. Galloway, D.K., Markwardt, C.B., Morgan, E.H., et al.: Discovery of the accretion-powered millisecond X-ray pulsar IGR J00291+5934. *Astrophys. J. Lett.* **622**(1), L45–L48 (2005). <https://doi.org/10.1086/429563>
54. Galloway, D.K., Morgan, E.H., Krauss, M.I., et al.: Intermittent pulsations in an accretion-powered millisecond pulsar. *Astrophys. J. Lett.* **654**, L73 (2007). <https://doi.org/10.1086/510741>
55. Ghosh, P., Lamb, F.K.: Accretion by rotating magnetic neutron stars. III. Accretion torques and period changes in pulsating X-ray sources. *Astrophys. J.* **234**, 296–316 (1979). <https://doi.org/10.1086/157498>
56. Ghosh, P., Lamb, F.K.: Plasma physics of accreting neutron stars. In: Ventura, J., Pines, D. (eds.) *NATO Advanced Science Institutes (ASI) Series C*. NATO Advanced Science Institutes (ASI) Series C, vol. 344, p. 363 (1991)
57. Gierliński, M., Poutanen, J.: Physics of accretion in the millisecond pulsar XTE J1751-305. *Mon. Not. R. Astron. Soc.* **359**(4), 1261–1276 (2005). <https://doi.org/10.1111/j.1365-2966.2005.09004.x>
58. Gierliński, M., Done, C., Barret, D.: Phase-resolved X-ray spectroscopy of the millisecond pulsar SAX J1808.4-3658. *Mon. Not. R. Astron. Soc.* **331**(1), 141–153 (2002). <https://doi.org/10.1046/j.1365-8711.2002.05174.x>
59. Giles, A.B., Greenhill, J.G., Hill, K.M., et al.: The optical counterpart of XTE J0929-314: the third transient millisecond X-ray pulsar. *Mon. Not. R. Astron. Soc.* **361**(4), 1180–1186 (2005). <https://doi.org/10.1111/j.1365-2966.2005.09255.x>
60. Hartman, J.M., Patruno, A., Chakrabarty, D., et al.: The long-term evolution of the spin, pulse shape, and orbit of the accretion-powered millisecond pulsar SAX J1808.4-3658. *Astrophys. J.* **675**(2), 1468–1486 (2008). <https://doi.org/10.1086/527461>
61. Hartman, J.M., Patruno, A., Chakrabarty, D., et al.: A decade of timing an accretion-powered millisecond pulsar: the continuing spin down and orbital evolution of SAX J1808.4-3658. *Astrophys. J.* **702**(2), 1673–1678 (2009). <https://doi.org/10.1088/0004-637X/702/2/1673>
62. Hartman, J.M., Watts, A.L., Chakrabarty, D.: The luminosity and energy dependence of pulse phase lags in the accretion-powered millisecond pulsar SAX J1808.4-3658. *Astrophys. J.* **697**(2), 2102–2107 (2009). <https://doi.org/10.1088/0004-637X/697/2/2102>
63. Hartman, J.M., Galloway, D.K., Chakrabarty, D.: A double outburst from IGR J00291+5934: implications for accretion disk instability theory. *Astrophys. J.* **726**(1), 26 (2011). <https://doi.org/10.1088/0004-637X/726/1/26>
64. Hessels, J.W.T., Ransom, S.M., Stairs, I.H., et al.: A radio pulsar spinning at 716 Hz. *Science* **311**(5769), 1901–1904 (2006). <https://doi.org/10.1126/science.1123430>
65. Homer, L., Charles, P.A., Chakrabarty, D., et al.: The optical counterpart to SAX J1808.4-3658: observations in quiescence. *Mon. Not. R. Astron. Soc.* **325**(4), 1471–1476 (2001). <https://doi.org/10.1046/j.1365-8711.2001.04567.x>
66. Iacolina, M.N., Burgay, M., Burderi, L., et al.: Searching for pulsed emission from XTE J0929-314 at high radio frequencies. *Astron. Astrophys.* **497**(2), 445–450 (2009). <https://doi.org/10.1051/0004-6361/200810677>
67. Iacolina, M.N., Burgay, M., Burderi, L., et al.: Search for pulsations at high radio frequencies from accreting millisecond X-ray pulsars in quiescence. *Astron. Astrophys.* **519**, A13 (2010). <https://doi.org/10.1051/0004-6361/201014025>
68. Iaria, R., di Salvo, T., Burderi, L., et al.: Detailed study of the X-ray and optical/UV orbital ephemeris of X1822-371. *Astron. Astrophys.* **534**, A85 (2011). <https://doi.org/10.1051/0004-6361/201117334>

69. Ibragimov, A., Poutanen, J.: Accreting millisecond pulsar SAX J1808.4-3658 during its 2002 outburst: evidence for a receding disc. *Mon. Not. R. Astron. Soc.* **400**(1), 492–508 (2009). <https://doi.org/10.1111/j.1365-2966.2009.15477.x>
70. Jackson, J.D.: Classical Electrodynamics, 2nd edn. Wiley, New York (1975). <https://cds.cern.ch/record/100964>
71. Jonker, P.G., van der Klis, M.: Discovery of an X-Ray pulsar in the low-mass X-ray binary 2A 1822-371. *Astrophys. J. Lett.* **553**(1), L43–L46 (2001). <https://doi.org/10.1086/320510>
72. Kaaret, P., Morgan, E.H., Vanderspek, R., et al.: Discovery of the millisecond X-ray pulsar HETE J1900.1-2455. *Astrophys. J.* **638**(2), 963–967 (2006). <https://doi.org/10.1086/498886>
73. Kluźniak, W., Rappaport, S.: Magnetically torqued thin accretion disks. *Astrophys. J.* **671**(2), 1990–2005 (2007). <https://doi.org/10.1086/522954>
74. Krimm, H.A., Markwardt, C.B., Deloye, C.J., et al.: Discovery of the accretion-powered millisecond pulsar SWIFT J1756.9-2508 with a low-mass companion. *Astrophys. J. Lett.* **668**(2), L147–L150 (2007). <https://doi.org/10.1086/522959>
75. Kuiper, L., Tsygankov, S.S., Falanga, M., et al.: High-energy characteristics of the accretion-powered millisecond pulsar IGR J17591-2342 during its 2018 outburst. e-prints. arXiv:2002.12154 (2020)
76. Manchester, R. N., Hobbs, G. B., Teoh, A., et al.: The Australia Telescope National Facility pulsar catalogue. *Astron. J.* **129**, 1993–2006 (2005). <https://doi.org/10.1086/428488>
77. Marino, A., Di Salvo, T., Gambino, A.F., et al.: Evidence of a non-conservative mass transfer for XTE J0929-314. *Astron. Astrophys.* **603**, A137 (2017). <https://doi.org/10.1051/0004-6361/201730464>
78. Marino, A., Di Salvo, T., Burderi, L., et al.: Indications of non-conservative mass transfer in AMXPs. *Astron. Astrophys.* **627**, A125 (2019). <https://doi.org/10.1051/0004-6361/201834460>
79. Markwardt, C.B., Swank, J.H.: XTE J1814-338. *IAU Circ.* **8144**, 1 (2003)
80. Markwardt, C.B., Swank, J.H., Strohmayer, T.E., et al.: Discovery of a second millisecond accreting pulsar: XTE J1751-305. *Astrophys. J. Lett.* **575**(1), L21–L24 (2002). <https://doi.org/10.1086/342612>
81. Mata Sánchez, D., Muñoz-Darias, T., Casares, J., et al.: The donor of Aquila X-1 revealed by high-angular resolution near-infrared spectroscopy. *Mon. Not. R. Astron. Soc.* **464**(1), L41–L45 (2017). <https://doi.org/10.1093/mnras/slw172>
82. Mazzola, S.M., Iaria, R., Di Salvo, T., et al.: Updated orbital ephemeris of the ADC source X 1822-371: a stable orbital expansion over 40 years. *Astron. Astrophys.* **625**, L12 (2019). <https://doi.org/10.1051/0004-6361/201935665>
83. Miller, J.M., Wijnands, R., Méndez, M., et al.: XMM-newton spectroscopy of the accretion-driven millisecond X-ray pulsar XTE J1751-305 in outburst. *Astrophys. J. Lett.* **583**(2), L99–L102 (2003). <https://doi.org/10.1086/368105>
84. Mukherjee, D., Bult, P., van der Klis, M., et al.: The magnetic-field strengths of accreting millisecond pulsars. *Mon. Not. R. Astron. Soc.* **452**(4), 3994–4012 (2015). <https://doi.org/10.1093/mnras/stv1542>
85. Özel, F., Freire, P.: Masses, Radii, and the equation of state of neutron stars. *Annu. Rev. Astron. Astrophys.* **54**, 401–440 (2016). <https://doi.org/10.1146/annurev-astro-081915-023322>
86. Papitto, A., di Salvo, T., Burderi, L., et al.: Timing of the accreting millisecond pulsar XTE J1814-338. *Mon. Not. R. Astron. Soc.* **375**(3), 971–976 (2007). <https://doi.org/10.1111/j.1365-2966.2006.11359.x>
87. Papitto, A., Di Salvo, T., D'Aì, A., et al.: XMM-Newton detects a relativistically broadened iron line in the spectrum of the ms X-ray pulsar SAX J1808.4-3658. *Astron. Astrophys.* **493**(3), L39–L43 (2009). <https://doi.org/10.1051/0004-6361:200811401>
88. Papitto, A., Riggio, A., di Salvo, T., et al.: The X-ray spectrum of the newly discovered accreting millisecond pulsar IGR J17511-3057. *Mon. Not. R. Astron. Soc.* **407**(4), 2575–2588 (2010). <https://doi.org/10.1111/j.1365-2966.2010.17090.x>

89. Papitto, A., Bozzo, E., Ferrigno, C., et al.: The discovery of the 401 Hz accreting millisecond pulsar IGR J17498-2921 in a 3.8 h orbit. *Astron. Astrophys.* **535**, L4 (2011). <https://doi.org/10.1051/0004-6361/201117995>
90. Papitto, A., Riggio, A., Burderi, L., et al.: Spin down during quiescence of the fastest known accretion-powered pulsar. *Astron. Astrophys.* **528**, A55 (2011). <https://doi.org/10.1051/0004-6361/201014837>
91. Papitto, A., Di Salvo, T., Burderi, L., et al.: The pulse profile and spin evolution of the accreting pulsar in Terzan 5, IGR J17480-2446, during its 2010 outburst. *Mon. Not. R. Astron. Soc.* **423**(2), 1178–1193 (2012). <https://doi.org/10.1111/j.1365-2966.2012.20945.x>
92. Papitto, A., Ferrigno, C., Bozzo, E., et al.: Swings between rotation and accretion power in a binary millisecond pulsar. *Nature* **501**(7468), 517–520 (2013). <https://doi.org/10.1038/nature12470>
93. Papitto, A., D'Aì, A., Di Salvo, T., et al.: The accretion flow to the intermittent accreting millisecond pulsar, HETE J1900.1-2455, as observed by XMM-Newton and RXTE. *Mon. Not. R. Astron. Soc.* **429**(4), 3411–3422 (2013). <https://doi.org/10.1093/mnras/sts605>
94. Papitto, A., Torres, D.F., Rea, N., Tauris, T.M.: Spin frequency distributions of binary millisecond pulsars. *Astron. Astrophys.* **566**, A64 (2014). <https://doi.org/10.1051/0004-6361/201321724>
95. Papitto, A., Bozzo, E., Sanchez-Fernandez, C., et al.: The 2015 outburst of the accreting millisecond pulsar IGR J17511-3057 as seen by INTEGRAL, Swift, and XMM-Newton. *Astron. Astrophys.* **596**, A71 (2016). <https://doi.org/10.1051/0004-6361/201628238>
96. Papitto, A., Ambrosino, F., Stella, L., et al.: Pulsating in unison at optical and X-ray energies: simultaneous high time resolution observations of the transitional millisecond pulsar PSR J1023+0038. *Astrophys. J.* **882**(2), 104 (2019). <https://doi.org/10.3847/1538-4357/ab2fdf>
97. Parfrey, K., Tchekhovskoy, A.: General-relativistic simulations of four states of accretion onto millisecond pulsars. *Astrophys. J. Lett.* **851**(2), L34 (2017). <https://doi.org/10.3847/2041-8213/aa9c85>
98. Patruno, A.: The accreting millisecond X-ray pulsar IGR J00291+5934: evidence for a long timescale spin evolution. *Astrophys. J.* **722**(1), 909–918 (2010). <https://doi.org/10.1088/0004-637X/722/1/909>
99. Patruno, A.: Evidence of fast magnetic field evolution in an accreting millisecond pulsar. *Astrophys. J. Lett.* **753**(1), L12 (2012). <https://doi.org/10.1088/2041-8205/753/1/L12>
100. Patruno, A.: The slow orbital evolution of the accreting millisecond pulsar IGR J0029+5934. *Astrophys. J.* **839**(1), 51 (2017). <https://doi.org/10.3847/1538-4357/aa6986>
101. Patruno, A., Altamirano, D., Hessels, J.W.T., et al.: Phase-coherent timing of the accreting millisecond pulsar SAX J1748.9-2021. *Astrophys. J.* **690**(2), 1856–1865 (2009). <https://doi.org/10.1088/0004-637X/690/2/1856>
102. Patruno, A., Wijnands, R., van der Klis, M.: An alternative interpretation of the timing noise in accreting millisecond pulsars. *Astrophys. J. Lett.* **698**(1), L60–L63 (2009). <https://doi.org/10.1088/0004-637X/698/1/L60>
103. Patruno, A., Altamirano, D., Messenger, C.: The long-term evolution of the accreting millisecond X-ray pulsar SwiftJ1756.9-2508. *Mon. Not. R. Astron. Soc.* **403**(3), 1426–1432 (2010). <https://doi.org/10.1111/j.1365-2966.2010.16202.x>
104. Patruno, A., Bult, P., Gopakumar, A., et al.: Accelerated orbital expansion and secular spin-down of the accreting millisecond pulsar SAX J1808.4-3658. *Astrophys. J. Lett.* **746**(2), L27 (2012). <https://doi.org/10.1088/2041-8205/746/2/L27>
105. Patruno, A., Watts, A.L.: Accreting millisecond X-ray pulsars. e-prints. arXiv:1206.2727 (2012)
106. Patruno, A., Maitra, D., Curran, P.A., et al.: The reflares and outburst evolution in the accreting millisecond pulsar SAX J1808.4-3658: a disk truncated near co-rotation? *Astrophys. J.* **817**(2), 100 (2016). <https://doi.org/10.3847/0004-637X/817/2/100>

107. Patruno, A., Haskell, B., Andersson, N.: The spin distribution of fast-spinning neutron stars in low-mass X-ray binaries: evidence for two subpopulations. *Astrophys. J.* **850**(1), 106 (2017). <https://doi.org/10.3847/1538-4357/aa927a>
108. Pintore, F., Sanna, A., Di Salvo, T., et al.: Broad-band spectral analysis of the accreting millisecond X-ray pulsar SAX J1748.9-2021. *Mon. Not. R. Astron. Soc.* **457**(3), 2988–2998 (2016). <https://doi.org/10.1093/mnras/stw176>
109. Poutanen, J.: Accretion-powered millisecond pulsars. *Adv. Space Res.* **38**(12), 2697–2703 (2006). <https://doi.org/10.1016/j.asr.2006.04.025>
110. Psaltis, D.: Probes and tests of strong-field gravity with observations in the electromagnetic spectrum. *Living Rev. Relativ.* **11**(1), 9 (2008). <https://doi.org/10.12942/lrr-2008-9>
111. Rappaport, S.A., Fregeau, J.M., Spruit, H.: Accretion onto fast X-ray pulsars. *Astrophys. J.* **606**(1), 436–443 (2004). <https://doi.org/10.1086/382863>
112. Riggio, A., Di Salvo, T., Burderi, L., et al.: Spin-up and phase fluctuations in the timing of the accreting millisecond pulsar XTE J1807-294. *Astrophys. J.* **678**(2), 1273–1278 (2008). <https://doi.org/10.1086/533578>
113. Riggio, A., Burderi, L., di Salvo, T., et al.: Secular spin-down of the AMP XTE J1751-305. *Astron. Astrophys.* **531**, A140 (2011). <https://doi.org/10.1051/0004-6361/201014883>
114. Riggio, A., Papitto, A., Burderi, L., et al.: Timing of the accreting millisecond pulsar IGR J17511-3057. *Astron. Astrophys.* **526**, A95 (2011). <https://doi.org/10.1051/0004-6361/201014322>
115. Riggio, A. et al.: IGR J17511-3057 In preparation (2022)
116. Romanova, M.M., Ustyugova, G.V., Koldoba, A.V., et al.: Propeller-driven outflows and disk oscillations. *Astrophys. J. Lett.* **635**(2), L165–L168 (2005). <https://doi.org/10.1086/499560>
117. Sanna, A., Di Salvo, T., Burderi, L., et al.: On the timing properties of SAX J1808.4-3658 during its 2015 outburst. *Mon. Not. R. Astron. Soc.* **471**(1), 463–477 (2017). <https://doi.org/10.1093/mnras/stx1588>
118. Sanna, A., Papitto, A., Burderi, L., et al.: Discovery of a new accreting millisecond X-ray pulsar in the globular cluster NGC 2808. *Astron. Astrophys.* **598**, A34 (2017). <https://doi.org/10.1051/0004-6361/201629406>
119. Sanna, A., Pintore, F., Bozzo, E., et al.: Spectral and timing properties of IGR J00291+5934 during its 2015 outburst. *Mon. Not. R. Astron. Soc.* **466**(3), 2910–2917 (2017). <https://doi.org/10.1093/mnras/stw3332>
120. Sanna, A., Riggio, A., Burderi, L., et al.: Study of the accretion torque during the 2014 outburst of the X-ray pulsar GRO J1744-28. *Mon. Not. R. Astron. Soc.* **469**(1), 2–12 (2017). <https://doi.org/10.1093/mnras/stx635>
121. Sanna, A., Bahramian, A., Bozzo, E., et al.: Discovery of 105 Hz coherent pulsations in the ultracompact binary IGR J16597-3704. *Astron. Astrophys.* **610**, L2 (2018). <https://doi.org/10.1051/0004-6361/201732262>
122. Sanna, A., Bozzo, E., Papitto, A., et al.: XMM-Newton detection of the 2.1 ms coherent pulsations from IGR J17379-3747. *Astron. Astrophys.* **616**, L17 (2018). <https://doi.org/10.1051/0004-6361/201833205>
123. Sanna, A., Ferrigno, C., Ray, P.S., et al.: NuSTAR and NICER reveal IGR J17591-2342 as a new accreting millisecond X-ray pulsar. *Astron. Astrophys.* **617**, L8 (2018). <https://doi.org/10.1051/0004-6361/201834160>
124. Sanna, A., Pintore, F., Riggio, A., et al.: SWIFT J1756.9-2508: spectral and timing properties of its 2018 outburst. *Mon. Not. R. Astron. Soc.* **481**, 1658 (2018). <https://doi.org/10.1093/mnras/sty2316>
125. Sanna, A., Pintore, F., Riggio, A., et al.: NICER and SWIFT/XRT detect a new outburst of the accreting millisecond X-ray pulsar SWIFT J1756.9-2508. *Astronomer's Telegram* **12882**, 1 (2019)
126. Sanna, A., Burderi, L., Gendreau, K.C., et al.: Timing of the accreting millisecond pulsar IGR J17591-2342: evidence of spin-down during accretion. *e-prints. arXiv:2003.05069* (2020)
127. Sanna, A. et al.: SAX J1748.9-2021. In preparation (2022)
128. Sanna, A. et al.: SAX J1808.4-3658. In preparation (2022)

129. Spitkovsky, A.: Time-dependent force-free pulsar magnetospheres: axisymmetric and oblique rotators. *Astrophys. J. Lett.* **648**(1), L51–L54 (2006). <https://doi.org/10.1086/507518>
130. Strohmayer, T., Keek, L.: IGR J17062-6143 is an accreting millisecond X-ray pulsar. *Astrophys. J. Lett.* **836**(2), L23 (2017). <https://doi.org/10.3847/2041-8213/aa5e51>
131. Tailo, M., D'Antona, F., Burderi, L., et al.: Evolutionary paths of binaries with a neutron star – I. The case of SAX J1808.4-3658. *Mon. Not. R. Astron. Soc.* **479**(1), 817–828 (2018). <https://doi.org/10.1093/mnras/sty1637>
132. Tauris, T.M., Konar, S.: Torque decay in the pulsar (P,dot {P}) diagram. Effects of crustal ohmic dissipation and alignment. *Astron. Astrophys.* **376**, 543–552 (2001). <https://doi.org/10.1051/0004-6361:20010988>
133. van Paradijs, J., McClintock, J.E.: Absolute visual magnitudes of low-mass X-ray binaries. *Astron. Astrophys.* **290**, 133–136 (1994)
134. Wang, Y.M.: Disc accretion by magnetized neutron stars – a reassessment of the torque. *Astron. Astrophys.* **183**, 257–264 (1987)
135. Wang, Z., Breton, R.P., Heinke, C.O., et al.: Multiband studies of the optical periodic modulation in the X-ray binary SAX J1808.4-3658 during its quiescence and 2008 outburst. *Astrophys. J.* **765**(2), 151 (2013). <https://doi.org/10.1088/0004-637X/765/2/151>
136. Wang, L., Steeghs, D., Casares, J., et al.: System mass constraints for the accreting millisecond pulsar XTE J1814-338 using Bowen fluorescence. *Mon. Not. R. Astron. Soc.* **466**(2), 2261–2271 (2017). <https://doi.org/10.1093/mnras/stw3312>
137. Wijnands, R., van der Klis, M.: A millisecond pulsar in an X-ray binary system. *Nature* **394**(6691), 344–346 (1998). <https://doi.org/10.1038/28557>
138. Wijnands, R., van der Klis, M.: The broadband power spectra of X-ray binaries. *Astrophys. J.* **514**(2), 939–944 (1999). <https://doi.org/10.1086/306993>
139. Will, C.M.: The confrontation between general relativity and experiment: a centenary perspective. *Prog. Theor. Phys. Suppl.* **163**, 146–162 (2006). <https://doi.org/10.1143/PTPS.163.146>
140. Zhang, B., Harding, A. K., Muslimov, A. G.: Radio pulsar death line revisited: is PSR J2144-3933 anomalous? *Astrophys. J. Lett.* **531**(2), L135 (2000). <https://doi.org/10.1086/312542>
141. Ziolkowski, J., Zdziarski, A.A.: Non-conservative mass transfer in stellar evolution and the case of V404 Cyg/GS 2023+338. *Mon. Not. R. Astron. Soc.* **480**(2), 1580–1586 (2018). <https://doi.org/10.1093/mnras/sty1948>

Chapter 5

Nuclear-Powered X-ray Millisecond Pulsars



Sudip Bhattacharyya

Abstract Nuclear-powered X-ray millisecond pulsars are the third type of millisecond pulsars, which are powered by thermonuclear fusion processes. The corresponding brightness oscillations, known as *burst oscillations*, are observed during some thermonuclear X-ray bursts, when the burning and cooling accreted matter gives rise to an azimuthally asymmetric brightness pattern on the surface of the spinning neutron star. Apart from providing neutron star spin rates, this X-ray timing feature can be a useful tool to probe the fundamental physics of neutron star interior and surface. This chapter presents an overview of the relatively new field of nuclear-powered X-ray millisecond pulsars.

5.1 Introduction

Most of the known millisecond pulsars (MSPs), i.e., rapidly spinning neutron stars, are powered by the stellar spin or rotational kinetic energy (see Chap. 1; [12]). There is also a small set of known MSPs, which are powered by the gravitational potential energy released from the matter accreted by the neutron star from its binary companion (see Chap. 4; [103]). In this chapter, however, we will discuss a third set of MSPs, which are powered by nuclear fusion reactions in the accreted matter accumulated on the neutron star surface [130].

Both the second and third types of MSPs are subsets of low-mass X-ray binary (LMXB) systems. In such a system, a neutron star accretes matter from a low-mass object filling its Roche lobe (see Chap. 4; [12]). This object could be a main sequence star, an evolved star, a white dwarf or even a brown dwarf (see Chap. 7). An LMXB primarily emits X-rays, as the blackbody temperatures of the inner part of the accretion disk and the neutron star surface are ~ 1 keV. Consequently, both types of MSPs, i.e., accretion-powered millisecond X-ray pulsars (AMXPs) and

S. Bhattacharyya (✉)
Tata Institute of Fundamental Research, Mumbai, India
e-mail: sudip@tifr.res.in

nuclear-powered millisecond X-ray pulsars (NMXP)s are typically observed in X-rays. There is also a partial overlap between these two types of MSPs, i.e., some AMXPs are also NMXP, and vice versa [130].

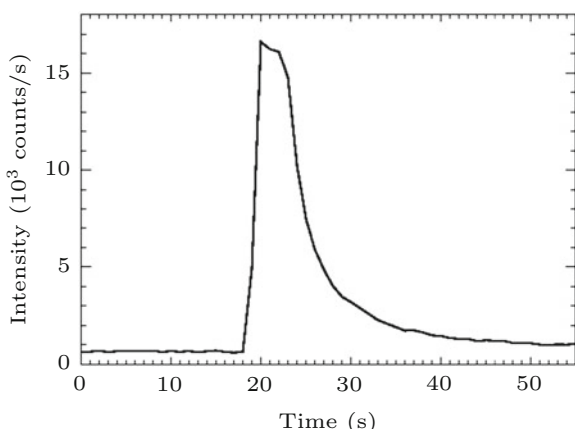
The three types of pulsations are useful to probe some distinctly different aspects of physics. Therefore, even though NMXP are much less explored than spin-powered MSPs, the study of the former is a uniquely important field of research by its own right. This is because, apart from providing the neutron star spin rates, which all pulsars do, nuclear-powered pulsations can be useful to probe the supranuclear density degenerate core matter of neutron stars (see Chap. 9; [11]) and the stellar surface physics in extreme conditions, such as strong gravity, high magnetic field, intense radiation and rapid stellar spin.

Nuclear-powered pulsations are also called burst oscillations, as this feature is the brightness oscillations observed during thermonuclear X-ray bursts originated on the neutron star surface. It is, therefore, imperative to briefly describe these bursts, in order to understand NMXP.

5.1.1 Thermonuclear X-ray Bursts

Thermonuclear X-ray bursts are eruptions in X-rays, intermittently observed from many neutron star LMXBs [54, 56, 111]. These bursts were discovered as sharp short-duration intensity rises in X-ray light curves in 1970's [9, 62]. The most common among these are type-I X-ray bursts, which show an intensity rise typically by a factor of ~ 10 in $\approx 0.5\text{--}5$ s, a somewhat flat intensity peak, and then a relatively slow decay in $\approx 10\text{--}100$ s (see Fig. 5.1). For a given LMXB, bursts may occur once in a few hours to days, and the typical energy emitted is $\sim 10^{39}$ erg [111]. Soon after the discovery, it was understood that these bursts originate from the surface of the neutron star. This conclusion was primarily based on the observational fact

Fig. 5.1 The X-ray light curve of a typical thermonuclear (type-I) X-ray burst observed from an LMXB with the *Rossi X-ray Timing Explorer (RXTE)* satellite. The rise, peak and decay parts of the burst are clearly seen (see Sect. 5.1.1)



that the burst emission area, inferred from the energy spectral analysis, matched well with the expected stellar surface area [65, 123]. Soon, it was also realized that the nuclear burning of the accreted matter accumulated on the stellar surface gives rise to these bursts [71, 81, 111]. The primary evidence for this is, at least for some cases, the ratio of the total fluence of all the bursts to that of the non-burst emission in a data set roughly tallies with the ratio of the expected nuclear energy release per nucleon (a few MeV) to the expected accretion-induced gravitational energy release per nucleon (~ 200 MeV) [11]. This also implies that this nuclear burning is unstable and intermittent, as otherwise the effect of the nuclear energy release would not be seen as a burst over and above the gravitational energy release due to accretion (see Fig. 5.1). Such an instability can happen when the nuclear energy generation rate is more temperature sensitive than the cooling rate. However, a stable nuclear burning of the accumulated accreted matter can also happen continuously, which could affect the profile, recurrence time and other properties of thermonuclear bursts.

The observed properties of a burst are determined by its ignition condition, specific nuclear reactions and energy generation, and energy and material transport. The burst ignition happens in the so-called ocean on an accreting neutron star's crust [130]. This ocean, made of the accreted matter and its ashes, is expected to have layers of various chemical compositions at various depths. At the top, there should be hydrogen-rich and helium-rich layers of a thickness of hundreds of cm, with a density of $\sim 10^{5-6}$ g cm $^{-3}$ at the bottom. Below this, there should be first a carbon-rich layer of thickness $\sim 10^4$ cm, and then layers of heavier nuclei [72, 130]. The thickness and density of layers also depend on previous bursts and stable nuclear burning, as well as the chemical composition of the accreted matter. For example, while hydrogen-rich matter is accreted for many LMXBs, the composition is different for an ultra-compact X-ray binary (UCXB) with a hydrogen deficient and heavier element rich dwarf companion star [69]. The ignition of the layer of a particular chemical composition depends on the column density and the temperature at the bottom of that layer. Note that the accretion rate is an important parameter which determines when the ignition column density and temperature will be reached. Moreover, the stellar gravity and spin rate, energy injection from the bottom, e.g., from the crust, and a pattern of temperature and chemical distributions, for example, due to the history of previous bursts, could also affect the ignition condition.

The next important aspect of thermonuclear X-ray bursts is nuclear reactions and energy generation, which have the following theoretically identified regimes for increasing accretion rate per unit neutron star surface area (\dot{m}) [23].

Regime 1: Mixed hydrogen and helium bursts should occur via the CNO (carbon-nitrogen-oxygen) cycle due to an unstable hydrogen ignition for a temperature $T > 10^7$ K and $\dot{m} < 900$ gm cm $^{-2}$ sec $^{-1}$ ($Z_{\text{CNO}}/0.01)^{1/2}$ (Z_{CNO} is the mass fraction of CNO; [23]).

Regime 2: For a higher \dot{m} , i.e., 900 gm cm $^{-2}$ sec $^{-1}$ ($Z_{\text{CNO}}/0.01)^{1/2} < \dot{m} < 2 \times 10^3$ gm cm $^{-2}$ sec $^{-1}$ ($Z_{\text{CNO}}/0.01)^{13/18}$, which may imply $T > 8 \times 10^7$ K, hydrogen should burn to produce helium in a stable manner via the “hot”

CNO cycle [48], and hence no thermonuclear burst should be triggered. This, however, is expected to build a helium layer below the hydrogen layer, and if no hydrogen is left when the helium ignition condition is satisfied, we can expect a short (~ 10 s) but very intense helium burst caused by the unstable triple-alpha reaction of the pure helium ($3\alpha \rightarrow ^{12}\text{C}$).

- Regime 3:* For an even higher m , i.e., $m > 2 \times 10^3 \text{ gm cm}^{-2} \text{ sec}^{-1}$ ($Z_{\text{CNO}}/0.01)^{13/18}$, although hydrogen burns in a stable manner via the “hot” CNO cycle, sufficient amount of hydrogen can remain unburnt when the helium ignition condition is satisfied. As a result, a mixed hydrogen and helium burst should be triggered by the helium ignition. Such a burst can be much longer (~ 100 s) than a helium burst, and should produce heavy elements beyond the iron group via the rp (rapid-proton) process [106].
- Regime 4:* When the accretion rate is very high, i.e., a considerable fraction of the Eddington rate, the nuclear burning should be stable and no burst is expected to occur, as the helium burning becomes less temperature sensitive than the cooling rate [7, 125].

While different types of bursts, as mentioned above, have been identified from their observed properties, such as duration, peak luminosity and intensity profile, so far it has not been possible to confirm this theoretical picture for most sources, and usually bursts do not occur in a regular manner and in correlation with the accretion rate, as expected. This could be due to the effects of parameters with unknown values, for example the area on which the accreted matter falls, and processes about which we have a limited knowledge, such as the nuclear reaction chain, continuous stable burning and hence the depletion of fuel, ignition conditions as mentioned above, and energy and material transport. Nevertheless, a clear correlation between burst properties and the accretion rate has been observed for the LMXBs GS 1826–238 and IGR J17480–2446 [33, 37, 53, 85].

Energy and material transport is the next aspect which decides the observed properties of thermonuclear X-ray bursts. It has been found from the theory and simulations that energy can be transferred by radiation, convection and conduction [57, 89, 109, 130, 135, 138]. Convection causes material transport, and hence is interesting for multiple reasons. For example, convection should contribute to the flame spreading on the neutron star surface after the ignition of a burst [109]. For photospheric radius expansion (PRE) bursts, i.e., strong bursts for which the radiation pressure temporarily pushes the stellar photosphere away from the neutron star surface, heavy elements could be transported to the stellar surface due to convection, providing a potential tool to probe nuclear reactions and to measure the stellar compactness [135]. Convection could also explain the rare thermonuclear bursts with short recurrence times [77]. This shows that a departure from the above mentioned simple accretion rate based burst model could happen due to complex processes such as convection.

Finally, we note that, in addition to type-I X-ray bursts, long bursts, i.e., bursts of longer durations of ≈ 30 min and fluence of $\approx 10^{41}$ erg have been observed

from several LMXBs (e.g., [66, 68, 76]). Even longer ($\sim 1\text{--}3$ h) and more energetic ($\sim 10^{42}$ erg) thermonuclear bursts, viz., superbursts, have also been observed from some sources (e.g., [43, 67, 78–80]). The latter bursts could originate from the thermally unstable ^{12}C fusion in the carbon-rich layer of the ocean [26, 124, 137].

5.1.2 Burst Oscillations: Discovery and Growth of the Field

With this basic knowledge of thermonuclear X-ray bursts, here we will briefly describe how the field of nuclear-powered pulsations, or burst oscillations, has developed over the last two-and-a-half decades. As soon as the first MSP was discovered in radio [8], it was proposed that an MSP is an old neutron star spun-up in its LMXB phase, in which it gains angular momentum by accretion [1, 104] (see Sect. 4.1). But no millisecond period in an LMXB was found for more than a decade. In 1995, the *Rossi X-ray Timing Explorer (RXTE)* satellite was launched. The Proportional Counter Array (PCA) on-board *RXTE* had a large area and high time resolution, and hence was ideal to detect millisecond period X-ray signals [70]. Indeed, soon after the launch, coherent millisecond period brightness oscillations at a frequency of ≈ 363 Hz were discovered in six thermonuclear X-ray bursts observed from the LMXB 4U 1728–34 [115]. The root mean square (rms) amplitudes of this timing feature were in the range of 2.5%–10%, and the frequency had an upward drift of ≈ 1.5 Hz for a few seconds, after which the oscillations became almost coherent during the burst decay. Because of this effective coherence, and since a near-millisecond spin period is expected for a neutron star in an LMXB, the burst oscillation frequency was thought to be the stellar spin frequency. Therefore, the simplest explanation of this feature was a spin modulated inhomogeneous burst emission, which could explain the observed rms amplitudes.

Burst oscillations from multiple neutron star LMXBs were discovered in the next few years [110, 120], and the finding of a remarkable stability of the asymptotic oscillation frequency of two sources over a period of ~ 1.5 years strongly indicated that this frequency is the neutron star spin frequency [118]. Nevertheless, this could not be established beyond doubt. In fact, based on a model of another millisecond period timing feature, viz., kilohertz quasiperiodic oscillations [127], as well as some observational indications, it was proposed that the burst oscillation frequency could be twice the stellar spin frequency [92]. But in 2003, Chakrabarty et al. reported that the oscillation frequency in the decay phase of thermonuclear bursts from the AMXP SAX J1808.4–3658 matched well with the known spin frequency (≈ 401 Hz) of this source [36]. This not only showed that a burst oscillation frequency is the neutron star spin frequency, but also provided a new way to measure the latter frequency. Detection of burst oscillations from more AMXPs has confirmed this (see Table 5.1).

The firm identification of the burst oscillation frequency with the neutron star spin frequency confirmed a new type of pulsars—the NMXPs. This also made the burst oscillation feature a promising tool to study the strong gravity and to measure

Table 5.1 Nuclear-powered millisecond X-ray pulsars

No.	Source name	Frequency (Hz)	Remarks
1	4U 1608–522 ^T	620	Oscillations in multiple bursts were reported using <i>RXTE</i> PCA observations [54, 63, 130]
2	SAX J1750.8–2900 ^T	601	A 5σ detection of oscillations in a burst was reported in 2002 [73] using <i>RXTE</i> PCA observations. Later, oscillations in more bursts were reported [54]
3	GRS 1741.9–2853 ^T	589	Oscillations in multiple bursts were reported using <i>RXTE</i> PCA observations [54, 116]
4	4U 1636–536	582	Oscillations in many bursts were reported using <i>RXTE</i> PCA observations [54, 61, 113, 119]
5	MXB 1659–298 ^T	567	Oscillations in multiple bursts were reported using <i>RXTE</i> PCA observations [54, 136]
6	EXO 0748–676 ^T	552	Oscillations in two bursts were reported in 2010 using <i>RXTE</i> PCA observations with a significance of 6.3σ [55]
7	Aql X-1 ^{T, IP}	550	Oscillations in multiple bursts were reported using <i>RXTE</i> PCA observations [130, 140]
8	SAX J1810.8–2609 ^T	532	A 5.75σ detection of oscillations in one burst was reported in 2018 using <i>RXTE</i> PCA observations [25]
9	1A 1744–361 ^T	530	Oscillations in one burst were reported with a significance of 5.02×10^{-7} in 2006 using <i>RXTE</i> PCA observations [19]. Later, oscillations in the same burst were confirmed [54]
10	KS 1731–260 ^T	524	Oscillations in multiple bursts were reported using <i>RXTE</i> PCA observations [54, 108]
11	SAX J1808.4–3658 ^{T, P}	401	Oscillations, with frequencies close to the accretion-powered pulsation frequency, in multiple bursts were reported using <i>RXTE</i> PCA observations [36, 54]
12	IGR J17498–2921 ^{T, P}	401	Oscillations, with frequencies close to the accretion-powered pulsation frequency, in two bursts were reported using <i>RXTE</i> PCA observations, one with 4.1σ significance [34, 84] and another with 8.8σ significance [34]
13	HETE J1900.1–2455 ^{T, IP}	377	Oscillations in one burst were reported in 2009 using <i>RXTE</i> PCA observations [134]. While the oscillations are relatively weak, the feature is considered robust due to the closeness of the corresponding frequency to the known accretion-powered pulsation frequency [24]
14	4U 1728–34	363	Oscillations in many bursts were reported using <i>RXTE</i> PCA observations [54, 115]
15	4U 1702–429	329	Oscillations in many bursts were reported using <i>RXTE</i> PCA observations [54, 90]

(continued)

Table 5.1 (continued)

No.	Source name	Frequency (Hz)	Remarks
16	XTE J1814–338 ^{T, P}	314	Oscillations, with frequencies close to the accretion-powered pulsation frequency, in many bursts were reported using <i>RXTE</i> PCA observations [54, 121]
17	IGR J17191–2821 ^T	294	Oscillations in multiple bursts were reported using <i>RXTE</i> PCA observations [3]
18	IGR J18245–2452 ^{T, IP}	254	Oscillations, with a frequency close to the accretion-powered and spin-powered pulsation frequencies, in one burst were reported in 2013 using <i>Swift</i> XRT observations [101, 102]
19	IGR J17511–3057 ^{T, P}	245	Oscillations, with frequencies close to the accretion-powered pulsation frequency, in multiple bursts were reported using <i>RXTE</i> PCA observations [4]

^T Transient source, ^P AMXP, ^{IP} Intermittent AMXP, ^{IP} Transitional MSP

some parameter values of neutron stars [11, 20]. The latter is required to probe the super-dense degenerate core matter of these stars (see Chap. 9).

Currently, 19 NMXPs are known (see Table 5.1), implying about 20% of burst sources are NMXPs [56]. In addition, tentative detection of burst oscillations has been reported for six neutron star LMXBs (see Table 5.2). Note that we have not included the burst oscillation source IGR J17480–2446, because the neutron star in this LMXB has a spin frequency of 11 Hz [114], and hence is not an MSP. Detection and observational studies of burst oscillations from so many sources, efforts to theoretically model and understand them, and use of this timing feature as a tool to probe various source properties have firmly established the field of NMXPs over the last two-and-a-half decades.

Nevertheless, it is quite challenging to detect burst oscillations and study their properties for the following reasons. Firstly, they appear only during thermonuclear bursts, which are typically irregular and have short duration and low duty cycle. In addition, most of the known NMXPs are transient sources (see Table 5.1), and we usually observe thermonuclear bursts during their outbursts, which are irregular and of low duty cycle. Next, these oscillations are usually seen only for a fraction of bursts even for known NMXPs, and even for a given burst this feature may be seen intermittently and for a small fraction of time, and with a frequency evolution (see Fig. 5.2). This is why the detection of burst oscillations often crucially depends on the used criteria [25, 56, 130]. Finally, not all X-ray instruments can detect this high-frequency feature. In fact, burst oscillations from all sources, except two, have so far been discovered or reported using *RXTE* PCA (see Tables 5.1 and 5.2). After *RXTE* was decommissioned in 2012, now *AstroSat* and *Neutron Star Interior Composition Explorer (NICER)* satellites are ideal to detect burst oscillations [27, 41, 88].

Table 5.2 Neutron star LMXBs with tentative detection of burst oscillations

No.	Source name	Frequency (Hz)	Remarks
1	XTE J1739–285 ^T	1122/386.5	Oscillations at 1122 Hz with $\lesssim 4\sigma$ significance in one burst were reported in 2007 using <i>RXTE</i> PCA observations [75]. However, this detection was not confirmed later for the same burst for independent time windows [54]. Another tentative detection of oscillations at 386.5 Hz was reported in 2021 from a burst observed with <i>NICER</i> [28]
2	GS 1826–24 ^T	611	Burst oscillations with $<4\sigma$ significance were reported in 2005 using <i>RXTE</i> PCA observations [126]
3	4U 0614+09	415	Oscillations with $\sim 4\sigma$ significance in one burst were reported in 2008 using <i>Swift</i> BAT observations [122]
4	MXB 1730–335 ^T	306	Burst oscillations with $\sim 2.5\sigma$ significance were reported in 2001 using <i>RXTE</i> PCA observations [49]
5	4U 1916–053	270	Oscillations with $\sim 4.6\sigma$ significance in one burst were reported in 2001 using <i>RXTE</i> PCA observations [52]
6	XB 1254–690	95	A 2σ candidate oscillation signal in one burst was reported in 2007 using <i>RXTE</i> PCA observations [10]

^T Transient source

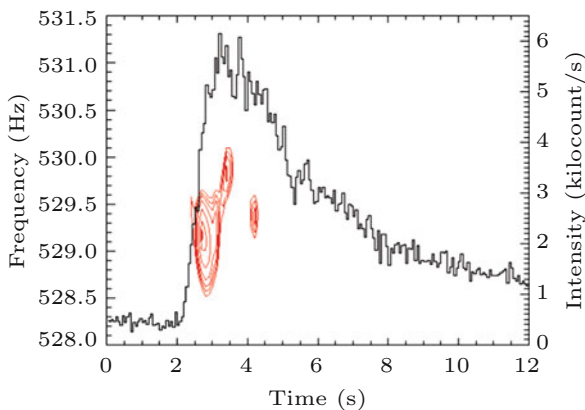


Fig. 5.2 A thermonuclear X-ray burst observed from the neutron star LMXB 1A 1744–361 with the *Rossi X-ray Timing Explorer (RXTE)* satellite (adapted from [19]). Dynamic power spectrum, i.e., X-ray brightness variation power as a function of frequency and time, is shown. The corresponding power contours (in red) suggest that burst oscillations can be present during only portions of a given burst, and their frequency could evolve (see Sect. 5.1.2). Credit: Bhattacharyya et al. ApJ, 639, L31 (2006) © AAS. Reproduced with permission

We will discuss the main observational aspects of burst oscillations in Sect. 5.2, except some of those related to thermonuclear flame-spreading on neutron stars. The theory and observations of such spreading, as well as the origin of oscillations during burst rise, will be presented in Sect. 5.3. In Sect. 5.4, we will discuss what may cause oscillations during burst decay. Finally, we will mention why burst oscillations are important and what is required to use them as a reliable tool, in Sect. 5.5.

5.2 Observational Aspects

In this section, we will discuss the main observational properties of burst oscillations. While burst oscillation models will be described in subsequent sections, here we will briefly mention certain physical effects, which might explain some of the observational aspects.

5.2.1 Frequency and Coherence

Burst oscillation frequency drifts by $\sim 1\text{--}3$ Hz in many thermonuclear X-ray bursts, but remains within a few Hz of the known neutron star spin frequency for AMXPs. A further evidence of the stellar spin connection of burst oscillation frequencies comes from a transitional MSP IGR J18245–2452 (see Sect. 6.4.2; [101]), because it has manifested itself as each of spin-powered, accretion-powered and nuclear-powered MSPs (Table 5.1). However, somewhat significant burst oscillation signals, at frequencies far from the known or believed stellar spin frequencies, have also been reported for some sources. For example, a $\sim 5.5\sigma$ oscillation signal was found at 45 Hz in the average power spectrum of many thermonuclear bursts from EXO 0748–676 in 2004 [129]. But in 2010, 6.3σ oscillations in two bursts from the same source were reported at 552 Hz [55], which is believed to be approximately the neutron star spin frequency. Note that the 45 Hz signal was not confirmed by further analyses [24]. Similarly, an oscillation signal at 410 Hz was reported for a burst from SAX J1748.9–2021 [74]. But this source was later found to be an intermittent AMXP with the stellar spin frequency of 442 Hz, and the significance of the 410 Hz signal decreased below 3σ for a revised number of trials [2].

Burst oscillation frequency typically drifts upwards, although exceptions, such as a downward drift and the presence of two simultaneous oscillations at frequencies separated by a few Hz, are observed in $\sim 5\%$ cases [95]. Upward drifting frequencies usually approach an apparent saturation frequency, known as the asymptotic frequency v_a . This frequency is determined by modelling the frequency evolution with the formula $v(t) = v_a(1 - \delta_v e^{-t/\tau})$, where t , δ_v , and τ are time, and fractional drift and drift timescale of the frequency, respectively [111]. Note that the frequency evolution is usually estimated using the phase connection technique [94, 95]. The

fractional dispersion in asymptotic frequencies over several years has been found to be typically less than 10^{-3} for multiple sources ([95, 111, 130] and references therein). Such a high stability strongly points to the neutron star spin frequency, and hence ν_a , when measured, is usually considered to be the stellar spin frequency for non-AMXPs. This assumption has been tested for two intermittent AMXPs, Aql X-1 and HETE J1900.1–2455, for which ν_a is 0.5 Hz and ~ 1 Hz below the known stellar spin frequencies, respectively ([130] and references therein).

The frequency evolution $\nu(t)$ is characterized either by fitting data with a formula, such as $\nu(t) = \nu_a(1 - \delta_\nu e^{-t/\tau})$, $\nu(t) = \nu_0 + \dot{\nu}t + \ddot{\nu}t^2$, etc., for the entire oscillation duration, or using several constant frequency values in shorter time bins. The modelling with a formula can give a highly coherent signal, with a coherence $Q (= \nu / \Delta\nu)$ as high as, for example, ~ 4000 [112]. Note that an evolution of frequency is not detected for many burst oscillation signals for the following reasons: oscillations are weak, short-lived or intermittent, or genuinely there is no evolution. Even when there is a frequency drift, the evolution may not be smooth on short timescales. This may be because of two simultaneous signals with a small frequency difference, or a discontinuous frequency evolution, or discrete phase jumps [95]. The saturation or asymptotic frequency is usually measured in the decay phase, because a burst rise duration is typically only ~ 1 s, and hence it is more challenging to detect a frequency evolution in the rising phase. Nevertheless, such an evolution and an indication of a saturation frequency have been found for the rise of some bursts, a clear example of which is shown in Fig. 5.3.

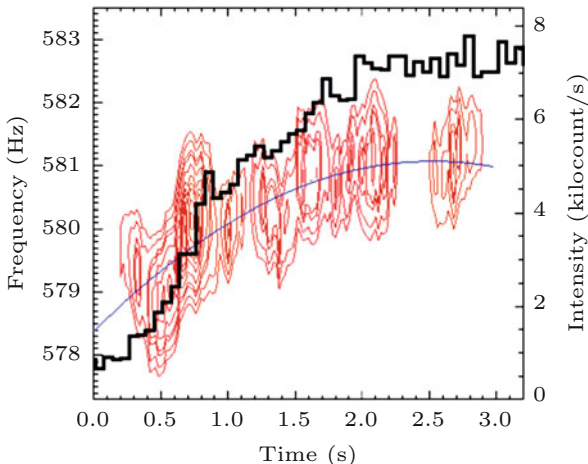


Fig. 5.3 Rise of a thermonuclear X-ray burst (black histogram) observed from the neutron star LMXB 4U 1636–536 with the *Rossi X-ray Timing Explorer (RXTE)* satellite (adapted from [13]). Dynamic power spectrum, i.e., burst rise oscillation power as a function of frequency and time, is shown. The corresponding power contours (in red) and the best-fit frequency evolution curve (in blue) suggest that the burst oscillation frequency drifts upward by a few Hz to an apparent saturation value (see Sect. 5.2.1). Credit: Bhattacharyya and Strohmayer ApJ, 634, L157 (2005) © AAS. Reproduced with permission

A drift of a burst oscillation frequency, typically $\approx 1\%$ in a few seconds, cannot be caused by the stellar spin evolution, as that would require an unphysically large torque. Note that an azimuthally asymmetric brightness pattern on the spinning neutron star surface should give rise to burst oscillations. Therefore, in order to explain the frequency drift, this pattern may move and/or change shape/size in the azimuthal direction. A simple model proposed to explain this is the following [116]. A ~ 10 m thick layer of accumulated accreted matter could expand to a thickness of about ~ 30 m during a burst, and hence in order to conserve the angular momentum, its rotation frequency should decrease by $\delta\nu \approx 2\nu(20m/R)$, where ν and R are the stellar spin frequency and radius, respectively [111]. This may explain why at the beginning we observe a burst oscillation frequency, which is typically ~ 2 Hz less than the stellar spin frequency. As the burning layer cools down, its thickness decreases, and hence the burst oscillation frequency is expected to increase towards the stellar spin frequency in a few seconds, as observed. However, this explanation has following problems. (1) Observations of a frequency drift of ≈ 3.6 Hz for 4U 1916–053 [52] and ~ 5 Hz for MXB 1659–298 [136] may imply an unphysically large increase of burning layer thickness during the burst. (2) A frequency increase by a few Hz has also been observed during the rising phase of bursts (see Fig. 5.3 for an example), when the burning layer should not cool down. (3) If the burning layer slips at a rate of a few Hz with respect to the neutron star, an azimuthal asymmetry could disappear in a fraction of a second, and hence burst oscillations might not be observed for as long as a few seconds.

5.2.2 Amplitude

The average fractional root mean square (rms) amplitude of burst oscillations is typically in the range of 0.02–0.2, with a median of ~ 0.05 [54, 96, 130]. However, for burst oscillations detected at the beginning of the rise of bursts, the fractional rms amplitude is typically found to be higher ($\gtrsim 0.2$, and sometimes as high as ~ 0.6 ; [35, 119]). It was also noticed soon after the discovery of the burst oscillation feature [117, 119], and later confirmed with extensive analyses [35], that the burst oscillation amplitude decreases with time during burst rise. This is expected for thermonuclear flame-spreading on the neutron star surface, as we will discuss in Sect. 5.3.

If oscillations are detected during both rise and decay portions of a burst, the oscillation amplitude can decrease until the burst peak, and then can again increase and finally decrease in the decay phase [87]. The fractional rms amplitude during burst decay is typically small (~ 0.1 ; [54, 88]). But recently very large burst decay oscillation amplitudes (fractional rms ~ 0.4 –0.5) have been measured for two bursts observed from 4U 1728–34 with the *NICER* satellite [88]. These oscillations, however, have been detected above 6 keV, and hence are somewhat unusual. Such high amplitude values could be very useful to constrain models (see Sect. 5.4).

Burst oscillation amplitude usually changes throughout a burst, sometimes smoothly, but in other cases erratically. While oscillations can be detected in any portion of a burst—rise, peak or decay, they do not appear during the peak of a PRE burst, confirming that oscillations are stellar surface phenomena. The short durations and/or intermittence of oscillations in many bursts (see Sect. 5.2.1) could be due to low observed X-ray count rates and/or apparently erratic low oscillation amplitudes. From a systematic study of the rise of 161 bursts from 4U 1636–536, it was found that intermittent non-detections of oscillations cannot be solely due to low observed X-ray count rates [35]. Detection of burst decay oscillations, on the other hand, could be linked to the apparent burst emission area evolution estimated from spectral analyses, as found for two NMXPs—4U 1636–53 and 4U 1728–34 [141, 142].

It has also been found for non-AMXPs that the oscillation fractional amplitude of the strongest signal during a burst can be both low and high (~ 0.05 – 0.2) in relatively softer source spectral states, but is typically low (~ 0.05 – 0.1) in harder spectral states [56, 100]. This may cause burst oscillations to be usually detected in softer states, which are thought to be linked with higher accretion rates [54, 56, 98]. Oscillations are also mostly found for bursts with higher peak fluxes and shorter durations, which are likely helium bursts on many occasions (see Sect. 5.1.1), and are often PRE bursts [56]. However, detection of oscillations does not depend on separation time and fluence of bursts [56].

5.2.3 *Harmonic Content*

Burst oscillations could originate from a hot spot or bright region on a spinning neutron star surface, and Doppler and time delay effects are expected to make the oscillation profile more asymmetric and narrowly peaked ([96] and references therein). This would cause larger amplitudes of the fundamental and overtones of oscillations. In such a case, the first overtone of the signal is expected to be detected, at least for some bursts. But a harmonic content has not been significantly detected for any individual burst from a non-AMXP or an intermittent AMXP [96, 134]. A theoretical study suggested that such a lack of harmonic content implies a hot spot near the spinning pole or a hot spot covering nearly half the stellar surface [96]. It is not known if one of these could be true for burst decay oscillations, since the cause of such oscillations is not yet understood (Sect. 5.4). However, during the burst rise, an expanding hot spot due to the thermonuclear flame-spreading is believed to cause oscillations (see Sect. 5.3). In this case, while a large hot spot is expected towards the end of the burst rise, the hot spot should be relatively small at the beginning (Sect. 5.3). Hence, unless the spot is very close to the spinning pole, there should be a significant harmonic content in oscillations at the beginning of a burst. Indeed, a significant first overtone was found at the beginning of burst rise, by stacking several

bursts observed from the non-AMXP 4U 1636–536 with *RXTE* [13]. A stacking was required to improve the statistics, as the observed X-ray count rates were low at the beginning of burst rise.

5.2.4 Energy Dependence

Burst oscillation fractional amplitude increases with photon energy for non-AMXPs and intermittent AMXPs [97, 134], although such a trend is not always observationally clear [38]. This trend is not unexpected, as the non-burst emission of a source peaks in a lower energy band, and hence the brightness contrast between burst and non-burst emissions are lesser in lower energies. Such an increasing brightness contrast with energy should cause an increasing fractional amplitude, as observed [38].

Photons of one energy band may arrive later than those of another band. If higher energy photons follow the lower energy photons, then it is a hard lag, and if the former photons precede the latter ones, then it is a soft lag. Detection of such an energy dependent phase lag for burst oscillations could be very useful to probe the origin of this timing feature. For example, a hard lag may imply that softer photons from a burst are upscattered to higher energy photons by a hot electron cloud [82]. A soft lag, on the other hand, could be produced by one of the following mechanisms. (1) As the hot spot on a spinning stellar surface moves towards the observer, the photons emitted from this spot at an earlier spin phase should be Doppler-shifted to higher energies [47]. (2) High energy photons could be Compton downscattered in a relatively cool atmosphere [44]. (3) A hot spot could laterally expand and cool [44]. (4) Burst photons could be scattered by an accretion disk rotating in the same direction of the neutron star spin [105].

An indication of hard lags for burst decay oscillations was found by averaging groups of bursts observed from individual sources [97]. However, it was later reported that the phase lags of oscillations during some of these individual bursts were consistent with soft lags [6]. More recently, a detailed analysis of *RXTE* data from several sources has shown that oscillations from different bursts from the same source could have either of no lag, hard lag, soft lag or mixed lag [38]. Explanation of a hard lag is challenging, because a Compton upscattering should decrease the fractional amplitude of oscillations, while relatively large fractional amplitudes in high-energy bands have been observed for hard lags [97]. In addition, it has recently been found for the soft state of the neutron star LMXB 4U 1728–34 that the burst emission is not significantly reprocessed by a hot electron cloud [22]. Moreover, it is particularly challenging to explain the hard lag for oscillations during the burst rise [38], when an expanding hot spot on the spinning neutron star might cause a soft lag due to the Doppler shift [47]. However, the current detection of phase lags are mostly marginal [130], and a stronger detection with future instruments will be required to understand burst oscillation phase lags.

5.2.5 Connection with Accretion-Powered Pulsations

Similar to burst oscillations, accretion-powered pulsations also originate from an azimuthal asymmetry on or near the neutron star surface. For the latter feature, a sufficiently strong stellar magnetic field channels the accreted matter on to magnetic poles (see Chap. 4). The resulting hot polar regions, which are rotating hot spots, can give rise to the observed accretion-powered pulsations. Studies of those sources, which are both NMXPs and AMXPs, particularly persistent AMXPs, can therefore be useful to probe several important questions, such as, if stellar magnetic field and polar regions contribute to the burst oscillation mechanism and if this mechanism is different for AMXPs and non-AMXPs in some respects. To this end, the first aspect to check is how the burst oscillation frequency behaves with respect to the accretion-powered pulsation frequency, or the *pulsar frequency*. Oscillation frequency does not significantly drift during the burst decay of persistently accretion-powered and nuclear-powered X-ray millisecond pulsars (ANMXPs), and typically remains close to the pulsar frequency. While for XTE J1814–338, the burst oscillation frequency is extremely stable, being within $\sim 10^{-8}$ Hz of the pulsar frequency, for SAX J1808.4–3658, IGR J17511–3057 and IGR J17498–2921, the former frequency is within a few mHz, ~ 0.05 Hz and ~ 0.25 Hz of the latter frequency, respectively [4, 34, 36, 121, 130, 131, 133]. These indicate that during the burst decay of ANMXPs, and particularly for XTE J1814–338, burst oscillation and accretion-powered pulsation mechanisms are closely related.

For the burst rise of SAX J1808.4–3658, however, the burst oscillation frequency increased from a lower value by a few Hz, and appeared to overshoot the pulsar frequency [16, 36] (see also Fig. 5.4). This and other simultaneous burst rise properties indicated an expanding hot spot due to thermonuclear flame-spreading [16], which should be unrelated to accretion-powered pulsations. An upward frequency drift of ~ 0.1 Hz and a similar overshooting was also reported for IGR J17511–3057 [4, 130]. But for XTE J1814–338, the oscillation frequency did not drift even during the burst rise, except for one burst, for which the frequency decreased by ~ 0.1 Hz.

The next aspect to check is if burst oscillations and accretion-powered pulsations of an ANXP are phase-locked when their frequencies are consistent with each other, and if so, what the constant phase offset is. A phase-locking with the zero phase offset might indicate that almost the same hot spot, that is the one at a magnetic polar cap, generates the two sets of pulsations. One implication of a non-zero offset might be burst oscillations due to a hot spot located at a constant longitude separation with a polar cap. However, burst oscillations could have soft or hard lags (see Sect. 5.2.4) and accretion-powered pulsations typically have soft lags [44, 130]. Therefore, the phase offset between these two sets of pulsations can also be energy dependent. This was found for the ANXP XTE J1814–338. For this source, while the two sets of pulsations were phase-locked with a zero offset at lower energies, there could be a non-zero offset at higher energies [121, 133]. This is because, while accretion-powered pulsations showed soft lags of up to 50

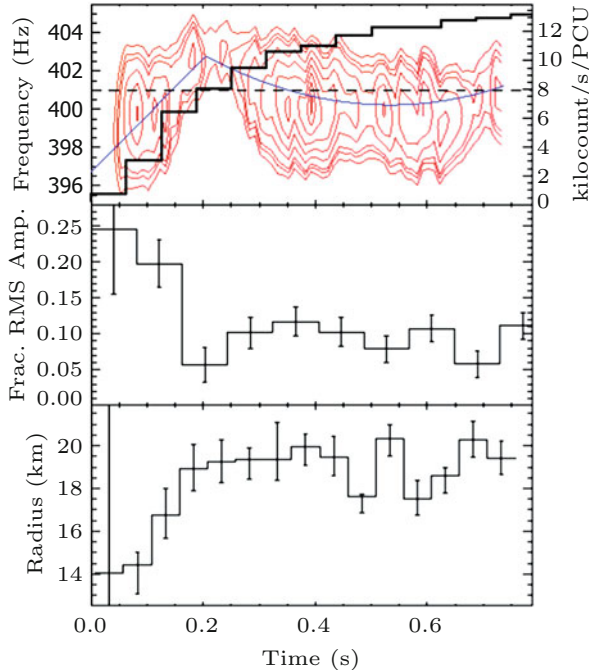


Fig. 5.4 *Upper panel:* Rise of a thermonuclear X-ray burst (black histogram) observed from the AMXP SAX J1808.4–3658 with the *Rossi X-ray Timing Explorer (RXTE)* satellite. The power contours (in red) of the dynamic power spectrum of burst rise oscillations, the best-fit frequency evolution curve (in blue) and the pulsar spin frequency (the horizontal dashed line) are shown. *Middle panel:* The fractional rms amplitude evolution of burst rise oscillations. *Lower panel:* Evolution of an apparent radius (assuming 10 kpc source distance), which is proportional to the square root of the burning area, as inferred from spectral fitting (adapted from [16]; see also Sects. 5.2.5 and 5.3.2). Credit: Bhattacharyya and Strohmayer ApJ, 642, L161 (2006) © AAS. Reproduced with permission

μ s, no evidence of lags was found for burst oscillations [132]. Accretion-powered pulsations and burst oscillations have been reported to be phase-locked also for another ANMXP, IGR J17511–3057 [4, 130].

Burst oscillations appear to be present in all observed bursts of ANMXPs. Moreover, oscillations were observed throughout the bursts, except during the peak of PRE bursts, for two ANMXPs: SAX J1808.4–3658 and XTE J1814–338. These aspects are different from other burst oscillation sources, for which only a fraction of bursts shows oscillations, that too usually for portions of a burst. For ANMXPs, burst oscillation amplitudes are usually close to the accretion-powered pulsation amplitudes [36, 130, 131]. This is not surprising if both sets of pulsations originate from essentially the same hot spot, perhaps at a magnetic polar cap, as mentioned above. However, burst oscillation amplitudes were found to be somewhat lower than accretion-powered amplitudes for some bursts from XTE J1814–338, which may

indicate a larger burning region, perhaps due to a higher degree of fuel spread [131]. Besides, the decreasing fractional amplitude during the burst rise for SAX J1808.4–3658 implies the thermonuclear flame-spreading, as mentioned above ([16]; see Fig. 5.4).

Unlike non-AMXPs (except 4U 1636–536) and intermittent AMXPs (see Sect. 5.2.3), the harmonic content of burst oscillations from XTE J1814–338 and IGR J17511–3057 has been detected [4, 121]. This supports the hot spot origin of burst oscillations from ANMXPs. However, a difference between the harmonic contents of burst oscillations and accretion-powered pulsations for a given ANMXP may indicate that beaming and other effects could also contribute to this feature [131].

While the burst oscillation fractional amplitude for non-AMXPs and intermittent AMXPs increases with photon energy (see Sect. 5.2.4), this behaviour appears to be opposite for both burst oscillations and accretion-powered pulsations from ANMXPs [130, 132]. While this further supports related mechanisms for the two sets of pulsations from ANMXPs, the decrease of the fractional amplitude with energy is not yet fully understood (but see [132] and references therein).

5.2.6 Superburst Oscillations

Brightness oscillations during an interval of ~ 800 s around the peak of a superburst from the known NMXP 4U 1636–536 were observed with *RXTE* [113]. The oscillation frequency was measured to be ≈ 582 Hz, which is a fraction of a Hz greater than the asymptotic frequency measured from type-I X-ray bursts of this source [61]. This is similar to intermittent AMXPs, for which the accretion-powered pulsation frequency is ~ 0.5 –1 Hz greater than the burst oscillation asymptotic frequency (see Sect. 5.2.1). The superburst oscillation frequency did not drift if the stellar orbital motion is taken into account, and the coherence Q ($> 4.5 \times 10^5$) was much higher than that observed for burst oscillations. In fact, both these properties are reminiscent of accretion-powered pulsations. The fractional rms amplitude of the superburst oscillations was measured to be ~ 0.01 , which is lower than those for oscillations found from type-I X-ray bursts from 4U 1636–536 [113]. Note that if these oscillations were generated only from the non-burst emission, this amplitude would be a few percent, which is typical for AMXPs [103]. A harmonic content of the superburst oscillations was not detected, with a first overtone upper limit of $\sim 6\%$ of the fundamental amplitude [113]. Note that harmonic content has also not been detected for oscillations in individual bursts from non-AMXPs and intermittent AMXPs (see Sect. 5.2.3). Even for accretion-powered pulsations, pulse profiles are sinusoidal in most cases, and when there is a harmonic content, overtones do not usually contribute to the pulsation amplitude by more than $\sim 5\%$ [103]. Finally, soft lags were reported for the superburst oscillations [6]. Note that, while burst oscillations have soft lags in some cases (see Sect. 5.2.4), accretion-powered pulsations typically have soft lags [103].

Therefore, superburst oscillations from 4U 1636–536 were clearly somewhat different from type-I X-ray burst oscillations, particularly if we consider frequency, coherence and fractional amplitude. What could have caused such oscillations? A model based on surface modes (see Sect. 5.4.1) could not explain some of the main observed properties [40]. However, the properties of these oscillations, as discussed above, appear to be consistent with those of accretion-powered pulsations from intermittent AMXPs. Could then 4U 1636–536 be an intermittent AMXP, and were the superburst oscillations accretion-powered pulsations? This could be possible, if the bursting activities around the superburst peak due to ^{12}C fusion in the deep carbon-rich layer of the ocean (see Sect. 5.1.1) would temporarily uncover a larger magnetic field, which might have been buried by the accreted material. However, given that only one instance of superburst oscillations is known to date, this is a speculation, albeit not unreasonable, at this time.

5.3 Burst Rise Oscillations and Thermonuclear Flame-Spreading

Burst oscillations are mostly detected, and their properties, as well as time evolution of these properties, have more extensively been studied for burst decay periods [56, 130]. This is because such a period lasts for $\sim 10\text{ s}$ to tens of seconds, and oscillations are also typically seen at least for a few seconds. On the other hand, burst rise duration is only sub-second to a few seconds, during which burst intensity, spectral properties and oscillation properties evolve rapidly. These make the detection and study of burst rise oscillations more challenging. But while more effort has been given to probe burst decay oscillations, burst rise oscillations are perhaps more important due to the following reasons. (1) The origin of the azimuthally asymmetric brightness pattern is known for burst rise. Thermonuclear flame-spreading gives rise to this pattern, at least for non-AMXPs, and also for some AMXPs, as we will discuss in this section. But we do not have the most basic understanding, i.e., how such a pattern originates, for burst decay oscillations (see Sect. 5.4). (2) Whatever is the reason of the asymmetric pattern for burst decay, it should depend on burst ignition and flame-spreading during burst rise (see Sect. 5.4). Therefore, it is perhaps not possible to fully understand burst decay oscillations without understanding burst rise oscillations. (3) Because of the above points, and an expanding hot spot origin, burst rise oscillations are likely a more reliable tool to constrain neutron star parameters, and hence to probe the supra-nuclear density degenerate core matter of neutron stars ([11]; see Sect. 5.1).

5.3.1 Theory of Flame-Spreading

A thermonuclear burst should be ignited at some point on the neutron star surface, because, given that burst durations are much shorter than time separations between bursts, it is very unlikely that ignition conditions can be met simultaneously all over the surface [45, 107]. It was noted that bursts should preferentially be ignited at or very close to the equator, because the spin-induced reduced gravity should lead to a larger accumulation of the accreted matter at the equator [109]. However, for higher accretion rates, ignition may occur at higher latitudes [42].

After ignition, a thermonuclear flame-spreading on the stellar surface to burn the fuel, i.e., the accumulated accreted matter, is expected. This spreading could happen via deflagration [51] or detonation [50, 143]. Detonation could be possible, if the nuclear burning timescale is less than the vertical sound crossing time, which is not expected for NMXP [109]. Therefore, flames should spread on the stellar surface by deflagration.

A theoretical study of flame-spreading on NMXP, considering the effects of the Coriolis force and the puffed up burning layers, were reported in 2002 [109]. According to this study, initially flames should spread by geostrophic flow, rapidly and almost isotropically, with a typical speed $v_{\text{geostrophic}} \approx \sqrt{gh} \sim 4500 \text{ km s}^{-1}$. Here, g and h are the gravitational acceleration and the burning region scale height, respectively. However, when the burning region becomes relatively large, with the Rossby number less than 1, the Coriolis force becomes important, and flames start spreading with a significantly slower ageostrophic speed. This speed v_{flame} is $\sim \sqrt{gh}/ft_n \sim 5-10 \text{ km s}^{-1}$ for a weak turbulent viscosity, and $\sim \sqrt{gh}/ft_n \sim 100-300 \text{ km s}^{-1}$ for a dynamically important turbulent viscosity [35, 109]. Here, t_n is the nuclear burning time scale and $f = 2\Omega \sin \theta$ is the Coriolis parameter, with Ω being the neutron star angular speed and θ being the latitude of the burning front. Therefore, the flame speed is latitude dependent and anisotropic [109]. A few further theoretical studies on flame propagation have been reported since 2002 (e.g., [29–32, 46]), some of which have considered the effects of magnetic field and instability, and used simulations. Note that the expanding burning region, which remains somewhat confined by the Coriolis force, should naturally give rise to brightness oscillations observed during the burst rise. The above-mentioned theoretical results are important to understand various aspects of such burst rise oscillations, as we will discuss in Sect. 5.3.2.

5.3.2 Evidence of Flame-Spreading

An expanding burning region on a spinning neutron star should give rise to brightness oscillations with a decreasing fractional amplitude, as an increasingly larger fraction of such a region is expected to remain visible throughout the stellar spin period. Such an amplitude evolution of burst rise oscillations should, therefore,

be a signature of thermonuclear flame-spreading. In addition, since the burst X-ray spectrum is typically well described with a blackbody, the burst emission area should be proportional to the best-fit blackbody normalization value. An increase of this normalization with time during burst rise could, therefore, provide an independent evidence of flame-spreading, although systematics might affect the inferred burst emission area [21]. Hence, the study of evolution of burst intensity, spectral properties and oscillation properties during the burst rise can be tools to probe flame-spreading. However, in order to use these observational aspects as tools, one needs to divide the burst rise period into a number of smaller time bins, and significantly detect features like oscillations and measure their properties in each bin. This is an extremely challenging goal, given a typical burst rise duration is only ~ 1 s.

In 1997, an evidence of decreasing fractional amplitude of burst rise oscillations was reported for the NMXP 4U 1728–34 [117]. Soon after this, more indications of plausible flame-spreading were found from oscillations and spectral analyses during burst rise (e.g., [119, 128]). In 2005, a better than 3σ detection of harmonic content of oscillations during the initial part of burst rise was reported for the NMXP 4U 1636–536 [13]. This and the finding of a gradual decrease of the harmonic power is expected for an expanding burning region. During 2006–07, observational indications of flame-spreading were reported for multiple bursts from two NMXPs. One of them was the ANMXP SAX J1808.4–3658, for which the oscillation frequency was found to increase rapidly by a few Hz and overshoot the pulsar frequency (see Sect. 5.2.5). With a detailed analysis it appeared that during the rise of one burst, the oscillation frequency could have increased by a few Hz in just first ~ 0.1 s, then decreased, and then increased again by a few Hz, all in just ~ 0.5 s [16]. For another burst from the same source, the oscillation frequency increased by a few Hz and appeared to overshoot the pulsar frequency in the first ~ 0.2 s, and then decreased and remained almost same for the next ~ 0.5 s [16]. During the first ~ 0.2 s, when this frequency rapidly increased, the oscillation fractional amplitude quickly decreased, and the apparent radius, which is proportional to the square-root of the burst emission area, increased fast (see Fig. 5.4). For the next ~ 0.5 s, both the amplitude and the apparent radius maintained near-constant values. Such an evolution and the anti-correlation between the oscillation fractional amplitude and the burst emission area are expected for the flame-spreading during burst rise. For another burst from the same source, which was a precursor to a big burst, a joint spectral and temporal modelling indicated an expanding burning region [17]. Analyses of burst oscillations and X-ray spectra also indicated thermonuclear flame-spreading, and a temporary burning front stalling, for non-PRE double-peaked bursts from 4U 1636–536 [14, 15].

It was found that, if the burning region expands isotropically, the oscillation fractional amplitude first decreases slowly, and then more rapidly, making the evolution profile upward convex [18]. But if this region expands in a latitude-dependent and anisotropic manner, which captures some features of the effects of the Coriolis force (see Sect. 5.3.1), the oscillation fractional amplitude first decreases rapidly, and then rather slowly, making the evolution profile upward concave [18]. It

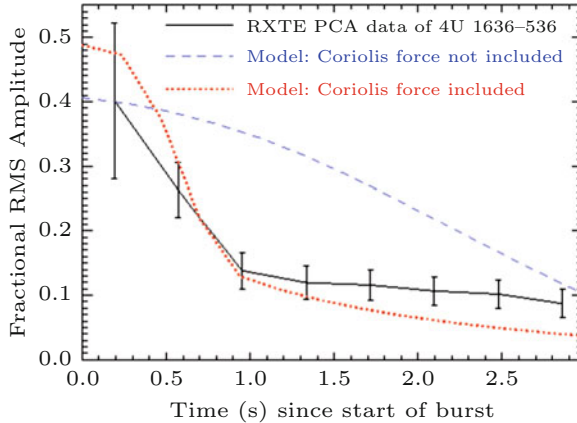


Fig. 5.5 Evolution of fractional rms amplitude of burst oscillations (black solid line with error bars) during the rise of a thermonuclear X-ray burst observed from the neutron star LMXB 4U 1636–536 with the *Rossi X-ray Timing Explorer (RXTE)* satellite (adapted from [18]). Two example models (not fit to data)—one for a uniformly expanding circular hot spot without considering the Coriolis force effect (blue dashed curve) and another for flame spreading including the salient features of the Coriolis force (red dotted line)—are shown (see Sect. 5.3.2)

was reported for two bursts from 4U 1636–536 and SAX J1808.4–3658 that a model of isotropic spreading cannot explain the observed oscillation fractional amplitude evolution, while a model including the salient features of the Coriolis force can, at least qualitatively [18]. This is shown in Fig. 5.5.

All the indications of thermonuclear flame-spreading mentioned above are for a few individual bursts, and a quantitative, systematic and extensive study to establish a plausible decreasing trend of oscillation fractional amplitude during burst rise was missing. Besides, when an observed fractional amplitude evolution during burst rise was studied, a sufficiently significant detection of oscillations in each independent time bin was not always considered. In 2014, a comprehensive study using the rising portions of the *RXTE*-observed thermonuclear X-ray bursts from 10 NMXP sources was reported [35]. The rise times of bursts from all 10 sources were divided into 0.25 s independent bins. Such a short bin was ideal to track oscillation fractional amplitude evolution, particularly at the beginning of burst rise, when the amplitude appears to evolve quickly. For a given time bin, the fractional rms amplitude was measured and an error was estimated, only if oscillations in that bin was detected with at least 3σ significance. Otherwise, an upper limit of the fractional rms amplitude was estimated. These made the analyses systematic and uniform across the bursts and sources. Moreover, the stringent detection criterion, given that a short 0.25 s bin has a small number of total counts, contributed to the reliability of the conclusions. With this criterion, oscillations in at least one bin was detected during the rise of 51 bursts. By fitting the fractional rms amplitude evolution, including upper limits, with empirical models, the decreasing trend was detected with 4σ significance for the best case, which is by far the strongest evidence of thermonuclear flame-spreading

by this method till now [35]. Moreover, an opposite trend was not found in any burst. A quantitative analysis also revealed that the fractional amplitude profiles are upward concave, which implied latitude-dependent flame speeds, likely because the effects of the Coriolis force are important [35]. This is what was theoretically predicted (see Sect. 5.3.1). Besides, even without considering the details, the finding of flame-spreading during ~ 2 s implied an average flame speed of $\sim 15 \text{ km s}^{-1}$, which indicated a weak turbulent viscosity (see Sect. 5.3.1).

It is, however, puzzling, why not all bursts, not even all bursts from NMXPs, show oscillations, at least during the burst rise. This could be somewhat understood based on the ignition location [35, 91]. As mentioned in Sect. 5.3.1, most bursts are likely ignited at or very close to the equator. Therefore, a very large equatorial flame speed (see Sect. 5.3.1) should ignite the entire equatorial belt in a tiny fraction of a second, making the burning region azimuthally symmetric. The subsequent symmetric northward and southward flame-spreading naturally should not give rise to oscillations in most bursts. However, if ignition happens at higher latitudes, possibly for higher accretion rates [42], an azimuthally asymmetric burning region may survive for an observable duration, and burst oscillations can be detected. This is perhaps why burst oscillations are preferentially seen at higher accretion rates (see Sect. 5.2.2). How long burst rise oscillations can be observed would then depend on exactly at what latitude and in which hemisphere the burst has been ignited. But, if a burst is ignited at a very high latitude, oscillation amplitude could be very small depending on the observer's line of sight, and the burning region may become azimuthally almost symmetric soon after the ignition [15]. Note that for ANMXPs, it is likely that a burst is ignited at a magnetic polar cap because of its higher temperature, and then the flames may spread for some sources, like SAX J1808.4–3658 [16], and may not spread much for some other sources, like XTE J1814–338 [121, 131].

5.4 What Causes Burst Decay Oscillations?

Oscillations during burst decay of ANMXPs could be caused by an azimuthal brightness asymmetry due to a magnetic polar cap (see Sect. 5.2.5), although this is not yet established. It is, however, more challenging to explain the observed burst decay oscillations for non-AMXPs and intermittent AMXPs. This is because, after a likely thermonuclear flame-spreading all over the neutron star surface during burst rise, it is not clear how an azimuthally asymmetric brightness pattern survives on the stellar surface. Therefore, while several models, including those based on surface oscillation modes [64], cooling wake [45, 87], vortices [109] and convective patterns [58], have been proposed, the cause of the asymmetry is not yet known with certainty. Here we briefly describe two main models, based on surface modes and cooling wake.

5.4.1 Surface Modes

Thermonuclear flame-spreading during the rise of a burst could excite waves in the ocean and the upper atmosphere of the neutron star, which could persist throughout a large fraction of the burst decay period [64]. Height differences due to these waves could give rise to an azimuthally asymmetric temperature, and hence brightness, pattern, and therefore, burst decay oscillations [130]. As the stellar surface cools down, the frequency of the waves may evolve, which could, in principle, explain the observed oscillation frequency drift (see Sect. 5.2.1). Different families of modes could be excited. But it was found that observations are best explained for the buoyant Rossby modes or r-modes, which are driven by a latitudinal variation of the Coriolis force, and the buoyancy [64, 130]. It is, however, not clear, why, among all the plausible modes, only some specific r-modes would be excited. Moreover, while the surface mode model can explain the observed absence of a significant harmonic content and the energy-dependence of amplitude [64, 83], this model cannot entirely explain the magnitudes of frequency drift and fractional amplitude. The predicted frequency drift is typically much higher than that observed [87, 130], although inclusion of the relativistic effects and use of improved models for the ocean cooling can reduce this discrepancy [39]. Besides, while this surface mode model can explain the lower values of observed burst decay oscillation fractional amplitudes, it is not clear if this model can explain higher observed amplitude values [87]. Particularly, it is not likely that the surface mode model would be able to explain fractional rms amplitudes as high as $\sim 0.4\text{--}0.5$, observed from 4U 1728–34 ([88]; see Sect. 5.2.2).

5.4.2 Cooling Wake

A ‘cooling wake’, i.e., a temperature asymmetry during the cooling of the stellar surface, is a natural consequence of thermonuclear flame-spreading during the burst rise. Such a cooling wake could give rise to an azimuthally asymmetric brightness pattern, which might explain burst decay oscillations [45]. However, it has been found that for a ‘canonical’ cooling, for which either each portion on the stellar surface heats up and cools down in the same way or the cooling timescale varies with latitude, unusually long burst rise times are required to produce the higher values of observed oscillation fractional amplitudes [87]. A canonical cooling also predicts a correlation between burst rise times and the decay oscillation amplitudes [87], which is not observed [38]. On the other hand, for an ‘asymmetric’ cooling model, for which different parts of the stellar surface cool at considerably different rates, higher oscillation fractional amplitudes can be produced, and there is no requirement of a correlation between burst rise times and the decay oscillation amplitudes [87]. While the asymmetric cooling wake mechanism has so far not been studied much, it is strongly connected to the thermonuclear flame-spreading during burst rise, and

together they might provide a natural and self-consistent mechanism for both rise and decay oscillations [87]. However, the origin of an asymmetry in the cooling is not yet understood.

5.5 Conclusion

Observations, primarily with the *RXTE* satellite, have confirmed the following points about burst oscillations: (1) the oscillations originate due to an azimuthally asymmetric brightness pattern on the surface of a spinning neutron star [111, 130], (2) the oscillation frequencies are very close to (typically within 1% of) the stellar spin frequency [36], and (3) oscillations during burst rise are mainly caused by thermonuclear flame-spreading on the stellar surface, except for some AMXPs [35, 117]. Nevertheless, many aspects of burst oscillations are still not well-understood. The main problem is to understand the origin of oscillations during burst decay, when the fuel on the entire neutron star surface is expected to be already burnt. But, even for burst rise, several aspects, such as what causes the frequency drift (see Figs. 5.3 and 5.4) and why hard lags are observed [38], are not understood. Some puzzling aspects of burst oscillations are why they are not detected from all bursting neutron star LMXBs, why they are not detected from all bursts for most NMXPs and why they are intermittent and short-lived for many bursts. While we have discussed some of these points for burst rise in Sect. 5.3.2 (see also [35]), in order to understand burst oscillations, first we need to either detect or at least put stringent upper limits on this feature in sub-second time bins throughout bursts, including in the time bins at the very beginning of the burst rise, when burst count rates are relatively small. Then it is required to measure all burst properties, such as, oscillation frequency, amplitudes of the fundamental and plausible overtones, energy-dependence of amplitudes and phase, etc., in conjunction with burst spectral properties, in all such time bins, which would give the time evolution of these properties and likely correlations among them. These will require observations with future large area X-ray instruments with a sufficient time resolution. Note that the accretion-powered emission may evolve during a burst, and hence could introduce significant systematics into measured burst properties [22, 35, 139]. In order to reliably measure these properties, it is therefore essential to characterize the accretion-powered emission, and hence the broadband spectra of NMXPs. These could perhaps be achieved by simultaneous observations with two mutually well-calibrated instruments, one for softer X-rays, like a larger area version of *NICER* [59], and another for harder X-rays, like a larger area and better spectral resolution version of *AstroSat* Large Area X-ray Proportional Counters (LAXPC; [5]). Another technique, i.e., pulse phase polarimetry, could also be used to probe burst oscillations in the future [60].

Burst oscillation light curves should be affected by various physical effects, such as Doppler shift, special relativistic beaming, gravitational red shift and light bending, etc. Therefore, a modelling of such phase-folded and energy-resolved light

curves can be useful to estimate source parameters, including neutron star mass and radius, and hence to understand the supra-nuclear density degenerate stellar core matter [20, 86, 93, 99]. In addition, studies of burst oscillations can be very useful to probe the extreme environments of the atmosphere, and even the crust, of neutron stars, which are affected by strong gravity, high magnetic field, intense radiation and rapid stellar spin. As an example, an observational evidence from oscillations that flame-spreading happens throughout the burst rise of ~ 2 s could put a constraint on the viscosity (see Sect. 5.3.2). However note that, only when the origin and physics of burst oscillations are sufficiently well-understood, NMXPs can be reliably used to probe the fundamental physics of neutron star interior and surface.

References

1. Alpar, M.A., Cheng, A.F., Ruderman, M.A., Shaham, J.: A new class of radio pulsars. *Nature* **300**, 728–730 (1982). <https://doi.org/10.1038/300728a0>
2. Altamirano, D., Casella, P., Patruno, A., Wijnands, R., van der Klis, M.: Intermittent millisecond X-ray pulsations from the neutron star X-ray transient SAX J1748.9-2021 in the globular cluster NGC 6440. *Astrophys. J.* **674**, L45 (2008). <https://doi.org/10.1086/528983>
3. Altamirano, D., Linares, M., Patruno, A., Degenaar, N., Wijnands, R., Klein-Wolt, M., van der Klis, M., Markwardt, C., Swank, J.: Type I X-ray bursts, burst oscillations and kHz quasi-periodic oscillations in the neutron star system IGR J17191-2821. *Mon. Not. R. Astron. Soc.* **401**, 223–230 (2010). <https://doi.org/10.1111/j.1365-2966.2009.15627.x>
4. Altamirano, D., Watts, A., Linares, M., Markwardt, C.B., Strohmayer, T., Patruno, A.: Type I X-ray bursts and burst oscillations in the accreting millisecond X-ray pulsar IGR J17511-3057. *Mon. Not. R. Astron. Soc.* **409**, 1136–1145 (2010). <https://doi.org/10.1111/j.1365-2966.2010.17369.x>
5. Antia, H.M., Yadav, J.S., Agrawal, P.C., Chauhan, J.V., Manchanda, R.K., Chitnis, V., Paul, B., Dedhia, D., Shah, P., Gujar, V.M., Katoch, T., Kurhade, V.N., Madhwani, P., Manojkumar, T.K., Nikam, V.A., Pandya, A.S., Parmar, J.V., Pawar, D.M., Pahari, M., Misra, R., Navalgund, K.H., Pandiyar, R., Sharma, K.S., Subbarao, K.: Calibration of the Large Area X-ray Proportional Counter (LAXPC) instrument on board AstroSat. *Astrophys. J. Suppl. Ser.* **231**, 10 (2017). <https://doi.org/10.3847/1538-4365/aa7a0e>
6. Artigue, R., Barret, D., Lamb, F.K., Lo, K.H., Miller, M.C.: Testing the rotating hotspot model using X-ray burst oscillations from 4U 1636-536. *Mon. Not. R. Astron. Soc.* **433**, L64–L68 (2013). <https://doi.org/10.1093/mnrasl/slt059>
7. Ayasli, S., Joss, P.C.: Thermonuclear processes on accreting neutron stars – a systematic study. *Astrophys. J.* **256**, 637–665 (1982). <https://doi.org/10.1086/159940>
8. Backer, D.C., Kulkarni, S.R., Heiles, C., Davis, M.M., Goss, W.M.: A millisecond pulsar. *Nature* **300**, 615–618 (1982). <https://doi.org/10.1038/300615a0>
9. Belian, R.D., Conner, J.P., Evans, W.D.: The discovery of X-ray bursts from a region in the constellation Norma. *Astrophys. J.* **206**, L135–L138 (1976). <https://doi.org/10.1086/182151>
10. Bhattacharyya, S.: Timing properties of XB 1254-690. *Mon. Not. R. Astron. Soc.* **377**, 198–202 (2007). <https://doi.org/10.1111/j.1365-2966.2007.11587.x>
11. Bhattacharyya, S.: Measurement of neutron star parameters: a review of methods for low-mass X-ray binaries. *Adv. Space Res.* **45**, 949–978 (2010). <https://doi.org/10.1016/j.asr.2010.01.010>
12. Bhattacharya, D., van den Heuvel, E.P.J.: Formation and evolution of binary and millisecond radio pulsars. *Phys. Rep.* **203**(1–2), 1–124 (1991). [https://doi.org/10.1016/0370-1573\(91\)90064-S](https://doi.org/10.1016/0370-1573(91)90064-S)

13. Bhattacharyya, S., Strohmayer, T.E.: Evidence for harmonic content and frequency evolution of oscillations during the rising phase of X-ray bursts from 4U 1636-536. *Astrophys. J.* **634**, L157–L160 (2005). <https://doi.org/10.1086/499100>
14. Bhattacharyya, S., Strohmayer, T.E.: A non-PRE double-peaked burst from 4U 1636-536: evidence of burning front propagation. *Astrophys. J.* **636**, L121–L124 (2006). <https://doi.org/10.1086/500199>
15. Bhattacharyya, S., Strohmayer, T.E.: Signature of temporary burning front stalling from a non-photospheric radius expansion double-peaked burst. *Astrophys. J.* **641**, L53–L56 (2006). <https://doi.org/10.1086/503768>
16. Bhattacharyya, S., Strohmayer, T.E.: Spreading of thermonuclear flames on the neutron star in SAX J1808.4-3658: an observational tool. *Astrophys. J.* **642**, L161–L164 (2006). <https://doi.org/10.1086/504841>
17. Bhattacharyya, S., Strohmayer, T.E.: An unusual precursor burst with oscillations from SAX J1808.4-3658. *Astrophys. J.* **656**, 414–419 (2007). <https://doi.org/10.1086/510359>
18. Bhattacharyya, S., Strohmayer, T.E.: Thermonuclear flame spreading on rapidly spinning neutron stars: indications of the coriolis force? *Astrophys. J.* **666**, L85–L88 (2007). <https://doi.org/10.1086/521790>
19. Bhattacharyya, S., Strohmayer, T.E., Markwardt, C.B., Swank, J.H.: The discovery of a neutron star with a spin frequency of 530 Hz in A1744-361. *Astrophys. J.* **639**, L31–L34 (2006). <https://doi.org/10.1086/501438>
20. Bhattacharyya, S., Strohmayer, T.E., Miller, M.C., Markwardt, C.B.: Constraints on neutron star parameters from burst oscillation light curves of the accreting millisecond pulsar XTE J1814-338. *Astrophys. J.* **619**, 483–491 (2005). <https://doi.org/10.1086/426383>
21. Bhattacharyya, S., Miller, M.C., Galloway, D.K.: Systematic variation in the apparent burning area of thermonuclear bursts and its implication for neutron star radius measurement. *Mon. Not. R. Astron. Soc.* **401**, 2–6 (2010). <https://doi.org/10.1111/j.1365-2966.2009.15632.x>
22. Bhattacharyya, S., Yadav, J.S., Sridhar, N., Chauhan, J.V., Agrawal, P.C., Antia, H.M., Pahari, M., Misra, R., Katoch, T., Manchanda, R.K., Paul, B.: Effects of thermonuclear X-ray bursts on non-burst emissions in the soft state of 4U 1728-34. *Astrophys. J.* **860**, 2 (2018). <https://doi.org/10.3847/1538-4357/aac495>
23. Bildsten, L.: Theory and observations of type I X-ray bursts from neutron stars. In: AIP Conference Proceedings, vol. 522, pp. 359–369 (2000). <https://doi.org/10.1063/1.1291736>
24. Bilous, A.V., Watts, A.L.: A uniform search for thermonuclear burst oscillations in the RXTE legacy data set. *Astrophys. J. Suppl. Ser.* **245**, 19 (2019). <https://doi.org/10.3847/1538-4365/ab2fe1>
25. Bilous, A.V., Watts, A.L., Galloway, D.K., in't Zand, J.J.M.: A millisecond oscillation in the bursting X-ray flux of SAX J1810.8-2609. *Astrophys. J.* **862**, L4 (2018). <https://doi.org/10.3847/2041-8213/aad09c>
26. Brown, E.F., Bildsten, L.: The ocean and crust of a rapidly accreting neutron star: implications for magnetic field evolution and thermonuclear flashes. *Astrophys. J.* **496**, 915–933 (1998). <https://doi.org/10.1086/305419>
27. Bult, P., Jaisawal, G.K., Guver, T., Strohmayer, T.E., Altamirano, D., Arzoumanian, Z., Ballantyne, D.R., Chakrabarty, D., Chenevez, J., Gendreau, K.C., Guillot, S., Ludlam, R.M.: A NICER thermonuclear burst from the millisecond X-ray pulsar SAX J1808.4-3658. *Astrophys. J.* **885**, L1 (2019). <https://doi.org/10.3847/2041-8213/ab4ae1>
28. Bult, P., Altamirano, D., Arzoumanian, Z., Bilous, A.V., Chakrabarty, D., Gendreau, K.C., Guver, T., Jaisawal, G.K., Kuulkers, E., Malacaria, C., Ng, M., Sanna, A., Strohmayer, T.E.: The X-ray bursts of XTE J1739-285: a NICER sample. *Astrophys. J.* **907**, 79 (2021). <https://doi.org/10.3847/1538-4357/abd54b>
29. Cavecchi, Y., Spitkovsky, A.: Three-dimensional instability of flame fronts in type I X-ray bursts. *Astrophys. J.* **882**, 142 (2019). <https://doi.org/10.3847/1538-4357/ab3650>
30. Cavecchi, Y., Watts, A.L., Braithwaite, J., Levin, Y.: Flame propagation on the surfaces of rapidly rotating neutron stars during Type I X-ray bursts. *Mon. Not. R. Astron. Soc.* **434**, 3526–3541 (2013). <https://doi.org/10.1093/mnras/stt1273>

31. Cavecchi, Y., Watts, A.L., Levin, Y., Braithwaite, J.: Rotational effects in thermonuclear type I bursts: equatorial crossing and directionality of flame spreading. *Mon. Not. R. Astron. Soc.* **448**, 445–455 (2015). <https://doi.org/10.1093/mnras/stu2764>
32. Cavecchi, Y., Levin, Y., Watts, A.L., Braithwaite, J.: Fast and slow magnetic deflagration fronts in type I X-ray bursts. *Mon. Not. R. Astron. Soc.* **459**, 1259–1275 (2016). <https://doi.org/10.1093/mnras/stw728>
33. Chakraborty, M., Bhattacharyya, S.: X-ray bursts from the terzan 5 transient IGR J17480-2446: nuclear rather than gravitational. *Astrophys. J.* **730**, L23 (2011). <https://doi.org/10.1088/2041-8205/730/2/L23>
34. Chakraborty, M., Bhattacharyya, S.: Thermonuclear X-ray bursts from the 401-Hz accreting pulsar IGR J17498-2921: indication of burning in confined regions. *Mon. Not. R. Astron. Soc.* **422**, 2351–2356 (2012). <https://doi.org/10.1111/j.1365-2966.2012.20786.x>
35. Chakraborty, M., Bhattacharyya, S.: Evidence of thermonuclear flame spreading on neutron stars from burst rise oscillations. *Astrophys. J.* **792**, 4 (2014). <https://doi.org/10.1088/0004-637X/792/1/4>
36. Chakrabarty, D., Morgan, E.H., Munoz, M.P., Galloway, D.K., Wijnands, R., van der Klis, M., Markwardt, C.B.: Nuclear-powered millisecond pulsars and the maximum spin frequency of neutron stars. *Nature* **424**, 42–44 (2003). <https://doi.org/10.1038/nature01732>
37. Chakraborty, M., Bhattacharyya, S., Mukherjee, A.: Terzan 5 transient IGR J17480-2446: variation of burst and spectral properties with spectral states. *Mon. Not. R. Astron. Soc.* **418**, 490–499 (2011). <https://doi.org/10.1111/j.1365-2966.2011.19499.x>
38. Chakraborty, M., Bahar, Y.E., Gogus, E.: Time- and energy-dependent characteristics of thermonuclear burst oscillations. *Astrophys. J.* **851**, 79 (2017). <https://doi.org/10.3847/1538-4357/aa984e>
39. Chambers, F.R.N., Watts, A.L.: Relativistic ocean r-modes during type-I X-ray bursts. *Mon. Not. R. Astron. Soc.* **491**, 6032–6044 (2020). <https://doi.org/10.1093/mnras/stz3449>
40. Chambers, F.R.N., Watts, A.L., Cavecchi, Y., Garcia, F., Keek, L.: Superburst oscillations: ocean and crustal modes excited by carbon-triggered type I X-ray bursts. *Mon. Not. R. Astron. Soc.* **477**, 4391 (2018). <https://doi.org/10.1093/mnras/sty895>
41. Chauhan, J.V., Yadav, J.S., Misra, R., Agrawal, P.C., Antia, H.M., Pahari, M., Sridhar, N., Dedhia, D., Katoch, T., Madhwani, P., Manchanda, R.K., Paul, B., Shah, P.: AstroSat/LAXPC detection of millisecond phenomena in 4U 1728-34. *Astrophys. J.* **841**, 41 (2017). <https://doi.org/10.3847/1538-4357/aa6d7e>
42. Cooper, R.L., Narayan, R.: The latitude of type I X-ray burst ignition on rapidly rotating neutron stars. *Astrophys. J.* **657**, L29–L32 (2007). <https://doi.org/10.1086/513077>
43. Cornelisse, R., Heise, J., Kuulkers, E., Verbunt, F., in't Zand, J.J.M.: The longest thermonuclear X-ray burst ever observed? A BeppoSAX Wide Field Camera observation of 4U 1735-44. *Astron. Astrophys.* **357**, L21–L24 (2000)
44. Cui, W., Morgan, E.H., Titarchuk, L.G.: Soft phase lags of pulsed emission from the millisecond X-ray pulsar SAX J1808.4-3658. *Astrophys. J.* **504**, L27–L30 (1998). <https://doi.org/10.1086/311569>
45. Cumming, A., Bildsten, L.: Rotational evolution during Type I X-ray bursts. *Astrophys. J.* **544**, 453–474 (1998). <https://doi.org/10.1086/317191>
46. Eiden, K., Zingale, M., Harpole, A., Willcox, D., Cavecchi, Y., Katz, M.P.: Dynamics of laterally propagating flames in X-ray bursts. I. Burning front structure. *Astrophys. J.* **894**, 6 (2020). <https://doi.org/10.3847/1538-4357/ab80bc>
47. Ford, E.C.: Lag of low-energy photons in an X-ray burst oscillation: Doppler delays. *Astrophys. J.* **519**, L73–L75 (1999). <https://doi.org/10.1086/312108>
48. Fowler, W.A., Hoyle, F.: Nucleosynthesis in Massive Stars and Supernovae. University of Chicago Press, Chicago (1965)
49. Fox, D.W., Lewin, W.H.G., Rutledge, R.E., Morgan, E.H., Guerriero, R., Bildsten, L., van der Klis, M., van Paradijs, J., Moore, C.B., Dotani, T., Asai, K.: Search for millisecond periodicities in type I X-ray bursts of the Rapid Burster. *Mon. Not. R. Astron. Soc.* **321**, 776–782 (2001). <https://doi.org/10.1046/j.1365-8711.2001.04085.x>

50. Fryxell, B.A., Woosley, S.E.: A two-dimensional model for gamma-ray bursts. *Astrophys. J.* **258**, 733–739 (1982). <https://doi.org/10.1086/160121>
51. Fryxell, B.A., Woosley, S.E.: Finite propagation time in multidimensional thermonuclear runaways. *Astrophys. J.* **261**, 332–336 (1982). <https://doi.org/10.1086/160344>
52. Galloway, D.K., Chakrabarty, D., Muno, M.P., Savov, P.: Discovery of a 270 hertz X-ray burst oscillation in the X-ray dipper 4U 1916-053. *Astrophys. J.* **549**, L85–L88 (2001). <https://doi.org/10.1086/319143>
53. Galloway, D.K., Cumming, A., Kuulkers, E., Bildsten, L., Chakrabarty, D., Rothschild, R.E.: Periodic thermonuclear X-ray bursts from GS 1826-24 and the fuel composition as a function of accretion rate. *Astrophys. J.* **601**, 466–473 (2004). <https://doi.org/10.1086/380445>
54. Galloway, D.K., Muno, M.P., Hartman, J.M., Psaltis, D., Chakrabarty, D.: Thermonuclear (type I) X-ray bursts observed by the rossi X-ray timing explorer. *Astrophys. J. Suppl. Ser.* **179**, 360 (2008). <https://doi.org/10.1086/592044>
55. Galloway, D.K., Lin, J., Chakrabarty, D., Hartman, J.M.: Discovery of a 552 Hz burst oscillation in the low-mass X-ray binary EXO 0748–676. *Astrophys. J.* **711**, L148–L151 (2010). <https://doi.org/10.1088/2041-8205/711/2/L148>
56. Galloway, D.K., in't Zand, J., Chenevez, J., Wörpel, H., Keek, L., Ootes, L., Watts, A.L., Gisler, L., Sanchez-Fernandez, C., Kuulkers, E.: The multi-instrument burst archive (MINBAR). *Astrophys. J. Suppl. Ser.* **249**, 32 (2020). <https://doi.org/10.3847/1538-4365/ab9f2e>
57. Garcia, F., Chambers, F.R.N., Watts, A.L.: Thermal convection in rotating spherical shells: temperature-dependent internal heat generation using the example of triple- α burning in neutron stars. *Phys. Rev. Fluids* **3**, 123501 (2018). <https://doi.org/10.1103/PhysRevFluids.3.123501>
58. Garcia, F., Chambers, F.R.N., Watts, A.L.: Polar waves and chaotic flows in thin rotating spherical shells. *Phys. Rev. Fluids* **4**, 074802 (2019). <https://doi.org/10.1103/PhysRevFluids.4.074802>
59. Gendreau, K., Arzoumanian, Z.: Searching for a pulse. *Nat. Astron.* **1**, 895–895 (2017). <https://doi.org/10.1038/s41550-017-0301-3>
60. Ghosh, P., Angelini, L., Baring, M., Baumgartner, W., Black, K., Dotson, J., Harding, A., Hill, J., Jahoda, K., Kaaret, P., Kallman, T., Krawczynski, H., Krolik, J., Lai, D., Markwardt, C., Marshall, H., Martoff, J., Morris, R., Okajima, T., Petre, R., Poutanen, J., Reynolds, S., Scargle, J., Schnittman, J., Serlemitsos, P., Soong, Y., Strohmayer, T., Swank, J., Tawara, Y., Tamagawa, T.: White paper on GEMS study of polarized X-rays from neutron stars. e-prints. arXiv:1301.5514 (2013)
61. Giles, A.B., Hill, K.M., Strohmayer, T.E., Cummings, N.: Burst oscillation periods from 4U 1636-53: a constraint on the binary Doppler modulation. *Astrophys. J.* **568**, 279–288 (2002). <https://doi.org/10.1086/338890>
62. Grindlay, J., Gursky, H., Schnopper, H., Parsignault, D.R., Heise, J., Brinkman, A.C., Schrijver, J.: Discovery of intense X-ray bursts from the globular cluster NGC 6624. *Astrophys. J.* **205**, L127–L130 (1976). <https://doi.org/10.1086/182105>
63. Hartman, J.M., Chakrabarty, D., Galloway, D.K., Muno, M.P., Savov, P., Mendez, M., van Straaten, S., Salvo, T.D.: Discovery of 619 Hz thermonuclear burst oscillations in the low-mass X-ray binary 4U 1608-52. *Bull. Am. Astron. Soc.* **35**, 865 (2003)
64. Heyl, J.S.: r-Modes on rapidly rotating, relativistic stars. I. Do type I bursts excite modes in the neutron star ocean? *Astrophys. J.* **600**, 939–945 (2004). <https://doi.org/10.1086/379966>
65. Hoffman, J.A., Lewin, W.H.G., Doty, J.: Observations of the X-ray burst source MXB 1636-53. *Astrophys. J.* **217**, L23–L28 (1977). <https://doi.org/10.1086/182531>
66. in't Zand, J.J.M., Verbunt, F., Kuulkers, E., Markwardt, C.B., Bazzano, A., Cocchi, M., Cornelisse, R., Heise, J., Natalucci, L., Ubertini, P.: Discovery of the neutron star nature of SLX 1737-282. *Astron. Astrophys.* **389**, L43–L46 (2002). <https://doi.org/10.1051/0004-6361:20020631>
67. in't Zand, J.J.M., Cornelisse, R., Cumming, A.: Superbursts at near-Eddington mass accretion rates. *Astron. Astrophys.* **426**, 257–265 (2004). <https://doi.org/10.1051/0004-6361:20040522>

68. in't Zand, J.J.M., Cumming, A., van der Sluys and F. Verbunt, M., Pols, O.R.: On the possibility of a helium white dwarf donor in the presumed ultracompact binary 2S 0918-549. *Astron. Astrophys.* **441**, 675–684 (2005). <https://doi.org/10.1051/0004-6361:20053002>
69. in't Zand, J.J.M., Bassa, C.G., Jonker, P.G., Keek, L., Verbunt, F., Méndez, M., Markwardt, C.B.: An X-ray and optical study of the ultracompact X-ray binary A 1246-58. *Astron. Astrophys.* **485**, 183–194 (2008). <https://doi.org/10.1051/0004-6361:200809361>
70. Jahoda, K., Markwardt, C.B., Radeva, Y., Rots, A.H., Stark, M.J., Swank, J.H., Strohmayer, T.E., Zhang, W.: Calibration of the rossi X-ray timing explorer proportional counter array. *Astrophys. J. Suppl. Ser.* **163**, 401–423 (2006). <https://doi.org/10.1086/500659>
71. Joss, P.C.: X-ray bursts and neutron-star thermonuclear flashes. *Nature* **270**, 310–314 (1977). <https://doi.org/10.1038/270310a0>
72. Joss, P.C.: Thermonuclear flashes on accreting neutron stars. *Comm. Astrophys.* **8**, 109 (1979)
73. Kaaret, P., in't Zand, J.J.M., Heise, J., Tomsick, J.A.: Discovery of millisecond variability in the neutron star X-ray transient SAX J1750.8-2900. *Astrophys. J.* **575**, 1018–1024 (2002). <https://doi.org/10.1086/341336>
74. Kaaret, P., in't Zand, J.J.M., Heise, J., Tomsick, J.A.: Discovery of X-ray burst oscillations from a neutron star X-ray transient in the globular cluster NGC 6440. *Astrophys. J.* **598**, 481–485 (2003). <https://doi.org/10.1086/375053>
75. Kaaret, P., Prieskorn, Z., in't Zand, J.J.M., Brandt, S., Lund, N., Mereghetti, S., Gotz, D., Kuulkers, E., Tomsick, J.A.: Evidence of 1122 Hz X-ray burst oscillations from the neutron star X-ray transient XTE J1739-285. *Astrophys. J.* **657**, L97–L100 (2007). <https://doi.org/10.1086/513270>
76. Kaptein, R.G., in't Zand, J.J.M., Kuulkers, E., Verbunt, F., Heise, J., Cornelisse, R.: Discovery of 1RXS J171824.2-402934 as an X-ray burster. *Astron. Astrophys.* **358**, L71–L74 (2000)
77. Keek, L., Heger, A.: Thermonuclear bursts with short recurrence times from neutron stars explained by opacity-driven convection. *Astrophys. J.* **842**, 113 (2017). <https://doi.org/10.3847/1538-4357/aa7748>
78. Keek, L., in't Zand, J.J.M., Kuulkers, E., Cumming, A., Brown, E.F., Suzuki, M.: First superburst from a classical low-mass X-ray binary transient. *Astron. Astrophys.* **479**, 177–188 (2008). <https://doi.org/10.1051/0004-6361:20078464>
79. Kuulkers, E.: The observers' view of (very) long X-ray bursts: they are super! *Nucl. Physics B. Suppl. Ser.* **132**, 466–475 (2004). <https://doi.org/10.1016/j.nuclphysbps.2004.04.081>
80. Kuulkers, E.: Probable superbursts in 4U 0614+091 and 4U 1608-522. *Astronomer's Telegram* **483**, 1 (2005)
81. Lamb, D.Q., Lamb, F.K.: Nuclear burning in accreting neutron stars and X-ray bursts. *Astrophys. J.* **220**, 291–302 (1978). <https://doi.org/10.1086/155905>
82. Lee, H.C., Miller, G.S.: Comptonization and QPO origins in accreting neutron star systems. *Mon. Not. R. Astron. Soc.* **299**, 479–487 (1998). <https://doi.org/10.1046/j.1365-8711.1998.01842.x>
83. Lee, U., Strohmayer, T.E.: Light curves of oscillating neutron stars. *Mon. Not. R. Astron. Soc.* **361**, 659–672 (2005). <https://doi.org/10.1111/j.1365-2966.2005.09198.x>
84. Linares, M., Altamirano, D., Strohmayer, A.W.T., Chakrabarty, D., Patruno, A., van der Klis, M., Wijnands, R., Casella, P., Armas-Padilla, M., Cavecchi, Y., Degenaar, N., Kalamkar, M., Kaur, R., Yang, Y., Rea, N.: RXTE detection of a thermonuclear burst from IGR J17498-2921: distance estimate and burst oscillations. *Astronomer's Telegram* **3568**, 1 (2011)
85. Linares, M., Altamirano, D., Chakrabarty, D., Cumming, A., Keek, L.: Millihertz quasi-periodic oscillations and thermonuclear bursts from Terzan 5: a showcase of burning regimes. *Astrophys. J.* **748**, 82 (2012). <https://doi.org/10.1088/0004-637X/748/2/82>
86. Lo, K.H., Miller, M.C., Bhattacharyya, S., Lamb, F.K.: Determining neutron star masses and radii using energy-resolved waveforms of X-ray burst oscillations. *Astrophys. J.* **776**, 19 (2013). <https://doi.org/10.1088/0004-637X/776/1/19>
87. Mahmoodifar, S., Strohmayer, T.E.: X-ray burst oscillations: from flame spreading to the cooling wake. *Astrophys. J.* **818**, 93 (2016). <https://doi.org/10.3847/0004-637X/818/1/93>

88. Mahmoodifar, S., Strohmayer, T.E., Bult, P., Altamirano, D., Arzoumanian, Z., Chakrabarty, D., Gendreau, K.C., Guillot, S., Homan, J., Jaisawal, G.K., Keek, L., Wolff, M.T.: NICER observation of unusual burst oscillations in 4U 1728-34. *Astrophys. J.* **878**, 145 (2019). <https://doi.org/10.3847/1538-4357/ab20c4>
89. Malone, C.M., Nonaka, A., Almgren, A.S., Bell, J.B., Zingale, M.: Multidimensional modeling of type I X-ray bursts. I. Two-dimensional convection prior to the outburst of a pure ^4He accretor. *Astrophys. J.* **728**, 118 (2011). <https://doi.org/10.1088/0004-637X/728/2/118>
90. Markwardt, C.B., Strohmayer, T.E., Swank, J.H.: Observation of kilohertz quasi-periodic oscillations from the atoll source 4U 1702-429 by the Rossi X-ray timing explorer. *Astrophys. J.* **512**, L125–L129 (1999). <https://doi.org/10.1086/311886>
91. Maurer, I., Watts, A.L.: Ignition latitude and the shape of type I X-ray bursts. *Mon. Not. R. Astron. Soc.* **383**, 387–398 (2008). <https://doi.org/10.1111/j.1365-2966.2007.12558.x>
92. Miller, M.C.: Evidence for antipodal hot spots during X-ray bursts from 4U 1636-536. *Astrophys. J.* **515**, L77–L80 (1999). <https://doi.org/10.1086/311970>
93. Miller, M.C., Lamb, F.K.: Bounds on the compactness of neutron stars from brightness oscillations during X-ray bursts. *Astrophys. J.* **499**, L37–L40 (1998). <https://doi.org/10.1086/311335>
94. Munro, M.P., Fox, D.W., Morgan, E.H., Bildsten, L.: Nearly coherent oscillations in type I X-ray bursts from KS 1731-260. *Astrophys. J.* **542**, 1016–1033 (2000). <https://doi.org/10.1086/317031>
95. Munro, M.P., Chakrabarty, D., Galloway, D.K., Psaltis, D.: The frequency stability of millisecond oscillations in thermonuclear X-ray bursts. *Astrophys. J.* **580**, 1048–1059 (2002). <https://doi.org/10.1086/343793>
96. Munro, M.P., Ozel, F., Chakrabarty, D.: The amplitude evolution and harmonic content of millisecond oscillations in thermonuclear X-ray bursts. *Astrophys. J.* **581**, 550–561 (2002). <https://doi.org/10.1086/344152>
97. Munro, M.P., Ozel, F., Chakrabarty, D.: The energy dependence of millisecond oscillations in thermonuclear X-ray bursts. *Astrophys. J.* **595**, 1066–1076 (2003). <https://doi.org/10.1086/377447>
98. Munro, M.P., Galloway, D.K., Chakrabarty, D.: The effect of neutron star rotation on the properties of thermonuclear X-ray bursts. *Astrophys. J.* **608**, 930–934 (2004). <https://doi.org/10.1086/420812>
99. Nath, N.R., Strohmayer, T.E., Swank, J.H.: Bounds on compactness for low-mass X-ray binary neutron stars from X-ray burst oscillations. *Astrophys. J.* **564**, 353–360 (2002). <https://doi.org/10.1086/324132>
100. Ootes, L.S., Watts, A.L., Galloway, D.K., Wijnands, R.: The accretion rate dependence of burst oscillation amplitude. *Astrophys. J.* **834**, 21 (2017). <https://doi.org/10.3847/1538-4357/834/1/21>
101. Papitto, A., Ferrigno, C., Bozzo, E., Rea, N., Pavan, L., Burderi, L., Burgay, M., Campana, S., di Salvo, T., Falanga, M., Filipović, M.D., Freire, P.C.C., Hessels, J.W.T., Possenti, A., Ransom, S.M., Riggio, A., Romano, P., Sarkissian, J.M., Stairs, I.H., Stella, L., Torres, D.F., Wieringa, M.H., Wong, G.F.: Swings between rotation and accretion power in a binary millisecond pulsar. *Nature* **501**(7468), 517–520 (2013). <https://doi.org/10.1038/nature12470>
102. Patruno, A.: Burst oscillations in the X-ray binary IGR J18245-2452 in M28. *Astronomer's Telegram* **5068**, 1 (2013)
103. Patruno, A., Watts, A.L.: Accreting millisecond X-ray pulsars. In: Belloni, T., Mendez, M., Zhang, C.M. (eds.) *Timing neutron stars: pulsations, oscillations and explosions*. ASSL, Springer, Berlin (2012)
104. Radhakrishnan, V., Srinivasan, G.: On the origin of the recently discovered ultra-rapid pulsar. *Curr. Sci.* **51**, 1096–1099 (1982)
105. Sazonov, S.Y., Sunyaev, R.A.: Scattering in the inner accretion disk and the waveforms and polarization of millisecond flux oscillations in LMXBs. *Astron. Astrophys.* **373**, 241–250 (2001). <https://doi.org/10.1051/0004-6361:20010624>

106. Schatz, H., Aprahamian, A., Barnard, V., Bildsten, L., Cumming, A., Ouellette, M., Rauscher, T., Thielemann, F.K., Wiescher, M.: End point of the rp process on accreting neutron stars. *Phys. Rev. Lett.* **86**, 3471–3474 (2001). <https://doi.org/10.1103/PhysRevLett.86.3471>
107. Shara, M.M.: Localized thermonuclear runaways and volcanoes on degenerate dwarf stars. *Astrophys. J.* **261**, 649–660 (1982). <https://doi.org/10.1086/160376>
108. Smith, D.A., Morgan, E.H., Bradt, H.: Rossi X-ray timing explorer discovery of coherent millisecond pulsations during an X-ray burst from KS 1731-260. *Astrophys. J.* **479**, L137–L140 (1997). <https://doi.org/10.1086/310604>
109. Spitkovsky, A., Levin, Y., Ushomirsky, G.: Propagation of thermonuclear flames on rapidly rotating neutron stars: extreme weather during type I X-ray bursts. *Astrophys. J.* **566**, 1018–1038 (2002). <https://doi.org/10.1086/338040>
110. Strohmayer, T.E.: Oscillations during thermonuclear x-ray bursts. *Adv. Space Res.* **28**, 511–522 (2001). [https://doi.org/10.1016/S0273-1177\(01\)00422-7](https://doi.org/10.1016/S0273-1177(01)00422-7)
111. Strohmayer, T.E., Bildsten, L.: New views of thermonuclear bursts. In: Lewin, W.H.G., van der Klis, M. (eds.) *Compact Stellar X-ray Sources*, vol. 39, pp. 113–156. Cambridge University Press, Cambridge (2006)
112. Strohmayer, T.E., Markwardt, C.B.: On the frequency evolution of X-ray brightness oscillations during thermonuclear X-ray bursts: evidence of coherent oscillations. *Astrophys. J.* **516**, L81–L85 (1999). <https://doi.org/10.1086/312009>
113. Strohmayer, T.E., Markwardt, C.B.: Evidence for a millisecond pulsar in 4U 1636-53 during a superburst. *Astrophys. J.* **577**, 337–345 (2002). <https://doi.org/10.1086/342152>
114. Strohmayer, T.E., Markwardt, C.B.: EXO 1745-248 is an 11 Hz eclipsing pulsar. *Astronomer's Telegram* **2929**, 1 (2010)
115. Strohmayer, T.E., Zhang, W., Swank, J.H., Smale, A., Titarchuk, L., Day, C., Lee, U.: Millisecond X-ray variability from an accreting neutron star system. *Astrophys. J.* **469**, L9 (1996). <https://doi.org/10.1086/310261>
116. Strohmayer, T.E., Jahoda, K., Giles, A.B., Lee, U.: Millisecond pulsations from a low-mass X-ray binary in the galactic center region. *Astrophys. J.* **486**, 355–362 (1997). <https://doi.org/10.1086/304522>
117. Strohmayer, T.E., Zhang, W., Swank, J.H.: 363 HZ oscillations during the rising phase of bursts from 4U 1728-34: evidence for rotational modulation. *Astrophys. J.* **487**, L77–L80 (1997). <https://doi.org/10.1086/310880>
118. Strohmayer, T.E., Zhang, W., Swank, J.H., Lapidus, I.: The long-term stability of oscillations during thermonuclear X-ray bursts: constraining the binary X-ray mass function. *Astrophys. J.* **503**, L147–L150 (1998). <https://doi.org/10.1086/311545>
119. Strohmayer, T.E., Zhang, W., Swank, J.H., White, N.E., Lapidus, I.: On the amplitude of burst oscillations in 4U 1636-54: evidence for nuclear-powered pulsars. *Astrophys. J.* **498**, L135–L139 (1998). <https://doi.org/10.1086/311322>
120. Strohmayer, T.E., Swank, J.H., Zhang, W.: The periods discovered by RXTE in thermonuclear flash bursts. *Nucl. Phys. B, Proc. Suppl.* **69**, 129–134 (1999). [https://doi.org/10.1016/S0920-5632\(98\)00195-9](https://doi.org/10.1016/S0920-5632(98)00195-9)
121. Strohmayer, T.E., Markwardt, C.B., Swank, J.H., in't Zand, J.: X-ray bursts from the accreting millisecond pulsar XTE J1814-338. *Astrophys. J.* **596**, L67–L70 (2003). <https://doi.org/10.1086/379158>
122. Strohmayer, T.E., Markwardt, C.B., Kuulkers, E.: Discovery of the spin frequency of 4U 0614+09 with the swift burst alert telescope. *Astrophys. J.* **672**, L37 (2008). <https://doi.org/10.1086/526546>
123. Swank, J.H., Becker, R.H., Boldt, E.A., Holt, S.S., Pravdo, S.H., Serlemitsos, P.J.: Spectral evolution of a long X-ray burst. *Astrophys. J.* **212**, L73–L76 (1977). <https://doi.org/10.1086/182378>
124. Taam, R.E., Picklum, R.E.: Nuclear fusion and carbon flashes on neutron stars. *Astrophys. J.* **224**, 210–216 (1978). <https://doi.org/10.1086/156367>

125. Taam, R.E., Woosley, S.E., Lamb, D.Q.: The effect of deep hydrogen burning in the accreted envelope of a neutron star on the properties of X-ray bursts. *Astrophys. J.* **459**, 271–277 (1996). <https://doi.org/10.1086/176890>
126. Thompson, T.W.J., Rothschild, R.E., Tomsick, J.A., Marshall, H.L.: Chandra and RXTE spectra of the burster GS 1826-238. *Astrophys. J.* **634**, 1261–1271 (2005). <https://doi.org/10.1086/497104>
127. van der Klis, M.: Rapid X-ray variability. In: Lewin, W.H.G., van der Klis, M. (eds.) *Compact stellar X-ray sources*, vol. 39, pp. 39–112. Cambridge University Press, Cambridge (2006)
128. van Straaten, S., van der Klis, M., Kuulkers, E., Méndez, M.: An atlas of burst oscillations and spectral properties in 4U 1728-34. *Astrophys. J.* **551**, 907–920 (2001). <https://doi.org/10.1086/320234>
129. Villarreal, A.R., Strohmayer, T.E.: Discovery of the neutron star spin frequency in EXO 0748–676. *Astrophys. J.* **614**, L121–L124 (2004). <https://doi.org/10.1086/425737>
130. Watts, A.L.: Thermonuclear burst oscillations. *Annu. Rev. Astron. Astrophys.* **50**, 609–640 (2012). <https://doi.org/10.1146/annurev-astro-040312-132617>
131. Watts, A.L., Strohmayer, T.E., Markwardt, C.B.: Analysis of variability in the burst oscillations of the accreting millisecond pulsar XTE J1814-338. *Astrophys. J.* **634**, 547–564 (2005). <https://doi.org/10.1086/496953>
132. Watts, A.L., Strohmayer, T.E.: The energy dependence of burst oscillations from the accreting millisecond pulsar XTE J1814-338. *Mon. Not. R. Astron. Soc.* **373**, 769–780 (2006). <https://doi.org/10.1111/j.1365-2966.2006.11072.x>
133. Watts, A.L., Patruno, A., van der Klis, M.: Coherence of burst oscillations and accretion-powered pulsations in the accreting millisecond pulsar XTE J1814-338. *Astrophys. J.* **688**, L37–L40 (2008). <https://doi.org/10.1086/594365>
134. Watts, A.L., Altamirano, D., Linares, M., Patruno, A., Casella, P., Cavecchi, Y., Degenaar, N., Rea, N., Soleri, P., van der Klis, M., Wijnands, R.: Discovery of burst oscillations in the intermittent accretion-powered millisecond pulsar HETE J1900.1-2455. *Astrophys. J.* **698**, L174–L177 (2009). <https://doi.org/10.1088/0004-637X/698/2/L174>
135. Weinberg, N.N., Bildsten, L., Schatz, H.: Exposing the nuclear burning ashes of radius expansion type I X-ray bursts. *Astrophys. J.* **639**, 1018–1032 (2006). <https://doi.org/10.1086/499426>
136. Wijnands, R., Strohmayer, T., Franco, L.M.: Discovery of nearly coherent oscillations with a frequency of 567 Hz during type I X-ray bursts of the X-ray transient and eclipsing binary X1658-298. *Astrophys. J.* **549**, L71–L75 (2001). <https://doi.org/10.1086/319128>
137. Woosley, S.E., Taam, R.E.: Gamma-ray bursts from thermonuclear explosions on neutron stars. *Nature* **263**, 101–103 (1976). <https://doi.org/10.1038/263101a>
138. Woosley, S.E., Heger, A., Cumming, A., Hoffman, R.D., Pruet, J., Rauscher, T., Fisker, J.L., Schatz, H., Wiescher, B.A.B.M.: Models for type I X-ray bursts with improved nuclear physics. *Astrophys. J. Suppl. Ser.* **151**, 75–102 (2004). <https://doi.org/10.1086/381533>
139. Worper, H., Galloway, D.K., Price, D.J.: Evidence for accretion rate change during type I X-ray bursts. *Astrophys. J.* **772**, 94 (2013). <https://doi.org/10.1088/0004-637X/772/2/94>
140. Zhang, W., Jahoda, K., Kelley, R.L., Strohmayer, T.E., Swank, J.H., Zhang, S.N.: Millisecond oscillations in the persistent and bursting flux of aquila X-1 during an Outburst. *Astrophys. J.* **495**, L9–L12 (1998). <https://doi.org/10.1086/311210>
141. Zhang, G., Méndez, M., Belloni, T., Homan, J.: Coherent oscillations and the evolution of the apparent emission area in the decaying phase of radius-expansion bursts from 4U 1636-53. *Mon. Not. R. Astron. Soc.* **436**, 2276–2285 (2013). <https://doi.org/10.1093/mnras/stt1728>
142. Zhang, G., Méndez, M., Zamfir, M., Cumming, A.: The link between coherent burst oscillations, burst spectral evolution and accretion state in 4U 1728-34. *Mon. Not. R. Astron. Soc.* **455**, 2004–2017 (2016). <https://doi.org/10.1093/mnras/stv2482>
143. Zingale, M., Timmes, F.X., Fryxell, B., Lamb, D.Q., Olson, K., Calder, A.C., Dursi, L.J., Ricker, P., Rosner, R., MacNeice, P., Tufo, H.M.: Helium detonations on neutron stars. *Astrophys. J. Suppl. Ser.* **133**, 195–220 (2001). <https://doi.org/10.1086/319182>

Chapter 6

Transitional Millisecond Pulsars



Alessandro Papitto and Domitilla de Martino

Abstract Millisecond pulsars in tight binaries have recently challenged our understanding of physical processes governing the evolution of binaries and the interaction between astrophysical plasma and electromagnetic fields. Transitional systems that showed changes from rotation-powered to accretion-powered states and vice versa have bridged the populations of radio and accreting millisecond pulsars, eventually demonstrating the tight evolutionary link envisaged by the recycling scenario. A decade of discoveries and theoretical efforts have just grasped the complex phenomenology of transitional millisecond pulsars from the radio to the gamma-ray bands. This chapter summarizes the main properties of the three transitional millisecond pulsars discovered so far, as well as of candidates and related systems, discussing the various models proposed to cope with their multifaceted behaviour.

6.1 Introduction

The observation of dramatic changes of state taking place over a few weeks is what defines *transitional* millisecond pulsars (tMSP). These transitions involve a rotation-powered regime, in which the (radio) pulsar wind prevents the infall of the matter lost by the low-mass companion (see Chaps. 1–3), and an accretion regime in which these systems emit intense high-energy radiation like X-ray binaries (see Chap. 4). During the transitions the luminosity changes by at least an order of magnitude, likely due to variations in the mass inflow rate. The discovery of tMSPs has been a key achievement in the investigation of the evolution of MSPs. The recycling scenario developed in the early 1980s had postulated that radio MSPs were spun up

A. Papitto (✉)

INAF–Osservatorio Astronomico di Roma, Monte Porzio Catone (Roma), Italy
e-mail: alessandro.papitto@inaf.it

D. de Martino

INAF–Osservatorio Astronomico di Capodimonte, Napoli, Italy
e-mail: domitilla.demartino@inaf.it

in a previous Gyr-long phase of mass accretion ([4, 21, 24, 78, 144]; see Sect. 4.1). It implied that these fast-spinning neutron stars (NSs) were descendants of low-mass (donor mass $< 1 M_{\odot}$) X-ray binaries (LMXBs). The discovery of radio MSPs in globular clusters [119] and of accreting MSPs (AMXPs) in a handful of X-ray transients [204] underpinned this theory. Eventually, in 2009 a radio MSP binary was recognised to have been previously surrounded by an accretion disc [11]. A few years later, the same binary and two more systems were surprisingly found to switch back and forth accretion and rotation-powered regimes over much shorter timescales than the secular recycling binary evolution [19, 130, 173]. Whether these MSPs represent an intermediate evolutionary stage before they end as radio pulsars that completely devour their companions, or rather experience a distinct evolutionary path, has still to be assessed (see Chap. 7). Certainly, they have provided us with a unique occasion to observe the different possible outcomes of the interaction between a quickly spinning magnetized NS and the plasma lost by a companion star as they unfold over timescales accessible to the human life.

TMSPs bridge a few classes of MSPs (see Sect. 6.2). The interplay between the gravitational pull exerted by the NS on the mass lost by the companion and the outward pressure of the pulsar wind determines whether an MSP behaves either as a rotation or as an accretion-powered source (see Sect. 6.3). As of December 2021, we currently know three transitional MSPs (see Sect. 6.4). They have shown radio pulsar states (Sect. 6.5.1), a bright accretion outburst in one of them (Sect. 6.5.2), but also an enigmatic X-ray *sub-luminous* disc state, which gave us a brand new view of how LMXBs may behave at low mass accretion rates (Sect. 6.5.3). The properties of tMSPs during such an X-ray faint accretion state are so peculiar are so peculiar that they are key signatures to identify candidates that will likely perform a transition in the future (Sect. 6.5.4). Like in many cases, the discovery of tMSPs raised far more questions than it answered. What makes a system transitional? Are all MSPs in binaries with an orbital period shorter than a day transitional? How does the pulsar magnetic field interact with the inflowing gas? Are the rotation and accretion powered regimes mutually exclusive, or do we rather see them mixed in the sub-luminous state? In Sect. 6.6 we discuss current models attempting to explain the enigmatic behaviour of these MSPs.

6.2 The Population of Millisecond Pulsar Binaries

As of December 2021, we know 21 accreting and 622 rotation-powered MSPs, here defined by a spin period < 30 ms. Figure 6.1 shows the observed binary characteristics.

AMXPs (see Chap. 4) are all found in X-ray transients, which undergo occasional outbursts reaching an X-ray luminosity up to $\sim 10^{36}\text{--}10^{38}$ erg s $^{-1}$, interleaved by long periods of quiescence ($L_X \sim 10^{31}\text{--}10^{32}$ erg s $^{-1}$). They are harboured in tight ($P_{orb} < 1$ day) binary systems (see orange symbols in Fig. 6.1), and half of them

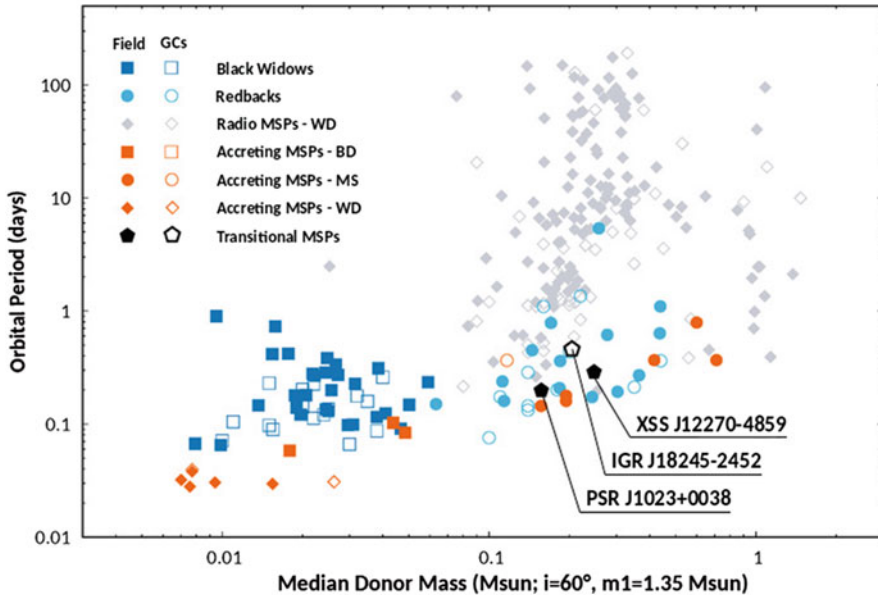


Fig. 6.1 Orbital period and median mass (evaluated from the pulsar timing parameters assuming an inclination of 60° and an NS mass of $1.35 M_{\odot}$) of black widows (blue squares), redbacks (cyan circles), non-interacting radio MSPs with a white dwarf companion (grey diamonds), AMXPs (orange symbols with shape depending on the donor type, squares for brown dwarfs, circles for main-sequence stars and diamonds for white dwarfs) and tMSPs (black pentagons). Filled and hollow symbols mark sources found in the Galactic field and globular clusters, respectively

showed thermonuclear type-I bursts. Only IGR J18245-2452 has been also detected as a radio pulsar in quiescence, so far.

Rotation-powered radio MSPs (see Chap. 1) are much more numerous. They amount to about 413 in the Galactic field¹ and 209 in 36 globular clusters.² Here, we mainly address the ~ 100 MSPs in compact binaries ($P_{orb} < 1$ day), most of which show irregular radio eclipses due to the presence of intrabinary material. Dubbed “spiders” [84, 149, 176], these binaries include “black widows” with very low-mass companions (defined by $< 0.06 M_{\odot}$) and “redbacks” with a hydrogen-rich secondary with a minimum mass of at least $\approx 0.1 M_{\odot}$ (see Fig. 6.1, Sects. 1.4.3 and 3.6). When rotation powered, the three known tMSPs are redbacks. Searches of yet unidentified *Fermi* gamma-ray sources (see [161, 176] and Sect. 2.4) with suitable spectral parameters have turned out to be the main technique to discover these otherwise elusive eclipsing radio MSPs.

¹ See the list maintained by D. Lorimer & E. Ferrara, available at <http://astro.phys.wvu.edu/GalacticMSPs/GalacticMSPs.txt>.

² See the list maintained P. Freire, available at <http://www.naic.edu/~pfreire/GCpsr.html>.

6.3 Changes of State in Millisecond Pulsars

The multifaceted behaviour of MSPs in tight binaries stems from the balance between the outward pressure exerted by the pulsar wind on the mass lost by the companion star, and the inward gravitational pull applied by the NS gravitational field. Given the typical MSP spin-down power ($L_{sd} \simeq \text{a few} \times 10^{34} \text{ erg s}^{-1}$) and mass transfer rates ($\dot{M} \approx 10^{-3}\text{--}10^{-4} \dot{M}_{Edd}$), this balance enforces within the binary, if the system has a short orbital period ($P_{orb} < 1$ day) and a small size ($d \lesssim 10^{11} \text{ cm}$). On one hand, this means that the pulsar wind is terminated by the inflowing matter in an intrabinary shock. On the other, slight variations in the mass inflow rate may lead to very different outcomes, which in the case of tMSPs occur in quick succession.

In the recycling framework, it was assumed that the accretion and the rotation-powered phases were well distinct. A source was to be found in either one of the states depending on the prevailing of the gravitational or electromagnetic pressure [118, 167]. Figure 6.2 shows the radial dependence of these pressures and the three main possible outcomes. The ram pressure of plasma in radial free-fall is [61]:

$$P_{grav} = \frac{(2GM_*)^{1/2}\dot{M}}{4\pi r^{5/2}}, \quad (6.1)$$

where M_* is the NS mass. In the accretion phase, the high-density plasma fills the light cylinder of the pulsar³ and this was assumed to switch off the rotation-powered pulsar [168]. Some of the closed field lines forming the magnetosphere thread the disc albeit the very high diffusivity of the plasma, and are bent by the differential rotation of the disc material in Keplerian rotation. The disc is truncated at the accretion radius R_{acc} , where the resulting magnetic stress becomes dominant compared to the disc viscous stress (see also the discussion in Sect. 4.1). The determination of this radius is crucial to predict the accretion regime onto a magnetized rotator at different accretion rates. It strongly depends on the often unknown microphysics governing the disc/field interaction and is still a matter of debate (see, e.g., [36, 37]). Under the assumption that the magnetic field lines thread the disc over a large radial extent [83, 199], it turns out that the accretion radius R_{acc} is approximately equal to a fraction ξ of the Alfvén radius R_A , obtained by equating the gravitational energy density (see Eq. 6.1) with the largest possible magnetic stress:

$$P_{em}(r) = \frac{\mu^2}{8\pi r^6}; \quad r < R_{LC} \quad (6.2)$$

³ The light cylinder of a pulsar is defined as the cylinder aligned with spin axis, with a radius $R_{LC} = c/2\pi\nu = c/2\pi v \simeq 80 v_{600} \text{ km}$ (v_{600} is the spin frequency in units of 600 Hz), where the co-rotating speed of the field lines equals the speed of light. Field lines that would close beyond the light cylinder are forced to open by the causality principle, thus producing the pulsar wind.

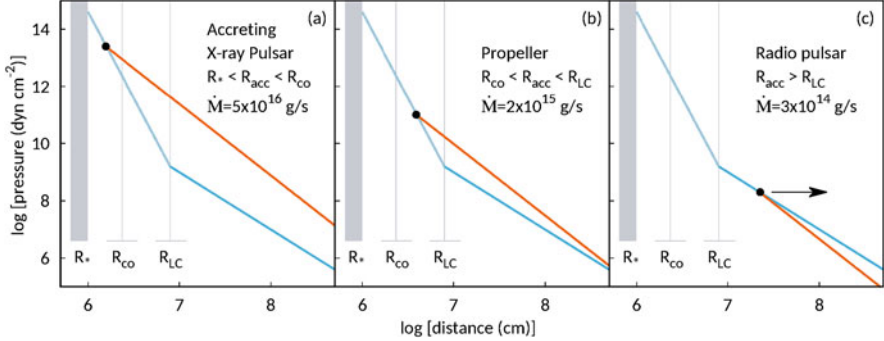


Fig. 6.2 Dependence of the pressure exerted by the in-flowing plasma (orange lines, Eq. 6.1) and by the electromagnetic field (cyan lines, Eqs. 6.2 and 6.5) on the distance from a pulsar with a magnetic dipole moment of 10^{26} G cm^3 (corresponding to a field strength at the magnetic poles of $5 \times 10^7 \text{ G}$). Grey vertical lines mark the NS radius (R_*), the corotation radius (R_{co}) and the light cylinder radius (R_{LC}) for a pulsar spinning at 600 Hz (corresponding to $\simeq 1.67 \text{ ms}$). The three panels represent the possible states depending on the value of the mass accretion rate considered, accreting X-ray pulsar ($R_* < R_{acc} < R_{co}$), propeller ($R_{co} < R_{acc} < R_{LC}$) and rotation-powered radio pulsar ($R_{acc} > R_{LC}$). The arrow indicates evaporation of the intrabinary matter due to the unstable equilibrium in the latter case

where $\mu = B_* R_*^3 / 2$ is the NS magnetic dipole moment, B_* is the field strength at the magnetic poles of the NS, and R_* is the NS radius. This yields:

$$R_{acc} = \xi R_A = \xi \frac{\mu^{4/7}}{\dot{M}^{2/7} (2GM_*)^{1/7}} \simeq 15.4 \xi 0.5 \mu_{26}^{4/7} \dot{m}_{16}^{-2/7} m_{1.4}^{-1/7} \text{ km}, \quad (6.3)$$

where $\xi 0.5$, μ_{26} , \dot{m}_{16} and $m_{1.4}$ are the respective quantities in units of 0.5, 10^{26} G cm^3 , 10^{16} g s^{-1} and $1.4 M_\odot$. Alternatively, if the diffusivity of the field lines is low, the magnetic field lines are unable to slip through the disc fast enough, and so they twist and open. The interaction region is smaller and the scalings of the accretion radius are flatter, $R_{acc} \propto \mu^{2/5} M^{-1/5}$ [57, 171]. A series of 3D magnetohydrodynamic simulations of disc accretion onto a magnetized rotating star have indeed given results compatible with such an estimate [111]. However, given the small differences, Eq. 6.3 with $\xi \simeq 0.5$ is still widely used to describe the position of the magnetospheric radius in many astrophysical systems (see, however, [37] for the limitations of the applicability of the magnetospheric radius in Eq. 6.3).

The subsequent fate of the inflowing matter depends on whether it has enough angular momentum to overcome the centrifugal barrier set by the rotating pulsar magnetosphere at the disc truncation radius. The corotation radius defines where the disc material rotates at the NS spin frequency:

$$R_{co} = \left[\frac{GM_*}{(2\pi\nu)^2} \right]^{1/3} \simeq 23.6 m_{1.4}^{1/3} \nu_{600}^{-2/3} \text{ km}. \quad (6.4)$$

The inflowing material either freely accretes onto the NS if $R_{acc} < R_{co}$ (see panel [a] in Fig. 6.2) or bounces on the barrier set by the rotating magnetosphere in the so-called propeller state if $R_{acc} > R_{co}$ [99] (see panel [b] in Fig. 6.2).

As the mass accretion rate decreases, the accretion radius expands. When it approaches the corotation boundary, no net angular momentum can be transferred to the NS by the infalling plasma any more. Nevertheless, the field lines that thread the disc beyond the corotation radius, and possibly eject matter through the propeller effect, might still exert a spin-down torque [83, 145, 199]. This torque is assumed to limit the secular spin-up of an accreting NS in an LMXB to an equilibrium period of a few milliseconds for a weakly magnetized ($\approx 10^8\text{--}10^9$ G) NS. Realizing that the equilibrium period could be so short was actually the main foundation of the recycling scenario [172].

A further decrease of the mass accretion rate may push the accretion radius beyond the light cylinder, at which point a rotation-powered pulsar is assumed to switch on (see panel (c) in Fig. 6.2). Outside the light cylinder, a radiative solution describes the pulsar electromagnetic field and its pressure has a much flatter radial dependence than Eq. 6.2:

$$P_{em}(r) = \frac{L_{sd}}{4\pi r^2 c} \simeq \frac{k\mu^2}{4\pi^2 R_{LC}^4 r^2}; \quad r > R_{LC}. \quad (6.5)$$

Here $L_{sd} \simeq [\mu^2(2\pi\nu)^4/c^3](1 + \sin^2\alpha)$ is the pulsar spin-down power [170], and α is the magnetic colatitude. Since the inflow ram pressure has a steeper dependence on the distance ($P_{grav} \propto r^{-5/2}$, see Eq. 6.1) than P_{em} , the equilibrium for $R_{acc} > R_{LC}$ is expected to be unstable. In this regime the pulsar wind is then expected to expel altogether the intrabinary material from the system, a mechanism dubbed radio-ejection [43]. In the secular picture, the mass transfer is predicted to switch-off as soon as the donor star detaches from its Roche lobe under the effects of the irradiation by the high energy emission of the accreting NS [109, 157, 158]. This possibly occurs through tens of Myr-long cycles of mass accretion and pulsar radio-ejection, caused by the complex reaction of the donor radius and mass transfer rate to wind irradiation from the NS (see Sect. 7.6).

The idea that binary systems could perform state transitions between accretion and rotation-powered states on a shorter timescale of months/years emerged when many LMXBs hosting NSs were found to undergo transient outbursts (see, e.g., [202]). At the end of an outburst, the pulsar wind was expected to push the accretion disc beyond the light cylinder (i.e., case (c) of Fig. 6.2). This would allow the turn-on of a rotation-powered radio pulsar during the quiescent period of the transient [46, 174]. The radiation and the wind of relativistic particle so generated would eject the matter lost by the companion as soon as it entered the pulsar Roche lobe [43]. Only an increase of the inward pressure of the transferred matter would allow the X-ray binary to enter in a new accretion outburst. For many years, only circumstantial evidence supported this idea. A few eclipsing MSP binaries were found to expel material transferred from their companions [56] according to a radio

ejection scenario [41], but no transition to an accretion state was observed. On the other hand, accreting MSPs in quiescence gave indirect indications that a radio pulsar switched on, but a detection could not be achieved (see Sect. 6.5.2). The discovery of tMSPs has eventually filled the gap.

6.4 Transitional Millisecond Pulsars

6.4.1 PSR J1023+0038—FIRST J102347.6-003841

FIRST J102347.6–003841 was first detected in May 2000 as a variable 1.4 GHz radio source [35]. Double peaked emission lines of the Balmer series, He I and He II in the spectrum and the flickering light curve of its optical counterpart suggested it was a disc accreting binary, possibly a peculiar magnetized white dwarf [35, 181, 200]. In early 2002, the source underwent a dramatic change. An almost sinusoidal smooth modulation at the 4.75 h orbital period due to heating of the secondary appeared in the optical light curve [205]. Also, emission lines were replaced by a G-type star absorption spectrum [187, 200] indicating the disappearance of the accretion disc. Thorstensen et al. [187] first proposed that the binary hosted a quiescent NS, based on the large irradiating luminosity required to explain the optical light curve. The discovery of the 1.67 ms radio pulsar PSR J1023+0038 by the *Robert C. Byrd Green Bank Telescope* in 2007 eventually nailed down this enigmatic object as a redback radio MSP, which had an accretion disc in the previous decade [11]. Archival optical and infrared observations constrained the duration of the 2000/2001 disc episode to \sim 1.5–2 years [35, 181, 198, 205]. Since the end of June 2013, the re-emergence of double-peaked optical emission lines [87], the disappearance of radio pulsations [173], and the brightening of the X-ray, ultraviolet [139] and gamma-ray [173] emissions marked the beginning of a new active phase which is currently ongoing as of December 2021. The average X-ray luminosity in the disc state never exceeded $L_X \approx 5 \times 10^{33}$ erg s $^{-1}$ (at a parallax distance of 1.37 kpc, [71]), indicating that both the 2000/2001 and the 2013/current accretion episodes have been *sub-luminous* (see Sect. 6.5.3).

6.4.2 IGR J18245-2452—PSR J1824-2452I

The transient X-ray source IGR J18245–2452 in the globular cluster M28 was first detected by *INTEGRAL* in March 2013 during a bright accretion outburst ([75], $L_X \approx 10^{36}$ erg s $^{-1}$ at a distance of 5.5 kpc). The *XMM-Newton* detection of 3.9 ms X-ray pulsations identified it as an accreting MSP with a main sequence companion [130]. Cross-referencing with pulsar catalogues, it was realized that the source had been already observed as a radio MSP before (PSR J1824-2452I; [20]), making it the

first source both as a rotation-powered and as an AMXP [130]. Radio pulses were again observed after the end of the month-long X-ray outburst in 2013—two weeks since the last detection of the X-ray pulsar. Serendipitous *Chandra* [117, 130] and *Hubble Space Telescope* observations [129] revealed two more accretion episodes in 2008 and 2009, respectively, which unlike the 2013 outburst, had properties compatible with a *sub-luminous* disc state.

6.4.3 XSS J12270–4859—PSR J1227–4853

XSS J12270–4859 resembles very closely PSR J1023+0038 under many respects (see Table 6.1). First detected as a hard X-ray source [163], it was tentatively identified as a cataclysmic variable based on the emission lines of its optical spectrum [121] and for large amplitude (~ 1 mag) optical flickering [143]. The spatial coincidence of XSS J12270–4859 with a *Fermi*-LAT source suggested an atypical low-luminosity ($L_X \simeq L_\gamma \simeq \text{few} \times 10^{33} \text{ erg s}^{-1}$) X-ray binary [63, 65]. Its unusual properties were only later assessed to be typical of the *sub-luminous* state of tMSPs ([63–65, 95, 159], see Sect. 6.5). The disappearance of the emission lines in the optical spectrum and the 10-fold dimming observed in the radio, optical and X-ray bands (and to a lesser extent in gamma-rays [190]), demonstrated that XSS J12270–4859 had transitioned from a disc to a radio pulsar state between 2012 November 14 and December 21 [19]. *Giant Metrewave Radio Telescope* observations later detected 1.69 ms radio pulsations eclipsed for a large fraction of the orbit [156]. Since the end of 2012, XSS J12270–4859 still behaves as a rotation-powered redback pulsar.

6.5 The Three States of Transitional Millisecond Pulsars

6.5.1 The Rotation-Powered State

In the rotation-powered state, the known tMSPs behave as redbacks. They are relatively faint objects at all wavelengths, and most of the information we have gathered comes from the study of the closest ones, PSR J1023+0038 and PSR J1227–4853 (see Table 6.1).

Mass Ejection Irregular eclipses of the radio pulses occur mostly (but not only) when the secondary is at the inferior conjunction of the orbit. They are due to a thin, but dense layer of ionized material which the pulsar wind drives off from the surface of the donor or the inner Lagrangian point, and partly enshrouds the system. The eclipses of PSR J1023+0038 lasted up to $\sim 60\%$ of the orbit when observed at 350 MHz, but were shorter at higher frequencies ($\sim 25\%$ at 1.4 GHz), and nearly absent at ~ 3 GHz [10, 11]. Similarly behaved PSR J1227–4853, showing

Table 6.1 Main observed properties of tMSPs

	PSR J1023+0038	XSS J1227-4859	IGR J18245-2452	Ref.
P_{orb} (h)	4.75	6.91	11.03	[19, 130, 187]
P_{spin} (ms)	1.69	1.69	3.93	[11, 130, 156]
\dot{P} (10^{-20}) ^a	0.539 (RMSP)	1.086	<0.0013	[10, 100, 130, 156]
	0.713 (LMXB)			[10, 100, 130, 156]
$a \sin i$ (lt-s)	0.343	0.668	0.766	[11, 100, 130]
\dot{E} (10^{34} erg/s) ^b	4.43(4)	$8.9^{+0.2}_{-0.9}$	–	[10, 67]
M_{NS} (M_{\odot})	1.7(2)	–	–	[166]
B_{NS} (10^8 G)	1.9	2.3	0.7-35	[10, 130, 156]
i (deg)	46(2)	46–55	–	[64, 148, 166, 176]
d (kpc)	1.37(4)	$1.4^{+0.7}_{-0.2}$	5.5	[67, 71, 130]
Comp. spectral type	G5–F6	G5–F5	Low main seq.	[64, 129, 187]
Comp. mass (M_{\odot})	0.22(3)	0.15–0.36	0.17 ^c	[66, 130, 166]
X-ray properties ^d	$F_E \sim E^{-\Gamma}$			
<i>Disc state</i>				
$\Gamma_{X,disc}$	1.62(2)	1.70(2)	1.428(3)	
$L_{X,ave}$ (10^{33} erg/s)	5.2(1)	12(2)	11.2(5)	
$L_{X,low}$ (10^{33} erg/s)	0.87(4)	2.0(4)	2.0(3)	
$L_{X,high}$ (10^{33} erg/s)	7.9(1)	13(3)	13.1(6)	
$L_{X,flare}$ (10^{33} erg/s)	22(6)	70(8)	33	
<i>Rotation-powered state</i>				
$\Gamma_{X,rot}$	1.17(9)	1.2(1)	2.5 assumed	
$L_{X,rot}$ (10^{33} erg/s)	0.8(4)	$0.83^{+0.42}_{-0.9}$	<1	
<i>Gamma-ray properties</i> ^e $F_E \sim E^{-\Gamma}$				
<i>Disc state</i>				
$\Gamma_{\gamma,disc}$	2.41(2)(3)	2.36(6)(9)	–	
$L_{\gamma,disc}$ (10^{33} erg/s)	12.5(4)	21.9(7)	–	
<i>Rotation-powered state</i>				
$\Gamma_{\gamma,rot}$	2.31(3)(4)	2.42(3)(15)	–	
$L_{\gamma,rot}$ (10^{33} erg/s)	1.1(2)	8.6(8)	–	
<i>Radio properties</i> ^f $S_{\nu} \sim \nu^{\alpha}$				
<i>Disc state</i>				
$\alpha_{r,disc}$	-0.1(2)–0.2(2)	-0.1(0.1)	-0.2–0.8	
$L_{r,disc,ave}$ (10^{27} erg/s)	0.97	2.4(8)	123	

(continued)

Table 6.1 (continued)

	PSR J1023+0038	XSS J1227-4859	IGR J18245-2452	Ref.
$L_{r,disc,high}$ (10^{27} erg/s)	0.63	–	–	
$L_{r,disc,low}$ (10^{27} erg/s)	1.9	–	244	
<i>Rotation-powered state</i>				
$\alpha_{r,rot}$	2.8	–	–	
S_{v_0} (mJy) [v_0 (GHz)]	14 [1.6]	6.6 [0.607]	0.02 [2.0]	

^a Spin down rates in both RMSP and LMXB state determined only for PSR J1023+0038, taking into account also the Shklovskii effect and acceleration in the Galactic potential

^b Spin down luminosity assuming the canonical value for the moment of inertia 10^{45} g cm². The NS moment of inertia has been found to range from $1\text{--}4 \times 10^{45}$ g cm² by detailed general relativistic numerical computations using a sample of MSPs with precise NS masses and for several realistic NS EoS models [23]

^c Minimum mass

^d X-ray luminosity in the 0.3–79 keV range from [54]

^e Gamma-ray luminosity in the 0.1–300 GeV using fluxes from [190] and the reported distances at face value

^f Radio luminosity at 5 GHz using distances reported at face value and fluxes from [80, 130] for IGR J1824-2452, from [10, 11, 28, 54, 135, 147] for PSR J1023+0038, from [19, 156] for PSR J1227-4853

eclipses for \sim 40% of the orbit at 607 MHz and \sim 30% at 1.4 GHz [67, 156]. This behaviour can be ascribed to the frequency dependence of the optical depth of the material (e.g., $\propto v^{-2}$ for electron scattering, $\propto v^{-1}$ for cyclotron absorption [186]) which makes the ionized layer more transparent at high frequencies. The correlated variation of the continuum flux density and the mean pulsed flux density at the eclipse boundary observed from PSR J1227–4853 suggested cyclotron-synchrotron absorption rather than dispersion smearing or scattering [156]. Similar conclusions were also drawn for other spiders [40]. Shorter losses of the signal at random orbital phases and substantial variations of the dispersion measure were also observed. All these properties indicate that the enshrouding ionized plasma extends well beyond the Roche lobe of the donor.

The Binary Properties The radio pulsar timing indicated that the orbits of tMSPs and of many spiders are almost circular, with upper limits of the order of a few times 10^{-5} on the eccentricity. This is due to the tidal circularization which occurred during the secular LMXB phase. Irregular changes in the phase of the orbital modulation by a few seconds over timescales of a few months suggested fast apparent orbital period variations [10, 100]. They have been interpreted as a combination of the angular momentum carried by material ejected from the system, and the exchange of angular momentum between the orbit and the companion star due to changes of the mass quadrupole in the latter [7]. Magnetic cycles of the secondary could be the cause for such fluctuations, even though luminosity variations larger than observed would be expected. Recently, a model has been proposed to account for the timing anomalies produced by mass quadrupole

deformations in spiders, which is promising to gain insights on the internal structure of their irradiated stars [195].

The optical spectra of PSR J1023+0038 and PSR J1227–4853 displayed absorption features typical of the photosphere of mid G-type stars, primarily metallic and Balmer lines [64, 123, 166, 187]. No spectroscopy has been acquired for the faint counterpart of PSR J1824–2452I, so far. However, photometric observations located it in a position of the colour-magnitude diagram of the globular cluster consistent with a main-sequence star, just 0.5–1 mag below the turn-off point [129]. The lack of an optical and near-infrared polarization in PSR J1227–4853 suggested that the emission in these bands was only due to the donor photosphere [13]. However, near-ultraviolet photometry of both PSR J1023+0038 and PSR J1227–4853 revealed an excess over the companion emission [148]. This suggests that the emission of the intrabinary shock, which dominates at higher energies (see below), may also extend to the ultraviolet domain.

The optical light curves of these two tMSPs featured an almost sinusoidal modulation at the binary orbital period with an amplitude of $\approx 0.4\text{--}0.7$ mag. The emission attains a maximum and becomes bluer when the companion star is at the superior conjunction ([66, 148, 187, 205]; see the right panel of Fig. 6.3). These signatures are due to the irradiation of the donor by the high-energy emission of the pulsar and were also observed in many spiders many spiders [38, 152]. A dramatic change in the spectral type (see Table 6.1) between the inferior and the superior conjunction confirmed the heating of the donor [64, 166]. The light curves significantly departed from an symmetric shape around the flux maximum, suggesting that the heating source is asymmetric [177]. A significant contribution to the donor irradiation by an asymmetric intrabinary shock, and/or dynamics of the

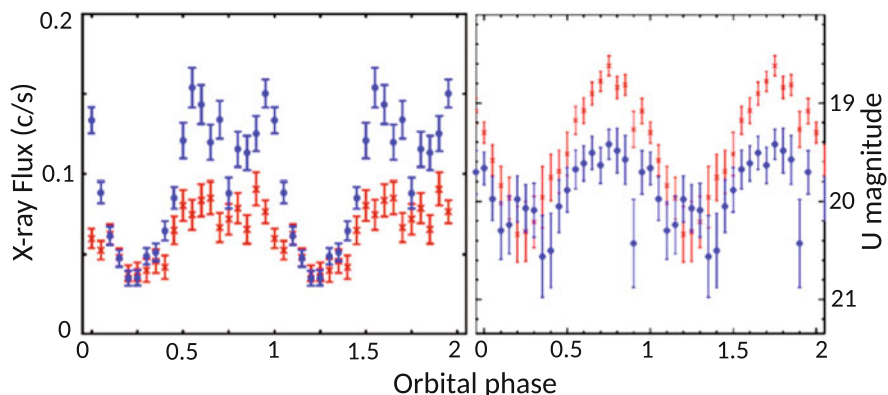


Fig. 6.3 X-ray (left panel) and optical (right panel) orbital modulation observed from PSR J1227–4853 on 2013, Dec 29 (red points) and 2014, Jun 27 (blue points). Phase 0 corresponds to the passage of the NS at the orbit ascending node. Credit: de Martino et al., MNRAS, 454, 2190 (2015), reproduced with permission of Oxford University Press on behalf of the Royal Astronomical Society

strongly heated donor surface were proposed as possible interpretations. Variations in the amplitude of the orbital modulation from epoch to epoch also suggested changes in the heating pattern [66, 166]. In both systems the irradiation persisted also during the disc state [26, 52, 64, 108, 134] with a different heating pattern likely due to disc shadowing of the donor star [166].

Modelling of the multi-colour optical orbital modulation and of the spectroscopic absorption line radial velocity is a technique commonly used to infer the component masses, the Roche lobe filling factor of the companion, and the binary inclination. It is especially powerful when coupled with the NS orbital ephemeris derived from the radio pulsar timing. However, for heated low-mass donors a degeneracy exists between the filling factor and the binary inclination, thus affecting the masses of the components [176]. The two tMSPs in the Galactic field are seen at moderate inclinations [66, 187] (see Table 6.1). While in PSR J1023+0038 the masses of both stars could be determined, for PSR J1227-4853 only the donor mass could be constrained. Modelling of the observed light curves and line radial velocity profiles suggested that the donor were slightly ($\simeq 80\text{--}95\%$) underfilling their Roche lobes [123, 166, 177].

The X-ray Properties and the Intrabinary Shock The X-ray luminosity of PSR J1023+0038 [9, 27, 96, 114, 185], PSR J1227-4853 [31, 66, 67] and PSR M28I [32, 117, 130] in the radio-pulsar state ($L_X \approx 1\text{--}2 \times 10^{32}$ erg s $^{-1}$, i.e. $\sim 0.1\text{--}0.2\%$ of the spin-down power) is at the bright end of the distribution observed in other redbacks ([116], see the bottom panel of Fig. 6.7). The X-ray spectra of tMSPs were largely non-thermal and described by a power law extending without a break up to ~ 70 keV (see Table 6.1). A soft thermal component possibly emitted by hot spots on the NS surface contributed at most to a few per cent of the 0.1–10 keV emission of PSR J1023+0038, while it was not significantly detected in PSR J1227-4853.

A large amplitude ($\gtrsim 25\%$) orbital variability characterized the X-ray emission of tMSPs (see the left panel of Fig. 6.3), similar to other redbacks ([150]; see also the discussion in Sect. 3.6). The maximum occurs when the companion is at the superior conjunction, in phase with the radio eclipses and the maximum of the optical emission. Only a slight spectral variability along the orbit has been seen, e.g. a hardening below 3 keV at the inferior conjunction of XSS J12270-4859, and a decrease in the amplitude above 25 keV ([67], Coti Zelati et al., in prep.). This excluded photoelectric absorption to explain the large orbital variability. The observed emission was better modelled with a synchrotron emission from the intrabinary shock created by the interaction of the pulsar wind with the material issued from the inner Lagrangian point, or directly at the donor surface ([12, 27], see Sect. 6.6.1). The occultation of the shock by the secondary star when it is at the inferior conjunction of the orbit determines the minimum of the X-ray emission. The orbital modulation was almost sinusoidal in PSR J1023+0038 with an enhanced emission at eclipse egress [9, 27]. In PSR J1227-4853, instead, the orbital light curve showed a quasi-sinusoidal shape at one epoch but double-peaked when observed 6 months apart. Concurrently, the amplitude of the X-ray modulation varied from 25% to 70% in anti-correlation with a similar change in

the amplitude of the optical modulation ([66], see Fig. 6.3). Double peaked orbital modulations were also observed from other redbacks such as PSR J2129-0429 [2] and PSR J2339-0533 [104], which also displayed subtle spectral changes along their orbits. The synchrotron emission is expected to be Doppler boosted at the pulsar inferior conjunction and de-boosted at superior conjunction, possibly explaining these features, at least partly ([12, 74], see also Sect. 6.6.1).

X-ray pulsations with a sinusoidal shape and a root-mean-square (rms) amplitude of $(11 \pm 2)\%$ were detected below 2.5 keV from PSR J1023+0038 [9]. The pulsed luminosity was a few $\times 10^{-4}$ times the spin-down power, similar to other rotation-powered X-ray MSPs [142]. Sinusoidal profiles are usually ascribed to the heated polar caps on the NS surface [210], although the thermal component observed in the X-ray spectrum was too faint to account for the observed pulse amplitude. A pulsed signal was not detected instead from either PSR J1227-4853 (within an upper limit of 10%, [132]) or PSR M28I (for which high time resolution data lacked [117, 130]).

The Gamma-ray Emission and Particle Acceleration MSPs are energetic enough to convert a few per cent of their spin-down power into emission at GeV energies, and tMSPs made no exception ([191], see also Chap. 2). They were characterised by a luminosity of a few $\times 10^{33}$ erg s $^{-1}$ (0.1–100 GeV) and a power law spectrum with photon index ~ 2.3 – 2.4 ([103, 127, 182, 183, 190], see Table 6.1). A marginally significant high energy cut-off at ~ 5 GeV could be detected only in PSR J1227-4853 [190]. Gamma-ray pulsations were reported at a significance of 3.7σ from PSR J1023+0038 [10] and 5σ from PSR J1227-4853 [103]. The gamma-ray (> 100 MeV) pulse profile featured a relatively broad peak almost aligned with the main peak of the radio pulse at 1.4 GHz. While an orbital modulation was not detected during the rotation-powered state of PSR J1023+0038, its presence in PSR J1227-4853 is controversial [103, 207].

6.5.2 Accretion Outbursts

So far, IGR J18245-2452 has been the only tMSP that has shown an accretion outburst with a similar peak X-ray luminosity ($L_X \simeq 5 \times 10^{36}$ erg s $^{-1}$) and duration (\sim three weeks) to other AMXPs. However, its X-ray emission was peculiar compared to other AMXPs (see Chap. 4), especially because an extremely strong variability was seen in two \sim one day-long *XMM-Newton* observations performed a few days apart ([130], see Fig. 6.4). It had an rms amplitude of more than 90% and its Fourier power density spectrum was described with a power law $P(\nu) \propto \nu^{-\gamma}$ with index $\gamma = 1.2$, extending over six decades in frequency (10 $^{-4}$ –100 Hz). Two states could be identified with a flux differing by two orders of magnitude ([80], see Fig. 6.5). In the high-intensity state ($L_X \simeq$ a few $\times 10^{36}$ erg s $^{-1}$, corresponding to a mass accretion rate of $\sim 10^{16}$ g s $^{-1} \simeq 10^{-2} \dot{M}_{Edd}$), a power law $F(E) \propto E^{-\Gamma}$ with $\Gamma \simeq 1.7$ characterized the X-ray energy spectrum. This is typical of AMXPs and is usually interpreted as Compton up-scattering of soft photons coming from

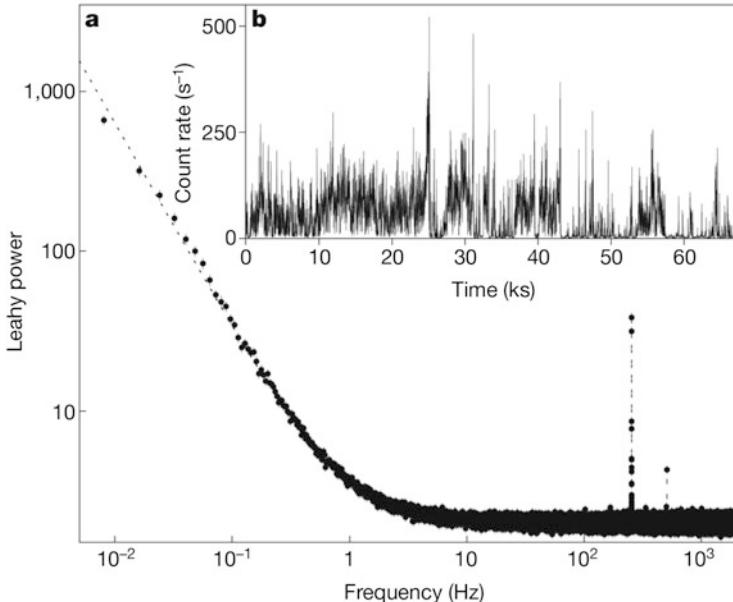


Fig. 6.4 X-ray power density spectrum and light curve (inset) of IGR J18245–2452 observed by *XMM-Newton* during its 2013 outburst. Credit: Papitto et al., *Nature*, 501, 517 (2013), reproduced with permission of Springer Nature

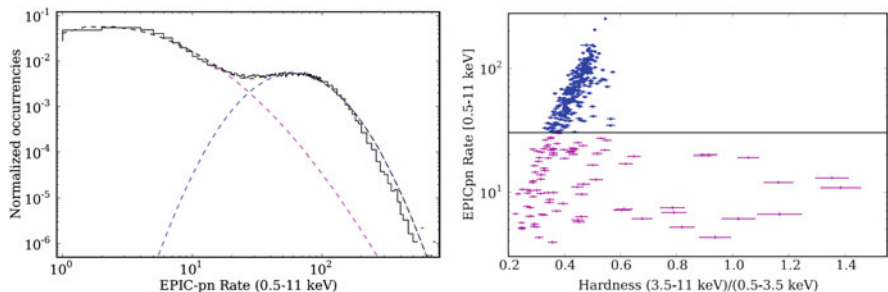


Fig. 6.5 Histogram of the X-ray count rates (top panel) and hardness-intensity diagram (bottom panel) of IGR J18245–2452 observed by *XMM-Newton* during its 2013 outburst, showing the bi-modal distribution of count rate and energy spectra. Credit: Ferrigno et al., *A&A*, 567, A77 (2014), reproduced with permission © ESO

the NS surface by hot electrons in the accretion columns. The spectrum became significantly harder, $\Gamma \simeq 0.9$, in the low-intensity state ($L_X \simeq \text{a few} \times 10^{34} \text{ erg s}^{-1}$, corresponding to $\dot{M} \sim 10^{14} \text{ g s}^{-1} = 10^{-4} \dot{M}_{Edd}$), and an additional partial covering absorption component was required. Together with a strongly variable emission observed at GHz radio frequencies, this suggested the presence of outflowing material [80]. The spectral hardening characterizing the low-intensity state also

made the average spectrum of IGR J18245–2452 the hardest of all AMXPs [62]. The X-ray pulse profile showed two sinusoidal peaks per cycle. Pulsations were present at all flux levels up to 60 keV, and the amplitude correlated with flux up to an rms of $\sim 20\%$. In the lower intensity-harder flux state the amplitude was instead lower ($\sim 5\%$) and the shape different. This peculiar behaviour was interpreted in terms of a fast switching between accretion and weak to strong propeller states [80, 155].

Other Accreting MSPs in Quiescence IGR J18245–2452 has been the only AMXP detected as a radio pulsar in quiescence, so far. However, many indirect pieces of evidence suggest that a radio pulsar may have switched on also in other AMXPs. When in quiescence, AMXPs are relatively faint compared to other soft X-ray transients ($10^{31}\text{--}10^{33}$ erg s $^{-1}$; see, e.g., [203]) and show a non-thermal power-law spectrum, possibly originating from an intrabinary shock [50]. On the other hand, a soft thermal component was found to be hardly detectable, giving stringent constraints on the rapidity of the cooling of the NS atmosphere after an accretion outburst [92]. Such a faint X-ray emission could not account for the optical flux of the irradiated companion, requiring the more intense spin-down power of a rotation-powered pulsar [42, 48, 60]. AMXPs in quiescence spin down at a rate compatible with magneto-rotational torques ([89]; see Sect. 4.3.3) and their orbit showed a rapid and complex evolution similar to black widow pulsars (see Sect. 4.3.4), possibly due to the ejection of matter from the system [73] and/or angular momentum exchange between the binary and the donor [140]. *Fermi*-LAT data also unveiled a gamma-ray counterpart of the closest ($d = 3.5$ kpc) AMXP known, SAX J1808.4–3658 ([68]; see Sect. 2.2). The luminosity measured during the ten years between August 2008 and 2018 (in which three outbursts have also occurred) was $L_\gamma = (6 \pm 1) \times 10^{33}$ erg s $^{-1}$. This is compatible with the values observed from rotation-powered MSPs, although pulsations could not be detected.

However, despite thorough searches, radio pulses were not detected from AMXPs other than IGR J18245–2452 [44, 97, 98], down to an upper limit of 30 μ Jy (at 2 GHz) in the case of SAX J1808.4–3658 [140], which is located at a distance of 3.5 kpc and is the closest AMXP known. An unfavourable inclination (although the radio beams of MSPs are very large), absorption of radio waves at low frequencies (where most of the radio power is emitted) by matter enshrouding the binary, and/or the larger distances of AMXPs (most are located in the Galactic bulge) than transitional systems are possible reasons. Worth noticing is that IGR J18245–2452 was sporadically detected as a faint radio pulsar with a flux density of 10–20 μ Jy at 2 GHz, i.e. close to the sensitivity limit, because the M28 cluster where it resides (located at a distance of 5.5 kpc) is rich of MSPs, and thus was deeply surveyed in the radio domain [20, 130, 147].

6.5.3 The Sub-luminous Disc State

All the three tMSPs showed an enigmatic accretion disc state characterized by an X-ray luminosity of $\sim 10^{33}\text{--}10^{34}$ erg s $^{-1}$, fainter than outbursts of AMXPs ($10^{36}\text{--}10^{37}$ erg s $^{-1}$) and brighter than rotation-powered MSPs and quiescent AMXPs ($10^{30}\text{--}10^{32}$ erg s $^{-1}$). PSR J1023+0038 has a *sub-luminous* disc for nine years (and counting), with a little change of its properties, if any. XSS J12270–4859 behaved as such between 2003 and 2012, and possibly since earlier times. Shorter episodes were also recorded in PSR J1023+0038 and IGR J18245–2452 (see Sect. 6.4).

The Intensity Modes The *high* (sometimes termed *active*) and the *low* (*passive*) intensity modes observed in the X-ray light curves together with sporadic flares, are perhaps the defining characteristics of tMSPs in the *sub-luminous* state. The top-left panel of Fig. 6.6 shows an X-ray light curve observed from PSR J1023+0038; the *high* and *low* modes are plotted with blue and red points, respectively, while flares are shown with green symbols. Most of the information about these intensity modes has been obtained from observations of PSR J1023+0038 [26, 47, 52, 139, 185], although they have also been observed from XSS J12270–4859 [63, 65, 159] and IGR J18245–2452 [117, 130] (see [116] for a comparative study). PSR J1023+0038 lies for $\sim 80\%$ of the time in the *high* mode, emitting a roughly constant 0.5–10 keV X-ray luminosity of $\sim 3 \times 10^{33}$ erg s $^{-1}$. Unpredictably, sharp transitions to the *low* mode occurs on a timescale of ~ 10 s. The X-ray luminosity observed in the *low* mode is also roughly constant and about one order of magnitude fainter than in the *high* mode, but still a few times brighter than the rotation-powered state (see Table 6.1). The transition from the *low* to *high* mode are characterized by a similar

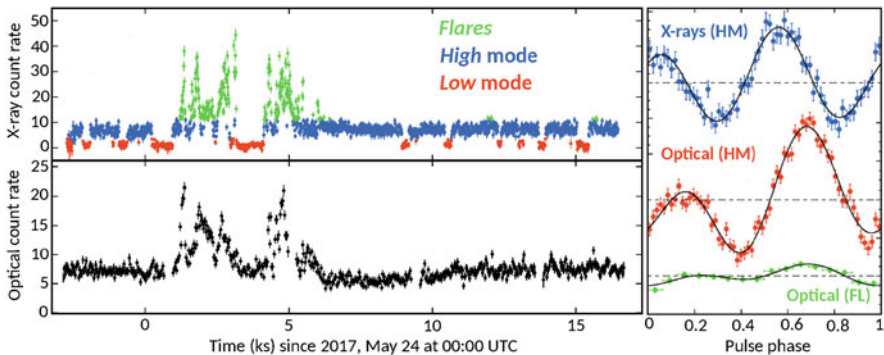


Fig. 6.6 X-ray (top-left panel) and optical (bottom-left panel) light curves of PSR J1023+0038 in the *sub-luminous* disc state observed simultaneously by *XMM-Newton*. *High mode*, *low mode* and flares are plotted in blue, red and green, respectively. The right panel shows the X-ray pulse profile during the *high* mode (blue points) and the optical pulse profiles in the *high* (red points) and flares (green points) detected by *SiFAP2* at the *INAF TNG Galileo Telescope*. Credit: Papitto et al., ApJ, 882, 104 (2019) © AAS. Reproduced with permission

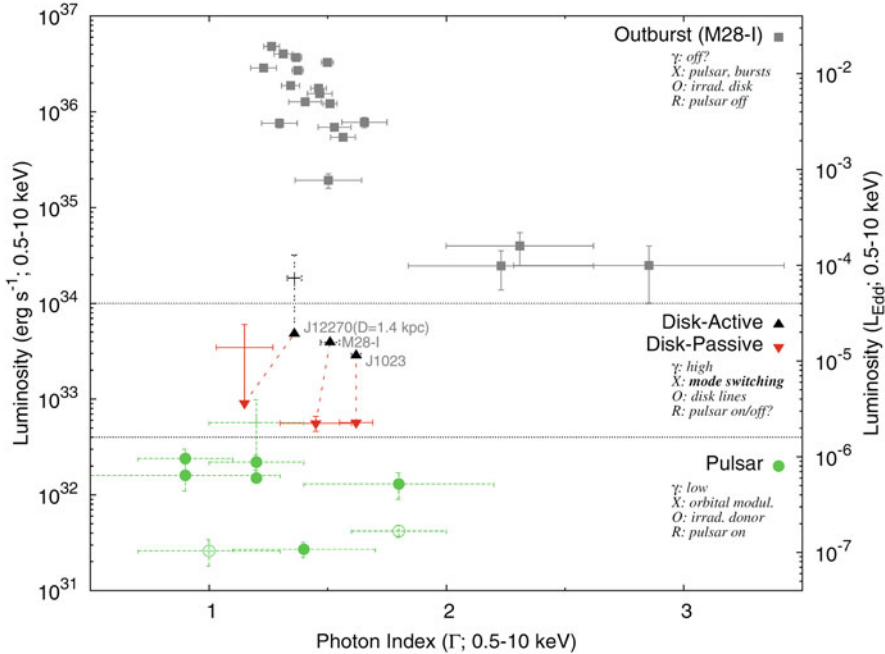


Fig. 6.7 0.5–10 keV X-ray luminosity and power-law spectral index of tMSPs in outburst (M28I=IGR J18245–2452) (top panel), in the *high*/active and *low*/passive modes in the *sub-luminous* disc state (middle panel), and of tMSPs and redbacks in the radio pulsar state (bottom panel). Credit: Linares et al., ApJ, 795, 72 (2014) © AAS. Reproduced with permission

timescale. The duration of these modes ranges from a few tens of seconds to a few hours, although there does not seem to be a characteristic length or recurrence time, nor a correlation between waiting times, duration or luminosity. The luminosity of the *high* and *low* modes have been stable within $\sim 10\%$ in the many observations of PSR J1023+0038 performed so far, without any modulation at the orbital period.

The spectrum of the X-ray emission observed in the *high* mode was described by an absorbed power-law with an index of $\Gamma_X = 1.4\text{--}1.6$, significantly softer than in the radio pulsar state, $\Gamma \simeq 1.1\text{--}1.2$ ([26, 53, 116], see Table 6.1 and Fig. 6.7). The power-law extends up to at least ~ 80 keV without any evidence for a cut-off [185]. A thermal component with a temperature of ~ 130 eV and contributing to a few per cent of the total flux was also detected at soft X-ray energies in PSR J1023+0038 [26]. Its properties are compatible with the emission coming from the inner rings of a disc truncated ~ 20 km from the pulsar [47]. In the *low* mode, the thermal component disappears and the power-law spectrum becomes slightly softer than in the *high* mode ($\Gamma \simeq 2.0$, [47, 53]).

The X-ray modes observed from XSS J12270–4859 had similar properties. However, the energy spectrum observed in the *low* modes which occurred after a flare was harder than in the *high* mode [63, 65, 116]. The tail of the flaring

emission likely contaminated those spectra, indicating that the flaring mechanism is independent of the *high-to-low* mode transitions [125]. An additional partial covering neutral absorber was required to model the spectra of these *low* modes, suggesting a refilling of the matter reservoir close to the NS after a flare [65]. The *high* and *low* modes observed in IGR J18245–2452 had a similar luminosity ratio (~ 7), but lasted significantly longer (up to 20 h) and showed slower transitions (~ 500 –1000 s), although shorter timescales could not be probed due to the particular observing mode [117, 130].

Flat-bottomed dips were also observed in high-cadence optical observations of PSR J1023+0038 [164, 165]. The ingress/egress times were slightly longer (~ 20 s) than those of X-ray *low* modes, whereas the duration was similar. A bi-modal distribution of the optical flux was also found from a lower cadence *Kepler K-2* monitoring [108]. However, simultaneous optical/X-ray *XMM-Newton* observations have not revealed such dips in B-band data [14, 26], possibly because the optical *low* modes are energy dependent. The lack of simultaneous detection of optical dips and X-ray *low* modes has prevented to establish the relationship between these phenomena, so far. Flares and hints of flat-bottomed dips were also found in near-infrared K_s-band photometric light curves [164]. An enhancement of the near-infrared emission, possibly a flare, was also observed right after an X-ray *low-to-high* mode transition [135]. *Low* and *high* modes were much more evident in the ultraviolet, they occurred simultaneously with the X-rays displaying variations by ~ 25 –30% in both PSR J1023+0038 [94] and XSS J12270–4859 [63, 65].

The gamma-ray brightening of PSR J1023+0038 when switching from the rotation-powered to the *sub-luminous* disc state, and the gamma-ray dimming of XSS J12270–4859 in the reverse transition, have been certainly one of the most unexpected features of tMSPs⁴ (see also the discussion in Sect. 2.3). AMXPs in outburst (and in general LMXBs) have not been detected in gamma-rays, so far.⁵ On the other hand, the GeV gamma-ray emission of tMSPs in the *sub-luminous* state became a few times brighter than in the rotation-powered state and slightly brighter than in the X-ray band (see Table 6.1). The \sim tenfold gamma-ray brightening observed from PSR J1023+0038 in 2013 took place in a month, or less [173, 190]. The transition of XSS J12270–4859 in the opposite direction was smoother and less pronounced ($L_{\gamma, \text{disc}} \sim 2.5 L_{\gamma, \text{rot}}$) [103, 190]. The gamma-ray spectra of both tMSPs in the disc state were well described by a power law with index $\Gamma_\gamma \approx 2.0$ with marginal evidence of a cutoff between 4 and 10 GeV ([190], see Table 6.1). A high-energy (> 5 GeV) component was recently claimed to emerge in the spectrum of PSR J1023+0038 at orbital phases corresponding to the pulsar descending node [208], but confirmation with a higher counting statistics is warranted. So far, only upper limits have been set to the emission in the TeV regime [3].

⁴ The M28 globular cluster to which IGR J18245–2452 belongs, hosts a population of gamma-ray emitting MSPs [206] that made a gamma-ray brightening difficult to detect.

⁵ Note that AMXPs are generally farther ($d \simeq 5$ –8 kpc) than the two tMSPs in the Galactic field ($d \sim 1.5$ kpc).

The Radio Emission In the *sub-luminous* state of PSR J1023+0038, radio (0.3–5 GHz) pulsations have not been detected in either of the X-ray modes. Upper limits of 0.1–1 mJy were set, i.e. more than an order of magnitude lower than in the radio pulsar state [26, 139, 173]. As the radio emission could be absorbed by the intrabinary material, this does not necessarily imply the complete quenching of the radio pulsar.

A radio continuum emission with a flat or a slightly inverted spectrum was instead seen from both PSR J1023+0038 and XSS J12270–4859 [72, 95]. Similar spectra are ubiquitous among accreting X-ray binaries in the hard state and are interpreted in terms of partially self-absorbed synchrotron emission from outflowing material, e.g. in a compact jet [79]. Different correlations hold between the X-ray and the radio luminosity of X-ray binaries hosting black holes and NSs; the latter are generally fainter radio sources at a given X-ray luminosity [55, 82, 101]. In a $L_{\text{radio}} - L_X$ diagram (see Fig. 6.8), tMSPs fall in the radio-bright end of the range expected by propagating the correlation for bright accreting NSs to a lower X-ray luminosity, especially when the peak radio luminosity is considered.

Simultaneous radio and X-ray observations of PSR J1023+0038 unveiled an anti-correlated pattern of variability [28]. When the source switched from the *high* to the

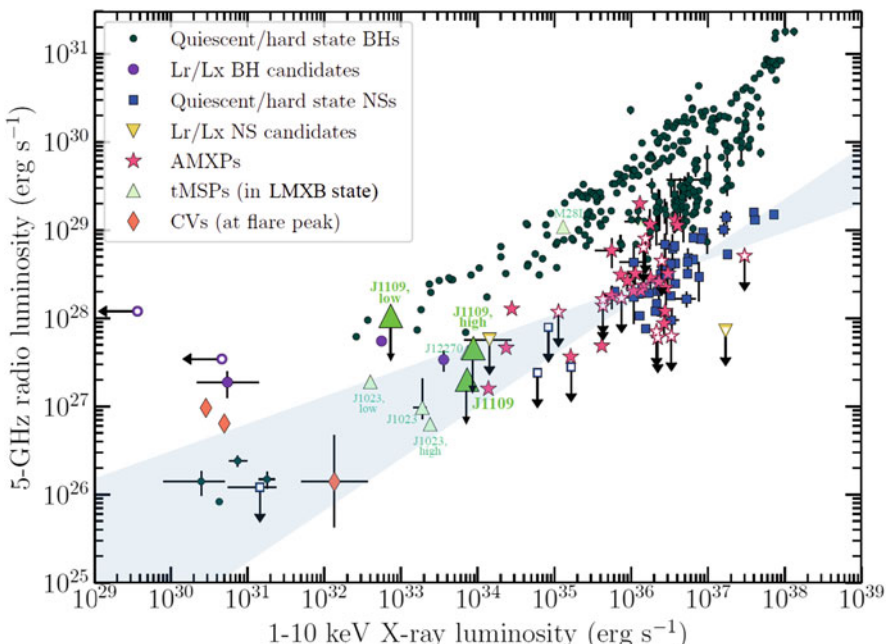


Fig. 6.8 Radio vs. X-ray luminosity plane for different classes of accreting compact objects. The tMSPs in the *sub-luminous* disc state are plotted with green symbols. The cyan shaded area encloses the 3σ confidence interval on the correlation holding for accreting NSs [82]. Credit: Coti Zelati et al., A&A, 622, A211 (2019), reproduced with permission © ESO

low X-ray mode, the radio flux suddenly increased and its spectrum became steeper. The decay of the radio emission was instead shallower; it started earlier than the *low-high* mode transition and ended $\sim 30\text{--}60$ s later. This phenomenology suggested that optically thin emission from expanding plasmoids becomes dominant when the source drops into the *low* mode. Sporadic radio flares up to a few mJy have also been observed in this source [35]. In particular, a radio flare with evolving synchrotron features typical of accretion driven outflows was observed to occur a few minutes after a bright X-ray flare, although other radio flares were observed when the source was in the *high* X-ray mode without any appreciable variability [28].

The Optical and UV Emission The optical brightness of tMSPs in the *sub-luminous* state is $\sim 1\text{--}2$ magnitudes brighter than in the rotation-powered state, due to the contribution of the newly-formed accretion disc [19, 88, 129]. On the other hand, the donor stars were still found to be heated at a similar level as in the rotation-powered state (see Sect. 6.5.1). The V and R band emissions in PSR J1023+0038 were found to be linearly polarized at $\sim 1\%$ level possibly due to Thomson scattering within the disc [13, 85].

The optical spectra were dominated by a blue continuum and strong, double-peaked emission lines of H and He produced in an optically thick accretion disc [26, 52, 64, 64, 200]. Modelling of the spectrum of PSR J1023+0038 observed during the 2000–2001 accretion state with a simple disc model gave a temperature in the range $(2\text{--}34) \times 10^3$ K, and inner and outer radii of $R_{in} \sim 10^9$ cm and $R_{out} \simeq 6 \times 10^9$ cm, respectively [200]. The inner disc radius is larger than the Alfvén radius, indicating that the optical emission originated in the outer disc regions. Similar results were obtained modelling the UV spectrum [93]. In XSS J12270–4859, Doppler tomography showed that the hotter regions producing the He II emission lines were similarly far-out [64].

Flares were observed simultaneously in the X-ray, UV, optical, and near-infrared bands both from PSR J1023+0038 [26, 85] and XSS J12270–4859 [63–65, 160], suggesting a common underlying process. X-ray flares emitted most of the energy ($L_X \simeq 6 \times L_{opt}$). They lasted from less than a minute to a few hours [26, 63, 100], even though extended episodes lasting up to ten hours have been observed in PSR J1023+0038 [185]. The brightest observed flares attained an X-ray luminosity of $\approx 2\text{--}7 \times 10^{34}$ erg s $^{-1}$ in the 0.3–79 keV band, ([26, 185], see Table 6.1), slightly exceeding the pulsar spin-down power.

The most prominent optical flares of PSR J1023+0038 had amplitudes of $\sim 0.5\text{--}1$ mag and lasted up to 14 h; they traced the brightest flares seen in X-rays with both positive and negative lags of up to ~ 250 s [26]. An 80-days long *Kepler K2* coverage observed optical flares for 15–22% of the time (depending on the flare identification algorithm, [108, 134]), much more frequently than X-ray flares observed at other epochs ($\simeq 2\%$, [100]). This showed that the flaring activity is highly unpredictable and cannot be easily parameterized. Multi-band simultaneous observations of a bright event suggested that the flare emission became hotter and more optically thin, like in an accretion disc corona and/or hot fireball ejecta [165]. Similar indications were also found in XSS J12270–4859

[65]. Remarkably, the optical emission lines observed from XSS J12270–4859 [64] and PSR J1023+0038 [85] showed a tendency to disappear during intervals characterized by enhanced flaring emission, compatible with the onset of an outflow. The emergence of an additional polarized component during the flares, possibly due to Thomson scattering from ejected matter, also supported this hypothesis [85]. Flaring variability observed in the near-infrared lagged the optical variability by ~ 10 s, and was tentatively attributed to the reprocessing of the optical emission produced close to the light cylinder by a stream of matter ejected by the system further out [14].

Pulses X-ray pulsations at the NS spin period were detected only during the *high* mode in both PSR J1023+0038 ([8], see the right panel of Fig. 6.6) and XSS J12270–4859 [132]. They had an rms amplitude of $\sim 6\text{--}7\%$ and were modelled with two sinusoidal harmonic components. Pulsations instead disappeared during the *low* modes and the flares, with upper limits of $\sim 1\text{--}2\%$. A quasi-coherent timing solution measured over the interval Nov 2013–Dec 2015 remarkably found that PSR J1023+0038 was spinning down in the disc state at a rate $(32 \pm 2)\%$ larger than in the radio pulsar state [100].⁶

Quite surprisingly, also the optical emission observed from PSR J1023+0038 turned out to be pulsed with an rms amplitude of $\simeq 1\%$ [5, 106, 135, 209]. This made PSR J1023+0038 the first optical MSP ever detected. Optical pulsations were present in the *high* mode and disappeared in the *low* mode with an upper limit of $A < 0.034\%$ ([135]; see the right panel of Fig. 6.6). Optical and X-ray pulsations had a similar shape with the optical lagging the X-rays by $\sim (200 \pm 70)\mu\text{s}$. Subsequent measurements with instruments least affected by systematics confirmed the presence of a $100 - 200\mu\text{s}$ lag (Illiano et al., in prep.). The spectral energy distribution of the pulsed emission from the optical to the X-ray band was found to nicely match a power-law relation $F_\nu \propto \nu^{-0.7}$ (see Fig. 6.9). Pulsations later observed in the UV band showed a similar pulse amplitude [102]. All these properties indicate that the optical/UV and the X-ray pulsations share a common underlying mechanism [135]. Interestingly, the optical pulses were also detected during flares with an amplitude \sim six times lower than that in the *high* mode [135]. The spin-down rate determined from optical pulsations measured between Jan 2018 and Jan 2020 was $\sim 20\%$ lower than that measured from X-ray pulses at earlier epochs, and very close to the value observed in the radio pulsar state [45]. The difference in the spin-down rate measured from the optical and the X-ray pulsations at different epochs has to be investigated with further long-term coverage in both domains.

⁶ The fractional change reported here is slightly larger than the value quoted in [100], $(26.8 \pm 0.4)\%$, because it takes into account the Shklovskii effect and acceleration in the Galactic potential [71].

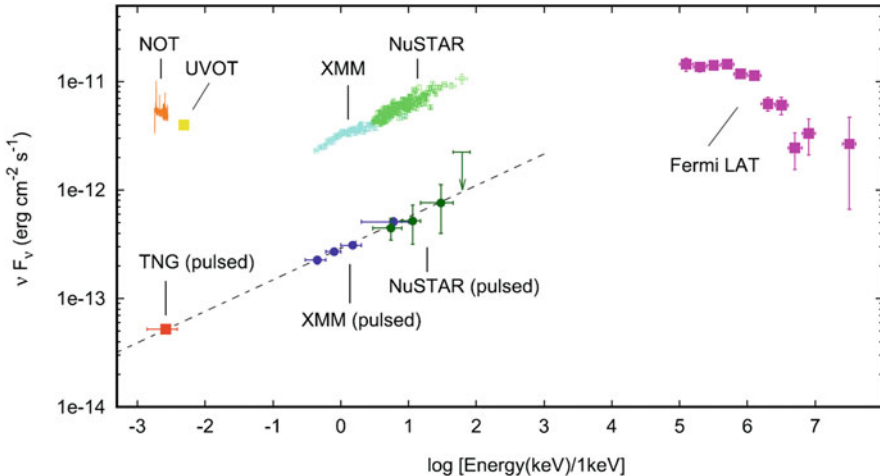


Fig. 6.9 Spectral energy distribution of the optical/UV/X-rays/gamma-rays total and pulsed emission of PSR J1023+0038 in the *sub-luminous* disc state. Credit: Papitto et al., ApJ, 882, 104 (2019) © AAS. Reproduced with permission

6.5.4 Candidate Transitional Millisecond Pulsars

Stimulated by the discovery of the three tMSPs, searches for new candidates started just after. Searching for a counterpart to a yet unidentified gamma-ray source, with peculiar time variability (such as the *high-low* modes and flares) and spectral properties in the optical (e.g., double peaked emission lines and a blue continuum) and X-ray bands ($L_X(0.3\text{--}79 \text{ keV}) \simeq (0.5\text{--}1) \times L_\gamma(0.1\text{--}300, \text{ GeV})$), as well as a power law-shaped spectrum with a photon index $\Gamma \sim 1.7$), turned out to be the most efficient way to identify candidate tMSPs in the *sub-luminous* disc state.

RX J154439.4–112820 was found within the error circle of 3FGL J1544.6–1125. The spectrum of the optical counterpart showed prominent H and He emission lines, consistent with the presence of an accretion disc [122]. The X-ray light curve displayed *high* and *low* modes differing by a factor of ≈ 10 in flux, with transitions occurring on a timescale of ≈ 10 s [30]. The power-law shaped X-ray spectrum, featuring a photon index $\Gamma \simeq 1.7$ and marginal spectral variability, was also similar to those shown by tMSPs in the *sub-luminous* disc state [25]. The long-term optical light curve revealed variability by 0.5 mag and in some occasions enhancements by $\approx 1.0\text{--}1.5$ mag [25], reminiscent of the optical flares observed in tMSPs. A variable radio emission with a flat spectrum was also detected [101], placing the source in a similar region of the radio vs. X-ray luminosity plane of the other tMSPs in the *sub-luminous* disc state (see Fig. 6.8). Optical time-resolved spectroscopy measured a period of 5.8 h and an inclination of $5\text{--}8^\circ$, implying that the system is seen almost face-on [39]. Adopting a distance prior to the *Gaia* eDR3 parallax [81], based on the Galactic model by [17], gave a distance of $2.8^{+1.0}_{-0.8}$ kpc. The corresponding X-ray and

gamma-ray luminosity are $\simeq 8.1 \times 10^{33} \text{ erg s}^{-1}$ and $1.3 \times 10^{34} \text{ erg s}^{-1}$, respectively, very similar to those of tMSPs in the *sub-luminous* disc state.

CXOU J110926.4–650224 (also known as IGR J11098–6457 [188]) is a hard X-ray source located within the error circle of FL8Y J1109.8–6500. The typical modes shown by tMSPs in the *sub-luminous* disc state were easily recognized in its X-ray light curve, and also the energy spectrum was similar to those of the tMSPs [54]. Its variable optical counterpart showed disc emission lines, and a variable and flaring radio counterpart with typical tMSP characteristics was also found [55]. At a distance in the range $\sim 4\text{--}11$ kpc, derived from *Gaia* eDR3, the X-ray luminosity is $\simeq 0.7\text{--}5.4 \times 10^{34} \text{ erg s}^{-1}$, of the same order of the gamma-ray luminosity $\simeq 0.5\text{--}3.7 \times 10^{34} \text{ erg s}^{-1}$ [55].

Recently, a variable optical and X-ray source has also been found within the error circle of the gamma-ray source **4FGL J0407.7–5702** [124]. The optical spectrum showed double peaked H and He emission lines and a blue continuum indicating the presence of an accretion disc. The X-ray spectrum was also found to be compatible to those observed in tMSPs. The ratio of the X-ray to gamma-ray luminosity was similar to that shown by other sources in the *sub-luminous* disc state, making it a strong candidate tMSP. The comparison of the flux observed in the optical, X-ray and gamma-ray bands with those of other tMSPs in the disc state, and the lack of a significant Gaia parallax, have suggested a distance larger than 5 kpc. This would make it the farthest tMSP known. Although the distribution of the count rates observed in the X-ray band featured two peaks, the phenomenology of the light curve makes an interpretation in terms of the usual *high*–*low* modes somewhat difficult although the time spent in one or other mode can be different from source to source.

The gamma-ray source **3FGL J0427.9–6704** was recently associated with an accreting eclipsing X-ray binary with an 8.8 h period and a hard X-ray spectrum extending up to ~ 50 keV [175]. The eclipses were observed both in the X-ray and the gamma-ray light curves, demonstrating the association of the counterpart, and indicating that the high energy emission arose very close to the compact object [107, 175]. The bright and variable emission of the radio counterpart was instead not eclipsed, indicating an origin further out. The X-ray luminosity of this source ($5 \times 10^{33} \text{ erg s}^{-1}$ at 2.3 kpc) was of the same order of that observed at gamma-ray energies, similar to tMSPs in the *sub-luminous* state. However, the simultaneous X-ray and optical/ultraviolet light curves did not reveal the typical intensity modes of tMSPs, as the source was found to be flaring most of the time [115]. Modelling of the optical orbital modulation and of the radial velocity of lines originating from the surface of the $\sim 0.6 M_{\odot}$ companion star indicated a relatively massive $\sim 1.8\text{--}1.9 M_{\odot}$ NS [175]. On the other hand, a recent study based on much higher quality photometric data found a lower, although not highly constrained, mass for the primary ($1.43^{+0.33}_{-0.19} M_{\odot}$, [107]).

The low-energy counterpart of the gamma-ray source **4FGL J0540.0–7552** also showed the presence of an accretion disc and extreme X-ray and optical variability [178]. Its X-ray spectrum was described by a $\Gamma \simeq 1.8$ power-law and the ratio

of the X-ray (0.5–10 keV) to gamma-ray (0.1–100 GeV) flux was $\simeq 0.1$, much higher than the values observed from redbacks ($\simeq 0.01$), although slightly lower than the range observed from other tMSPs in the same bands (0.26–0.43; [124]). Unlike all the other candidate tMSP, it showed evidence for a state transition from a rotation-powered to a *sub-luminous* disc state which took place in 2013, in both the optical, X-ray and gamma-ray wavebands. Similar to 3FGL J0427.9-6704, its X-ray emission in the *sub-luminous* disc state was dominated by flares, suggesting that flare-dominated emission might be a common feature of at least a subset of tMSPs.

These characteristics listed above make these five sources very strong candidate tMSPs in the *sub-luminous* disc state, although the lack of precise orbital ephemeris has hampered the detection of X-ray pulsations, so far.

The recent release of the 4th *Fermi*-LAT catalogue [1] and its newest 10-yr DR2 version[18]⁷, with a forthcoming DR3 version (Fermi LAT collaboration 2021, in preparation), enhanced the search for MSP binaries associated with an X-ray and optical counterpart. However, discriminating between redbacks and tMSPs in the disc state has been sometimes not immediate. For instance, a few redbacks such as 3FGL J0838.8-2829 [86, 146], PSR J1048+2339 [126, 176], PSR J1628-3205 [51, 176], and 4FGL J2339.6-0533/PSRJ2339-0533 [105, 141, 151], the black widow PSR J1311-3430 [154] and the recently discovered long-period (> 1 d) MSP binaries 2FGL J0846.0+2820 [179] and 3FGL J1417.5-4402 [175, 180] occasionally displayed emission lines in their optical spectra. While they may hint to a disc origin, the emission lines could be also ascribed to a magnetically driven wind of the companion or to the intra-binary shock. The recently identified source 4FGL J0935.3+0901 has an optical counterpart with double-peaked emission lines, features gamma-ray properties similar to tMSPs, and showed an enhancement by a factor about 8 between Dec. 2010 and Jul. 2013 with significant spectral change [201]. However, its X-ray-to-gamma-ray flux ratio (~ 40) was more typical of spiders in the rotational-powered state rather than of tMSPs in the *sub-luminous* disc state. Simultaneous photometric and spectroscopic observations will be crucial to understand the connection of variable heating and the appearance of emission lines.

Recently, very faint persistent or quasi-persistent X-ray binaries with a luminosity $\sim 10^{33}$ – 10^{35} erg s $^{-1}$, have also been proposed to harbour tMSPs in the *sub-luminous* disc state [91]. These sources would switch on as radio pulsars as soon as the X-ray luminosity drops below $\sim 10^{32}$ erg s $^{-1}$. However, given the relatively low X-ray luminosity involved, detecting a state transition is only possible for close-by sources or deeply observed fields, such as the Galactic Centre and globular clusters.

Terzan 5 CX1 (CXOU J174805.05–244641.0) is a variable hard X-ray source in the dense globular cluster Terzan 5. A comprehensive study of several *Chandra* observations spanning 13 years found it twice in a bright state with $L_X \sim 2 \times 10^{33}$ erg s $^{-1}$ (in 2003 and 2016), and twice in a much fainter state $L_X \sim 10^{32}$ erg s $^{-1}$

⁷ https://fermi.gsfc.nasa.gov/ssc/data/access/lat/10yr_catalog/.

(between 2009 and 2014) with a harder spectrum than the bright state [15]. This behaviour was reminiscent of the changes of state of tMSPs. A faint optical counterpart with colours compatible with the cluster main sequence was also identified. Follow-up radio continuum observations also revealed a faint ($\sim 20 \mu\text{Jy}$ at 3 GHz) radio source, which placed CX1 close to the position of PSR J1023+0038 in the X-ray/radio luminosity diagram. These properties make it a strong candidate tMSP to be searched in beamed-formed radio observations to reveal the yet to be discovered pulsar. Large changes in the X-ray flux from **Ter 5 A (CXOU 174802.26–244637.5)**, likely the counterpart of the 11.6 ms redback PSR J1748-2446A, also suggested that two transitions to an accretion disc state might have taken place in 2011 and 2013 [33].

XMM J174457–2850.3 is a faint X-ray transient in the Galactic Centre region. The detection of a 2 hr-long type-I X-ray burst proved that it hosts an accreting NS [70]. This source exhibited a few-weeks long outbursts up to $\sim 10^{36} \text{ erg s}^{-1}$, but for most of the time, it lay in quiescence with a luminosity of $\sim 5 \times 10^{32} \text{ erg s}^{-1}$. Also, it was occasionally found to linger for several months at an intermediate level of $10^{33}–10^{34} \text{ erg s}^{-1}$ [69]. The X-ray spectrum was described by a $\Gamma \sim 1.4$ power-law, much harder than that generally observed from LMXBs at the same luminosity level. The properties of these three luminosity states resembled those observed in the tMSP IGR J18245–2452 [130]. However, no meaningful search for fast pulsations could be performed either in X-rays due to the low statistic of available data [69], or in the radio band due to the large (6.5 kpc) distance of the source.

Recently, a catalogue of more than 1100 X-ray sources in 38 globular clusters has been compiled to complement the MAVERIC (Milky-way ATCA VLA Exploration of Radio-sources In Clusters) radio survey [16]. Among these, the brightest source in **NGC 6539**, [16] and the second brightest in **NGC 6652** [128], were identified as a candidate tMSP based on their X-ray properties, and the presence of a bright radio counterpart with a flat/slightly inverted spectrum. Interestingly, the latter also showed prolonged X-ray flaring, suggestive of the flare-dominated mode also seen from 3FGL J0427.9-6704 and 4FGL J0540.0-7552 (see above).

6.6 Models and Open Questions

6.6.1 The Rotation-Powered State

The relativistic wind of MSPs in close binaries is terminated by the interaction with the stream of matter issuing from the companion star or the companion star itself. Hence, they offer the opportunity to study the properties of the termination shock so created at much smaller distances than in pulsar wind nebulae (see also the discussion in Sect. 3.6). Already in late eighties, it was also predicted that high-energy photons generated by the particles accelerated at the termination shock would have been able to evaporate the late-type companion star [109, 157, 184].

Models were first applied to the case of the first black window pulsar discovered, PSR B1957+20 [12]. Given the relatively small size of the binary ($d \simeq 10^{11}$ cm), the magnetic field down-stream the shock is $B \gtrsim 3\sqrt{L_{sd}/cd^2} \approx 30$ G (for a magnetically dominated and isotropic wind emitted by a pulsar with spin-down power $L_{sd} \simeq 10^{34}$ erg s $^{-1}$). Synchrotron emission is thus the main cooling mechanism of the relativistic particles accelerated in the shock, yielding an X-ray output which exceeds the magnetospheric pulsar emission. A recent X-ray study of a large sample of MSPs indeed found that redbacks are brighter than black widows and isolated MSPs [113]. This indicates that a larger fraction of the pulsar wind of redbacks is intercepted at the shock surface compared to black widows.

The luminosity of the shock synchrotron emission depends on the strength of the magnetic field beyond the shock. Assuming that the efficiency of electron acceleration at the shock is similar to that of the Crab pulsar, the relatively bright X-ray luminosity observed from tMSPs required a pulsar wind dominated by the electromagnetic Poynting flux and focused along the equatorial plane of the pulsar (expected to be close to the orbital plane for a spun-up MSP) [27, 31, 67]. The index p of the power-law describing the electron population energy spectrum is related to the power-law index Γ of the X-ray spectrum as $p \sim 2\Gamma - 1$. The X-ray spectrum of both tMSPs [67, 185] and other redbacks observed with *NuSTAR* [2, 104, 110] extended up to at least 70 keV, and was consistent with a power-law with index $\Gamma \sim 1.1$ –1.2, implying $p \sim 1.3$. Such a value favours a shock-driven magnetic reconnection in a striped pulsar wind (see, e.g., [169] and Sect. 3.3.4) rather than diffusive shock acceleration. Even though the shock emission has to extend well above the 3–79 keV hard X-ray band covered by *NuSTAR* to be efficient enough in irradiating the secondary star [67], it must be limited below a few MeV not to exceed the pulsar spin-down power. The energy dependence of the orbital modulation marginally seen in two tMSPs (see Sect. 6.5.1) and PSR J2129-0429 [2] could also hint at a spatial variation of the p -index of the synchrotron emitting electrons.

The prediction that the X-ray emission was modulated at the binary orbital period due to the obscuration by the companion star and to Doppler boosting [12] was indeed confirmed in several MSP binaries [29, 150]. The phasing of the X-ray orbital modulation observed in tMSPs is similar to that observed in other redbacks; the X-ray flux attains a maximum when the pulsar is at the inferior conjunction of the orbit, in phase with the optical orbital variability [150]. On the contrary, the X-ray modulation of black widows displays a minimum when the pulsar is at the inferior conjunction of the orbit. To explain this, a different orientation of the shock in redbacks and black widows has been proposed by two groups [152, 196, 197], who have developed semi-empirical models to explain the radio, X-ray and optical behaviour. They argued that the shock which surrounds redbacks is oriented towards the pulsar due to the large companion wind momentum $\beta_w = \dot{M}_2 v_w c / \dot{E}$ (where v_w is the relative wind velocity and \dot{E} is the pulsar spin down energy \dot{M}_2 is the mass loss rate), while it surrounds the companion in black widows. The wind momentum ratio also sets the shock opening angle, which together with the binary inclination in turn determines the shape of the X-ray orbital light curve, single or double-peaked;

the width of the peaks depends instead on the boost parameter [74, 196]. Most redbacks showed a rather stable X-ray double-peaked modulation, while the tMSP PSR J1227-4853 displayed variations from single to double and again single-peaked shape over several months, indicating changes in the shock parameters [66, 67]. It was also noticed that systems prone to make or just after a transition, may indeed display variability in the shape of X-ray orbital modulation [196].

The stability of the shock over years is still an unresolved issue since a quasi-radial infall terminated outside the pulsar light cylinder is unstable on dynamical timescales ([43]; see Sect. 6.3). It was suggested that either a highly magnetized ($B \sim$ several kG) donor star with a low mass-loss rate ($\lesssim 10^{15} \text{ g s}^{-1}$, [10]), or a secondary star with a large mass loss rate but with an ADAF-like or heating-dominated flow, could bend the shock towards the pulsar helping make it stable [197]. This flow should be unmodulated and detectable at soft X-rays down to UV wavelengths and could explain the observed UV excess in PSR J1227-4538.

The companion star heating pattern inferred from high-quality optical photometric light curves of both redbacks and black widows did not match what expected from direct irradiation by the pulsar only, requiring also the illumination by the intrabinary shock [152]. An additional source of heating could arise if a fraction of the wind particles threads the companion field lines and is ducted to its surface; this would require a very active magnetic star displaying star-spots or flares [162, 197]. This possibility was claimed to explain the optical light curve of the strongly irradiated companion of the redback PSR J2215+5135 [162]. Asymmetries in the optical orbital modulation were also observed in the tMSP PSR J1227-4853, although no indication of a magnetically active star was found [66, 177].

6.6.2 The Accretion-Disc State

Transitional systems have shown a marked preference for the *sub-luminous* disc state than the bright X-ray outbursts typically seen in AMXPs. This made them more elusive to discover, and hard to reconcile with the typical classification scheme of X-ray transients. The main features of the *sub-luminous* state to explain are:

- its duration (more than ~ 10 years) and faintness (the accretion rate estimated from the X-ray luminosity is 5×10^{-5} times the Eddington rate);
- the *high* and *low* intensity modes with fast (~ 10 s) transitions seen in X-rays and UV, as well as in the optical and near-infrared, although with a still uncertain relationship with the other bands;
- the X-ray and optical pulsations detected in the *high* mode;
- the spin down of the NS at a rate similar to the rotation powered state;
- a flat-spectrum radio emission, showing flares and in at least one system a brightening simultaneous to the X-ray *low* modes;
- a brighter gamma-ray emission ($L_\gamma \gtrsim L_X$) than in the rotation-powered state;

- flares seen in the X-rays, UV, optical and near-infrared bands, with duration ranging from several minutes to hours.

Determining whether the multi-wavelength emission observed in the *sub-luminous* disc state is accretion or rotation-powered is the major challenge. This is not surprising since the accretion luminosity estimated from the X-ray flux is comparable to the pulsar spin-down power of MSP binaries ($\approx \text{few} \times 10^{34} \text{ erg s}^{-1}$), and both processes should be important. Most of the models proposed so far relied on the standard assumption that the source emission could be either accretion or rotation-powered. In the accretion-powered case the intrusion of high-density accreting plasma into the magnetosphere would easily suppress the acceleration of particles in the magnetosphere and the resulting emission [118, 167, 168]. On the other hand, the switch on of a rotation-powered radio pulsar would develop a radiation pressure which is able to eject the material lost by the companion [43]. However, the complications in applying one or the other assumption to the *sub-luminous* state of tMSPs have forced to consider models in which both rotation and accretion-powered mechanisms conspire to yield the puzzling emission properties listed above.

Enshrouded Radio Pulsar Models The unexpectedly bright gamma-ray emission of tMSPs first led Takata et al. [114, 182] and Coti Zelati et al. [52] to argue that a radio pulsar was hiding behind the enshrouding intrabinary matter [184]. They assumed that the pulsar wind truncated the disc far from the pulsar ($d \approx 10^9 - 10^{10} \text{ cm}$). The electrons accelerated in the shock would up-scatter the disc UV photons to yield the observed gamma-rays. These electrons would also interact with the field permeating the shock to emit synchrotron X-ray photons.

These models were proposed before the optical and X-ray pulsations had been discovered. Although the magnetosphere of a rotation-powered pulsar can actually produce pulsations in those wavebands, the efficiency in converting the spin-down power into the optical and X-ray pulsed emission observed from PSR J1023+0038 ($\eta_{\text{opt}} \sim \text{a few} \times 10^{-4}$ and $\eta_X \sim 6 \times 10^{-3}$, respectively) is higher than in young rotation-powered optical ($\eta_{\text{opt}} \sim 10^{-9}-10^{-5.5}$; see Fig. 3 in [5]) and X-ray pulsars ($\eta_X \sim 10^{-4}$ for a pulsar with the spin-down power of PSR J1023+0038; see [113]). Also, the X-ray efficiency should have increased by ~ 25 times after the formation of the disc. This would be hard to understand since the magnetospheric processes of the pulsar should not be affected by a disc truncated much further out. Furthermore, the synchro-curvature models which provided a successful modelling of the X-ray/gamma-ray emission of other MSPs [189, 192], failed to do so for tMSPs in the disc state.

Accretion/Propeller Models The detection of X-ray pulsations with similar properties of the pulses of AMXPs suggested that accretion onto the NS magnetic poles was taking place also in tMSPs [8, 132]. However, this would make tMSPs the faintest accreting X-ray pulsars known. This is a critical issue since the mass accretion rate deduced from the observed X-ray luminosity ($\dot{M} \simeq 5 \times 10^{13} \text{ g s}^{-1} = 5 \times 10^{-5} \dot{M}_{Edd}$) would place the accretion radius well beyond the corotation radius (e.g. $R_{\text{acc}} \sim 75 \text{ km}$ and $R_{\text{co}} \simeq 25 \text{ km}$ in PSR J1023+0038, see Eqs. 6.3 and 6.4). A

centrifugal barrier would be expected to inhibit completely the accretion inflow [99]. Magneto-hydrodynamic simulations [153] have shown that if the magnetosphere rotates only slightly faster than the disc matter ($R_{acc} \gtrsim R_{co}$), the propeller is *weak*; part of the inflowing mass manages to accrete and produce X-ray pulsations, the rest is bounced back to the disc in a non-collimated wind. Therefore, various attempts have been made to keep the accretion radius close to corotation at such a low \dot{M} , such as considering a high NS magnetic dipole inclination [36].

Papitto et al. [131, 133] argued instead that the mass accretion rate in the disc was higher than that deduced from the X-ray luminosity, so maintaining the accretion radius obtained with Eq. 6.3 close to the corotation surface. The propeller effect would eject most (>90%) of the disc mass with a low emission efficiency, and only a tiny fraction would make its way to the NS surface. Electrons would be accelerated at the magnetized ($B \sim 10^5\text{--}10^6$ G) turbulent disc/magnetosphere boundary and emit X-ray synchrotron photons. The Compton up-scattering of these photons up to a few GeVs in a few km-wide region would account for the gamma-ray emission.

Following D’Angelo et al. [57–59], it was alternatively proposed that the disc of tMSPs could be trapped in a low \dot{M} state, so avoiding the onset of a propeller [100]. The in-flowing matter would pile up at the corotation boundary rather than being ejected from the system, and the disc truncation radius would be locked close to the corotation boundary without any strong dependence on \dot{M} (see also [77] who obtained a similar result in the propeller framework).

The transitions between the *high* and *low* intensity modes could be due to a switching between an accretion/propeller and a rotation-powered state, respectively ([47, 117]; see the left panel of Fig. 6.10). In the *low* mode, the pulsar wind would be terminated in a shock beyond the light cylinder, which would hide the radio pulses [52] and produce the power-law shaped X-ray spectrum. In the *high* mode, the disc would get close to the corotation radius, with most of the emission produced at the boundary between the disc and the propellering magnetosphere [47]. The penetration of the disc within the light cylinder would force some magnetic field lines to open [136], explaining the slightly enhanced spin-down observed in the disc state compared to the radio pulsar state [45, 100, 137].

Bhattacharyya [22] has recently included such an additional spin-down component in the torque budget. The fraction of magnetic field lines opened by the disc intrusion inside the light cylinder was estimated from the observed increase of the γ -ray emission. The underlying non-standard assumption was that the magnetospheric processes invoked to explain the high energy emission in the rotation-powered state kept working in the disc state, even if the in-falling plasma was accreting onto the NS surface so driving the X-ray pulsations. Since the accretion torques are negligible compared to the pulsar spin-down torques, the overall budget could be ensured only by the inclusion of an additional spin-down torque. Such a component could be granted by the continuous gravitational radiation related to a permanent ellipticity of the NS yielding a quadrupole moment of $Q \simeq 1 - 2 \times 10^{36} \text{ g cm}^2$.

The increased spin-down due to the emission of gravitational waves had been first considered by Haskell and Patruno [90]. They assumed that asymmetries in pycno-nuclear reactions or an unstable r-mode developing in the accretion state only

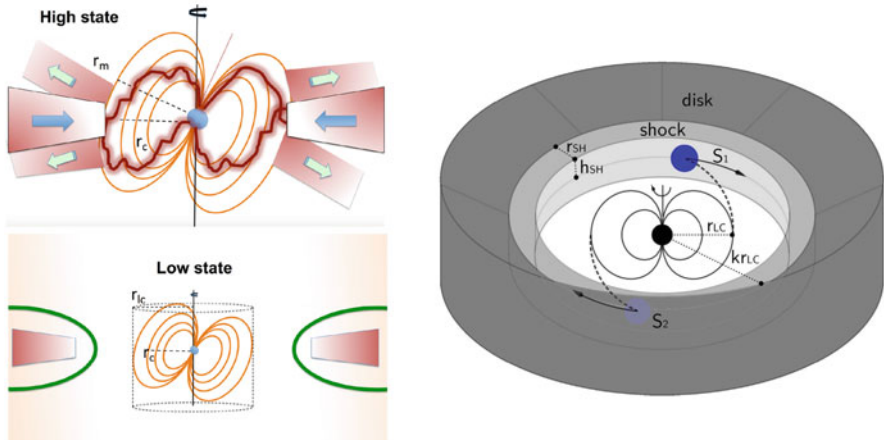


Fig. 6.10 *Left panel:* Cartoon view of the *high* and *low* mode transitions of PSR J1023+0038 in the *sub-luminous* disc state, according to the accretion/propeller interpretation [47, 117]. The disc extends down to the co-rotation radius in the *high* mode, whereas is bounced beyond the light cylinder radius in the *low* mode. Credit: Campana et al., A&A, 594, A31 (2016), reproduced with permission © ESO. *Right panel:* Sketch of the mini pulsar-wind nebula configuration proposed by [135] (see [194] for a similar geometry). Optical and X-ray synchrotron radiation is produced at S_1 and S_2 where the pulsar wind current sheets are terminated by the disk, and the particles there accelerated cool by interaction with the field that permeates the shock. Credit: Papitto et al., ApJ, 882, 104 (2019) © AAS. Reproduced with permission

could yield a NS mass quadrupole moment of $>4.4 \times 10^{35} \text{ g cm}^2$, strong enough to account for the observed increase of the spin-down. Deriving fully coherent X-ray and optical pulse timing solutions in the disc state, and a radio pulse timing solution at the onset of the next radio MSP phase will test this intriguing possibility, which predicts a gravitational wave amplitude in the range of the next generation interferometers such as the Einstein telescope.

Alternatively, Ertan [77] argued that the sub-luminous disc state and the radio pulsar state represented weak and strong propeller states, respectively (although there is no strong evidence of the presence of a disc extending close to the NS when radio pulses are observed); a decrease of the accretion radius in the weak propeller state would account for the increased propeller torque.

A Mini Pulsar-Wind Nebula The detection of relatively bright optical/UV pulsations from a tMSP in the disc state was hard to fit in the accretion framework [5, 135]⁸ The cyclotron self-absorbed optical emission produced in the accretion columns is expected to be much fainter than the values observed. A beaming of the emission by a factor of ~ 50 would be required to match the observations,

⁸ Similar difficulties hold to explain the optical/UV pulsations later detected during an X-ray accretion outburst of the AMXP SAX J1808.4–3658 [6].

but it seems unlikely given the sinusoidal shape of the pulses. The simultaneous appearance and disappearance of optical and X-ray pulsations, the similar shape and the possibility of describing the optical/X-ray pulsed spectral energy distribution with a single power-law, strongly suggested that they are produced by a common underlying process. As a consequence also the accretion interpretation of the X-ray pulses had to be questioned. Papitto et al. [135] and Veledina et al. [194] proposed that the disc was truncated just beyond the light cylinder also in the *high* mode and that both optical and X-ray pulsations originated at the pulsar wind termination shock (see the right panel of Fig. 6.10). In the so-called striped wind models (see, e.g., [34]), two current sheets carry the electromagnetic power of the pulsar wind outside the light cylinder. These would produce two rotating spots in the inner face of the wind/disc boundary in which particles are accelerated and quickly radiate optical and X-ray synchrotron photons, by interacting with the relatively strong field (\approx few $\times 10^5$ G) that permeates the shock. An observer would see these spots from a different angle at each rotational phase, so explaining the detection of coherent optical and X-ray pulsations. Indeed, the narrow emission and absorption lines observed at a few keV supported the presence of a hot and dense turbulent medium close to the light cylinder [53].

In the *low* intensity mode, the termination shock would be pushed outward and the pulsations would be smeared because the synchrotron emission time scale and the light travel time between different regions of the shock become longer [135]. In the *high* mode, the shock would instead approach the light cylinder, justifying the need of an additional absorbing component covering 30% of the emitting source to explain the change of the X-ray emission spectrum compared to the *low* mode [49, 125]. Alternatively, the *low* mode could be ascribed to the penetration of the disc plasma inside the light cylinder which would curb the termination shock emission [194].

Axisymmetric general-relativistic MHD simulations demonstrated that the pulsar electromagnetic wind can keep the plasma inflow beyond the light cylinder, creating a termination shock and inhibiting mass accretion [138]. Placing the termination shock close to the light cylinder would also help solve the stability issue of the equilibrium between the pulsar wind and the matter inflow beyond the light cylinder [76]. In this framework, episodes of magnetic reconnection at the termination shock, in the disc or from the donor star could also explain the observed flares [49].

Outflows The bright flat-spectrum radio emission [28, 72, 80] and the obscuration of the disc emission lines at certain orbital phases [65, 86] suggested that tMSPs launch outflows of plasma. The radio emission observed in the *high* mode is compatible with self-absorbed synchrotron emission from a compact jet, whose spectral break would be beyond the near-infrared band given the low accretion luminosity [14]. Less collimated outflows could also be launched by the propelling magnetosphere [131, 133] or by the pulsar wind [135].

On the other hand, a compact jet could hardly explain the radio brightening observed in the *low* X-ray intensity mode, since a correlation between the radio and X-ray luminosity would be expected. The sudden radio brightening at the onset

of an X-ray *low* mode indicated that the emission had to come from the vicinity of the NS. The launching of optically thin plasmoids by episodes of magnetic reconnection due to the complex field/disc interaction in the pulsar-wind framework [138] was considered the most likely explanation [28, 135, 194]. Reconnection of the magnetic field lines threading the disc, or of the donor star, could also explain the flares observed at all wavelengths [49].

The Variability Simulations of the complex interaction between the pulsar electromagnetic field and the disc plasma in a regime in which they have comparable energy densities [138, 153] helped understand the qualitative behaviour of tMSPs. However, they are limited to timescales of less than a second. The long-term changes of state, the *high-low* mode transitions and in general the flicker noise variability lasting up to a few hours, were clearly out of reach.

The swings between accretion and rotation-powered activity over a few years are generally attributed to changes in the ram pressure exerted by the matter captured by the gravitational field of the NS. However, it remains unclear what ultimately causes the \dot{M} to vary. A viscous disc instability is usually invoked to explain the transient behaviour of dwarf novae and X-ray binaries [112]. TMSPs challenged this interpretation since two very different accretion disc states were realized, a bright and a *sub-luminous* one. An advection dominated accretion flow may characterize the fainter state, and a more typical geometrically thin/optically thick disc may explain the former. However, it is puzzling that IGR J18245–2452 (and possibly XMM J174457–2850.3) was able to show both states just a few years apart. Also, it is not yet determined whether a disc-like flow manages to survive the pulsar wind pressure in the rotation-powered state (see Sect. 6.6.1). Variations in the mass-loss rate from the donor are unlikely driven by changes of its radius since the timescales involved are much longer even when high energy irradiation of the donor is considered. The magnetic activity of the secondary excited by its fast orbital-locked rotation is instead an intriguing possibility to drive surges of the mass transfer rate needed to squeeze the pulsar wind and start the formation of an accretion disc.

The driver of the recurring *high-low* mode transitions so frequently observed in the *sub-luminous* state, despite a chaotic and unstable disc/wind interaction, is also yet to determine. A flicker noise power-law extending to very low frequencies (10^{-3} – 10^{-4} Hz) characterized the X-ray power density spectra of both the bright outburst of IGR J18245–2452 and the *sub-luminous* states. Similar spectra have been sometimes observed from a few black hole binaries in the soft state, while the noise power density of AMXPs becomes flat below 0.1–1 Hz [193]. The fluctuations of the mass inflow rate in the outer disc, where the viscous time-scales are long, are usually invoked to explain such spectra [120]; these fluctuations must be able to propagate to the inner disc regions to produce the observed X-ray variability. In this framework, the *high-low* mode transitions occurring in tMSPs in the *sub-luminous* state (but also the two intensity states observed from IGR J18245–2452 in outburst, [80]) could reflect how the \dot{M} variations introduced in the outer disc eventually force the system into two well-defined luminosity states, related to the different regimes (accretion, propeller, radio pulsar) introduced earlier.

6.7 Conclusions

Almost a decade of observations of tMSPs demonstrated that variations in the mass inflow rate actually lead to very different states in quick succession. This unique property has allowed us to study the complex interaction between the in-flowing plasma and the pulsar electromagnetic field in different regimes.

Multi-wavelength and high-temporal resolution simultaneous observations of tMSPs have been crucial to glimpse the physical processes lying behind the *sub-luminous* disc state. Much has to be done yet, especially to understand the nature of the modes and the flares that characterise this state. For instance, establishing whether the X-ray and optical pulsations originate just outside the light cylinder, implying that the pulsar wind is terminated a few km away, would have important consequences to confirm the striped wind configuration and measure how it interacts with the surrounding matter. On one hand, searches for more optical MSPs in either accretion or rotation-powered systems will help assess the nature of optical pulsations. On the other, MHD simulations will help investigate the properties of the disc/wind intrabinary shock. In this regard, studies of tMSPs could play an important role as a benchmark for the theories that assume that a millisecond magnetar form after a double NS merger and powers a short gamma-ray burst (see Chap. 8).

Searches for new systems associated with gamma-ray sources and displaying a peculiar X-ray and optical behaviour are intensively ongoing. Together with the monitoring of redbacks and AMXPs, this will likely increase the number of confirmed tMSPs. This will be crucial to assess whether all the MSPs in tight binaries are potentially transitional, or other properties (e.g. magnetic activity of the secondary, NS magnetic dipole inclination, magnetic inclination) are required to yield the state transitions. Enlarging the sample has important consequences in the understanding of the population of short orbital period MSP binaries, rather than restricting to the case by case, as done so far.

Acknowledgments We acknowledge financial support from the Italian Space Agency (ASI) and National Institute for Astrophysics (INAF) under agreements ASI-INAF I/037/12/0 and ASI-INAF n.2017-14-H.0 and from INAF “Main streams”, Presidential Decree 43/2018 and “SKA/CTA projects”, Presidential Decree N. 70/2016. We acknowledge the extremely fruitful collaboration with F. Ambrosino, M. Baglio, E. Bozzo, L. Burderi, M. Burgay, S. Campana, P. Casella, F. Coti Zelati, P. D’Avanzo, T. Di Salvo, C. Ferrigno, A. Ghedina, A. Miraval Zanon, F. Meddi, E. Poretti, A. Possenti, N. Rea, A. Sanna, L. Stella, D. F. Torres, and many more with whom we have tackled the challenge of tMSPs in the last decade.

References

1. Abdollahi, S., et al.: Fermi large area telescope fourth source catalog. *Astrophys. J., Suppl. Ser.* **247**(1), 33 (2020). <https://doi.org/10.3847/1538-4365/ab6bcb>
2. Al Noori, H., Roberts, M.S.E., Torres, R.A., et al.: X-ray and optical studies of the redback system PSR J2129-0429. *Astrophys. J.* **861**(2), 89 (2018). <https://doi.org/10.3847/1538-4357/aac828>

3. Aliu, E., et al.: A search for very high energy gamma rays from the missing link binary pulsar J1023+0038 with VERITAS. *Astrophys. J.* **831**(2), 193 (2016). <https://doi.org/10.3847/0004-637X/831/2/193>
4. Alpar, M.A., Cheng, A.F., Ruderman, M.A., et al.: A new class of radio pulsars. *Nature* **300**(5894), 728–730 (1982). <https://doi.org/10.1038/300728a0>
5. Ambrosino, F., Papitto, A., Stella, L., et al.: Optical pulsations from a transitional millisecond pulsar. *Nat. Astron.* **1**, 854–858 (2017). <https://doi.org/10.1038/s41550-017-0266-2>
6. Ambrosino, F., Miraval Zanon, A., Papitto, A., et al.: Optical and ultraviolet pulsed emission from an accreting millisecond pulsar. *Nat. Astron.* **5**, 552 (2021). <https://doi.org/10.1038/s41550-021-01308-0>
7. Applegate, J.H., Shaham, J.: Orbital period variability in the eclipsing pulsar binary PSR B1957+20: evidence for a tidally powered star. *Astrophys. J.* **436**, 312 (1994). <https://doi.org/10.1086/174906>
8. Archibald, A.M., Bogdanov, S., Patruno, A., et al.: Accretion-powered pulsations in an apparently quiescent neutron star binary. *Astrophys. J.* **807**(1), 62 (2015). <https://doi.org/10.1088/0004-637X/807/1/62>
9. Archibald, A.M., Kaspi, V.M., Bogdanov, S., et al.: X-ray variability and evidence for pulsations from the unique radio pulsar/X-ray binary transition object FIRST J102347.6+003841. *Astrophys. J.* **722**(1), 88–95 (2010). <https://doi.org/10.1088/0004-637X/722/1/88>
10. Archibald, A.M., Kaspi, V.M., Hessels, J.W.T., et al.: Long-term radio timing observations of the transition millisecond pulsar PSR J1023+0038 (2013). arXiv e-prints arXiv:1311.5161
11. Archibald, A.M., Stairs, I.H., Ransom, S.M., et al.: A radio pulsar/X-ray binary link. *Science* **324**(5933), 1411 (2009). <https://doi.org/10.1126/science.1172740>
12. Arons, J., Tavani, M.: High-energy emission from the eclipsing millisecond pulsar PSR 1957+20. *Astrophys. J.* **403**, 249 (1993). <https://doi.org/10.1086/172198>
13. Baglio, M.C., D’Avanzo, P., Campana, S., et al.: Different twins in the millisecond pulsar recycling scenario: optical polarimetry of PSR J1023+0038 and XSS J12270-4859. *Astron. Astrophys.* **591**, A101 (2016). <https://doi.org/10.1051/0004-6361/201628383>
14. Baglio, M.C., Vincentelli, F., Campana, S., et al.: Peering at the outflow mechanisms in the transitional pulsar PSR J1023+0038: simultaneous VLT, XMM-Newton, and Swift high-time resolution observations. *Astron. Astrophys.* **631**, A104 (2019). <https://doi.org/10.1051/0004-6361/201936008>
15. Bahramian, A., Strader, J., Chomiuk, L., et al.: The MAVERIC survey: a transitional millisecond pulsar candidate in Terzan 5. *Astrophys. J.* **864**(1), 28 (2018). <https://doi.org/10.3847/1538-4357/aad68b>
16. Bahramian, A., Strader, J., Miller-Jones, J.C.A., et al.: The MAVERIC survey: Chandra/ACIS catalog of faint X-ray sources in 38 galactic globular clusters. *Astrophys. J.* **901**(1), 57 (2020). <https://doi.org/10.3847/1538-4357/aba51d>
17. Bailer-Jones, C.A.L., Rybizki, J., Fouesneau, M., et al.: Estimating distances from parallaxes. V. Geometric and photogeometric distances to 1.47 billion stars in gaia early data release 3. *Astron. J.*, 161, 147 (2021). <https://doi.org/10.3847/1538-3881/abd806>
18. Ballet, J., Burnett, T.H., Digel, S.W., et al.: Fermi large area telescope fourth source catalog data release 2 (2020). arXiv e-prints arXiv:2005.11208
19. Bassa, C.G., Patruno, A., Hessels, J.W.T., et al.: A state change in the low-mass X-ray binary XSS J12270-4859. *Mon. Notices Royal Astron. Soc.* **441**(2), 1825–1830 (2014). <https://doi.org/10.1093/mnras/stu708>
20. Bégin, S.: A search for fast pulsars in globular clusters. Master’s Thesis, University of British Columbia (2006)
21. Bhattacharya, D., van den Heuvel, E.P.J.: Formation and evolution of binary and millisecond radio pulsars. *Phys. Rep.* **203**(1-2), 1–124 (1991). [https://doi.org/10.1016/0370-1573\(91\)90064-S](https://doi.org/10.1016/0370-1573(91)90064-S)
22. Bhattacharyya, S.: The permanent ellipticity of the neutron star in PSR J1023+0038. *Mon. Notices Royal Astron. Soc.* **498**(1), 728–736 (2020). <https://doi.org/10.1093/mnras/staa2304>

23. Bhattacharyya, S., Bombaci, I., Band yopadhyay, D., et al.: Millisecond radio pulsars with known masses: parameter values and equation of state models. *New. Astron.* **54**, 61–71 (2017). <https://doi.org/10.1016/j.newast.2017.01.008>
24. Bisnovatyi-Kogan, G. S., Komberg, B. V.: Pulsars and close binary systems. *Sov. Ast.* **2**, 130 (1976).
25. Bogdanov, S.: A NuSTAR observation of the gamma-ray-emitting X-ray binary and transitional millisecond pulsar candidate 1RXS J154439.4-112820. *Astrophys. J.* **826**(1), 28 (2016). <https://doi.org/10.3847/0004-637X/826/1/28>
26. Bogdanov, S., Archibald, A.M., Bassa, C., et al.: Coordinated X-ray, ultraviolet, optical, and radio observations of the PSR J1023+0038 system in a low-mass X-ray binary state. *Astrophys. J.* **806**(2), 148 (2015). <https://doi.org/10.1088/0004-637X/806/2/148>
27. Bogdanov, S., Archibald, A.M., Hessels, J.W.T., et al.: A Chandra X-ray observation of the binary millisecond pulsar PSR J1023+0038. *Astrophys. J.* **742**(2), 97 (2011). <https://doi.org/10.1088/0004-637X/742/2/97>
28. Bogdanov, S., Deller, A.T., Miller-Jones, J.C.A., et al.: Simultaneous Chandra and VLA observations of the transitional millisecond pulsar PSR J1023+0038: anti-correlated X-ray and radio variability. *Astrophys. J.* **856**(1), 54 (2018). <https://doi.org/10.3847/1538-4357/aaeb9>
29. Bogdanov, S., Grindlay, J.E., van den Berg, M.: An X-ray variable millisecond pulsar in the globular cluster 47 tucanae: closing the link to low-mass X-ray binaries. *Astrophys. J.* **630**(2), 1029–1036 (2005). <https://doi.org/10.1086/432249>
30. Bogdanov, S., Halpern, J.P.: Identification of the high-energy gamma-ray source 3FGL J1544.6-1125 as a transitional millisecond pulsar binary in an accreting state. *Astrophys. J. Lett.* **803**(2), L27 (2015). <https://doi.org/10.1088/2041-8205/803/2/L27>
31. Bogdanov, S., Patruno, A., Archibald, A.M., et al.: X-ray observations of XSS J12270-4859 in a new low state: a transformation to a disk-free rotation-powered pulsar binary. *Astrophys. J.* **789**(1), 40 (2014). <https://doi.org/10.1088/0004-637X/789/1/40>
32. Bogdanov, S., van den Berg, M., Servillat, M., et al.: Chandra X-ray observations of 12 millisecond pulsars in the globular cluster M28. *Astrophys. J.* **730**(2), 81 (2011). <https://doi.org/10.1088/0004-637X/730/2/81>
33. Bogdanov, S., Bahramian, A., Heinke, C. O., et al.: A Deep Chandra X-ray observatory study of the millisecond pulsar population in the globular cluster Terzan 5. *Astrophys. J.* **912**, 124 (2021). <https://doi.org/10.3847/1538-4357/abee78>
34. Bogovalov, S.V.: On the physics of cold MHD winds from oblique rotators. *Astron. Astrophys.* **349**, 1017–1026 (1999)
35. Bond, H.E., White, R.L., Becker, R.H., et al.: FIRST J102347.6+003841: the first radio-selected cataclysmic variable. *Publ. Astron. Soc. Pac.* **114**(802), 1359–1363 (2002). <https://doi.org/10.1086/344381>
36. Bozzo, E., Ascenzi, S., Ducci, L., et al.: Magnetospheric radius of an inclined rotator in the magnetically threaded disk model. *Astron. Astrophys.* **617**, A126 (2018). <https://doi.org/10.1051/0004-6361/201732004>
37. Bozzo, E., Stella, L., Vietri, M., et al.: Can disk-magnetosphere interaction models and beat frequency models for quasi-periodic oscillation in accreting X-ray pulsars be reconciled? *Astron. Astrophys.* **493**(3), 809–818 (2009). <https://doi.org/10.1051/0004-6361:200810658>
38. Breton, R.P., van Kerkwijk, M.H., Roberts, M.S.E., et al.: Discovery of the optical counterparts to four energetic Fermi millisecond pulsars. *Astrophys. J.* **769**(2), 108 (2013). <https://doi.org/10.1088/0004-637X/769/2/108>
39. Britt, C.T., Strader, J., Chomiuk, L., et al.: Orbital dynamics of candidate transitional millisecond pulsar 3FGL J1544.6-1125: an unusually face-on system. *Astrophys. J.* **849**(1), 21 (2017). <https://doi.org/10.3847/1538-4357/aa8e41>

40. Broderick, J.W., Fender, R.P., Breton, R.P., Stewart, A.J., et al.: Low-radio-frequency eclipses of the redback pulsar J2215+5135 observed in the image plane with LOFAR. *Mon. Notices Royal Astron. Soc.* **459**(3), 2681–2689 (2016). <https://doi.org/10.1093/mnras/stw794>
41. Burderi, L., D'Antona, F., Burgay, M.: PSR J1740-5340: accretion inhibited by radio ejection in a binary millisecond pulsar in the globular cluster NGC 6397. *Astrophys. J.* **574**(1), 325–331 (2002). <https://doi.org/10.1086/340891>
42. Burderi, L., Di Salvo, T., D'Antona, F., et al.: The optical counterpart to SAX J1808.4-3658 in quiescence: evidence of an active radio pulsar? *Astron. Astrophys.* **404**, L43–L46 (2003). <https://doi.org/10.1051/0004-6361:20030669>
43. Burderi, L., Possenti, A., D'Antona, F., et al.: Where may ultrafast rotating neutron stars be hidden? *Astrophys. J. Lett.* **560**(1), L71–L74 (2001). <https://doi.org/10.1086/324220>
44. Burgay, M., Burderi, L., Possenti, A., et al.: A search for pulsars in quiescent soft X-ray transients. I. *Astrophys. J.* **589**(2), 902–910 (2003). <https://doi.org/10.1086/374690>
45. Burtovoi, A., Zampieri, L., Fiori, M., et al.: Spin-down rate of the transitional millisecond pulsar PSR J1023+0038 in the optical band with Aqueye+. *Mon. Notices Royal Astron. Soc.* (2020). <https://doi.org/10.1093/mnrasl/slaa133>
46. Campana, S., Colpi, M., Mereghetti, S., et al.: The neutron stars of soft X-ray transients. *Astron. Astrophys. Rev.* **8**(4), 279–316 (1998). <https://doi.org/10.1007/s001590050012>
47. Campana, S., Coti Zelati, F., Papitto, A., et al.: A physical scenario for the high and low X-ray luminosity states in the transitional pulsar PSR J1023+0038. *Astron. Astrophys.* **594**, A31 (2016). <https://doi.org/10.1051/0004-6361/201629035>
48. Campana, S., D'Avanzo, P., Casares, J., et al.: Indirect evidence of an active radio pulsar in the quiescent state of the transient millisecond pulsar SAX J1808.4-3658. *Astrophys. J. Lett.* **614**(1), L49–L52 (2004). <https://doi.org/10.1086/425495>
49. Campana, S., Miraval Zanon, A., Coti Zelati, F., et al.: Probing X-ray emission in different modes of PSR J1023+0038 with a radio pulsar scenario. *Astron. Astrophys.* **629**, L8 (2019). <https://doi.org/10.1051/0004-6361/201936312>
50. Campana, S., Stella, L., Gastaldello, F., et al.: An XMM-Newton study of the 401 Hz accreting pulsar SAX J1808.4-3658 in quiescence. *Astrophys. J. Lett.* **575**(1), L15–L19 (2002). <https://doi.org/10.1086/342505>
51. Cho, P.B., Halpern, J.P., Bogdanov, S.: Variable heating and flaring of three redback millisecond pulsar companions. *Astrophys. J.* **866**(1), 71 (2018). <https://doi.org/10.3847/1538-4357/aade92>
52. Coti Zelati, F., Baglio, M.C., Campana, S., et al.: Engulfing a radio pulsar: the case of PSR J1023+0038. *Mon. Notices Royal Astron. Soc.* **444**(2), 1783–1792 (2014). <https://doi.org/10.1093/mnras/stu1552>
53. Coti Zelati, F., Campana, S., Braito, V., et al.: Simultaneous broadband observations and high-resolution X-ray spectroscopy of the transitional millisecond pulsar PSR J1023+0038. *Astron. Astrophys.* **611**, A14 (2018). <https://doi.org/10.1051/0004-6361/201732244>
54. Coti Zelati, F., Papitto, A., de Martino, D., et al.: Prolonged sub-luminous state of the new transitional pulsar candidate CXOU J110926.4-650224. *Astron. Astrophys.* **622**, A211 (2019). <https://doi.org/10.1051/0004-6361/201834835>
55. Coti Zelati, F., Hugo, B., Torres, D. F., et al.: Simultaneous X-ray and radio observations of the transitional millisecond pulsar candidate CXOU J110926.4-650224. The discovery of a variable radio counterpart. *Astron. Astrophys.* **655**, A52 (2021). <https://doi.org/10.1051/0004-6361/202141431>
56. D'Amico, N., Possenti, A., Manchester, R.N., et al.: An eclipsing millisecond pulsar with a possible main-sequence companion in NGC 6397. *Astrophys. J. Lett.* **561**(1), L89–L92 (2001). <https://doi.org/10.1086/324562>
57. D'Angelo, C.R., Spruit, H.C.: Episodic accretion on to strongly magnetic stars. *Mon. Notices Royal Astron. Soc.* **406**(2), 1208–1219 (2010). <https://doi.org/10.1111/j.1365-2966.2010.16749.x>

58. D'Angelo, C.R., Spruit, H.C.: Long-term evolution of discs around magnetic stars. *Mon. Notices Royal Astron. Soc.* **416**(2), 893–906 (2011). <https://doi.org/10.1111/j.1365-2966.2011.19029.x>
59. D'Angelo, C.R., Spruit, H.C.: Accretion discs trapped near corotation. *Mon. Notices Royal Astron. Soc.* **420**(1), 416–429 (2012). <https://doi.org/10.1111/j.1365-2966.2011.20046.x>
60. D'Avanzo, P., Campana, S., Casares, J., et al.: The optical counterparts of accreting millisecond X-ray pulsars during quiescence. *Astron. Astrophys.* **508**(1), 297–308 (2009). <https://doi.org/10.1051/0004-6361/200810249>
61. Davidson, K., Ostriker, J.P.: Neutron-star accretion in a stellar wind: model for a pulsed X-ray source. *Astrophys. J.* **179**, 585–598 (1973). <https://doi.org/10.1086/151897>
62. De Falco, V., Kuiper, L., Bozzo, E., et al.: The transitional millisecond pulsar IGR J18245-2452 during its 2013 outburst at X-rays and soft gamma-rays. *Astron. Astrophys.* **603**, A16 (2017). <https://doi.org/10.1051/0004-6361/201730600>
63. de Martino, D., Belloni, T., Falanga, M., et al.: X-ray follow-ups of XSS J12270-4859: a low-mass X-ray binary with gamma-ray Fermi-LAT association. *Astron. Astrophys.* **550**, A89 (2013). <https://doi.org/10.1051/0004-6361/201220393>
64. de Martino, D., Casares, J., Mason, E., et al.: Unveiling the redback nature of the low-mass X-ray binary XSS J1227.0-4859 through optical observations. *Mon. Notices Royal Astron. Soc.* **444**(4), 3004–3014 (2014). <https://doi.org/10.1093/mnras/stu1640>
65. de Martino, D., Falanga, M., Bonnet-Bidaud, J.M., et al.: The intriguing nature of the high-energy gamma ray source XSS J12270-4859. *Astron. Astrophys.* **515**, A25 (2010). <https://doi.org/10.1051/0004-6361/200913802>
66. de Martino, D., Papitto, A., Belloni, T., et al.: Multiwavelength observations of the transitional millisecond pulsar binary XSS J12270-4859. *Mon. Notices Royal Astron. Soc.* **454**(2), 2190–2198 (2015). <https://doi.org/10.1093/mnras/stv2109>
67. de Martino, D., Papitto, A., Burgay, M., et al., Belloni, T.M.: NuSTAR and Parkes observations of the transitional millisecond pulsar binary XSS J12270-4859 in the rotation-powered state. *Mon. Notices Royal Astron. Soc.* **492**(4), 5607–5619 (2020). <https://doi.org/10.1093/mnras/staa164>
68. de Óña Wilhelmi, E., Papitto, A., Li, J., Rea, N., et al.: SAX J1808.4-3658, an accreting millisecond pulsar shining in gamma rays? *Mon. Notices Royal Astron. Soc.* **456**(3), 2647–2653 (2016). <https://doi.org/10.1093/mnras/stv2695>
69. Degenaar, N., Wijnands, R., Miller, J.M., et al.: The Swift X-ray monitoring campaign of the center of the Milky Way. *J. High Energy Astrophys.* **7**, 137–147 (2015). <https://doi.org/10.1016/j.jheap.2015.03.005>
70. Degenaar, N., Wijnands, R., Reynolds, M.T., et al.: The peculiar galactic center neutron star X-ray binary XMM J174457-2850.3. *Astrophys. J.* **792**(2), 109 (2014). <https://doi.org/10.1088/0004-637X/792/2/109>
71. Deller, A.T., Archibald, A.M., Brisken, W.F., et al.: A parallax distance and mass estimate for the transitional millisecond pulsar system J1023+0038. *Astrophys. J. Lett.* **756**(2), L25 (2012). <https://doi.org/10.1088/2041-8205/756/2/L25>
72. Deller, A.T., Moldon, J., Miller-Jones, J.C.A., et al.: Radio imaging observations of PSR J1023+0038 in an LMXB state. *Astrophys. J.* **809**(1), 13 (2015). <https://doi.org/10.1088/0004-637X/809/1/13>
73. di Salvo, T., Burderi, L., Riggio, A., et al.: Orbital evolution of an accreting millisecond pulsar: witnessing the banquet of a hidden black widow? *Mon. Notices Royal Astron. Soc.* **389**(4), 1851–1857 (2008). <https://doi.org/10.1111/j.1365-2966.2008.13709.x>
74. Dubus, G., Lamberts, A., Fromang, S.: Modelling the high-energy emission from gamma-ray binaries using numerical relativistic hydrodynamics. *Astron. Astrophys.* **581**, A27 (2015). <https://doi.org/10.1051/0004-6361/201425394>
75. Eckert, D., Del Santo, M., Bazzano, A., et al.: IGR J18245-2452: a new hard X-ray transient discovered by INTEGRAL. *Astronomer's Telegram* **4925**, 1 (2013)
76. Ekşİ, K.Y., Alpar, M.A.: Disks surviving the radiation pressure of radio pulsars. *Astrophys. J.* **620**(1), 390–397 (2005). <https://doi.org/10.1086/425959>

77. Ertan, Ü.: Accretion and propeller torque in the spin-down phase of neutron stars: The case of transitional millisecond pulsar PSR J1023+0038. *Mon. Notices Royal Astron. Soc.* **479**(1), L12–L16 (2018). <https://doi.org/10.1093/mnrasl/sly089>
78. Fabian, A.C., Pringle, J.E., Verbunt, F., et al.: Do galactic bulge X-ray sources evolve into millisecond pulsars? *Nature* **301**(5897), 222–223 (1983). <https://doi.org/10.1038/301222a0>
79. Fender, R.: Disc-jet-wind coupling in black hole binaries, and other stories. *Astron. Nachr.* **337**(4–5), 381 (2016). <https://doi.org/10.1002/asna.201612317>
80. Ferrigno, C., Bozzo, E., Papitto, A., et al.: Hiccup accretion in the swinging pulsar IGR J18245-2452. *Astron. Astrophys.* **567**, A77 (2014). <https://doi.org/10.1051/0004-6361/201322904>
81. Gaia Collaboration: Gaia early data release 3. Summary of the contents and survey properties. *Astron. Astrophys.* **649**, A1 (2021). <https://doi.org/10.1051/0004-6361/202039657>
82. Gallo, E., Degenaar, N., van den Eijnden, J.: Hard state neutron star and black hole X-ray binaries in the radio:X-ray luminosity plane. *Mon. Notices Royal Astron. Soc.* **478**(1), L132–L136 (2018). <https://doi.org/10.1093/mnrasl/sly083>
83. Ghosh, P., Lamb, F.K.: Accretion by rotating magnetic neutron stars. III. Accretion torques and period changes in pulsating X-ray sources. *Astrophys. J.* **234**, 296–316 (1979). <https://doi.org/10.1086/157498>
84. Guillemot, L., Octau, F., Cognard, I., et al.: Timing of PSR J2055+3829, an eclipsing black widow pulsar discovered with the Nançay Radio Telescope. *Astron. Astrophys.* **629**(1), A92 (2019). <https://doi.org/10.1051/0004-6361/201936015>
85. Hakala, P., Kajava, J.J.E.: Variable polarisation and Doppler tomography of PSR J1023+0038—Evidence for the magnetic propeller during flaring? *Mon. Notices Royal Astron. Soc.* **474**(3), 3297–3306 (2018). <https://doi.org/10.1093/mnras/stx2922>
86. Halpern, J.P., Bogdanov, S., Thorstensen, J.R.: X-ray and optical study of the gamma-ray source 3FGL J0838.8–2829: identification of a candidate millisecond pulsar binary and an asynchronous polar. *Astrophys. J.* **838**(2), 124 (2017). <https://doi.org/10.3847/1538-4357/838/2/124>
87. Halpern, J.P., Gaidos, E., Sheffield, A., Price-Whelan, A.M., et al.: Optical observations of the binary MSP J1023+0038 in a new accreting state. *Astronomer's Telegram* **5514**, 1 (2013)
88. Halpern, J.P., Gaidos, E., Sheffield, A., et al.: Optical observations of the binary MSP J1023+0038 in a new accreting state. *Astronomer's Telegram* **5514**, 1 (2013)
89. Hartman, J.M., Patruno, A., Chakrabarty, D., et al.: The long-term evolution of the spin, pulse shape, and orbit of the accretion-powered millisecond pulsar SAX J1808.4-3658. *Astrophys. J.* **675**(2), 1468–1486 (2008). <https://doi.org/10.1086/527461>
90. Haskell, B., Patruno, A.: Are gravitational waves spinning down PSR J 1023 +0038 ? *Phys. Rev. Lett.* **119**(16), 161103 (2017). <https://doi.org/10.1103/PhysRevLett.119.161103>
91. Heinke, C.O., Bahramian, A., Degenaar, N., et al.: The nature of very faint X-ray binaries: hints from light curves. *Mon. Notices Royal Astron. Soc.* **447**(4), 3034–3043 (2015). <https://doi.org/10.1093/mnras/stu2652>
92. Heinke, C.O., Jonker, P.G., Wijnands, R., et al.: Further constraints on thermal quiescent X-ray emission from SAX J1808.4-3658. *Astrophys. J.* **691**(2), 1035–1041 (2009). <https://doi.org/10.1088/0004-637X/691/2/1035>
93. Hernandez Santisteban, J.V.: Multi-wavelength Observations of Accreting Compact Objects. Ph.D. Thesis, University of Southampton (2016)
94. Jaodand, A.: Unravelling the nature of transitional millisecond pulsars. Ph.D. Thesis, University of Amsterdam (2019)
95. Hill, A.B., Szostek, A., Corbel, S., et al.: The bright unidentified γ-ray source 1FGL J1227.9-4852: can it be associated with a low-mass X-ray binary? *Mon. Notices Royal Astron. Soc.* **415**(1), 235–243 (2011). <https://doi.org/10.1111/j.1365-2966.2011.18692.x>

96. Homer, L., Szkody, P., Chen, B., et al.: XMM-Newton and optical follow-up observations of SDSS J093249.57+472523.0 and SDSS J102347.67+003841.2. *Astron. J.* **131**(1), 562–570 (2006). <https://doi.org/10.1086/498346>
97. Iacolina, M.N., Burgay, M., Burderi, L., et al.: Searching for pulsed emission from XTE J0929-314 at high radio frequencies. *Astron. Astrophys.* **497**(2), 445–450 (2009). <https://doi.org/10.1051/0004-6361/200810677>
98. Iacolina, M.N., Burgay, M., Burderi, L., et al.: Search for pulsations at high radio frequencies from accreting millisecond X-ray pulsars in quiescence. *Astron. Astrophys.* **519**, A13 (2010). <https://doi.org/10.1051/0004-6361/201014025>
99. Illarionov, A.F., Sunyaev, R.A.: Why the number of galactic X-ray stars is so small? *Astron. Astrophys.* **39**, 185 (1975)
100. Jaodand, A., Archibald, A.M., Hessels, J.W.T., et al.: Timing observations of PSR J1023+0038 during a low-mass X-ray binary state. *Astrophys. J.* **830**(2), 122 (2016). <https://doi.org/10.3847/0004-637X/830/2/122>
101. Jaodand, A., Deller, A. T., Gusinskaia, N., et al.: Quasi-simultaneous radio/X-ray observations of the candidate transitional millisecond pulsar 3FGL J1544.6-1125 during its low-luminosity accretion-disc state (2021). arXiv:2110.10706
102. Jaodand, A.D., Hernández Santisteban, J.V., Archibald, A.M., et al., Discovery of UV millisecond pulsations and moding in the low mass X-ray binary state of transitional millisecond pulsar J1023+0038, arXiv:2102.13145
103. Johnson, T.J., Ray, P.S., Roy, J., et al.: Discovery of gamma-ray pulsations from the transitional redback PSR J1227-4853. *Astrophys. J.* **806**(1), 91 (2015). <https://doi.org/10.1088/0004-637X/806/1/91>
104. Kandel, D., Romani, R.W., An, H.: The synchrotron emission pattern of intrabinary shocks. *Astrophys. J.* **879**(2), 73 (2019). <https://doi.org/10.3847/1538-4357/ab24d9>
105. Kandel, D., Romani, R. W., Filippenko, A. V., et al.: Heated poles on the companion of redback PSR J2339-0533 *Astrophys. J.*, 903, 39 (2020). <https://doi.org/10.3847/1538-4357/abb6fd>
106. Karpov, S., Beskin, G., Plokhotnichenko, V., et al.: The study of coherent optical pulsations of the millisecond pulsar PSR J1023+0038 on Russian 6-m telescope. *Astron. Nachr.* **340**(7), 607–612 (2019). <https://doi.org/10.1002/asna.201913663>
107. Kennedy, M.R., Breton, R.P., Clark, C.J., et al.: Optical, X-ray, and γ -ray observations of the candidate transitional millisecond pulsar 4FGL J0427.8-6704 (2020). arXiv e-prints arXiv:2003.13718
108. Kennedy, M.R., Clark, C.J., Voisin, G., et al.: Kepler K2 observations of the transitional millisecond pulsar PSR J1023+0038. *Mon. Notices Royal Astron. Soc.* **477**(1), 1120–1132 (2018). <https://doi.org/10.1093/mnras/sty731>
109. Kluzniak, W., Ruderman, M., Shaham, J., et al.: Nature and evolution of the eclipsing millisecond binary pulsar PSR1957 + 20. *Nature* **334**(6179), 225–227 (1988). <https://doi.org/10.1038/334225a0>
110. Kong, A.K.H., Hui, C.Y., Takata, J., et al.: A NuSTAR observation of the gamma-ray emitting millisecond pulsar PSR J1723-2837. *Astrophys. J.* **839**(2), 130 (2017). <https://doi.org/10.3847/1538-4357/aa6aa2>
111. Kulkarni, A.K., Romanova, M.M.: Analytical hotspot shapes and magnetospheric radius from 3D simulations of magnetospheric accretion. *Mon. Notices Royal Astron. Soc.* **433**(4), 3048–3061 (2013). <https://doi.org/10.1093/mnras/stt945>
112. Lasota, J.P.: The disc instability model of dwarf novae and low-mass X-ray binary transients. *New Astron. Rev.* **45**(7), 449–508 (2001). [https://doi.org/10.1016/S1387-6473\(01\)00112-9](https://doi.org/10.1016/S1387-6473(01)00112-9)
113. Lee, J., Hui, C.Y., Takata, J., et al.: X-ray census of millisecond pulsars in the galactic field. *Astrophys. J.* **864**(1), 23 (2018). <https://doi.org/10.3847/1538-4357/aad284>
114. Li, K.L., Kong, A.K.H., Takata, J., et al.: NuSTAR observations and broadband spectral energy distribution modeling of the millisecond pulsar binary PSR J1023+0038. *Astrophys. J.* **797**(2), 111 (2014). <https://doi.org/10.1088/0004-637X/797/2/111>

115. Li, K.L., Strader, J., Miller-Jones, J.C.A., et al.: The flare-dominated accretion mode of a radio-bright candidate transitional millisecond pulsar (2020). arXiv e-prints arXiv:2004.14573
116. Linares, M.: X-ray states of redback millisecond pulsars. *Astrophys. J.* **795**(1), 72 (2014). <https://doi.org/10.1088/0004-637X/795/1/72>
117. Linares, M., Bahramian, A., Heinke, C., et al.: The neutron star transient and millisecond pulsar in M28: from sub-luminous accretion to rotation-powered quiescence. *Mon. Notices Royal Astron. Soc.* **438**(1), 251–261 (2014). <https://doi.org/10.1093/mnras/stt2167>
118. Lipunov, V.M.: The ecology of rotators. *Astrophys. Space Sci.* **132**(1), 1–51 (1987). <https://doi.org/10.1007/BF00637779>
119. Lyne, A.G., Brinklow, A., Middleditch, J., et al.: The discovery of a millisecond pulsar in the globular cluster M28. *Nature* **328**(6129), 399–401 (1987). <https://doi.org/10.1038/328399a0>
120. Lyubarskii, Y.E.: Flicker noise in accretion discs. *Mon. Notices Royal Astron. Soc.* **292**(3), 679–685 (1997). <https://doi.org/10.1093/mnras/292.3.679>
121. Masetti, N., Morelli, L., Palazzi, E., et al.: Unveiling the nature of INTEGRAL objects through optical spectroscopy. V. Identification and properties of 21 southern hard X-ray sources. *Astron. Astrophys.* **459**(1), 21–30 (2006). <https://doi.org/10.1051/0004-6361:20066055>
122. Masetti, N., Sbarufatti, B., Parisi, P., et al.: BL Lacertae identifications in a ROSAT-selected sample of Fermi unidentified objects. *Astron. Astrophys.* **559**, A58 (2013). <https://doi.org/10.1051/0004-6361/201322611>
123. McConnell, O., Callanan, P.J., Kennedy, M., et al.: Roche lobe underfilling of the secondary star in PSR J102347.6+003841? *Mon. Notices Royal Astron. Soc.* **451**(4), 3468–3472 (2015). <https://doi.org/10.1093/mnras/stv1197>
124. Miller, J.M., Swihart, S.J., Strader, J., et al.: A new candidate transitional millisecond pulsar in the sub-luminous disk state: 4FGL J0407.7–5702 (2020). arXiv e-prints arXiv:2009.09054
125. Miraval Zanon, A., Campana, S., Ridolfi, A., et al.: X-ray study of high-and-low luminosity modes and peculiar low-soft-and-hard activity in the transitional pulsar XSS J12270-4859. *Astron. Astrophys.* **635**, A30 (2020). <https://doi.org/10.1051/0004-6361/201936356>
126. Miraval Zanon, A., D’Avanzo, P., Ridolfi, A., et al.: Evidence of intra-binary shock emission from the redback pulsar PSR J1048+2339. *Astron. Astrophys.* **649**, A120 (2021). <https://doi.org/10.1051/0004-6361/202040071>
127. Nolan, P.L., et al.: Fermi large area telescope second source catalog. *Astrophys. J., Suppl. Ser.* **199**(2), 31 (2012). <https://doi.org/10.1088/0067-0049/199/2/31>
128. Paduano, A., Bahramian, A., Miller-Jones, J. C. A., et al.: The MAVERIC survey: simultaneous chandra and VLA observations of the transitional millisecond pulsar candidate NGC 6652B. *Mon. Notices Royal Astron. Soc.* **506**, 4107 (2021). <https://doi.org/10.1093/mnras/stab1928>
129. Pallanca, C., Dalessandro, E., Ferraro, F.R., et al.: The optical counterpart to the X-ray transient IGR J1824-24525 in the globular cluster M28. *Astrophys. J.* **773**(2), 122 (2013). <https://doi.org/10.1088/0004-637X/773/2/122>
130. Papitto, A., Ferrigno, C., Bozzo, E., Rea, et al.: Swings between rotation and accretion power in a binary millisecond pulsar. *Nature* **501**(7468), 517–520 (2013). <https://doi.org/10.1038/nature12470>
131. Papitto, A., Torres, D.F., Li, J.: A propeller scenario for the gamma-ray emission of low-mass X-ray binaries: the case of XSS J12270-4859. *Mon. Notices Royal Astron. Soc.* **438**(3), 2105–2116 (2014). <https://doi.org/10.1093/mnras/stt2336>
132. Papitto, A., de Martino, D., Belloni, T.M., et al.: X-ray coherent pulsations during a sub-luminous accretion disc state of the transitional millisecond pulsar XSS J12270-4859. *Mon. Notices Royal Astron. Soc.* **449**, L26–L30 (2015). <https://doi.org/10.1093/mnrasl/slv013>
133. Papitto, A., Torres, D.F.: A Propeller model for the sub-luminous state of the transitional millisecond pulsar PSR J1023+0038. *Astrophys. J.* **807**(1), 33 (2015). <https://doi.org/10.1088/0004-637X/807/1/33>

134. Papitto, A., Rea, N., Coti Zelati, F., et al.: The first continuous optical monitoring of the transitional millisecond pulsar PSR J1023+0038 with Kepler. *Astrophys. J. Lett.* **858**(2), L12 (2018). <https://doi.org/10.3847/2041-8213/aabee9>
135. Papitto, A., Ambrosino, F., Stella, L., et al.: Pulsating in unison at optical and X-ray energies: simultaneous high time resolution observations of the transitional millisecond pulsar PSR J1023+0038. *Astrophys. J.* **882**(2), 104 (2019). <https://doi.org/10.3847/1538-4357/ab2fdf>
136. Parfrey, K., Spitkovsky, A., Beloborodov, A.M.: Torque enhancement, spin equilibrium, and jet power from disk-induced opening of pulsar magnetic fields. *Astrophys. J.* **822**(1), 33 (2016). <https://doi.org/10.3847/0004-637X/822/1/33>
137. Parfrey, K., Spitkovsky, A., Beloborodov, A.M.: Simulations of the magnetospheres of accreting millisecond pulsars. *Mon. Notices Royal Astron. Soc.* **469**(3), 3656–3669 (2017). <https://doi.org/10.1093/mnras/stx950>
138. Parfrey, K., Tchekhovskoy, A.: General-relativistic simulations of four states of accretion onto millisecond pulsars. *Astrophys. J. Lett.* **851**(2), L34 (2017). <https://doi.org/10.3847/2041-8213/aa9c85>
139. Patruno, A., Archibald, A.M., Hessels, J.W.T., et al.: A new accretion disk around the missing link binary system PSR J1023+0038. *Astrophys. J. Lett.* **781**(1), L3 (2014). <https://doi.org/10.1088/2041-8205/781/1/L3>
140. Patruno, A., Jaodand, A., Kuiper, L., et al.: Radio pulse search and X-ray monitoring of SAX J1808.4-3658: what causes its orbital evolution? *Astrophys. J.* **841**(2), 98 (2017). <https://doi.org/10.3847/1538-4357/aa6f5b>
141. Pletsch, H. J. & Clark, C. J.: gamma-ray timing of redback PSR J2339-0533: hints for gravitational quadrupole moment changes. *Astrophys. J.* **807**, 18 (2015). <https://doi.org/10.1088/0004-637X/807/1/18>
142. Possenti, A., Cerutti, R., Colpi, M., et al.: Re-examining the X-ray versus spin-down luminosity correlation of rotation powered pulsars. *Astron. Astrophys.* **387**, 993–1002 (2002). <https://doi.org/10.1051/0004-6361:20020472>
143. Pretorius, M.L.: Time-resolved optical observations of five cataclysmic variables detected by INTEGRAL. *Mon. Notices Royal Astron. Soc.* **395**(1), 386–393 (2009). <https://doi.org/10.1111/j.1365-2966.2009.14521.x>
144. Radhakrishnan, V., Srinivasan, G.: On the origin of the recently discovered ultra-rapid pulsar. *Curr. Sci.* **51**, 1096–1099 (1982)
145. Rappaport, S.A., Fregeau, J.M., Spruit, H.: Accretion onto fast X-ray pulsars. *Astrophys. J.* **606**(1), 436–443 (2004). <https://doi.org/10.1086/382863>
146. Rea, N., Coti Zelati, F.C., Esposito, P., et al.: Multiband study of RX J0838-2827 and XMM J083850.4-282759: a new asynchronous magnetic cataclysmic variable and a candidate transitional millisecond pulsar. *Mon. Notices Royal Astron. Soc.* **471**(3), 2902–2916 (2017). <https://doi.org/10.1093/mnras/stx1560>
147. Ridolfi, A., Gautam, T., Freire, P. C. C., et al.: Eight new millisecond pulsars from the first MeerKAT globular cluster census. *Mon. Notices Royal Astron. Soc.* **504**, 1407 (2021). <https://doi.org/10.1093/mnras/stab790>
148. Rivera Sandoval, L.E., Hernández Santisteban, J.V., Degenaar, N., et al.: Mid-UV studies of the transitional millisecond pulsars XSS J12270-4859 and PSR J1023+0038 during their radio pulsar states. *Mon. Notices Royal Astron. Soc.* **476**(1), 1086–1099 (2018). <https://doi.org/10.1093/mnras/sty291>
149. Roberts, M.S.E.: Surrounded by spiders! New black widows and redbacks in the Galactic field. In: van Leeuwen, J. (ed.) *Neutron Stars and Pulsars: Challenges and Opportunities after 80 years*, IAU Symposium, vol. 291, pp. 127–132 (2013). <https://doi.org/10.1017/S174392131202337X>
150. Roberts, M.S.E., Al Noori, H., Torres, R.A., et al.: X-ray and optical properties of black widows and redbacks. In: Weltevrede, P., Perera, B.B.P., Preston, L.L., Samidas, S. (eds.) *Pulsar Astrophysics the Next Fifty Years*, IAU Symposium, vol. 337, pp. 43–46 (2018). <https://doi.org/10.1017/S1743921318000480>

151. Romani, R.W. & Shaw, M.S.: The orbit and companion of probable γ -ray pulsar J2339-0533. *Astrophys. J. Lett.*, **743**, L26 (2011). <https://doi.org/10.1088/2041-8205/743/2/L26>
152. Romani, R.W., Sanchez, N.: Intra-binary shock heating of black widow companions. *Astrophys. J.* **828**(1), 7 (2016). <https://doi.org/10.3847/0004-637X/828/1/7>
153. Romanova, M.M., Blinova, A.A., Ustyugova, G.V., et al.: Properties of strong and weak propellers from MHD simulations. *New. Astron.* **62**, 94–114 (2018). <https://doi.org/10.1016/j.newast.2018.01.011>
154. Romanova, M.M., Owocki, S.P.: Accretion, outflows, and winds of magnetized stars. *Space Sci. Rev.* **191**(1–4), 339–389 (2015). <https://doi.org/10.1007/s11214-015-0200-9>
155. Romanova, M.M., Ustyugova, G.V., Koldoba, A.V., et al.: The propeller regime of disk accretion to a rapidly rotating magnetized star. *Astrophys. J. Lett.* **616**(2), L151–L154 (2004). <https://doi.org/10.1086/426586>
156. Roy, J., Ray, P.S., Bhattacharyya, B., et al.: Discovery of Psr J1227-4853: a transition from a low-mass X-ray binary to a redback millisecond pulsar. *Astrophys. J. Lett.* **800**(1), L12 (2015). <https://doi.org/10.1088/2041-8205/800/1/L12>
157. Ruderman, M., Shaham, J., Tavani, M.: Accretion turnoff and rapid evaporation of very light secondaries in low-mass X-ray binaries. *Astrophys. J.* **336**, 507 (1989). <https://doi.org/10.1086/167029>
158. Ruderman, M., Shaham, J., Tavani, M., et al.: Late evolution of very low mass X-ray binaries sustained by radiation from their primaries. *Astrophys. J.* **343**, 292 (1989). <https://doi.org/10.1086/167704>
159. Saitou, K., Tsujimoto, M., Ebisawa, K., et al.: Suzaku X-ray study of an anomalous source XSS J12270-4859. *Publ. Astron. Soc. Pac. Jpn.* **61**, L13 (2009). <https://doi.org/10.1093/pasj/61.L13>
160. Saitou, K., Tsujimoto, M., Ebisawa, K., et al.: Near-infrared and X-ray observations of XSS J12270-4859. *Publ. Astron. Soc. Pac. Jpn.* **63**, S759–S769 (2011). <https://doi.org/10.1093/pasj/63.sp3.S759>
161. Salvetti, D., Mignani, R.P., De Luca, A., et al.: A multiwavelength investigation of candidate millisecond pulsars in unassociated γ -ray sources. *Mon. Notices Royal Astron. Soc.* **470**(1), 466–480 (2017). <https://doi.org/10.1093/mnras/stx1247>
162. Sanchez, N., Romani, R.W.: B-ducted heating of black widow companions. *Astrophys. J.* **845**(1), 42 (2017). <https://doi.org/10.3847/1538-4357/aa7a02>
163. Sazonov, S.Y., Revnivtsev, M.G.: Statistical properties of local active galactic nuclei inferred from the RXTE 3–20 keV all-sky survey. *Astron. Astrophys.* **423**, 469–480 (2004). <https://doi.org/10.1051/0004-6361:20047150>
164. Shahbaz, T., Dallilar, Y., Garner, A., et al.: Evidence for hot clumpy accretion flow in the transitional millisecond pulsar PSR J1023+0038. *Mon. Notices Royal Astron. Soc.* **477**(1), 566–577 (2018). <https://doi.org/10.1093/mnras/sty562>
165. Shahbaz, T., Linares, M., Nevado, S.P., et al.: The binary millisecond pulsar PSR J1023+0038 during its accretion state—I. Optical variability. *Mon. Notices Royal Astron. Soc.* **453**(4), 3461–3473 (2015). <https://doi.org/10.1093/mnras/stv1686>
166. Shahbaz, T., Linares, M., Rodríguez-Gil, P., et al.: The binary millisecond pulsar PSR J1023+0038—II. Optical spectroscopy. *Mon. Notices Royal Astron. Soc.* **488**(1), 198–212 (2019). <https://doi.org/10.1093/mnras/stz1652>
167. Shvartsman, V.F.: The influence of stellar wind on accretion. *Sov. Ast.* **14**, 527 (1970)
168. Shvartsman, V.F.: Neutron stars in binary systems should not be pulsars. *Sov. Ast.* **15**, 342 (1971)
169. Sironi, L., Keshet, U., Lemoine, M.: Relativistic shocks: particle acceleration and magnetization. *Space Sci. Rev.* **191**(1–4), 519–544 (2015). <https://doi.org/10.1007/s11214-015-0181-8>
170. Spitkovsky, A.: Time-dependent force-free pulsar magnetospheres: axisymmetric and oblique rotators. *Astrophys. J. Lett.* **648**(1), L51–L54 (2006). <https://doi.org/10.1086/507518>
171. Spruit, H.C., Taam, R.E.: An instability associated with a magnetosphere-disk interaction. *Astrophys. J.* **402**, 593 (1993). <https://doi.org/10.1086/172162>

172. Srinivasan, G., van den Heuvel, E.P.J.: Some constraints on the evolutionary history of the binary pulsar PSR1913+16. *Astron. Astrophys.* **108**, 143–147 (1982)
173. Stappers, B.W., Archibald, A.M., Hessels, J.W.T., et al.: A state change in the missing link binary pulsar system PSR J1023+0038. *Astrophys. J.* **790**(1), 39 (2014). <https://doi.org/10.1088/0004-637X/790/1/39>
174. Stella, L., Campana, S., Colpi, M., et al.: Do quiescent soft X-ray transients contain millisecond radio pulsars? *Astrophys. J. Lett.* **423**, L47 (1994). <https://doi.org/10.1086/187232>
175. Strader, J., Li, K.L., Chomiuk, L., et al.: A new γ -ray loud, eclipsing low-mass X-ray binary. *Astrophys. J.* **831**(1), 89 (2016). <https://doi.org/10.3847/0004-637X/831/1/89>
176. Strader, J., Swihart, S., Chomiuk, L., et al.: Optical spectroscopy and demographics of redback millisecond pulsar binaries. *Astrophys. J.* **872**(1), 42 (2019). <https://doi.org/10.3847/1538-4357/aafbaa>
177. Stringer, J. G., Breton, R. P., Clark, C. J., et al.: Optical photometry of two transitional millisecond pulsars in the radio pulsar state. *Mon. Notices Royal Astron. Soc.*, 507, 2174 (2021). <https://doi.org/10.1093/mnras/stab2167>
178. Strader, J., Swihart, S. J., Urquhart, R., et al.: Multiwavelength evidence for a new flare-mode transitional millisecond pulsar. *Astrophys. J.*, 917, 69 (2021). <https://doi.org/10.3847/1538-4357/ac0b47>
179. Swihart, S.J., Strader, J., Johnson, T.J., et al.: 2FGL J0846.0+2820: a new neutron star binary with a giant secondary and variable γ -ray emission. *Astrophys. J.* **851**(1), 31 (2017). <https://doi.org/10.3847/1538-4357/aa9937>
180. Swihart, S.J., Strader, J., Shishkovsky, L., et al.: A multiwavelength view of the neutron star binary 1FGL J1417.7-4402: a progenitor to canonical millisecond pulsars. *Astrophys. J.* **866**(2), 83 (2018). <https://doi.org/10.3847/1538-4357/aadcab>
181. Szkody, P., Fraser, O., Silvestri, N., et al.: Cataclysmic variables from the Sloan Digital Sky Survey. II. The second year. *Astron. J.* **126**(3), 1499–1514 (2003). <https://doi.org/10.1086/377346>
182. Takata, J., Li, K.L., Leung, G.C.K., et al.: Multi-wavelength emissions from the millisecond pulsar binary PSR J1023+0038 during an accretion active state. *Astrophys. J.* **785**(2), 131 (2014). <https://doi.org/10.1088/0004-637X/785/2/131>
183. Tam, P.H.T., Hui, C.Y., Huang, R.H.H., et al.: Evidence for gamma-ray emission from the low-mass X-ray binary system first J102347.6+003841. *Astrophys. J. Lett.* **724**(2), L207–L211 (2010). <https://doi.org/10.1088/2041-8205/724/2/L207>
184. Tavani, M.: “Hidden” millisecond pulsars. *Astrophys. J. Lett.* **379**, L69 (1991). <https://doi.org/10.1086/186156>
185. Tendulkar, S.P., Yang, C., An, H., et al.: NuSTAR observations of the state transition of millisecond pulsar binary PSR J1023+0038. *Astrophys. J.* **791**(2), 77 (2014). <https://doi.org/10.1088/0004-637X/791/2/77>
186. Thompson, C., Blandford, R.D., Evans, C.R., et al.: Physical processes in eclipsing pulsars: eclipse mechanisms and diagnostics. *Astrophys. J.* **422**, 304 (1994). <https://doi.org/10.1086/173728>
187. Thorstensen, J.R., Armstrong, E.: Is FIRST J102347.6+003841 really a cataclysmic binary? *Astron. J.* **130**(2), 759–766 (2005). <https://doi.org/10.1086/431326>
188. Tomsick, J.A., Chaty, S., Rodriguez, J., et al.: Chandra localizations and spectra of integral sources in the galactic plane: the cycle 9 sample. *Astrophys. J.* **701**(1), 811–823 (2009). <https://doi.org/10.1088/0004-637X/701/1/811>
189. Torres, D.F.: Order parameters for the high-energy spectra of pulsars. *Nat. Astron.* **2**, 247–256 (2018). <https://doi.org/10.1038/s41550-018-0384-5>
190. Torres, D.F., Ji, L., Li, J., et al.: A search for transitions between states in redbacks and black widows using seven years of Fermi-LAT observations. *Astrophys. J.* **836**(1), 68 (2017). <https://doi.org/10.3847/1538-4357/836/1/68>
191. Torres, D.F., Li, J.: The high-energy emission of millisecond pulsars (2020). arXiv e-prints arXiv:2004.03128

192. Torres, D.F., Viganò, D., Coti Zelati, F., et al.: Synchrocurvature modelling of the multifrequency non-thermal emission of pulsars. *Mon. Notices Royal Astron. Soc.* **489**(4), 5494–5512 (2019). <https://doi.org/10.1093/mnras/stz2403>
193. van Straaten, S., van der Klis, M., Wijnands, R.: Relations between timing features and colors in accreting millisecond pulsars. *Astrophys. J.* **619**(1), 455–482 (2005). <https://doi.org/10.1086/426183>
194. Veledina, A., Nättälä, J., Beloborodov, A.M.: Pulsar wind-heated accretion disk and the origin of modes in transitional millisecond pulsar PSR J1023+0038. *Astrophys. J.* **884**(2), 144 (2019). <https://doi.org/10.3847/1538-4357/ab44c6>
195. Voisin, G., Breton, R.P., Summers, C.: A spider timing model: accounting for quadrupole deformations and relativity in close pulsar binaries. *Mon. Notices Royal Astron. Soc.* **492**(2), 1550–1565 (2020). <https://doi.org/10.1093/mnras/stz3430>
196. Wadiasingh, Z., Harding, A.K., Venter, C., et al.: Constraining relativistic bow shock properties in rotation-powered millisecond pulsar binaries. *Astrophys. J.* **839**(2), 80 (2017). <https://doi.org/10.3847/1538-4357/aa69bf>
197. Wadiasingh, Z., Venter, C., Harding, A.K., et al.: Pressure balance and intrabinary shock stability in rotation-powered-state redback and transitional millisecond pulsar binary systems. *Astrophys. J.* **869**(2), 120 (2018). <https://doi.org/10.3847/1538-4357/aaed43>
198. Wang, X., Wang, Z., Morrell, N.: Infrared observations of the millisecond pulsar binary J1023+0038: evidence for the short-term nature of its interacting phase in 2000–2001. *Astrophys. J.* **764**(2), 144 (2013). <https://doi.org/10.1088/0004-637X/764/2/144>
199. Wang, Y.M.: On the torque exerted by a magnetically threaded accretion disk. *Astrophys. J. Lett.* **449**, L153 (1995). <https://doi.org/10.1086/309649>
200. Wang, Z., Archibald, A.M., Thorstensen, J.R., et al.: SDSS J102347.6+003841: a millisecond radio pulsar binary that had a hot disk during 2000–2001. *Astrophys. J.* **703**(2), 2017–2023 (2009). <https://doi.org/10.1088/0004-637X/703/2/2017>
201. Wang, Z., Xing, Y., Zhang, J., et al.: A compact X-ray emitting binary in likely association with 4FGL J0935.3+0901. *Mon. Notices Royal Astron. Soc.* **493**(4), 4845–4851 (2020). <https://doi.org/10.1093/mnras/staa655>
202. White, N.E.: X-ray binaries. *Astron. Astrophys. Rev.* **1**(1), 85–110 (1989). <https://doi.org/10.1007/BF00872485>
203. Wijnands, R., Degenaar, N., Page, D.: Cooling of accretion-heated neutron stars. *J. Astrophys. Astron.* **38**(3), 49 (2017). <https://doi.org/10.1007/s12036-017-9466-5>
204. Wijnands, R., van der Klis, M.: A millisecond pulsar in an X-ray binary system. *Nature* **394**(6691), 344–346 (1998). <https://doi.org/10.1038/28557>
205. Woudt, P.A., Warner, B., Pretorius, M.L.: High-speed photometry of faint cataclysmic variables - IV. V356 Aql, Aqr1, FIRST J1023+0038, H α 0242–2802, GI Mon, AO Oct, V972 Oph, SDSS 0155+00, SDSS 0233+00, SDSS 1240-01, SDSS 1556-00, SDSS 2050-05, FH Ser. *Mon. Notices Royal Astron. Soc.* **351**(3), 1015–1025 (2004). <https://doi.org/10.1111/j.1365-2966.2004.07843.x>
206. Wu, J.H.K., Hui, C.Y., Wu, E.M.H., et al.: Search for pulsed γ -ray emission from globular cluster M28. *Astrophys. J. Lett.* **765**(2), L47 (2013). <https://doi.org/10.1088/2041-8205/765/2/L47>
207. Xing, Y., Wang, Z.: Fermi observation of the transitional pulsar binary XSS J12270-4859. *Astrophys. J.* **808**(1), 17 (2015). <https://doi.org/10.1088/0004-637X/808/1/17>
208. Xing, Y., Wang, Z.X., Takata, J.: Possible modulated γ -ray emission from the transitional millisecond pulsar binary PSR J1023+0038. *Res. Astron. Astrophys.* **18**(10), 127 (2018). <https://doi.org/10.1088/1674-4527/18/10/127>
209. Zampieri, L., Burtovoi, A., Fiori, M., et al.: Precise optical timing of PSR J1023+0038, the first millisecond pulsar detected with Aqueye+ in Asiago. *Mon. Notices Royal Astron. Soc.* **485**(1), L109–L113 (2019). <https://doi.org/10.1093/mnrasl/slz043>
210. Zavlin, V.E.: Studying millisecond pulsars in X-rays. *Astrophys. Space Sci.* **308**(1-4), 297–307 (2007). <https://doi.org/10.1007/s10509-007-9297-y>.

Chapter 7

Origin and Binary Evolution of Millisecond Pulsars



Francesca D'Antona and Marco Tailo

Abstract We review the channels of formation, the orbital and the spin evolution of neutron stars (NSs) in binary systems that lead to the formation of millisecond pulsars (MSP), in the context of the recycling scenario. The basics of binary evolution and the key concepts of angular momentum losses are given. After discussing the case of Cataclysmic Variables and long-period MSP binaries with a compact companion, we focus on the evolution of systems with a short orbital period and a low companion mass, in which the recycling phase can be caught ‘in the act’. Irradiation of the companion by the NS (either in the accretion or in the radio MSP stage) plays a central role in the evolution of these systems, possibly causing cyclic LMXB stages which would help to explain the high positive \dot{P}_{orb} 's of some LMXB systems, and account for the (apparently) different birthrates of LMXB and MSP. Irradiation by the MSP may also be able to drive the donor to a stage in which either radio-ejection (in the redbacks) or mass loss due to the companion expansion, may govern the evolution to the black widow stage and to the final disruption of the companion.

7.1 Introduction

Understanding millisecond pulsars (MSP) has a particular appeal for stellar evolution, for its breadth among a number of still open problems, first of all those belonging to the neutron star (NS) formation, such as the different paths to supernova explosions, the supernova kicks and the initial mass distribution of NSs. In addition, the binary evolution to the MSP stage is either affected by crude parametrization of difficult phases (common envelope, systemic angular momentum

F. D'Antona (✉)

INAF–Rome Observatory, Address of Institute, Roma, Italy

e-mail: francesca.dantona@inaf.it; francesca.dantona@oa-roma.inaf.it

M. Tailo

Dipartimento di Fisica e Astronomia ‘Galileo Galilei’, Univ. di Padova, Padova, Italy

losses) or by subtle issues, such as the description of ‘illumination’ by X-rays or by the MSP energy loss, and its effect on the structure of the companion star in the short and long term evolution. Thus this review focuses on a few problems and ignores most of the surrounding rich physics of these objects.

We shortly discuss the channels of neutron star (NS) formation in single and binary stellar evolution and deal with the problem of the high frequency of MSP in Globular Clusters (GCs) in Sect. 7.2. Then we summarize basic concepts of binary evolution in Sect. 7.3. As a comparison key study, we discuss the secular evolution of Cataclysmic Binaries (CBs) in Sect. 7.4, and give a coarse comparison between the orbital period distribution of these systems and that of MSP and low mass X-ray binary systems. Sect. 7.5 discusses the evolution of different classes of MSP binaries, those having compact remnant companions, while Sect. 7.6 deals with the evolution of low mass—short period LMXB and MSP. The role of ‘irradiation’ or ‘illumination’ is discussed and found relevant, together with ‘radio-ejection’ and ‘evaporation’ to explain the different period distribution of the binary MSP.

7.2 The Origin of Millisecond Pulsars

The topic consists of two generally independent problems: the formation of neutron stars (NS) and the acceleration of the NS to millisecond periods. The fact that MSPs are statistically much more abundant in Globular Clusters points to an important formation role for these stellar ensembles.

7.2.1 *The Formation of Single Neutron Stars*

The evolution of single stars as a function of their initial mass is schematically shown in Fig. 7.1, from the work by Karakas and Lattanzio [55] which we take as general reference for this Section. The mass boundaries between different kinds of evolutionary paths must be regarded as indicative only, because the precise mass values depends both on physical inputs (e.g. the metallicity) and on the assumptions made on those inputs of evolution which are not known from first principles (e.g. mass loss or core overshooting) and thus have to be educatedly parametrized.

Masses which ignite helium in the core within the age of the Universe ($\gtrsim 0.8 M_\odot$) and up to $\sim 7 M_\odot$ develop carbon–oxygen (C–O) cores. Their evolution proceeds along the Asymptotic Giant Branch (AGB) phase, through thermal pulses [48] and mass loss. Finally they become C–O white dwarfs (WDs). In a small range of masses above $7 M_\odot$, which develop C–O core masses $1.1 \lesssim M_{\text{C–O}}/M_\odot \lesssim 1.35$, carbon is ignited in conditions of semi-degeneracy, the energy released is able to expand the core, which is further processed to become an oxygen–Neon (O–Ne) core. Above the core, the star experiences thermal pulses and mass-loss (‘super-AGB’ evolution). The final outcome is generally an O–Ne WD. If the core can grow

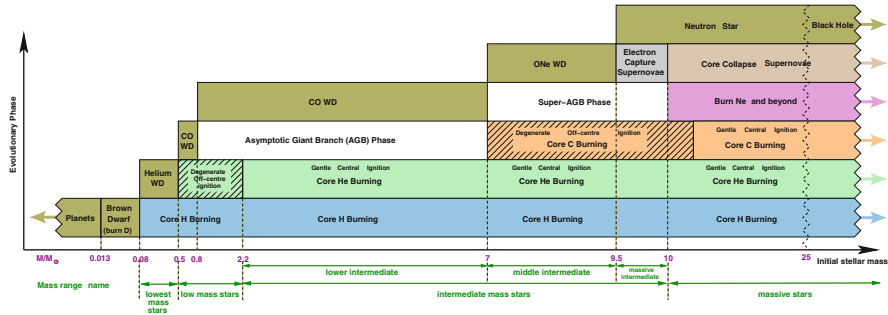


Fig. 7.1 The scheme shows how the initial stellar mass determines the main nuclear burning phases, as well as the fate of the final remnant. NS are the remnants of ecSN and CCSN, from $M \sim 9.5\text{--}25 M_{\odot}$. Credit: Karakas & Lattanzio, Publ. Astron. Soc. Pac., 31, e030 (2014), reproduced with permission of the Cambridge University Press

beyond the Chandrasekhar limit, electron captures occur before the core can ignite Neon. The depletion of electron pressure in the core induces the core collapse to nuclear densities in the event named “electron-capture supernova” (ecSN)¹. In larger masses, the supernova explosion occurs when the star has ignited all elements up to iron, and the core collapse is caused by the iron ignition (core collapse supernova, CCSN). Up to an initial mass estimated to be $\sim 20\text{--}25 M_{\odot}$, the remnant of CCSNs are neutron stars, while above a black hole is formed.

Thus NS can be born from either ecSN or CCSN, from an initial mass range $\sim 9.5\text{--}25 M_{\odot}$.

7.2.2 Formation of Neutron Stars in Binaries

The scheme of neutron star formation is largely modified when we deal with the evolution of binary systems. In general, the mass range of both CCSN and ecSN become larger.

- 1 **CCSN:** The binary channel to CCSN also includes the so-called delayed Type II SN, exploding in binaries in which the mass necessary for the event is obtained by mass exchange [119].
- 2 **ecSN:** The binary evolution has an important role which can end in a higher frequency of ecSN events, as described by Podsiadlowski et al. [83]. In binaries beginning mass transfer when the donor is evolving through the Herzsprung gap, before reaching the giant branch location, the star may avoid the second dredge up (2DU) phase which in single stars reduces the mass of the helium core remnant

¹ In Fig. 7.1 ecSN occur for an initial mass range of $\sim 0.5 M_{\odot}$, but this value is very dependent on the modelization of the evolution of super-AGB phase [84].

from the main sequence evolution. This He-core mass is the dominant factor in the following evolution, as it is converted into the initial C-O core mass by helium burning. If, for a given initial mass, the C-O core is larger, the larger is its probability to become an ecSN instead of a plain O-Ne WD.

- 3 **AIC ecSN:** in an interacting binary containing an O-Ne WD, accretion may push the WD above the Chandrasekhar mass, in an ecSN event named “accretion induced collapse” (AIC) (e.g. [39, 73]).

7.2.3 *The MSP Formation*

We recall that timing measurements allow to detect the spin period of pulsars (P_s) and its time derivative (\dot{P}_s). The hypothesis that the loss of rotational energy of the pulsar equals the amount of magnetic dipole radiation emitted yields an estimate of the average strength of the dipole component of the pulsar magnetic field at the surface (B_s). A spin-down age may also be defined by $\tau = \frac{P_s}{2\dot{P}_s}$. The P_s and \dot{P}_s data then allow to build the B_s versus P_s diagram, which best describes the evolution of pulsars (see, e.g., Fig. 4.1). MSP are identified as a class of ‘old’ NSs. The very low \dot{P}_s ’s ($< 10^{-18}$), a modest loss of rotational energy due to emission of magnetodipole waves, imply that their magnetic field is 3–5 orders of magnitude lower than that of young pulsar. Thus these pulsars have high τ and are visible as MSP for gigayears after their formation.

Soon after the discovery of the first MSP, PSR 1937+21 (a single NS, but possibly previously host in a binary [6]), a model was proposed to explain its 1.55 ms spin period as due to accretion of mass and angular momentum from a binary companion. PSR 1937+21 was then recognized as a “recycled”² pulsar [4]. The reader is referred to Sects. 4.1 and 6.3 for a the discussion of the recycling scenario and its observational tests.

7.2.3.1 *The Lack of Sub-millisecond Pulsars and the Radio-Ejection*

The spin evolution of NS depends on important details, e.g. on the role of the neutron star matter equation of state and of the same NS spin in determining the NS radius, on how the magnetic field of the NS is modified by accretion, and on the disk description itself. The minimum observed spin period of MSP (1.55 ms) can be obtained by the modest mass accretion $\sim 0.1 M_\odot$, for any assumption on the equation of state for the neutron star matter, and is much longer that the limiting period P_{sh} below which the star becomes unstable to mass shedding at its equator [24]. Further, a reasonable transfer of $\sim 0.3 M_\odot$ appears sufficient to bring the NS

² This term had already been used to describe the status of the pulsar in the Hulse-Taylor binary NS PSR B1913+16, discovered in 1974.

down to its maximum spin well below 1 ms [18], posing the problem of why we do not see sub-millisecond pulsars.

Apart that observing such short periods is a challenging task, it is possible that the energetic MSPs do not allow further accretion. Nevertheless, the corotation radius is close to the NS surface, so a strong energy loss from the NS is needed to efficiently get rid, via the propeller mechanism, of the matter further lost by the donor during its whole secular evolution. Burderi et al. [19] proposed instead that a ‘radio-ejection’ mechanism sets in when two circumstances happen together: the radio pulsar becomes active and the magnetic pressure due to the NS overcomes the disk internal pressure, so that it the disk becomes unstable and the MSP prevents further accretion directly at the inner Lagrangian point. The specific angular momentum associated to this mass loss will be dominant to estimate the further secular evolution (see Sect. 7.6). The radio-ejection conditions depend on a high power of the pulsar spin, but it is more efficient than the propeller, as the mass loss is driven by the system secular evolution and not by the rotational energy loss of the MSP. The role of radio-ejection may be important (e.g. in the case of PSR J1740–53; see [17]) and affect many MSP binaries.

7.2.4 *Binary and Single MSPs and the Globular Clusters Environment*

The recycling model implies that there has been a stage of the NS life during which it has been a component of an interacting binary. The (few) single MSPs observed are generally regarded as previous binaries whose companion has been fully evaporated by the pulsar radiation, if it is the remnant of an LMXB. Was the NS formed with the same companion which later on caused the recycling? This is possible in particular cases, but not strictly necessary for the bulk of MSPs found in Globular Clusters (GC), where binaries containing NS may be formed by tidal capture, binary exchanges or direct collisions [51]. MSPs in the field should then be the outcome of the evolution of pristine binary systems (see Sect. 7.5.1, 7.5.2, 7.5.3),³ while MSPs in GCs can result both from the evolution of primordial systems and from new binaries formed after the NS formation by means of dynamical interactions [56]. In fact, the dynamical role of the GC environment must be overwhelming, as $\sim 40\%$ of MSPs are found in GCs, despite the Galaxy is 10^3 times more massive than the entire GC system.⁴ A similar overabundance holds for LMXBs, reinforcing the hypothesis.

The dominant presence of MSPs and LMXBs in GCs poses the question that the GC must retain at least a fraction of the NS. This is not so obvious, as, in fact, we

³ Note anyway the scenario proposed by Grindlay et al. [43]: also the bulge LMXBs may have been formed in GCs, later on destroyed by repeated tidal stripping and shocking in the galactic plane.

⁴ MSPs in the galactic field are 252, and those in GCs are 149 at the time of writing (Dec. 2019).

expect that most of the NS born from CCSN are expelled from clusters, as there is a momentum kick resulting from the supernova, due to the explosion asymmetries. The kick is a consequence of non radial hydrodynamic instabilities, such as neutrino driven convection or accretion shock instability (see [52] and references therein) in the collapsing stellar core.

The average observed kick velocities are very large, obviously much larger than the escape velocity from typical clusters. The important issue is then to look at the constraints on the fraction of *low velocity* pulsars. It is estimated that the average 3D initial pulsar velocity in the galactic disk is ~ 400 Km/s, with a 1D rms velocity of $\sigma = 265$ Km/s [47] and in these conditions only a fraction as low as 3×10^{-3} have space velocities below 60 Km/s and could be retained in GCs. In other models [37] the fraction of pulsars below 60 Km/s varies in the ample range 0.012–0.135.

The binary channels are favoured for the NS retention, as we expect that their SN are subject to smaller kicks,⁵ thanks to two different possible reasons:

1. some CCSN explosions may occur in an ‘ultra-stripped’ progenitor, already deprived of its hydrogen envelope by previous mass loss and transfer to the companion, so they eject a small mass, often with a low binding energy. In this case, at least the ultra-stripped CCSN with relatively small iron cores may lead to fast explosions and get small kicks;
2. a smaller energy of explosion—because the H-envelope is small—also occurs in the ecSN due to accretion induced collapse (AIC) of an O–Ne WD [70], and in single ecSN, as these latter events occur at the lower mass edge of the SN explosions range. A smaller kick velocity is produced as a consequence. The explosions are under-energetic because there is too little mass to absorb neutrinos—see e.g. the numerical simulations in [29].

Synthetic computation of NS formation and evolution to MSP in GCs can be found. The recent numerical study [118] shows that GCs born with the typical present-day mass of $M_{GC} = 2\text{--}5 \times 10^5 M_\odot$ may produce up to 10–20 MSP, while initially more massive GCs of $\sim 10^6 M_\odot$ can produce ~ 100 MSP. The larger number is to be ascribed both to the larger number of NS formed, keeping the same assumptions on the formation channels, and to the lower escape velocity ($v_e \propto \sqrt{M_{GC}}$).

As far as the initial mass of globular clusters is concerned, it is important to point out that a number of recent studies have indeed concluded that many clusters must have been initially significantly more massive and lost a significant fraction of their initial mass [8, 62, 114]. Several models for the formation of multiple stellar populations also require globular clusters to be initially more massive (see Gratton et al. [42] for a review). The MSP production in globular clusters could therefore be significantly larger [118].

⁵ The dependence of the kick velocity on the mass ejected in the SN event is tentatively taken into account in [15, 16, 41].

7.3 Concepts of Binary Evolution

Interacting binary evolution is a necessary ingredient for the formation of an MSP, and in many cases for the formation of the NS itself. We summarize here the main properties of binary interaction and take notice of the relevance of some concepts for the case of MSP evolution.

The first important summary review is by Paczynski [75], whose basic definitions and relevant concepts are still used, also in this short summary.

7.3.1 *The Roche Lobe and the Radius Evolution of Single Stars*

The most important way of how mass can be transferred from one star to the other is the ‘Roche-lobe overflow’ (RLOF). The definition of Roche lobe for a binary component is based on the potential surfaces defined by the gravitational potential of the two orbiting masses plus the centrifugal force acting on a mass-less test particle in a reference frame co-rotating with the binary, in a number of simplifying assumptions (the orbit has zero eccentricity, the gravitational fields of the stars can be approximated as those of point masses, and stellar rotation is synchronised with the orbital motion). The gravitational potential has five ‘Lagrangian points’ where the gradient of the effective potential is zero. Three points lie along the line that connects the two stars. The equipotential surface that passes through L1 (the critical Roche-Lobe potential) connects the gravitational spheres of influence of the two stars. If one star begins filling its Roche lobe, matter can flow through the L1 point into the Roche lobe of the other star. Approximating the Roche lobe volume with a sphere, the Roche lobe radius of the component M_d (R_{RLd}) can be evaluated with the expression by Eggleton [31]:

$$\frac{R_{RLd}}{a} = \frac{0.49q^{-2/3}}{0.6q^{-2/3} + \ln(1 + q^{-1/3})} \quad (7.1)$$

where a is the orbital separation, $q = M_d/M_{acc}$ is the mass ratio, and M_{acc} is the mass of the companion (the accreting component, if mass transfer takes place).

The expression by Kopal [74] is still very useful for $q \lesssim 0.5$:

$$\frac{R_{RLd}}{a} = \frac{2}{3^{4/3}} \left(\frac{M_d}{M_d + M_{acc}} \right)^{1/3} \quad (7.2)$$

This expression, coupled with Kepler’s third law:

$$\left(\frac{2\pi}{P_{\text{orb}}} \right)^2 a^3 = G(M_d + M_{acc}) \quad (7.3)$$

provides a useful relation between the orbital period P_{orb} , the mass and radius of the donor, in the hypothesis that the donor fills the Roche lobe:

$$P_{\text{orb}} = \frac{9\pi}{\sqrt{2G}} R_{RLd}^{3/2} M_d^{-1/2} \simeq 9 h \left(\frac{R_{RLd}}{R_\odot} \right)^{3/2} \left(\frac{M_d}{M_\odot} \right)^{-1/2} \quad (7.4)$$

Equation 7.4 is an useful first order evaluation of the donor possible mass-radius relations, depending on its structure (main sequence, giant, white dwarf, mixed H–He degenerate remnant).

A binary in which both component are inside their Roche lobe is ‘detached’. The life of an interacting binary begins when one of the component becomes a mass ‘donor’, filling its Roche lobe and beginning mass transfer to the companion. Three cases of mass exchange are defined by Paczynski [75]. Case A occurs when the donor fills the Roche lobe during the main sequence stage; case B occurs when it is out of the main sequence, or during the red giant branch evolution; case C occurs when the donor is evolving through the AGB that is when it burns hydrogen and helium in a shell From Eq. 7.1 which case applies depends on the separation a and on the mass ratio q .

Role for MSP: The historical subdivision in case A, B and C is still important to understand the previous evolution of MSP binaries, whose former donor is now a compact object (see Sect. 7.5).

7.3.2 The Radius Change due to Mass Loss

The most important property of mass transfer is its stability, and this depends on the comparison of the response of the stellar radius, to the concomitant response of the Roche lobe radius to mass loss. We define three *mass-radius exponents*, from which three different *timescales of mass transfer* depend.

Mass–Radius Exponents

adiabatic: $\zeta_S = \left(\frac{\partial \log R_d}{\partial \log M_d} \right)_S$ —change at constant entropy

equilibrium: $\zeta_{eq} = \left(\frac{\partial \log R_d}{\partial \log M_d} \right)$ —change preserving hydrostatic and thermal equil.

Roche lobe: $\zeta_{RLd} = \left(\frac{\partial \log R_{RLd}}{\partial \log M_d} \right)$

Timescales of Mass Transfer

Nuclear: $\zeta_{RLd} < \min(\zeta_S, \zeta_{eq})$. The mass transfer is stable, mass loss is due to the *expansion* of the donor caused by nuclear evolution, while the donor remains in hydrostatic and thermal equilibrium. The approximate timescale (for core–H burning) is $\tau_{nuc} \sim 10 \text{ Gyr} \frac{M}{M_\odot} \frac{L_\odot}{L}$. If τ_{nuc} is too long (for masses having a timescale of hydrogen burning longer than the age of the Universe), systemic angular momentum losses may act as a driver, on the timescale of *contraction* of the Roche lobe radius;

Thermal: $\zeta_S > \zeta_{RLd} > \zeta_{eq}$. The mass transfer is driven by the expansion of the donor, for example when it crosses the Hertzsprung gap after the end of the core–hydrogen burning phase. The star remains in hydrostatic equilibrium, and the mass loss is limited by the thermal readjustment at a maximum value $\dot{M}_{max} = -M_d/\tau_{KH}$, where $\tau_{KH} \sim (GM^2)/(2RL) \sim 15 \text{ Myr} (M/M_\odot)^2 (R/R_\odot) (L_\odot/L)$

Dynamical: $\zeta_{RLd} > \zeta_S$. The adiabatic response of the donor is unable to keep it within the Roche lobe. The growing mass transfer rates reach values $\dot{M}_{max} = -M_d/\tau_{dyn}$. The evolution is catastrophic, as the star reacts to perturbations to hydrostatic equilibrium on the dynamical timescale $\tau_{dyn} \sim \sqrt{R^3/GM} \sim 0.04(M_\odot/M)^{1/2} (R_\odot/R)^{3/2} \text{ yr}$.

Figure 7.2 exemplifies these three cases.

A typical situation in which dynamical mass transfer ensues is the case of an evolving giant beginning to transfer mass to a less massive companion, as $\zeta_S \sim -1/3$ for the convective giant envelope, while $\zeta_{RL} > 0$ (the system becomes tighter). This leads to the “common envelope” (CE) evolution [76] that is assumed to be responsible for, e.g., the formation of cataclysmic binaries [76], and of the double WD merging leading to Type I supernovae [49, 115]. Unfortunately, quantitative computations have been rare [67], as the spiraling-in process of two stars (or a star and a core) embedded in a CE involves a large number of hydrodynamic and thermodynamic processes, occurring on a wide range of time and length scales. Simple expressions have been worked out and widely adopted in the literature. The common assumption is that the gravitational energy lost from the orbit when the mass losing star spirals in towards the companion is partially deposited into rotation and partially into heating of the envelope, and, in principle, it can cause the envelope ejection when it exceeds the binding energy. Thus an efficiency parameter is defined as: $\alpha_{ce} = \frac{\Delta E_{\text{binding}}}{\Delta E_{\text{orb}}}$ and in the simplest case it is evaluated by:

$$\alpha_{ce} \frac{GM_c M_2}{a_f} = \frac{GM_1^2}{a} \quad (7.5)$$

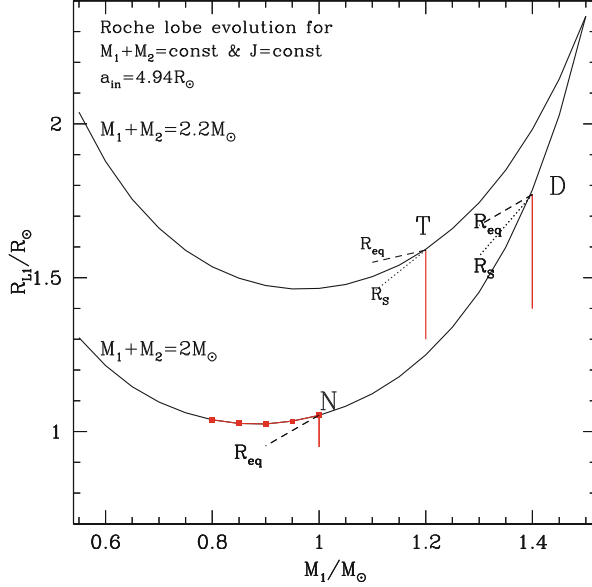


Fig. 7.2 Roche lobe radius in conservative evolution starting from an initial separation $a_{in}=4.94R_{\odot}$ for two examples with different total mass. A possible donor evolves at constant mass, increasing radius, until it meets the Roche lobe. Thereon, the evolution depends on whether the stellar equilibrium radius R_{eq} remains inside the lobe (evolution on the nuclear timescale), as from the point N, which can follow the Roche lobe conservative evolution—red squares), or it becomes larger, and the evolution is on the thermal timescale (T), or, if the adiabatic radius also becomes bigger than the lobe radius, the system is unstable to dynamic mass transfer (D)

where M_1 and M_2 are the initial masses of donor and companion, M_c is the core mass of the donor (for example the mass of the helium core in case B Roche lobe overflow) and a and a_f are the initial and final separations before and after the CE [49]. More elaborated expressions are available (e.g. [64]), but the parametrization remains highly uncertain.

The total derivative of radius and Roche lobe radius with respect to time can be written as:

$$\frac{d \ln R_d}{dt} = \zeta_S \frac{d \ln M_d}{dt} + \left(\frac{\partial \ln R_d}{\partial t} \right)_{\dot{M}=0} \quad (7.6)$$

$$\frac{d \ln R_{RLd}}{dt} = \zeta_{RLd} \frac{d \ln M_d}{dt} + \left(\frac{\partial \ln R_{RLd}}{\partial t} \right)_{\dot{M}=0} \quad (7.7)$$

The radius varies *independently* of mass loss on its timescale $\tau_{R_d} = (\partial \ln R_d / \partial t)_{\dot{M}=0}^{-1}$ due both to thermal relaxation (a contraction, or an expansion) and nuclear evolution (generally an expansion). If the system is isolated, but primary angular momentum (J) loss mechanisms are present (for example, magnetic braking

and gravitational radiation), also the Roche lobe radius varies in time independently of mass loss, on the timescale $\tau_J = J/\dot{J} = 2(\partial \ln R_{RLd}/\partial t)_{\dot{M}=0}^{-1}$

7.3.3 The Losses of Angular Momentum: Primary Mechanisms

The orbital angular momentum of binaries J can be written as:

$$J^2 = J_{\text{orb}}^2 = G \frac{M_d^2 M_{\text{acc}}^2}{M} a(1 - e^2) \quad (7.8)$$

where G is the gravitational constant, e the system eccentricity and the total mass is $M = M_d + M_{\text{acc}}$. Differentiating we obtain the general orbital evolution equation

$$2 \frac{\dot{J}}{J} = \frac{\dot{a}}{a} + 2 \frac{\dot{M}_d}{M_d} + 2 \frac{\dot{M}_{\text{acc}}}{M_{\text{acc}}} - \frac{\dot{M}}{M} - \frac{2e\dot{e}}{(1 - e^2)} \quad (7.9)$$

For $e = 0$ and conservative mass transfer ($\dot{J} = 0$ and $\dot{M}_{\text{acc}} = -\dot{M}_d$), Eq. 7.9 reduces to:

$$\frac{\dot{a}}{a} = -2 \left(1 - \frac{M_d}{M_{\text{acc}}} \right) \frac{\dot{M}_d}{M_d} \quad (7.10)$$

As $\dot{M}_d < 0$, we find the well known result that the separation *increases* when the donor is the less massive component, and *decreases* in the opposite case. A simple way to understand this result is to see it from the point of view that total AM is constant: mass transfer to the more massive component brings matter *closer* to the center of mass, to a status of smaller AM, thus AM must be added to the orbit, which becomes wider. The reverse occurs when matter is transferred to the lighter component, and thus has to achieve AM from the orbit.

In the general case, we must consider all the possible angular momentum variations. We can write

$$\frac{\dot{J}}{J} = \frac{\dot{J}_{GR}}{J} + \frac{\dot{J}_{MB}}{J} + \frac{\dot{J}_{ml}}{J} \quad (7.11)$$

The two first terms are primary losses, as they act also when the binary is detached, the third one is the consequence of mass loss.

Magnetic Braking: (MB AML) \dot{J}_{MB}/J The single stars having a convective envelope ($M \lesssim 1.3M_{\odot}$) are known to slow down during their main sequence lifetime [96, 97]. The presence of the convective envelope produces a dynamo magnetic field, and turbulence and wind mass loss. Schatzman [94] pointed out that

the winds of these stars are magnetically constrained to corotate with the star, out to distances large compared with the stellar radius, so that even a very small amount of mass loss would yield a proportionally much greater loss of angular momentum. This ‘magnetic braking’ is schematized in various parametric ways in the literature, mainly calibrated on the Skumanich relation [96] that the stellar angular velocity decreases as the age at power $-1/2$. In [112] the expression (in cgs units) is:

$$\frac{\dot{J}_{MB}}{J} \simeq -0.5 \times 10^{-28} f_{mb}^{-2} \frac{k^2 R_d^4}{a^5} \frac{GM_d^3}{M_d M_{acc}} s^{-1} \quad (7.12)$$

where R_d is the radius of the mass-losing star; k^2 is its gyration radius and f_{mb} is a constant of order unity. Several other (parametric anyway) formulations have been tested and adopted in the literature.

Gravitational Radiation (GR AML) \dot{J}_{GR}/J From general relativity

$$\frac{\dot{J}_{GR}}{J} = \frac{32G^3}{5c^5} \frac{M_d M_{acc} M}{a^4} s^{-1} \quad (7.13)$$

where c is the speed of light in vacuum. This term is especially significant for close orbits, and in particular for short period cataclysmic binaries. Note that gravitational radiation is a physical consequence of the general relativity, but the magnetic braking formulation resides on parameters and functional dependences which are, at best, semiempirical. In fact, calibration of the magnetic braking losses is done by comparison of the results of binary evolution with the properties of the relevant classes of objects.

Consequential AML \dot{J}_{ml}/J If the mass transfer is non conservative, and a fraction α of mass is lost by the system, this mass will carry away angular momentum, and we can write:

$$\dot{J}_{ml} = \alpha \dot{M} j_{spec} \quad (7.14)$$

where j_{spec} is the specific AM of the mass leaving the system. It is useful to write again J_{orb} , for circular orbit in terms of the orbital angular velocity $\omega = \sqrt{(GM/a^3)}$:

$$J_{orb} = \frac{M_d M_{acc}}{M} a^2 \omega \quad (7.15)$$

to explicit how j_{spec} is written in terms of the total AM of the binary. A typical case considered in the literature is the loss of AM occurring when a nova explosion expels the accumulated hydrogen rich envelope. In this case we can make the assumption that the nova shell is lost with the specific angular momentum of the WD [95]. In cases of mass transfer rates larger than the Eddington limit, a typical assumption is that the mass lost by the donor (\dot{M}) is acquired by the accretor up to the Eddington

mass accretion rate (\dot{M}_{Edd} in modulus) but the rest is lost with the specific AM of the accretor $j_{acc} = a_{acc}^2 \omega = [M_d/(M_{acc}M)]J_{orb}$ (being $a_{acc} = (M_d/M)a$ the distance of M_{acc} from the center of mass), and:

$$\frac{\dot{J}_{ml}}{J} = \frac{M_d}{M_{acc}M} (\dot{M} + |\dot{M}_{Edd}|) \quad (7.16)$$

In the case of wind mass loss from the donor, the associated specific AML is probably that of the donor, while, specifically for low mass companions of MSP in the radio-ejection phase, it has been proposed that the mass lost by this mechanism carries away the specific AM at the inner Lagrangian point L1, which is $j_{L1} = d_{L1}^2 \omega$, where d_{L1} is the distance between L1 and the binary center of mass. In this case we can write:

$$\frac{\dot{J}_{ml}}{J} = \frac{M}{M_d M_{acc}} \frac{d_{L1}^2}{a^2} \times \alpha \dot{M} \quad (7.17)$$

where the fraction is $\alpha=1$ for radio-ejection. Note that, fixed \dot{M} , the AM lost is minimum if the mass is lost from the accretor (which is the mass closer to the barycentre) much larger if the loss is from L1, and a bit larger if the loss is directly from the donor.

Role for MSP: MB and GR AML are both considered in the secular binary evolution of short period binary MSP. A role for consequential AML is probably played both during the super-Eddington phases of mass transfer and during the mass loss induced on the companion by the action of the MSP radiation, both in the case of evaporation and in the case of radio-ejection. Whatever the choice for the specific AML associated to mass loss from the system, the term is so important that it may qualitatively affect the result of binary evolution.

7.3.4 The Approach of a Donor to the Roche Lobe Contact

Stars have extended atmospheres, so mass flow from the donor begins when the photospheric radius is still smaller than the Roche lobe radius. While the mass flow through the inner Lagrangian point is a complicated hydrodynamical problem, a simple expression to estimate it in the ‘optically thin’ case was developed by Ritter [88].

$$\dot{M} = -\dot{M}_0 \exp\left(\frac{(R_d - R_{RLd})}{H_p}\right) \quad (7.18)$$

and $\dot{M}_0 = (1/\sqrt{e})\rho_{ph}v_s Q$, where v_s and Q are the isothermal sound speed and the effective cross section of the flow at L1, and ρ_{ph} is the photospheric density.

Equation 7.18 shows that the mass transfer rate increases exponentially while the stellar radius approaches the Roche lobe, until the stationary situation is reached, when $R_d = R_{RLd}$ and $dR_d/dt = dR_{RLd}/dt$. In [88] we find the discussion of the evolution of the mass transfer rate and in [28] numerical examples of the different approach to stationary mass loss for different initial donor masses.

We can explicitly write down the acceleration by differentiating Eq. 7.18, and assuming that \dot{M}_0 is constant:

$$\ddot{\dot{M}} = \dot{M} \frac{R_d}{H_p} \left[\frac{d \ln R_d}{dt} - \frac{d \ln R_{RLd}}{dt} \right] \quad (7.19)$$

Substituting the derivatives as written in Eq. 7.6 and 7.7, we write:

$$\ddot{\dot{M}} = \dot{M} \frac{R_d}{H_p} \left[(\zeta_S - \zeta_{RLd}) \frac{d \ln M_d}{dt} + \left(\frac{\partial \ln R_d}{\partial t} \right)_{\dot{M}=0} + \left(\frac{\partial \ln R_{RLd}}{\partial t} \right)_{\dot{M}=0} \right] \quad (7.20)$$

and using the definition of thermal relaxation and AML timescales, we get the timescale of mass transfer:

$$\tau_{\dot{M}} = \frac{\dot{M}}{\ddot{\dot{M}}} = \frac{H_p}{R_d} \left[\frac{\dot{M}}{M_d} (\zeta_S - \zeta_{RLd}) + \frac{1}{\tau_{R_d}} - \frac{2}{\tau_J} \right]^{-1} \quad (7.21)$$

At first, when the donor is still well within its Roche lobe, the dominant term in Eq. 7.21 is the third one, the timescale of angular momentum loss, and

$$\tau_{\dot{M}} = \frac{\dot{M}}{\ddot{\dot{M}}} \sim \frac{H_p}{2R_d} \tau_J \quad (7.22)$$

As soon as the radius reaction to mass loss becomes effective, the first term enters into play, as well as the thermal relaxation term. In the stable case, at the end the two first terms balance the third one and a stationary value for \dot{M} is achieved

$$-\dot{M}_d = \frac{M_d}{\zeta_S - \zeta_{RLd}} \left[\frac{1}{\tau_{Rd}} - \frac{2}{\tau_J} \right] \quad (7.23)$$

The stationary mass transfer in the conservative case is also found directly from Eqs. 7.6 and 7.7, by requiring that the radius of the donor and of the Roche lobe, and their respective time derivatives are equal. Notice that Eq. 7.23 requires that $\zeta_S > \zeta_{RLd}$ for dynamically stable mass transfer (Sect. 7.3.2).

The approach to the stationary rate thus depends on the characteristic timescales of the donor under consideration. The timescale of non-stationary mass transfer (Eq. 7.22) is only $H_p/2R_d \simeq 10^{-4}$ of the secular evolution timescale τ_J .

Role for accreting MSP: Primary losses of AM dominate the timescale and average mass transfer rate for binaries with scarcely evolved companions. If, for any reason, the mass transfer timescale becomes shorter (and thus \dot{M} larger) a lower \dot{M} at a following epoch will be necessary. In CBs the irradiation will produce short duration ‘limit cycles’ (King et al. [57]). In LMXBs this produces cycles of mass transfer followed by fully detached stages (see Sect. 7.6.2).

7.4 Cataclysmic Binaries as a Comparison Key Study

We summarize here the concepts framing the secular evolution of Cataclysmic binaries (CBs), semi-detached systems consisting of a quasi-main-sequence donor and a WD companion, because they can be (in part) applied to study the evolution of binaries with NS companions.

At $P_{\text{orb}} \lesssim 10$ h the donor of CBs must be a scarcely evolved quasi-MS star, thus primary AML is required to keep the Roche lobe radius in constant contact with the donor radius, allowing stable mass transfer. A ‘standard’ model has been developed to account for the observational properties of different classes of CBs. In particular, the non-magnetic CBs shows a shortage of stars at orbital periods between ~ 3.2 h and ~ 2.15 h (period gap), as shown in Fig. 7.3.

We can write the mass–radius relation as a power law:

$$\frac{R}{R_{\odot}} = f \left(\frac{M_d}{M_{\odot}} \right)^{\alpha} \quad (7.24)$$

where $f \sim 1$ and $\alpha \sim 1$ for low mass main sequence stars. We can get rid of the dependence of the orbital period on the radius of the mass-losing component in Eq. 7.4, and obtain:

$$P_{\text{orb}}^2 \propto M_d^{3\alpha-1} \quad (7.25)$$

The logarithm derivative provides:

$$\frac{\dot{P}_{\text{orb}}}{P_{\text{orb}}} = \frac{3\alpha - 1}{2} \frac{\dot{M}_d}{M_d} \quad (7.26)$$

The typical average mass transfer rates observed above the gap are $\sim 10^{-9} M_{\odot}/\text{yr}$, too large to be provided by GR AML, while they can be met with a reasonable choice of parameters of MB AML from Eq. 7.12. For a typical mass of $0.4M_{\odot}$ the mass loss timescale is $\sim 0.4/10^{-9} \sim 5 \times 10^8$ yr, similar to the thermal timescale. Such a mass loss keeps the donor out of thermal equilibrium, meaning that its radius remains somewhat larger than the MS radius (or that $\alpha < 1$ in Eq. 7.24). The best model to describe the presence of the period gap is to

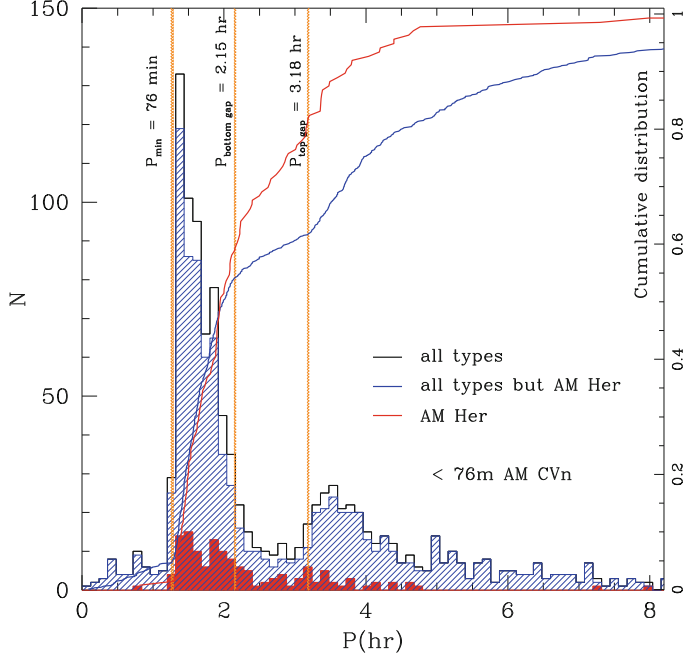


Fig. 7.3 Period distribution of CBs from the 7th Edition, Release 7.21 (March 2014) of the Catalog by Ritter and Kolb [89]. The cumulative distribution is normalized to the total numbers in the catalogue, but only periods up to 8 h are shown. The differential distribution shows separately the Polars (AM Her) and the sample not including the polars. The minimum period and the boundaries of the 2–3 h period gap are highlighted. The gap is well defined by the flattening in the cumulative distribution of CBs, but is not present in the distribution of Polars

recognize that the donor becomes fully convective at $P_{\text{orb}} \sim 3$ h.⁶ This change of structure corresponds to a readjustment of the magnetic field in a way that MB AML becomes suddenly much smaller, and allows the donor to contract back to thermal equilibrium. Thus the donor detaches from the Roche lobe and mass transfer stops. It is mainly GR AML that, at this stage, will shrink the orbit and bring the donor again into contact at a period ~ 2 h. The “disrupted magnetic braking” model was first proposed by Ritter [87]. AM Her or polar CBs (in which the spin of a highly magnetized WD is locked with the P_{orb}) are found in the period gap in the proportion expected if there is no discontinuous behaviour. MB is probably less efficient in these systems, because synchronous rotation allows the connection between the lines of the magnetic fields of donor and of the WD, and there are few open lines left for the wind to carry away angular momentum [117].

⁶ At $P_{\text{orb}} = 3$ h the donor has a mass $\sim 0.2 M_{\odot}$. In MS models, full convection is reached at $\sim 0.35 M_{\odot}$, but thermal disequilibrium modifies the structure and these mass losing models achieve full convection at a smaller mass.

Below the gap, the evolution of CBs resumes and proceeds at lower mass loss rate, $\dot{M} \sim \text{few} \times 10^{-11} M_{\odot}/\text{yr}$. This can be easily provided by pure GR AML. Even the timescale for such a low mass transfer rate becomes shorter than the thermal timescale, and the low mass donor is driven out of thermal equilibrium and preserves a larger radius. Electron degeneracy becomes increasingly important in the structure approaching the transition to brown dwarf, the mass radius exponent α lowers, the period reaches a minimum when $\alpha \sim 1/3$ (Eq. 7.26), and begins increasing again. Nuclear burning is still active at the minimum period, even if the stellar mass is well below the ‘standard’ minimum mass for core hydrogen burning ($M \sim 0.08 M_{\odot}$), because the structure is not in thermal equilibrium and thus keeps a larger central temperature. Paczynski [77, 78] proposed that the minimum period observed in the period distribution of CBs at 80 min (actually at ~ 76 min, according to the more complete modern inventory, see Fig. 7.3) is due to GR AML. Thus, in spite of the need to calibrate the parameters in the description, the qualitative (and quantitative) picture of the secular evolution of CBs is settled. For a fresh and updated summary see [58].

7.4.1 Extension of the CB Evolution Scheme to X-ray Binaries

While the scenario for the evolution of CBs was building up, some bright galactic X-ray sources were discovered in binaries in the hours period range, and appeared to be the counterparts of CBs, where a NS accretor had replaced the WD.⁷ It was then a natural extension to adopt a similar secular evolution scheme [86].

In this context, Tutukov et al. [110] gave the first description of the ‘bifurcation’ period (P_{bif}) between systems evolving towards short or long P_{orb} . The evolution arrow depends on which timescale prevails. If the AML prevails on the H-core nuclear burning ($\tau_J < \tau_{\text{nuc}}$) mass loss will erode the non evolved MS star, in the typical secular evolution described above; if the H-core burning prevails ($\tau_J > \tau_{\text{nuc}}$) mass loss can not prevent the formation of a H-exhausted core, the stellar radius increases and the system follows a standard ‘case B’ evolution. In [32, 85] we find the first discussions of binary evolution above P_{bif} for the MSP case, and see Sect. 7.6.5.

Systems starting mass loss at periods close to the bifurcation have the arrow of evolution pointing towards shorter periods, but an advanced core hydrogen exhaustion, or even a very small helium core ($\sim 0.02\text{--}0.03 M_{\odot}$) is already present. The radius for a fully degenerate hydrogen–helium core with hydrogen mass

⁷ Interesting to note that two of the few X-ray binaries with determined periods hinting for the analogy with CB evolution were 4U 1626–67 [68], with $P_{\text{orb}}=41$ min, well below P_{min} , and Cyg X3, with a $P_{\text{orb}}=4.8$ h. This latter, in spite of its ‘typical’ period of a few hours, is indeed the final stage of a high mass interacting binary, a black hole accreting from a mass losing Wolf-Rayet star [111].

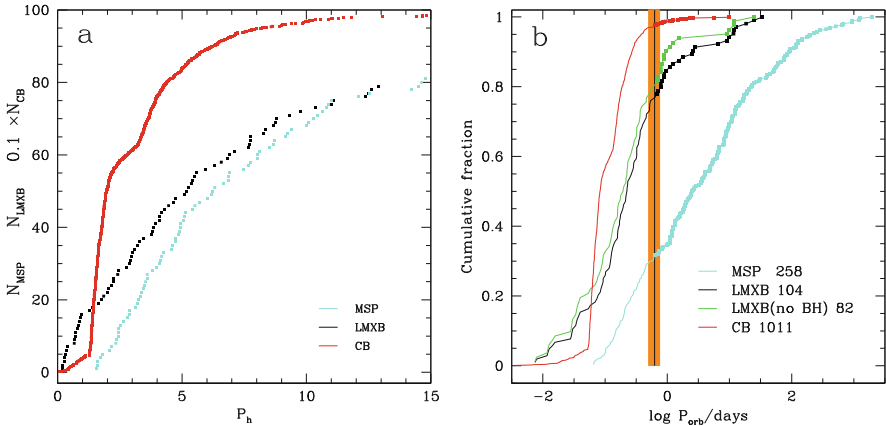


Fig. 7.4 Panel a: comparison of the cumulative number counts for LMXB, MSP and CBs as a function of P_{orb} in the range 0–15 h. Note the different scale for the very abundant CB sample. Panel b: the same comparison highlights with dots the systems above the bifurcation period (orange band)

fraction X can be approximated [74] by:

$$\frac{R_d}{R_\odot} = 0.013(1 + X)^{3/2} \left(\frac{M_d}{M_\odot} \right)^{-1/3} \quad (7.27)$$

Thus the stellar radius is smaller for each given mass. According to Eq. 7.4, these systems may evolve to ‘ultrashort’ periods [38]. The ultracompact LMXBs 4U 1626–67 ($P_{\text{orb}} = 41$ min; [68]) and 4U 1915–05 ($P_{\text{orb}} = 50$ min; [23]) should have degenerate donors remnants of cores in which hydrogen has been partially depleted. The formation of ultracompact binaries in the field may also be due to different pathways through intermediate mass X-ray binaries evolution for a He-star plus NS [22].

7.4.2 Comparisons and the Birthrate Problem

Figure 7.4 shows the cumulative distribution versus P_{orb} for the classes of objects we have been examining. The LMXB and pulsar data are taken respectively from the Ritter LMXB catalogue and from the Australian Telescope National Facility (ATNF) pulsar catalogue.⁸ No completeness study is considered here, but the catalogue of the high luminosity non transient LMXBs is complete, and it is

⁸ <https://www.atnf.csiro.au/research/pulsar/psrcat/>.

improbable that the shape of the distribution is altered when the pulsars database becomes more complete.

In Fig. 7.4a ($P_{\text{orb}} < 15 \text{ hr}$) we see that neither the LMXB nor the MSP distributions show clear indications of the minimum period and period gap, well recognized in the CB distribution. The scarcely populated tail of the distribution of CBs, composed by binaries whose donor is a low mass WD (the AM CVn binaries), is in percentage much more populated in the LMXB sample. On the contrary, *there are no binary MSP below $\sim 2 \text{ hr}$* , so it is clear that the LMXB evolution below P_{bif} has no obvious correspondence with the evolution of CBs in the same P_{orb} range (see Sect. 7.6).

In Fig. 7.4b we see that there are only $\sim 5\%$ of CBs above 8 h period and only few objects above P_{bif} . On the contrary, at $P_{\text{orb}} > P_{\text{bif}}$ there are several LMXB, and most of the MSP (for this latter category, this is simply due to the fact that these systems are endpoints of the evolution).

The total number of MSPs in the catalogues is 2.5 times that of LMXBs. When completeness studies are performed on both samples, the long-standing problem of discrepancy between the birthrates emerges. First Kulkarni and Narayan [59] noticed that the birthrate of galactic LMXB is 10–100 smaller than the birthrate of MSP. This latter is now estimated as $B_{\text{MSP}} \sim 2.5 \times 10^{-6} \text{ yr}^{-1}$ [61]. The birthrate of LMXB can be simply computed as $B_{\text{LMXB}} \sim N_{\text{LMXB}}/\tau_{\text{LMXB}}$, as the LMXB sample does not suffer of any significant incompleteness factor (greatly affecting, on the contrary, the MSP number counts). As $N_{\text{LMXB}} \sim 100$, to obtain the same birthrate of MSP, we need a $\tau_{\text{LMXB}} \sim 4 \times 10^7 \text{ yr}$, much shorter than the typical MB AML ($\sim 5 \times 10^8 \text{ yr}$) or GR AML ($\sim 10^9 \text{ yr}$) timescales.

Solution proposed for this discrepancy are indeed variegated,⁹ including the role of AIC in the direct formation of MSPs, without passing through the LMXB phase [73], the direct formation of NS having a low magnetic field [69] and the role of ‘evaporation’, the ablation of low mass donors through the wind excited by the high energy pulsar radiation impact, see Sect. 7.6.4). In Sect. 7.6.2 we discuss that the irradiation cycles, plus a late final ablation, can be a reasonable explanation for this puzzle.

7.5 The P_{orb} Versus M_d Plane as a Tracer of the NS to MSP Evolution

MSP formation follows a variety of binary channels (see, e.g. [14, 107]), and in most cases the binaries are now detached. We make a rapid excursion on the MSP systems where the companion is a remnant of the evolution of intermediate and high mass binaries, and consider the MSP remnants of the case B evolution of LMXB.

⁹ We quote here that the presence of single MSPs in the field (and the numerical overabundance of MSPs with respect to their supposed progenitors interacting X-ray binaries) has risen the suspect that some MSPs may have been born directly with their present low magnetic field and rapid spin [69].

Once we accept the concept that MSPs are recycled, generally old or very old neutron stars, the plot of companion mass (M_c) versus orbital period (P_{orb}) provides a snapshot of the evolutionary path through which the neutron star has been accelerated.¹⁰

M_c is generally not well determined. We know the projected orbital velocity of the NS itself, through the MSP spin Doppler effect, and so we have the mass function of the companion $M_c^3 \sin^3 i / (M_c + M_{\text{NS}})^2$, where i is the orbital inclination angle. Thus the minimum NS mass M_c can be constrained by assuming a standard value for the NS mass, while an ‘average’ mass is derived by fixing an ‘average’ inclination ($M_{\text{MSP}} = 1.35 M_{\odot}$ and $i = 60^\circ$ in the ATNF catalog). Anyway the value assumed for the NS mass is itself a lower limit, if we consider that MSP must have accreted 0.1-0.2 M_{\odot} to reach their spin. Strader et al. [99] have determined the average mass of 24 confirmed or candidate redbacks components by optical spectroscopy, and the average NS mass is $\sim 1.8 M_{\odot}$, consequently their also find larger M_c 's.

Data with available information are shown in Fig. 7.5, where we also show the subdivision of different loci in the plane (inspired by T. Tauris [104]) for the field MSP.

7.5.1 Double NS Remnants

The possible evolutionary histories of double NS binaries (DNS) have been originally studied in view of the importance of the Hulse–Taylor binary PSR B1913+16, and more recently because the merging of the two NS components is a possible source of gravitational waves bursts, as occurred in the LIGO/Virgo events GW 170817 [2] and GW 190425[1].¹¹

DNS occupy the region of highest M_c highlighted by the yellow colored region in Fig. 7.5, and are born from high mass binaries evolution. In the figure we may also notice that the spins of the MSP component are not extreme, meaning that the primary NS is only partially recycled.

The evolutionary paths to DNS [14, 107] begin with the more massive of the two high mass components undergoing a CCSN and leaving a remnant NS, which may receive a high kick at birth. After some time, the secondary, now the more massive component, will evolve off the main sequence out of its Roche lobe, and fully lose the hydrogen envelope in a CE phase. The binary will be then a NS plus a ‘naked’ helium star companion, and may undergo a further phase of mass transfer

¹⁰ We use from now on the term M_c for the NS companion, both for the detached systems and for the still interacting systems. When discussing the secular evolution, in some cases, we will go back to the term ‘donor’ mass M_d .

¹¹ GW 190425 has a total mass of $3.4^{+0.3}_{-0.1} M_{\odot}$, 5σ larger than the galactic population mean, pointing to a peculiar formation mechanism. Nevertheless, among the possible explanations (see [1]), the high mass of the primary component points towards recognizing it as a NS which has been subject to non negligible accretion after its formation, that is an MSP.

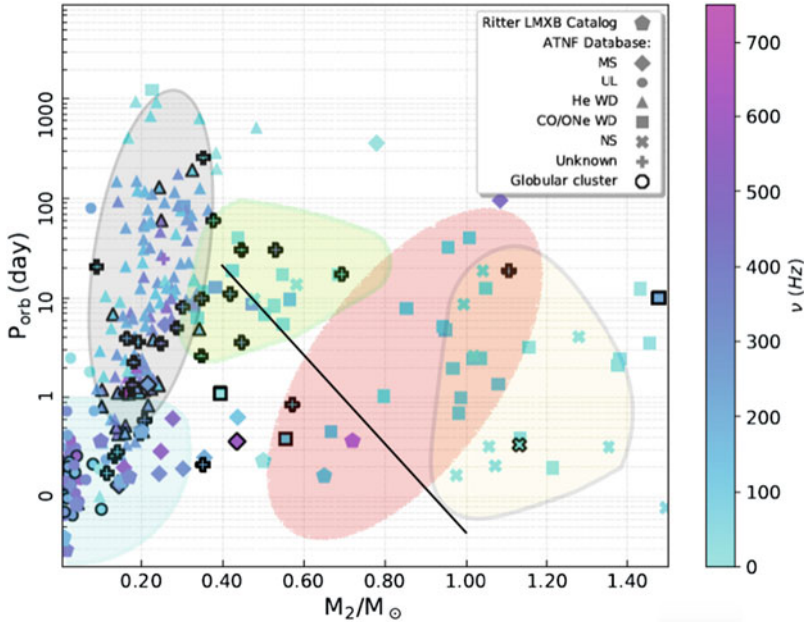


Fig. 7.5 P_{orb} versus average companion mass of LMXBs [89] and MSPs from the ATNF Pulsar Catalogue 2018 are shown with different symbols according to their nature. The colors correspond to the pulsar spin, according to the scale on the right. The diagonal line is the relation minimum $P_{\text{orb}}(M_c)$ for case B evolution [102] leading to systems with CO WD companions. The outcomes ($P_{\text{orb}} \gtrsim 1$ d), in which the companion is a helium WD, are highlighted in grey. The green–yellow shape highlights the location of remnants of Case A and early case B evolution of IMXBs; the red region highlights the remnants of IMXB case C evolution, including a CE phase. NS–NS remnants, highlighted in yellow, result from HMXBs

(the case BB, see, e.g. [30]), during which again the donor helium star overfills its Roche lobe. In both phases of mass loss after the first CCSN, the binary may appear as a HMXB. Eventually, a second CCSN will occur, and the DNS will be formed, unless the natal kick of the second SN explosion unbinds the system. The sequence of events is quite uncertain, because it depends both on the outcome of (two) CE evolutions, and on the uncertainty in the distribution of natal kicks [105].

A different formation channel is possible in GCs: the MSP is formed through one of the other binary evolution paths described below, and the remnant donor mass suffers an exchange interaction with another NS in the GC core, resulting in the exchange of the former donor (the lighter star in the triple) with the NS. The three body interaction may be able to eject the newly formed binary to the outskirts of the GC, from which it may go back to the core due to dynamical friction on a timescale longer than 100 Myr. Such evolution has been suggested to explain the location of the binary pulsar PSR B2127+11C, in the GC M 15, far from the cluster core [81]. The exchange interaction is also testified by the high eccentricity ($e = 0.681$) of this system, and Phinney and Sigurdsson [81] argue that similar interactions,

in a shorter period system, may lead to ejection of the newly formed DNS from the GC or to NS merging by orbital decay due to GR. More recently, Andrews and Mandel [5] consider a sub-population of short-period, high eccentricity field DNS and notice that they have properties similar to PSR B2127+11C. Rejecting the formation channel of these eccentric DNS in a single binary, they argue that they could have been formed in, and then ejected from, GCs.

7.5.2 Intermediate Mass Cases A, B or C

The central region of the data of Fig. 7.5 contains the end-product of the evolution of intermediate mass binaries at different stage of interaction (cases A and B—region highlighted in green—or case C-highlighted in red and characterised by the companion Carbon Oxygen ($M \gtrsim 0.45 M_{\odot}$) or Oxygen–Neon ($M \gtrsim 1.05 M_{\odot}$). We refer the reader to the outline in [106] and references therein for an extensive discussion.

7.5.3 The Evolution to MSPs with Companion Low Mass White Dwarfs

Figure 7.6 shows the lower side of the P_{orb} vs. M_d plane. The evolution above P_{bif} at a first look appears to be standard (e.g. [116]). Giants at $M \lesssim 2.2 M_{\odot}$ increase their radius around the growing of the helium degenerate core. If the donor mass is larger than the NS mass, initially mass transfer proceeds on the thermal timescale and P_{orb} decreases. When the mass ratio is reversed, the mass transfer proceeds on the nuclear timescale and is ideal to accelerate the pulsar, which will emerge when the donor, lost the majority of its hydrogen envelope, contracts to become a helium WD. Thus the period distribution of MSP with He–WD companion, from a few to hundreds of days, represents the frozen endpoints of binary evolution. The existence of a He-core mass vs. radius relation—almost independent of the total mass—implies, that there will be a well defined period at which the donor detaches from the Roche lobe for each core mass, and thus there is a relation between the WD remnant mass and P_{orb} (see [63] and the red line in Fig. 7.6 for a recent expression).

A class of systems progenitors of these MSP with He–WD companions may be the recently discovered systems 1FGL J1417.7–4407 ($P_{\text{orb}} = 5.4$ d, [101]) and PSR J1306–40 ($P_{\text{orb}} = 1.096$ d [100]), dubbed ‘huntsman’ pulsars (referred to the classification of companions of MSP in different classes of spiders (see Sect. 7.6). We discuss in Sect. 7.6.5 the ambiguity in the evolution of such systems, with reference to the similar case of PSR J1740-5340.

From the ‘bifurcation’ of the evolutionary tracks, either towards long P_{orb} and degenerate companion, or to short P_{orb} for core H-burning companions, we expect

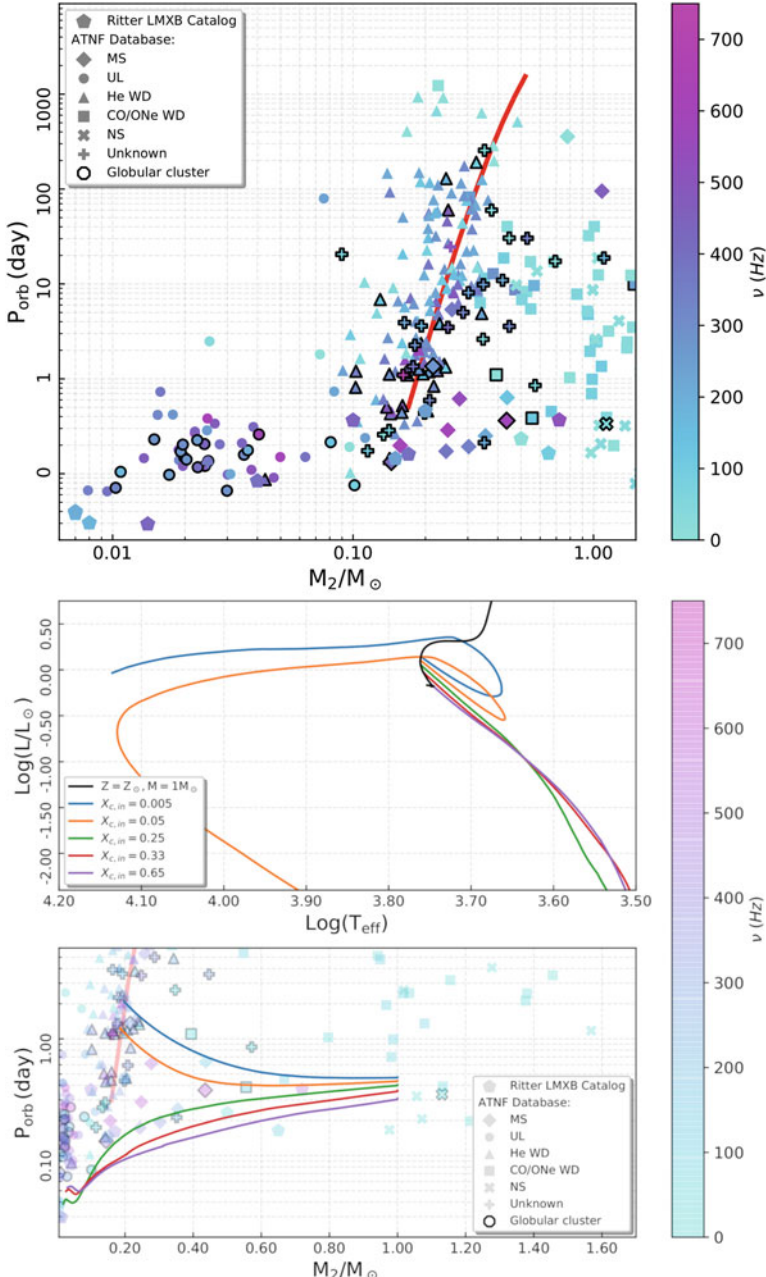


Fig. 7.6 In the top panel, the P_{orb} versus $\log(M_d)$ plot is shown for the lower mass side, where we see well the location of helium WD companions at $P_{\text{orb}} \gtrsim 1$ d. Analytic expression from [63] is plotted for masses from 0.15 to $0.5 M_\odot$. The bottom panel shows typical ‘classic’ evolutionary tracks of the donors in the HR diagram (upper panel) and in the P_{orb} versus $\log(M_d)$ plane (bottom)

a dearth of systems in the region $0.3 \text{ d} \lesssim P_{\text{orb}} \lesssim \text{few days}$. This dearth of system is not observed (see Sect. 7.6.5).

7.6 Short Period, Low-mass Companion Systems: The Mixed Bag

Overall, the evolution starting below P_{bif} results to be the most interesting in the $P_{\text{orb}}\text{--}M_c$ plane, because it also hosts systems which are not necessarily at the end point of their orbital evolution, and contains both LMXB (or AMXP) and MSP systems. We show in Fig. 7.7 the P_{orb} vs. M_c data with their identification, from A. Patruno's catalogue.¹² In spite minimum M_c is plotted, there is no doubt that the true M_c at any given period is *smaller* than the donor masses of CBs. Overall, this region of the $P_{\text{orb}}\text{--}M_c$ plane includes:

- **AMXP**: accreting millisecond X-ray pulsars (see Chap. 4). They include MSPs with shortest P_{orb} . Companions may be H-rich, He- or CO- WDs [20, 80].
- **Radio MSP binaries** (see Chap. 1): in these (detached) systems the companion may be a H-burning dwarf or a He-WD. These latter companions are also found at $P_{\text{orb}} < P_{\text{bif}}$. In many system the companion is not yet identified.
- **Redbacks** (see Sects. 1.4.3, 3.6, 2.4 and Chap. 6): the red dots (GC) and triangles (field) in Fig. 7.7 mark the systems called ‘redbacks’ [90], showing extended radio eclipses, associated with circumbinary material, and $0.1 \lesssim M_c/M_\odot \lesssim 0.7$ [99], on almost circular orbits with periods $0.1 \text{ d} \lesssim P_{\text{orb}} \lesssim 1.37 \text{ d}$ (note that some redbacks are at $P_{\text{orb}} > P_{\text{bif}}$).
- **Transitional MSP** (see Chap. 6): a class of redbacks switching from the AMXP to the radio MSP stage [79] on timescales of months.
- **Black widows** (see Sects. 1.4.3 and 3.6) are defined as the family of pulsars in a P_{orb} range similar to the range of redbacks, but with companions having $M_c \lesssim 0.05 M_\odot$.

To explain this variety of systems, the evolution of the donor must include physical inputs due to the NS (and MSP, when accelerated) nature of the accretor, the main reason why the period distribution of LMXB and MSP binaries at $P_{\text{orb}} < P_{\text{bif}}$ is very different from the ‘standard’ CB evolution (Sect. 7.4.2 and Fig. 7.4). When the NS is very close to the companion, the donor suffers from different kinds of irradiation and its structure changes accordingly. Other phenomena as the “radio-ejection” ([17], see Sect. 7.2.3.1) can also be at the basis of the modified evolution.

¹² www.apatruno.wordpress.com/about/millisecond-pulsar-catalogue/.

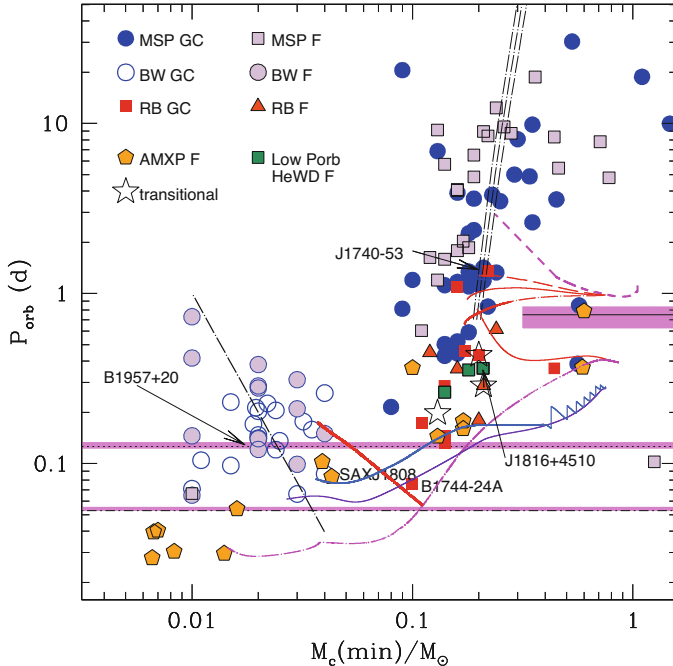


Fig. 7.7 Minimum M_c versus P_{orb} plane (data taken from the Millisecond Pulsar Catalogue compiled by A. Patruno, <https://apatruno.wordpress.com/about/millisecond-pulsar-catalogue/>). P_{bif} , the 3 h period gap, and the $P_{\text{min}}=76$ m of CBs are highlighted in pink. Most AMXPs (yellow pentagons) are at $P_{\text{orb}} < P_{\text{min}}$. Grey squares (GC) and blue dots (field) are standard MSP with (mainly He-) WD companions, and three green squares mark the lowest P_{orb} MSP with He-WD M_c in the field (see [50]). Red squares and triangles are the redbacks, and the open stars show transitional MSP. Above P_{bif} , we show three different evolutions starting at $M_0=1.05 M_\odot$, in case A, but with an advanced consumption of the core hydrogen. The violet dashed curve and the red lines represent evolution with increasing specific angular momentum losses associated to the mass lost from the system when radio-ejection sets in. Shorter final P_{orb} corresponds to stronger specific AML. Below P_{bif} , starting from $0.85 M_\odot$, the dash-dotted magenta line is a standard binary evolution starting in late case A, with no illumination and reaching a minimum period well below 76 m, as the hydrogen content of the core is very small. The violet and blue lines are taken from [103] and represent a standard case A evolution (no illumination) and an evolution with illumination $\epsilon_X = \epsilon_{MSP} = 0.01$. This latter passes through the location of the AMXP SAX J 1808.4-3658. The diagonal dot-dashed lines are an evolution starting from a thermal equilibrium configuration at $\sim 0.12 M_\odot$ and including a strong MSP illumination (red line, see text) and a typical evolution with evaporation (black line, from [12])

7.6.1 The Radius Reaction when a Source of Irradiation Is Present

The total stellar radius derivative in Eq. 7.6 includes the terms independent on the mass loss, and due to nuclear evolution and thermal relaxation. There is another

powerful way of radius change, whose effect is important when the donor has a convective envelope, and it is the ‘irradiation’ or ‘illumination’ term. We write explicitly:

$$\left(\frac{\partial \ln R_d}{\partial t} \right)_{M=0} = \left(\frac{\partial \ln R_d}{\partial t} \right)_{\text{th. rel.}} + \left(\frac{\partial \ln R_d}{\partial t} \right)_{\text{ill}} \quad (7.28)$$

(the negligible term $(\partial \ln R_d / \partial t)_{\text{nuc}}$ is dropped). The importance of the last term was first shown in [82], addressing the change in the structure of stars with a convective envelope immersed in the X-ray radiation field of the accreting NS. Afterwards, the problem received attention by considering the evolution of the companion of MSP irradiated by the MSP power [27] or accreting NS irradiated by the X-ray flux [11, 26, 44], with the main attention focused on the onset of mass transfer.

When the donor, having an unperturbed luminosity L_* , finds itself immersed in a “heating” bath of luminosity L_h , the stellar surface suddenly can not emit L_* , so its structure (its T_{eff}) must adjust so that the star can emit *both* the intrinsic and the heating luminosity:

$$L_{\text{tot}} = L_* + L_h = 4\pi R^2 \sigma T_{\text{eff}}^4 \quad (7.29)$$

where $L_h = 4\pi R^2 \sigma T_b^4$ defines the temperature of the radiation bath T_b . This is not a problem for the stars having radiative envelopes, as they can adjust easily the temperature gradient in the external layers to do it, and, in fact, illumination is totally irrelevant for donors of $M \gtrsim 1.5 M_\odot$. But, for smaller masses, the stellar envelope is convective, and throughout the envelope the temperature gradient is adiabatic, and dictated by thermodynamics (apart from the upper over-adiabatic surface layers). Thus the surface perturbation is immediately felt *at the bottom of the convective envelope*. Starting from a configuration of thermal equilibrium ($L_* = L_{\text{nuc}}$), the star reacts approximately only on the thermal timescale of the convective envelope itself, longer for smaller masses having deeper convective envelopes ($\sim 10^8$ yr for a $0.5 M_\odot$), but in any case long enough that a “fully bloated” configuration (those studied in [82]) can not be reached.

A better physical approach to describe the irradiation comes by considering that an irradiation flux $F_{\text{irr}} = L_h/(4\pi R^2)$ is deposited below the photosphere. The illumination, which in principle affects at most half of the donor surface, is thus distributed on the back side of the star on a timescale much shorter than any of the evolutionary timescale into play, and mainly shorter than τ_{conv} . The ways in which the flux can be distributed and becomes symmetric has been considered by several studies, notably in [45, 113]. The nature of the illumination source is relevant, because it determines the depth at which the energy flux penetrates into the envelope: the depth is larger for a harder X-ray flux, but even a soft X-ray spectrum allows $\sim 10\%$ of flux deposited in the adiabatic part of the convective envelope [113], and can be circulated to the dark side on a timescale close to the

sound speed. When the deposition density becomes a few tens of g cm⁻², the effect on the radius derivative becomes close to that of symmetric illumination [44].

When the problem was initially approached [113], the idea about MSP illumination was that a role was played by the relativistic e⁺-e⁻ pairs and γ ray photons present in the beam composition. *Fermi* LAT observations have shown that the γ -ray emission power from MSP may be a considerable fraction (10-90%) of the spin down energy ([3]; see Chap. 2). Thus the MSP illumination has the potential to be much more symmetric and effective than the illumination from X-rays during the accretion stages. The roles of illumination by the X-rays in a LMXB, or by the pulsar radiation in a MSP are indeed very different as we are going to discuss.

7.6.2 *The Consequence of X-ray Irradiation: Mass Transfer Cycles*

Independent from the ‘symmetry’ of illumination, the activation of the NS as an X-ray source is such that it affects at least a fraction of the donor surface, altering the ways in which the stellar luminosity (equal to $4\pi R^2$ times the flux, in standard conditions) is emitted, if about a half of the 4π solid angle is blocked by the X-rays. This will affect the radius and the mass transfer at least in a transitory ways.

At first the donor is in thermal equilibrium. As soon as the Roche lobe approaches to the stellar radius, mass transfer begins, following Eq. 7.18, and most of the gravitational energy liberated by mass accretion on the NS will be emitted in the X-ray region of the spectrum, L_X . A fraction ϵ of the intercepted power of the X-ray luminosity at the surface of the donor having radius R_d , in the binary having separation a will be the illumination power:

$$L_{ill} = \epsilon \times \left(\frac{R_d}{2a} \right)^2 \times L_X \quad (7.30)$$

For typical conditions of LMXB systems, very small ϵ is enough to provoke cycles of mass transfer followed by epochs of detachment. The cycles depend on the fact that the average \dot{M} through the secular evolution is eventually due to the systemic AML, so if \dot{M} becomes larger than the average, at some stage, because of the additional radius increase due to illumination, it must be reduced in the following stage. The illumination cycles in CBs are due to the (much weaker) UV irradiation of the accreting WD: these have been formally studied by King et al. [57], showing that they induce a modulation of the mass transfer rate around the rate dictated by the systemic AML. The effect can explain the differences in mass transfer found for CBs having similar orbital periods.

7.6.2.1 Mass Transfer Cycles and the Redbacks

The cycles of mass-transfer due to X-rays illumination in LMXBs are particularly important, as they may be relevant to understand: After early computations [26, 44, 45], recently the evolution of LMXBs with illumination has been afforded in [11–13, 103].

Equation 7.20 is modified by illumination, as there is a further perturbative factor for the stellar radius:

$$\ddot{M} = \dot{M} \frac{R_d}{H_p} \left[(\zeta_S - \zeta_{RLd}) \frac{d \ln M_d}{dt} + \left(\frac{\partial \ln R_d}{\partial t} \right)_{ill} \right. \\ \left. + \left(\frac{\partial \ln R_d}{\partial t} \right)_{th.\,rel.} + \left(\frac{\partial \ln R_{RLd}}{\partial t} \right)_{\dot{M}=0} \right] \quad (7.31)$$

The term $(\partial \ln R_d / \partial t)_{ill}$ is positive and acts to enhance the mass transfer rate, contrary to the relaxation term $(\partial \ln R_d / \partial t)_{th.\,rel.}$, negative for this kind of donor. The Roche lobe will follow the radius increase, and the orbital period will increase. In the first stage, \dot{M} increases, and so increases L_{ill} while the radius reacts on the thermal timescale of its convective envelope. The larger is the donor mass, the smaller is the convective envelope extension—and the thermal timescale at its bottom—and the faster is the radius increase and the larger the \dot{M} peak. The limitation in the mass transfer rate is not due to the impinging radiation level (ϵ), but only to the interplay between the radius expansion due to illumination and the thermal relaxation. As soon as the radius begins to decrease due to the thermal relaxation of the envelope, \dot{M} decreases, together with the illumination source (proportional to \dot{M}), and the radius tends to go back to its thermal equilibrium radius. In the X-ray phase the period has increased due to the anomalous mass transfer, so that the donor finds itself within the Roche lobe and mass transfer stops until the AML brings it back into contact.

The onset of mass transfer for different initial masses and different fractions of irradiation due to the X-ray luminosity are shown in the Fig. 7.8. The larger is the donor mass, the longer is the interval between the LMXB phases and the higher the peak of mass transfer reached. The dominant factor in the play is the thermal timescale of the convective envelope, which increases with decreasing the mass.

The orbital period derivative \dot{P}_{orb} measured in LMXBs is not directly linked to the secular evolution, that is to the angular momentum losses which are the primary drivers of standard evolution, but *to the phase at which we are looking at the system, along the cycles of mass transfer*.

The cyclic evolution is unavoidable for all masses which have convective envelopes, thus $M \lesssim 1 M_\odot$. In the larger masses the cycles lead to super-Eddington mass transfer rates, and only a minor fraction of the mass lost by the donor can be accreted. The high mass loss means that a few cycles of LMXB will be sufficient to reduce the mass quickly, and the probability to catch an LMXB system with a donor mass in the range $0.4 \lesssim M/M_\odot \lesssim 1$ is small. Thus a reason why the donors have

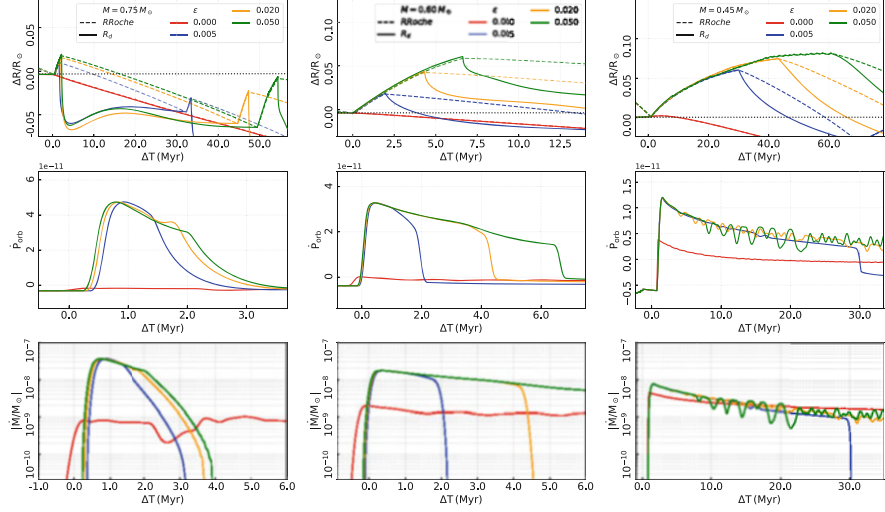


Fig. 7.8 Top panels: radius evolution during the first cycles of mass transfer in binaries containing a NS and a main sequence donor of $0.75 M_{\odot}$ (left panel), $0.6 M_{\odot}$ (center) and $0.45 M_{\odot}$ (right). Note the different timescales in the abscissa. Mass transfer is computed following the non stationary phases by Eq. 7.18 in Sect. 7.3.4, and the mass loss rate is shown in the bottom panels, in an enlarged scale which covers the first cycle of mass transfer only. This same time scale is used in the Central panels, plotting the derivative of the orbital period. The red line shows the evolution driven by AML only, not considering illumination. The radius decreases and the \dot{P}_{orb} is negative during the whole evolution. The other lines show the evolution for different fractions of illumination ϵ from 0.5 to 5%. The maximum radius expansion increases with ϵ , and the system detaches almost suddenly when the radius increase due to illumination is overcome by thermal relaxation. The dashed lines represent the Roche lobe evolution, which closely follows the radius expansion until detachment, while the following contraction occurs on the timescale of AML, until the stellar and Roche radius meet again and the new cycle begins. Of course, the interval of detachment is longer when ϵ is larger. Note that the *maximum* \dot{P}_{orb} is independent on ϵ

smaller mass than the values found for donors in CBs at similar P_{orb} may be linked to the occurrence of super-Eddington cycles of mass transfer.

In the range $M/M_{\odot} \lesssim 0.4$ the cycles become longer. Nevertheless, the mass transfer remains unstable and thus the system is active as LMXB only for a fraction of the AML timescale. From Fig. 7.8, considering the shorter recurrence between cycles ($\epsilon = 0.005$), the LMXB phase is $\sim 1/15$, $1/10$ and $1/4$ of the entire cycle, thus fully solving the birthrate problem.

In the case displayed, and in [103], each cycle spans from 30–50 Myr ($0.75 M_{\odot}$) to 20–90 Myr ($0.6 M_{\odot}$) to 70–140 Myr. This kind of cycles is compatible with the positive \dot{P}_{orb} 's found for some AMXPs (see Sect. 4.3.4).

In particular, the $\dot{P}_{\text{orb}}=3.6\div3.8 \times 10^{-12}$ [93] measured during the outbursts in SAX J1808, can be reproduced by standard evolution including X-ray irradiation and MSP irradiation with $\epsilon = 0.01$ [103].

The cyclic evolution also accounts for the higher frequency of systems at $0.1 \lesssim M/M_\odot \lesssim 0.2$. In fact, only $\sim 10\%$ of the total secular evolution time is spent at masses $\gtrsim 0.2 M_\odot$, the evolution slows down at smaller M_c because the detachment periods become longer.

Summarizing, the X-ray cycles may be relevant to understand:

1. the difference in the birthrate of MSP and LMXBs: the birthrate of LMXBs is reduced, as the timescale of the mass-exchange phases is much shorter than the timescale imposed by systemic AML;
2. the faster evolution observed for some LMXBs by measuring their \dot{P}_{orb} , in particular the high positive \dot{P}_{orb} 's;
3. the large differences in \dot{P}_{orb} , for very similar systems.
4. the cyclic detachment allows to initiate the interaction of the MSP with the companion (MSP illumination, evaporation or radio-ejection) at any stage along the secular evolution, as soon as the NS has been accelerated. There is no need to invoke detachment at, say, the period gap.

7.6.3 The MSP Illumination

There is a further consequence of the cyclic detachment: when the NS has been accelerated to MSP, the pulsar power may catch on and become the most important source of perturbation of the companion evolution: the pulsar emission in the γ -ray spectrum [3] represents a long lived illumination source, and is more ‘symmetric’ and effective than the X-rays during the accretion stage, thanks to its deep penetration into the donor envelope. Thus the X-ray cycles are the way the low mass system is able to recycle the NS companion to millisecond spin periods.

The illumination due to the MSP may be the key to understand the lack of standard MSP binaries below $P_{\text{orb}}=2$ h (other models are available as well).

First, the NS has to be accelerated to the MSP phase, so the presence of an illumination due to the MSP depends on the precise effect of the NS spin-up and spin-down mechanisms. The spin-up problem has been afforded numerically in early works in e.g. [60, 71] and more recently in [103].

According to the Larmor formula, the pulsar luminosity can be written as:

$$L_{\text{MSP}} = \frac{2}{3c^3} \mu^2 \left(\frac{2\pi}{P_s} \right)^4 \text{erg/s} \quad (7.32)$$

where μ is the magnetic momentum of the pulsar in $G \text{ cm}^3$, c is the speed of light and P_s the spin period in seconds. With the typical values of magnetic momentum, derived from the MSP spin down, the MSP luminosity is much smaller than the X-ray luminosity in the typical LMXB regime, resulting to be $10^{32}\text{--}10^{35}$ erg/s, to be compared with $L_X \sim 10^{38}$ erg/s in systems accreting at Eddington rate.

Nevertheless, even a small fraction of MSP illumination is sufficient to allow the donor to remain much more expanded than obtained by the thermal disequilibrium due only to systemic mass loss mechanisms [103], and the minimum period reached by these systems will be much larger than the 80 min of CBs, depending mostly on the fraction of MSP illumination allowed. The results of the computation in [103] show explicitly that the important factor to produce long term effects is the action of the MSP spin-down luminosity, even at the low level of 1% efficiency as in the case shown in Fig.7.7 (blue line). X-ray illumination only is totally ineffective in the long term and the evolution is very similar to the standard evolution (violet in Fig. 7.7).

Thus the role of the X-ray illumination for the secular evolution is almost negligible, but it allows the existence of cycles of mass transfer, so that the system is detached for most of the time, and the much more efficient and symmetric illumination due to the MSP spin down luminosity is the true responsible for the peculiarity of the binary evolution in the MSP binaries.

7.6.4 *The ‘Evaporation’ Model: A Role for the Black Widows Stage?*

We have seen in the preceding section that at least some systems in the BW region ($M_c \lesssim 0.05 M_\odot$ and $P_{\text{orb}} \sim 2\text{--}20 \text{ hr}$) can result from standard evolution from a main sequence donor, with a small degree of illumination in both X-ray and MSP stages. But the BWs are most probably the result of a variety of possible evolutionary paths, and generally ‘evaporation’ is indicated as the dominant active mechanism.

The first evidence of the effect of the role played by a close MSP on the binary evolution was the discovery of wind mass loss from the companions of two MSP:

1. PSR B1957+20 [40] at $P_{\text{orb}}=9.2 \text{ h}$, with an $M_c \sim 0.025 M_\odot$. The companion eclipses the pulsar for $\sim 50 \text{ m}$, and delays the pulses for a few minutes before and twenty minutes after the eclipse, indicating the presence of surrounding plasma.
2. PSR B1744-24A (J1748-2446A) in the GC Terzan 5 [66, 72], at $P_{\text{orb}}=1.8 \text{ h}$ with variable eclipse duration from 1/3 to 1/2 of the orbit. Thus the eclipsing region is much larger than the Roche lobe of the companion having $M_c \sim 0.1 M_\odot$. This MSP system becomes then a prototype of redbacks.

Does the impinging radiation from the MSP cause a wind mass loss with an associated AML due to the MSP pressure acting on the wind? When these systems were observed, already a model predicting ‘evaporation’ from a close companion of an MSP had been developed by Ruderman et al. [92]. The physics of evaporation presents several big question marks. The efficiency in producing the wind (‘wind driving’) is the first quantity to be understood (or parametrized). The following problem is how AM is lost from the system during the wind phase, as the period evolution largely depends on this input [33, 36, 108]. SPH simulations in 2D and

3D [109], led to the proposal of a model of self-excited evolution of LMXB [9], in which the mass and AML due to the evaporation stimulated further mass loss till the reduction of the companion of the MSP to the planetary mass stage.

A ‘fast evaporation’ model was developed by Stevens et al. [98] to account for the presence of ‘planets’, companions of a few Earth masses, around pulsars [7], that would be formed in the thick disk around the NS, due to the evaporation of the MSP companion. In this study, the authors propose a simple expression for the evaporation:

$$\dot{M}_{\text{evap}} = \zeta L_{\text{MSP}} \left(\frac{R_d}{a} \right)^2 \quad (7.33)$$

where R_d and a are the donor radius and the separation. The normalizing factor ζ is estimated by requiring that the pulsar luminosity L_{MSP} intercepted (times an efficiency factor f) is equal to the kinetic luminosity of a thermal wind with speed equal to the escape velocity v_{esc} from the stellar surface:

$$f L_{\text{MSP}} \left(\frac{R_d}{2a} \right)^2 = \frac{1}{2} \dot{M}_{\text{evap}} v_{\text{esc}}^2 \quad (7.34)$$

This assumption is very important for the model, because the brown dwarf donor will inflate ($M \propto R^{-3}$) losing mass adiabatically, v_{esc} becomes smaller and evaporation faster.

The evaporation model has been applied in several recent works [10, 12, 21].

Chen et al. [21] focus on the bimodal distribution of MSP of low M_c , between the region of $M_c \gtrsim 0.5 M_\odot$, populated by redbacks and the region of $M_c \lesssim 0.05 M_\odot$, populated by BWs. They suggest that in both regions evolution is dominated by evaporation, but at different efficiency. The model proposes that the NS has been accelerated by a standard LMXB evolution until the system detaches due to the radius contraction at the period gap. At this point, the donor may recover its equilibrium radius, if f is small, or begin the evaporation phase, if f is large. In the latter case, the system will find itself in the redbacks region, in the first case it will populate the BW region. The reason for different values of efficiency may reside simply in the distribution of angles between the orbital angular momentum and the pulsar magnetic axis. This model anyway has to include further hypotheses to account for the redbacks having M_c larger than the typical $0.2 M_\odot$ at which the period gap would appear.

This model is interesting because it proposes a unique mechanism both for the redback and BW stage. We will see in Sect. 7.6.5 a different proposal linked to illumination and radio-ejection for redbacks. Further, we have seen in Sect. 7.6.2 that the structure of the companion modified by illumination delays reaching of a fully convective structure to below $0.1 M_\odot$, and anyway X-ray cycles predict detachment at any stage, independent of the presence or not of a period gap. Thus it is more

probable that evaporation has a role mainly after the binary has already reached a short period during the previous evolution.

Benvenuto et al. [10–12] model the evolution of black widows through evaporation. The simple prescription in Eq. 7.34 [98] is adopted, fixing the efficiency at $f = 0.1$. The evolution is followed through cycles of mass transfer (see Sect. 7.6.2) until the mass-radius relation of the donor reverses, at the minimum period (see Sect. 7.4) and then the evaporation acts to increase the orbital period. Different degrees of hydrogen consumption in the donor are followed. The progenitor of BW, in this scenario, evolve when the initial period of the binary is close to the bifurcation. Benvenuto et al [12] show that the range in their models is $P_{\text{orb}} \sim 0.6\text{--}1\text{ d}$ for $M_{\text{in}}=1.5\text{--}3 M_{\odot}$. The starting relatively large initial masses are necessary to reach the observed average density of the companion and the mass ratio of some BW binaries. The partial hydrogen consumption in the core is also consistent with the very hydrogen poor spectrum of the companion of PSR J131-3430 [91]. Other BWs have standard hydrogen rich companion spectra, so the BWs appear to be a mixed bag themselves.

We must not forget that the BW binaries might not be the end point of the secular evolution in a single binary. King et al. [56] noticed that BWs are more abundant in GCs than in the Galactic field, and in particular, GC MSP binary lack the rich population of remnants of case B evolutions of intermediate and high mass present in the field (see Fig. 7.5) where the systems above the line of minimum P_{orb} for these evolutions are all in the field). Thus they suggested a two-stage formation: first a binary evolution leading to the acceleration of the NS, generally in a case B evolution, leaving a loosely bound WD companion; a second event would be an exchange interaction by which the low mass WD is substituted by a main sequence star (of mass most probably close to the turnoff mass of the epoch of the exchange) leaving a high eccentric orbit. Tides at periastron reduce the eccentricity and, added to further encounters, lead to a closer orbit. The further evolution would be dominated by radio-ejection and lead the system to a BW stage. Field BWs then require the ejection of the system from the parent GC.

The BW companion can be the same star which spun up the NS only if the detachment occurs at short P_{orb} , and that GR can bring the MSP and the companion close enough to start evaporation on a timescale shorter than the age of the Universe.

An alternate path to the BW region occurs if we consider the effect of MSP illumination [27] during the time of action of GR in a detached stage such that the low mass companion has reached thermal equilibrium again.¹³ If the L_{MSP} is indeed 10–90% of the spin down energy, as implied by the gamma ray observations, the donor expands to its Roche lobe and goes on expanding while mass is lost by the system, and P_{orb} increases. In Fig. 7.7 we show the possible path starting at

¹³ This case is different from those discussed in [103]—e.g., the evolution passing through SAX J1808 in Fig. 7.7—where the donor was never able to go back to full thermal equilibrium, thanks to the small X-ray and MSP irradiation, at the detachments following the X-ray cycles. In the case here examined, the evolution starts with a companion in thermal equilibrium, and for this reason the effect of the MSP irradiation is larger, see, e.g. the models in [27].

$0.12 M_{\odot}$ and ending at $0.04 M_{\odot}$ and $P_{\text{orb}} \sim 5$ h, in the middle of the BW region. The timescale of this evolution will be $\sim 0.5\text{--}1 \times 10^9$ yr, if the mass loss is dominated by the companion expansion due to the illumination. If evaporation also is active, the timescale becomes shorter. The advantage of including illumination is that the companion will be always close to Roche lobe filling, and the mechanism will be more effective (see Eq. 7.34).

7.6.5 The Evolution Close to P_{bif}

In Fig. 7.7, the two red squares (redbacks in GCs) just above P_{bif} , are PSR J1748–2446ad, the fastest MSP at 716 Hz found in the GC Terzan 5 at $P_{\text{orb}} \sim 26.26$ h [46], and PSR J1740–5340, the partially obscured MSP in NGC 6397 at $P_{\text{orb}} \sim 32.5$ h [25]. The radio eclipses in both these systems are of variable length, leading to model the companion as a star losing circumbinary material, as it would occur in the ‘radio-ejection’ model. As PSR J1740–5340 belongs to a Globular Cluster, the initial mass of the MSP companion can not have been larger than the turnoff mass for this cluster. Working on this hypothesis, Burderi et al. [17] reproduced the present location of the donor in the color magnitude diagram, starting the evolution with mass transfer in early case B, from a slightly evolved $0.85 M_{\odot}$. They presented the case that the system is now in the radio-ejection phase. Nevertheless, in the published computations the companion mass at the period of PSR J1740–5340 would be still much larger than the observed mass ($\sim 0.5 M_{\odot}$, versus $\sim 0.3 M_{\odot}$). Exploratory evolutions include larger losses of orbital angular momentum associated with the evolution are shown in Fig. 7.9: the track in [17] is represented by the continuous line starting at $M = 0.85 M_{\odot}$, while some other tracks start from the stage reached at $P_{\text{orb}} \sim 26$ h. These latter are computed in the hypothesis that the NS initiates radio-ejection already at 26 h, it does not accrete any more and there is more or less specific angular momentum loss associated with the loss of mass from the system. Some of these tracks (full line and magenta dashed line) can indeed represent the M_c – P_{orb} status of PSR J1740–5340, as also has been modelled by Ergma and Sarna [34] who were able to fit the MSP companion with M_c close to the observed range of values.

7.6.5.1 An Alternative Path for the Short- P_{orb} MSP with He-WD Companions?

The peculiar evolution of binaries starting close to P_{bif} when the mass transfer is non conservative was studied by Ergma, Sarna and Antipova [35], who found out that when the mass is fully lost the systems evolve towards shorter P_{orb} , leaving an MSP plus low mass WD system. They did not specify a mechanism to account for the mass loss, but were then able to characterise a range of initial periods for which the final P_{orb} would depend on the loss of mass and AM from the system.

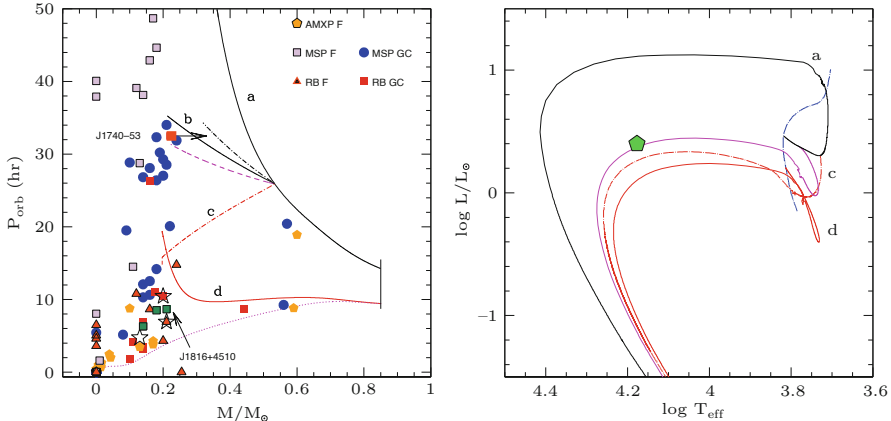


Fig. 7.9 Evolution of the companion of PSR J1740-5340, whose plausible mass range is limited by the red square (minimum mass) and the black arrow ($M_c \lesssim 0.35 M_\odot$). The location at the turnoff of the Globular Cluster NGC 6397 implies an initial mass $\sim 0.85 M_\odot$. Left panel: Standard evolution with radio-ejection begins at $P=29$ h, assuming that the mass is lost with the specific AM at the Lagrangian point (curve a [17]) and predicts $M_c \sim 0.5 M_\odot$ at $P_{\text{orb}}=32.5$ d. A larger loss of specific angular momentum is needed to fit the system data (e.g. curve b). In the extreme assumption (curve c) that the specific AML is 20% larger than at the donor location, P_{orb} decreases. We show also two evolutionary tracks starting with a much less evolved stage of the donor of $0.85 M_\odot$, with different primary losses of angular momentum. In the right panel some of the evolutionary tracks are shown in the theoretical HR diagram, where also the $0.85 M_\odot$ track is shown (dash dotted blue line). Case c, d of the left panel evolve to the WD stage at luminosities below the main sequence starting location, and may be able to represent the locus of the peculiar companion of PSR J1816+4510 (green pentagon [53])

In analogy, we have shown in Fig. 7.9 that the low donor mass and short P_{orb} of PSR J1740-5340 can be reproduced by including significant angular momentum losses associated with the mass lost from the binary due to radio-ejection (corresponding to the redback stage). In a similar way, the specific AML of evolutionary tracks starting from an $1.05 M_\odot$ donor (of composition close to that of the GC Terzan 5) may be adjusted in order to reproduce the $P_{\text{orb}} \sim 26$ h of PSR J1748-2446ad (full red line in Fig. 7.7).

The evolution computed for PSR J1740-5340, but including AML greater than that due to mass lost with the specific AM of the donor, evolves to a very short period of about 0.5 d (red dot-dashed line), where the mass loss stops and the companion is now a low mass He-WD. Thus the radio-ejection phase may produce remnant systems such as, discussed in Sect. 7.6, of an MSP with a He-WD companions at very short P_{orb} (~ 0.3 d), possibly easing the difficulty mentioned by Istrate et al. [50].

The MSP with He-WDs at short period may then represent an important hint of evolution with strong consequential AML due to the influence of the MSP on the mass loss from the system. Indeed, the lowest P_{orb} of such MSPs is PSR J0751+1807 at $P_{\text{orb}}=6.3$ h [65], PSR J1738+0333 at $P_{\text{orb}}=8.51$ h and

PSR J1816+4510, at $P_{\text{orb}}=8.66$ h [53]. In this last system, the spectrum of the optical component resembles that of a hot (~ 16500 K) proto-WD, but it has a lower gravity and larger radius, and it shows numerous helium and metallic lines, more similar to the non degenerate companions of redbacks. In addition, the radio MSP eclipses for $\sim 10\%$ of the orbit [54], a feature again more similar to the redbacks behaviour. PSR J1816+4510 could represent the final stage of evolution of a binary in radio-ejection, following the stage in which it appears as a redback, and before the fully detached MSP plus He-WD stage. We show its location as a green pentagon in the HR diagram in Fig. 7.9, where we see that the high T_{eff} and relatively low gravity $\log g = 5$ [53] are in good agreement with the evolutionary tracks including high specific AML during the radio-ejection phase. From this point of view, the transitional systems could also be linked to this peculiar evolution.

We must explicitly note that the X-ray irradiation cycles described so far have no relation whatsoever with the ‘transitional’ MSP, switching from the AMXP to the radio MSP on a timescale of a few weeks (see Chap. 6). Such a rapid change can not be related to any of the timescales (systemic AML, thermal stellar timescale or thermal timescale of the convective envelope) so far investigated. Nevertheless, the study of irradiation shows that the thermal disequilibrium during the secular evolution is such that the stellar radius and the Roche lobe radius are kept close to each other in a very unstable situation which might well be subject to other shorter term variations. Any physical mechanism causing the transition from MSP to AMXP on weeks timescale deals with a system in which the companion barely fills its Roche lobe, in a stage of thermal instability.

If the redbacks are a mixed bag of systems with pre-WD or core–hydrogen burning companions, one must ask if there is a preferential class to which the transitional objects preferentially belong.

7.7 Summary and (a few of the) Questions Left Open

In spite of all the work done in the latest forty years, there are still problems in the binary evolution of MSP, and of their multifaceted characteristics. We have specifically dealt mostly with the low mass—short P_{orb} region, which is populated by very different characteristic systems, for which many questions remain open, first of all the question of next Section.

7.7.1 Why the Evolution Close to P_{bif} Has Such a Dominant Role?

We have seen that many of the secular evolution paths of short P_{orb} —low M_c systems need to have begun close to the bifurcation period. In particular:

1. the radius of donors of AMXPs having P_{orb} shorter than 76 min is the exposed core of a star which has partially depleted its initial hydrogen content (Sect. 7.4.1);
2. the location of some redbacks in the $P_{\text{orb}}-\dot{M}_c$ plane also implies that mass transfer began when the donor was substantially evolved off the MS; but not yet in the giant stage (Sect. 7.6.5);
3. the presence of helium WD companions of MSP at periods 3–9 h (Sect. 7.6.5.1)
4. the presence of helium companions to BWs (Sect. 7.6.4).

All these hints together point to an important role for P_{bif} , both for donors of intermediate mass and for donors of low mass such as those evolving today in GCs. We leave the problem open, keeping an eye on the idea by King, Davies and Beer [56] that some configurations are ‘the price of promiscuity’ and are due to the evolution of MSP systems in GCs (see also Sect. 7.6.4), where binaries, in which the NS has already formed, may suffer exchange interactions with other stars in the field of the GC, and the most suitable candidates to replace the former companion are the most massive stars alive at the epoch of the encounters. At least a fraction of NS formed in GCs are retained there (see Sect. 7.2.4). The fact that 40% of MSPs are found in GCs, which include today only 10^{-3} of the galactic mass, implies that GCs are the favourite locus for accelerating the NS to MSP and for providing the best environment for the occurrence of some paths of secular evolution. Even if the idea that the BWs in the field can be in many cases escaped from GCs [56] may look ad hoc, it has even been proposed that *all* bulge LMXBs may have been formed in GCs, later on destroyed by repeated tidal stripping and shocking in the galactic plane [43]; further, some double neutron stars may have formed by three body interactions in GCs and ejected in the field (see Sect. 7.5.1), a relevant point to understand mergers of DNS in old stellar environments, as observed in the detection by LIGO of the event GW 170817.

7.7.2 Conclusions

We summarize here the results concerning the secular evolution of short period systems only:

1. the redbacks can be mostly in a phase of radio-ejection, losing mass directly at the Lagrangian point and evolving towards either shorter or longer P_{orb} according to the stage of evolution of the donor at the beginning of the mass transfer phase;
2. the systems with He-WD companions at short P_{orb} (<0.5 d) may be remnants of the evolution of the class of redbacks like PSR J740–5340, whose companion has lost and is losing mass and angular momentum due to radio-ejection. Mass exchange began after the donor developed a small helium core, and evolved off the main sequence turnoff. By losing enough specific AM, systems similar to this may evolve to shorter and shorter P_{orb} . Some may become ‘transitional’ systems;

3. the redback stage may begin because X-ray illumination on donors with convective envelopes occurs for a limited fraction of cycles, lasting tens to hundreds of million years, during which the system is mostly detached. Thus the companion will be subject to the MSP power in all the stages when there is no mass transfer. This is the most favourable situation to either begin the evaporation [11] or a radio-ejection phase [17]. Possibly, radio-ejection acts at longer P_{orb} , while evaporation is dominant for closer orbits and smaller masses.
4. the X-ray cycles may explain the positive large \dot{P}_{orb} of systems like SAX J1808, and the large number of MSP binaries, compared to accreting systems, both LMXB or AMXPs;
5. evaporation and MSP illumination may be competing in dominating the evolution in the black widow stage;
6. the ‘transitional’ stage is an open question.

Acknowledgments We thank Michela Mapelli, Alessandro Papitto and Enrico Vesperini for comments and suggestions.

References

1. Abbott, B.P., Abbott, R., Abbott, T.D., et al., LIGO scientific collaboration, virgo collaboration: GW190425: observation of a compact binary coalescence with total mass $\sim 3.4 \text{ M}_\odot$. *Astrophys. J. Lett.* **892**(1), L3 (2020). <https://doi.org/10.3847/2041-8213/ab75f5>
2. Abbott, B.P., Abbott, R., Abbott, T.D., et al., LIGO scientific collaboration, virgo collaboration: GW170817: observation of gravitational waves from a binary neutron star inspiral. *Phys. Rev. Lett.* **119**(16), 161101 (2017). <https://doi.org/10.1103/PhysRevLett.119.161101>
3. Abdo, A.A., Ajello, M., Allafort, A., et al.: The second fermi large area telescope catalog of gamma-ray pulsars. *Astrophys. J., Suppl. Ser.* **208**(2), 17 (2013). <https://doi.org/10.1088/0067-0049/208/2/17>
4. Alpar, M.A., Cheng, A.F., Ruderman, M.A., Shaham, J.: A new class of radio pulsars. *Nature* **300**(5894), 728–730 (1982). <https://doi.org/10.1038/300728a0>
5. Andrews, J.J., Mandel, I.: Double neutron star populations and formation channels. *Astrophys. J. Lett.* **880**(1), L8 (2019). <https://doi.org/10.3847/2041-8213/ab2ed1>
6. Backer, D.C., Kulkarni, S.R., Heiles, C., et al.: A millisecond pulsar. *Nature* **300**(5893), 615–618 (1982). <https://doi.org/10.1038/300615a0>
7. Bailes, M., Lyne, A.G., Shemar, S.L.: A planet orbiting the neutron star PSR1829-10. *Nature* **352**(6333), 311–313 (1991). <https://doi.org/10.1038/352311a0>
8. Baumgardt, H., Hilker, M., Sollima, A., Bellini, A.: Mean proper motions, space orbits, and velocity dispersion profiles of Galactic globular clusters derived from Gaia DR2 data. *Mon. Notices Royal Astron. Soc.* **482**(4), 5138–5155 (2019). <https://doi.org/10.1093/mnras/sty2997>
9. Becker, C.M., Tavani, M., Rappaport, S.A.: A study of self-excited evolution of low mass X-ray binaries. In: Fruchter, A.S., Tavani, M., Backer, D.C. (eds.) *Millisecond Pulsars. A Decade of Surprise*, Astronomical Society of the Pacific Conference Series, vol. 72, p. 145 (1995)
10. Benvenuto, O.G., De Vito, M.A., Horvath, J.E.: Evolutionary trajectories of ultracompact “black widow” pulsars with very low mass companions. *Astrophys. J. Lett.* **753**(2), L33 (2012). <https://doi.org/10.1088/2041-8205/753/2/L33>

11. Benvenuto, O.G., De Vito, M.A., Horvath, J.E.: Understanding the evolution of close binary systems with radio pulsars. *Astrophys. J. Lett.* **786**, L7 (2014). <https://doi.org/10.1088/2041-8205/786/1/L7>
12. Benvenuto, O.G., De Vito, M.A., Horvath, J.E.: Exploring the formation of ‘Black Widows’. *Mon. Notices Royal Astron. Soc.* **449**(4), 4184–4191 (2015). <https://doi.org/10.1093/mnras/stv259>
13. Benvenuto, O.G., De Vito, M.A., Horvath, J.E.: Evolution of redback radio pulsars in globular clusters. *Astron. Astrophys.* **598**, A35 (2017). <https://doi.org/10.1051/0004-6361/201628692>
14. Bhattacharya, D., van den Heuvel, E.P.J.: Formation and evolution of binary and millisecond radio pulsars. *Phys.Rep.* **203**(1-2), 1–124 (1991). [https://doi.org/10.1016/0370-1573\(91\)90064-S](https://doi.org/10.1016/0370-1573(91)90064-S)
15. Bray, J.C., Eldridge, J.J.: Neutron star kicks and their relationship to supernovae ejecta mass. *Mon. Notices Royal Astron. Soc.* **461**(4), 3747–3759 (2016). <https://doi.org/10.1093/mnras/stw1275>
16. Bray, J.C., Eldridge, J.J.: Neutron star kicks - II. Revision and further testing of the conservation of momentum ‘kick’ model. *Mon. Notices Royal Astron. Soc.* **480**(4), 5657–5672 (2018). <https://doi.org/10.1093/mnras/sty2230>
17. Burderi, L., D’Antona, F., Burgay, M.: PSR J1740-5340: accretion inhibited by radio ejection in a binary millisecond pulsar in the globular cluster NGC 6397. *Astrophys. J.* **574**(1), 325–331 (2002). <https://doi.org/10.1086/340891>
18. Burderi, L., Possenti, A., Colpi, M., et al.: Neutron stars with submillisecond periods: a population of high-mass objects? *Astrophys. J.* **519**(1), 285–290 (1999). <https://doi.org/10.1086/307353>
19. Burderi, L., Possenti, A., D’Antona, F., et al.: Where may ultrafast rotating neutron stars be hidden? *Astrophys. J. Lett.* **560**(1), L71–L74 (2001). <https://doi.org/10.1086/324220>
20. Campana, S., Di Salvo, T.: Accreting Pulsars: Mixing-up Accretion Phases in Transitional Systems. *Astrophysics and Space Science Library*, vol. 457, p. 149 (2018). https://doi.org/10.1007/978-3-319-97616-7_4
21. Chen, H.L., Chen, X., Tauris, T.M., Han, Z.: Formation of black widows and redbacks—two distinct populations of eclipsing binary millisecond pulsars. *Astrophys. J.* **775**(1), 27 (2013). <https://doi.org/10.1088/0004-637X/775/1/27>
22. Chen, W.C., Podsiadlowski, P.: Evolution of intermediate-mass X-ray binaries driven by the magnetic braking of AP/BP Stars. I. Ultracompact X-ray binaries. *Astrophys. J.* **830**(2), 131 (2016). <https://doi.org/10.3847/0004-637X/830/2/131>
23. Chou, Y., Grindlay, J.E., Bloser, P.F.: Timing analysis of the light curve of the dipping-bursting X-ray binary X1916-053. *Astrophys. J.* **549**(2), 1135–1144 (2001). <https://doi.org/10.1086/319443>
24. Cook, G.B., Shapiro, S.L., Teukolsky, S.A.: Rapidly rotating neutron stars in general relativity: realistic equations of state. *Astrophys. J.* **424**, 823 (1994). <https://doi.org/10.1086/173934>
25. D’Amico, N., Possenti, A., Manchester, R.N., et al.: An eclipsing millisecond pulsar with a possible main-sequence companion in NGC 6397. *Astrophys. J. Lett.* **561**(1), L89–L92 (2001). <https://doi.org/10.1086/324562>
26. D’Antona, F.: Modeling the onset of mass transfer in low-mass X-ray binaries. *Mem. Soc. Astron. It.* **65**, 285 (1994)
27. D’Antona, F., Ergma, E.: Evolution of binaries with a low mass component immersed in a radiation field. I—effect of irradiation by a millisecond pulsar companion. *Astron. Astrophys.* **269**, 219–230 (1993)
28. D’Antona, F., Mazzitelli, I., Ritter, H.: The turn-on of mass transfer in cataclysmic binaries. *Astron. Astrophys.* **225**, 391–404 (1989)
29. Dessart, L., Burrows, A., Ott, C.D., et al.: Multidimensional simulations of the accretion-induced collapse of white dwarfs to neutron stars. *Astrophys. J.* **644**(2), 1063–1084 (2006). <https://doi.org/10.1086/503626>

30. Dewi, J.D.M., Pols, O.R., Savonije, G.J., van den Heuvel, E.P.J.: The evolution of naked helium stars with a neutron star companion in close binary systems. *Mon. Notices Royal Astron. Soc.* **331**(4), 1027–1040 (2002). <https://doi.org/10.1046/j.1365-8711.2002.05257.x>
31. Eggleton, P.P.: Aproximations to the radii of Roche lobes. *Astrophys. J.* **268**, 368–369 (1983). <https://doi.org/10.1086/160960>
32. Ergma, E.: The relation between white dwarf mass and orbital period for binary millisecond radio pulsars orbital period $1 \leq P_{\text{orb}} \leq 20$ days. *Astron. Astrophys.* **315**, L17–L18 (1996)
33. Ergma, E., Fedorova, A.V.: Orbital evolution of binaries with ultra-rapid pulsars. *Astron. Astrophys.* **265**, 65–70 (1992)
34. Ergma, E., Sarna, M.J.: Eclipsing binary millisecond pulsar PSR J1740-5340—evolutionary considerations and observational test. *Astron. Astrophys.* **399**, 237–241 (2003). <https://doi.org/10.1051/0004-6361:20021689>
35. Ergma, E., Sarna, M.J., Antipova, J.: The evolution of short-period binary pulsars: a systematic study. *Mon. Notices Royal Astron. Soc.* **300**(2), 352–358 (1998). <https://doi.org/10.1046/j.1365-8711.1998.01761.x>
36. Ergma, E.V., Fedorova, A.V.: Is it possible to evaporate the companion stars of ultra-rapid pulsars? *Astron. Astrophys.* **242**, 125 (1991)
37. Faucher-Giguère, C.A., Kaspi, V.M.: Birth and evolution of isolated radio pulsars. *Astrophys. J.* **643**(1), 332–355 (2006). <https://doi.org/10.1086/501516>
38. Fedorova, A.V., Ergma, E.V.: Evolution of binaries with ultrashort periods—systematic study. *Astrophys Space Sci.* **151**(1), 125–134 (1989). <https://doi.org/10.1007/BF00643634>
39. Freire, P.C.C., Tauris, T.M.: Direct formation of millisecond pulsars from rotationally delayed accretion-induced collapse of massive white dwarfs. *Mon. Notices Royal Astron. Soc.* **438**(1), L86–L90 (2014). <https://doi.org/10.1093/mnrasl/slt164>
40. Fruchter, A.S., Stinebring, D.R., Taylor, J.H.: A millisecond pulsar in an eclipsing binary. *Nature* **333**(6170), 237–239 (1988). <https://doi.org/10.1038/333237a0>
41. Giacobbo, N., Mapelli, M.: Revising natal kick prescriptions in population synthesis simulations. *Astrophys. J.* **891**(2), 141 (2020). <https://doi.org/10.3847/1538-4357/ab7335>
42. Gratton, R., Bragaglia, A., Carretta, E., et al.: What is a globular cluster? An observational perspective. *A&A Rev.* **27**(1), 8 (2019). <https://doi.org/10.1007/s00159-019-0119-3>
43. Grindlay, J.E., Hertz, P.: Galactic bulge X-ray burst sources from disrupted globular clusters? In: Lamb, D.Q., Patterson, J. (eds.) *Cataclysmic Variables and Low-Mass X-ray Binaries*, p. 79 (1985). <https://doi.org/10.1007/978-94-009-5319-2-9>
44. Hameury, J.M., King, A.R., Lasota, J.P.: LMXB evolution: illumination effects. In: Fruchter, A.S., Tavani, M., Backer, D.C. (eds.) *Millisecond Pulsars. A Decade of Surprise*, Astronomical Society of the Pacific Conference Series, vol. 72, p. 149 (1995)
45. Hameury, J.M., King, A.R., Lasota, J.P., Raison, F.: Structure and evolution of X-ray heated compact binaries. *Astron. Astrophys.* **277**, 81–92 (1993)
46. Hessels, J.W.T., Ransom, S.M., Stairs, I.H., et al.: A radio pulsar spinning at 716 Hz. *Science* **311**(5769), 1901–1904 (2006). <https://doi.org/10.1126/science.1123430>
47. Hobbs, G., Lorimer, D.R., Lyne, A.G., Kramer, M.: A statistical study of 233 pulsar proper motions. *Mon. Notices Royal Astron. Soc.* **360**(3), 974–992 (2005). <https://doi.org/10.1111/j.1365-2966.2005.09087.x>
48. Iben I.J.: Thermal pulses: p-capture, alpha -capture, s-process nucleosynthesis; and convective mixing in a star of intermediate mass. *Astrophys. J.* **196**, 525–547 (1975). <https://doi.org/10.1086/153433>
49. Iben I.J., Tutukov, A.V.: Supernovae of type I as end products of the evolution of binaries with components of moderate initial mass. *Astrophys. J. Suppl. Ser.* **54**, 335–372 (1984). <https://doi.org/10.1086/190932>

50. Istrate, A.G., Tauris, T.M., Langer, N.: The formation of low-mass helium white dwarfs orbiting pulsars . Evolution of low-mass X-ray binaries below the bifurcation period. *Astron. Astrophys.* **571**, A45 (2014). <https://doi.org/10.1051/0004-6361/201424680>
51. Ivanova, N., Heinke, C.O., Rasio, F.A., et al.: Formation and evolution of compact binaries in globular clusters—II. Binaries with neutron stars. *Mon. Notices Royal Astron. Soc.* **386**(1), 553–576 (2008). <https://doi.org/10.1111/j.1365-2966.2008.13064.x>
52. Janka, H.T., Melson, T., Summa, A.: Physics of core-collapse supernovae in three dimensions: a sneak preview. *Ann. Rev. Nucl. Part. Sci.* **66**(1), 341–375 (2016). <https://doi.org/10.1146/annurev-nucl-102115-044747>
53. Kaplan, D.L., Bhalerao, V.B., van Kerkwijk, M.H., et al.: A metal-rich low-gravity companion to a massive millisecond pulsar. *Astrophys. J.* **765**(2), 158 (2013). <https://doi.org/10.1088/0004-637X/765/2/158>
54. Kaplan, D.L., Stovall, K., Ransom, S.M., et al.: Discovery of the optical/ultraviolet/gamma-ray counterpart to the eclipsing millisecond pulsar J1816+4510. *Astrophys. J.* **753**(2), 174 (2012). <https://doi.org/10.1088/0004-637X/753/2/174>
55. Karakas, A.I., Lattanzio, J.C.: The Dawes review 2: nucleosynthesis and stellar yields of low- and intermediate-mass single stars. *Publ. Astron. Soc. Pac. Aust.* **31**, e030 (2014). <https://doi.org/10.1017/pasa.2014.21>
56. King, A.R., Davies, M.B., Beer, M.E.: Black widow pulsars: the price of promiscuity. *Mon. Notices Royal Astron. Soc.* **345**(2), 678–682 (2003). <https://doi.org/10.1046/j.1365-8711.2003.06990.x>
57. King, A.R., Frank, J., Kolb, U., Ritter, H.: Mass transfer cycles in cataclysmic variables. *Astrophys. J. Lett.* **444**, L37 (1995). <https://doi.org/10.1086/187854>
58. Knigge, C.: Cataclysmic variables: eight breakthroughs in eight years (2011). arXiv e-prints arXiv:1101.2901
59. Kulkarni, S.R., Narayan, R.: Birthrates of low-mass binary pulsars and low-mass X-ray binaries. *Astrophys. J.* **335**, 755 (1988). <https://doi.org/10.1086/166964>
60. Lavagetto, G., Burderi, L., D’Antona, F., et al.: The different fates of a low-mass X-ray binary—I. Conservative mass transfer. *Mon. Notices Royal Astron. Soc.* **348**(1), 73–82 (2004). <https://doi.org/10.1111/j.1365-2966.2004.07299.x>
61. Levin, L., Bailes, M., Barsdell, B.R., et al.: The high time resolution universe pulsar survey—VIII. The Galactic millisecond pulsar population. *Mon. Notices Royal Astron. Soc.* **434**(2), 1387–1397 (2013). <https://doi.org/10.1093/mnras/stt1103>
62. Li, H., Gnedin, O.Y.: Star cluster formation in cosmological simulations—III. Dynamical and chemical evolution. *Mon. Notices Royal Astron. Soc.* **486**(3), 4030–4043 (2019). <https://doi.org/10.1093/mnras/stz1114>
63. Lin, J., Rappaport, S., Podsiadlowski, P., et al.: LMXB and IMXB evolution: I. The binary radio pulsar PSR J1614-2230. *Astrophys. J.* **732**(2), 70 (2011). <https://doi.org/10.1088/0004-637X/732/2/70>
64. Livio, M., Soker, N.: The common envelope phase in the evolution of binary stars. *Astrophys. J.* **329**, 764 (1988). <https://doi.org/10.1086/166419>
65. Lundgren, S.C., Zepka, A.F., Cordes, J.M.: A millisecond pulsar in a 6 hour orbit: PSR J0751+1807. *Astrophys. J.* **453**, 419 (1995). <https://doi.org/10.1086/176402>
66. Lyne, A.G., Manchester, R.N., D’Amico, N., et al.: An eclipsing millisecond pulsar in the globular cluster Terzan 5. *Nature* **347**(6294), 650–652 (1990). <https://doi.org/10.1038/347650a0>
67. Meyer, F., Meyer-Hofmeister, E.: Formation of cataclysmic binaries through common envelope evolution. *Astron. Astrophys.* **78**, 167–176 (1979)
68. Middleditch, J., Mason, K.O., Nelson, J.E., White, N.E.: 4U 1626-67 : A prograde spinning X-ray pulsar in A 2500 S binary system. *Astrophys. J.* **244**, 1001–1021 (1981). <https://doi.org/10.1086/158772>
69. Miller, M.C., Hamilton, D.P.: Implications of the PSR 1257+12 planetary system for isolated millisecond pulsars. *Astrophys. J.* **550**(2), 863–870 (2001). <https://doi.org/10.1086/319813>

70. Miyaji, S., Nomoto, K.: On the collapse of 8–10 M_{sun} stars due to electron capture. *Astrophys. J.* **318**, 307 (1987). <https://doi.org/10.1086/165368>
71. Muslimov, A.G., Sarna, M.J.: Formation of low-mass binaries with millisecond pulsars. *Mon. Notices Royal Astron. Soc.* **262**(1), 164–174 (1993). <https://doi.org/10.1093/mnras/262.1.164>
72. Nice, D.J., Thorsett, S.E., Taylor, J.H., Fruchter, A.S.: Observations of the eclipsing binary pulsar in Terzan 5. *Astrophys. J. Lett.* **361**, L61 (1990). <https://doi.org/10.1086/185827>
73. Nomoto, K.: Evolution of 8–10 M_{sun} stars toward electron capture supernovae. II. Collapse of an O + NE + MG core. *Astrophys. J.* **322**, 206 (1987). <https://doi.org/10.1086/165716>
74. Paczyński, B.: Gravitational waves and the evolution of close binaries. *Acta Astron.* **17**, 287 (1967)
75. Paczyński, B.: Evolutionary processes in close binary systems. *Annu. Rev. Astron. Astrophys.* **9**, 183 (1971). <https://doi.org/10.1146/annurev.aa.09.090171.001151>
76. Paczynski, B.: Common envelope binaries. In: Eggleton, P., Mitton, S., Whelan, J. (eds.) *Structure and Evolution of Close Binary Systems*, IAU Symposium, vol. 73, p. 75 (1976)
77. Paczynski, B.: Evolution of cataclysmic binaries. *Acta Astron.* **31**, 1–12 (1981)
78. Paczynski, B., Sienkiewicz, R.: Gravitational radiation and the evolution of cataclysmic binaries. *Astrophys. J. Lett.* **248**, L27–L30 (1981). <https://doi.org/10.1086/183616>
79. Papitto, A., de Martino, D., Belloni, T.M., et al.: X-ray coherent pulsations during a sub-luminous accretion disc state of the transitional millisecond pulsar XSS J12270-4859. *Mon. Notices Royal Astron. Soc.* **449**(1), L26–L30 (2015). <https://doi.org/10.1093/mnrasl/slv013>
80. Patruno, A., Watts, A.L.: Accreting millisecond X-ray pulsars (2012). arXiv e-prints arXiv:1206.2727
81. Phinney, E.S., Sigurdsson, S.: Ejection of pulsars and binaries to the outskirts of globular clusters. *Nature* **349**(6306), 220–223 (1991). <https://doi.org/10.1038/349220a0>
82. Podsiadlowski, P.: Irradiation-driven mass transfer low-mass X-ray binaries. *Nature* **350**, 136–138 (1991). <https://doi.org/10.1038/350136a0>
83. Podsiadlowski, P., Langer, N., Poelarends, A.J.T., et al.: The effects of binary evolution on the dynamics of core collapse and neutron star kicks. *Astrophys. J.* **612**(2), 1044–1051 (2004). <https://doi.org/10.1086/421713>
84. Poelarends, A.J.T., Herwig, F., Langer, N., Heger, A.: The supernova channel of super-AGB stars. *Astrophys. J.* **675**(1), 614–625 (2008). <https://doi.org/10.1086/520872>
85. Pylyser, E., Savonije, G.J.: Evolution of low-mass close binary systems with a compact mass accreting component. *Astron. Astrophys.* **191**, 57–70 (1988)
86. Rappaport, S., Joss, P.C., Webbink, R.F.: The evolution of highly compact binary stellar systems. *Astrophys. J.* **254**, 616–640 (1982). <https://doi.org/10.1086/159772>
87. Ritter, H.: Magnetic braking and the period gap of cataclysmic binaries. *Astron. Astrophys.* **145**(1), 227–231 (1985)
88. Ritter, H.: Turning on and off mass transfer in cataclysmic binaries. *Astron. Astrophys.* **202**, 93–100 (1988)
89. Ritter, H., Kolb, U.: Catalogue of cataclysmic binaries, low-mass X-ray binaries and related objects (Seventh edition). *Astron. Astrophys.* **404**, 301–303 (2003). <https://doi.org/10.1051/0004-6361:20030330>
90. Roberts, M.S.E.: Surrounded by spiders! New black widows and redbbacks in the Galactic field. In: van Leeuwen, J. (ed.) *Neutron Stars and Pulsars: Challenges and Opportunities after 80 years*, IAU Symposium, vol. 291, pp. 127–132 (2013). <https://doi.org/10.1017/S174392131202337X>
91. Romani, R.W., Filippenko, A.V., Silverman, J.M., et al.: PSR J1311-3430: a heavyweight Neutron star with a flyweight helium companion. *Astrophys. J. Lett.* **760**(2), L36 (2012). <https://doi.org/10.1088/2041-8205/760/2/L36>
92. Ruderman, M., Shaham, J., Tavani, M.: Accretion turnoff and rapid evaporation of very light secondaries in low-mass X-ray binaries. *Astrophys. J.* **336**, 507 (1989). <https://doi.org/10.1086/167029>

93. Sanna, A., Di Salvo, T., Burderi, L., et al.: On the timing properties of SAX J1808.4-3658 during its 2015 outburst. *Mon. Notices Royal Astron. Soc.* **471**, 463–477 (2017). <https://doi.org/10.1093/mnras/stx1588>
94. Schatzman, E.: A theory of the role of magnetic activity during star formation. *Ann. Astrophys.* **25**, 18 (1962)
95. Schenker, K., Kolb, U., Ritter, H.: Properties of discontinuous and nova-amplified mass transfer in cataclysmic variables. *Mon. Notices Royal Astron. Soc.* **297**(2), 633–647 (1998). <https://doi.org/10.1046/j.1365-8711.1998.01529.x>
96. Skumanich, A.: Time scales for CA II emission decay, rotational braking, and lithium depletion. *Astrophys. J.* **171**, 565 (1972). <https://doi.org/10.1086/151310>
97. Soderblom, D.R.: Rotational studies of late-type stars. II. Ages of solar-type stars and the rotational history of the Sun. *Astrophys. J., Suppl. Ser.* **53**, 1–15 (1983). <https://doi.org/10.1086/190880>
98. Stevens, I.R., Rees, M.J., Podsiadlowski, P.: Neutron stars and planet-mass companions. *Mon. Notices Royal Astron. Soc.* **254**, 19P–22 (1992). <https://doi.org/10.1093/mnras/254.1.19P>
99. Strader, J., Swihart, S., Chomiuk, L., et al.: Optical spectroscopy and demographics of redback millisecond pulsar binaries. *Astrophys. J.* **872**(1), 42 (2019). <https://doi.org/10.3847/1538-4357/aafbaa>
100. Swihart, S.J., Strader, J., Chomiuk, L., Shishkovsky, L.: PSR J1306-40: an X-ray luminous redback with an evolved companion. *Astrophys. J.* **876**(1), 8 (2019). <https://doi.org/10.3847/1538-4357/ab125e>
101. Swihart, S.J., Strader, J., Shishkovsky, L., et al.: A multiwavelength view of the neutron star binary 1FGL J1417.7-4402: a progenitor to canonical millisecond pulsars. *Astrophys. J.* **866**(2), 83 (2018). <https://doi.org/10.3847/1538-4357/aadcab>
102. Taam, R.E., King, A.R., Ritter, H.: On a theoretical interpretation of the period gap in binary millisecond pulsars. *Astrophys. J.* **541**(1), 329–334 (2000). <https://doi.org/10.1086/309392>
103. Tailo, M., D'Antona, F., Burderi, L., et al.: Evolutionary paths of binaries with a neutron star—I. The case of SAX J1808.4 - 3658. *Mon. Notices Royal Astron. Soc.* **479**(1), 817–828 (2018). <https://doi.org/10.1093/mnras/sty1637>
104. Tauris, T.M.: Five and a half roads to form a millisecond pulsar. In: Schmidtobreick, L., Schreiber, M.R., Tappert, C. (eds.) *Evolution of Compact Binaries*, Astronomical Society of the Pacific Conference Series, vol. 447, p. 285 (2011)
105. Tauris, T.M., Kramer, M., Freire, P.C.C., et al.: Formation of double neutron star systems. *Astrophys. J.* **846**(2), 170 (2017). <https://doi.org/10.3847/1538-4357/aa7e89>
106. Tauris, T.M., Langer, N., Kramer, M.: Formation of millisecond pulsars with CO white dwarf companions—II. Accretion, spin-up, true ages and comparison to MSPs with He white dwarf companions. *Mon. Notices Royal Astron. Soc.* **425**(3), 1601–1627 (2012). <https://doi.org/10.1111/j.1365-2966.2012.21446.x>
107. Tauris, T.M., van den Heuvel, E.P.J.: Formation and Evolution of Compact Stellar X-Ray Sources, vol. 39, pp. 623–665 (2006)
108. Tavani, M.: Birthrates of galactic millisecond pulsars and their low-mass X-ray binary precursors. *Astrophys. J. Lett.* **366**, L27 (1991). <https://doi.org/10.1086/185902>
109. Tavani, M., Brookshaw, L.: Hidden slow pulsars in binaries. *Astrophys. J. Lett.* **413**, L39 (1993). <https://doi.org/10.1086/186954>
110. Tutukov, A.V., Fedorova, A.V., Ergma, E.V., Yungelson, L.R.: Evolution of low-mass close binaries—the minimum orbital period. *Sov. Astron. Lett.* **11**, 52–56 (1985)
111. van den Heuvel, E.P.J., De Loore, C.: The nature of X-ray binaries III. Evolution of massive close binaries with one collapsed component - with a possible application to Cygnus X-3. *Astron. Astrophys.* **25**, 387 (1973)
112. Verbunt, F., Zwaan, C.: Magnetic braking in low-mass X-ray binaries. *Astron. Astrophys.* **100**, L7–L9 (1981)
113. Vilhu, O., Ergma, E., Fedorova, A.: The X-ray heating and evolution of LMXB's. *Astron. Astrophys.* **291**, 842–846 (1994)

114. Webb, J.J., Leigh, N.W.C.: Back to the future: estimating initial globular cluster masses from their present-day stellar mass functions. *Mon. Notices Royal Astron. Soc.* **453**(3), 3278–3287 (2015). <https://doi.org/10.1093/mnras/stv1780>
115. Webbink, R.F.: Double white dwarfs as progenitors of R Coronae Borealis stars and type I supernovae. *Astrophys. J.* **277**, 355–360 (1984). <https://doi.org/10.1086/161701>
116. Webbink, R.F., Rappaport, S., Savonije, G.J.: On the evolutionary status of bright, low-mass X-ray sources. *Astrophys. J.* **270**, 678–693 (1983). <https://doi.org/10.1086/161159>
117. Webbink, R.F., Wickramasinghe, D.T.: Cataclysmic variable evolution: AM Her binaries and the period gap. *Mon. Notices Royal Astron. Soc.* **335**(1), 1–9 (2002). <https://doi.org/10.1046/j.1365-8711.2002.05495.x>
118. Ye, C.S., Kremer, K., Chatterjee, S., et al.: Millisecond pulsars and black holes in globular clusters. *Astrophys. J.* **877**(2), 122 (2019). <https://doi.org/10.3847/1538-4357/ab1b21>
119. Zapartas, E., de Mink, S.E., Izzard, R.G., et al.: Delay-time distribution of core-collapse supernovae with late events resulting from binary interaction. *Astron. Astrophys.* **601**, A29 (2017). <https://doi.org/10.1051/0004-6361/201629685>

Chapter 8

Millisecond Magnetars



Simone Dall’Osso and Luigi Stella

Abstract Two classes of X-ray/gamma-ray sources, the Soft Gamma Repeaters and the Anomalous X-ray Pulsars have been identified with isolated, slowly spinning *magnetars*, neutron stars whose emission draws energy from their extremely strong magnetic field ($\sim 10^{15}$ – 10^{16} G). Magnetars are believed to form with millisecond spin period and to represent an important fraction of the whole young neutron star population. Newborn magnetars can convert very quickly their rotational energy into electromagnetic and/or gravitational waves, by virtue of their magnetic field strength and fast spins. This chapter provides a brief summary of astrophysical problems and scenarios in which millisecond magnetars are believed to play a key role: these include Gamma Ray Bursts, Supernovae, Gravitational Wave events and Fast Radio Bursts.

8.1 Introduction

The idea that neutron stars (NSs) may possess surface magnetic fields in excess of $B_{\text{crit}} = 4.3 \times 10^{14}$ G, the field for which the cyclotron energy equals the electron rest mass, predates the discovery of radio pulsars [210]. Substantially lower magnetic fields, typically in the $\sim 10^{11}$ – 10^{13} G range, were derived in the late 1960s and 1970s from the application of the rotating magnetic dipole model to the spin-down of classical radio pulsars and the measurement of cyclotron resonant scattering features in the X-ray spectra of accreting pulsars [152, 201]. Supra-critical B-fields

S. Dall’Osso
Gran Sasso Science Institute, L’Aquila, Italy

INFN–Laboratori Nazionali del Gran Sasso, L’Aquila, Italy
e-mail: simone.dalloso@gssi.it

L. Stella (✉)
INAF–Osservatorio Astronomico di Roma, Roma, Italy
e-mail: luigi.stella@inaf.it

did not receive much attention for many years to follow. The idea was resurrected and developed especially in interpreting the properties of two classes of high energy sources, the Soft Gamma Repeaters (SGRs; [85]) and the Anomalous X-ray Pulsars (AXPs; [130]). The former were identified after the soft, sub-second long γ -ray flares emitted by the proto-typical class member SGR 0526-66 [126], while the latter initially comprised the four persistent X-ray pulsars 1E 2259+586, 1E 1048.1-5937, 4U 0142+61 and RX J1838.4-0301, with spin periods $\sim 5\text{--}10$ s, X-ray luminosities largely in excess of their putative spindown power and no signs of companion stars from which they may accrete material [130, 205]. The subsequent detection of persistent X-ray pulsations from SGRs, with similar spin period, spindown power and X-ray luminosity as AXPs (e.g. SGR 1806-20; [83]), and SGR-like flares from AXPs (e.g. 1E 2259+586; [58]), demonstrated the close relation between the two classes.

A few tens SGRs and AXPs are presently known in our Galaxy (plus one in the LMC); they are isolated X-ray/soft gamma-ray sources displaying pulsations at relatively slow spin periods of $\sim 1\text{--}12$ s and with spin-down ages of $\sim 240\text{--}10^5$ yr.¹ Their association to supernova remnants in about one third of the cases and location close to the galactic plane further testify to their very young age. Some are persistent X-ray sources (typical luminosities in the $10^{34}\text{--}10^{35}$ erg/s range) and others are transients, which spend most of the time in quiescence at very low luminosity levels and undergo month/year-long outbursts during which their properties closely resemble those of persistent AXPs and SGRs. The emission of subsecond duration X-ray bursts with peak luminosities of $\sim 10^{38}\text{--}10^{41}$ erg/s during sporadic periods of activity is a defining characteristic of both classes. On rare occasions more extreme events known as intermediate and giant flares, lasting from several second to minutes, have been observed which involve much larger energy releases, up to $\sim 10^{44}\text{--}10^{46}$ ergs. Occasionally radio pulsations at the spin period or individual radio bursts have been observed in a few AXPs and SGRs.

In many cases the measured spin-down rate implies rotational energy losses that are about two orders of magnitude smaller than the $\sim 10^{34}\text{--}10^{35}$ erg/s persistent X-ray luminosity. Therefore the main source of power of AXPs/SGRs cannot be rotation: that is unlike classical radio pulsars. The highly super-Eddington luminosity of sub-second bursts and, even more so, giant flares rules out accretion as their powering mechanism. Reviews of the properties of AXPs/SGRs are found e.g. in [127, 167, 211].

In a series of papers Robert Duncan and Chris Thompson introduced the magnetar model and proposed that the emission of AXPs and SGRs is generated (mostly) at the expense of their magnetic energy [48, 195–197]. The model² envisages that the external magnetic field of magnetars drives angular momentum losses via magnetic dipole radiation and pulsar wind as in rotation-powered pulsars, whereas the energy release resulting from instabilities of their inner, mainly toroidal

¹ For the lower limit of this range see [49].

² For a basic tutorial see <http://solomon.as.utexas.edu/magnetar.html>.

magnetic field is responsible for the bulk of the emission. According to the magnetar model energy is fed to the magnetosphere as magnetic field's helicity propagates from the interior outwards. Impulsive high-energy bursts originate in sudden energy injections resulting from *crust-quakes*; persistent emission, in turn, arises from the gradual untwisting of the magnetosphere. Giant flares are believed to originate from large-scale rearrangements of the inner B-field or catastrophic instabilities in the magnetosphere [103, 198].

Several arguments, besides spin-down via magnetic dipole radiation, indicate external field strengths of $B_d \sim 10^{14}\text{--}10^{15}$ G for the majority of presently-known AXPs and SGRs [196, 206]. In a few class members, as well as in some radio pulsars displaying magnetar-like bursting activity, sub-critical values $B_d \sim 10^{13}$ G have been inferred, which are close to the upper end of the distribution in rotationally powered neutron stars [168, 169]. The strength of the interior magnetic field is estimated through energy arguments. The B-field energy is $E_{B,\text{int}} \simeq (B_{\text{int}}^2/8\pi)(4\pi R_*^3/3) \sim 2 \times 10^{47} B_{\text{int},15}^2 R_{*,6}^2$ erg with R_* the neutron star radius. All subscripts in this chapter indicate power of 10 values in CGS units, e.g. $B_{15} \equiv B/(10^{15}\text{G})$ and $R_6 \equiv R/(10^6\text{ cm})$, unless specified otherwise. $E_{B,\text{int}}$ must be high enough to power the emission of SGRs and AXPs over their lifetime, as estimated from the spin-down age and/or the age of the supernova remnants they are associated to. The persistent emission of the brightest members of the two classes ($\sim 10^{34}\text{--}10^{35}$ erg/s) provides an interior field estimate of $B_{\text{int}} \sim 10^{15}$ G. The energy release and estimated recurrence rate of the initial sub-second spike of the 2004 Dec 27 giant flare from SGR 1806-20 implies an energy release in the $\sim 10^{49}$ erg range, which converts to $B_{\text{int}} \approx 10^{16}$ G [189]. Additional studies indicate that magnetars contain interior B-fields well in excess of their already strong exterior dipoles (e.g. [39, 113, 168, 169, 172, 199]), and numerical work dedicated to understanding their characteristic burst activity reached similar conclusions (e.g. [163, 202]), pointing to values of $B_{\text{int},15} \sim 5\text{--}20$. AXPs and SGRs, i.e. *classical magnetars*, possess a rotational energy of $E_{\text{rot}} \sim 10^{44}\text{--}10^{46}$ erg, in most cases much lower than their magnetic energy.

According to current estimates [10] magnetars form at a comparable rate to that of ordinary NSs. The collapse of massive stars is believed to be their main formation channel, naturally relating newborn magnetars to core collapse supernovae (CCSNe; see Sect. 8.3) and long gamma-ray bursts (GRBs) in the collapsar scenario (see Sect. 8.2). Based on the stellar population properties of their associated open cluster, progenitor masses of two classical magnetars have been constrained to $\sim(30\text{--}45)$ M_\odot in two cases [12, 144] and $M \sim (15\text{--}19)$ M_\odot in another case [44].

Very high values of the internal B-field are key to the magnetar model. Conservation of the progenitor's magnetic flux during core collapse, the so-called *fossil field* scenario, is expected to give rise to a maximum strength in the $\sim 10^{14}$ G range, and only in a small fraction of the cases (for a review see [52]). Dynamo action in the proto-neutron star (PNS) seconds after its formation is required to generate stronger fields. This is likely driven by the interplay of differential rotation, which stretches the field in a predominantly toroidal configuration, and the onset of Tayler

or magneto-rotational instabilities to close the dynamo loop [48, 166, 188]. The resulting B-field amplification draws from the energy of differential rotation, which may amount to $\sim 10\%$ of the rotational energy of the PNS, $E_{\text{rot}} = I\Omega^2/2 \approx 2 \times 10^{52} I_{45} P_{-3}^{-2}$ erg. Here I is the moment of inertia, Ω the angular velocity and P the spin period. The Tayler dynamo has been estimated to saturate at $\sim 1\%$ of the energy density in differential rotation [15]. The amplified B-field energy may thus represent a fraction f_{-3} of the PNS rotational energy, implying that magnetars are born with much larger rotational than magnetic energy. It is their fast spindown, due to the strong magnetic dipole field, which makes them magnetically-dominated at a later age, $\sim 10^3\text{--}10^5$ yr, when they are observed as AXPs/SGRs. Relating the inner B-field to the fraction f of spin energy in the PNS that goes to magnetic energy gives $B_{\text{int}} \approx 10^{16} G f_{-3}^{1/2} I_{45}^{1/2} P_{-3}^{-1} R_6^{-3/2}$. An interior B-field $\sim 10^{16}$ G would thus require a magnetar spin period of $\sim (1\text{--}2)$ ms at birth.³ Correspondingly, an angular momentum of order $\sim 10^{48}\text{--}10^{49}$ g cm²/s must be retained in the progenitors’ core pre-collapse or transferred by fallback accretion to the PNS.

That a stable, ms-spinning magnetar may form in a binary NS (BNS) merger was first shown in numerical simulations by [63] and further studied, e.g. [7, 72, 182] especially in the aftermath of the BNS merger GW 170817. The large orbital angular momentum of the two NSs at the time of coalescence guarantees a remnant’s ms-spin period and rotational energy of $\gtrsim 3 \times 10^{52}$ erg. Also in this case differential rotation leads to the fast growth of a $\sim 10^{16}$ G, mostly azimuthal B-field inside the merger remnant. In [148] it was found that, in the early phases, the large-scale dipolar B-field (B_d) contains only a fraction of the poloidal magnetic field energy, most of it being concentrated in smaller-scale, higher-order multipoles. The possibility to form stable magnetars in BNS mergers depends sensitively on the not well constrained maximum mass of a NS, which is set by the equation of state of ultradense matter. For component masses of $\sim 1.3 M_\odot$, most NS mergers may end up producing a BH, possibly after the formation of a short-lived supramassive or hypermassive NS, temporarily sustained against collapse by centrifugal forces (due to rigid or differential rotation, respectively). However, if the maximum NS mass is $\gtrsim (2.3\text{--}2.4) M_\odot$, the formation of a stable, massive NS is possible in a sizeable fraction of cases (e.g. [38, 160]).

Other channels may lead to the formation of millisecond magnetars: besides BNS mergers, accretion induced-collapse of a white dwarf, merging of two white dwarfs or a white dwarf and a NS (e.g. [222] and references therein). Recent reviews on classical magnetars are [50, 80, 128, 203].

³ Note that the virial limit of $\lesssim 10^{17}$ G holds for NS interior B-fields (e.g. [171]).

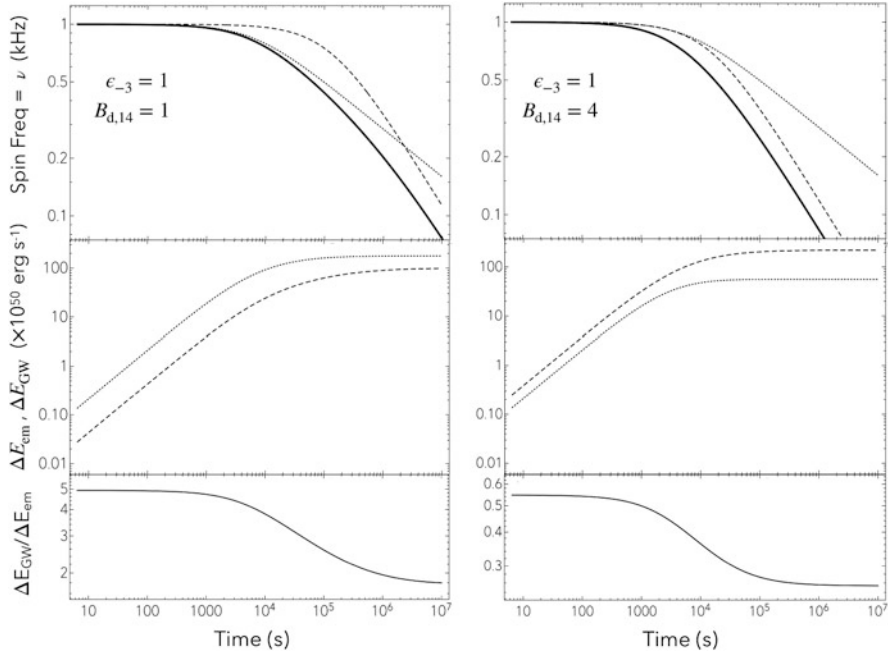


Fig. 8.1 Spindown of 1-ms spin NS subject to magnetic dipole and GW losses. The two panels represent a GW-dominated (left) and EM-dominated (right) spindown, respectively. In both cases, the upper row depicts the spin frequency evolution (continuous), with the dotted (dashed) curve showing the spin evolution if only GW (EM) losses were in place. The middle row shows the total spin energy lost to GWs (dotted) and EM radiation (dashed) vs. time (i.e. the two luminosities integrated up to that time). The lower row reports the ratio of the radiated energies vs. time

The bulk of a newborn magnetar rotational energy can be radiated away with enormous power in two main ways (e.g. [152]; see Fig. 8.1):

- (a) in the electromagnetic (EM) channel via magnetic dipole radiation, thanks to their intense (external) dipole B-fields. The EM luminosity is⁴

$$L_{\text{EM}}(t) = \frac{\mu_d^2 \Omega^4(t)}{c^3} = \frac{E_{\text{rot}}}{\tau_{\text{EM}}} \left(1 + \frac{t}{\tau_{\text{EM}}}\right)^{-2} \approx 10^{47} \frac{E_{\text{rot},52}}{\tau_{\text{EM},5}} \left(1 + \frac{t}{\tau_{\text{EM}}}\right)^{-2} \text{ erg s}^{-1} \quad (8.1)$$

where τ_{EM} is the characteristic time in which half of the initial spin energy is lost

$$\tau_{\text{EM}} = E_{\text{rot}}/L_{\text{EM}}(t=0) \approx 1.4 \times 10^5 P_{-3}^2 B_{\text{d},14}^{-2} I_{45} R_6^{-6} \text{ s}. \quad (8.2)$$

⁴This holds when the magnetic dipole is aligned with the spin axis. In general, if they are misaligned by an angle χ , the rhs of Eq. 8.1 must be multiplied by $(1 + \sin^2 \chi)$ [185].

- (b) in the gravitational wave (GW) channel, e.g. as a result of the ellipticity ϵ_B (and thus the mass quadrupole moment $Q \sim \epsilon_B I$) induced by their ultra-strong (internal) magnetic field. The GW luminosity is⁵

$$\begin{aligned} L_{\text{GW}}(t) &= 32G Q^2 \Omega^6(t) / 5c^5 = \\ &= \frac{E_{\text{rot}}}{\tau_{\text{GW}}} \left(1 + \frac{2t}{\tau_{\text{GW}}}\right)^{-3/2} \approx 10^{48} \frac{E_{\text{rot},52}}{\tau_{\text{GW},4}} \left(1 + \frac{2t}{\tau_{\text{GW}}}\right)^{-3/2} \text{erg s}^{-1}. \end{aligned} \quad (8.3)$$

The magnetically-induced ellipticity (see Sect. 8.4) is $\epsilon_B \sim 4 \times 10^{-4} B_{\text{int},16}^2 R_6^4 M_{1.4}^{-2}$, $M_{1.4}$ being the PNS mass in units of $1.4 M_\odot$. The characteristic spin-down time is

$$\tau_{\text{GW}} = E_{\text{rot}} / L_{\text{GW}}(t=0) \approx 1.8 \times 10^4 P_{-3}^4 B_{\text{int},16}^{-4} M_{1.4}^4 I_{45}^{-1} R_6^{-8} \text{ s}. \quad (8.4)$$

Magnetars are thus believed to be rotationally powered in their early infancy and magnetically-powered (*i.e.* *classical magnetars*) in their youth. Newborn, millisecond spinning magnetars have been invoked as the power source for a variety of short-lived paroxysmal phenomena, such as GRBs (Sect. 8.2), SNe (Sect. 8.3), GW events (Sect. 8.4) and Fast Radio Bursts (FRBs, Sect. 8.5), by virtue of the very fast rate at which they can tap and radiate away their rotational energy.⁶

8.2 Millisecond Magnetars as Gamma-Ray Burst Central Engines

GRBs are among the most powerful cosmic explosions, releasing $E_0 \sim 10^{49}\text{--}10^{52}$ erg, once corrected for a typical beaming $f_b \sim 10^2$, in a relativistic jet of photons, pairs, magnetic fields and a small amount of baryons [67, 132, 153, 158, 181] (see [88] for a recent review). The jet moves with bulk Lorentz factor $\Gamma \gtrsim 10^2$, sending a relativistic shock-wave through the circumstellar and/or interstellar medium.

Photons from the relativistic jet, Doppler-boosted to γ -rays (up to $\gtrsim 100$ MeV, or even \gtrsim GeV in some cases; e.g. [3]), form the GRB *prompt* phase. Based on their duration, GRBs are classified as long (> 2 s) or short (< 2 s; [84]). This classification captures fundamental differences between the two GRB groups, including (i) their

⁵ This holds when the magnetic symmetry axis is orthogonal to the rotation axis. In general, when they are misaligned by a tilt angle χ , the rhs of Eq. 8.3 must be multiplied by $(1 + 15 \sin^2 \chi) / 16$.

⁶ They may release magnetic energy as well, though this channel involves a smaller reservoir and there is no simple prescription for the power that can be liberated; this possibility has been discussed in relation to FRBs and the low-luminosity end of the short-GRB population.

characteristic luminosities, long GRBs typically being \sim 1–2 decades brighter and more energetic than short GRBs, (ii) their spectral properties, with long GRBs presenting a softer low-energy part of the spectrum (while the distributions in peak energy are very similar, with $E_p \sim 10^2$ – 10^3 keV; [59, 60]), and (iii) their progenitors and host galaxies.

Long GRBs are usually associated to a young stellar population as indicated by their often irregular, star-forming galaxy hosts and, within these hosts, to regions with the highest star-formation rate [55]. Some long GRBs were found to be associated with powerful type Ic SN (e.g. [57, 73]), a class of core collapse supernovae lacking H and He lines and thus originating from progenitors whose H- and He-rich envelopes were stripped before collapse (see Sect. 8.3). The comparatively small size of the progenitor at the time of collapse thus facilitates the break-out of a GRB jet from the star [125, 212, 214]. This suggested, in particular, a connection with WR stars⁷ [110, 212], which have $M > 20 M_\odot$ at birth (e.g. [30]) and suffer large mass losses during their evolution. At the time of collapse, they may have $M \gtrsim 10 M_\odot$ and $R \sim (1\text{--}10) R_\odot$, as observed in the Milky Way (e.g. [215]).

Concerning short GRBs, at least a fraction of them are produced by BNS mergers (and, possibly, BH-NS systems with not too large mass ratio), which track an old stellar population and are typically found in the outskirts of their massive host galaxies. GW events provide an estimated rate of $\sim 10^3$ Gpc $^{-3}$ yr $^{-1}$ for BNS mergers [2]. The short-GRB rate at $L_{\gamma,\text{iso}} > 10^{50}$ erg/s is $\sim (0.5\text{--}3)$ Gpc $^{-3}$ yr $^{-1}$ [61, 62, 209]. The two rates can be reconciled if GRBs jets have a typical beaming ~ 500 , or a jet core size $\theta_c \sim 3.5^\circ$: this matches nicely the estimated jet core size in GRB 170817A (see below) [61, 142, 143, 200].

The characteristic energies and fast variability time scales of prompt emission (down to $\Delta t \sim 1$ ms) suggest that GRBs originate in catastrophic events, involving the binding energy $W \sim GM^2/R \sim 10^{53} (M/M_\odot)^2 R_6^{-1}$ erg of a stellar mass compact object, or its somewhat lower rotational energy. Two possible central engines fulfilling these broad requirements for prompt emission have been considered:

- (a) Hyper-accreting black holes (BHs) surrounded by an ultra-high density, thick accretion disk of high angular momentum fallback material from the progenitor star [145, 164, 212]. The innermost stable circular orbit in the Schwarzschild potential requires that the specific angular momentum $\ell > \sqrt{12GM/c} = \sqrt{3}r_s c \sim 5 \times 10^{16} (M/3M_\odot) \text{ cm}^2 \text{ s}^{-1}$ (e.g. [180]), where r_s is the Schwarzschild radius, placing a lower limit to ℓ in the pre-collapse stellar core for a disk to form. The jet-launching mechanism lies in the interaction of the inflowing disk plasma with the spinning BH, mediated by the plasma-frozen B-field which endows the BH with an effective magnetosphere as long as matter inflow continues [13, 109, 192, 193]. The accretion (viscous) timescale in a thick disk, $t_v \sim r^{3/2}/\alpha\sqrt{GM}h^2 \sim 0.1\text{--}20 (M/3M_\odot)$ s for radii $\sim (3\text{--}100) r_s$ and

⁷ We note in passing that the two classical magnetars for which a progenitor mass of $\sim (30\text{--}45) M_\odot$ has been derived are associated to young open clusters (< 8 Myr) hosting WR stars.

typical parameter values (viscosity $\alpha \sim 0.01$, thickness-to-radius ratio $h \sim 0.5$), in agreement with the duration of the prompt emission.

(b) Millisecond spinning, highly magnetised NSs, independently proposed as GRB central engines as far back as 1992 [48, 204]. Early suggestions focused on the release of their large magnetic energy reservoir, due to the short characteristic timescales of magnetic instabilities/reconnection events. If instead the (even larger) spin energy of a millisecond magnetar is responsible for the prompt GRB emission, a more powerful mechanism than the classical dipole formula (Eqs. 8.1–8.2) is required for plausible values of B_d and P . It was then proposed that energy may be extracted very efficiently, in the first $\lesssim 30$ s of the NS life, by a strong neutrino-driven MHD wind from the NS surface.⁸ i.e. on a timescale much shorter than τ_{EM} [17, 137, 140]. Observationally, the (beaming-corrected) energy needed to power even the brightest prompt emissions rarely exceeds $\sim 10^{52}$ erg. On the other hand, the maximum spin energy of a NS is $\sim (3\text{--}8) \times 10^{52}$ erg, depending on its mass and equation of state [42, 116]. Thus, a GRB prompt phase requires a fraction of the maximum spin energy of a millisecond magnetar. Moreover, the specific angular momentum of the latter is $\ell = \sqrt{2IE_{\text{rot}}}/M \approx 3 \times 10^{15} R_6^2 P_{-3}^{-1} \text{ cm}^2 \text{s}^{-1}$, imposing a less demanding constraint on the angular momentum of the progenitor’s core compared to an hyper-accreting BH.

In both long and short GRBs the measured prompt γ -ray emission may amount to a seizable fraction of the total energy release ($\gtrsim 50\%$; [51, 218]), challenging theoretical models and requiring an efficient mechanism to convert the jet power to high-energy radiation. Proposed mechanisms for the prompt emission include internal shocks generated by collision of shells traveling at different values of Γ (e.g. [33, 170]) or by internal magnetic dissipation (e.g. [47, 107, 220]), with a possible contribution from bulk Comptonisation of photospheric emission (e.g. [8, 69, 175, 208])). Due to the observed fast variability, causality requires that the size of the prompt-emitting region be $\lesssim c\Delta t\Gamma^2 \sim 3 \times 10^{11} \Delta t_{-3} \Gamma_{100}^2 \text{ cm}$.

GRB *afterglows* are observed from X-ray to radio wavelengths for timescales of weeks/months in some cases and originate from the relativistic shock-wave resulting from the jet interaction with the surrounding medium [133, 154, 176]. Afterglows

⁸ During this short time, the enhanced spin down luminosity can be expressed as [137]

$$L_{\text{wind}} = L_{\text{EM}} (R_L/R_Y)^2 \times \max \left[\sigma_0^{-1/3}, 1 \right]. \quad (8.5)$$

Here $R_L = c/\Omega$ is the light cylinder, $R_Y \leq R_L$ the equatorial radius of the closed magnetosphere and $\sigma_0 = \phi^2 \Omega^2 / (\dot{M}c^3)$ the magnetization parameter of the wind, where \dot{M} is the neutrino-driven mass loss from the NS surface and ϕ the magnetic flux threading the NS surface and linked to open B-field lines. In the early stages the closed magnetosphere is small, i.e. a large fraction of the NS magnetic flux is linked to open B-field lines, hence $R_Y \ll R_L$. In addition, the neutrino-driven wind is strongest, carrying a sufficiently large mass outflow to ensure a low magnetization ($\sigma_0 \ll 1$): as a result, $L_{\text{wind}} \gg L_{\text{EM}}$. Later, as the mass loss rate drops, σ_0 grows quickly and the wind approaches a force-free condition ($\sigma_0 \rightarrow \infty$) while the closed magnetosphere expands, $R_Y \rightarrow R_L$. Thus $L_{\text{wind}} \rightarrow L_{\text{EM}}$ and the classic magneto-dipole spindown kicks in.

are produced farther out from the central engine, at a distance $>10^{16}$ cm, where, having swept up a mass $M_{\text{dec}} \sim E_0 / (\Gamma^2 c^2) \sim 10^{-7} M_\odot E_{0.51} (\Gamma/100)^{-2}$, the *external shock* decelerates and converts its kinetic energy to the energy of relativistic particles that radiate it away.

At the end of the prompt phase, the X-ray lightcurves of most long GRBs show a short-lived, steep flux decay $\propto t^{-3}$ (or steeper), followed by a shallow decay phase, or *plateau*, which is always flatter than $t^{-0.8}$ (typical index ~ -0.5) and lasts up to $t \gtrsim 10^4$ s [147]. Short GRBs display a similar phenomenology, albeit less frequently and on typically ~ 10 times shorter timescales. Plateaus usually end with a smooth transition to the so-called normal decay law (slightly steeper than $\sim t^{-1}$) that characterises afterglows, a behaviour expected from the decelerating shock-wave (Fig. 8.2, top panel).

The occurrence of the X-ray plateau cannot be explained by invoking spectral transitions in the emitting region, because observations indicate a constant X-ray spectrum throughout the whole duration of the plateau. Since X-ray plateaus are observed in long as well as short GRBs, any explanation for this feature should be general enough to hold in both classes of events. A straightforward interpretation involves the presence of a long-lived central engine, releasing power at a nearly constant rate for the typical duration ($\lesssim 10^4$ s in long GRBs and $\lesssim 10^3$ s in short GRBs; [215]; see also [191]). The energy may be injected in the afterglow-producing external shock, e.g. through a (magnetized) wind, constantly refreshing its kinetic energy and thus maintaining a constant level of radiation [32, 43, 66, 219]. Alternatively, the power from the central engine may give rise to an additional emission component temporarily outshining the external shock emission (e.g. [101, 174, 184]).

The plateau durations in long GRBs, $\sim 10^3$ – 10^4 s or longer in some cases, place a strong constraint on the central engine activity. Models with a central BH were devised in which the density profile in the progenitor star is tuned to provide the long-term time-varying mass accretion rate through the ultradense disk, as required to account for the X-ray afterglow light curve shape (e.g. [87]). By contrast, a millisecond spinning magnetar would have just the right spin down luminosity and plateau duration (Eq. 8.1), thus offering a straightforward interpretation. This idea was put forward [32, 219] well before the Swift discovery of X-ray plateaus. By using the magnetic dipole spindown formulae (Eq. 8.1), [101] and [174] obtained fits of X-ray plateaus in short GRBs deriving birth spin periods $P \sim (0.5\text{--}10)$ ms and dipole magnetic fields $B_d \sim (10^{14}\text{--}10^{16})$ G.

In [43], the luminosity evolution of a relativistic external shock was calculated based on a more advanced model including (i) energy injection from the magnetar spin down, (ii) radiative losses with efficiency as a free parameter, (c) a simple hydrodynamic prescription for the evolution of Γ with (observer's) time. The solution to this model was used to fit 4 long GRB plateaus, deriving $B_d \sim (10^{14}\text{--}10^{15})$ G and $P \sim (1\text{--}5)$ ms as birth parameters (Fig. 8.2, bottom panel). Application to a sample of 64 long GRBs confirmed previous results and extended the birth parameter ranges [11]. This work also confirmed the existence of a

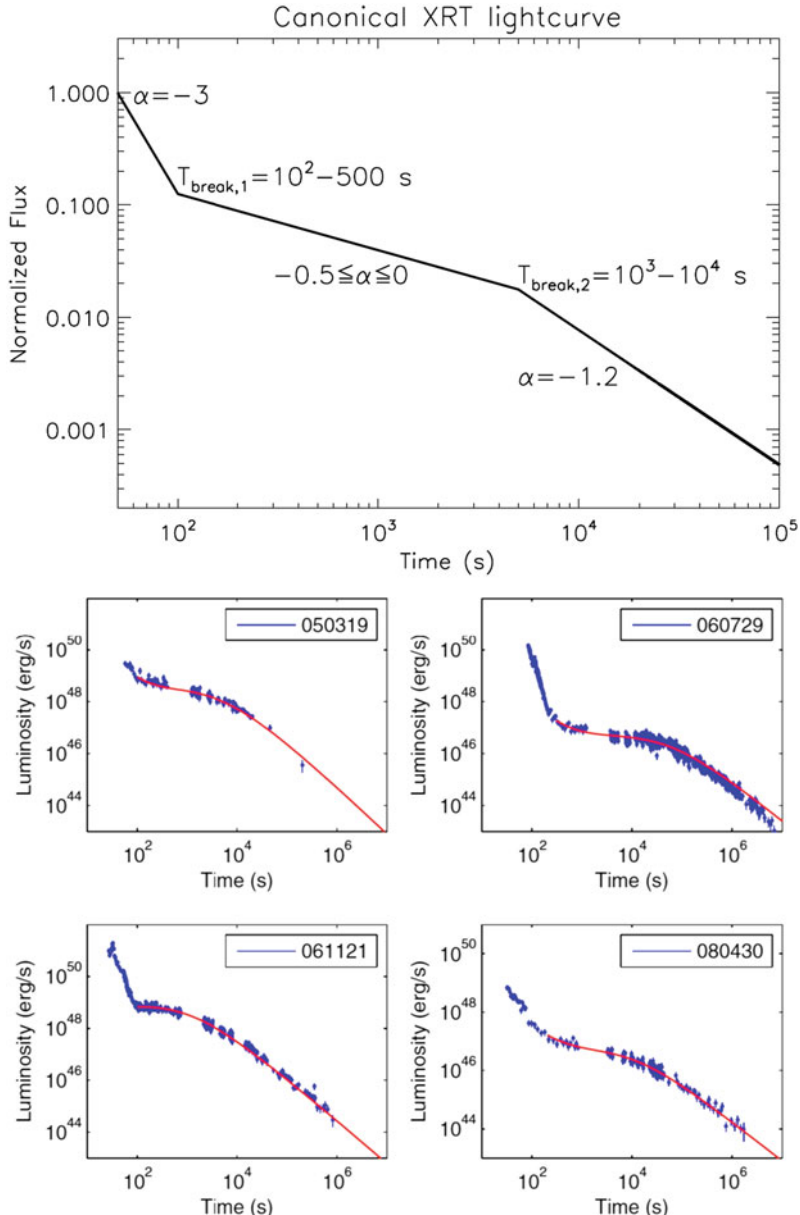


Fig. 8.2 *Top panel:* sketch of the canonical GRB X-ray light-curve. The prompt phase ends with a steep flux decay ($\alpha_1 > 3$), which is followed by a shallow decay phase ($0 \leq \alpha_2 < 0.8$; “plateau”) accompanied by a spectral hardening. The plateau joins smoothly to the so-called “normal” decay, i.e. the one expected from standard afterglow theory. Credit: Corsi et al. ApJ, 702, 1171 (2009) © AAS. Reproduced with permission. *Bottom panel:* plateau light-curve fits of four selected GRBs with an energy injection model invoking the spindown luminosity of a millisecond magnetar. Radiative losses are also included parametrically. Credit: Dall'Osso et al., A&A, 526, A121 (2011) © ESO. Reproduced with permission

correlation between the plateau luminosity and its duration, which had been first discovered in [34] and further studied in, e.g., [35–37] (Fig. 8.3, top panel). The model was extended with a more general expression for the magnetar spindown [190], and used to fit the light curves of 51 long and short GRBs with X-ray plateaus, obtaining $P \sim (0.8\text{--}20)$ ms and $B_d \sim (0.5\text{--}20) \times 10^{15}$ G (cf. [93]). A correlation between P - and B_d -values was found, with short GRBs lying systematically on the long-spin and strong- B_d end of the distribution while long GRBs occupy the opposite extreme (Fig. 8.3, bottom panel).

A test of the energy injection model with magnetar spin-down vs. a fireball model with no energy injection in two particular short-GRBs concluded that the data favor the former model with great significance, requiring NS matter to have a relatively stiff equation of state, with a maximum non-rotating mass of $\approx 2.3 M_\odot$ [177].

An open problem for the magnetar scenario is the great diversity observed in the joint optical/X-ray light curves of GRB plateaus (e.g. [66, 95, 155]). Approximately half of GRB afterglows appear to display an achromatic behaviour [88], in which the optical and X-ray emission have a similar temporal evolution as expected if they were both produced by the forward shock. However, in other afterglows these two components evolve differently [88], even though the X-ray light curve, from the start of the plateau through the transition to normal decay, typically does not show any spectral evolution. The X-ray behaviour would thus suggest that the transitions are still due to geometrical and/or hydrodynamical factors, but the optical behaviour argues against this possibility. This points to the existence of two separate emission regions at least in a fraction of GRBs (see, however, [66]). In the magnetar scenario, this may occur if the NS spin energy is not injected in the external shock but rather gives rise to a magnetar wind nebula (MWN) as envisaged in ([184]; cf. [117, 139]). In this case, the X-ray plateau would reflect the emission from the MWN, while the optical would be dominated by emission from the forward shock. This may be possible in short GRBs, whereas in long GRBs the observed X-rays would hardly be able to diffuse through the several M_\odot of ejecta in a $\sim 10^4$ s timescales.

The discovery of the gravitational signal GW 170817 and of the associated short GRB 170817A (e.g. [96]) confirmed the BNS merger nature of at least some short GRB progenitors. Broadband afterglow observations showed that a relativistic structured jet [134, 173] was launched right after the merger [61, 142], having a wide angular profile of kinetic energy with a narrow core ($\theta_c \sim 5^\circ$) and an extended decaying tail at larger angles [120, 143, 200]. Following this discovery it was proposed [149] that the X-ray plateau of GRBs can be interpreted as a consequence of the jet's extended angular profile—combined with its relativistic motion—when observed along the jet axis, requiring a relatively large emission radius, $R > 10^{14}\text{--}10^{15}$ cm. It was further shown that steep decays and plateaus that follow the prompt are generic features of structured jets even if observed off-axis, although their slopes and durations depend sensitively on the viewing angle [6]. In this alternative scenario the plateau carries signatures of the jet structure, but not of the central engine. Therefore all considerations about a magnetar central engine (but the plateau) remain unaltered.

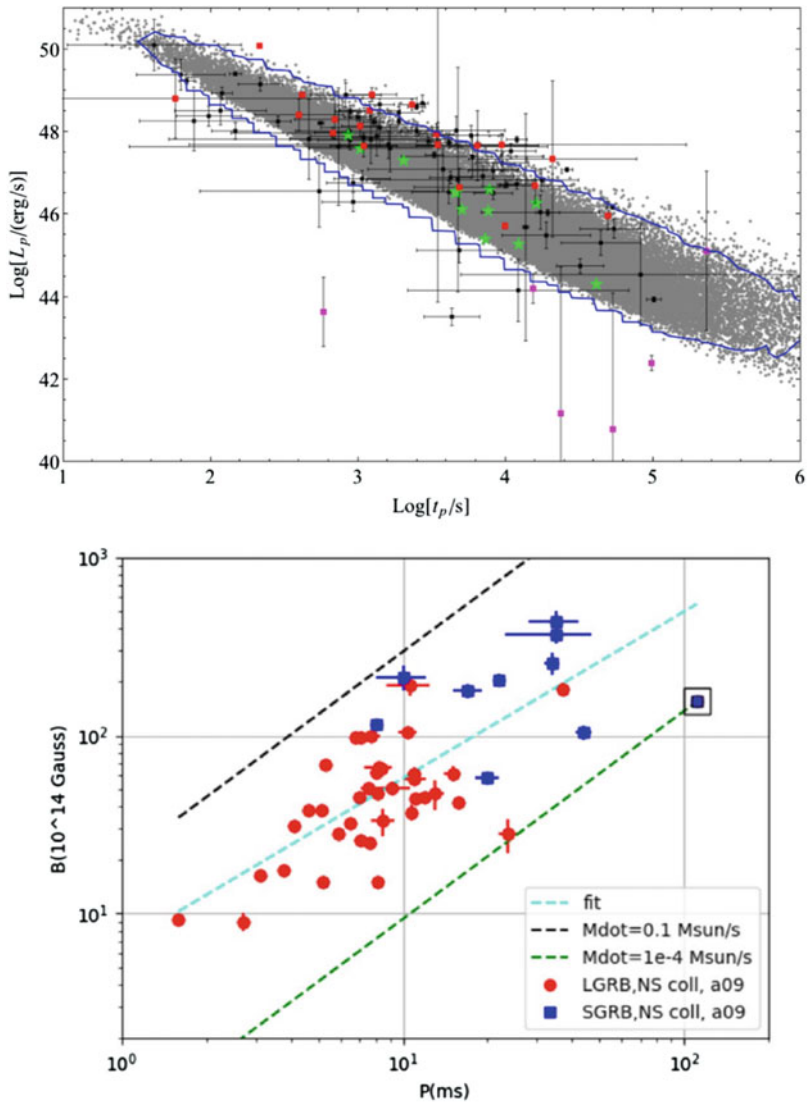


Fig. 8.3 *Top panel:* the anti-correlation between the luminosity at the end of the plateau (L_p) and the plateau duration (t_p) for a large sample of long GRBs. Credit: Bernardini et al., A&A, 539, A3 (2012) © ESO. Reproduced with permission.; *Bottom panel:* the B_d vs. P correlation for a sample of long *and* short GRB plateaus that were fitted with an energy injection model invoking a spinning down millisecond magnetar. Reproduced with permission. It was noted that this correlation matches the well studied “spin-equilibrium” line for accreting NS in galactic binaries, once the mass accretion rate is normalised to typical values expected in a GRB prompt phase ($M \sim 10^{-4}\text{--}0.1 \text{ M}_\odot \text{ s}^{-1}$). Credit: Stratta et al., ApJ, 869, 155 (2018) © AAS

8.3 Millisecond Magnetars and Supernovae

A group of stellar explosions exceeding by 1–2 orders of magnitude the peak luminosity of standard SNe has been identified and studied in the last two decades. These events, termed SuperLuminous SNe (SLSNe), occur ~ 100 times less frequently than SNe and are broadly classified into hydrogen-poor (SLSNe—I) and hydrogen-rich (SLSNe—II) types (for reviews see [56, 74]). They are believed to arise in the core collapse of massive stars (~ 20 – $40 M_{\odot}$). Different scenarios have been investigated to explain the extra energy required to power SLSNe and attain peak luminosities of \sim few $\times (10^{44}$ – 10^{45}) erg/s; among these the formation of a millisecond spinning magnetar appears to be especially promising, particularly in relation to SLSNe—I.

Originally proposed to interpret the characteristics of a peculiar Type Ib SN (SN 2005bf, [112]), the magnetar model for SLSNe was further developed in [45, 78, 213]. The model envisages that the spin-down power of the newborn millisecond magnetar is emitted in the electromagnetic channel in the form of magnetic dipole radiation and pulsar wind, and deposited deep in the expanding SN layers, from which it diffuses outwards. We summarise here the basic features of the simple model by [78].

In the core-collapse of the progenitor star of radius R_* , a mass M_{ej} is ejected with velocity v_{ej} , such that the initial energy of the SN is $E_{\text{SN}} = M_{\text{ej}}v_{\text{ej}}^2/2 \sim 10^{51}$ erg. In the absence of other energy sources (such as decay of ^{56}Ni , fallback accretion or magnetar spin-down), self-similar adiabatic evolution ensues with expansion time $t_{\text{e}} = R_*/v_{\text{ej}}$. The internal energy decreases as $E_{\text{int}} \sim E_{\text{SN}}(R_*/R)$, with $R = v_{\text{ej}}t$ the radius of the remnant. When the age of the remnant equals the radiative diffusion timescale $t_{\text{d}} \sim (\kappa M_{\text{ej}}/v_{\text{ej}}c)^{1/2}$ (here κ is the opacity) the light curve attains its maximum luminosity of $\sim E_{\text{SN}}t_{\text{e}}/t_{\text{d}}^2 \lesssim 10^{43}$ erg/s.

For plausible amounts of ^{56}Ni the extra heat source provided by radioactive decay is not enough to reach maximum luminosities up to $\sim 10^{45}$ erg/s. Instead the rotational power of a newborn magnetar suffices. The bulk of its rotational energy E_{rot} is released on a spin-down timescale τ_{EM} (Eq. 8.1) which is shorter than t_{d} if

$$B_{\text{d},14}P_{-2}^{-1} > 2M_{\text{ej},5}^{-3/8}E_{51}^{1/8}, \quad (8.6)$$

here $M_{\text{ej},5} = M_{\text{ej}}/5M_{\odot}$. The rotational energy of the remnant will become dominant when $E_{\text{SN}}(R_*/R) < E_{\text{rot}}$ (since usually $(R_*/R) \ll 1$ this condition does not require extreme values of E_{rot}). In this case the SN attains a peak luminosity of

$$L_{\text{p}} \sim E_{\text{rot}}\tau_{\text{EM}}/t_{\text{d}}^2 \sim 5 \times 10^{43}B_{\text{d},14}^{-2}M_{\text{ej},5}^{-3/2}E_{51}^{-1/2}\text{erg/s} \quad (8.7)$$

The above model provides only rough estimates, which nevertheless capture the characteristic scales of the magnetar scenario. In their more advanced model [78] explore other effects such as those arising from magnetar energy release for $t > \tau_{\text{EM}}$

and derive analytical expressions for the SN light curve in the regimes arising from a different hierarchy of timescales.

Magnetar models were applied to SLSNe light curve fitting by a number of authors. Based on the analysis of the bolometric light curve of 5 SLSNe-I, [75] estimated the following ranges for the magnetar parameter $P_{-3} \sim 1.7\text{--}7$, $B_{d,14} \sim 3\text{--}7$, $E_{51} \sim 0.4\text{--}7$ and an ejected mass of $M_{ej} \sim 2.3\text{--}8.6 M_\odot$. By fitting of the multicolor light curves of 38 SLSNe-I with a more general model [146] derived the following (1σ) parameter ranges: $P_{-3} \sim 1.2\text{--}4$, $B_{d,14} \sim 0.2\text{--}1.8$, $E_{51} \sim 2\text{--}10$ and $M_{ej} \sim 2.2\text{--}13 M_\odot$. Applications to hydrogen-rich SLSNe (SLSNe-II) have also been proposed [151].

Millisecond magnetar models for SLSNe also face some difficulties: for instance early or late bumps in the light curves are not straightforwardly interpreted, and the observationally-determined ejected masses are sometimes 3–4 times larger than predicted. It has been proposed that the shock breakout of a magnetar-inflated bubble, or of a GRB-related relativistic jet, crossing the SN ejecta can produce an early-time secondary maximum in the SN light-curve as a specific signature [79, 118]. 1D models and simulations are probably inadequate to capture such complex features in light curves and spectra. Multidimensional simulations of magnetar winds embedded in young remnants offer a better perspective and the first 3D studies have recently become available (see e.g. [23]).

Accretion of fallback matter onto a newly formed fast spinning magnetar shortly after collapse may also contribute determining the magnetar properties as well as the energy release into the exploding SN envelope. In [161] the fallback matter inflow rate is parametrised with an initial growth (scaling as $\propto t^{1/2}$) followed a few hundred seconds later by a decrease, with the characteristic time dependence of fallback ($\propto t^{-5/3}$). If accretion of fallback matter onto the proto-magnetar does take place, the total amount of accreted matter must be small enough (several tenths of solar mass) that the maximum NS mass is not exceeded and collapse to a BH does not take place. This in turn requires that the initial spin is in the millisecond range, $B_d \geq 10^{15} \text{ G}$ and fallback does not involve large masses. Under these circumstances at the end of the accretion phase, when the NS magnetospheric radius

$$r_m \simeq 10^6 B_{d,15}^{4/7} M_{1.4}^{-1/7} \dot{M}_{31}^{-2/7} \text{ cm} \quad (8.8)$$

becomes larger than the corotation radius

$$r_c \simeq 1.7 \times 10^6 M_{1.4}^{1/3} P_{-3}^{2/3} \text{ cm}, \quad (8.9)$$

fallback matter will be flung outwards at the expense of the proto-magnetar rotational energy by the so-called *propeller* mechanism. Collision of this matter with the ejecta will shock-heat, creating a cavity deep inside the expanding envelope and depositing $\sim 10^{51}\text{--}10^{52} \text{ erg}$ in the SN in \sim tens of seconds. At the end of the propeller phase energy losses will be dominated by (slower-decreasing) dipole spin-down. The large energy release by the propeller in the early stages adds up to the

whole budget of the SN, giving rise to a fast and powerful evolution. In this scenario the energy injection takes place at later times, at variance with standard models for SLSNe in which the magnetar dipole spin-down losses directly power the observed light-curve.

In [135] an extensive study of fallback in millisecond magnetar models for both GRBs and SLSNe is presented in which additional regimes and effects are explored. Among these it is considered that fallback accretion might spin up an initially non-maximally rotating protomagnetar, at the same time enhancing the spin-down luminosity with respect to the standard dipole formula (see footnote 5). This effect is found to reduce the gap in the range of initial spin periods and B-fields required to model GRBs and SLSNe with millisecond magnetar models.

An open issue with the above scenarios (and, more generally, core collapse formation of millisecond magnetars) is that the Supernova Remnants (SNRs) originating in stellar explosions which receive an additional energy of $\sim 10^{51}\text{--}10^{52}$ erg from magnetar spin-down should be distinctly different from shell-type SNRs hosting lower magnetic field NSs. This is contradicted by the SNRs associated to classical magnetars, which display fairly standard features [207],[121]. Possible way outs have been proposed. A very fast expanding envelope may dissipate all its energy in several hundred years and make the SNRs too faint to be detected: in fact more than half presently-known magnetars are not associated to SNRs. Alternatively the bulk of the rotational energy of millisecond magnetar could be released in the GW channel, thus leaving the expanding remnant unaffected ([41]; see Sect. 8.4).

8.4 Gravitational Waves from Millisecond Spinning Magnetars

The huge rotational energy of millisecond magnetars may also give rise to powerful GW emission if the NS develops a sufficiently large, time-varying mass quadrupole moment (Q). Non axisymmetric shape distortions, caused e.g. by a superstrong interior B-field or by an extreme rotation rate, can produce this effect. The interior B-field generally induces an ellipsoidal deformation of a NS shape. If the spin axis of the ellipsoidal NS is *not aligned* with one of the principal axes, the NS will undergo free-body precession. In these conditions, a viscosity-driven secular instability⁹ can operate [31, 76]: viscosity will dissipate spin (precession) energy while conserving angular momentum (L), hence the NS will end up spinning, after a few viscous times (τ_{visc}), around the axis with the largest moment of inertia.¹⁰

Let us approximate for clarity the NS as a biaxial ellipsoid with $I_x = I_y \neq I_z$, where (x, y, z) are the directions of the three principal axes and z represents the

⁹ Secular instabilities arise from the fact that lower-energy states are accessible to the fluid if it can get rid of its excess energy, e.g. via GW-emission or viscosity on timescales \gg the dynamical time.

¹⁰ Indeed, for a constant $L = I\Omega$, the spin energy $T = L^2/2I$ is minimised by maximising I .

symmetry axis. Oblate ellipsoids are characterised by $I_z > I_x$: thus, viscous dissipation will lead them to spin around the z -axis, with an axisymmetric shape in the orthogonal plane ($I_x = I_y$). Prolate ellipsoids have the opposite property, $I_x > I_z$, and therefore will spin-flip and end up rotating, after a time $\sim \tau_{\text{visc}}$, around the x -axis with the non-axisymmetric shape in the orthogonal plane (the symmetry axis is orthogonal to the spin axis). The former case would result in $Q = 0$, hence no GW emission. The latter case instead maximises $Q \sim \epsilon I_x$, where the ellipticity $\epsilon = (I_x - I_z) / I_x$, thus making the NS an efficient GW emitter under suitable circumstances according to Eq. 8.3 [31, 38, 40–42, 90, 91, 189].

In the dynamo scenario, a toroidal component is expected to dominate the interior B-field of magnetars [63, 188, 195, 197]. The azimuthal magnetic field, in turn, induces a prolate shape distortion of the NS, with ellipticity ϵ_B and with the magnetic axis as its symmetry axis (e.g. [31] and references therein). Thus, newborn magnetars are ideal candidates for the spin-flip instability which, combined with the ms spin, makes them optimal GW sources among newborn NS.

The magnetically-induced ellipticity is determined by both the strength and geometry of the interior B-field (e.g., [4, 26, 38, 70, 122, 123]). Dimensionally $\epsilon_B \sim E_B / W$, where the NS magnetic energy $E_B \sim 2 \times 10^{49} B_{\text{int},16}^2 R_6^3 \text{ erg}$. Models of the magnetic field distribution in NSs consider mixed toroidal/poloidal components, like e.g. the so-called *twisted-torus* configuration in which a toroidal field (B_ϕ) is confined within the NS core, in a torus-shaped region pierced by poloidal field lines, (B_p). The dipole component of B_p forms the exterior dipole B-field, B_d . Stability arguments [15, 16] require the toroidal-to-poloidal magnetic energy ratio $E_{B,\phi}/E_{B,p} \gtrsim 0.5$, while the maximum value for this ratio is less constraining and can be $\sim 10^2$ – 10^3 , depending on the structure and size of the torus-shaped region (e.g. [4, 38, 64]). Thus, B_ϕ can largely dominate the interior magnetic energy and the corresponding ϵ_B -value. In this case we may write

$$\epsilon_B = k (E_{B,\phi} / W) \approx 4 \times 10^{-4} (k/4) B_{\text{int},16}^2 R_6^4 M_{1.4}^{-2}, \quad (8.10)$$

where the geometrical factor k is ≈ 4 for a uniform B-field [31] and can be a few times larger in twisted-torus configurations (e.g. [4, 38, 122, 123]).

The spin-flip instability is generic to all rotating stars with misaligned toroidal B-fields [31, 76, 131]. However, since $L_{\text{GW}} \propto \epsilon_B^2 \Omega^6$ and $L_{\text{EM}} \propto B_d^2 \Omega^4$, it can lead to strong GW signals only in millisecond spinning NS provided that (i) the magnetically-induced ellipticity is $\epsilon_B \gtrsim 5 \times 10^{-4}$, requiring an interior magnetic field $B_{\text{int}} \gtrsim 10^{16} \text{ G}$, (ii) the exterior magnetic dipole field is $B_d \lesssim \text{a few} \times 10^{14} \text{ G}$, in order to prevent magnetic dipole radiation from dominating the spindown and choking the GW signal (in the latter case a bright EM transient may result, e.g. a GRB X-ray plateau or a SLSN); (iii) viscous dissipation of free-body precession

acts on a timescale $\tau_{\text{visc}} < \tau_{\text{EM}}$, to allow GWs to kick in while the NS still retains its original spin.¹¹

The GW signal emitted by the millisecond magnetar, once its symmetry axis has become perpendicular to the spin axis (orthogonal rotator), has frequency $f_{\text{GW}} = 2/P = \Omega/\pi$ and a relatively simple shape: a sinusoidal oscillation with decreasing amplitude ($h \propto \Omega^2$) and frequency ($f_{\text{GW}} \propto \Omega$), resembling in many respects a *time-reversed chirp* lasting $\sim h$ ([42]). The horizon distance for ideal matched-filter searches with Advanced LIGO/Virgo is estimated to be ~ 20 Mpc [31, 40, 189] within which one expects, conservatively, ¹² $\gtrsim 0.3$ magnetars per year to be formed [42], given a local rate of SN Ibc+II $\sim 7 \times 10^{-5}$ Mpc⁻³ yr⁻¹ [94].

Very fast rotation leads also to a large mass quadrupole moment (Q) in fluid bodies, regardless of the B-field strength. The corresponding symmetry axis is aligned with the spin axis, hence no GW emission ensues. However when the kinetic-to-binding energy ratio $T/|W| \gtrsim 0.27$ (here $T = E_{\text{rot}}$), the fluid becomes *dynamically unstable* [19], transitioning to a new stable state on a timescale $\tau_{\text{dyn}} \sim 2\pi\sqrt{R^3/(GM)} \lesssim 1$ ms. In the stable state the rotating body has a highly elongated, non-axisymmetric shape (bar-like) and $\lesssim 1$ ms spin, thus emitting GWs according to Eq. 8.3, with ϵ related to the degree of asymmetry of the bar. The high energy threshold makes the dynamical instability unlikely to occur ([46]; see, however, [183]). Indeed, as the PNS is spun up by angular momentum conservation in the progenitor's collapsing core, it becomes subject to a *secular* bar-mode instability already at $T/|W| \gtrsim 0.14$. This is the fastest growing (f -mode, $\ell = m = 2$, $\tau_f \sim 1-10^5$ s; [89]) among the so-called CFS (Chandrasekhar-Friedmann-Schutz) instabilities [20, 54], that are secular GW-driven frame-dragging instabilities¹³ of fast-rotating stars.

In the case of the f -mode, the fluid becomes prone to a non-axisymmetric, elliptical deformation of its shape (Riemann-S ellipsoid) with $\epsilon = (a_1^2 - a_2^2)/(a_1^2 + a_2^2)$, a_1 and a_2 being the semi-major axes of the elliptical cross-section orthogonal to the spin axis. The elliptical pattern rotates, in the inertial frame, at the angular frequency Ω_p , leading to GW emission which provides the required energy sink for the instability to grow, up to a large saturation amplitude ($\epsilon \lesssim 10^{-2}$; [29, 89]). Superposed to the pattern rotation is a field of internal motions with vorticity ζ and angular frequency Λ such that, in the inertial frame, the rotation of fluid particles has angular frequency¹⁴ $\Omega = \Omega_p + \Lambda$. At the onset of the instability, the energy lost to GWs drives the growth of the mode amplitude without affecting Ω_p and Λ (the total circulation is conserved, see [29]). Once the mode saturates GW losses

¹¹ At these early times the NS temperature is $T \sim (3-10) \times 10^9$ K ([40, 42, 91]), implying the main dissipative term should be bulk viscosity. The latter requires a periodic pressure perturbation in the fluid NS to activate out-of-equilibrium chemical reactions. The precessional motion of the fluid NS provides such a perturbation, the amplitude of which is still debated (e.g. [42, 90, 91]).

¹² For this estimate, we adopt a minimum magnetar birth rate of one per 10 CCSNe..

¹³ As long as viscosity can be neglected.

¹⁴ Λ is the angular frequency of internal motions in the frame co-rotating with the elliptical pattern.

start reducing Ω_p : the NS then follows a sequence of Riemann-S ellipsoids with decreasing pattern rotation and constant Λ , towards a final state which has interior fluid motions (vorticity ζ) but a stationary (non-radiating) non-axisymmetric shape (Dedekind ellipsoid). We note that, up to this point, the model does not require the NS to have a magnetar-like B-field but only a millisecond spin.

As with spin-flip, magnetic dipole radiation due to the exterior B_d introduces an additional sink for the NS spin energy. The latter is $E_{\text{rot}} \gtrsim 5 \times 10^{52}$ erg if the secular instability sets in. It was shown in [29] that this extra energy loss can (a) accelerate the instability growth rate and the NS evolution along the same sequence of Riemann-S ellipsoids and (b) extract a fraction of E_{rot} releasing it in the EM window. Because Ω (and Ω_p) is constant during the growth of the f -mode, a constant EM luminosity would result, $\sim 10^{47}$ erg s $^{-1}$ for typical magnetar parameters, which would account e.g. for an early GRB X-ray plateau. Like with the spin-flip instability, the NS spin down is initially only due to magnetic dipole radiation. However, in a time $\tau_f \lesssim 10^3$ s the f -mode amplitude becomes large enough to make GW emission dominant. The early EM signal would thus be followed, after $\lesssim 10^3$ s, by a long-lived GW signal (lasting $\sim \tau_f$) at the nearly constant frequency $f = 2\nu_p = \Omega_p/\pi$. Both signals would then fade rapidly due to the strong NS spindown (Fig. 8.4).

Therefore, a $\sim 10^3$ s long GRB X-ray plateau followed by a $\sim 10^3$ s GW signal at $f < 1$ kHz may represent the signature of a newborn magnetar with spin energy $E_{\text{rot}} > 5 \times 10^{52}$ erg. The X-ray plateau would carry information about the NS spin and dipole magnetic field (B_d), while the GW signal tracks the f -mode amplitude (ϵ) and its pattern frequency (Ω_p), in principle different from that associated to the plateau ([29]). The pattern rotation has a lower frequency (Ω_p) than $\Omega = \Omega_p + \Lambda$: this offers an advantage for GW signal detection, by placing its frequency in the range $\sim (0.1\text{--}1)$ kHz, where the Advanced LIGO/Virgo sensitivity is higher. For optimal NS parameters, the GW signal may reach a peak $h \sim 10^{-26}$ Hz $^{-1/2}$ at an horizon distance $d \sim 100$ Mpc for Advanced LIGO/Virgo with ideal matched-filter searches[29].

In contrast to ideal matched-filter, realistic signal searches are strongly limited by computational resources and must be carried out with sub-optimal methods. Currently, four different dedicated pipelines exist for LIGO/Virgo data implementing four different detection techniques [1]: STAMP (Stochastic Transient Analysis Multidetector Pipeline), HMM (Hidden Markov Model) tracking, ATrHough (Adaptive Transient Hough) and FreqHough (Generalized FrequencyHough). The discovery of the BNS merger GW 170817, at the distance of only 40 Mpc, provided a first performance test for such pipelines. No NS signal was revealed, but it was shown with real data that the O2 horizon for the 4 pipelines ranged between 0.2 and 0.9 Mpc ([1]), independent of the particular emission model. The foreseen sensitivity improvements in the years to come imply a realistic horizon ~ 3 Mpc for Advanced interferometers, and $\sim 20\text{--}30$ Mpc with 3rd generation detectors.

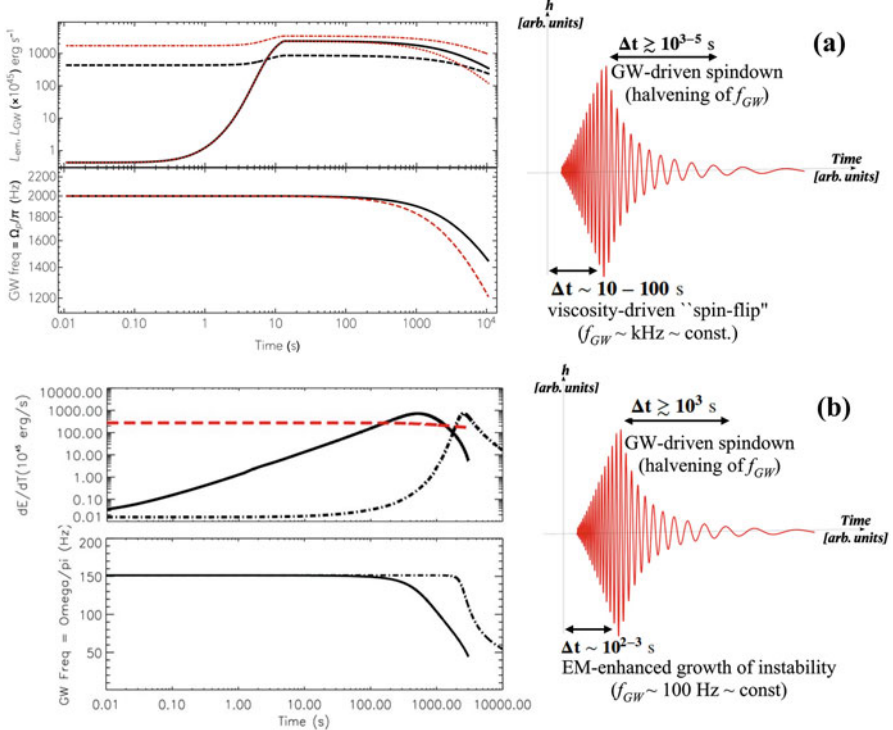


Fig. 8.4 (a) Spin-Flip. *Upper left:* the GW (continuous) and EM (dashed) spindown luminosity of a 1 ms-magnetar with initial tilt angle $\chi = 3^\circ$, $\epsilon_{B,-3} = 1$ and $B_{d,14} = 1$ (black). GWs (dotted) and EM (dot-dashed) luminosity with a three times stronger dipole B-field and all other parameters fixed (red). The GW fast rise follows the growth of the tilt angle (see footnote 5). The EM emission grows as well, by a factor 2, due to a term $(1 + \sin^2 \chi)$ in Eq. 8.1 (see footnote 4). *Lower left:* Signal frequency vs. time with the weaker (continuous, black) and stronger (dashed, red) dipole B-field. *Right panel:* Sketch of the time evolution of the GW signal (strain). (b) Bar-mode. *Upper left:* GW (continuous, black) and EM (dashed, red) luminosity of a NS with $B_{d,14} = 1$ (adapted from [29]). *Lower left:* signal frequency (twice the rotation frequency of the elliptical pattern) vs. time (from [29]). *Right panel:* same as in (a). Credit: Corsi et al., ApJ, 702, 1171 (2009) © AAS. Reproduced with permission

To summarize this section, the huge reservoir of rotational energy of millisecond magnetars ($\sim 10^{-2} M_\odot c^2$) and their extreme interior B-fields allow for strong GW signals to be emitted, potentially carrying orders of magnitude more energy than the GW signals expected from core-collapse or *ordinary* NS ($< 10^{-5} M_\odot c^2$; e.g. [5, 178]). This makes newborn magnetars potentially detectable in GWs over a much larger volume than any other isolated NS source ($> 10^{3.5}$ times larger), hence at a substantially higher rate despite their relative rarity. The shape of their GW signals carries the signature of the mechanism that has produced them, and provides insights into the physical properties of newborn magnetars.

8.5 Fast Radio Bursts and Millisecond Magnetars

Fast Radio Bursts (FRBs) are another class of astrophysical transients which has drawn much interest into young magnetars and the possibility that they are endowed with ultra-strong interior B-fields and large spin energy. FRBs are single, (sub)-millisecond radio pulses with GHz peak flux densities $S_\nu \sim (0.1\text{--}10)$ Jy and very large dispersion measures (the electron column density along the line of sight to the source) $\text{DM} \sim 100\text{--}2600 \text{ pc cm}^{-3}$, which exceed the values in our galaxy. Assuming that the extra-DM is due to the intergalactic medium, typical comoving distances in the Gpc range, isotropic emitted energies of $E_{\text{iso}} \sim 10^{38}\text{--}10^{40}$ erg, and brightness temperatures, $T_b > 10^{33}\text{--}10^{36}$ K were derived (see, e.g., [27, 82, 157, 165, 217] for recent reviews). First discovered in Parkes archival data [97], for long their nature remained uncertain, their astronomical origin being supported by (i) the precise scaling of the arrival times of individual pulses with frequency ($\propto \nu^{-2}$), as expected from radio waves propagating through a cold plasma and (ii) the duration of the decaying tail of individual pulses vs. frequency ($\propto \nu^{-4.4}$), as expected from waves scattered by a medium with a Kolmogorov spectrum of inhomogeneities. Eventually, the discovery of the repeating FRB121102 [179, 187] and the identification of its host galaxy at $z \approx 0.193$ [21] established FRBs as genuine extragalactic phenomena. More recently a second repeater was discovered (FRB180814; [25]), soon followed by seventeen new ones ([53, 114]), indicating that the fraction of repeating FRBs may be much higher than originally thought.

Their short durations imply FRBs are associated to compact sources, i.e. the size of the emitting region should be $\lesssim c\Delta t\Gamma_2^2 \approx 3 \times 10^7 \text{ cm } \Delta t_{-3}\Gamma^2$. In contrast to GRB jets, where the pair-production opacity for γ -ray photons places a strong constraint on the bulk Lorentz factor, different models for FRBs have widely different requirements on the source bulk motion, from non-relativistic (e.g. [104, 108]) to extremely relativistic ($\Gamma \sim 10^2\text{--}10^3$ or even up to 10^5 in shock models [9, 119]; see below).

Accounting for beaming $f_b = \Delta\Omega/4\pi$ within a solid angle $\Delta\Omega$, the energy released by FRBs is

$$E_{\text{FRB}} = E_{\text{iso}} f_b = \frac{S_\nu \Delta\nu \Delta t d_L^2}{1+z} f_b \simeq 10^{38} \text{ erg } \frac{S_\nu}{1 \text{ Jy}} \frac{\Delta\nu_9}{0.5} \Delta t_{-3} d_{L,\text{Gpc}}^2 f_b , \quad (8.11)$$

where $\Delta\nu_9$ is the bandwidth in GHz and the last equality is for a luminosity distance $d_L \approx 1 \text{ Gpc}$ ($z \approx 0.2$, or $\text{DM} \sim 300 \text{ pc cm}^{-3}$; e.g. [157]).

Besides FRB121102, the repeater FRB180916 is to date the only other source of the class with an identified host galaxy and measured redshift, $z \approx 0.0337$ (150 Mpc; [114]), again consistent with its DM. This source displays also an enigmatic ~ 16 d periodicity in its bursting activity [24, 92, 216]. FRB121102 has a persistent radio source counterpart with luminosity $\nu L_\nu \approx 10^{39} \text{ erg s}^{-1}$ at 1.4 GHz and a flat spectrum $\propto \nu^{-0.2}$ up to ~ 10 GHz beyond which it steepens to

$\alpha \sim -1$. Based on its emission properties an estimated age $\gtrsim 30$ yrs was derived for the persistent radio source, hence for FRB 121102's progenitor [136, 159].

The puzzling features of FRBs boosted a flurry of theoretical models invoking compact object progenitors (see [162]). If all FRBs are produced by a single type of progenitors, the existence of repeaters demonstrates that, despite their energy, FRBs are not produced in one-time-only catastrophic events (e.g. a NS collapsing to a BH). NSs play a major role in FRB models, either as isolated sources of magnetically-powered flares or as members of binary systems (see, e.g., [68, 71]).

The progenitors of FRBs must meet the constraint of their estimated all-sky rate $\sim 10^{3-4}$ events/day, or a rate density $\sim 10^{4-5} f_b^{-1} \text{ Gpc}^{-3} \text{ yr}^{-1}$ up to $z \approx 0.5$ ($\sim 36 \text{ Gpc}^3$). If repeating FRBs dominated the population, as suggested by the many already discovered, a much lower birth rate of FRB sources would be implied. A burst rate $\dot{N}_0 \sim 1$ per day is estimated for FRB121102 [98], while the estimated age of this source suggests an active lifetime $\tau_{\text{active}} \gtrsim 30$ yr. If these values were typical of FRBs, each repeater would produce $N_{\text{FRB}} \sim 10^4 \dot{N}_0 (\tau_{\text{active}}/30 \text{ yrs})$ FRBs and the corresponding source birth rate would be $\mathcal{R} \sim (1-10) f_b^{-1} \dot{N}_0^{-1} (\tau_{\text{active}}/30 \text{ yrs})^{-1} \text{ Gpc}^{-3} \text{ yr}^{-1}$. This is a small fraction of the rate of core collapse supernovae (CCSN) $\sim 3 \times 10^5 \text{ Gpc}^{-3} \text{ yr}^{-1}$ ([111]) and roughly comparable to the SLSN and (beaming-corrected) GRB rates [98, 99, 146]. Overall, a small fraction of all CCSN remnants broadly fit into this picture, possibly a small subset of the magnetar population [115].

A digression on ordinary radio pulsars is in order here. Their NSs are known to produce highly collimated beams of coherent radio waves with very large brightness temperatures,

$$T_b = \frac{S_\nu}{2k_B} \left(\frac{cd}{\nu R} \right)^2 \gtrsim \frac{S_\nu}{2k_B} \left(\frac{d}{\nu \Delta t} \right)^2 \approx 3 \times 10^{20} \frac{S_\nu}{\text{mJy}} \left(\frac{d_{\text{kpc}}}{\nu_9 \Delta t_{-3}} \right)^2 \text{ K}, \quad (8.12)$$

k_B being Boltzmann's constant and d the distance. While the radio mechanism in pulsars is not fully understood yet, it is well established that it is powered by the NS electromagnetic spin down (Eq. 8.1) with a characteristically low [65] radio efficiency,¹⁵ $\epsilon_r \sim 10^{-5} \gamma_6 (L_{\text{EM,38}}/4.6)^{-1/2}$, primarily limited by the ability of the NS magnetosphere to accelerate a large number of electrons to relativistic energies ($\gamma \sim 10^6$).

Some radio pulsars sporadically emit Giant Pulses (GPs) with very short duration ($\sim \mu\text{s}$) and much larger fluence than ordinary radio pulses. GPs can be interpreted as highly beamed, rotation-powered pulses [28]. The brightest GP from the Crab pulsar had a peak fluence $\sim 2 \text{ MJy}$ at $\sim 9 \text{ GHz}$ (2.5 GHz bandwidth; [28]), implying that $\sim 10^{28} \text{ erg}$ were released in its $\sim 0.4 \text{ ns}$ duration ($T_b \sim 10^{41} \text{ K}$). By virtue of Eqs. 8.11 and 8.12 this requires $\epsilon_r/f_b < 0.05$, or $f_b > 2 \times 10^{-4}$ for $\epsilon_r \sim 10^{-5}$, in order not to exceed the spindown power being transferred to relativistic

¹⁵ Normalized to the spindown power of the Crab pulsar and an acceleration potential $\varphi \sim 10^{12} \text{ V}$.

particles. Even smaller f_b values may in general be expected of coherent radiation, in principle allowing for brighter rotationally-powered GPs from the Crab pulsar [28].

These ideas become challenging when extended to interpret FRBs as extreme versions of spindown-powered GPs. Indeed, FRBs typically release $> 10^8$ times more energy than the brightest GP, which can’t be ascribed to beaming alone. Moreover, a rotation-powered burst with beaming f_b and duration Δt would have fluence

$$F_\nu = S_\nu \Delta t \approx 8 (\epsilon_r/f_b) L_{\text{EM},40} \Delta t_{-3} (\Delta\nu_9)^{-1} d_{\text{Gpc}}^{-2} \text{ mJyms} \quad (8.13)$$

which, for a typical detection threshold of ~ 1 Jy ms, requires $(\epsilon_r/f_b) L_{\text{EM},40} \Delta t_{-3} \gtrsim 10^2 \Delta\nu_9 d_{\text{Gpc}}^2$. Recall that $\epsilon_r/f_b \sim 10^{-2}$ in the Crab’s brightest GP and $\epsilon_r/f_b \lesssim 10^{-3}$ for its more typical GPs; even allowing for a large $\epsilon_r/f_b = 1$ in FRBs and a small bandwidth $\Delta\nu_9 \approx 0.1$, $L_{\text{EM},40} \gtrsim 10$ would still be required, which only holds for a young NS of age (Eq. 8.1)

$$t \lesssim I_{45} R_6^{-3} \left[5.5 (B_{d,14} d_{\text{Gpc}})^{-1} (\epsilon_r/f_b)^{1/2} - 0.0045 P_{-3}^2 B_{d,14}^{-2} R_6^{-3} \right] \text{ yrs}, \quad (8.14)$$

where the spin period and B-field refer to birth values. The limit in Eq. 8.14 is consistent with the estimated age of FRB 121102, i.e. $\gtrsim 30$ yr, only for $P_{-3} < 8$ and $B_{d,14} < 0.2$. Rotation-powered FRB models may thus be viable only for young, ms-spinning NSs with moderately strong dipole B-fields (cf. [106, 118]) under favourable assumptions on the other parameters in Eq. 8.14.

Due to these difficulties, the magnetic field was considered as an alternative energy source for NS-powered FRBs. Moreover, their characteristic range of energies and timescales, as well as the bursting activity of repeating FRBs, are reminiscent, broadly speaking, of the X/ γ -ray behaviour of classical magnetars (e.g., [50, 80]). This led several authors to propose extragalactic magnetars as possible/likely progenitors of FRBs (e.g. [9, 80, 81, 86, 99, 100, 102, 104, 108, 136, 138]). In this scenario, FRBs are powered by the release of the magnetic energy reservoir of their progenitors, which is $\gg 10^{47}$ erg and thus largely sufficient to power FRB activity for very long times, in analogy with the X/ γ -ray bursts/flare of galactic magnetars. Several mechanisms are proposed for coherent radio emission of $\sim 10^{36}\text{--}10^{40}$ erg on a \sim ms timescale: (a) magnetospheric models envision particle bunches emitting curvature radiation in a very strong B-field close to the NS ([99, 100, 104, 105, 108]); (b) external models point to a synchrotron maser, excited in the interaction of a flare-induced plasma outflow with a surrounding highly magnetised wind, produced by previous flares or by the magnetar spindown, i.e. a magnetar wind nebula [80, 86, 102, 136, 138].

Observationally, rotation-powered and magnetically-powered models have proven difficult to disentangle. So far polarization and rotation measure studies (e.g. [18, 124, 141, 156]), aimed at revealing signatures of highly magnetized

progenitors, have not led to firm conclusions. On the other hand, the lack of energetic radio flares from AXPs/SGRs represented for long a criticality for magnetar-based scenarios. Two very intense radio pulses were reported in association with X-ray bursts from a transient galactic magnetar,¹⁶ but their energy was down by ~ 5 orders of magnitude even with respect to the weakest known FRB (FRB 180916 which released $E_{\text{iso}} \sim 5 \times 10^{36}$ erg; [114]). The situation changed dramatically with the recent discovery of a bright radio flare temporally coincident with an X-ray burst in the classical magnetar SGR 1935+2154 [14, 129, 194]. The event contained two 0.5-ms sub-bursts separated by a quiescent period of ~ 28 ms. Its fluence, constrained by STARE observations to be > 1.5 MJy ms at 3 GHz, implies an isotropic-equivalent energy $\sim 10^{35}$ erg at a distance ~ 9.5 kpc [14], just a factor ~ 40 less than FRB 180916. This crucial discovery demonstrated that: (a) magnetars are capable of producing radio bursts with similar properties to those of extragalactic FRBs; (b) magnetar FRBs can be associated to X-ray bursts, as envisaged in many of the proposed models; (c) the radio bursts are almost exactly simultaneous with the peaks of the X-ray bursts, favoring models in which the emission in the two bands is co-located, either both produced in the NS magnetosphere or in the shock region within the magnetar wind nebula; (d) the FRB-like flare of SGR 1935+2154 could not be powered by the instantaneous spindown luminosity ($\sim 10^{35}$ erg s $^{-1}$) of the NS. A mechanism for the long-term accumulation of rotation power, capable of releasing it on a \sim ms timescale, e.g. via some kind of instability,¹⁷ may still be consistent with the energetics of the event; (e) the radio-to-X-ray fluence ratio $\sim 10^{-5}$ [115, 194] was, at least in this event, within the relatively narrow range predicted by external shock models (e.g. [119]), and in contrast to the expectations from other models (see [22] for a thorough discussion).

The repeater FRB 121102, which has been emitting sporadic bursts since its discovery [150], offers a unique test of the energetic requirements in the magnetar scenario. In [186] 11 bursts were studied, which released a total isotropic-equivalent $\sim 4.5 \times 10^{39}$ erg. With a total on-source time ~ 15.8 h, these imply a long-term average luminosity¹⁸ [99]

$$\langle L_{\text{FRB}} \rangle \approx 8 \times 10^{34} \left(f_{\text{b,tot}} / \epsilon_r \right) \text{ erg s}^{-1}, \quad (8.15)$$

where $f_{\text{b,tot}} = 11 \times \langle f_{\text{b}} \rangle$ is the sum of the beaming factors of the 11 bursts. Multiplying $\langle L_{\text{FRB}} \rangle$ by $\tau_{\text{active}} \gtrsim 30$ yrs gives a minimal energy $E_{\min} \sim 8 \langle f_{\text{b}} \rangle / \epsilon_r \times 10^{44}$ ergs, which translates to a minimal B-field $B_{\min} = (6 E_{\min} / R_*^3)^{1/2} \approx 6 \times 10^{13} (f_{\text{b}} / \epsilon_r)^{1/2}$ G. Thus, if FRB 121102 hosts a magnetar, values of $f_{\text{b}} / \epsilon_r \gtrsim 10^4 - 10^5$ would imply a magnetic energy $\sim 10^{49} - 10^{50} (\tau_{\text{active}} / 30 \text{ yr})$ erg, or a minimum $B_{\text{int}} \sim (0.6 - 2) \times 10^{16} (\tau_{\text{active}} / 30 \text{ yr})^{1/2}$ G. As discussed above, $f_{\text{b}} / \epsilon_r \sim 10^2 - 10^3$ is

¹⁶ Israel et al. [77].

¹⁷ NS glitches represent an example of this kind of processes.

¹⁸ The same result is obtained using VLA or Green Bank data ([99]).

estimated in radio pulsar GPs. In the magnetar SGR 1935+2154, on the other hand, the measured radio-to-X-ray fluence suggests $f_b/\epsilon_r \sim 10^4\text{--}10^5$ if the X-rays were not beamed, or only mildly beamed.

An independent test of the magnetar scenario is based only on the persistent radio counterpart of FRB 121102. With a luminosity $vL_v \sim 10^{39}$ erg s⁻¹ and flat spectrum up to ~ 10 GHz, beyond which a turnover appears, the source is straightforwardly interpreted as a synchrotron nebula, with size $R < 0.7$ pc and $\tau_{\text{age}} \sim 30\text{--}100$ yrs [136]. Its radio luminosity is consistent with the spindown power of a young, moderately magnetized and ms-spinning NS (Eq. 8.14). However, its spectral properties—in particular the peak at ~ 10 GHz—can only be explained with a number of emitting particles $N \gtrsim 10^{52} (t_{\text{age}}/30 \text{ yr})^{2/3}$, too large to be provided by the typical mechanism of pulsar wind nebulae¹⁹ (PWN) with the current spindown power [80]. $N \gtrsim 10^{52}$ may instead be provided in two possible ways:

- (i) in the early stages of the nebula lifetime, when R was much smaller and its large compactness $\ell = L_{\text{EM}}\sigma_T/(Rm_ec^3)$ allowed a much more efficient pair-production than typical of PWNs ([80, 136]). Following [80] two possible solutions can be found which would provide $\sim 10^{52}$ particles to the nebula well before its current age. One is a moderately magnetized NS, with $B_d \gtrsim 10^{13}$ G and birth spin $P \gtrsim 6$ ms, the other a $B_d \gtrsim 10^{15}$ G NS with any $P \sim (1\text{--}40)$ ms.
- (ii) during the whole $\gtrsim 30$ yrs lifetime of the remnant, if the central engine has continuously released magnetic energy through flares at its current rate (assuming $f_b/\epsilon_r > 10^4$), and if each flare released radiation (in erg) and particles (electrons) with a similar ratio $N_{\text{part}}/E_{\text{rad}} \gtrsim 10^2 \text{ erg}^{-1}$ to that estimated in the Giant Flare from the classical magnetar SGR 1806-20 [80].

In either case the constraints from the persistent radio source agree with those obtained from the FRBs indicating that a highly magnetized NS is a likely central engine in FRB 121102, and further suggesting it was spinning at \sim millisecond period at birth.

¹⁹ The spectral peak at $v \sim 10$ GHz and the luminosity $L_v \sim 10^{29}$ erg s⁻¹ Hz⁻¹ below the peak lead to the conclusion that the energy of the emitting particles peaks at $\gamma_e \sim 10^2/B^{1/2}$, where B (in gauss) is the magnetic field strength in the emitting region, and that $NB \sim 2 \times 10^{50}$ G ([80]). Moreover, the constraint that the particle cooling break $v_c = 10em_ec/(\sigma_T^2 B^3 t^2)$ be > 10 GHz implies $B < 0.03 (t_{\text{age}}/30 \text{ yr})^{-2/3} (v_c,9/10)^{-1/3}$ G, from which $N > 7 \times 10^{51} t_9^{2/3} (v_c,9/10)^{1/3}$ is derived. Particles are accelerated at the NS surface to relativistic energies, giving rise to an electrical current $i = \mu\Omega^2/c$ and leading to copious pair-production in the magnetosphere. Pairs are produced at the rate $\dot{N}^\pm \sim 2Mi/e$, where the multiplicity M is the number of e^\pm pairs per accelerated particle, and typically $M \lesssim 10^3$ in PWNe. Because $L_{\text{EM}} \sim i^2/c$, the NS in FRB121102 should produce pairs with a multiplicity $M \sim 10^7\text{--}10^{10}$ in order to inject 10^{52} particles, given the spindown luminosity $\sim 10^{39}$ erg s⁻¹. This is several orders of magnitude larger than typical in PWNe, pointing to a different mechanism or to very different conditions existing in this source.

8.6 Conclusions

Our knowledge of GRBs and SNe, including SLSNe, has advanced a great deal in the last two decades; the pace of discovery in GW and FRB studies has been very fast in recent years. In all these areas, models involving millisecond spinning magnetars appear to be promising for interpreting paroxysmal phenomena that characterise these sources. Direct evidence for the presence of such extremely powerful central engines is still lacking.

An unambiguous signature of newborn magnetars would be the detection of fast, rapidly-evolving periodic signals arising from the star rotation. Searches in the electromagnetic channels face serious difficulties. It is hard to image ways in which a newborn magnetar's signal could emerge out of the huge matter depth of an expanding SN envelope, or out of the relativistic shocks (or even an \sim h-old magnetar wind nebula) of a GRB. Recurrent FRBs from repeaters, should they occur at fixed rotational phases, may allow detection of the underlying magnetar periodic signal in a manner similar to that of Rotating Radio Transients (RRATs) [221]. As GW signals are intrinsically locked to the star rotation and travel unimpeded they provide better prospects for revealing the characteristic signal of newborn, fast spinning magnetars. The detectability of their hours-long, time-reversed chirps is presently limited to an horizon of \sim 3 Mpc by a combination of detector sensitivity and computing power.

Research in these frontier areas will likely be thriving even faster in the years to come, both through observations and theoretical studies; a wealth of new results and, possibly, some surprises are to be expected.

Acknowledgments We wish to thank G. Ghisellini, B. Margalit, B. Metzger and A. Papitto for careful reading of the manuscript and helpful comments and suggestions. LS acknowledges financial contributions from ASI-INAF agreements 2017-14-H.O and I/037/12/0 and from “iPeska” research grant (P.I. Andrea Possenti) funded under the INAF call PRIN-SKA/CTA (resolution 70/2016).

References

1. Abbott, B.P., Abbott, R., Abbott, T.D., et al., LIGO Scientific Collaboration, Virgo Collaboration: search for gravitational waves from a long-lived remnant of the binary neutron star merger GW170817. *ApJ* **875**(2), 160 (2019). <https://doi.org/10.3847/1538-4357/ab0f3d>
2. Abbott, B.P., Abbott, R., Abbott, T.D., et al., LIGO Scientific Collaboration, Virgo Collaboration: GWTC-1: a gravitational-wave transient catalog of compact binary mergers observed by LIGO and Virgo during the first and second observing runs. *Phys. Rev. X* **9**(3), 031040 (2019). <https://doi.org/10.1103/PhysRevX.9.031040>
3. Ajello, M., Arimoto, M., Axelsson, M., et al.: A decade of gamma-ray bursts observed by Fermi-LAT: the second GRB catalog. *ApJ* **878**(1), 52 (2019). <https://doi.org/10.3847/1538-4357/ab1d4e>

4. Akgün, T., Reisenegger, A., Mastrano, A., Marchant, P.: Stability of magnetic fields in non-barotropic stars: an analytic treatment. *MNRAS* **433**(3), 2445–2466 (2013). <https://doi.org/10.1093/mnras/stz913>
5. Andersson, N., Baker, J., Belczynski, K., et al.: The transient gravitational-wave sky. *Classical Quantum Gravity* **30**(19), 193002 (2013). <https://doi.org/10.1088/0264-9381/30/19/193002>
6. Ascenzi, S., Oganesyan, G., Salafia, O.S., et al.: High latitude emission from structured jet of Gamma-Ray Bursts observed off-axis (2020). arXiv e-prints arXiv:2004.12215
7. Baiotti, L., Rezzolla, L.: Binary neutron star mergers: a review of Einstein’s richest laboratory. *Rep. Progr. Phys.* **80**(9), 096901 (2017). <https://doi.org/10.1088/1361-6633/aa67bb>
8. Beloborodov, A.M.: Collisional mechanism for gamma-ray burst emission. *MNRAS* **407**(2), 1033–1047 (2010). <https://doi.org/10.1111/j.1365-2966.2010.16770.x>
9. Beloborodov, A.M.: Blast waves from magnetar flares and fast radio bursts. *ApJ* **896**(2), 142 (2020). <https://doi.org/10.3847/1538-4357/ab83eb>
10. Beniamini, P., Hotokezaka, K., van der Horst, A., Kouveliotou, C.: Formation rates and evolution histories of magnetars. *MNRAS* **487**(1), 1426–1438 (2019). <https://doi.org/10.1093/mnras/stz1391>
11. Bernardini, M.G., Margutti, R., Zaninoni, E., Chincarini, G.: A universal scaling for short and long gamma-ray bursts: $E_{X,iso} - E_{\gamma,iso} - E_{pk}$. *MNRAS* **425**(2), 1199–1204 (2012). <https://doi.org/10.1111/j.1365-2966.2012.21487.x>
12. Bibby, J.L., Crowther, P.A., Furness, J.P., Clark, J.S.: A downward revision to the distance of the 1806-20 cluster and associated magnetar from Gemini Near-Infrared Spectroscopy. *MNRAS* **386**(1), L23–L27 (2008). <https://doi.org/10.1111/j.1745-3933.2008.00453.x>
13. Blandford, R.D., Znajek, R.L.: Electromagnetic extraction of energy from Kerr black holes. *MNRAS* **179**, 433–456 (1977). <https://doi.org/10.1093/mnras/179.3.433>
14. Bochenek, C.D., Ravi, V., Belov, K.V., et al.: A fast radio burst associated with a Galactic magnetar (2020). arXiv e-prints arXiv:2005.10828
15. Braithwaite, J.: A differential rotation driven dynamo in a stably stratified star. *A&A* **449**(2), 451–460 (2006). <https://doi.org/10.1051/0004-6361:20054241>
16. Braithwaite, J.: Axisymmetric magnetic fields in stars: relative strengths of poloidal and toroidal components. *MNRAS* **397**(2), 763–774 (2009). <https://doi.org/10.1111/j.1365-2966.2008.14034.x>
17. Bucciantini, N., Quataert, E., Metzger, B.D., et al.: Magnetized relativistic jets and long-duration GRBs from magnetar spin-down during core-collapse supernovae. *MNRAS* **396**(4), 2038–2050 (2009). <https://doi.org/10.1111/j.1365-2966.2009.14940.x>
18. Caleb, M., Keane, E.F., van Straten, W., et al.: The survey for pulsars and extragalactic radio bursts—III. Polarization properties of FRBs 160102 and 151230. *MNRAS* **478**(2), 2046–2055 (2018). <https://doi.org/10.1093/mnras/sty1137>
19. Chandrasekhar, S.: Ellipsoidal figures of equilibrium (1969)
20. Chandrasekhar, S.: The effect of gravitational radiation on the secular stability of the maclaurin spheroid. *ApJ* **161**, 561 (1970). <https://doi.org/10.1086/150560>
21. Chatterjee, S., Law, C.J., Wharton, R.S., et al.: A direct localization of a fast radio burst and its host. *Nature* **541**(7635), 58–61 (2017). <https://doi.org/10.1038/nature20797>
22. Chen, G., Ravi, V., Lu, W.: The multiwavelength counterparts of fast radio bursts. *ApJ* **897**(2), 146 (2020). <https://doi.org/10.3847/1538-4357/ab982b>
23. Chen, K.J., Woosley, S.E., Whalen, D.J.: Three-dimensional Simulations of Magnetar-powered Superluminous Supernovae. *ApJ* **893**(2), 99 (2020). <https://doi.org/10.3847/1538-4357/ab7db0>
24. Chime/Frb Collaboration, Amiri, M., Andersen, B.C., Bandura, K.M., et al.: Periodic activity from a fast radio burst source. *Nature* **582**(7812), 351–355 (2020). <https://doi.org/10.1038/s41586-020-2398-2>

25. CHIME/FRB Collaboration, Andersen, B.C., Bandura, K., Bhardwaj, M., et al.: CHIME/FRB discovery of eight new repeating fast radio burst sources. *ApJ* **885**(1), L24 (2019). <https://doi.org/10.3847/2041-8213/ab4a80>
26. Ciolfi, R., Rezzolla, L.: Twisted-torus configurations with large toroidal magnetic fields in relativistic stars. *MNRAS* **435**, L43–L47 (2013). <https://doi.org/10.1093/mnrasl/slt092>
27. Cordes, J.M., Chatterjee, S.: Fast radio bursts: an extragalactic enigma. *ARA&A* **57**, 417–465 (2019). <https://doi.org/10.1146/annurev-astro-091918-104501>
28. Cordes, J.M., Wasserman, I.: Supergiant pulses from extragalactic neutron stars. *MNRAS* **457**(1), 232–257 (2016). <https://doi.org/10.1093/mnras/stv2948>
29. Corsi, A., Mészáros, P.: Gamma-ray burst afterglow plateaus and gravitational waves: multi-messenger signature of a millisecond magnetar? *ApJ* **702**(2), 1171–1178 (2009). <https://doi.org/10.1088/0004-637X/702/2/1171>
30. Crowther, P.A.: Physical properties of wolf-rayet stars. *ARA&A* **45**(1), 177–219 (2007). <https://doi.org/10.1146/annurev.astro.45.051806.110615>
31. Cutler, C.: Gravitational waves from neutron stars with large toroidal B fields. *Phys. Rev. D* **66**(8), 084025 (2002). <https://doi.org/10.1103/PhysRevD.66.084025>
32. Dai, Z.G., Lu, T.: Gamma-ray burst afterglows and evolution of postburst fireballs with energy injection from strongly magnetic millisecond pulsars. *A&A* **333**, L87–L90 (1998)
33. Daigne, F., Mochkovitch, R.: Gamma-ray bursts from internal shocks in a relativistic wind: temporal and spectral properties. *MNRAS* **296**(2), 275–286 (1998). <https://doi.org/10.1046/j.1365-8711.1998.01305.x>
34. Dainotti, M.G., Cardone, V.F., & Capozziello, S.: A time-luminosity correlation for γ -ray bursts in the X-rays. *MNRAS* **391**, L79 (2008). <https://doi.org/10.1111/j.1745-3933.2008.00560.x>
35. Dainotti, M.G., Willingale, R., Capozziello, S., et al.: Discovery of a tight correlation for gamma-ray burst afterglows with “canonical” light curves. *ApJ* **722**, L215 (2010). <https://doi.org/10.1088/2041-8205/722/2/L215>
36. Dainotti, M.G., Ostrowski, M., & Willingale, R.: Towards a standard gamma-ray burst: tight correlations between the prompt and the afterglow plateau phase emission. *MNRAS* **418**, 2202 (2011). <https://doi.org/10.1111/j.1365-2966.2011.19433.x>
37. Dainotti, M.G., Petrosian, V., Singal, J., Ostrowski, M.: Determination of the intrinsic luminosity time correlation in the X-ray afterglows of gamma-ray bursts. *ApJ* **774**(2), 157 (2013). <https://doi.org/10.1088/0004-637X/774/2/157>
38. Dall’Osso, S., Giacomazzo, B., Perna, R., Stella, L.: Gravitational waves from massive magnetars formed in binary neutron star mergers. *ApJ* **798**(1), 25 (2015). <https://doi.org/10.1088/0004-637X/798/1/25>
39. Dall’Osso, S., Granot, J., Piran, T.: Magnetic field decay in neutron stars: from soft gamma repeaters to ‘weak-field magnetars’. *MNRAS* **422**(4), 2878–2903 (2012). <https://doi.org/10.1111/j.1365-2966.2012.20612.x>
40. Dall’Osso, S., Shore, S.N., Stella, L.: Early evolution of newly born magnetars with a strong toroidal field. *MNRAS* **398**(4), 1869–1885 (2009). <https://doi.org/10.1111/j.1365-2966.2008.14054.x>
41. Dall’Osso, S., Stella, L.: Newborn magnetars as sources of gravitational radiation: constraints from high energy observations of magnetar candidates. *ApSS* **308**(1–4), 119–124 (2007). <https://doi.org/10.1007/s10509-007-9323-0>
42. Dall’Osso, S., Stella, L., Palomba, C.: Neutron star bulk viscosity, ‘spin-flip’ and GW emission of newly born magnetars. *MNRAS* **480**(1), 1353–1362 (2018). <https://doi.org/10.1093/mnras/sty1706>
43. Dall’Osso, S., Stratta, G., Guetta, D., et al.: Gamma-ray bursts afterglows with energy injection from a spinning down neutron star. *A&A* **526**, A121 (2011). <https://doi.org/10.1051/0004-6361/201014168>
44. Davies, B., Figer, D.F., Kudritzki, R.P., et al.: The Progenitor Mass of the Magnetar SGR1900+14. *ApJ* **707**(1), 844–851 (2009). <https://doi.org/10.1088/0004-637X/707/1/844>

45. Dessart, L., Hillier, D.J., Waldman, R., et al.: Superluminous supernovae: ^{56}Ni power versus magnetar radiation. *MNRAS* **426**(1), L76–L80 (2012). <https://doi.org/10.1111/j.1745-3933.2012.01329.x>
46. Dimmelmeier, H., Ott, C.D., Marek, A., Janka, H.T.: Gravitational wave burst signal from core collapse of rotating stars. *Phys. Rev. D* **78**(6), 064056 (2008). <https://doi.org/10.1103/PhysRevD.78.064056>
47. Drenkhahn, G., Spruit, H.C.: Efficient acceleration and radiation in Poynting flux powered GRB outflows. *A&A* **391**, 1141–1153 (2002). <https://doi.org/10.1051/0004-6361:20020839>
48. Duncan, R.C., Thompson, C.: Formation of Very Strongly Magnetized Neutron Stars: Implications for Gamma-Ray Bursts. *ApJ* **392**, L9 (1992). <https://doi.org/10.1086/186413>
49. Esposito, P., Rea, N., Borges, A., et al.: A very young radio-loud magnetar. *ApJ* **896**(2), L30 (2020). <https://doi.org/10.3847/2041-8213/ab9742>
50. Esposito, P., Rea, N., Israel, G.L.: Magnetars: a short review and some sparse considerations (2018). arXiv e-prints arXiv:1803.05716
51. Fan, Y., Piran, T.: Gamma-ray burst efficiency and possible physical processes shaping the early afterglow. *MNRAS* **369**(1), 197–206 (2006). <https://doi.org/10.1111/j.1365-2966.2006.10280.x>
52. Ferrario, L., Melatos, A., Zrake, J.: Magnetic field generation in stars. *Space Sci. Rev.* **191**(1–4), 77–109 (2015). <https://doi.org/10.1007/s11214-015-0138-y>
53. Fonseca, E., Andersen, B.C., Bhardwaj, M., et al.: Nine new repeating fast radio burst sources from CHIME/FRB. *ApJ* **891**(1), L6 (2020). <https://doi.org/10.3847/2041-8213/ab7208>
54. Friedman, J.L., Schutz, B.F.: Secular instability of rotating Newtonian stars. *ApJ* **222**, 281–296 (1978). <https://doi.org/10.1086/156143>
55. Fruchter, A.S., Levan, A.J., Strolger, L., et al.: Long γ -ray bursts and core-collapse supernovae have different environments. *Nature* **441**(7092), 463–468 (2006). <https://doi.org/10.1038/nature04787>
56. Gal-Yam, A.: The most luminous supernovae. *ARA&A* **57**, 305–333 (2019). <https://doi.org/10.1146/annurev-astro-081817-051819>
57. Galama, T.J., Vreeswijk, P.M., van Paradijs, J., et al.: An unusual supernova in the error box of the γ -ray burst of 25 April 1998. *Nature* **395**(6703), 670–672 (1998). <https://doi.org/10.1038/27150>
58. Gavriil, F.P., Kaspi, V.M., Woods, P.M.: Magnetar-like X-ray bursts from an anomalous X-ray pulsar. *Nature* **419**(6903), 142–144 (2002). <https://doi.org/10.1038/nature01011>
59. Ghirlanda, G., Ghisellini, G., Celotti, A.: The spectra of short gamma-ray bursts. *A&A* **422**, L55–L58 (2004). <https://doi.org/10.1051/0004-6361:20048008>
60. Ghirlanda, G., Nava, L., Ghisellini, G., et al.: Short versus long gamma-ray bursts: spectra, energetics, and luminosities. *A&A* **496**(3), 585–595 (2009). <https://doi.org/10.1051/0004-6361/200811209>
61. Ghirlanda, G., Salafia, O.S., Paragi, Z., et al.: Compact radio emission indicates a structured jet was produced by a binary neutron star merger. *Science* **363**(6430), 968–971 (2019). <https://doi.org/10.1126/science.aau8815>
62. Ghirlanda, G., Salafia, O.S., Pescalli, A., et al.: Short gamma-ray bursts at the dawn of the gravitational wave era. *A&A* **594**, A84 (2016). <https://doi.org/10.1051/0004-6361/201628993>
63. Giacomazzo, B., Perna, R.: Formation of stable magnetars from binary neutron star mergers. *ApJ* **771**(2), L26 (2013). <https://doi.org/10.1088/2041-8205/771/2/L26>
64. Glampedakis, K., Lasky, P.D.: The freedom to choose neutron star magnetic field equilibria: Table 1. *MNRAS* **463**(3), 2542–2552 (2016). <https://doi.org/10.1093/mnras/stw2115>
65. Goldreich, P., Julian, W.H.: Pulsar electrodynamics. *ApJ* **157**, 869 (1969). <https://doi.org/10.1086/150119>
66. Gompertz, B.P., van der Horst, A.J., O'Brien, P.T., et al.: Broad-band modelling of short gamma-ray bursts with energy injection from magnetar spin-down and its implications for radio detectability. *MNRAS* **448**(1), 629–641 (2015). <https://doi.org/10.1093/mnras/stu2752>
67. Goodman, J.: Are gamma-ray bursts optically thick? *ApJ* **308**, L47 (1986). <https://doi.org/10.1086/184741>

68. Gourdji, K., Rowlinson, A., Wijers, R.A.M.J., Goldstein, A.: Constraining a neutron star merger origin for localized fast radio bursts. *MNRAS* **497**(3), 3131–3141 (2020). <https://doi.org/10.1093/mnras/staa2128>
69. Guiriec, S., Daigne, F., Hascoët, R., et al.: Evidence for a photospheric component in the prompt emission of the short GRB 120323A and its effects on the GRB hardness-luminosity relation. *ApJ* **770**(1), 32 (2013). <https://doi.org/10.1088/0004-637X/770/1/32>
70. Haskell, B., Samuelsson, L., Glampedakis, K., Andersson, N.: Modelling magnetically deformed neutron stars. *MNRAS* **385**(1), 531–542 (2008). <https://doi.org/10.1111/j.1365-2966.2008.12861.x>
71. Hessels, J.W.T.: Fast radio bursts and their possible neutron star origins (2018). arXiv e-prints arXiv:1804.06149
72. Hinderer, T., Rezzolla, L., Baiotti, L.: Gravitational waves from merging binary neutron-star systems. *Astrophys. Space Sci. Lib.* **457**, 575 (2018). <https://doi.org/10.1007/978-3-319-97616-7-10>
73. Hjorth, J., Sollerman, J., Møller, P., et al.: A very energetic supernova associated with the γ -ray burst of 29 March 2003. *Nature* **423**(6942), 847–850 (2003). <https://doi.org/10.1038/nature01750>
74. Inserra, C.: Observational properties of extreme supernovae. *Nat. Astron.* **3**, 697–705 (2019). <https://doi.org/10.1038/s41550-019-0854-4>
75. Inserra, C., Smartt, S.J., Jerkstrand, A., et al.: Super-luminous type Ic supernovae: catching a magnetar by the tail. *ApJ* **770**(2), 128 (2013). <https://doi.org/10.1088/0004-637X/770/2/128>
76. Jones, P.B.: The secular variation of pulsar magnetic dipole moments. *ApSS* **45**(2), 369–381 (1976). <https://doi.org/10.1007/BF00642671>
77. Israel, G.L., Burgay, M., Rea, N., Esposito, P., Possenti, A., Dall’Osso, S., Stella, L., Pilia, M., Tiengo, A., Ridnaia, A., Lien A.Y., Frederiks, D.D., Bernardini, F.: X-ray and radio bursts from the magnetar 1E 1547.0-5408. *ApJ* **907**(1), id.7 (2021). <https://doi.org/10.3847/1538-4357/abca95>
78. Kasen, D., Bildsten, L.: Supernova light curves powered by Young magnetars. *ApJ* **717**(1), 245–249 (2010). <https://doi.org/10.1088/0004-637X/717/1/245>
79. Kasen, D., Metzger, B.D., Bildsten, L.: Magnetar-driven shock breakout and double-peaked supernova light curves. *ApJ* **821**(1), 36 (2016). <https://doi.org/10.3847/0004-637X/821/1/36>
80. Kaspi, V.M., Beloborodov, A.M.: Magnetars. *ARA&A* **55**(1), 261–301 (2017). <https://doi.org/10.1146/annurev-astro-081915-023329>
81. Katz, J.I.: How soft gamma repeaters might make fast radio bursts. *ApJ* **826**(2), 226 (2016). <https://doi.org/10.3847/0004-637X/826/2/226>
82. Katz, J.I.: Fast radio bursts. *Prog. Part. Nucl. Phys.* **103**, 1–18 (2018). <https://doi.org/10.1016/j.ppnp.2018.07.001>
83. Kouveliotou, C., Dieters, S., Strohmayer, T., et al.: An X-ray pulsar with a superstrong magnetic field in the soft γ -ray repeater SGR1806-20. *Nature* **393**(6682), 235–237 (1998). <https://doi.org/10.1038/30410>
84. Kouveliotou, C., Meegan, C.A., Fishman, G.J., et al.: Identification of two classes of gamma-ray bursts. *ApJ* **413**, L101 (1993). <https://doi.org/10.1086/186969>
85. Kouveliotou, C., Norris, J.P., Cline, T.L., et al.: SMM hard X-ray observations of the soft gamma-ray repeater 1806-20. *ApJ* **322**, L21 (1987). <https://doi.org/10.1086/185029>
86. Kulkarni, S.R., Ofek, E.O., Neill, J.D.: The arecibo fast radio burst: dense circum-burst medium (2015). arXiv e-prints arXiv:1511.09137
87. Kumar, P., Narayan, R., Johnson, J.L.: Properties of gamma-ray burst progenitor stars. *Science* **321**(5887), 376 (2008). <https://doi.org/10.1126/science.1159003>
88. Kumar, P., Zhang, B.: The physics of gamma-ray bursts and relativistic jets. *PhR* **561**, 1–109 (2015). <https://doi.org/10.1016/j.physrep.2014.09.008>
89. Lai, D., Shapiro, S.L.: Gravitational radiation from rapidly rotating nascent neutron stars. *ApJ* **442**, 259 (1995). <https://doi.org/10.1086/175438>
90. Lander, S.K., Jones, D.I.: Non-rigid precession of magnetic stars. *MNRAS* **467**(4), 4343–4382 (2017). <https://doi.org/10.1093/mnras/stx349>

91. Lander, S.K., Jones, D.I.: Magnetar birth: rotation rates and gravitational-wave emission. *MNRAS* **494**(4), 4838–4847 (2020). <https://doi.org/10.1093/mnras/staa966>
92. Levin, Y., Beloborodov, A.M., Bransgrove, A.: Precessing flaring magnetar as a source of repeating FRB 180916.J0158+65. *ApJ* **895**(2), L30 (2020). <https://doi.org/10.3847/2041-8213/ab8c4c>
93. Li, L., Wu, X.F., Lei, W.H., et al.: Constraining the type of central engine of GRBs with swift data. *ApJS* **236**(2), 26 (2018). <https://doi.org/10.3847/1538-4365/aabaf3>
94. Li, W., Chornock, R., Leaman, J., et al.: Nearby supernova rates from the Lick Observatory Supernova Search—III. The rate-size relation, and the rates as a function of galaxy Hubble type and colour. *MNRAS* **412**(3), 1473–1507 (2011). <https://doi.org/10.1111/j.1365-2966.2011.18162.x>
95. Liang, E.W., Zhang, B.B., Zhang, B.: A comprehensive analysis of swift XRT data. II. Diverse physical origins of the shallow decay segment. *ApJ* **670**(1), 565–583 (2007). <https://doi.org/10.1086/521870>
96. LIGO Scientific Collaboration, Virgo Collaboration, *Fermi* gamma-ray burst monitor, INTEGRAL: gravitational waves and gamma-rays from a binary neutron star merger: GW170817 and GRB 170817A. *ApJ* **848**(2), L13 (2017). <https://doi.org/10.3847/2041-8213/aa920c>
97. Lorimer, D.R., Bailes, M., McLaughlin, M.A., et al.: A bright millisecond radio burst of extragalactic origin. *Science* **318**(5851), 777 (2007). <https://doi.org/10.1126/science.1147532>
98. Lu, W., Kumar, P.: A universal EDF for repeating fast radio bursts? *MNRAS* **461**(1), L122–L126 (2016). <https://doi.org/10.1093/mnrasl/slw113>
99. Lu, W., Kumar, P.: On the radiation mechanism of repeating fast radio bursts. *MNRAS* **477**(2), 2470–2493 (2018). <https://doi.org/10.1093/mnras/sty716>
100. Lu, W., Kumar, P., Narayan, R.: Fast radio burst source properties from polarization measurements. *MNRAS* **483**(1), 359–369 (2019). <https://doi.org/10.1093/mnras/sty2829>
101. Lyons, N., O'Brien, P.T., Zhang, B., et al.: Can X-ray emission powered by a spinning-down magnetar explain some gamma-ray burst light-curve features? *MNRAS* **402**(2), 705–712 (2010). <https://doi.org/10.1111/j.1365-2966.2009.15538.x>
102. Lyubarsky, Y.: A model for fast extragalactic radio bursts. *MNRAS* **442**, L9–L13 (2014). <https://doi.org/10.1093/mnrasl/slu046>
103. Lyutikov, M.: Explosive reconnection in magnetars. *MNRAS* **346**(2), 540–554 (2003). <https://doi.org/10.1046/j.1365-2966.2003.07110.x>
104. Lyutikov, M.: Free electron laser in magnetars/fast radio bursts (2020). arXiv e-prints arXiv:2006.16029
105. Lyutikov, M.: Radius-to-frequency mapping and FRB frequency drifts. *ApJ* **889**(2), 135 (2020). <https://doi.org/10.3847/1538-4357/ab55de>
106. Lyutikov, M., Burzawa, L., Popov, S.B.: Fast radio bursts as giant pulses from young rapidly rotating pulsars. *MNRAS* **462**(1), 941–950 (2016). <https://doi.org/10.1093/mnras/stw1669>
107. Lyutikov, M., Pariev, V.I., Blandford, R.D.: Polarization of prompt gamma-ray burst emission: evidence for electromagnetically dominated outflow. *ApJ* **597**(2), 998–1009 (2003). <https://doi.org/10.1086/378497>
108. Lyutikov, M., Popov, S.: Fast Radio Bursts from reconnection events in magnetar magnetospheres (2020). arXiv e-prints arXiv:2005.05093
109. MacDonald, D., Thorne, K.S.: Black-hole electrodynamics—an absolute-space/universal-time formulation. *MNRAS* **198**, 345–382 (1982). <https://doi.org/10.1093/mnras/198.2.345>
110. MacFadyen, A.I., Woosley, S.E.: Collapsars: gamma-ray bursts and explosions in “failed supernovae”. *ApJ* **524**(1), 262–289 (1999). <https://doi.org/10.1086/307790>
111. Madau, P., Dickinson, M.: Cosmic star-formation history. *ARA&A* **52**, 415–486 (2014). <https://doi.org/10.1146/annurev-astro-081811-125615>
112. Maeda, K., Tanaka, M., Nomoto, K., et al.: The unique type Ib supernova 2005bf at nebular phases: a possible birth event of a strongly magnetized neutron star. *ApJ* **666**(2), 1069–1082 (2007). <https://doi.org/10.1086/520054>

113. Makishima, K., Enoto, T., Hiraga, J.S., et al.: Possible evidence for free precession of a strongly magnetized neutron star in the magnetar 4U 0142+61. *Phys. Rev. Lett.* **112**(17), 171102 (2014). <https://doi.org/10.1103/PhysRevLett.112.171102>
114. Marcote, B., Nimmo, K., Hessels, J.W.T., et al.: A repeating fast radio burst source localized to a nearby spiral galaxy. *Nature* **577**(7789), 190–194 (2020). <https://doi.org/10.1038/s41586-019-1866-z>
115. Margalit, B., Beniamini, P., Sridhar, N., Metzger, B.D.: Implications of a “fast radio burst” from a Galactic magnetar (2020). arXiv e-prints arXiv:2005.05283
116. Margalit, B., Metzger, B.D.: Constraining the maximum mass of neutron stars from multi-messenger observations of GW170817. *ApJ* **850**(2), L19 (2017). <https://doi.org/10.3847/2041-8213/aa991c>
117. Margalit, B., Metzger, B.D.: A concordance picture of FRB 121102 as a flaring magnetar embedded in a magnetized ion-electron wind nebula. *ApJ* **868**(1), L4 (2018). <https://doi.org/10.3847/2041-8213/aaedad>
118. Margalit, B., Metzger, B.D., Berger, E., et al.: Unveiling the engines of fast radio bursts, superluminous supernovae, and gamma-ray bursts. *MNRAS* **481**(2), 2407–2426 (2018). <https://doi.org/10.1093/mnras/sty2417>
119. Margalit, B., Metzger, B.D., Sironi, L.: Constraints on the engines of fast radio bursts. *MNRAS* **494**(4), 4627–4644 (2020). <https://doi.org/10.1093/mnras/staa1036>
120. Margutti, R., Alexander, K.D., Xie, X., et al.: The binary neutron star event LIGO/Virgo GW170817 160 days after merger: synchrotron emission across the electromagnetic spectrum. *ApJ* **856**(1), L18 (2018). <https://doi.org/10.3847/2041-8213/aab2ad>
121. Martin, J., Rea, N., Torres, D.F., Papitto, A.: Comparing supernova remnants around strongly magnetized and canonical pulsars. *MNRAS* **444**(3), 2910–2924 (2014). <https://doi.org/10.1093/mnras/stu1594>
122. Mastrano, A., Lasky, P.D., Melatos, A.: Neutron star deformation due to multipolar magnetic fields. *MNRAS* **434**(2), 1658–1667 (2013). <https://doi.org/10.1093/mnras/stt1131>
123. Mastrano, A., Melatos, A., Reisenegger, A., Akgün, T.: Gravitational wave emission from a magnetically deformed non-barotropic neutron star. *MNRAS* **417**(3), 2288–2299 (2011). <https://doi.org/10.1111/j.1365-2966.2011.19410.x>
124. Masui, K., Lin, H.H., Sievers, J., et al.: Dense magnetized plasma associated with a fast radio burst. *Nature* **528**(7583), 523–525 (2015). <https://doi.org/10.1038/nature15769>
125. Matzner, C.D.: Supernova hosts for gamma-ray burst jets: dynamical constraints. *MNRAS* **345**(2), 575–589 (2003). <https://doi.org/10.1046/j.1365-8711.2003.06969.x>
126. Mazets, E.P., Golentskii, S.V., Ilinskii, V.N., et al.: Observations of a flaring X-ray pulsar in Dorado. *Nature* **282**(5739), 587–589 (1979). <https://doi.org/10.1038/282587a0>
127. Mereghetti, S.: The strongest cosmic magnets: soft gamma-ray repeaters and anomalous X-ray pulsars. *A&AR* **15**(4), 225–287 (2008). <https://doi.org/10.1007/s00159-008-0011-z>
128. Mereghetti, S., Pons, J.A., Melatos, A.: Magnetars: properties, origin and evolution. *Space Sci. Rev.* **191**(1–4), 315–338 (2015). <https://doi.org/10.1007/s11214-015-0146-y>
129. Mereghetti, S., Savchenko, V., Ferrigno, C., et al.: INTEGRAL discovery of a burst with associated radio emission from the magnetar SGR 1935+2154 (2020). arXiv e-prints arXiv:2005.06335
130. Mereghetti, S., Stella, L.: The very low mass x-ray binary pulsars: a new class of sources? *ApJ* **442**, L17 (1995). <https://doi.org/10.1086/187805>
131. Mestel, L., Takhar, H.S.: The internal dynamics of the oblique rotator. *MNRAS* **156**, 419 (1972). <https://doi.org/10.1093/mnras/156.4.419>
132. Meszaros, P., Rees, M.J.: Relativistic fireballs and their impact on external matter: models for cosmological gamma-ray bursts. *ApJ* **405**, 278 (1993). <https://doi.org/10.1086/172360>
133. Mészáros, P., Rees, M.J.: Optical and long-wavelength afterglow from gamma-ray bursts. *ApJ* **476**(1), 232–237 (1997). <https://doi.org/10.1086/303625>
134. Mészáros, P., Rees, M.J.: Collapsar jets, bubbles, and Fe lines. *ApJ* **556**(1), L37–L40 (2001). <https://doi.org/10.1086/322934>

135. Metzger, B.D., Beniamini, P., Giannios, D.: Effects of Fallback Accretion on Protomagnetar Outflows in Gamma-Ray Bursts and Superluminous Supernovae. *ApJ* **857**(2), 95 (2018). <https://doi.org/10.3847/1538-4357/aab70c>
136. Metzger, B.D., Berger, E., Margalit, B.: Millisecond magnetar birth connects FRB 121102 to superluminous supernovae and long-duration gamma-ray bursts. *ApJ* **841**(1), 14 (2017). <https://doi.org/10.3847/1538-4357/aa633d>
137. Metzger, B.D., Giannios, D., Thompson, T.A., et al.: The protomagnetar model for gamma-ray bursts. *MNRAS* **413**(3), 2031–2056 (2011). <https://doi.org/10.1111/j.1365-2966.2011.18280.x>
138. Metzger, B.D., Margalit, B., Sironi, L.: Fast radio bursts as synchrotron maser emission from decelerating relativistic blast waves. *MNRAS* **485**(3), 4091–4106 (2019). <https://doi.org/10.1093/mnras/stz700>
139. Metzger, B.D., Piro, A.L.: Optical and X-ray emission from stable millisecond magnetars formed from the merger of binary neutron stars. *MNRAS* **439**(4), 3916–3930 (2014). <https://doi.org/10.1093/mnras/stu247>
140. Metzger, B.D., Quataert, E., Thompson, T.A.: Short-duration gamma-ray bursts with extended emission from protomagnetar spin-down. *MNRAS* **385**(3), 1455–1460 (2008). <https://doi.org/10.1111/j.1365-2966.2008.12923.x>
141. Michilli, D., Seymour, A., Hessels, J.W.T., et al.: An extreme magneto-ionic environment associated with the fast radio burst source FRB 121102. *Nature* **553**(7687), 182–185 (2018). <https://doi.org/10.1038/nature25149>
142. Mooley, K.P., Deller, A.T., Gottlieb, O., et al.: Superluminal motion of a relativistic jet in the neutron-star merger GW170817. *Nature* **561**(7723), 355–359 (2018). <https://doi.org/10.1038/s41586-018-0486-3>
143. Mooley, K.P., Frail, D.A., Dobie, D., et al.: A strong jet signature in the late-time light curve of GW170817. *ApJ* **868**(1), L11 (2018). <https://doi.org/10.3847/2041-8213/aaeda7>
144. Munoz, M., Clark, J., Crowther, P., et al.: A neutron star with a massive progenitor in westerlund 1. *Astrophys. J. Lett.* **636**(1), L41–L44 (2006). <https://doi.org/10.1086/499776>
145. Narayan, R., Piran, T., Kumar, P.: Accretion models of gamma-ray bursts. *ApJ* **557**(2), 949–957 (2001). <https://doi.org/10.1086/322267>
146. Nicholl, M., Guillotin, J., Berger, E.: The magnetar model for type I superluminous supernovae. I. Bayesian analysis of the full multicolor light-curve sample with MOSFiT. *ApJ* **850**(1), 55 (2017). <https://doi.org/10.3847/1538-4357/aa9334>
147. Nousek, J.A., Kouveliotou, C., Grupe, D., et al.: Evidence for a canonical gamma-ray burst afterglow light curve in the swift XRT data. *ApJ* **642**(1), 389–400 (2006). <https://doi.org/10.1086/500724>
148. Obergaulinger, M., Aloy, M.Á.: Evolution of the surface magnetic field of rotating proto-neutron stars. In: *Journal of Physics Conference Series, Journal of Physics Conference Series*, vol. 932, p. 012043 (2017). <https://doi.org/10.1088/1742-6596/932/1/012043>
149. Oganesyan, G., Ascenzi, S., Branchesi, M., et al.: Structured jets and X-ray plateaus in gamma-ray burst phenomena. *ApJ* **893**(2), 88 (2020). <https://doi.org/10.3847/1538-4357/ab8221>
150. Oppermann, N., Yu, H.R., Pen, U.L.: On the non-Poissonian repetition pattern of FRB121102. *MNRAS* **475**(4), 5109–5115 (2018). <https://doi.org/10.1093/mnras/sty004>
151. Orellana, M., Bersten, M.C., Moriya, T.J.: Systematic study of magnetar-powered hydrogen-rich supernovae. *A&A* **619**, A145 (2018). <https://doi.org/10.1051/0004-6361/201832661>
152. Ostriker, J.P., Gunn, J.E.: On the nature of pulsars. I. Theory. *ApJ* **157**, 1395 (1969). <https://doi.org/10.1086/150160>
153. Paczynski, B.: Gamma-ray bursters at cosmological distances. *ApJ* **308**, L43–L46 (1986). <https://doi.org/10.1086/184740>
154. Paczynski, B., Rhoads, J.E.: Radio transients from gamma-ray bursters. *ApJ* **418**, L5 (1993). <https://doi.org/10.1086/187102>

155. Panaiteescu, A., Mészáros, P., Burrows, D., et al.: Evidence for chromatic X-ray light-curve breaks in Swift gamma-ray burst afterglows and their theoretical implications. *MNRAS* **369**(4), 2059–2064 (2006). <https://doi.org/10.1111/j.1365-2966.2006.10453.x>
156. Petroff, E., Burke-Spolaor, S., Keane, E.F., et al.: A polarized fast radio burst at low Galactic latitude. *MNRAS* **469**(4), 4465–4482 (2017). <https://doi.org/10.1093/mnras/stx1098>
157. Petroff, E., Hessels, J.W.T., Lorimer, D.R.: Fast radio bursts. *A&AR* **27**(1), 4 (2019). <https://doi.org/10.1007/s00159-019-0116-6>
158. Piran, T., Shemi, A., Narayan, R.: Hydrodynamics of relativistic fireballs. *MNRAS* **263**, 861 (1993). <https://doi.org/10.1093/mnras/263.4.861>
159. Piro, A.L.: The impact of a supernova remnant on fast radio bursts. *ApJ* **824**(2), L32 (2016). <https://doi.org/10.3847/2041-8205/824/2/L32>
160. Piro, A.L., Giacomazzo, B., Perna, R.: The fate of neutron star binary mergers. *ApJ* **844**(2), L19 (2017). <https://doi.org/10.3847/2041-8213/aa7f2f>
161. Piro, A.L., Ott, C.D.: Supernova fallback onto magnetars and propeller-powered supernovae. *ApJ* **736**(2), 108 (2011). <https://doi.org/10.1088/0004-637X/736/2/108>
162. Platts, E., Weltman, A., Walters, A., et al.: A living theory catalogue for fast radio bursts. *PhR* **821**, 1–27 (2019). <https://doi.org/10.1016/j.physrep.2019.06.003>
163. Pons, J.A., Perna, R.: Magnetars versus high magnetic field pulsars: a theoretical interpretation of the apparent dichotomy. *ApJ* **741**(2), 123 (2011). <https://doi.org/10.1088/0004-637X/741/2/123>
164. Popham, R., Woosley, S.E., Fryer, C.: Hyperaccreting black holes and gamma-ray bursts. *ApJ* **518**(1), 356–374 (1999). <https://doi.org/10.1086/307259>
165. Rane, A., Lorimer, D.: Fast radio bursts. *J. Astrophys. Astron.* **38**(3), 55 (2017). <https://doi.org/10.1007/s12036-017-9478-1>
166. Raynaud, R., Guilet, J., Janka, H.T., Gastine, T.: Magnetar formation through a convective dynamo in protoneutron stars. *Sci. Adv.* **6**(11), eaay2732 (2020). <https://doi.org/10.1126/sciadv.aay2732>
167. Rea, N., Esposito, P.: Magnetar outbursts: an observational review. *Astrophys. Space Sci. Proc.* **21**, 247 (2011). https://doi.org/10.1007/978-3-642-17251-9_21
168. Rea, N., Esposito, P., Turolla, R., et al.: A low-magnetic-field soft gamma repeater. *Science* **330**(6006), 944 (2010). <https://doi.org/10.1126/science.1196088>
169. Rea, N., Israel, G.L., Esposito, P., et al.: A new low magnetic field magnetar: the 2011 outburst of swift J1822.3-1606. *ApJ* **754**(1), 27 (2012). <https://doi.org/10.1088/0004-637X/754/1/27>
170. Rees, M.J., Meszaros, P.: Unsteady outflow models for cosmological gamma-ray bursts. *ApJ* **430**, L93 (1994). <https://doi.org/10.1086/187446>
171. Reisenegger, A.: Stable magnetic equilibria and their evolution in the upper main sequence, white dwarfs, and neutron stars. *A&A* **499**(2), 557–566 (2009). <https://doi.org/10.1051/0004-6361/200810895>
172. Rodríguez Castillo, G.A., Israel, G.L., Tiengo, A., et al.: The outburst decay of the low magnetic field magnetar SWIFT J1822.3-1606: phase-resolved analysis and evidence for a variable cyclotron feature. *MNRAS* **456**(4), 4145–4155 (2016). <https://doi.org/10.1093/mnras/stv2490>
173. Rossi, E., Lazzati, D., Rees, M.J.: Afterglow light curves, viewing angle and the jet structure of γ -ray bursts. *MNRAS* **332**(4), 945–950 (2002). <https://doi.org/10.1046/j.1365-8711.2002.05363.x>
174. Rowlinson, A., O'Brien, P.T., Metzger, B.D., et al.: Signatures of magnetar central engines in short GRB light curves. *MNRAS* **430**(2), 1061–1087 (2013). <https://doi.org/10.1093/mnras/sts683>
175. Ryde, F.: Is thermal emission in gamma-ray bursts ubiquitous? *ApJ* **625**(2), L95–L98 (2005). <https://doi.org/10.1086/431239>
176. Sari, R., Piran, T., Narayan, R.: Spectra and light curves of gamma-ray burst afterglows. *ApJ* **497**(1), L17–L20 (1998). <https://doi.org/10.1086/311269>
177. Sarin, N., Lasky, P.D., Ashton, G.: X-ray afterglows of short gamma-ray bursts: magnetar or fireball? *ApJ* **872**(1), 114 (2019). <https://doi.org/10.3847/1538-4357/aaf9a0>

178. Sathyaprakash, B.S., Schutz, B.F.: Physics, astrophysics and cosmology with gravitational waves. *Living Rev. Relativ.* **12**(1), 2 (2009). <https://doi.org/10.12942/lrr-2009-2>
179. Scholz, P., Spitler, L.G., Hessels, J.W.T., et al.: The repeating fast radio burst FRB 121102: multi-wavelength observations and additional bursts. *ApJ* **833**(2), 177 (2016). <https://doi.org/10.3847/1538-4357/833/2/177>
180. Shapiro, S.L., Teukolsky, S.A.: Black Holes, White Dwarfs, and Neutron Stars: The Physics of Compact Objects. Wiley, London (1983)
181. Shemi, A., Piran, T.: The appearance of cosmic fireballs. *ApJ* **365**, L55 (1990). <https://doi.org/10.1086/185887>
182. Shibata, M., Fujibayashi, S., Hotokezaka, K., et al.: Modeling GW170817 based on numerical relativity and its implications. *Phys. Rev. D* **96**(12), 123012 (2017). <https://doi.org/10.1103/PhysRevD.96.123012>
183. Shibata, M., Sekiguchi, Y.I.: Three-dimensional simulations of stellar core collapse in full general relativity: Nonaxisymmetric dynamical instabilities. *Phys. Rev. D* **71**(2), 024014 (2005). <https://doi.org/10.1103/PhysRevD.71.024014>
184. Siegel, D.M., Ciolfi, R.: Electromagnetic emission from long-lived binary neutron star merger remnants. I. Formulation of the problem. *ApJ* **819**(1), 14 (2016). <https://doi.org/10.3847/0004-637X/819/1/14>
185. Spitkovsky, A.: Time-dependent force-free pulsar magnetospheres: axisymmetric and oblique rotators. *ApJ* **648**(1), L51–L54 (2006). <https://doi.org/10.1086/507518>
186. Spitler, L.G., Cordes, J.M., Hessels, J.W.T., et al.: Fast radio burst discovered in the arecibo pulsar ALFA survey. *ApJ* **790**(2), 101 (2014). <https://doi.org/10.1088/0004-637X/790/2/101>
187. Spitler, L.G., Scholz, P., Hessels, J.W.T., et al.: A repeating fast radio burst. *Nature* **531**(7593), 202–205 (2016). <https://doi.org/10.1038/nature17168>
188. Spruit, H.C.: The source of magnetic fields in (neutron-) stars. In: Strassmeier, K.G., Kosovichev, A.G., Beckman, J.E. (eds.) *Cosmic Magnetic Fields: From Planets, to Stars and Galaxies*. IAU Symposium, vol. 259, pp. 61–74 (2009). <https://doi.org/10.1017/S1743921309030075>
189. Stella, L., Dall'Osso, S., Israel, G.L., Vecchio, A.: Gravitational radiation from newborn magnetars in the Virgo cluster. *ApJ* **634**(2), L165–L168 (2005). <https://doi.org/10.1086/498685>
190. Stratta, G., Dainotti, M.G., Dall'Osso, S., et al.: On the magnetar origin of the GRBs presenting X-ray afterglow plateaus. *ApJ* **869**(2), 155 (2018). <https://doi.org/10.3847/1538-4357/aadd8f>
191. Suvorov, A.G., Kokkotas, K.D.: Evidence for Magnetar Precession in X-Ray Afterglows of Gamma-Ray Bursts. *Astrophys. J. Lett.* **892**(2), L34 (2020). <https://doi.org/10.3847/2041-8213/ab8296>
192. Tchekhovskoy, A.: Simulations of jet formation by accreting black holes. In: American Astronomical Society Meeting Abstracts, American Astronomical Society Meeting Abstracts, p. 223.04 (2020)
193. Tchekhovskoy, A., Narayan, R., McKinney, J.C.: Efficient generation of jets from magnetically arrested accretion on a rapidly spinning black hole. *MNRAS* **418**(1), L79–L83 (2011). <https://doi.org/10.1111/j.1745-3933.2011.01147.x>
194. The CHIME/FRB Collaboration, ., Andersen, B.C., Bandura, K.M., Bhardwaj, M., et al.: A bright millisecond-duration radio burst from a Galactic magnetar (2020). arXiv e-prints arXiv:2005.10324
195. Thompson, C., Duncan, R.C.: Neutron star dynamos and the origins of pulsar magnetism. *ApJ* **408**, 194 (1993). <https://doi.org/10.1086/172580>
196. Thompson, C., Duncan, R.C.: The soft gamma repeaters as very strongly magnetized neutron stars—I. Radiative mechanism for outbursts. *MNRAS* **275**(2), 255–300 (1995). <https://doi.org/10.1093/mnras/275.2.255>
197. Thompson, C., Duncan, R.C.: The soft gamma repeaters as very strongly magnetized neutron stars. II. Quiescent neutrino, X-ray, and alfven wave emission. *ApJ* **473**, 322 (1996). <https://doi.org/10.1086/178147>

198. Thompson, C., Duncan, R.C.: The giant flare of 1998 August 27 from SGR 1900+14. II. Radiative mechanism and physical constraints on the source. *ApJ* **561**(2), 980–1005 (2001). <https://doi.org/10.1086/323256>
199. Tiengo, A., Esposito, P., Mereghetti, S., et al.: A variable absorption feature in the X-ray spectrum of a magnetar. *Nature* **500**(7462), 312–314 (2013). <https://doi.org/10.1038/nature12386>
200. Troja, E., Piro, L., Ryan, G., et al.: The outflow structure of GW170817 from late-time broadband observations. *MNRAS* **478**(1), L18–L23 (2018). <https://doi.org/10.1093/mnrasl/sly061>
201. Truemper, J., Pietsch, W., Reppin, C., et al.: Evidence for strong cyclotron line emission in the hard X-ray spectrum of Hercules X-1. *ApJ* **219**, L105–L110 (1978). <https://doi.org/10.1086/182617>
202. Turolla, R., Zane, S., Pons, J.A., et al.: Is SGR 0418+5729 indeed a waning magnetar? *ApJ* **740**(2), 105 (2011). <https://doi.org/10.1088/0004-637X/740/2/105>
203. Turolla, R., Zane, S., Watts, A.L.: Magnetars: the physics behind observations. A review. *Rep. Progr. Phys.* **78**(11), 116901 (2015). <https://doi.org/10.1088/0034-4885/78/11/116901>
204. Usov, V.V.: Millisecond pulsars with extremely strong magnetic fields as a cosmological source of γ -ray bursts. *Nature* **357**(6378), 472–474 (1992). <https://doi.org/10.1038/357472a0>
205. van Paradijs, J., Taam, R.E., van den Heuvel, E.P.J.: On the nature of the ‘anomalous’ 6-s X-ray pulsars. *A&A* **299**, L41 (1995)
206. Vietri, M., Stella, L., Israel, G.L.: SGR 1806-20: evidence for a superstrong magnetic field from quasi-periodic oscillations. *ApJ* **661**(2), 1089–1093 (2007). <https://doi.org/10.1086/517506>
207. Vink, J., Kuiper, L.: Supernova remnant energetics and magnetars: no evidence in favour of millisecond proto-neutron stars. *MNRAS* **370**(1), L14–L18 (2006). <https://doi.org/10.1111/j.1745-3933.2006.00178.x>
208. Vurm, I., Lyubarsky, Y., Piran, T.: On thermalization in gamma-ray burst jets and the peak energies of photospheric spectra. *ApJ* **764**(2), 143 (2013). <https://doi.org/10.1088/0004-637X/764/2/143>
209. Wanderman, D., Piran, T.: The rate, luminosity function and time delay of non-Collapsar short GRBs. *MNRAS* **448**(4), 3026–3037 (2015). <https://doi.org/10.1093/mnras/stv123>
210. Woltjer, L.: X-rays and type I supernova remnants. *ApJ* **140**, 1309–1313 (1964). <https://doi.org/10.1086/148028>
211. Woods, P.M., Thompson, C.: Soft gamma repeaters and anomalous X-ray pulsars: magnetar candidates, vol. 39, pp. 547–586 (2006)
212. Woosley, S.E.: Gamma-ray bursts from stellar mass accretion disks around black holes. *ApJ* **405**, 273 (1993). <https://doi.org/10.1086/172359>
213. Woosley, S.E.: Bright supernovae from magnetar birth. *ApJ* **719**(2), L204–L207 (2010). <https://doi.org/10.1088/2041-8205/719/2/L204>
214. Woosley, S.E.: Models for gamma-ray burst progenitors and central engines (2011). arXiv e-prints arXiv:1105.4193
215. Zhang, B.: The physics of gamma-ray bursts (2018). <https://doi.org/10.1017/9781139226530>
216. Zhang, B.: Astrophysics: A fast radio burst with an unexpected repeat period (2020). arXiv e-prints arXiv:2006.10727
217. Zhang, B.: The physical mechanisms of fast radio bursts. *Nature* **587**(7832), 45–53 (2020). <https://doi.org/10.1038/s41586-020-2828-1>
218. Zhang, B., Liang, E., Page, K.L., et al.: GRB radiative efficiencies derived from the swift data: GRBs versus XRFs, long versus short. *ApJ* **655**(2), 989–1001 (2007). <https://doi.org/10.1086/510110>
219. Zhang, B., Mészáros, P.: Gamma-ray burst afterglow with continuous energy injection: signature of a highly magnetized millisecond pulsar. *ApJ* **552**(1), L35–L38 (2001). <https://doi.org/10.1086/320255>
220. Zhang, B., Yan, H.: The internal-collision-induced magnetic reconnection and turbulence (ICMART) model of gamma-ray bursts. *ApJ* **726**(2), 90 (2011). <https://doi.org/10.1088/0004-637X/726/2/90>

221. Zhang, Y.G., Gajjar, V., Foster, G., et al.: Fast radio burst 121102 pulse detection and periodicity: a machine learning approach. *ApJ* **866**(2), 149 (2018). <https://doi.org/10.3847/1538-4357/aad31>
222. Zhong, S.Q., Dai, Z.G.: Magnetars from neutron star-white dwarf mergers: application to fast radio bursts. *ApJ* **893**(1), 9 (2020). <https://doi.org/10.3847/1538-4357/ab7bdf>

Chapter 9

The Equation of State of Neutron Star Matter



Ignazio Bombaci

Abstract Neutron stars are remarkable natural laboratories that allow us to investigate the fundamental constituents of matter and their interactions under extreme conditions that cannot be reproduced in terrestrial laboratories. This chapter gives a brief pedagogical introduction to the physics of matter at very high densities (i.e. up to several times the density of atomic nuclei) that hopefully could be useful to researchers in pulsars' astrophysics and related areas.

9.1 Introduction

With central densities exceeding by several times the density of atomic nuclei ($\rho_0 \simeq 2.6 \times 10^{14} \text{ g/cm}^3$) neutron stars (NSs) are the densest macroscopic objects in the universe. They represent the limit beyond which gravity overwhelms all the other forces of nature and leads to the formation of a black hole. Neutron stars thus represent incomparable natural laboratories that allow us to investigate the constituents of matter and their interactions under extreme conditions that cannot be reproduced in any terrestrial laboratory, and to explore the phase diagram of quantum chromodynamics (QCD) in a region which is presently inaccessible to numerical calculations of QCD on a space-time lattice.

The global properties of NSs (mass, radius, maximum mass, maximum spin frequency, etc.) primarily depend on the equation of state (EoS) of strong interacting matter, i.e. on the thermodynamic relation between the matter pressure (P), the energy density (ϵ) and the temperature (T). The EoS of dense matter is also a basic ingredient for modeling various astrophysical phenomena related to NSs, as core-collapse supernovae and binary neutron star (BNS) mergers.

Determining the correct EoS model which describes NSs is a fundamental problem of nuclear physics, particle physics and astrophysics, and major efforts

I. Bombaci (✉)

Dipartimento di Fisica “Enrico Fermi”, Università di Pisa, INFN Sezione di Pisa, Pisa, Italy
e-mail: ignazio.bombaci@unipi.it

have been made during the last few decades to solve it by measuring different NS properties using the data collected by various generations of X-ray and γ -ray satellites and by ground-based radio telescopes.

The recent detection of gravitational waves from the binary neutron star mergers, GW170817 [1, 2] and GW190425 [3] is giving a big boost to the research on dense matter physics. Gravitational wave signals, from BNS inspiral and especially from the BNS post-merger phase, offer in fact a unique opportunity to test different dense matter EoS models. Gravitational wave astronomy thus opened a new window to explore matter under extreme conditions.

The accurate measurements of the masses, ¹ $M = 1.97 \pm 0.04 M_{\odot}$ [4] and $M = 2.01 \pm 0.04 M_{\odot}$ [5], of the NSs in PSR J1614-2230 and PSR J0348+0432 respectively, and the recent mass measurement $M = 2.14^{+0.10}_{-0.09} M_{\odot}$ [6] for the neutron star in the millisecond pulsar J0740+6620, have ruled out all the EoS models which cannot support such high values of stellar masses.

In principle, in a *microscopic* approach, the EoS of dense matter should be derived starting from the matter constituents and their mutual interactions using quantum theory of many-body systems (see e.g. [7]). This is a very ambitious goal, and its level of difficulty depends on what *degrees of freedom* (constituents particles) we chose to describe dense matter and on how we model their mutual interactions (particularly the strong interaction).

Due to the large values of the stellar central density, various particle species and phases of dense matter are expected in NS interiors. In particular various “exotic” constituents, as for example hyperons, or a phase with deconfined quarks, are expected in neutron star interiors. Thus different types of “neutron stars” (nucleon stars, hyperon stars, hybrid stars, strange stars) are hypothesized to exist.

In this chapter, we do not discuss the techniques to constrain “neutron star” EoS models, which can be found in several existing reviews (e.g., [8–10]).

9.2 Neutron Star Physics in a Nutshell: Basic Concepts

As we already mentioned in Sect. 9.1, different particle species and different phases of dense matter are expected in neutron star interiors. This can be understood by the following basic arguments.

1. Gravity holds matter together at increasingly high density as one moves from the neutron star surface to its center. Thus gravity acts as a piston to compress matter at extreme densities.
2. Stellar constituents are different species of identical fermions² (n , p , \dots , e^- , μ^-), consequently they must have an antisymmetric wave function for particle

¹ Stellar masses will be given in unit of the mass of the Sun, $M_{\odot} = 1.988 \times 10^{33}$ g.

² The star may also contain species of identical bosons as in the case of negative pions (π^-) or negative kaons (K^-) condensation.

exchange. Thus, in the non-interacting quasi-particle approximation, the particles for each fermionic species must obey the Pauli principle. As a consequence their chemical potentials ($\mu_n, \mu_p, \dots, \mu_e, \mu_\mu$) are rapidly increasing function of the density.

3. Finally the weak interaction change the isospin and strangeness content of dense matter to minimize the energy per baryon of the system.

Thus following Harrison et al. [11] (see also [12]) by *catalyzed matter*, we mean matter at baryon number density n , in which the baryons and leptons abundances ($Y_i = n_i/n$) are such as to absolutely minimize the total energy per baryon (ε/n). Such matter is in equilibrium with respect to the strong and weak (“chemical equilibrium”) interactions.³ For a multicomponent system in chemical equilibrium, the abundances of its constituents are fixed uniquely by two thermodynamic variables, e.g. by the baryon number density n and the total entropy per baryon s . The EoS can then be expressed as:

$$\rho = \rho(n, s) = \rho_0 + \frac{1}{c^2} \varepsilon' \quad (9.1)$$

$$P = P(n, s) = n \left(\frac{\partial \varepsilon}{\partial n} \right)_s - \varepsilon \quad (9.2)$$

where $\rho = \varepsilon/c^2$ is the total mass density, inclusive of rest-mass density $\rho_0 = \varepsilon_0/c^2$. The total energy density is denoted as $\varepsilon = \varepsilon_0 + \varepsilon'$ and the internal energy density ε' includes the total kinetic energy density of all the particles plus the potential energy density due to the interactions among the particles of the system (this potential energy density does not include the gravitational potential energy density). Finally P is the total pressure.

In addition, one must know how the entropy per baryon depends on the baryon number density. Then one gets a one-parameter EoS

$$\rho = \rho(n, s(n)), \quad P = P(n, s(n)), \quad (9.3)$$

to be used to solve the stellar structure equations in general relativity.

A neutron star cools, within a few hours after birth, to temperatures in the range of 10^7 – 10^9 K [15]. These temperatures are very small when compared to nuclear matter energy scale (Fermi energies). Typical values for the Fermi energy in the core of a neutron star are of the order of tens to hundreds MeV (as the density increases going towards the center).⁴ Then we assume $s(n) = 0$ (or equivalently

³ The Coulomb interaction, together with finite size effects (mainly surface effects), is responsible for the formation of the so called *nuclear pasta* phases in the neutron star crust [13]. For the same physical reasons, similar *quark matter pasta* phases could appear inside hybrid stars [14].

⁴ $k_B T = 1$ MeV corresponds to $T \simeq 1.134 \times 10^{10}$ K.

$T(n) = 0$) within the whole star. We refer to such a state of matter as *cold catalyzed matter*.

The first theoretical calculation of the structure of a neutron star was performed in 1939 by J. Robert Oppenheimer and George M. Volkoff [16]. At that time, the theoretical and experimental investigation of the nuclear force was just at the beginning. The Yukawa's theory on the nuclear interaction based on meson exchange dates from 1935. But the important feature of a strong short distance repulsion between two nucleons was recognized only at the beginning of 1950s. Moreover, the first systematic experimental data on the phase shifts measured in nucleon-nucleon (NN) scattering experiments, and the first phenomenological NN potentials where available only in the late 1950s (for an historical outline on the early stages of the concept of nuclear forces see ref. [17]).

In view of this poor knowledge of the nuclear interaction, Oppenheimer and Volkoff disregarded it completely and assumed in their calculation [16] the EoS of an ideal relativistic Fermi gas of neutrons. This extreme approximation reveals the main features of neutron stars' properties. The most important of these features is the existence of a maximum possible mass for neutron stars, which according to the Oppenheimer–Volkoff calculations is $M_{max} = 0.71M_\odot$.

In the following, before we undertake our main task, regarding the influence of the strong interaction on the equation of state of dense matter and on neutron stars' structure, we imagine to “switch off” the strong interaction and focus on the role played by the weak interaction and the Pauli principle on dense matter physics.

9.2.1 The Role of Weak Interaction and Pauli Principle

An isolated neutron is unstable with respect to the decay process



having a mean life $\tau = (880.2 \pm 1.0)$ s ~ 14 min 40 s. The neutron decay is caused by the weak interaction and releases an energy $Q = (m_n - m_p - m_e)c^2 \simeq 0.78$ MeV which is shared by the three particles in the final state.

Consider now a system of *stable*⁵ non-interacting neutrons with a given baryon number density n_n .

What happens to the system if we “turn on” the weak interaction?

Do all neutrons decay to protons, electrons and electron-type anti-neutrinos?

The answer is yes, but below a threshold baryon density n^* that we will evaluate in the next pages. For densities above n^* the neutron decay process (9.4) is Pauli-blocked and the system will reach an equilibrium configuration with appropriate concentrations Y_i of the different particles.

⁵ i.e. imagine for a moment to “switch off” the weak interaction.

9.2.1.1 Inverse β -decay

To answer the above questions consider a system of protons and electrons with number densities $n_p = n_e$ (i.e. an electric charge neutral system), and neglect both the electromagnetic interactions between the particle and the strong interaction between protons. We refer to this system as an ideal $\{p, e^-\}$ -gas. We want to calculate the value n^* of the baryon density above which the inverse β -decay process



is energetically possible. We consider protons and neutrons as two ideal non-relativistic gases and electrons as an ideal ultra-relativistic gas (i.e. we neglect the electron rest mass).⁶ Under these conditions the chemical potential μ_p for protons (inclusive of its rest energy) can be written as:

$$\mu_p = \frac{\hbar^2}{2m_p} k_{F_p}^2 + m_p c^2 \quad (9.6)$$

where k_{F_p} (the Fermi momentum of protons in units of the reduced Plank's constant \hbar) is related to the proton number density n_p by the equation

$$n_p = \frac{1}{3\pi^2} k_{F_p}^3. \quad (9.7)$$

The electron chemical potential is given by $\mu_e = \hbar c k_{F_e}$, where the electron Fermi momentum k_{F_e} is related to the electron number density n_e by an equation similar to eq. (9.7). The threshold density n^* for the inverse β -decay (9.5) is set by the condition

$$\mu_p + \mu_e = m_n c^2 \quad (9.8)$$

which is valid for the neutrino-free matter ($\mu_{\nu_e} = \mu_{\bar{\nu}_e} = 0$).⁷

The charge neutrality condition implies $k_{F_p} = k_{F_e}$, thus the threshold density condition can be written as

$$\hbar c k_{F_p} \left(1 + \frac{1}{2} \frac{\hbar k_{F_p}}{m_p c} \right) = (m_n - m_p) c^2. \quad (9.9)$$

As we have already supposed (and we can verify a posteriori) at these densities protons are non relativistic, thus $\frac{\hbar}{m_p c} k_{F_p} \ll 1$, consequently from the previous

⁶ This is possible if the electron Fermi momentum satisfies $k_{F_e} \gg \frac{m_e c}{\hbar} = \tilde{\chi}_e^{-1}$, thus for densities $\rho \gg m_p \frac{1}{3\pi^2} \tilde{\chi}_e^{-3} \simeq 9.814 \times 10^5 \text{ g/cm}^3$.

⁷ Neutrino are trapped in neutron star interior for a few tens of second after their birth [15].

equation the threshold value for the proton Fermi momentum is

$$k_{F_p}^* \sim \frac{(m_n - m_p)c^2}{\hbar c} \simeq 6.537 \times 10^{-3} \text{ fm}^{-1}. \quad (9.10)$$

The corresponding threshold baryon density is thus $n_p^* \simeq 0.944 \times 10^{31} \text{ cm}^{-3} = 9.44 \times 10^{-9} \text{ fm}^{-3}$ and the threshold mass density is $\rho^* \simeq m_p n_p^* \simeq 1.58 \times 10^7 \text{ g/cm}^3$.

A more accurate determination of the inverse β -decay threshold density can be obtained considering fully relativistic electrons, i.e. considering the effect of the electron rest mass on their chemical potential ($\mu_e = [(\hbar c k_{F_e})^2 + (m_e c^2)^2]^{1/2}$). In this case one has:

$$k_{F_p}^* = k_{F_e}^* = \frac{1}{\lambda_e} \left[\left(\frac{m_n - m_p}{m_e} \right)^2 - 1 \right]^{1/2} \quad (9.11)$$

where $\lambda_e = \hbar/(m_e c) = 386.16 \text{ fm}$ is the electron reduced Compton's wave length. Thus one has $\rho^* \simeq m_p n_p^* \simeq 1.22 \times 10^7 \text{ g/cm}^3$.

9.2.1.2 β -stable Nuclear Matter

Consider now a system of ideal non-relativistic neutrons and protons (with number densities n_n and n_p respectively) and ideal ultra-relativistic electrons (with density n_e): ideal $\{n, p, e^-\}$ -gas. The equilibrium conditions for the weak processes (9.4) and (9.5) and the charge neutrality condition can be written as

$$\mu_e = \mu_n - \mu_p \quad (9.12)$$

$$n_e = n_p \quad (9.13)$$

where, as before, we consider neutrino-free matter. At nucleon densities $n = n_n + n_p$ which are much larger than the threshold density n^* for the inverse β decay processes, we can neglect the neutron-proton mass difference. In this case from Eqs. (9.12) and (9.13) one can easily obtain the proton fraction $Y_p = n_p/n$ in β -equilibrium as the solution of the following equation:

$$\frac{(3\pi^2)^{1/3}}{2} \lambda_N \left[(1 - Y_p)^{2/3} - Y_p^{2/3} \right] n^{1/3} - Y_p^{1/3} = 0, \quad (9.14)$$

where $\lambda_N = \hbar/(m_N c)$ is the nucleon reduced Compton's wave length, with $m_N = 938.92 \text{ MeV}/c^2$ being the average nucleon mass. For example at nuclear matter saturation density $n_0 = 0.16 \text{ fm}^{-3}$ one has $Y_p \sim 0.005$, whereas at $n = 5n_0 = 0.8 \text{ fm}^{-3}$ one has $Y_p \sim 0.021$. Thus up to several times the nuclear saturation

density n_0 , the ideal $\{n, p, e^-\}$ -matter is almost pure neutron matter, as assumed by Oppenheimer and Volkoff in their paper [16].

As we will discuss in some detail in the following pages, the nuclear interaction substantially modifies the composition of matter, producing a much larger proton fraction in β -stable nuclear matter.

9.2.1.3 The Muon Threshold

An isolated muon ($m_\mu = 105.658 \text{ MeV}/c^2$) is unstable with respect to the weak decay process

$$\mu^- \rightarrow e^- + \bar{\nu}_e + \nu_\mu \quad (9.15)$$

having a mean life $\tau = 2.197 \times 10^{-6} \text{ s}$.

In dense $\{n, p, e^-\}$ -matter, when the electron chemical potential μ_e is sufficiently high, it is energetically convenient to turn electrons into muons via the weak process

$$e^- \rightarrow \mu^- + \bar{\nu}_\mu + \nu_e. \quad (9.16)$$

To calculate the threshold density for muons' appearance in dense matter, we consider a charge neutral ideal $\{n, p, e^-\}$ -gas in a regime where neutrons and protons are non-relativistic and electrons ultra-relativistic. We further consider neutrino-free matter i.e. $\mu_{\nu_e} = \mu_{\bar{\nu}_e} = \mu_{\nu_\mu} = \mu_{\bar{\nu}_\mu} = 0$.

The threshold density for muons' appearance is set by the condition:

$$\mu_e = m_\mu c^2. \quad (9.17)$$

Thus, at threshold, the electron Fermi momentum k_{F_e} must be equal to the inverse muon reduced Compton's wave length $\tilde{\lambda}_\mu^{-1} = m_\mu c / \hbar$. The charge neutrality condition $n_p = n_e$ (at threshold $n_\mu = 0$) implies $k_{F_p} = k_{F_e}$, and the chemical equilibrium between neutrons, protons and electrons gives $\mu_n - \mu_p = \mu_e$.

For ideal non-relativistic neutron and proton gases, and neglecting the neutron-proton mass difference one thus gets:

$$\frac{\hbar^2}{2m_N} (k_{F_n}^2 - k_{F_p}^2) = m_\mu c^2, \quad (9.18)$$

which can be rewritten in terms of the total nucleon density $n = n_n + n_p$ as

$$(3\pi^2)^{2/3} \left(n - \frac{1}{3\pi^2} \tilde{\lambda}_\mu^{-3} \right)^{2/3} - \tilde{\lambda}_\mu^{-2} - 2\tilde{\lambda}_N^{-1} \tilde{\lambda}_\mu^{-1} = 0. \quad (9.19)$$

With simple algebra from this equation one gets for the threshold nucleon density for muons' appearance

$$n = \frac{1}{3\pi^2} \tilde{\chi}_\mu^{-3} \left[1 + \left(1 + 2 \frac{m_N}{m_\mu} \right)^{3/2} \right] = 0.43 \text{ fm}^{-3}, \quad (9.20)$$

where we have used $\tilde{\chi}_\mu = 1.87 \text{ fm}$. Thus the threshold mass density for muons' appearance in (ideal) dense nuclear matter is

$$\rho \simeq n m_N \simeq 7.2 \times 10^{14} \text{ g/cm}^3. \quad (9.21)$$

which is about 2.7 times the value of the central density $\rho_0 \simeq 2.6 \times 10^{14} \text{ g/cm}^3$ at the center of heavy atomic nuclei.

9.3 Nuclear Matter and Nucleon Stars

We now undertake the main task of this chapter and investigate the role of the strong interaction on the EoS of dense matter and on the properties of neutron stars. In the present work, we will not discuss the properties and the EoS of the neutron star crust (see e.g. [13]), but we will focus on the study of the EoS describing the thermodynamic properties of the neutron star core.

In the simplest and conservative picture the core of a NS is modeled as an electrically neutral uniform fluid of neutrons, protons, electrons and muons in equilibrium with respect to the weak interaction (β -stable nuclear matter). These neutron stars are often called *nucleon stars*. Even in this simplified picture, the microscopic determination of the EoS from the underlying nuclear interactions remains a formidable theoretical problem. In fact, one has to determine the EoS to extreme conditions of high density and high neutron-proton asymmetry, i.e. in a regime where the EoS is poorly constrained by nuclear data and experiments.

A prerequisite of any EoS of dense matter to be used in NS structure calculations, in core-collapse supernovae and in BNS mergers numerical simulations, relates to its capability to reproduce some basic empirical properties of nuclear matter at and around the nuclear saturation density $n_0 = 0.16 \text{ fm}^{-3}$ (cf. Sect. 9.3.1.1).

The nuclear symmetry energy (cf. Sect. 9.3.1) is one of the most relevant quantities to control the composition, and the pressure of β -stable nuclear matter [18, 19], and therefore many NS attributes such as the radius, moment of inertia, and crustal properties [20, 21].

Another important issue is related to the role of three-nucleon interactions (TNIs) on the EoS at high density. In fact, it is well known that TNIs are essential to reproduce the experimental binding energy of few-nucleon ($A = 3, 4$) systems [22, 23] and the empirical saturation point ($n_0 = 0.16 \text{ fm}^{-3}$, $(E/A)_0 = -16 \text{ MeV}$) of symmetric nuclear matter.

As shown by various microscopic calculations⁸ [24–28] of the EoS of β -stable nuclear matter, based on realistic nucleon-nucleon (NN) interactions supplemented with TNI, it is possible to obtain NS sequences with maximum mass $M_{max} > 2 M_\odot$ and thus in agreement with presently measured masses. However, the value of M_{max} strongly depends on the strength of the TNI at high density [27], thus indicating that few-body nuclear systems properties and/or nuclear matter saturation properties can not be used to constrain the TNI at high density. In addition, the central density for the maximum mass configuration for these neutron stars is in the range $n_c(M_{max}) = (6\text{--}8) n_0$.

In the present work, we do not make any attempt to discuss the various quantum many-body methods used to derive the EoS of nuclear matter, or more generally of baryonic matter (when other baryons are considered in addition to nucleons). We also do not attempt to make a review of recent studies on the neutron star matter EoS.

With the purpose of illustrating basic NS properties and discussing various possibilities for their inner structure, we will make use of some *representative* EoS models. Some of these are very popular EoS models, widely used in many astrophysical applications, and others are models on which the present author has worked on during his research activity.

9.3.1 Isospin-Asymmetric Nuclear Matter

The energy per nucleon $\tilde{E} \equiv E/A$ of isospin-asymmetric nuclear matter, with neutron number density n_n and proton number density n_p , contains the information to give a complete thermodynamic description of the system at zero temperature. $\tilde{E}(n_n, n_p)$ can be expressed as a function of the total nucleon number density $n = n_n + n_p$ and of the isospin-asymmetry parameter (shortly the asymmetry parameter),

$$\beta = \frac{n_n - n_p}{n} = 1 - 2 Y_p , \quad (9.22)$$

where $Y_p = n_p/n$ is the proton fraction. The case $\beta = 0$ corresponds to symmetric nuclear matter (SNM) i.e. matter with $n_n = n_p$, whereas the case with $\beta = 1$ corresponds to pure neutron matter (PNM).

⁸ Including those considered in the present chapter.

Due to the charge symmetry of the nuclear interactions, \tilde{E} must be the same exchanging all neutrons to protons and vice versa, thus \tilde{E} must depend on even-power of the asymmetry parameter:⁹

$$\tilde{E}(n, \beta) = \tilde{E}(n, 0) + S_2(n) \beta^2 + S_4(n) \beta^4 + \dots, \quad (9.23)$$

where the first term $\tilde{E}(n, 0) \equiv \tilde{E}_{SNM}(n)$ is the energy per nucleon of SNM, and the function in front of the β^2 term, is the nuclear symmetry energy

$$E_{sym}(n) \equiv S_2(n) = \frac{1}{2} \left. \frac{\partial^2 \tilde{E}}{\partial \beta^2} \right|_{\beta=0}. \quad (9.24)$$

Microscopic calculations of asymmetric nuclear EoS [18] show that terms $S_k(n)$ with $k > 2$ in Eq. (9.23) can be neglected, then one can safely use the so-called “parabolic approximation” in the asymmetry parameter β for the energy per particle of asymmetric nuclear matter up to $\beta = 1$,

$$\tilde{E}(n, \beta) = \tilde{E}(n, 0) + E_{sym}(n) \beta^2. \quad (9.25)$$

In the parabolic approximation the symmetry energy can be written as the difference between the energy per particle of PNM and SNM

$$E_{sym}(n) = \tilde{E}(n, \beta=1) - \tilde{E}(n, \beta=0). \quad (9.26)$$

This greatly reduces the numerical effort in all the quantum many-body approaches to derive the EoS of isospin-asymmetric and β -stable nuclear matter.

9.3.1.1 The Empirical Saturation Point of SNM

Due to the saturation properties of nuclear interactions, $\tilde{E}_{SNM}(n)$ has a minimum at a density n_0 which is set by the condition $[\partial \tilde{E}_{SNM}/\partial n]_{n_0} = 0$. The corresponding value of the energy per nucleon $\tilde{E}_0 \equiv \tilde{E}_{SNM}(n_0)$ is called the saturation energy. These two quantities (n_0 , \tilde{E}_0) locate the so called *saturation point* of SNM, which represents its ground state.

The empirical value for n_0 is obtained from the measured values of the central density of heavy nuclei (e.g. from electron-nucleus scattering experiments) taking

⁹ Notice that the presence of tiny charge-symmetry breaking (CSB) and charge-independence breaking (CIB) terms in the nuclear interaction (for a review, see e.g. [29]) could invalidate Eq. (9.23). For example a CSB component in the NN interaction produces a linear (and more generally odd-power) β -term in Eq. (9.23) [30]. However, it has been numerically demonstrated by various authors (e.g. [30] and [31]) that the effects on $\tilde{E}(n, \beta)$ and on the nuclear symmetry energy of CSB and CIB terms in the nucleon-nucleon interaction are essentially negligible.

into account corrections due to the finite size of atomic nuclei and to the Coulomb interaction which is not considered in nuclear matter. The value of the saturation energy \tilde{E}_0 corresponds to the volume coefficient (with a minus sign) of the semi-empirical Bethe–Weizsäcker mass formula, which is obtained from the fit of measured nuclear masses. From the above quoted experimental information one thus get the empirical saturation point of SNM:

$$n_0 = 0.16 \pm 0.01 \text{ fm}^{-3}, \quad \tilde{E}_0 = -16 \pm 1 \text{ MeV}. \quad (9.27)$$

9.3.1.2 The Incompressibility of SNM

Around the saturation density the energy per particle of SNM can be expanded as

$$\tilde{E}(n, 0) = \tilde{E}_0 + \frac{1}{2!} K_0 \left(\frac{n - n_0}{3n_0} \right)^2 + \frac{1}{3!} Q_0 \left(\frac{n - n_0}{3n_0} \right)^3 + \dots \quad (9.28)$$

The coefficient

$$K_0 = 9n_0^2 \left. \frac{\partial^2 \tilde{E}(n, 0)}{\partial n^2} \right|_{n_0} \quad (9.29)$$

is called the incompressibility of SNM. Its value can be extracted from experimental data on giant resonance in atomic nuclei. The empirical value for this quantity is in the range [32, 33]:

$$K_0 = 180 - 260 \text{ MeV}. \quad (9.30)$$

9.3.1.3 Properties of the Nuclear Symmetry Energy Around the Saturation Point

The symmetry energy can be expanded in series around the saturation density

$$E_{sym}(n) = E_{sym}(n_0) + L \left(\frac{n - n_0}{3n_0} \right) + \frac{1}{2!} K_{sym} \left(\frac{n - n_0}{3n_0} \right)^2 + \frac{1}{3!} Q_{sym} \left(\frac{n - n_0}{3n_0} \right)^3 + \dots \quad (9.31)$$

where $E_{sym}^0 \equiv E_{sym}(n_0)$ is the value of the symmetry energy at the saturation density, and the parameter

$$L = 3n_0 \left. \frac{\partial E_{sym}(n)}{\partial n} \right|_{n_0} \quad (9.32)$$

is called the symmetry energy *slope parameter*. The values of these two quantities can be extracted using various nuclear physics experimental data (see e.g. [34]). For example E_{sym}^0 corresponds to the symmetry coefficient of the semi-empirical Bethe–Weizsäcker mass formula, obtained from the fit of measured nuclear masses. The values for these two quantities lies in the ranges [34] :

$$E_{sym}^0 = (25\text{--}37) \text{ MeV}, \quad L = (30\text{--}90) \text{ MeV}. \quad (9.33)$$

9.3.1.4 Saturation Properties of Nuclear Matter for EoS Models

In Fig. 9.1 we plot the energy per nucleon of SNM as a function of the nucleon number density for the following four representative microscopic EoS models: WFF [24], APR [26], BL [28] and KVLBG [35] (case $\beta = \infty$ and $r_3 = 1.4$ fm in their Table I). All these EoS models have been obtained within quantum many-body approaches starting from two-body and three-body nuclear interactions. The properties of these EoS models, at the calculated saturation point, are reported in Table 9.1.

Notice that the WFF EoS does not reproduce the empirical saturation point of SNM, whereas in the case of the APR EoS an ad hoc density dependent correction term has been added by the authors of Ref. [26] to their microscopic results (see Tab VI last column and pag. 1815 in Ref. [26]) to reproduce the empirical saturation point of SNM.

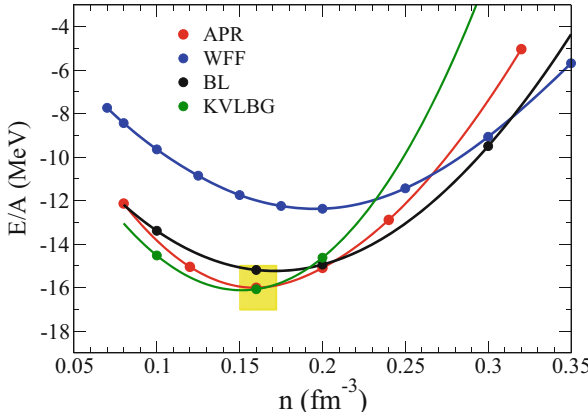


Fig. 9.1 Energy per nucleon of SNM as a function of the nucleon density n for the four considered EoS models. The yellow box represents the empirical saturation “point” Eq. (9.27). The curve for the APR EoS has been obtained by the authors of Ref. [26] adding an ad hoc density dependent correction term to their microscopic results to reproduce the empirical saturation point of SNM (see Tab VI last column and pag. 1815 in Ref. [26])

Table 9.1 Properties of nuclear matter for the EoS models (first column) used in this work: saturation density n_0 (second column) and corresponding energy per nucleon E/A (third column) for symmetric nuclear matter; symmetry energy E_{sym}^0 (fourth column), and its slope parameter L (fifth column); incompressibility K_0 (sixth column) at the calculated saturation density

EoS model	n_0 (fm $^{-3}$)	\tilde{E}_0 (MeV)	E_{sym}^0 (MeV)	L (MeV)	K_0 (MeV)
WFF	0.19	-12.4	31.0	56.5	209
APR ^a	0.16	-16.0	33.9	59.4	266
BL	0.17	-15.2	35.4	76.0	190
KVLBG	0.15	-16.1	35.2	70.2	251
Empirical	0.16 ± 0.01	-16 ± 1	25–37	30–90	180–260

^aThese results have been obtained by APR adding an ad hoc density dependent correction term to their microscopic results to reproduce the empirical saturation point of SNM (see Tab VI last column and pag. 1815 in Ref. [26])

9.3.2 β -stable Nuclear Matter: Role of the Nuclear Interactions

In this subsection we want to emphasize the role played by the nuclear interactions on the composition of β -stable nuclear matter. We consider the case of neutrino-free matter.

At any given value of the nucleon number density n , the composition of β -stable nuclear matter is obtained solving the following equations:

$$\mu_e = \mu_n - \mu_p, \quad \mu_\mu = \mu_e, \quad (9.34)$$

$$n_p = n_e + n_\mu. \quad (9.35)$$

It can be shown that the difference between the neutron and proton chemical potentials (neglecting their mass difference) can be written as:

$$\hat{\mu} \equiv \mu_n - \mu_p = -\frac{\partial \tilde{E}(n, Y_p)}{\partial Y_p} \Big|_n = 2 \frac{\partial \tilde{E}(n, \beta)}{\partial \beta} \Big|_n, \quad (9.36)$$

where the partial derivatives are taken for constant nucleon number density n .

To begin with, we neglect for the moment the presence of muons. In this case the β -stability conditions (9.34) and (9.35) reduce to Eqs. (9.12) and (9.13). At the densities found in the neutron star core ($\rho > 10^{14}$ g/cm 3) electrons can be considered as an ideal ultra-relativistic gas, so

$$n_e = \frac{1}{3\pi^2} \frac{1}{(\hbar c)^3} \mu_e^3. \quad (9.37)$$

Using the chemical equilibrium condition $\mu_e = \mu_n - \mu_p$ and Eq. (9.36), from the charge neutrality condition $n_e = n_p = Y_p n$ one gets:

$$3\pi^2(\hbar c)^3 n Y_p + \left(\frac{\partial \tilde{E}(n, Y_p)}{\partial Y_p} \Big|_n \right)^3 = 0 \quad (9.38)$$

which defines in an implicit way the proton fraction $Y_p = Y_p(n)$ at β -equilibrium and can be solved numerically for each given and fixed value of the nucleon number density n .

From Eq. (9.38) we see that the composition of β -stable nuclear matter is ruled not only by the weak interaction but also by the strong interaction which enters in the energy per nucleon $\tilde{E}(n, Y_p)$.

In the parabolic approximation (9.25) for $\tilde{E}(n, Y_p)$ one has

$$\left. \frac{\partial \tilde{E}(n, Y_p)}{\partial Y_p} \right|_n = -4E_{sym}(n)(1 - 2Y_p), \quad (9.39)$$

thus the proton fraction $Y_p(n)$ is the solution of the equation

$$3\pi^2(\hbar c)^3 n Y_p - \left[4E_{sym}(n)(1 - 2Y_p) \right]^3 = 0. \quad (9.40)$$

Consequently the composition of β -stable nuclear matter is a result of the density dependence of the nuclear symmetry energy.

In the density region for which $Y_p \ll 1/2$, an approximate solution of the equilibrium condition (9.40) is

$$Y_p(n) \simeq \frac{1}{3\pi^2} \frac{1}{n} \left(\frac{4E_{sym}(n)}{\hbar c} \right)^3 \quad (9.41)$$

which exhibits the high sensitivity of Y_p to the value of the symmetry energy and to its density dependence.

In Fig. 9.2 we plot the symmetry energy for the four considered microscopic nuclear matter EoS models. In the same figure, to quantify the influence of the nuclear interactions on this quantity, we plot the symmetry energy for an ideal {n, p}-system (black dotted curve). It is apparent that $E_{sym}(n)$ is heavily influenced by the nuclear interactions, and its behavior at large density ($n > 2n_0$) is still quite uncertain. The two bands in Fig. 9.2 represent the constraints on the symmetry energy obtained in Ref. [36] using the excitation energies to isobaric analog states (IAS) in nuclei (yellow band labeled IAS) and with the additional constraints from neutron skin thickness Δr_{np} of heavy nuclei [36, 37] (orange band labeled IAS+ Δr_{np}). Notice that some of the considered EoS models (particularly the WFF EoS) do not fulfill the above mentioned empirical constraints.

To illustrate the role of the nuclear interactions on the composition of β -stable nuclear matter, we plot in Fig. 9.3 the particle fractions $Y_i = n_i/n$ for the various

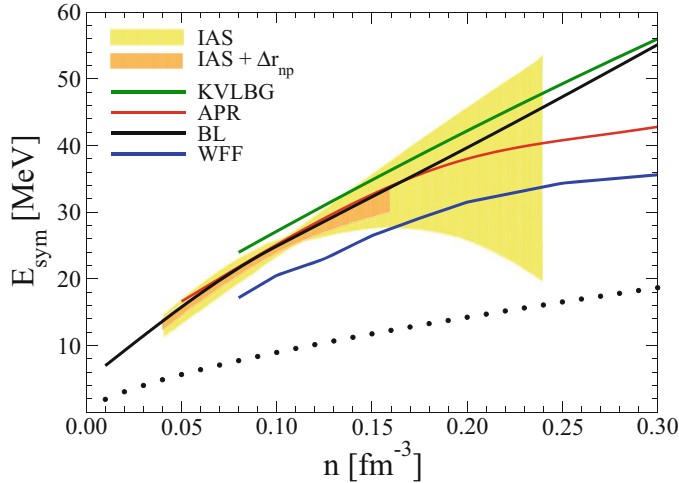


Fig. 9.2 Nuclear symmetry energy as a function of the nucleon number density for the four considered EoS models. The black dotted curve represents $E_{sym}(n)$ for an ideal $\{n, p\}$ -gas. The yellow band, labeled IAS, represents the constraints on the symmetry energy obtained in [36] using the excitation energies of isobaric analog states (IAS) in nuclei. The additional constraints from neutron skin thickness Δr_{np} of heavy nuclei [36, 37] give the more limited region covered by the orange band labeled IAS+ Δr_{np}

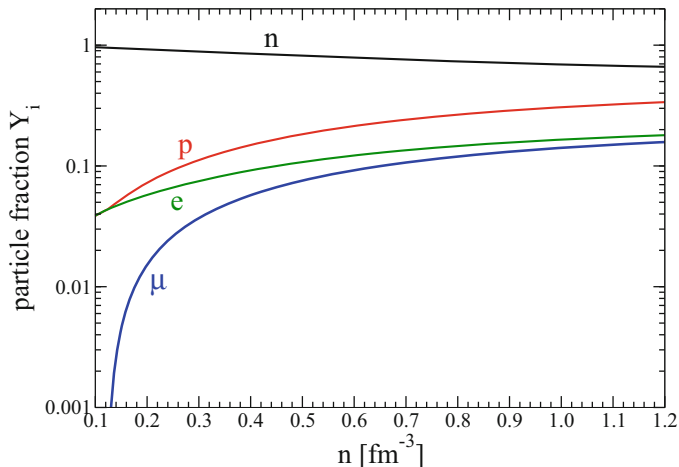


Fig. 9.3 Particle fractions $Y_i = n_i/n$ of β -stable nuclear matter as a function of the nucleon number density for the BL EoS model

matter constituents in the case of the BL EoS model. As one can see, neutrons are still the most abundant species, but now the proton fraction Y_p is much higher with respect to the case where nuclear interactions are ignored (ideal gas). For example, one has $Y_p(n_0) = 5.7 \times 10^{-2}$ and $Y_p(5n_0) = 26.6 \times 10^{-2}$, to be compared with the

values reported in Sect. 9.2.1.2 for the ideal gas. These results are also in line with the previous discussion on the role of the symmetry energy (cf. Eq. (9.40)) and with the results reported in Fig. 9.2.

Due to charge neutrality, a large proton fraction also implies a large electron fraction Y_e . Thus the nuclear interactions have the effect to lower the threshold density for muons' appearance in dense matter. In the case of the BL EoS, the muon threshold density is $n^* = 0.12 \text{ fm}^{-3} = 0.75 n_0$, to be compared with the one for the ideal {n, p, e}-gas: $n^* = 0.43 \text{ fm}^{-3} = 2.7 n_0$.

9.3.3 Nucleon Stars Properties

Once one has determined the particle fractions $Y_i(n)$ in β -stable matter, the nucleonic contribution $\varepsilon_N(n)$ to the total energy density is given by

$$\varepsilon_N(n) = n \tilde{E}(n, Y_p(n)) + m_n n_n + m_p n_p . \quad (9.42)$$

The nucleonic contribution $P_N(n)$ to the total pressure can thus be computed using the thermodynamic relation

$$P_N(n) = \mu_n n_n + \mu_p n_p - \varepsilon(n) . \quad (9.43)$$

Finally the leptonic contributions ε_L and P_L , to the total energy density and total pressure respectively, are computed using the expressions for relativistic ideal Fermi gases of electrons and muons.

The structural properties of non-rotating neutron stars can be obtained integrating numerically the equation for hydrostatic equilibrium in general relativity [16, 38]

$$\frac{dP}{dr} = -G \frac{m(r)\varepsilon(r)}{c^2 r^2} \left(1 + \frac{P(r)}{\varepsilon(r)}\right) \left(1 + \frac{4\pi r^3 P^3(r)}{c^2 m(r)}\right) \left(1 - \frac{2Gm(r)}{c^2 r}\right)^{-1}, \quad (9.44)$$

and

$$\frac{dm(r)}{dr} = \frac{4\pi}{c^2} r^2 \varepsilon(r) , \quad (9.45)$$

where G is the gravitational constant and $m(r)$ is the gravitational mass enclosed within a sphere of radial coordinate r (surface area $4\pi r^2$).

Starting with a central energy density $\varepsilon_c \equiv \varepsilon(r = 0)$, we integrate out Eqs. (9.44) and (9.45) until the energy density equals the one corresponding to the density of iron $\varepsilon_{surf}/c^2 = 7.86 \text{ g/cm}^3$. This condition determines the stellar surface and specifies the neutron star radius R (through the surface area $4\pi R^2$) and the stellar gravitational mass

$$M \equiv m(R) = \frac{4\pi}{c^2} \int_0^R dr r^2 \varepsilon(r). \quad (9.46)$$

The total baryon number of a star with central baryon density $n_c = n(r = 0)$ is given by

$$N_B = 4\pi \int_0^R dr r^2 n(r) \left(1 - \frac{2Gm(r)}{c^2 r}\right)^{-1/2}, \quad (9.47)$$

and the baryonic mass (or “rest mass”) of the neutron star is

$$M_B = m_u N_B \quad (9.48)$$

where m_u is a baryonic mass unit that we take equal to $m_u = m(^{12}\text{C})/12 = 1.6605 \times 10^{-24} \text{ g}$. Other choices for m_u are sometimes used in the literature as $m_u = m_n$ or $m_u = m(^{56}\text{Fe})/56$. These choices for m_u only make a small change in the calculated stellar binding energy since $\Delta\mathcal{B}/(M_B c^2) \sim 0.01$.

The total binding energy of the star is thus

$$\mathcal{B} = (M_B - M) c^2 \quad (9.49)$$

which represents the total energy liberated during the neutron star birth.

The stellar structure equations (9.44), (9.45) and (9.47) have been integrated using the microscopic EoS (in tabular form) for β -stable nuclear matter described in the previous sections to model the neutron star core, whereas to model the stellar crust (i.e. for nucleonic density $\leq 0.08 \text{ fm}^{-3}$) we have used the SLy4 [39] EoS.

In Fig. 9.4 we plot the gravitational mass as a function of the radius in the case of nucleon stars for the considered EoS models. Notice that all the considered EoS models are compatible with present measured neutron star masses and particularly with the mass $M = 2.01 \pm 0.04 M_\odot$ [5] of the neutron stars in PSR J0348+0432. The cyan and magenta regions give the mass and radius values for the high mass and low mass components respectively, extracted [2] from the gravitational wave signal for the event GW178017 in the case of low-spin priors for the two inspiraling NSs. The properties of the maximum mass configuration for the considered EOS models are reported in Table 9.2.

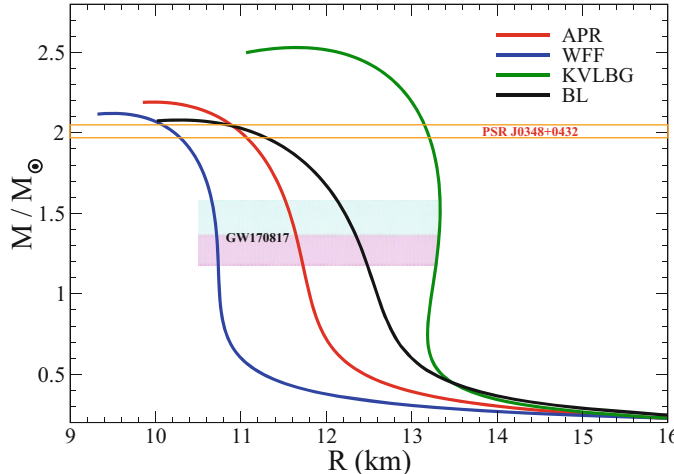


Fig. 9.4 Gravitational mass as a function of the stellar radius in the case of nucleon stars for the considered EoS models. The strip with boundaries marked with orange lines stands for the measured mass $M = 2.01 \pm 0.04 M_{\odot}$ of the neutron stars in PSR J0348+0432. The cyan and magenta regions give the mass and radius values for the high mass and low mass components respectively, extracted [2] from the gravitational wave signal for the event GW170817 in the case of low-spin priors for the two inspiraling neutron stars

Table 9.2 Maximum mass configuration properties for different EoS models. Stellar gravitational maximum mass M , corresponding radius R , central baryon number density n_c , central density ρ_c and baryonic maximum mass M_B . The stellar masses are given in unit of the solar mass $M_{\odot} = 1.989 \times 10^{33}$ g

EoS model	$M (M_{\odot})$	R (km)	n_c (fm $^{-3}$)	ρ_c (g/cm 3)	$M_B (M_{\odot})$
WFF	2.12	9.50	1.247	3.012×10^{15}	2.60
APR	2.19	9.97	1.146	2.787×10^{15}	2.65
BL	2.08	10.28	1.156	2.737×10^{15}	2.45
KVLBG	2.53	11.65	0.845	2.025×10^{15}	3.06

9.4 Hyperons in Neutron Stars: The Hyperon Puzzle

Just as nucleons, hyperons are baryons.¹⁰ However they possess an additional quantum number S , called *strangeness*, which is zero for nucleons. The strangeness quantum number is related to their quark structure. In fact, hyperons contain at least one strange (s) quark, whereas nucleons are formed by up (u) and down (d) quarks.

¹⁰ Hadrons, i.e. particles subject to the strong interaction, can be classified in two groups: baryons if they have spin $J = 1/2, 3/2, 5/2, \dots$, or mesons if they have spin $J = 0, 1, 2, \dots$. According to the hadrons' quark model, baryons are colorless bound states of three quarks ($q_1 q_2 q_3$), and mesons are colorless quark–anti-quark ($q_1 \bar{q}_2$) bound states.

Table 9.3 Properties of the baryons belonging to the $J^P = (1/2)^+$ baryon octet. I_3 is the isospin 3rd component

Baryon name	Isospin	I_3	\mathcal{S}	Quarks	Mass (MeV/c ²)	Mean life
n	1/2	-1/2	0	udd	939.56	880 s
p	1/2	+1/2	0	uud	938.27	Stable
Λ	0	0	-1	uds	1115.68	2.63×10^{-10} s
Σ^-	1	-1	-1	dds	1197.43	1.48×10^{-10} s
Σ^0	1	0	-1	uds	1192.55	7.4×10^{-20} s ^a
Σ^+	1	+1	-1	uus	1189.37	0.80×10^{-10} s
Ξ^-	1/2	-1/2	-2	dss	1321.32	1.64×10^{-10} s
Ξ^0	1/2	+1/2	-2	uss	1314.90	2.90×10^{-10} s

^aThe Σ^0 decays via the electromagnetic process $\Sigma^0 \rightarrow \Lambda + \gamma$ followed by the weak decay of the Λ

The properties of the baryons belonging to the so called baryon octet $J^P = (1/2)^+$, i.e. having spin $J = 1/2$ and positive parity P , are listed in Table 9.3.

Other hyperons (Σ^{*-} , Σ^{*0} , Σ^{*+} , Ξ^{*-} , Ξ^{*0} and Ω^-) belong to the baryon decuplet $J^P = (3/2)^+$. Among these we mention the Ω^- hyperon, which is a sss quark state with strangeness $\mathcal{S} = -3$ and mass $m_{\Omega^-} = 1672$ MeV/c². Due to their large masses, hyperons of the baryon decuplet are not expected in neutron stars. In the following we thus consider only members of the baryon octet $J^P = (1/2)^+$.

Hyperons are unstable with respect to various weak decay processes. For example an isolated Λ particle mainly decays via the following mesonic decay modes

$$\Lambda \rightarrow p + \pi^- \quad (63.9\%) , \quad (9.50)$$

$$\Lambda \rightarrow n + \pi^0 \quad (35.8\%) , \quad (9.51)$$

where in parenthesis we give the branching ratio for each of the two processes. Other rare weak decay modes, as for example $\Lambda \rightarrow p + e^- + \bar{\nu}_e$, are also possible.

9.4.1 β -stable Hyperonic Matter

At the high densities found in the core of nucleon stars (see Table 9.2) hyperons are expected among the stellar constituents. Hyperons' formation in dense matter can be understood by the basic and general physical arguments discussed in Sect. 9.2. As soon as the chemical potentials of nucleons and electrons become sufficiently large, it is energetically convenient to convert nucleons into hyperons via weak interaction processes. For example the Λ hyperons can be formed through the weak process $p + e^- \rightarrow \Lambda + \nu_e$ when the Λ chemical potential fulfills the condition $\mu_\Lambda = \mu_p + \mu_e = \mu_n$. The Σ^- hyperons can be formed e.g. through the weak process

$n + e^- \rightarrow \Sigma^- + \nu_e$ when the Σ^- chemical potential fulfills the condition $\mu_{\Sigma^-} = \mu_n + \mu_e$ (we consider neutrino-free matter). Other hyperons can be formed with similar weak interaction processes. Thus at sufficiently large density, nuclear matter turns into *hyperonic matter* (also referred to as *hypernuclear matter*).

At any given value of the total baryon density

$$n = n_n + n_p + n_\Lambda + n_{\Sigma^-} + n_{\Sigma^0} + n_{\Sigma^+} + n_{\Xi^-} + n_{\Xi^0} \quad (9.52)$$

the composition of hyperonic matter (i.e. the values of the particle fractions $Y_i = n_i/n$ for the various particle species) is set by the following equations between the chemical potentials of the different constituents

$$\mu_p = \mu_n - \mu_e = \mu_{\Sigma^+} \quad (9.53)$$

$$\mu_n = \mu_\Lambda = \mu_{\Sigma^0} = \mu_{\Xi^0} \quad (9.54)$$

$$\mu_n + \mu_e = \mu_{\Sigma^-} = \mu_{\Xi^-} \quad (9.55)$$

$$\mu_\mu = \mu_e \quad (9.56)$$

with the additional condition given by electric charge neutrality

$$n_p + n_{\Sigma^+} = n_e + n_\mu + n_{\Sigma^-} + n_{\Xi^-}. \quad (9.57)$$

Once again we consider neutrino-free matter. The solution of Eqs. (9.52)–(9.57) give the composition $Y_i(n)$ ($i = n, p, \Lambda, \Sigma^-, \dots, e^-, \mu^-$) for β -stable hyperonic matter.

To begin with, to estimate the threshold baryon density $n^{*[\Lambda]}$ for Λ hyperons in dense matter, we neglect the strong interaction. We thus consider an ideal $\{n, p, e^-\}$ -gas in β -equilibrium. The Λ -threshold condition is given by $\mu_n = \mu_p + \mu_e = m_\Lambda c^2$. Assuming non-relativistic nucleons, one easily gets $n^{*[\Lambda]} = 0.86 \text{ fm}^{-3} = 5.4 n_0$.

To illustrate the role of the strong interaction on the threshold density values of different hyperons, we show in Fig. 9.5 (upper panel) the chemical potentials μ_i for the different stellar constituents. These results have been obtained [40, 41] within the many-body Brueckner-Hartree-Fock (BHF) approach and using the following interactions: the Argonne v18 (Av18) nucleon-nucleon (NN) interaction [42]; the TNI used in [25] to reproduce the empirical nuclear matter saturation point; the Nijmegen ESC08b potential [43] to describe the hyperon-nucleon (YN) interaction. No hyperon-hyperon (YY) interaction and no three-body interactions of the type nucleon-nucleon-hyperon (NNY), NYY and YYY have been considered [40, 41]. The onset of Λ hyperons occurs at $n^{*[\Lambda]} = 0.35 \text{ fm}^{-3} = 2.19 n_0$. Thus the strong interaction moves the Λ -threshold density to a lower value with respect to the one relative to the ideal $\{n, p, e^-\}$ -gas case. The Σ^- hyperon occurs at $n^{*[\Sigma^-]} = 0.64 \text{ fm}^{-3} = 4 n_0$. Notice that, due to the strong interaction, the hyperons chemical potential, below the corresponding threshold density, is not equal to its

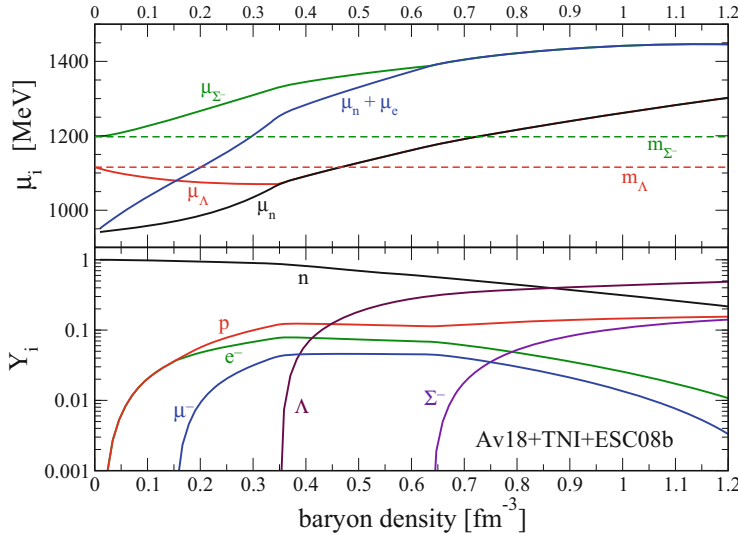


Fig. 9.5 Chemical potentials μ_i (upper panel) and concentrations Y_i (lower panel) of the different stellar constituents in β -stable hyperonic matter as a function of the total baryon density

corresponding rest mass energy $m_Y c^2$. The calculated threshold densities for Λ and Σ^- hyperons are thus well below the predicted central densities n_c^{max} (see Table 9.2) for the maximum mass configuration of nucleon stars.

The composition of β -stable hyperonic matter is reported in Fig. 9.5 (lower panel). Notice that at $n = 5 n_0$ hyperons represent about 43% of the total number of baryons.

9.4.2 Hyperon Stars

The effect of hyperons on the EoS is shown in Fig. 9.6 (upper panels), where we compare the EoS for β -stable pure nucleonic matter (curves Av18+TNI) with that of β -stable hyperonic matter (curves Av18+TNI+ESC08b). As we can see the presence of hyperons produces a significant reduction of the pressure of the system. As a consequence, solving the relativistic stellar structure equations, we find a considerable decrease of the stellar maximum mass from $M_{max} = 2.28 M_\odot$ to $M_{max} = 1.38 M_\odot$ when hyperons are included among the stellar constituents. The prediction of a value for $M_{max} < 2 M_\odot$ is a common feature of various hyperon stars structure calculations and particularly of those based on microscopic hyperonic matter EoSs [27, 44–47].

Thus, on the one hand the presence of hyperons in neutron stars seems unavoidable, on the other hand their presence results in a stellar maximum mass not

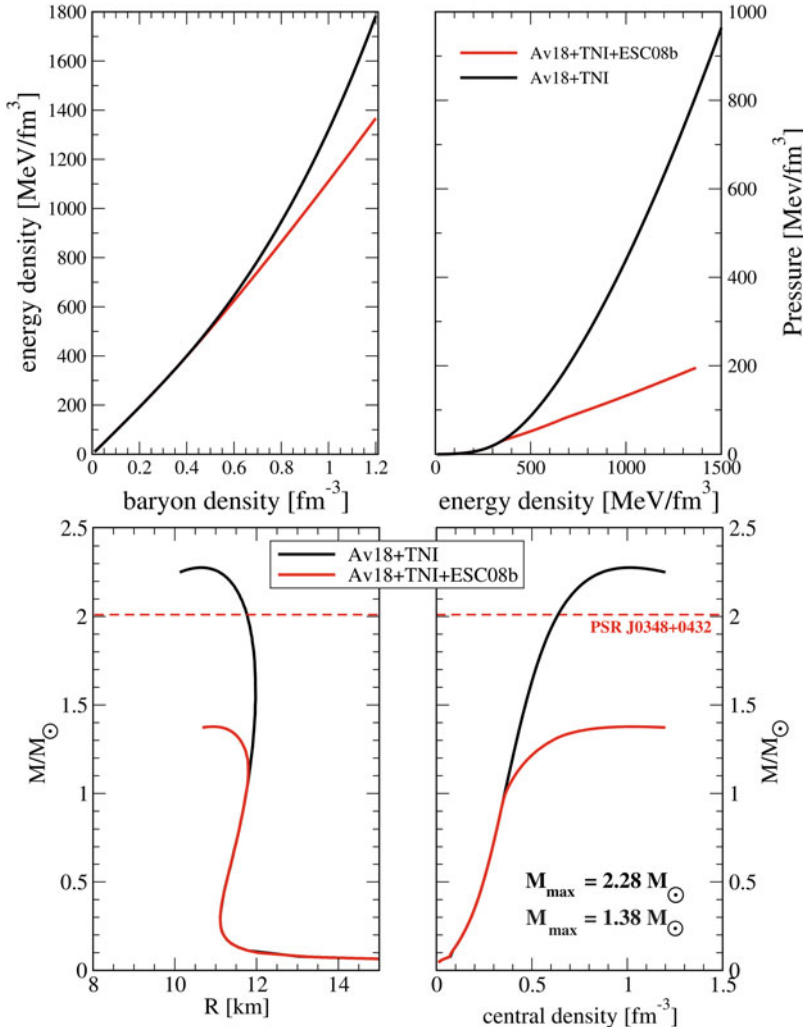


Fig. 9.6 Upper panels: EoS of β -stable matter illustrating the energy density as a function of the total baryon density (upper left panel) and the pressure versus the energy density (upper right panel). The upper (lower) curves refer to the case of nuclear (hyperonic) matter. Lower panels: gravitational mass as a function of the stellar radius (lower left panel) and of the central baryon density (lower right panel) in the case of nucleon stars (upper curves) and hyperon stars (lower curves). The dashed horizontal line represents the measured mass [5] of the neutron star in the pulsar PSR J0348+0432

compatible with measured NS masses. This baffling problem is known as the “hyperon puzzle” in neutron stars.

Clearly, one should try to trace back the origin of the hyperon puzzle to the underlying NY and YY two-body interactions or to the possible repulsive NNY,

NNY and YYY three-body interactions. Unfortunately, these two- and three-body strangeness $S \neq 0$ baryonic interactions are rather uncertain and poorly known. Basically this is due to the scarce amount of experimental data and to the considerable difficulties in their theoretical analysis. This situation is in sharp contrast to the case of the NN interaction, which is satisfactorily well known, mostly due to the large number of scattering data and to the huge amount of measured properties of stable and unstable nuclei. The study of hypernuclei (i.e. nuclei containing one or more hyperons) [48–52] and more in general of hypernuclear physics [53–55] is partially filling this gap and hopefully will give in the near future the possibility to have accurate and reliable description of the $S \neq 0$ baryonic interactions.

Presently, this is a very active research field both from an experimental [52, 56] and a theoretical [56, 57] point of view. Within this contest, the use of microscopic EoS of hyperonic matter in the study of NS structure is of fundamental importance for the understanding of strong interactions involving hyperons, and particularly to learn how these interactions behave in a dense many-body system.

9.4.3 Hyperonic Three-Body Interactions as Possible Solutions of the Hyperon Puzzle

As already mentioned TNIs play an important role in nuclei and in nuclear matter. Thus, within a unified description of the interactions between baryons, it is rather evident to suppose the existence of hyperonic three-body interactions. The NNA interaction was in fact first hypothesized [58, 59] at the end of the 1950s, i.e. during the early days of hypernuclear physics, as an important ingredient to calculate the binding energy of hypernuclei. Since then the NNA interaction received considerable attention in many other studies on hypernuclei [60–68]. It is thus quite natural to expect that hyperonic three-body interactions can influence the EoS of dense matter and can represent a likely candidate to solve the hyperon puzzle [69–73].

To emphasize the effect of hyperonic three-body interactions on the EoS of hyperonic matter and on M_{max} , we consider the simplified situation where we include only the Λ hyperons and ignore the possible appearance of other hyperon species. We thus consider a $\{\text{n}, \text{p}, \Lambda, e^-, \mu^-\}$ -system in β -equilibrium and under the influence of NN, NNN and N Λ interactions, to which we add a NNA three-body interaction (see Ref. [72] for more details).

The composition of β -stable hyperonic matter is presented in the upper left panel of Fig. 9.7. The continuous lines (labeled as NSC97a) display the particle fractions Y_i when only NN, NNN, and N Λ interactions are included, whereas the dashed lines (labeled as NSC97a+NN Λ_1) display the particle fractions when the NNA three-body interaction is added. The effect of the NNA interaction is twofold. First it shifts the Λ -threshold density to a larger value with respect to the case in which the

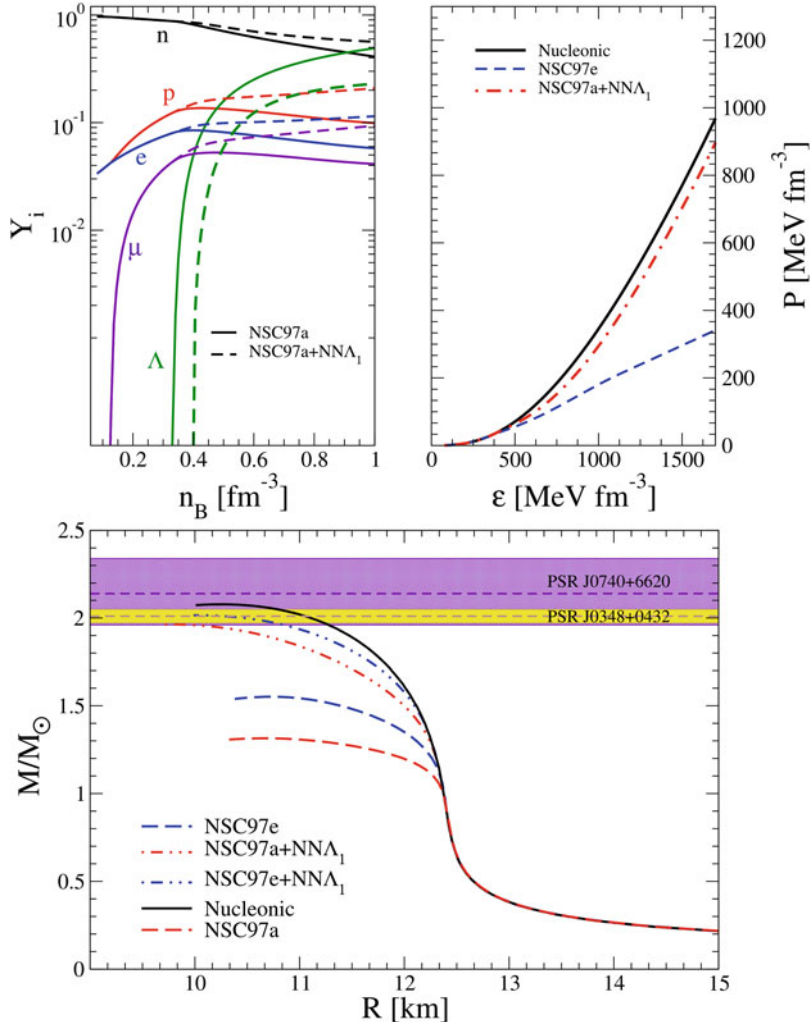


Fig. 9.7 Upper left panel: particle fractions Y_i in β -stable hyperonic matter as a function of the baryon density. The continuous lines (labeled as NSC97a) display the particle fractions Y_i when only NN, NNN, and $N\Lambda$ interactions are included, whereas the dashed lines (labeled as NSC97a+NNA₁) display the particle fractions when the NNA three-body interaction is added. Upper right panel: EoS for β -stable hyperonic matter including (dot-dashed line) or not including (dashed line) the NNA interaction. The EoS for pure nucleonic matter (continuous line) is also shown for comparison. Lower panel: mass-radius sequences for the various EoS models with (dot-dashed lines) and without (dashed lines) the NNA interaction. Results for nucleon stars (continuous line) are shown for comparison. The two colored bands represent the measured masses of the neutron stars in PSR J0348+0432 and PSR J0740+6620. The results reported in this figure are adapted from Ref. [72] where the reader can find more details on the strong interaction models used to derive the EoS. Credit: Logoteta et al., Eur. Phys. J. A 55, 207 (2019). License: CC BY 4.0

NN Λ interaction is not included. Second it strongly reduces the Λ concentration and consequently increases back the neutron and proton concentrations. The effect of the NN Λ interaction on the EoS can be examined looking at the results reported in the upper right panel of Fig. 9.7, where we plot the total pressure P as function of the total energy density ε for β -stable matter. The continuous line represent the EoS for nucleonic matter under the influence of NN and NNN interactions. The inclusion of the Λ hyperons and of a N Λ interaction produces a sizable softening of the EoS (dashed line) i.e. strongly reduces the pressure. When the NN Λ interaction is added the pressure abundantly increases (dot-dashed line) and the EoS is stiffened, almost back to the nucleonic case.

Next in the lower panel of Fig. 9.7, we plot the mass-radius equilibrium sequences for various EoS models with (dot-dashed lines) and without (dashed lines) the NN Λ interaction. Notice that two different models (NSC97a and NSC97e) for the N Λ interaction have been used (see Ref. [72] for more details). The mass-radius curve for nucleon stars (continuous line) is shown for comparison. The two colored bands represent the measured masses of the neutron stars in the pulsar PSR J0348+0432 [5] and PSR J0740+6620 [6]. These results thus give a strong indications that hyperonic three-body interactions could represent a likely solution of the hyperon puzzle in neutron stars [72].

9.5 Quark Matter in Neutron Stars

Neutron star structure calculations (see e.g. Table 9.2) based on a large variety of modern EoS of nuclear or hyperonic matter, predict a maximum stellar central density (the one for the maximum mass star configuration) in the range of 4–8 times the saturation density n_0 of nuclear matter. Thus the core of a neutron star is one of the best candidates in the universe where a transition from a phase where quarks are confined within baryons and mesons (hadronic matter) to a quark deconfined phase (quark matter) could occur. This possibility was realized by several researchers [74–79] soon after the introduction of quarks as the fundamentals building blocks of hadrons.

Neutron stars which possess a quark matter core either as a mixed phase of deconfined quarks and hadrons or as a pure quark matter phase are called *hybrid stars* [14]. In the following the more conventional neutron stars in which no fraction of quark matter is present, will be referred to as *hadronic stars* (HSs). This family thus includes nucleon stars (Sect. 9.3) and hyperon stars (Sect. 9.4), or compact stars containing a Bose–Einstein condensate of negative pions (π^-) or negative kaons (K^-) (not discussed in this chapter).

According to the quark model, baryons are bound states of three quarks ($q_1 q_2 q_3$), and mesons are quark–anti-quark ($q_1 \bar{q}_2$) bound states. Each quark has spin 1/2 (thus quarks are fermions) and baryon number 1/3. There are six different *flavors* of quarks: up (u), down (d), strange (s), charm (c), top (t) and bottom (b). Each quark possesses an electric charge, which is a fraction of the electron charge magnitude

Table 9.4 Properties of quarks: flavor, mass, electric charge Q/e in units of the electron charge magnitude $e = 1.602 \times 10^{19}$ C. Data from the Particle Data Group booklet, 2018 edition

Flavor	Mass	Q/e		Flavor	Mass	Q/e
u	$2.2^{+0.5}_{-0.4}$ MeV	$+\frac{2}{3}$		d	$4.7^{+0.5}_{-0.3}$ MeV	$-\frac{1}{3}$
s	95^{+9}_{-3} MeV	$-\frac{1}{3}$		c	$1.275^{+0.025}_{-0.035}$ GeV	$+\frac{2}{3}$
b	$4.18^{+0.04}_{-0.03}$ GeV	$-\frac{1}{3}$		t	$173.0^{+0.4}_{-0.4}$ GeV	$+\frac{2}{3}$

$e = 1.602 \times 10^{19}$ C. The values of the mass and electric charge for quarks of each flavor are listed in Table 9.4.

Quarks possess an internal degree of freedom, the *color* degree of freedom. The color charge is responsible for the strong interaction. There are three different colors a quark can carry. The colors are labeled *red*, *green*, and *blue* with associated anticolors. Quarks interact each other via the exchange of massless particles called gluons. Gluons themselves have color charge and so they mutually interact via the strong interaction. All the observed meson and baryon states are *colorless*, namely either color-anticolor combinations in the case of mesons, or equal mixture of *red*, *green*, and *blue* in the case of baryons.

The number density n_q for a given quark flavor is related to the corresponding Fermi momentum k_{F_q} by the equation

$$n_q = \frac{1}{\pi^2} k_{F_q}^3 . \quad (9.58)$$

Notice that the previous relation differs by a factor of three from the similar equation for an electron gas or for a proton gas (Eq. (9.7)). The extra factor of three is due to the color degree of freedom. Quark states, for any given flavor, are in fact degenerate with respect to spin ($v_{\text{spin}} = 2$) and with respect to color ($v_{\text{color}} = 3$). Since to each quark is assigned a baryon number $1/3$, the baryon number density for a system containing quarks of different flavors with partial number densities n_q is given by

$$n = \frac{1}{3} \sum_q n_q . \quad (9.59)$$

Weak interaction processes can change the quark flavor (see e.g. Eqs. (9.63)–(9.67)).

If quark matter is present in neutron stars, it can be shown that the chemical potential μ_s for the strange quark is larger than its rest energy. Thus the *s* quark must be included in the description of the stellar quark matter core, in addition to the *u* and *d* quarks [14].

We give now a simple argument to show why charm, bottom and top quarks are not expected in a neutron star core. The reason is that *c*, *b*, and *t* quarks are much more massive than *u*, *d*, and *s* quarks (see Table 9.4). We thus assume $m_u = m_d =$

$m_s = 0$ and consider an ideal $\{u, d, s, e^-\}$ -gas,¹¹ with $m_e = 0$, in equilibrium with respect to the weak interaction and with total electric charge equal to zero (see Eqs. (9.62)–(9.69) below). Under these hypothesis it can be shown that $n_u = n_d = n_s$ and $n_e = 0$. As a consequence the baryon density $n = (n_u + n_d + n_s)/3$ is $n = n_s$.

The creation of the charm quark, e.g. through the weak process

$$s \rightarrow c + e^- + \bar{\nu}_e, \quad (9.60)$$

requires the chemical potential of the s quark should be at least equal to the charm quark rest energy, consequently we get

$$\mu_s = \hbar c k_{F_s} = \hbar c (\pi^2 n_s)^{1/3} = \hbar c (\pi^2 n)^{1/3} \geq m_c c^2 = 1.275 \text{ GeV} \quad (9.61)$$

which implies $n \geq 27 \text{ fm}^{-3}$, i.e. a baryon number density at least equal to about 170 times the normal saturation density n_0 of nuclear matter, in other words a density much higher than the maximum expected central density in neutron stars.

Thus the quark matter phase expected in neutron stars is a mixture of u , d , and s quarks, together with an appropriate number of electrons to guarantee electric charge neutrality. This phase of dense matter is called strange quark matter (SQM). For consistency with the strangeness quantum number S assigned to hyperons and nucleons (see Table 9.3), quarks u and d have no strangeness ($S = 0$), whereas the s quark has strangeness $S = -1$.

9.5.1 β -stable Strange Quark Matter

The composition of β -stable SQM is determined by the requirement of electric charge neutrality

$$\frac{2}{3}n_u - \frac{1}{3}n_d - \frac{1}{3}n_s - n_e = 0 \quad (9.62)$$

and equilibrium with respect to the weak processes:



¹¹ The strong interaction between quarks can be neglected due to the asymptotic freedom of QCD which, for the purpose of the present estimate, is a reasonable approximation at the high densities found in neutron stars cores.

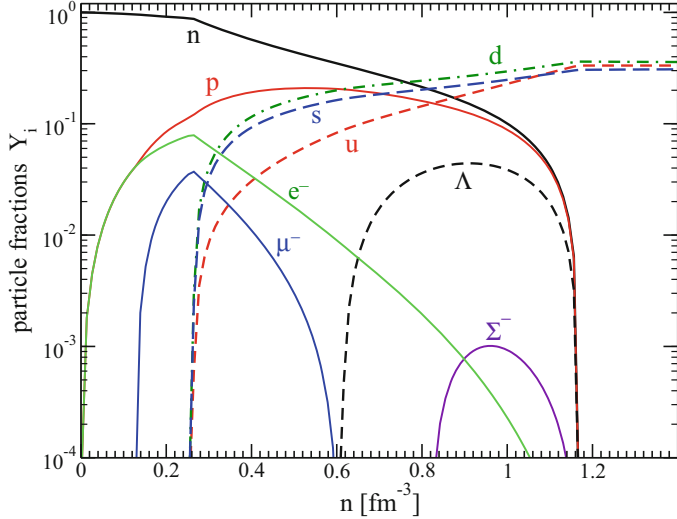


Fig. 9.8 Particle fractions Y_i for the different stellar constituents as a function of the baryon density n . The quark fraction is defined as $Y_i = n_i/(3n)$, since quarks have baryon number $1/3$, where n_i is the number density of quarks of flavor i (u, d, s). For nucleons, hyperons, electrons and muons $Y_i = n_i/n$. The hadronic phase is described by the GM3 EoS model and the quark phase by the bag model EoS with bag constant $B = 136.6 \text{ MeV/fm}^3$ and $m_s = 150 \text{ MeV}$, $m_u = m_d = 0$. See [14] for details on the EoS models and on the phase-transition modeling



which, in neutrino-free matter, can be written in terms of the corresponding chemical potentials as

$$\mu_d = \mu_s \equiv \mu \quad (9.68)$$

$$\mu = \mu_u + \mu_e. \quad (9.69)$$

Considering now two different EoS models, one for the hadronic phase and the other for the quark phase, and assuming a first-order transition between the two phases, one can construct the EoS for hybrid star matter as described in detail in the book by N. K. Glendenning [14].

As an example of the composition of hybrid star matter, we plot in Fig. 9.8 (see figure caption for informations on the EoS models) the particle fractions Y_i for the different stellar constituents as a function of the baryon density n . The hadronic phase extends up to $n \simeq 0.26 \text{ fm}^{-3}$. Above this density value one has the mixed hadron-quark phase which extend up to $n \simeq 1.16 \text{ fm}^{-3}$. Finally for larger densities one has a pure SQM phase.

It has been shown (see e.g. Ref. [80–84]) that several of the current models of hybrid stars are compatible with present measured NS masses.

9.5.2 Strange Stars

Even more intriguing than the existence of a quark matter core in a neutron star, is the possible existence of a new family of compact stars consisting completely of β -stable SQM. Such compact stars have been referred to in the literature, as *strange quark stars* or shortly *strange stars* (SSs). The investigation of such a possibility is extremely relevant not only for astrophysics, but for high energy physics too.

The possible existence of SS is a direct consequence of the so called strange matter hypothesis [85–87].

According to this hypothesis, SQM could be the true ground state of matter. In other words, the energy per baryon of SQM (at the baryon density where the pressure is equal to zero) is supposed to be less than the lowest energy per baryon found in atomic nuclei, which is about 930.4 MeV for the most bound nuclei (^{56}Fe , ^{58}Fe , and ^{62}Ni).

If the strange matter hypothesis is true, then a nucleus with A nucleons, could in principle lower its energy by converting to a *strangelet* (i.e. a drop of SQM). However, this process requires a very high-order simultaneous weak interactions to convert about a number A of u and d quarks of the nucleus into s quarks. The probability for such a process is thus proportional to G_F^{2A} , where G_F is the Fermi constant. As a consequence, for a large enough baryon number ($A > A_{\min} \sim 5$), this probability is extremely low, and the mean-life time for an atomic nucleus to decay to a strangelet is much higher than the age of the universe. In addition, finite size effects (surface and shell effects) place a lower limit ($A_{\min} \sim 10\text{--}10^3$, depending on the assumed model parameters) on the baryon number of a stable strangelet even if bulk SQM is stable [88–90].

On the other hand, a step by step production of s quarks, at different times, would produce hyperons in the nucleus, i.e. a system (hypernucleus) with a higher energy per baryon with respect to the original nucleus. Thus, according to the strange matter hypothesis, the ordinary state of matter, in which quarks are confined within hadrons, is a metastable state having a mean-life time much higher than the age of the universe.

The success of traditional nuclear physics, in explaining an astonishing amount of experimental data, provides a clear indication that quarks in a nucleus are confined within protons and neutrons. Thus, the energy per baryon for a droplet of u , d quark matter (non-strange quark matter) must be higher than the energy per baryon of a nucleus with the same baryon number. These stability conditions in turn may be used to constrain the parameters entering in models for the EoS of SQM [88].

In summary, our present understanding of the properties of ultra-dense hadronic matter, does not allow us to exclude or to accept a priori the validity of the strange matter hypothesis. Thus strange stars may exist in the universe.

We consider only bare strange stars, i.e. we neglect the possible presence of a crust of normal (confined) matter above the deconfined quark matter core [91]. For stars with $M \sim 1 M_{\odot}$ the thickness of this crust is on the order of 10–100 m, therefore the presence of a crust will not affect the predicted value of the radius of strange star candidates [92–95].

Strange stars are the natural site for various possible color superconducting phases of quark matter [96, 97], and matter in their interiors might be characterized by the formation of different crystalline structures [98, 99]. These crystalline structures might be relevant to model pulsar glitches in strange stars.

Computations of fully general relativistic equilibrium sequences of rapidly spinning compact stars [100] are very important to study millisecond pulsars and other fast spinning compact objects. Recent work [101] has shown that rapidly spinning SSs can have gravitational masses and spin frequencies at least up to $\sim 3 M_{\odot}$ and ~ 1250 Hz, and thus fully consistent with present measured values for these quantities.

9.6 Two Coexisting Families of Compact Stars

According to the current accepted paradigm there exist in the universe only one family of neutron stars. Thus making accurate measurements of the mass and radius of several neutron stars, one could in principle determine the dense matter EoS solving the so called relativistic inverse stellar problem [102, 103].

In the following we discuss the possibility of having two coexisting families of compact stars: hadronic stars and quark stars (QSs) (i.e. hybrid stars or strange stars). This possibility and the stellar conversion mechanism to jump from the HS family to the QS family has been proposed several years ago in these papers [104–107] and since then has been investigated by many authors [108–121].

The basic assumption for the two-families scenario of compact stars is that in the low temperature T and high baryon chemical potential region of the QCD phase diagram (which is the one relevant for neutron star physics) the quark deconfinement transition is a first-order phase transition. This assumption is supported by several QCD inspired models [122, 123].

As it is well known, first-order phase transitions, in different physical systems, are triggered by the nucleation of a critical size drop of the new (stable) phase in a metastable mother phase. This is a very common phenomenon in nature (e.g. fog or dew formation in supersaturated vapor, ice formation in supercooled water) and plays an important role in many scientific disciplines (e.g. in atmospheric science, meteorology, cosmology, biology) as well as in many technical applications (e.g. in metallurgy).

One of the most exciting astrophysical consequences of the nucleation process of quark matter in the core of massive hadronic stars is that above a threshold value of their mass, HSs are metastable [104–107] to the “decay” (conversion) to QSs. This stellar conversion process liberates a huge amount of energy (a few 10^{53} erg) and it could be the energy source of Gamma Ray Bursts (GRBs) [124]. In addition, within this scenario, one has two coexisting families of compact stars, and the members of these two families could have similar values for their gravitational masses but different values for their radii [106].

The metastability of HSs originates from the finite size effects (which represent the driving “force” of first-order phase transitions) in the formation process of the first QM drop in the hadronic environment.

In cold ($T = 0$) bulk matter the quark deconfinement transition takes place at the *static transition point* defined by the Gibbs’ criterion for phase equilibrium

$$\mu_H = \mu_Q \equiv \mu_0, \quad P_H(\mu_0) = P_Q(\mu_0) \equiv P_0 \quad (9.70)$$

where $\mu_H = (\varepsilon_H + P_H)/n_H$ and $\mu_Q = (\varepsilon_Q + P_Q)/n_Q$ are the Gibbs energies per baryon (average chemical potentials) for the hadron and quark phase respectively, ε_H (ε_Q), P_H (P_Q) and n_H (n_Q) denote respectively the total (*i.e.*, including leptonic contributions) energy density, the total pressure and baryon number density for the hadronic (quark) phase.

Consider now the more realistic situation in which one takes into account the energy cost due to finite size effects (e.g. surface effects) in creating a drop of deconfined QM in the hadronic environment. As a consequence of these effects, the formation of a critical-size drop of QM is not immediate and it is necessary to have an overpressure $\Delta P = P - P_0$ with respect to the static transition point. Thus, above P_0 (see Fig. 9.9 left panel), hadronic matter is in a metastable state, and the formation of a real drop of QM occurs via a quantum nucleation mechanism.

Small localized fluctuations in the state variables of the metastable hadronic phase will give rise to virtual drops of the stable quark phase. These fluctuations are characterized by a time scale $v_0^{-1} \sim 10^{-23}$ s. This time scale is set by the strong interactions (responsible for the deconfinement phase transition), and it is many orders of magnitude shorter than the typical time scale for the weak interactions. Quark flavor must therefore be conserved during the deconfinement transition [106, 108, 125]. We refer to this form of deconfined matter, in which the flavor content is equal to that of the β -stable hadronic system at the same pressure, as the Q*-phase [106]. Soon after a critical size drop of Q*-matter is formed, the weak interactions will have enough time to act, changing the quark flavor fraction of the deconfined droplet to lower its energy, and a droplet of β -stable quark matter is formed (hereafter the Q-phase). This first seed of β -stable quark matter will trigger the conversion [124] of the HS to a QS (*i.e.* to a strange star or to an hybrid star depending on whether or not the strange matter hypothesis [85–87] is satisfied).

Thus, an HS having a central pressure larger than P_0 is metastable with respect to the conversion to a QS. These metastable HSs have a *mean-life time* which is related to the nucleation time τ to form the first critical-size drop of deconfined matter in

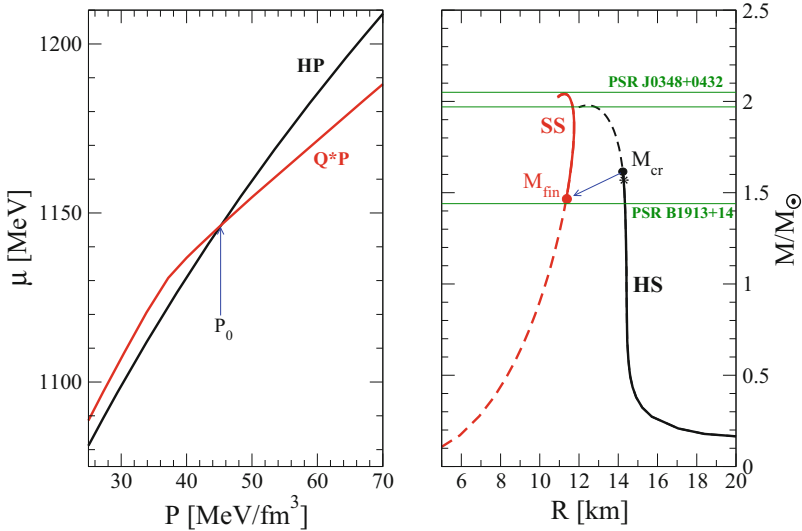


Fig. 9.9 Left panel: Gibbs energy per baryon versus pressure for the hadronic-phase (HP) and the quark phase in which the flavor content is equal to that of the β -stable hadronic system at the same pressure (Q^*P). Above P_0 the HP is metastable. Right panel: Mass-radius relation for hadronic stars (HS) and strange stars (SS). The configuration marked with an asterisk represents the HS for which the central pressure is $P_c = P_0$ and thus the nucleation time is $\tau = \infty$. The conversion process of the HS, with a gravitational mass equal to the critical mass M_{cr} , into the final SS is denoted by the full circles connected by an arrow. The lower horizontal green line represents the mass $M = 1.4398 \pm 0.0002 M_\odot$ [126] of the pulsar PSR B1913+16, whereas the higher horizontal green lines represent the mass $M = 2.01 \pm 0.04 M_\odot$ of PSR J0348+0432 [5]. Adaped from Ref. [120] where details on the employed EoS models can be found. Credit: Bhattacharyya et al., ApJ, 848, 65 (2017) © AAS. Reproduced with permission

their interior.¹² When τ is *short* compared to typical pulsar ages, the metastable HS will be likely converted to a stable QS. Following Ref. [104–106] we define as the *critical mass* configuration for the HS family the stellar configuration having a gravitational mass for which the nucleation time $\tau = \tau(P_c)$, at the center of the star, is equal to one year:¹³ $M_{cr} \equiv M^{HS}(\tau = 1 \text{ yr})$.

Since it is very unlikely to observe an HS with $M^{HS} > M_{cr}$, the critical mass M_{cr} plays the role of an *effective maximum mass* for the hadronic branch of compact stars [106]. Differently from the Oppenheimer–Volkov maximum mass M_{max}^{HS} , which is determined by the overall stiffness of the EoS for hadronic matter, the value of M_{cr} will depend in addition on the bulk properties of the EoS for quark

¹² The actual *mean-life time* of the HS will depend on the mass accretion or on the spin-down rate which modifies the nucleation time τ via an explicit time dependence of the stellar central pressure.

¹³ Since the nucleation time is extremely sensitive to the value of the stellar central pressure P_c and thus to its corresponding gravitational mass $M^{HS}(P_c)$ (see Fig. 4 and 5 in Ref. [106]), the critical mass value is not influenced by the particular choice $\tau = 1 \text{ yr}$.

matter and on the properties at the interface between the confined and deconfined phases of matter (e.g., the surface tension σ).

These findings are exemplified in the right panel of Fig. 9.9, where we show the mass-radius (MR) curve for hadronic stars (HS) and that for strange stars (SS).¹⁴ The configuration marked with an asterisk on the HS curve represents the HS for which the central pressure is equal to P_0 and thus the nucleation time is $\tau = \infty$. Above this point all the HS configurations are metastable. The black filled circle on the HS sequence represents the critical mass configuration M_{cr} , whereas the red filled circle on the SS curve represents the strange star which is formed from the conversion of the HS with $M^{HS} = M_{cr}$. As we can see, for the EoS parametrizations used in the calculations reported in Fig. 9.9 (see [120] for details on the employed EoS models), PSR B1913+16 is likely an HS, whereas PSR J0348+0432 is a SS.

We assume [124] that during the stellar conversion process the total number of baryons in the star, or in other words the stellar baryonic mass M_B , is conserved. Thus the total energy liberated in the stellar conversion is given [124] by the difference between the gravitational masses of the critical mass HS (M_{cr}) and that of the final QS (M_{fin}) configuration with the same baryonic mass: $E^{conv} = (M_{cr} - M_{fin})c^2$.

In the case of the EoS models used to get the results reported in Fig. 9.9 one has $E^{conv} = 2.67 \times 10^{53}$ erg. Using different EoS models for both the HM and the QM phases one has [104–106, 124] $E^{conv} = 0.5 – 4.0 \times 10^{53}$ erg.

This huge amount of released energy will cause a powerful neutrino burst, likely accompanied by intense gravitational waves emission, and conceivably it could cause a second delayed (with respect to the supernova forming the HS) explosion. Under favorable physical conditions this second explosion could be the energy source of a powerful GRB [104, 105, 124]. This scenario is thus able to explain a “delayed” connection between supernova explosions and GRBs.

The stellar conversion process, described so far, will start to populate the new branch of quark stars (strange stars for the case reported in Fig. 9.9) i.e. the part of the stellar sequence above the filled red circle in Fig. 9.9. Long term accretion on the QS can next produce stars with masses up to the maximum mass M_{max}^{QS} for the quark star configurations. Thus within this scenario one has two coexisting families of compact stars: HSs and QSs [106]. The quark star branch is occasionally referred to as the “third family” of compact stars, considering white dwarfs as the first family and HSs as the second family. Notice also that there is a range of values of stellar gravitational mass (see Fig. 9.9) where HSs and QSs with the same gravitational mass, but with different radius, can exist.

As discussed in [120], the possibility of having of two coexisting families of compact stars has very interesting implications for millisecond pulsars. In fact, performing fully general relativistic numerical computations of the structure of fast-spinning compact stars, the authors of Ref. [120] found that the HS to QS conversion process causes a simultaneous spin-up and decrease in gravitational mass of the

¹⁴ The SQM EoS used to calculate the QS configurations reported in Fig. 9.9 satisfies the strange matter hypothesis.

star. This is a new type of millisecond pulsar evolution through a new mechanism, which gives rise to relatively lower mass compact stars with higher spin rates. This could have considerable implications for the observed mass and spin distributions of millisecond pulsars [127]. Such a stellar conversion can also rescue some massive, spin-supported millisecond pulsars from collapsing into black holes [120].

Notice that for the EoS models used in [120] the stellar conversion process generates a SS with a radius (R_{SS}) smaller than the one (R_{HS}) of the critical mass HS (see the right panel of Fig. 9.9) and with a gravitational mass $M_{fin} < M_{cr}$ (i.e. $E^{conv} > 0$).

Within the two-families scenario, in the case of soft EoSs for the hadronic phase and stiff quark matter EoSs satisfying the strange matter hypothesis, it is possible to have a stellar conversion process which generates a SS with $R_{SS} > R_{HS}$ (and $M_{fin} < M_{cr}$) [121]. At first glance this process could seem not possible since the gravitational binding energy \mathcal{B}_G^{SS} of the final SS configuration is smaller than the gravitational binding energy \mathcal{B}_G^{HS} of the critical mass HS. However for a relativistic star the total binding energy \mathcal{B} can be written as the sum of two contributions [124] $\mathcal{B} = \mathcal{B}_G + \mathcal{B}_I$, the gravitational binding energy \mathcal{B}_G and the internal binding energy \mathcal{B}_I . The latter quantity includes the contribution of the internal energy (kinetic and strong interaction energies) of stellar matter. Thus the stellar conversion energy can be written [124] as $E^{conv} = (\mathcal{B}_I^{SS} - \mathcal{B}_I^{HS}) + (\mathcal{B}_G^{SS} - \mathcal{B}_G^{HS}) \equiv E_I^{conv} + E_G^{conv}$. As a consequence in the case of strange stars the gain in the internal binding energy could overcompensate (see Fig. 1 and Table I in [124]) the decrease of the gravitational binding energy thus producing an exothermic (i.e. $E^{conv} > 0$) process.

The conversion between stars having $R_{SS} > R_{HS}$ could have peculiar consequences for the evolution of millisecond pulsars (which have not yet been explored) and for binary compact star mergers. As an example of the latter case we mention the possibility that the secondary component of mass (2.50–2.67) M_\odot (a value in the mass-gap between NSs and black holes) of the binary merger GW190814 [128] was a strange quark star [129].

Finally, as pointed out and discussed in [106], the possibility of having metastable HSs, together with the expected existence of two distinct families of compact stars, demands an extension of the concept of maximum mass of a “neutron star” with respect to the *classical* one introduced in 1939 by Oppenheimer and Volkoff.

Acknowledgments I thank the editors of the present book, Sudip Bhattacharyya, Alessandro Papitto, and Dipankar Bhattacharya, for inviting me to write this chapter. I dedicate this work to my beloved son, Paride.

References

1. Abbott, B.P., et al.: LIGO scientific collaboration and Virgo collaboration. Phys. Rev. Lett. **119**, 161101 (2017)
2. Abbott, B.P., et al.: LIGO scientific collaboration and Virgo collaboration. Phys. Rev. Lett. **121**, 161101 (2018)

3. Abbott, B.P., et al.: LIGO scientific collaboration and Virgo collaboration. arXiv:2001.01761
4. Demorest, P.B., Pennucci, T., Ransom, S., Roberts, M., Hessels, J.: *Nature* **467**, 1081 (2010)
5. Antoniadis, J., et al.: *Science* **340**, 1233232 (2013)
6. Cromartie, H.T., Fonseca, E., M Ransom, S., et al.: *Nat. Astron.* **4**, 72 (2020)
7. Fetter, A.L., Walecka, J.D.: *Quantum Theory of Many-Particle Systems*. McGraw-Hill Book Company, New York (1971)
8. Bhattacharyya, S.: *Adv. Space Res.* **45**, 949 (2010)
9. Watts, A.L.: *AIP Conference Proceedings* **2127**, 020008 (2019). <https://doi.org/10.1063/1.5117798>
10. Miller, M.C.: Astrophysical constraints on dense matter in neutron stars. In: Belloni, T.M., Méndez, M., Zhang, C. (eds.) *Timing Neutron Stars: Pulsations, Oscillations and Explosions. Astrophysics and Space Science Library*, vol. 461. Springer, Berlin, Heidelberg (2021). https://doi.org/10.1007/978-3-662-62110-3_1
11. Harrison, B.K., Wakano, M., Wheeler, J.A.: *La Structure et l'Evolution de l'Univers*. Stoops, Brussels (1958)
12. Harrison, B.K., Thorne, K.S., Wakano, M., Wheeler, J.A.: *Gravitation Theory and Gravitational Collapse*. University of Chicago Press, Chicago (1965)
13. Chamel, N., Haensel, P.: *Living Rev. Relativ.* **11**, 10 (2008)
14. Glendenning, N.K.: *Compact Stars: Nuclear Physics, Particle Physics, and General Relativity*. Springer, New York (2000)
15. Prakash, M., Bombaci, I., Prakash, M., Ellis, J.P., Lattimer, J.M., Knorren, R.: *Phys. Rep.* **280**, 1 (1997)
16. J. R. Oppenheimer, G. M. Volkoff, *Phys. Rev.* **55**, 374 (1939)
17. Brown, L.M., Rechenberg, H.: *The Origin of the Concept of Nuclear Forces*. Institute of Physics Publishing, Bristol and Philadelphia (1996)
18. Bombaci, I., Lombardo, U.: *Phys. Rev. C* **44**, 1892 (1991)
19. Zuo, W., Bombaci, I., Lombardo, U.: *Eur. Phys. J. A* **50**, 12 (2014)
20. Lattimer, J.M.: *Gen. Rel. Grav.* **46**, 1713 (2014)
21. Lattimer, J.M., Prakash, M.: *Phys. Rep.* **621**, 127 (2016)
22. Kalantar-Nayestanaki, N., Epelbaum, E., Messchendorp, J.G., Nogga, A.: *Rep. Prog. Phys.* **75**, 016301 (2012)
23. Hammer, H.W., Nogga, A., Schenk, A.: *Rev. Mod. Phys.* **85**, 197 (2013)
24. Wiringa, R.B., Fiks, V., Fabrocini, A.: *Phys. Rev. C* **38**, 1010 (1988)
25. Baldo, M., Bombaci, I., Burgio, G.F.: *A&A* **328**, 274 (1997)
26. Akmal, A., Pandharipande, V.R., Ravenhall, D.G.: *Phys. Rev. C* **58**, 1804 (1998)
27. Li, Z.H., Schulze, H.-J.: *Phys. Rev. C* **78**, 028801 (2008)
28. Bombaci, I., Logoteta, D.: *A&A* **609**, A128 (2018)
29. Miller, G.A., Opper, A.K., Stephenson, E.J.: *Ann. Rev. Nucl. Part. Sci.* **56**, 253 (2006)
30. Haensel, P.: *J. Phys. G* **3**, 373 (1997)
31. Müther, H., Polls, A., Machleidt, R.: *Phys. Lett. B* **445**, 259 (1999)
32. Blaizot, J.P., Gogny, D., Grammaticos, B.: *Nucl. Phys. A* **265**, 315 (1976)
33. Shlomo, S., Kolomietz, V.K. Colò, G.: *Eur. Phys. J. A* **30**, 23 (2006)
34. Li, B.A., Han, X.: *Phys. Lett. B* **727**, 276 (2013)
35. Kievsky, A., Viviani, M., Logoteta, D., Bombaci, I., Girlanda, L.: *Phys. Rev. Lett.* **121**, 072701 (2018)
36. Danielewicz, P., Lee, J.: *Nucl. Phys. A* **922**, 1 (2014)
37. Roca-Maza, X., et al.: *Phys. Rev. C* **87**, 034301 (2013)
38. Tolman, R.C.: *Proc. Nat. Acad. Sci. (USA)* **20**, 169 (1934)
39. Gulminelli, F., Raduta, Ad.D.: *Phys. Rev. C* **92**, 055803 (2015)
40. Bombaci, I., Logoteta, D.: *EPJ Web of Conferences* **117**, 07005 (2016)
41. Bombaci, I.: *JPS Conf. Proc.* **17**, 101002 (2017)
42. Wiringa, R.B., Stoks, V.G.J., Schiavilla, R.: *Phys. Rev. C* **51**, 38 (1995)
43. Rijken, Th.A., Nagels, M.M., Yamamoto, Y.: *Nucl. Phys. A* **835**, 160, (2010)
44. Baldo, M., Burgio, G.F., Schulze, H.-J.: *Phys. Rev. C* **61**, 055801 (2000)

45. Vidaña, I., Polls, A., Ramos, A., Engvik, L., Hjorth-Jensen, M.: Phys. Rev. C **62**, 035801 (2000)
46. Schulze, H.-J., Rijken, Th.A.: Phys. Rev. C **84**, 035801 (2011)
47. Djapo, H., Schaefer, B.-J., Wambach, J.: Phys. Rev. C **81**, 035803 (2010)
48. Hashimoto, O., Tamura, H.: Progr. Part. Nucl. Phys. **57**, 564 (2006)
49. Millener, D.J.: Lect. Notes Phys. **724**, 31 (2007)
50. Rappold, C., et al., HypHI Collaboration: Nucl. Phys. A **913**, 170 (2013)
51. Feliciello, A., Nagae, T.: Rep. Progr. Phys. **78**, 096301 (2015)
52. Tamura, H., et al.: Proceedings, 11th International Conference on Hypernuclear and Strange Particle Physics (HYP 2012): Barcelona, Spain, October 1–5, 2012. Nuclear Phys., vol. A914, p. 99 (2013)
53. Botta, E., Bressani, T., Garbarino, G.: Eur. Phys. J. A **48**, 41 (2012)
54. Curceanu, C., et al.: Acta Phys. Pol. B **46**, 203 (2015)
55. Gal, A., Hungerford, E.V., Millener, D.J.: Rev. Mod. Phys. **88**, 035004 (2016)
56. Tolos, L., Fabbietti, L.: Progr. Part. Nucl. Phys. **112**, 103770 (2020)
57. Petschauer, S., Haidenbauer, J., Kaiser, N., Meißner, U.-G., Weise, W.: Front. Phys. **8**, 12 (2020)
58. Spitzer, R.: Phys. Rev. **110**, 1190 (1958)
59. Bach, G.G.: Nuovo Cimento **XI**, 73 (1959)
60. Dalitz, R.H.: 9th Int. Ann. Conf. on High-Energy Physics. Academy of Sciences, USSR, vol. I, p. 587 (1960)
61. Bodmer, A., Sampanthar, S.: Nucl. Phys. **31**, 251 (1962)
62. Conte, F., Iwao, S.: Nucl. Phys. **58**, 291 (1964)
63. Bodmer, A.R., Murphy, J.W.: Nucl. Phys. **64**, 593 (1965)
64. Gal, A.: Phys. Rev. **152**, 975 (1966); Gal, A.: Phys. Rev. Lett. **18**, 568 (1967)
65. Bhaduri, R.K., Losieau, B.A., Nogami, Y.: Ann. Phys. **44**, 57 (1967)
66. Gal, A., Soper, J.M., Dalitz, R.H.: Ann. Phys. **63**, 53 (1971)
67. Bodmer, A.R., Usmani, Q.N., Carlson, J.: Phys. Rev. C **29**, 684 (1984)
68. Yamamoto, Y.: Phys. Rev. C **36**, 2166 (1987)
69. Vidaña, I., Logoteta, D., Providencia, C., Polls, A., Bombaci, I.: Europhys. Lett. **94**, 11002 (2011)
70. Yamamoto, Y., Furumoto, T., Yasutake, N., Rijken, Th.: Phys. Rev. C **90**, 045805 (2014)
71. Lonardoni, D., Lovato, A., Gandolfi, S., Pederiva, F.: Phys. Rev. Lett. **114**, 092301 (2015)
72. Logoteta, D., Vidaña, I., Bombaci, I.: Eur. Phys. J. A **55**, 207 (2019)
73. Gerstung, D., Kaiser, N., Weise, W.: Eur. Phys. J. A **56**, 175 (2020)
74. Ivchenko, D., Kurdgelaidze, D.F.: Lett. Nuovo Cimento **2**, 13 (1969)
75. Itho, N.: Prog. Teor. Phys. **44**, 291 (1970)
76. Iachello, F., Langer, W.D., Lande, A.: Nucl. Phys. A **219**, 612 (1974)
77. Collins, J.C., Perry, M.J.: Phys. Rev. Lett. **34**, 1353 (1975)
78. Baym, G., Chin, S.A.: Phys. Lett. B **62**, 241 (1976)
79. Keister, B.D., Kisslinger, L.S.: Phys. Lett. B **64**, 117 (1976)
80. Lenzi, C.H., Lugones, G.: Astrophys. J. **759**, 57 (2012)
81. Bonanno, L., Sedrakian, A.: A&A **539**, A16 (2012)
82. Orsaria, M., Rodrigues, H., Weber, F., Contrera, G.A.: Phys. Rev. C **89**, 015806 (2014)
83. Bombaci, I., Logoteta, D.: MNRAS **433**, L79 (2013)
84. Whittenbury, D.L., Matevosyan, H.H., Thomas, A.W.: Phys. Rev. C **93**, 035807 (2016)
85. Bodmer, A.R.: Phys. Rev. D **4**, 1601 (1971)
86. Terazawa, H.: INS Rep. **336** (Univ. Tokyo, INS) (1979); J. Phys. Soc. Jpn. **58**, 3555 (1989); **58**, 4388 (1989); **59**, 1199 (1990)
87. Witten, E.: Phys. Rev. D **30**, 272 (1984)
88. Farhi, E., Jaffe, R.L.: Phys. Rev. D **30**, 2379 (1984)
89. Madsen, J.: Phys. Rev. D **50**, 3328 (1994)
90. Mustafa, M.G., Ansari, A.: Phys. Rev. D **53**, 5136 (1996)
91. Alcock, C., Farhi, E., Olinto, A.: Astrophys. J. **310**, 261 (1986)

92. Dey, M., Bombaci, I., Dey, J., Ray, S., Samanta, B.C.: Phys. Lett. B **438**, 123 (1998); Phys. Lett. B **447**, 352 (1999); Phys. Lett. B **467**, 303 (1999)
93. Li, X.-D., Bombaci, I., Dey, M., Dey, J., van den Heuvel, E.P.J.: Phys. Rev. Lett. **83**, 3776 (1999)
94. Li, X.-D., Ray, S., Dey, J., Dey, M., Bombaci, I.: Astrophys. J. **527**, L51 (1999)
95. Xu, R.X., Qiao, G.J., Zhang, B.: Astrophys. J. **522**, L109 (1999)
96. Casalbuoni, R., Nardulli, G.: Rev. Mod. Phys. **76**, 263 (2004)
97. Alford, M.G., Schmitt, A., Rajagopal, K., Schafer, T.: Rev. Mod. Phys. **80**, 455 (2008).
98. Anglani, R., Casalbuoni, R., Ciminale, M., Ippolito, N., Gatto, R., Mannarelli, M., Ruggeri, M.: Rev. Mod. Phys. **86**, 509 (2014)
99. Buballa, M., Carignano, S.: Progr. Part. Nucl. Phys. **81**, 39 (2015)
100. Bhattacharyya, S., Bombaci, I., Bandyopadhyay, D., Thampan, A.V., Logoteta, D.: New Astron. **54**, 61 (2017)
101. Bhattacharyya, S., Bombaci, I., Logoteta, D., Thampan, A.V.: MNRAS **457**, 3101 (2016)
102. Lindblom, L.: Astrophys. J. **398**, 569 (1992)
103. Riley, T.E., et al.: MNRAS **478**, 1093 (2018)
104. Berezhiani, Z., Bombaci, I., Drago, A., Frontera, F., Lavagno, A.: Nucl. Phys. B Proc. Suppl. **113**, 268 (2002)
105. Berezhiani, Z., Bombaci, I., Drago, A., Frontera, F., Lavagno, A.: Astrophys. J. **586**, 1250 (2003)
106. Bombaci, I., Parenti, I., Vidaña, I.: Astrophys. J. **614**, 314 (2004)
107. Drago, A., Lavagno, A., Pagliara, G.: Eur. Phys. J. A **19**, 197 (2004)
108. Lugones, G., Bombaci, I.: Phys. Rev. D **72**, 065021 (2005)
109. Drago, A., Lavagno, A., Parenti, I.: Astrophys. J. **659**, 1519 (2007)
110. Bombaci, I., Lugones, G., Vidaña, I.: A&A **462**, 1017 (2007)
111. Bombaci, I., Panda, P.K., Providencia, C., Vidaña, I.: Phys. Rev. D **77**, 083002 (2008)
112. Bombaci, I., Logoteta, D., Panda, P.K., Providencia, C., Vidaña, I.: Phys. Lett. B **680**, 448 (2009)
113. Bombaci, I., Logoteta, D., Providencia, C., Vidaña, I.: A&A **528**, A71 (2011)
114. Drago, A., Lavagno, A., Pagliara, G.: Phys. Rev. D **89**, 043014 (2014)
115. Bombaci, I., Logoteta, D., Vidaña, I., Providencia, C.: Eur. Phys. J. A **52**, 58 (2016)
116. Drago, A., Lavagno, A., Pagliara, G., Pigato, D.: Eur. Phys. J. A **52**, 40 (2016)
117. Drago, A., Pagliara, G.: Eur. Phys. J. A **52**, 41 (2016)
118. Drago, A., Lavagno, A., Metzger, B., Pagliara, G.: Phys. Rev. D **93**, 103001 (2016)
119. Pili, A.G., Bucciantini, N., Drago, A., Pagliara, G., Del Zanna, L.: MNRAS **462**, L26 (2016)
120. Bhattacharyya, S., Bombaci, I., Logoteta, D., Thampan, A.V.: Astrophys. J. **848**, 65 (2017)
121. Drago, A., Pagliara, G.: Phys. Rev. D **102**, 063003 (2020)
122. Hsu, S.D.H., Schwetz, M.: Phys. Lett. B **432**, 203 (1998)
123. Fodor, Z., Katz, S.D.: JHEP **04**, 050 (2004)
124. Bombaci, I., Datta, B.: Astrophys. J. **530**, L69 (2000)
125. Olesen, M.L.: Madsen, J.: Phys. Rev. D **49**, 2698 (1994)
126. Hulse, R.A., Taylor, J.H.: Astrophys. J. **195**, L51 (1975); Weisberg, J.M., Nice, D.J., Taylor, J. H.: Astrophys. J. **722**, 1030 (2010)
127. Patruno, A., Haskell, B., Andersson, N.: Astrophys. J. **850**, 106 (2017)
128. Abbott, R., et al.: Astrophys. J. Lett. **896**, L44 (2020)
129. Bombaci, I., Drago, A., Logoteta, D., Pagliara, G., Vidaña, I.: Phys. Rev. Lett. **126**, 162702 (2021)

Index

A

- Aberration, 64, 70–72
- Accreting millisecond pulsar, 37, 38, 41, 87
- Accretion column, 45, 170, 186
- Ageostrophic, 142
- Alfvén radius, 91, 160, 176
- Anomalous X-ray Pulsar (AXP), 245–248, 267
- Asymptotic Giant Branch (AGB), 202, 203, 208
- ATNF Pulsar Catalog, 3, 19, 36, 89, 218, 220, 221

B

- Balmer, 163, 167
- Barycentre, 106, 213
- Baryon decuplet, 299
- Baryon octet, 299
- Bethe–Weizsäcker mass formula, 291, 292
- Be X-ray binary, 40
- Binary neutron star (BNS), 23, 220, 248, 251, 255, 262, 281, 282, 288
- Binary orbit, 14, 77, 167, 182
- Binary properties of MSPs, 3
- Binary pulsar, 19, 20, 89, 221
- Birthrate, 201, 218, 219, 229, 230
- Black widow pulsars, 14, 24, 25, 35, 43, 46, 47, 77, 159, 180, 182, 224, 231, 232
- Bose–Einstein condensate, 305
- Bow shock, 77
- Brueckner–Hartree–Fock (BHF), 300

C

- Carbon–oxygen (C–O) core, white dwarf, 3, 202, 204
- Catalyzed matter, 283, 284
- CFS (Chandrasekhar–Friedmann–Schutz) instability, 261
- Charge–independence breaking (CIB), 290
- Charge–symmetry breaking (CSB), 290
- Chemical potential, 283, 285–287, 293, 299, 300, 307, 308, 310, 311
- Cherenkov telescopes, 35, 41, 65, 78
- Classical magnetar, 247, 248, 250, 251, 259, 266–268
- CNO cycle, 127, 128
- Common envelope (CE) evolution, 209, 221
- Compton hump, 97, 99
- Convective envelope, 211, 226, 228, 236, 238
- Core collapse supernova (CCSN), 203, 206, 220, 221, 247, 251, 261, 265
- Coriolis force, 142–146
- Corotation radius, 92, 93, 97, 99, 102, 161, 184, 185, 258
- Crab pulsar, 33, 35, 58, 62, 64, 65, 67, 79, 88, 90, 182, 265, 266
- Crustquake, 247
- Curvature radiation, 63, 66, 89, 266
- Cyclotron, 45, 64, 66, 166, 186, 245

D

- Dedekind ellipsoid, 262
- Deflagration, 142

Detonation, 142
 Diffusive shock acceleration (DSA), 78, 80
 Dispersion measure (DM), 11, 19, 20, 25, 27,
 166, 264
 Dynamo, 211, 247, 248, 260

E

Eddington limit, 91, 96, 98, 112, 128, 183, 212,
 213, 228–230, 246
 Einstein-at-Home, 49
 Einstein delay, 23
 Electron-capture supernova (ecSN), 203, 204,
 206
 Equation of state, 14, 20, 75, 93, 116, 126, 204

F

Fermi gas, 284, 296
 f-mode, 261, 262
 Force-free Inside Dissipative Outside (FIDO),
 69, 70, 72

G

Galactic centre, 16, 17
 Gamma-ray binary, 46
 Gamma-ray millisecond pulsar, 34, 35
 class, 62, 66–68
 Gamma-ray pulsar catalog, 35, 67
 Geostrophic, 142
 Giant Pulse (GP), 18, 265, 266, 268
 Gibbs, 311, 312
 Globular cluster, 14, 87, 180, 181, 205, 221
 Goldreich-Julian parameters, 59, 61, 63, 73–75
 Gravitational waves, 19, 20, 93, 117, 185

H

Hadronic star (HS), 305, 310–313
 Helium white dwarf (He-WD), 3, 221–223,
 225, 235, 237
 Hertzsprung gap, 209
 Hybrid star, 282, 283, 305, 308–311
 Hydrogen–helium core, 217
 Hyperon star, 282, 301, 302, 305
 Hyperon–hyperon (YY) interaction, 300
 Hyperon–nucleon (YN) interaction, 300

I

IGR J18245–2452, 41, 94, 97, 114, 131, 163
 Inner Lagrangian point, 90, 109, 164, 168, 205,
 213

Intra-binary material, 25, 45, 184
 Intra-binary shock, 46, 47, 76, 77, 80, 160,
 167, 168, 171, 181–184
 Irradiation, 38, 110, 162, 167, 183, 201, 202,
 215, 219, 224–229, 233, 236
 Isolated MSP, 14, 24

J

Jet, 40, 175, 187

K

Kaon, 282, 305
 Klein-Nishina effect, 65

L

Larmor formula, 88, 116, 230
 Light cylinder radius, 160, 187
 Lorentz force, 88
 Low-mass X-ray binary, 90, 93, 98, 114, 125,
 218, 228

M

Magnetar wind nebula (MWN), 255, 266, 267,
 269
 Magnetic Braking (MB), 90, 210, 212, 216
 Magnetic field decay, 90
 Magneto-rotational instability, 248
 Magnetospheric radius, 91, 92, 97, 160, 161,
 258

N

Nuclear powered millisecond pulsar, 37
 Nucleon-nucleon (NN) interactions, 289, 290,
 300, 303, 305
 Nucleon star, 282, 288, 289, 297–299, 301,
 302, 304, 305

O

Optical pulsations, 38, 45, 116, 177, 183, 186
 Orbital evolution, 107, 171
 Oxygen–Neon (O-Ne) core, white dwarf, 202

P

Pair-starved polar cap (PSPC), 63, 66, 67
 Parallax, 163, 178, 179
 Particle-in-Cell (PIC) model, 60, 71, 74
 Pauli principle, 283, 284
 Phase connection technique, 133

- Photospheric radius expansion (PRE) burst, 128, 136, 139
Pion, 282, 305
Post-Keplerian (PK) parameters, 23
P-Ṗ diagram, 1, 89, 90
Propeller effect, 40, 45, 92, 162, 185, 186, 205, 258
Proto-neutron star (PNS), 247, 248, 250, 261
Protomagnetar, 259
PSR B195720, 25
PSR J10230038, 41, 43, 45, 163
Pulsar current sheet, 65, 71, 186
Pulsar timing array (PTA), 20
Pulsar timing noise, 102, 103, 113
Pulsar wind, 25, 181, 182, 184
Pulsar wind/disk shock, 45, 187, 189
Pulse phase polarimetry, 147
Pure neutron matter (PNM), 289, 290
- Q**
Quantum chromodynamics (QCD), 281, 307, 310
Quark stars, 309, 310, 313
- R**
Radio frequency interference (RFI), 11, 13
Radio pulsar eclipse, 24, 25, 77, 164
Radio-ejection, 24, 109, 115, 162, 201, 202, 205, 213, 224, 230, 232, 234–237
Radiometer equation, 9
Radio-quiet pulsar, 35, 48
Recycling, 204
Recycling scenario, 2, 34, 58, 88, 94, 113, 129, 157
Redback pulsar, 14, 24, 25, 35, 43, 46, 47, 77, 159, 164, 180, 182, 224, 231, 232
Riemann-S ellipsoid, 261, 262
Roche-lobe overflow (RLOF), 168, 207
Rossby mode, 146
Rossby number, 142
Rotating Radio Transient (RRaT), 269
Rotating vector model (RVM), 7, 61
Rotation measure (RM), 19
Rp (rapid-proton) process, 128
- S**
SAX J1808.4–3658, 38, 39, 94, 98, 100, 102, 103, 107, 116, 130, 171, 225
Separatrix, 60, 70, 72
Shapiro delay, 17, 23
Shklovskii effect, 166, 177
- Skumanich relation, 212
Soft Gamma Repeater (SGR), 245–248, 267
Spin-down age, 89, 204, 246, 247
Spin-down power, 35, 45, 57, 58, 65, 67, 89, 90, 162, 168, 169, 171, 176, 182, 184, 257, 259
Spin frequency distribution, 37, 116
Spin frequency evolution, 38, 100, 103, 171, 177
Static transition point, 311
Strangelet, 309
Strange matter hypothesis, 309–311, 313, 314
Strangeness, 283, 298, 299, 303, 307
Strange quark matter (SQM), 307–309, 313
Strange star (SS), 282, 309–314
Striped-wind model, 65, 71, 182, 187
Strong equivalence principle, 24
Sub-luminous accretion disk state, 41, 172, 183
SuperLuminous SNe (SLSNe), 257–260, 265, 269
Symmetric nuclear matter (SNM), 289–293
- T**
Three-nucleon interactions (TNIs), 288, 289, 300, 303
Timing noise, 20
Transitional millisecond pulsar, 41, 94, 113, 236
candidate, 42, 178
moding, 41, 43, 172, 178, 183
Transitional MSPs, 14
Triple-alpha reaction, 128
Two-pole caustic, 62, 64, 66
- U**
Ultra-compact X-ray binary (UCXB), 127, 218
Unassociated Fermi source, 14, 25, 48, 77, 180, 189
UV pulsation, 38, 116
- V**
Vacuum gap, 63, 73, 74
Vela pulsar, 35, 58
- X**
XSS J12270–4859, 41, 43, 44, 164
- Y**
Yukawa’s theory, 284